

# Characterizing Electroactive Polymer Films: from Fundamentals to Fingerprints

---

Thesis submitted for the degree of

**Doctor of Philosophy**

at the University of Leicester

by

**Rachel Marie Sapstead (nee Brown)**

**MChem**

Department of Chemistry

University of Leicester

January 2014

# Characterizing Electroactive Polymer Films: from Fundamentals to Fingerprints

---

**Rachel Marie Sapstead**

Visualisation of latent fingerprints present on metallic surfaces has been demonstrated by means of spatially selective deposition of conducting copolymers. This novel technique utilises the inhibition of electrochemical processes on areas that have been masked by the fingerprint. This results in electropolymerisation between the ridges, generating a negative image of the fingerprint. The efficiency of recovery in forensically challenging scenarios of the copolymers was compared with the corresponding homopolymers.

An extension of this electrochromic enhancement to include fluorescence has been developed using a novel synthetic pathway aiming to create more free volume to aid the inclusion of bulky fluorophore moieties. The unique selectivity of neutron reflectivity (NR), with isotopic contrast variation, permitted the diagnosis of chemical and structural changes within the depth profile of the polymer during the incorporation of the fluorophore moieties.

The properties of conducting polymer films are determined by film composition and structure which, this thesis will show, can lead to different routes to electroneutrality maintenance during electrochemically controlled redox switching (doping/undoping). NR was used to quantify the diverse permeation characteristics of conventional solvents and ionic liquids into an electroactive copolymer. It revealed how the availabilities of these mechanisms are dictated by anion and cation sources and sinks in the film and liquid phases where molecular solvent *is/is not* present.

In multi-layered systems, the nature of the polymer/polymer interface is central to the rectifying (segregated) or capacitive (interdiffused) characteristics of the films, such that the spatial distribution of the different polymer components determines the optical and electronic properties of the films. These properties are important for the potential applications of these multi-component systems in energy storage. NR was used to probe the extent of segregation and solvation properties of multi-layer films and revealed the order the components are deposited has a great effect on the final film properties.

# Acknowledgements

---

It would not have been possible to write this doctoral thesis without the help and support of the kind people around me: including family, friends, colleagues and collaborators. Regrettably, it is only possible to give a particular mention to a few here.

I would like to begin by thanking my supervisor Professor A. Robert Hillman. His guidance and support have been invaluable to me throughout my PhD

Although only my name appears on the front of this thesis the nature of neutron reflectivity experiments means that they are performed with the help of a team. I would like to give a special thank you to Charlotte Stillwell-Beebee, Virginia Ferreira and Emma Smith for keeping me sane during experiments, especially during those inevitable middle of the night sample changes. The following instrument scientists went above and beyond to ensure that I got the maximum out of the beam time I was allocated and deserve a special mention: Erik B. Watkins and Robert Barker (ILL, Grenoble, France) and Robert M. Dalgliesh, Nina-Juliane Steinke and Maximilian Skoda (ISIS, Harwell, UK).

Above all, I would like to thank my husband Andrew for his unwavering support throughout the course of my PhD. My parents Sue and Kev and my brother Stuart have given me their unequivocal support as always. For these individuals in particular this mere expression of gratitude does not suffice.

# Contents

---

<b>Abstract</b>	<b>i</b>
<b>Acknowledgements</b>	<b>ii</b>
<b>Contents</b>	<b>iii</b>
<b>Abbreviations</b>	<b>vii</b>
<b>Chapter 1: Introduction</b>	<b>1</b>
<hr/>	
<b>1.1. Fingerprints</b>	<b>1</b>
1.1.1. What are Fingerprints?	1
1.1.2. Types of Fingerprint Patterns	2
1.1.3. Skin Anatomy	6
1.1.4. Types of Sweat	7
<b>1.2. The History of Fingerprints</b>	<b>9</b>
<b>1.3. Established Methods for Fingerprint Enhancement</b>	<b>11</b>
1.3.1. Powder Dusting	12
1.3.2. Ninhydrin Spraying	12
1.3.3. Fuming Methods	13
1.3.4. Chemical Dyes	15
1.3.5. Other Techniques	16
<b>1.4. Latent Print Development on Metal Surfaces</b>	<b>19</b>
<b>1.5. Electroactive Polymers</b>	<b>19</b>
1.5.1. Electronic Structure	20
1.5.2. Multicomponent Systems	22
<b>1.6. Electrochromic Enhancement of Latent Fingerprints</b>	<b>23</b>
<b>1.7. Deep Eutectic Solvents</b>	<b>27</b>
<b>1.8. Neutron Scattering</b>	<b>28</b>
<b>1.9. Objectives</b>	<b>30</b>
<b>1.10. References</b>	<b>32</b>

<b>Chapter 2: Methodology</b>	<b>42</b>
<hr/>	
<b>2.1. Electrochemical Methods</b>	<b>42</b>
2.1.1. Cyclic Voltammetry	42
<b>2.2. Microscopy</b>	<b>47</b>
2.2.1. Atomic Force Microscopy	47
2.2.2. Optical Profilometry	49
<b>2.3. Spectroscopy</b>	<b>50</b>
2.3.1. Fourier Transform Infrared Spectroscopy	50
2.3.2. X-ray Photo Electron Spectroscopy	50
<b>2.4. Neutron Reflectivity</b>	<b>51</b>
2.4.1. Data Analysis	61
<b>2.5. References</b>	<b>64</b>
<b>Chapter 3: Electrochromic Enhancement of Latent Fingerprints with Poly-(Pyrrole-co-EDOT)</b>	<b>69</b>
<hr/>	
<b>3.1. Introduction</b>	<b>69</b>
<b>3.2. Experimental</b>	<b>70</b>
3.2.1. Instrumentation	70
3.2.2. Procedures	71
3.2.3. Grading of Fingerprints	75
3.2.4. XPS Sample Preparation	76
<b>3.3. Results</b>	<b>76</b>
3.3.1. Electropolymerisation	76
3.3.2. Electrochromism of P(Py-co-EDOT): a Comparison to the Corresponding Homopolymers PPy and PEDOT	80
3.3.3. FTIR	94
3.3.4. XPS	96
3.3.5. 3D Profiling	103
3.3.6. Comparison with Traditional Fingerprint Enhancement Techniques	106
3.3.7. Over Oxidation	117
3.3.8. Application to Other Metal Surfaces and Pseudo Items of Evidence	118
<b>3.4. Conclusions</b>	<b>121</b>
<b>3.5. References</b>	<b>124</b>

<b>Chapter 4: A Neutron Reflectivity Study of the Fluorescent- -Electrochromic Enhancement of Latent Fingerprints</b>	<b>126</b>
<hr/>	
<b>4.1. Introduction</b>	<b>126</b>
<b>4.2. Experimental</b>	<b>128</b>
4.2.1. Monomer Synthesis	128
4.2.2. Electrode Preparation	129
4.2.3. Electropolymerisation	130
4.2.4. Post Polymerisation Chemical Modifications	130
4.2.1. Neutron Reflectivity	133
<b>4.3. Results</b>	<b>134</b>
4.3.1. Electropolymerisation	134
4.3.2. Post Polymerisation Chemical Modifications	138
4.3.3. Neutron Reflectivity	141
<b>4.4. Conclusions and Future Work</b>	<b>190</b>
<b>4.5. References</b>	<b>193</b>
<b>Chapter 5: Probing the Segregation and Solvation of Multi-Component Conducting Polymer Films</b>	<b>195</b>
<hr/>	
<b>5.1. Introduction</b>	<b>195</b>
<b>5.2. Experimental</b>	<b>196</b>
5.2.1. Monomer Synthesis	196
5.2.2. Electropolymerisation	198
5.2.3. Neutron Reflectivity Measurements	199
<b>5.3. Results: PEDOT/PPFP Systems</b>	<b>200</b>
5.3.1. Electrodeposition	200
5.3.2. Au/PEDOT/PPFP Bilayer	201
5.3.3. Au/PEDOT/PPFP/PEDOT Trilayer	212
<b>5.4. Results: PEDOT/PPy Systems</b>	<b>223</b>
5.4.1. Au/h4-PEDOT/d2-PPy Bilayer	223
5.4.2. Au/d2-PPy/h4-PEDOT Bilayer	236
<b>5.5. Conclusions</b>	<b>249</b>
<b>5.6. References</b>	<b>251</b>

<b>Chapter 6: Thiophene-Pyrrole Comonomer: a Promising Material for Rechargeable Batteries</b>	<b>253</b>
<hr/>	
<b>6.1. Introduction</b>	<b>253</b>
<b>6.2. Experimental</b>	<b>254</b>
6.2.1. Electrode Fabrication	255
6.2.2. Neutron Reflectivity Measurements	255
<b>6.3. Results</b>	<b>256</b>
6.3.1. Electropolymerisation of P(Th-Py)	256
6.3.2. Neutron Reflectivity	261
6.3.3. Atomic Force Microscopy	277
6.3.4. Electrochemical Characterisation	281
<b>6.4. Conclusions and Future Work</b>	<b>285</b>
<b>6.5. References</b>	<b>287</b>
<b>Chapter 7: Conclusions</b>	<b>289</b>
<hr/>	
<b>7.1. References</b>	<b>298</b>
<b>Publications</b>	<b>300</b>
<hr/>	

# Abbreviations

---

<b>NAFIS</b>	National Automated Fingerprint Intelligence System
<b>DFO</b>	1,8-diazafluoren-9-one
<b>MBD</b>	Methylene Blue Dye
<b>CBB</b>	Coomassie Brilliant Blue
<b>VMD</b>	Vacuum Metal Deposition
<b>SPR</b>	Small Particle Reagent
<b>HOMO</b>	Highest Occupied Molecular Orbital
<b>LUMO</b>	Lowest Unoccupied Molecular Orbital
<b>A<sup>-</sup></b>	Anion
<b>C<sup>+</sup></b>	Cation
<b>LbL</b>	Layer by Layer
<b>EDOT</b>	3,4-Ethylenedioxythiophene
<b>Ani</b>	Aniline
<b>Py</b>	Pyrrole
<b>ThPy</b>	Thiophene-pyrrole comonomer
<b>P(EDOT-co-Py)</b>	3,4-Ethylenedioxythiophene/pyrrole copolymer
<b>PyFmoc</b>	(9H-fluoren-9-yl)methyl 3-(1H-pyrrol-1-yl)propylcarbamate
<b>PyNH<sub>2</sub></b>	3-(pyrrol-1-yl)propylamine
<b>PFP</b>	Pentafluorophenyl 3-(pyrrol-1-yl)propanoate
<b>PyCN</b>	N-cyanoethylpyrrole
<b>PyCOOH</b>	3-(pyrrol-1-yl)propanoic Acid
<b>DES</b>	Deep Eutectic Solvents
<b>ILs</b>	Ionic Liquids
<b>LEDs</b>	Light Emitting Devices
<b>CV</b>	Cyclic Voltammetry
<b>AFM</b>	Atomic Force Microscopy
<b>FTIR</b>	Fourier Transform Infrared Spectroscopy
<b>XPS</b>	X-ray Photoelectron Spectroscopy
<b>NR</b>	Neutron Reflectivity
<b>SLD</b>	Scattering Length Density
<b>RGB</b>	Red Green Blue
<b>Fmoc</b>	9-fluorenylmethoxycarbonyl
<b>MPTS</b>	3-mercaptopropyltrimethoxysilane

# 1. Introduction

---

## 1.1. Fingerprints

Although fingerprints have been used as a means of biometric identification since the mid-1800s<sup>1</sup>, most of the significant advances have come within the past century<sup>2</sup>. There are three distinct types of fingerprint that can be recovered from a crime scene: patent (visible), plastic (impressions), and latent (invisible). Patent and plastic prints are easier to recover than latent prints, as they are visible to the naked eye, and can be recovered with ease by lifting/casting/photographing. Latent fingerprints, on the other hand, are invisible by nature and first have to be located and enhanced before they can be recovered.

### 1.1.1. What are Fingerprints?

Fingerprints are made up of individual friction ridges in the skin that group together to form patterns. These friction ridges are present on the fingers, thumbs, palms, toes, soles of feet and even lips. Fingerprints follow Locard's principle that every contact leaves a trace<sup>3</sup>: when a finger touches a surface it leaves behind traces of sweat and other substances that were present on the skin<sup>2</sup>. Fingerprints have provided law enforcement officers with an accurate means of identifying suspects for over a century. There are three main principles that determine the usefulness of fingerprints in identification: they are unique<sup>2</sup>, formed during pregnancy and remain unchanged throughout a person's life. Fingerprints can even survive minor burns and being 'cut' off because as the skin repairs itself the fingerprints are reformed<sup>2</sup>. It takes severe damage to the deeper layers of skin to totally eliminate a fingerprint. Another key characteristic, with regard to their application from a law enforcement perspective, is that fingerprints are one of the final features to leave the skin during decomposition. They are therefore an important tool in identifying bodies, even

several years after death<sup>4</sup>. Finally, the classification of fingerprints into three general types, loops, whorls and arches<sup>2</sup>, reduces the number of prints that need to be searched when looking for a match<sup>5</sup>.

### 1.1.2. Types of Fingerprint Patterns

All fingerprints can be categorised into one of three types of ridge patterns: loops (that account for 60 % of all prints), whorls (that make up 35 %) and arches (that form the remaining 5 %). These main groups can then be subdivided into smaller groups resulting in eight types of fingerprint patterns which are shown in **Figure 1.1**. Fingerprints are placed into one of these groups based on the shape of the friction ridges and the number of deltas present in the print. These are known as primary level characteristics. A delta is an area within a fingerprint where the ridges triangulate (see **Figure 1.3**). Arches have no deltas and are formed when ridgelines run from one side of the finger to the other making no backward turn. Arches are subdivided into *plain arches*, which curve at the top and *tented arches*, which push up to a point in the centre forming a distinct triangle. Loops have one delta and are made up of one or more ridges that start on one side and double back on themselves to end on the same side. Loops are distinguished further based upon the direction in which the loop flows: *radial loops* start and end at the radial side of the arm (thumb side), whereas *ulnar loops* flow to and from the ulna (little finger side). When it is unclear as to which hand a loop has come from, loops flowing from the left are referred to as *left slant loops* and loops flowing from the right are referred to as *right slant loops*. Whorls contain more than one delta; they are subcategorised into four groups: *plain*, *double loop*, *central-pocket* and *accidental loop whorls*. *Plain whorls* either form spiral ridges or concentric circles. *Central-pocket whorls* are loops containing whorls. *Double loop whorls* consist of two loops coming together to form an 'S-shape', and *accidental loop whorls* are whorls which do not lie in between two deltas<sup>6</sup>. A person can have fingerprints all of one type or a mixture of two or more.

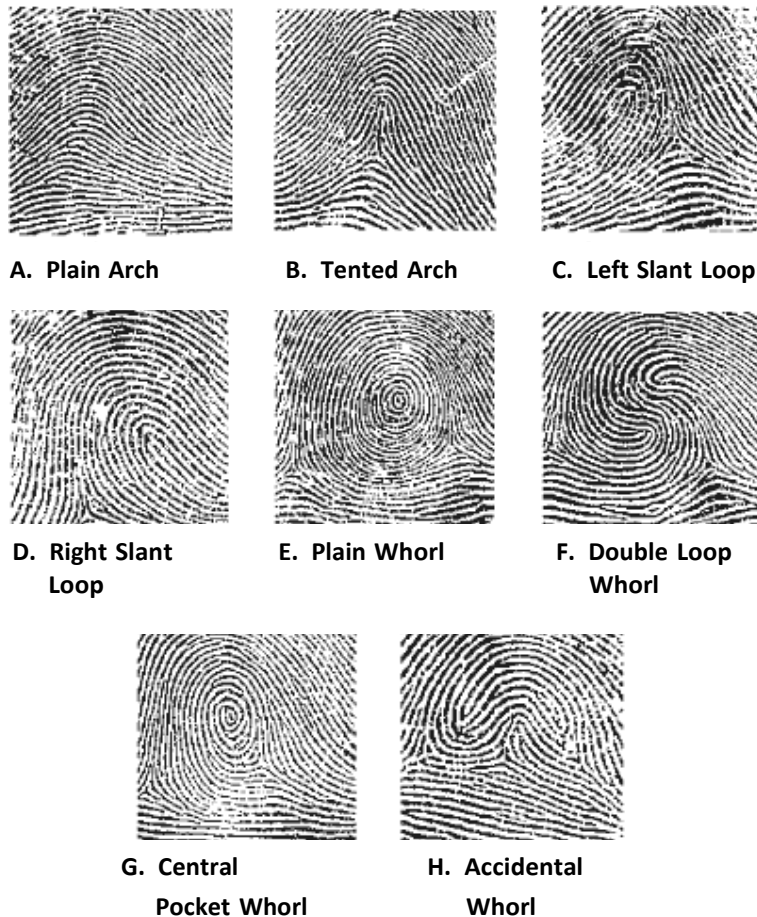


**Figure 1.1.** The eight types of fingerprint patterns<sup>7</sup>.

Once the pattern type has been determined, further comparison can then take place by evaluating certain 'points' within the print. A 'point' is a distinguishable characteristic within the print caused by breaks and more detailed patterns within the ridges. These are known as secondary level characteristics. There are seven classes of ridge points as shown in **Figure 1.2**. A *ridge ending* occurs when a ridge finishes. A *bifurcation* occurs when one ridge splits into two distinct ridges. A *lake* arises when two split ridges join back together reforming a single ridge after a bifurcation. A *dot* is a short, almost circular independent ridge. An *island* is a short independent ridge. A *spur* occurs if a bifurcation leaves one of the two forking ridges considerably shorter in length than the other. A *crossover* runs between two parallel ridges.

RIDGE CHARACTERISTICS	
	RIDGE ENDING
	BIFURCATION
	LAKE
	INDEPENDENT RIDGE
	DOT or ISLAND
	SPUR
	CROSSOVER

**Figure 1.2.** Examples of the different classes of ridge detail<sup>2</sup>.

The standard required for a lawful recognition of identification varies with different jurisdictions. According to the National Fingerprint Standard adopted in 1953 in the UK, the same sixteen 'points'/characteristics must have been identifiable in both the crime scene print and that of the suspect for the prints to be a lawful match. Now the number of points is viewed as less significant and it is left up to the fingerprint expert to decide whether or not the two are a match. As a result of this, a so called zero point system has been adopted in the U.K. since 2000. In order to make this comparison easier, computer based systems have been created. The current system is the National Automated Fingerprint Intelligence System (NAFIS). The NAFIS system scans and digitally stores fingerprints on a database. Current computers can search through 500,000 prints in less than a second when attempting to find a positive match for a print<sup>4</sup>. However, even with such powerful computers they can still only identify candidates for a match: the final assessment still has to be made by a human expert.

Computers can also be used to enhance the quality of recovered fingerprints by varying contrast, light, clarity and background. This can produce a clearer image making comparison easier.

Another way of evaluating fingerprints is to compare their ridge counts. This is the number of ridges present between the core of a fingerprint and its delta. However, for whorls it is slightly more complicated due to the presence of more than one delta. In this instance, both ridge counts are calculated but only the higher of the two is used for comparison. Also, because arches have no delta, they have a ridge count of zero, meaning ridge counts are useless when comparing arches.

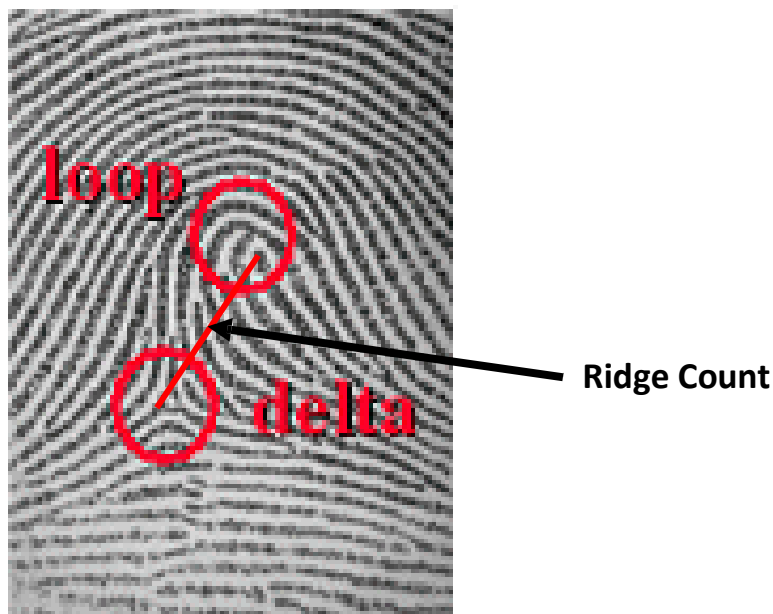


**Figure 1.3.** Ridge count of a right slant loop (here is equal to 7)<sup>2</sup>.

Tertiary level detail can also be seen and used in the identification process. The most common is the mapping of the positions of the sweat pores along the fingerprint ridges.

Forensic scientists classify fingerprints into three groups based on how they were deposited. The first type is patent fingerprints that are formed when a substance on the fingers, such as blood or paint, is transferred to an object leaving behind a visible print. The second type is plastic or impression prints that are three dimensional mouldings of the friction ridges that occur when a person touches a soft material such as wax or gum. Both patent and plastic prints can be photographed directly in order to record and compare. However, the third type

of print, known as latent, is invisible to the naked eye. Hence, in order to be seen, latent prints must be given characteristics which differentiate them from the surface on which they was left. This is a central issue in the work described in this thesis.

### **1.1.3. Skin Anatomy**

The skin is the largest organ in the human body and provides a protective covering from water and harmful substances. It is the site of the touch sensation and some bodily secretions and is also responsible for the production of essential vitamin D<sup>2</sup>. The thickness of the skin<sup>2</sup> in most areas of the body is no thicker than 2 mm but on the palms and soles can be as thin as 0.4 mm. The skin is made up of two distinct layers: the epidermis and the dermis. The epidermis is the outer region and consists of several layers of cells known as the stratum germinativum, stratum spinosum, stratum granulosum, stratum lucidum and stratum corneum. Together these layers have an average thickness of 75 to 150  $\mu\text{m}^2$ . The underlying layer is known as the dermis and is made up of collagen, elastin fibres, an interfibrillar gel and proteoglycans as well as salts and water. These form a dense fibroelastic connective tissue which contains the millions of secretory glands responsible for perspiration.

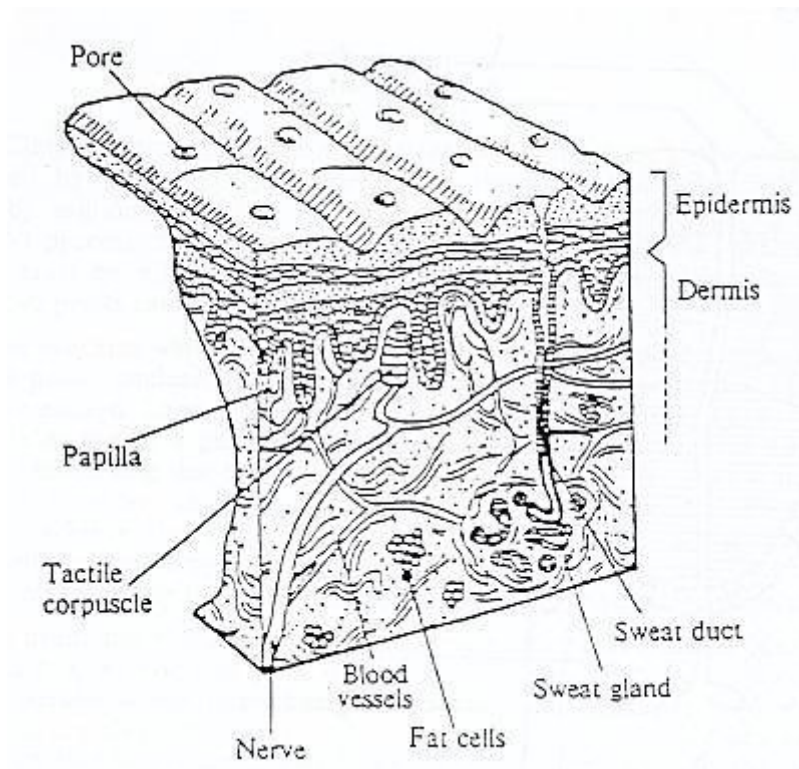


**Figure 1.4.** How friction ridges and pores are linked to sweat glands<sup>8</sup>.

#### 1.1.4. Types of Sweat

Latent fingerprints are produced from a number of natural secretions produced by the different sweat glands present in the skin. These secretions spread out from the pores and form a layer over the friction ridges. When an individual then touches something, these secretions get transferred to the object leaving behind a latent print.

In the medical community the composition of sweat from the various sweat glands has been extensively studied for a variety of reasons centralising around the diagnosis of disease. However, there is no guarantee that the composition of sweat within the glands will be representative of what is transferred to a surface because of contaminants such as cosmetics. Furthermore, once the secretions are exposed on a surface they are subjected to both bacterial and oxidative mechanisms which result in their degradation, which in turn changes the composition. This last point is of particular importance as it is rare that a forensic examiner will receive fingerprint evidence immediately after deposition. If there was a deeper

understanding of exactly how latent fingerprints degraded over time, enhancement techniques could be developed or modified to focus on a specific component of the sweat deposit that was known to withstand the test of time.

There are three types of sweat gland: apocrine, eccrine and sebaceous, each producing sweats of different compositions. The apocrine glands are located close to the hair follicles and have a large, coiled structure. However, as they are mainly situated within the axillary regions such as the armpits and genitals they rarely contribute to latent fingerprint deposits.

Eccrine glands on the other hand significantly contribute to the deposits as they densely populate the palm and sole areas. The sweat produced from these glands has a water content of over 98 %<sup>2</sup> but also contains various other compounds including inorganic salts which, in high enough levels, can lead to corrosion on metal surfaces<sup>9</sup>. Also present are relatively high levels of ammonia, and trace amounts of magnesium, iodide, bromide, fluoride, phosphate, sulphate, sulphur, and transition metals such as iron and copper. Amino acids are also present, which is crucial for development with ninhydrin (see **Section 1.3.2**). Some lipids will also be present due to sebaceous and epidermal contamination<sup>2</sup>. The amount of eccrine sweat secreted is dependent on the amount of water a person has consumed.

Sebaceous secretions also contribute to latent fingerprint depositions. They are confined to areas of the skin containing hair follicles, such as the face, and are absent on the palms. They produce an oily mixture known as sebum. The constituents of sebum include fatty acids, phospholipids, wax esters, sterols and the lipid squalene.

Plastic and patent prints are visible to the naked eye, thus the primary focus of forensic investigators is the recording of these prints through photographs and/or casts. Latent prints, on the other hand, are invisible to the naked eye and need to be enhanced before visualisation can occur. This will be the primary focus of this research.

The quality of enhanced latent prints depends on both the amount of perspiration on the finger and the surface of the object touched. Scene of crime officers collect latent fingerprint evidence from a variety of surfaces, which require a range of development techniques. For example, smooth, non-porous surfaces cannot absorb the perspiration transferred from the finger and can be enhanced using powder or superglue fuming and then either photographed or lifted. On the other hand, porous surfaces absorb the perspiration and have to be enhanced using a series of chemical techniques.

New techniques are constantly being developed to overcome the difficulties of problematic surfaces such as skin and metal, as well as to try and improve existing techniques. For example, methods such as powder dusting rely on the moisture components of the fingerprint residue, so if these components are destroyed by exposure to heat or simply through aging, there is nothing for the powders to adhere to. Research into the removal of latent fingerprints has also shown how heating to high temperatures (>600 °C) can totally remove the fingerprint residue<sup>10</sup>. This research also showed that acetone, rubbing and washing in warm, soapy water are all effective in removing fingerprint residues, which may make current methods fail, so it is important to develop a technique that will still work after such harsh conditions are applied.

## **1.2. The History of Fingerprints**

The use of fingerprints as a means of identification has been perfected over hundreds of years. The first recorded incident of a person studying fingerprints was in 1684 by English plant morphologist Nehemiah Grew<sup>2</sup>. He was fascinated by the ridges on his hands and produced detailed drawings and notes. The first paper to be published on the subject of fingerprints was by Joannes Purkinje in 1823. He classified fingerprints into nine categories including two loops, two arches and five whorls. He also reported on the function of the ridges, furrows and pores within the prints.

Sir William Herschel was the first to note that fingerprints remain unchanged throughout a person's life. He conducted an experiment to prove this by taking his own palm prints first in 1860 and then again in 1890. He noted that, excepting a few wrinkles, the ridge details had remained the same. He later used this concept in a prison in India as a means of identifying inmates. Around the same time Dr Henry Faulds was looking into the persistency of fingerprints by removing finger pads from his patients and comparing the healed fingerprints with the originals. He found them to be the same<sup>2</sup>.

A major breakthrough came with the recognition of fingerprint individuality by Sir Francis Galton in the late nineteenth century. This led to the replacement of the original anthropometric means of identification by fingerprints. This was further perfected towards the end of the nineteenth century by Sir Edward Henry who used Sir Francis Galton's ideas to develop his own classification system that today is used all over the world. He used the number of whorls a person has to categorise prints. Each whorl is given a numerical value based on which finger it is on. Even numbers on the form make up the numerator and the odd ones the denominator. In order to avoid a value of 0/0 for someone with no whorls a value of one is always added to both the numerator and the denominator. There are 1024 classes of fingerprints according to this system which significantly reduces the number of prints that have to be searched.

<b>Right Thumb</b> 16	<b>Right Forefinger</b> 16	<b>Right Middle</b> 8	<b>Right Ring</b> 8	<b>Right Little</b> 4
<b>Left Thumb</b> 4	<b>Left Forefinger</b> 2	<b>Left Middle</b> 2	<b>Left Ring</b> 1	<b>Left Little</b> 1

**Table 1.1** Values given to the whorls on each finger, which are added up to form the numerators and denominators in the totalled whorl pattern in Sir Edward Henry's method.

### 1.3. Established Methods for Fingerprint Enhancement

As latent deposits are invisible to the naked eye, they require enhancement before a comparison/identification can be made. There are many different methods currently employed by forensic examiners for this purpose, the most common of which include powder dusting, ninhydrin spraying, fuming methods and soaking in chemical dyes. Some of these methods target water soluble components whilst others target lipids. Choosing the most suitable technique for a specific sample is crucial in obtaining a good quality print for comparison. There are several factors that will affect the choice of technique, the most important being the nature of the surface (porosity, reflectivity and colour) and any environmentally induced changes. Ideally, fingerprint evidence should be enhanced at a crime scene to avoid any unnecessary aging of the prints or damage during transportation to a laboratory.

Maximum contrast between the enhancement material and the background material is essential in achieving a high quality image of the developed fingerprint. This is important as it is photographic images that will be used to determine a match both through computer systems, such as NAFIS, and fingerprint experts. Any new techniques being developed should take this into account and developing a method where the colour of the enhancement material could be changed would be desirable. Once a visible print has been developed, the

next step is documenting its place at the crime scene by taking a photograph. Afterwards, the print is lifted, using a specially designed adhesive strip, so that a comparison can be made.

### **1.3.1. Powder Dusting**

One of the most common methods for enhancing latent prints on a non-porous surface is powder dusting. This is because of their simple application and ease of collection. They are applied by 'twirling' a brush over the print. There are four main types of powders used: coloured, luminescent<sup>11-13</sup>, magnetic<sup>14,15</sup> and thermoplastic, all of which consist of small particles that stick mainly to residual oils in the perspiration left by friction ridges. Regular powders, such as Sudan Black and aluminium, contain a colorant to add contrast and a resinous polymer for adhesion. Luminescent powders are commonly used on multi-coloured surfaces. They contain either a natural or synthetic compound(s) that will fluoresce or phosphoresce under a light source such as a UV lamp or laser<sup>16-18</sup>. Magnetic powders are applied with a special applicator and are good for use on problematic surfaces such as human skin and leather<sup>2,19,20</sup>. Finally, thermoplastic powders (photocopier toner) become fused to the surface when exposed to heat.

The quality of a print developed using powder is reliant on a number of factors. For example, not all latent prints contain oils; some only contain amino acids and other compounds which powders are less likely to stick to. The powder used must be fine enough to show the ridge detail on the print. The powder must also be adherent enough to stick to the residue but not so adherent that it sticks to the rest of the surface. The powder must also be the right colour for the surface in question, for instance, darker powders cannot be used on dark surfaces.

### **1.3.2. Ninhydrin Spraying**

Ninhydrin is commonly employed on porous surfaces such as paper. The reaction of ninhydrin with amino acids found in latent prints is shown in **Figure 1.5**.

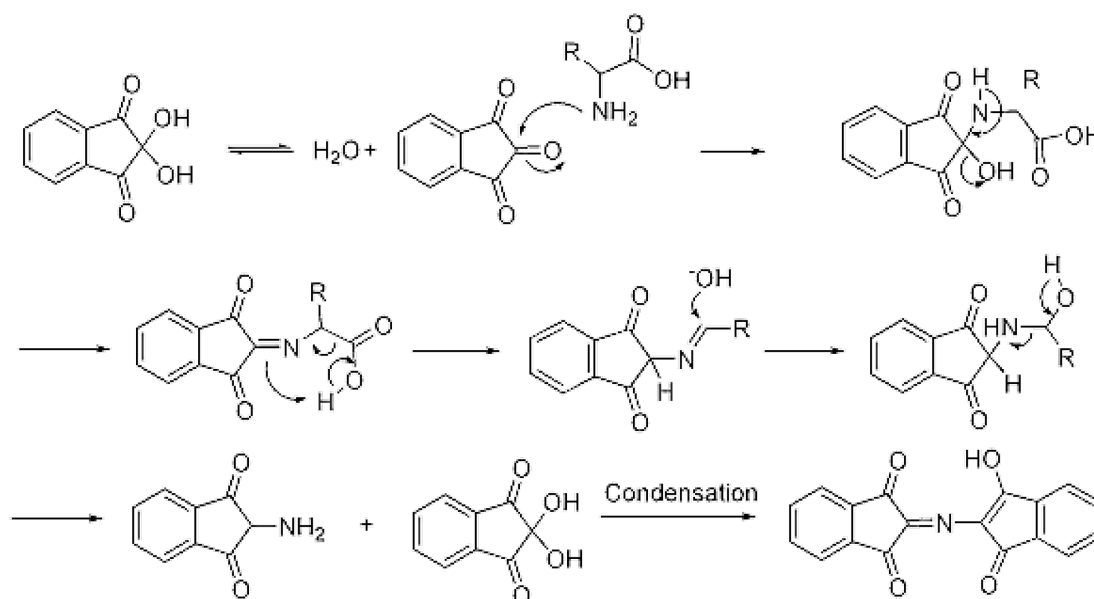


**Figure 1.5.** Reaction of Ninhydrin with amino acids<sup>21</sup>.

This produces a purple coloured fingerprint that can then be photographed. Unfortunately, ninhydrin development interferes with other techniques, so other more exploratory methods are often used beforehand. Despite this, ninhydrin is a popular reagent for use on porous surfaces as it is cheap and easy to produce. The technique for applying ninhydrin is portable and simple to use, allowing it to be used at crime scenes by individuals with minimal specialist training. Although fingerprints that are enhanced using ninhydrin can take a few days to develop fully, the process can be speeded up with heat and high humidity<sup>2</sup>. Amino acids are stable compounds and do not tend to migrate through pores in the paper. For this reason, ninhydrin can be used to develop latent fingerprints on porous materials.

### 1.3.3. Fuming Methods

Another technique for developing fingerprints left on porous surfaces is iodine fuming. When iodine crystals are warmed they produce a purple vapour which physically adsorbs to the fingerprint residue<sup>22</sup>. Iodine fuming has one main advantage over other techniques such as ninhydrin: it is a non-destructive technique, and the print that is produced quickly fades, allowing other enhancement techniques to be used afterwards. This allows for use on

important documents without risking any damage. On the other hand, because the print fades so quickly, iodine fuming has to be closely monitored and the print has to be photographed as soon as it is developed because it soon starts to disappear.

Cyanoacrylate (superglue) fuming is another fuming technique, this time for development of latent fingerprints on non-porous surfaces. Superglue is made up of alkyl-cyanoacrylates. When heated to boiling point (120 °C) in a confined space, the cyanoacrylate vapours adhere to the fatty acids and amino acids in the deposit as well as moisture in the air to form a sticky, white powder along the ridges in the fingerprint. Once developed, the fingerprint can be photographed and lifted directly or it can be further enhanced with powders or dyes and then imaged.

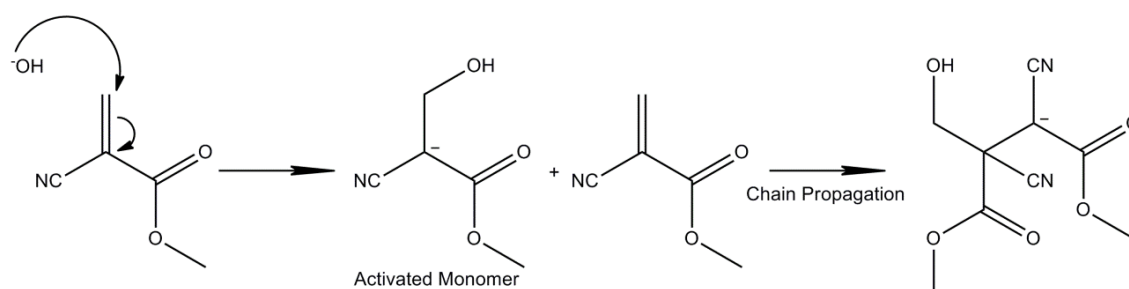


**Figure 1.6.** The mechanism for the anionic chain polymerisation reaction started by the reaction of the cyanoacrylate vapours with hydroxide ions<sup>23</sup>.

The electron withdrawing effects of the cyanide and ester substituents mean that the  $\text{CH}_2$  group on the double bond is highly electropositive and therefore open to nucleophilic attack from the hydroxide ion. This pushes the electrons from the double bond on to the other carbon forming a carbo-anion. This carbo-anion then attacks the  $\text{CH}_2$  group on another cyanoacrylate monomer forming a bond between the two monomers. This is repeated until polycyanoacrylates are formed. It is these polymers that react with the fatty and amino acids to form the hardened white powder that enhances the latent fingerprint.

### 1.3.4. Chemical Dyes

Chemical dyes are often used as a post treatment after cyanoacrylate enhancement in order to maximise the contrast. Gentian Violet is a chemical dye which stains the fatty acids in the sweat residue purple. In order to achieve this, the cyanoacrylate print is immersed in the solution for about a minute, after which the excess dye is removed by rinsing with water. Other dyes include Coumarin 540, Rhodamine 6G and Coomassie Brilliant Blue (CBB) (see **Figure 1.7**).

Fluorescent dyes, such as Rhodamine 6G, are commonly used on multicoloured surfaces as their fluorescence/phosphorescence, rather than colour, is used to achieve contrast. 1,8-diazafluoren-9-one (DFO) is another fluorescent technique that is used on porous surfaces. Like ninhydrin it reacts with the amino acids present in latent fingerprints, which can then be detected using a laser that causes it to fluoresce. The solution is made up of methanol, ethyl acetate, acetic acid and a small amount of DFO, which are sprayed onto the evidence and then oven dried. Methylene Blue dye (MBD) and Safranin O are also fluorescent dyes that are commonly used to further enhance prints after superglue fuming.

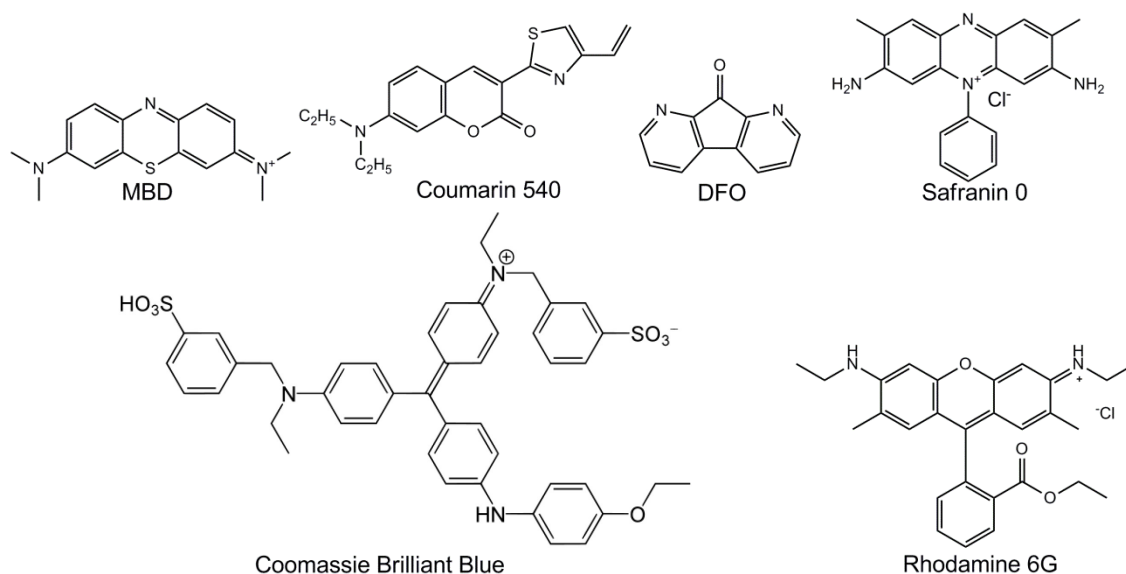


**Figure 1.7.** Structures of fluorescent materials commonly used in the enhancement of latent fingerprints.

### 1.3.5. Other Techniques

As well as fuming, iodine can be used as a spray that is effective in developing fingerprints on porous surfaces. It consists of two solutions: one is iodine in cyclohexane and the other is naphthoflavone and methylene chloride<sup>24</sup>. This spray technique is particularly effective on wallpaper, paint and other glossy surfaces at a crime scene that cannot be taken to the lab for further enhancement. It has even been proved more effective than ninhydrin. The spray reacts with the residual perspiration in the latent print making it appear dark blue. However, this technique is only effective on prints that are up to a week old; after that the development is less successful.

Another good technique for waxy or glossy surfaces is silver nitrate solution<sup>25</sup>. The evidence is soaked in the solution and is then exposed to bright light in order to develop the prints as silver nitrate is photosensitive. A photograph is then taken immediately as the prints do not stay visible for long in the absence of light.

Vacuum metal deposition (VMD) is occasionally used to enhance latent fingerprints left on non-porous surfaces<sup>26</sup>. A thin layer of gold and zinc is applied to the item under vacuum which enhances the prints. However, the use of gold and the need for a vacuum make this process expensive and non-portable; it also requires a more skilled operator, so it is rarely used.

Small particle reagent (SPR) is a technique used for developing latent prints on wet surfaces such as window glass, where the use of dry powders may destroy the prints. Small black particles of molybdenum disulphide adhere to the fatty residues in latent fingerprints. Like many enhancement methods, it depends on the amount of residue deposited by the finger when forming the print. This technique can even be used to examine surfaces underwater, providing the spray bottle is powerful enough to push the particles through the water.

The order in which enhancement techniques are applied to a piece of evidence is important in ensuring the successful recovery of any latent fingerprints. An example of the systematic approach to latent print enhancement is outlined in **Figure 1.8**. The standard development techniques described above are sufficient for most everyday surfaces. However, occasionally there are unusual conditions, such as previously wetted surfaces or human skin, which will require more specialised methods of enhancement. The majority of development techniques are destructive, which is undesirable. The use of treatments on the residue before visualisation is something that should be avoided if at all possible. Spectroscopic techniques are a way of achieving this<sup>27</sup> as they only measure the interaction between radiation and fingerprint matter.

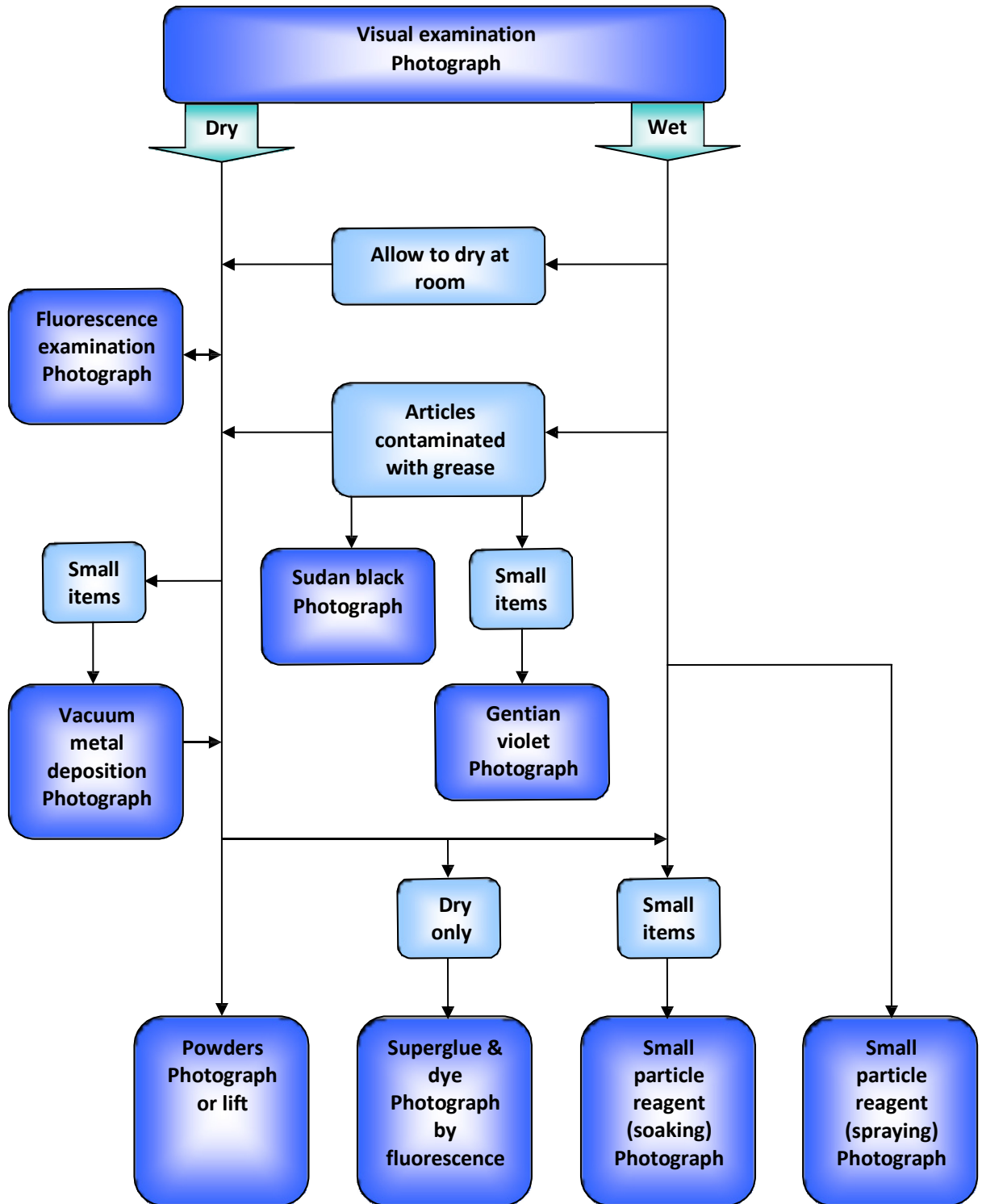


**Figure 1.8.** A systematic approach used for latent print enhancement on a non-porous surface<sup>15</sup>.

## 1.4. Latent Print Development on Metal Surfaces

Over 200,000 items of fingerprint evidence are processed each year in the UK, of which 20,000 are metallic items. Surprisingly, despite the range of methods available, less than 10% of these produce useable fingerprints. Given the prevalence of metallic objects - weapons, tools, handles – in criminal investigations this is an important challenge<sup>28-30</sup>.

The development of latent fingerprints on metal surfaces has been extensively researched because of the high quantity of metallic weapons. Commonly employed enhancement techniques for metal surfaces include powder dusting, vacuum metal deposition, cyanoacrylate fuming, dyeing and immersion in small particle suspensions<sup>17,31,32</sup>. Fluorescence has also been used for development on aluminium using cadmium sulphide nanocomposites which bond with the fatty and amino acid components in the deposits<sup>33</sup>. Williams et al have established a method for latent print visualisation using a Scanning Kelvin Probe<sup>34,35</sup>. This measures the potential difference between a vibrating probe tip and sample in order to obtain a work function map of the surface. The salts within the fingerprint deposit affect the magnitude of the potential difference. This method is successful on metal samples that have been exposed to high temperatures<sup>36</sup>. Fingerprints have also been successfully visualised on brass shell casings and discharged brass shell casings using this method, even after other techniques such as cyanoacrylate fuming have been employed<sup>37</sup>. Another technique involves running carbon powder balls over a brass casing, causing the carbon to adhere to the fingerprint deposit<sup>38</sup>.

## 1.5. Electroactive Polymers

Electroactive conducting polymers are organic polymers which can conduct electricity because of their molecular structure. Derivatives of the pyrrole and thiophene families can be chemically or electrochemically oxidised to form electronically conjugated polymers<sup>39-43</sup>. Interest in conducting polymers has been growing since the 1970's<sup>44-46</sup> due to their wide

spectrum of applications ranging from photo-voltaic devices<sup>47,48</sup> and organic-based light emitting devices<sup>49</sup> to integrated circuits<sup>50-53</sup> to use in the automotive industry<sup>54</sup>. The desire to extend this scope to further technological applications means that there is always a need to refine electrodeposition conditions in order to increase the stability of the resulting polymer and to extend to different substrates<sup>55</sup>.

### 1.5.1. Electronic Structure

Conducting polymers consist of a backbone of  $sp^2$  hybridised carbons. The nature of this type of hybridisation means that each carbon has three sigma bonds and a  $p_z$  orbital perpendicular to the plane of the carbon backbone containing one valence electron. The closeness of these orbitals on the backbone allows the valence electrons to delocalise, forming a  $\pi$  electron "cloud" along the polymer chain resulting in high mobility of the electrons. This means that electrons can be removed during oxidation (p- doped) forming a film with some empty  $p_z$  orbitals allowing the remaining electrons to move and conduct<sup>56</sup>.

According to **Equation 1.1**, colour changes occur due to the promotion of electrons from the highest occupied molecular orbital (HOMO) within the valence band to the lowest unoccupied molecular orbital (LUMO) in the conduction band. This causes light of a certain wavelength to be absorbed. The oxidation of undoped polymer creates mid gap states from both the valence and conduction bands. This leads to different transitions becoming available both to and from these mid gap states, causing a change in transition energy. This results in light of a different wavelength being absorbed causing a change in colour of the polymer film. The relative populations of the mid gap states depends on the potential of the film and therefore, the degree of oxidation<sup>57</sup>. During doping of the polymer, cations and anions move into/out of the film changing the positions of the HOMO and LUMO causing the transition energy to change further. **Equation 1.2** relates these transitions to a voltammogram.

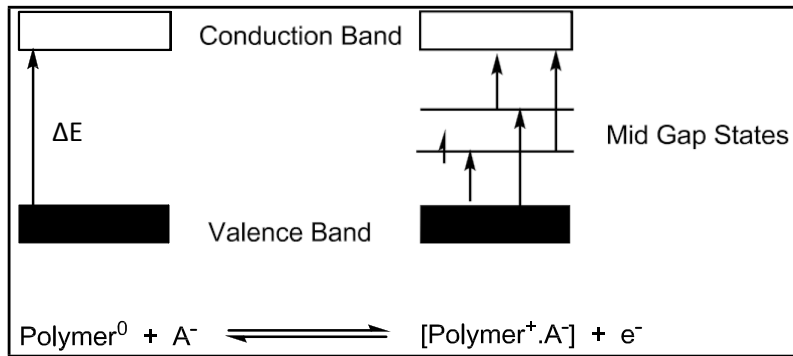


**Figure 1.9.** Molecular orbital diagram showing valence and conduction bands in undoped polymer as well as the mid gap states found in p-doped polymer.

### Equation 1.1

where  $E$  is energy (J),  $h$  is Planck's constant (J s);  $\nu$  is frequency ( $\text{s}^{-1}$ ).

### Equation 1.2

as work (J) = charge (C)  $\times$   $\Delta E$  and  $\Delta G = -W$ , where  $G$  is Gibbs energy ( $\text{J mol}^{-1}$ ),  $n$  is number of moles of electrons,  $F$  is Faraday's constant ( $\text{C mol}^{-1}$ ) and  $E$  is potential (V or  $\text{J C}^{-1}$ ).

When the polymer film is oxidised, electrons are removed from the dry side of the film. In order to maintain electroneutrality, anionic dopants ( $\text{A}^-$ ) and/or cations ( $\text{C}^+$ ) diffuse into/out of the film to balance the charge (**Figure 1.10**). As the oxidation potentials of most conducting polymers are lower than those of their corresponding monomers, they are simultaneously oxidised during polymerisation<sup>58</sup>.

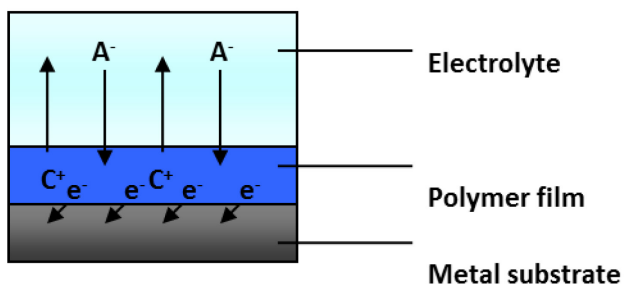


**Figure 1.10.** Cartoon representation of ion migration within a polymer film during oxidation.

Electrode surface modification using conducting polymers has been extensively researched since the term was first used by Murray et al. in 1975<sup>59-63</sup>. Applications of such modified electrodes range from supercapacitors and batteries, in items such as mobile phones and electrically powered vehicles<sup>64</sup>, to corrosion prevention<sup>65</sup> and the enhancement of latent fingerprints<sup>66,67</sup>.

### 1.5.2. Multicomponent Systems

Metal coordination complexes<sup>68,69</sup>, metal oxides<sup>70,71</sup>, viologens<sup>69,70</sup> and conjugated polymers<sup>69,70,72</sup> all exhibit electrochromic properties. Conducting polymers offer advantages over other electrochromic materials, such as inorganic metal oxides ( $\text{WO}_3/\text{IrO}_2$ ) and small organic molecules (viologens), due to their low processing costs, no dependence on the angle of visualisation, fast switching and the ability to tune the band gap and therefore colour by structure modification<sup>73</sup>. Most electroactive polymers are restricted to two colours or two shades of the same colour<sup>74</sup>. Changing the electronic character of the polymer backbone moves the position of the  $\pi - \pi^*$  transition across the electromagnetic spectrum so that when different conducting polymers are doped different optical properties are observed<sup>75,76</sup>. The electrochromic properties of conjugated polymers are the focus of this thesis.

One way to tune electrochromic properties is using copolymerisation of two distinct monomer units or homopolymerisation of a hybrid comonomer which can lead to the resulting polymer

having optical properties intermediate of the corresponding homopolymers or distinct new properties of its own<sup>73,77,78</sup>.

The layer-by-layer (LbL) fabrication technique relies on electrostatic or other molecular forces to construct multiple layers of different components. In the case of conducting polymers<sup>79,80</sup>, the use of multiple layers allows synergy or the combination of the properties of the individual components to create a polymer system with greater functionality. For example, charge storage capacity can increase compared to copolymers of the same monomer units and the individual<sup>81-83</sup>. Although the different components of the films are deposited sequentially there is reason to believe they may be considerably interdiffused which significantly increases the electroactivity of the films. On the other hand, if the layers retain a high degree of segregation both layers may experience different degrees of solvation.

Neutron reflectivity can be used to determine the spatial profiles of the individual polymer component. Reflectivity contrast can be manipulated by deuterating selective components to accurately determine absolute solvation levels to answer whether equal or differentiated solvation of the individual polymer components is seen in multi-layered systems.

## **1.6. Electrochromic Enhancement of Latent Fingerprints**

Current techniques for developing fingerprints, such as dusting, superglue fuming and wet powder application, rely on physical or chemical interaction between a reagent and the deposit left from handling an item or surface, resulting in a positive image of the fingerprint. A complementary technique has been explored that involves interaction of a reagent with a surface rather than the fingerprint deposit itself. This novel technique exploits the fingerprint deposit as an insulating mask blocking electrochemical processes, such as polymer deposition. This results in spatially selective deposition of the polymer on the bare metal surface in between the ridges of the fingerprint.

This first stage of the concept (illustrated in **Figure 1.12**) was described by Bersellini et al.<sup>84</sup>, who deposited polypyrrole electrochemically on fingerprinted metal surfaces such as Pt, Au, Ag and Ergal (Al alloy).

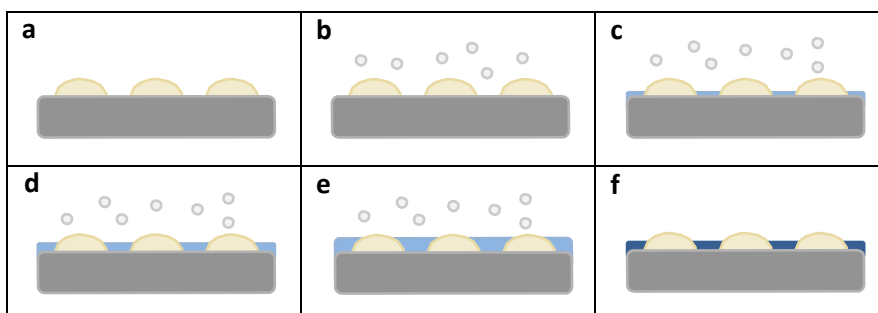


**Figure 1.11.** Schematic representation of strategy for visualizing latent fingerprints by deposition of electrochromic polymer: (a) surface with deposited fingerprint, prior to treatment; (b) fingerprinted surface immersed in monomer solution, prior to initiation of film deposition; (c) regions of bare (inter-ridge) surface covered with thin layer of polymer in early stages of deposition; (d) surface optimally covered with polymer; (e) excess polymer deposited, resulting in overfilling of trenches and partial obscuring of fingerprint deposit and (f) sample after transfer to monomer-free electrolyte and held at a different potential, generating a contrasting image (via a colour change) to that in (d).

The electrochromic enhancement explored here uses the electrochemical polymerisation of the respective monomers 3,4-ethylenedioxythiophene (EDOT) and aniline (Ani). The fundamental extension pursued in this case is subsequent potential control of the deposited polymer to vary its optical properties (colour). This can be achieved by transferring the fingerprinted object to a background electrolyte solution, following polymer deposition, where variation of applied potential allows reversible changes to polymer colour thereby optimising visual contrast. The practical significance of this is that one can then optimise fingerprint

visual contrast, yielding excellent second level detail and significant third level detail (see **Section 1.1.2**).

Visualisation of latent fingerprints present on metallic surfaces has been demonstrated by means of spatially selective deposition of the polymers polyaniline (PAni)<sup>85</sup> and poly(3,4-ethylenedioxythiophene) (PEDOT)<sup>86</sup>. The novel technique utilises the inhibition of the electrochemical processes on areas of the surface that have been masked by the fingerprint. This results in polymer deposition between the ridges, generating a negative image of the fingerprint (**Figure 1.13**).

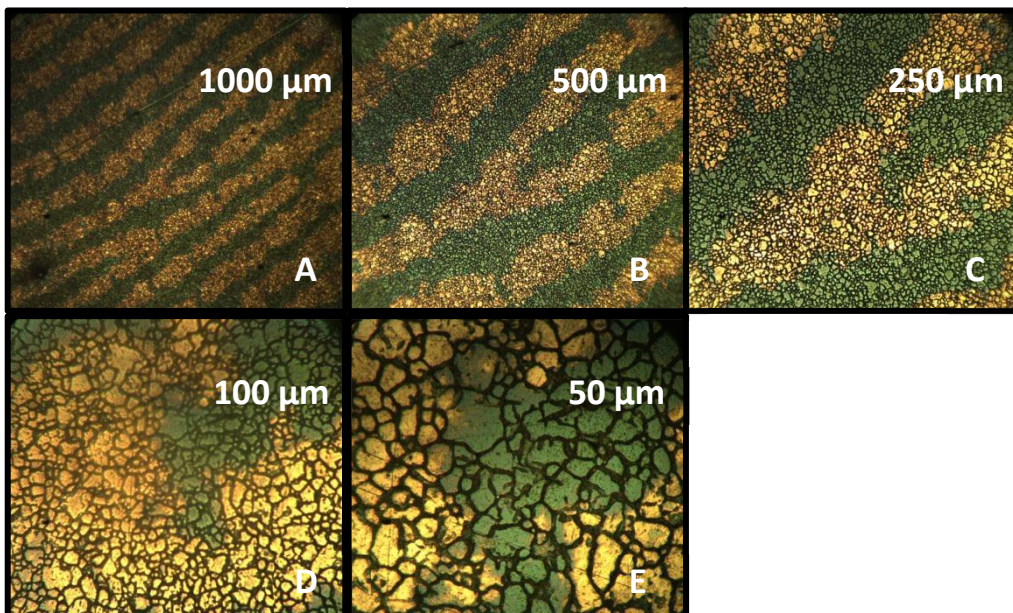


**Figure 1.12.** Secondary classification bifurcation point within a PEDOT developed fingerprint (1 day old, kept under water, 230 s deposition time) at the following magnifications; (A) x 5, (B) x 10, (C) x 20, (D) x 50 and (E) x 100 (see scale bars for absolute distances).

By variation of the applied potential, the polymer's colour can be continuously and reversibly adjusted, as different redox states have distinct optical properties, i.e. the polymers are electrochromic. This can be used to optimise visual contrast of the fingerprint.

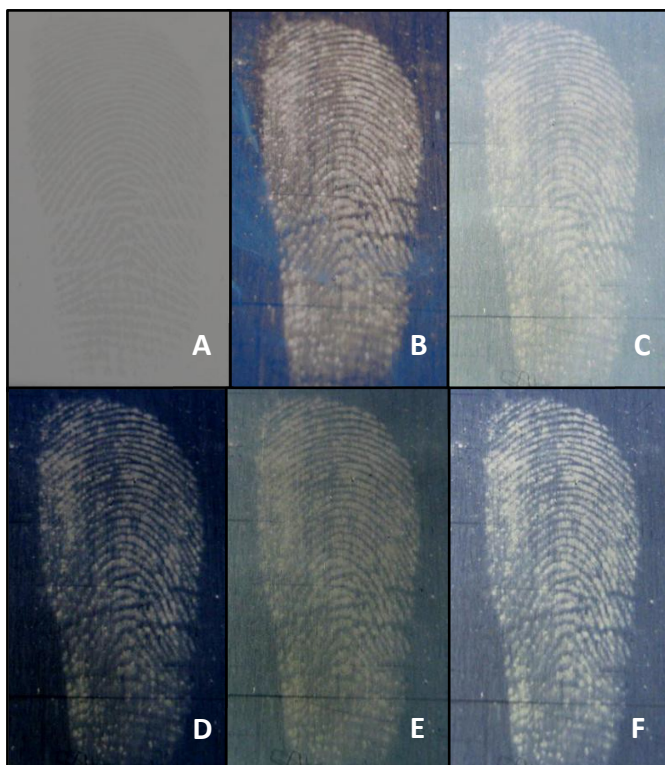


**Figure 1.13.** Effects of ambient medium and applied potential on a fingerprint image subjected to enhancement by PEDOT deposition. All images are for the same sebaceous fingerprint, deposited on stainless steel, then stored for 3 days in ambient laboratory conditions prior to the observations shown. (A) fingerprint prior to enhancement; (B-F) following PEDOT deposition; final image quality on the Bandey scale: grade 3. Sample environment: (B) *ex situ*; (C and D) *in situ* exposed to  $1 \text{ mol dm}^{-3} \text{ H}_2\text{SO}_4$ ; (E and F) *in situ* exposed to  $1 \text{ mol dm}^{-3} \text{ H}_2\text{SO}_4/0.01 \text{ mol dm}^{-3} \text{ SDS}$ . Applied potential: (C and E)  $0.80 \text{ V}$ ; (D and F)  $-0.80 \text{ V}$ .

The facility of the method to reveal fingerprints of various ages and subjected to plausible environmental histories has been demonstrated. A comparison of this enhancement methodology with commonly used fingerprint enhancement methods (dusting with powder, application of wet powder suspensions and cyanoacrylate fuming) showed promising

performance in a variety of scenarios of practical forensic interest. The electrochromic enhancement outperformed traditional techniques when the sample environment had significantly decreased the amount of fingerprint residue left on the surface, for example when subjected to high temperatures and when washed with soap<sup>87</sup>. This was attributed to the fact that an insulating layer of fingerprint residue is enough to prevent electropolymerisation so only a fraction of the original fingerprint deposit, which can be several microns thick<sup>88</sup>, is required for a successful enhancement. This is significantly less than the amount required by traditional development techniques.

## 1.7. Deep Eutectic Solvents

In energy storage devices the movement of ions and solvent through the polymer film during oxidation and reduction is crucial to both application and function, e.g. charging rate, metal ion permeability or adhesion stability.

Deep eutectic solvents (DESs) are a form of ionic liquids (ILs) that have been recently developed<sup>89</sup>. They form eutectic mixtures from quaternary ammonium salts, such as choline chloride, complexed with hydrogen bond donors, such as ethylene glycol and urea<sup>90</sup>. This is how DESs differ from conventional ILs, which interact through electrostatic forces between small ions. DESs consist of bulky cations (salt) and complex anions, which acts as a hydrogen bond donor or form metal halide bonds. DESs are highly conducting (*ca.* 1 to 10 mS cm<sup>-1</sup> at 30°C)<sup>91</sup>. This suggests that the ionic species in the DESs are fully dissociated and can move independently. Therefore, utilising DESs as electrolytes should mean a constant supply of dopant ions.

In this research Type III DESs were used. These consist of choline chloride (ChCl) and a hydrogen bond donor e.g. ethylene glycol (Ethaline). Ethaline 200 is made from 1 mole of choline chloride to 2 moles of ethylene glycol.

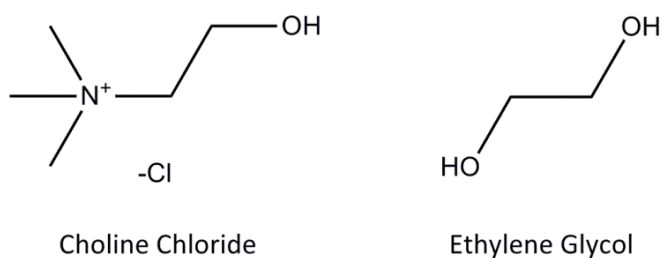


**Figure 1.14.** Structures of choline chloride and ethylene glycol.

## 1.8. Neutron Scattering

For many materials there are differences between the properties (density, composition, and solvation) of the bulk and interfacial or surface materials. To achieve vertical depth profiling, with high spatial resolution, a highly penetrating beam must be used<sup>92</sup>. Neutron scattering is a powerful technique for investigating air/liquid<sup>93-99</sup>, liquid/liquid<sup>100-105</sup> and solid/liquid<sup>106-111</sup> interfaces.

Neutrons are neutral, spin  $\frac{1}{2}$  particles which have been widely used to probe nanoscale structures over a range of length scales<sup>112-115</sup>. Like x-rays they can be used to investigate the structure of condensed matter in a non-destructive manner<sup>116</sup>. However, because of their electroneutrality, neutrons penetrate deep into a material and so are more able to probe the bulk material than x-ray photons, which are primarily used as a surface probing technique. One advantage of neutron scattering is that it emanates from an interaction with the nuclei, which varies irregularly with atomic number. X-rays on the other hand are scattered by electrons which means that the scattering ability (scattering cross section) is proportional to the atomic number. As a result of this, neutron scattering is a useful structural probe for materials containing elements with lower and/or similar atomic numbers. Neutrons can also distinguish between different isotopes as these possess different nuclear forces. This allows contrast variation using deuterium labelling as the scattering lengths ( $b$ ) vary greatly (H = -3.74 fm, D = 6.67 fm). Another significant characteristic of the neutron is that it possesses a magnetic moment; this allows it to interact with any unpaired electrons in a magnetic material

offering information on magnetic spin states<sup>117,118</sup>. Neutrons can be polarised to align their spins so that information regarding specific magnetic states within a material can be extracted<sup>119</sup>.

There are two ways of producing neutrons:

1. Fission reaction:  $^{235}\text{U} + \text{neutron} \rightarrow \text{fission fragments} + 2.52 \text{ neutrons} + 180 \text{ MeV}$ <sup>120</sup>.
2. Spallation reaction: a high energy proton hits a nucleus causing the release of a neutron. In this case the neutron beam is pulsed and the nature of the proton pulse determines the nature of the neutron pulse<sup>121</sup>.

For their practical applications, neutrons can be classified according to their energy: cold, thermal and hot. Cold neutrons probe larger distances or lower energy samples whereas hot neutrons probe small lattice spacing or higher energies.

Type of Neutron	Energy	Wavelength/Å
Cold	0.05 – 5 meV	4 – 40
Thermal	5 – 100 meV	0.9 – 4
Hot	100 meV – 1 eV	0.3 – 0.9

**Table 1.2** Properties of cold, thermal and hot neutrons<sup>80</sup>.

Thermal neutrons are at temperature equilibrium with the medium they are in. They are produced during nuclear reactions (fission and spallation). Hot and cold neutrons are made when thermal neutrons are heated or cooled using a moderator.

Neutrons obey the laws of quantum mechanics so may be considered a wave as well as a particle. Neutron beams are transported using neutron guides which utilise the concepts of reflectivity.

where  $n$  is the refractive index and  $N_b$  is the scattering length density which is equal to the sum of the bound coherent scattering lengths ( $b_c$ ) of the nuclei and the atomic number density ( $n_j$ ).

$$\Sigma$$

Equation 1.4

When the angle of incidence ( $\theta$ ) is below a critical angle ( $\theta_c$ ) then total external reflection is observed with none of the beam being transmitted.

$$\sqrt{\frac{\rho}{\rho_0}}$$

Equation 1.5

where  $\rho$  is the density ( $\text{g cm}^{-3}$ ) of the material.

This is the basic principle behind neutron guides that reduce loss of flux and allow bending of the neutron beam during transportation and help to focus beam onto a sample.

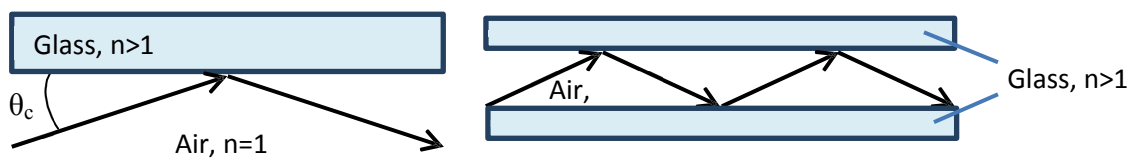


**Figure 1.15** Principle of neutron transport through glass guides.

The basic principles described above mean that neutrons can be employed in various scattering techniques to probe the properties/processes in condensed matter. For more information on the specific techniques employed in this thesis please refer to **Section 2.4**.

## 1.9. Objectives

In general terms, the objectives of this thesis relate to enhanced understanding of conducting polymer films and their practical applications, specifically in latent fingerprint visualization and in energy storage.

In the former instance, the aim is to visualize latent fingerprints on metallic surfaces, recovered from challenging environments. The means by which this is to be attempted involves electrochemically controlled deposition of conducting polymers based on thiophene- and pyrrole-type monomers and co-monomers. The specific objectives that follow from this are determination of the electrochemical and electrochromic behaviour of the resultant polymers and the efficiency of recovery of usable fingermarks from surfaces subject to various environments that simulate forensically challenging scenarios.

The above objectives represent natural evolution of preliminary work carried out before the commencement of this project. In a more novel departure from this electrochromic polymer approach, an additional goal is fluorescence-based fingerprint imaging. The specific objectives en route to this are development of a synthetic pathway to accommodation of bulky fluorophore moieties within sterically crowded polymer films and determination of the extent and spatial distribution of fluorophore immobilization within the polymer film.

In the case of energy storage, the goals are deposition, characterization and comparison of conducting polymer films based on thiophene- and pyrrole-based monomers. A key question is the effect of spatial distribution of the components: the objective is to explore this from the most intimate mixture of a co-monomer to segregated multi-layers. Additionally, the effect of medium on film charge storage is to be determined, by evaluation of film doping characteristics in a traditional electrolyte ( $\text{LiClO}_4/\text{acetonitrile}$ ) and a DES (Ethaline). The final objective, for promising systems, is evaluation of (electro)chemical stability to extensive redox cycling.

## 1.10. References

- <sup>1</sup> The International Biometric Group (2003): *The Henry Classification System*.
- <sup>2</sup> Henry C. Lee and R. E. Gaensslen, (2001): *Advances in Fingerprint Technology, 2<sup>nd</sup> Edition*. U.S.A, CRC Press LCC.
- <sup>3</sup> C. Champod, C. J. Lennard, P. Margot and M. Stoilovic (2004): *Fingerprints and Other Ridge Skin Impressions (International Forensic Science and Investigation)*, CRC Press, Boca Raton.
- <sup>4</sup> Fields, R., Molina, D. K., *J. Forensic Sci.*, 2008, **53**, 952-955.
- <sup>5</sup> D. P. Lyle, MD (2004): *Forensics for Dummies*. Indianapolis, Indiana: Wiley Publishing, Inc.
- <sup>6</sup> N. E. Genge (2004): *The Forensic Casebook, The science of Crime Scene Investigation*. Great Britain: Ebury Press, Random House.
- <sup>7</sup> How Stuff Works Express. Accessed 08/04/2008.  
  
<http://express.howstuffworks.com/gif/express-detective-prints.gif>
- <sup>8</sup> Australian Police. Accessed 25/11/2013.  
  
<http://www.australianpolice.com.au/dactyloscopy/friction-ridge-skin/>
- <sup>9</sup> Jensen, O., Nielsen, E., *Acta Dermatovener (Stockholm)*, 1979, **59**, 139-143.
- <sup>10</sup> Paterson, E., Bond, J. W., and Hillman, A. R., *J. Forensic Sci.*, 2010, **55(1)**, 221.
- <sup>11</sup> N. Akiba, N. Saitoh and K. Kuroki, *J. Forensic Sci.*, 2007, **55**, 180.

- <sup>12</sup>M. J. Choi, T. Smoother, A. A. Martin, A. M. McDonagh, P. J. Maynard, C. Lennard and C. Roux, *Forensic Sci. Int.*, 2007, **173**, 154.
- <sup>13</sup>J. Almog, G. Levinton-Shamuilov, Y. Cohen and M. Azoury, *J. Forensic Sci.*, 2007, **52**, 1057.
- <sup>14</sup>J. D. James, C. A. Pounds and B. Wilshire, *J. Forensic Sci.*, 1993, **38**, 391.
- <sup>15</sup>L. K. Seah, U. S. Dinish, W. F. Phang, Z. X. Chao and V. M. Murukeshan, *Forensic Sci. Int.*, 2005, **152**, 249.
- <sup>16</sup>Akiba, N., Saitoh, N., and Kuroki, K., *J. Forensic Sci.*, 2007, **55**, 180.
- <sup>17</sup>Choi, M. J., Smoother, T., Martin, A. A., McDonagh, A. M., Maynard, P. J., Lennard, C., and Roux, C., *Forensic Sci. Int.*, 2007, **173**, 154.
- <sup>18</sup>Almog, J., Levinton-Shamuilov, G., Cohen, Y., and Azoury, M., *J. Forensic Sci.*, 2007, **52**, 1057.
- <sup>19</sup>James, J. D., Pounds, C. A., and Wilshire, B., *J. Forensic Sci.*, 1993, **38**, 391.
- <sup>20</sup>Seah, L. K., Dinish, U. S., Phang, W. F., Chao, Z. X., and Murukeshan, V. M., *Forensic Sci. Int.*, 2005, 152, 249.
- <sup>21</sup>Jackson, A. R. W., Jackson, J. M., (2004): *Forensic Science*, Pearson Prentice House, Harlow, UK.
- <sup>22</sup>Almog, J., Sasson, Y., and Anah, A., *J. Forensic Sci.*, 1979, **24**, 431.
- <sup>23</sup>Czekanski, P., Fasola, M., and Allison, J., *J. Forensic Sci.*, 2006, **51**, 1323.

- <sup>24</sup>Siegel, J. A., Saukko, P. J., and Knupfer, G. C., (2000): *Encyclopedia of forensic sciences (Vol. 2)*, Academic Press.
- <sup>25</sup>United States Department of Justice: Federal Bureau of Investigation (1993): *Science of Fingerprints: Classification and Uses*, DIANE Publishing Co., Collingdale, United States.
- <sup>26</sup>Manual of fingerprint development techniques, ed. V. Bowman, Sandridge, UK, 2nd rev. edition, 2004: Police Scientific Development Branch, Home Office.
- <sup>27</sup>Crane, N. J., Bartick, E. G., Perlman, R. S., and Hoffman, S., *J. Forensic Sci.*, 2007, **52**, 48.
- <sup>28</sup>S. P. Wargacki, L. A. Lewis and M. D. Dadmun, *J. Forensic Sci.*, 2008, **53**, 1138–1144.
- <sup>29</sup>P. Cuce, G. Polimeni, A. P. Lazzaro and G. De Fulvio, *Forensic Sci. Int.*, 2004, **146**, 7–8.
- <sup>30</sup>M. Zhang and H. H. Girault, *Analyst*, 2009, **134**, 25–30.
- <sup>31</sup>Bowman, V., editor. *Manual of Fingerprint Development Techniques*. 2<sup>nd</sup> rev. ed. Sandridge, UK: Police Scientific Development Branch, Home Office, 2004.
- <sup>32</sup>Bandey, H., and Kent, T., *Superglue Treatment of Crime Scenes*. Sandridge, UK: Police Scientific Development Branch, Home Office, 2003.
- <sup>33</sup>Bouldin, K. K., Menzel, E. R., Takatsu, M., and Murdock, R. H., *J. Forensic Sci.*, 2000, **45**, 1239.
- <sup>34</sup>Williams, G., McMurray, H. M., and Worsley, D. A., *J. Forensic Sci.*, 2001, **46**, 1085.
- <sup>35</sup>Williams, G., and McMurray, N., *Forensic Sci. Int.*, 2007, **167**, 102.
- <sup>36</sup>Bond, J. W., *J. Forensic Sci.*, 2008, **53**.
- <sup>37</sup>Bond, J. W., and Heidel, C., *J. Forensic Sci.*, 2009, **54**, 892.

- <sup>38</sup>Bond, J. W., Review of Scientific Instruments, 2009, **80**, 075108.
- <sup>39</sup>P.M.S Monk, R.J. Mortimer, and D.R. Rosseinsky, *Electrochromism: Fundamentals and Applications*, VCH, Weinheim, 1995.
- <sup>40</sup>Higgins, S.J. *Chem. Soc. Rev.* **1997**, 26, 247.
- <sup>41</sup>Handbook of Conducting Polymers, 2<sup>nd</sup> Ed., Marcel Dekker, New York (1998) pp259-276.
- <sup>42</sup>Hyodo, K. *Electrochim. Acta* **1994**, 39, 265.
- <sup>43</sup>Roncali, J. *Chem. Rev.* **1992**, 92, 711.
- <sup>44</sup>Shirakawa, H., Louis, E., McDiarmid, A., Chiang, C., and Heeger, A. J., *J. Chem. Soc. Chem. Commun.*, 1977, 758.
- <sup>45</sup>Skotheim, T. A., Elsenbaumer, R. L., and Reynolds, J. R., *Handbook of conducting polymers 2<sup>nd</sup> edition*, Marcel Dekker, New York, 1988.
- <sup>46</sup>Nalwa, H. S., *Handbook of organic conductive molecules and polymers*, John Wiley and Sons, Chichester, 1997.
- <sup>47</sup>Halls, J. J. M., Walsh, C.A., Greenham, N.C., Marseglia, E.A., Friend, R.H., Moratti, S.C., Holmes, A.B. *Nature* **1995**, 376, 498.
- <sup>48</sup>Sariciftci, N.S., Smilowitz, L., Heeger, A.J, Wudl, F. *Science* **1992**, 258, 1474.
- <sup>49</sup>Friend, R.H., Gymer, R.W., Holmes, A.B., Burroughes, J.H., Marks, R.N., Taliani, C., Bradley, D.D.C.; Dos Santos, D.A., Brédas, J.L., Lögdlund, M., Salaneck, W.R. *Nature* **1999**, 397, 121.

- <sup>50</sup>Li, X.C., Siringhaus, H., Garnier, F., Holmes, A.B., Moratti, S.C., Feeder, N., Clegg, W., Teat, S.J., Friend, R.H. *J. Am. Chem. Soc.* **1998**, *120*, 2206.
- <sup>51</sup>Siringhaus, H., Tessler, N., Friend, R.H. *Science* **1998**, *280*, 1741.
- <sup>52</sup>Brown, A.R., Pomp, A., Hart, C.M., de Leeuw, D.M. *Science* **1995**, *270*, 972.
- <sup>53</sup>Garnier, F., Hajlaoui, R., Yassar, A., Srivastava, P. *Science* **1994**, *265*, 1684
- <sup>54</sup>De Paoli, M. A., and Gazotti, W. A., *J. Braz. Chem. Soc.*, 2002, **13**, 410.
- <sup>55</sup>Saraç, A. S., Sönmez, G., and Cebeci, F. Ç., *J. App. Electrochem.*, 2003, **33**, 295-301.
- <sup>56</sup>L.F. Ferreira, L.M. Souza, D.L. Franco, A.C.H. Castro, A.A. Oliveira, J.F.C. Boodts, A.G. Brito-Madurro, J.M. Madurro, *Materials Chemistry and Physics*, 2011, **129**, 46– 52
- <sup>57</sup>Skotheim, T. A., Reynolds, J. R., (2007) "*Handbook of Conducting Polymers, Third Edition: Conjugated Polymers, Processing and Applications*", Taylor and Francis Group, U.S.A.
- <sup>58</sup>Saunders, B. R., Fleming, R. J., and Murray, K. S., *Chem. Mater.*, 1995, **7**, 1082.
- <sup>59</sup>Moses, P. R., Wier, L., and Murray, R. W., *Anal. Chem.*, 1975, **47**, 1882.
- <sup>60</sup>Alkire, R., Kolb, D., & Lipkowsky, J. (2009): *Chemically modified electrodes*, Weinheim, Germany, Wiley-VCH.
- <sup>61</sup>Street, G. B. and Clarke, T. B., *IBM J. Res. Develop.*, 1981, **25**, 51-57.
- <sup>62</sup>Katz, H. E., Searson, P. C., and Poehler, T. O., *J. Mater. Res.*, 2010, **25**, 8.
- <sup>63</sup>Ates, M., *Materials Science and Engineering*, 2013, **33(4)**, 1853–1859.

- <sup>64</sup>G.A. Snook, P. Kao, A.S. Best, *Journal of Power Sources*, 196 (2011) 1–12
- <sup>65</sup>Michalik, A., and Rohwerder, M., *Z. Phys. Chem.*, 2005, **219**, 1547-1559.
- <sup>66</sup>Spotnitz, R., *IEEE Vehicle Power and Propulsion Conference*, 2005, 344.
- <sup>67</sup> Beresford, A. L., and Hillman, A. R., *Anal. Chem.*, 2010, **82(2)**, 483.
- <sup>68</sup> R.J. Mortimer and N.M. Rowley, Metal complexes as dyes for optical data storage and electrochromic materials, in J.A.McCleverty and T.J. Meyers, eds., *Comprehensive Coordination Chemistry – II: From Biology to Nanotechnology*, Elsevier, Oxford, Volume 9, M.D. Ward, ed (2003)
- <sup>69</sup> Mortimer, R.J.; Dyer, A.L.; Reynolds, J.R. *Displays* **2006**, 27, 2
- <sup>70</sup> Higgins, S.J. *Chem. Soc. Rev.* **1997**, 26, 247
- <sup>71</sup>C.G. Granqvist, *Handbook of Inorganic Electrochromic Materials*, Elsevier, Amsterdam, 1995
- <sup>72</sup> *Handbook of Conducting Polymers*, 2<sup>nd</sup> Ed., Marcel Dekker, New York (1998)
- <sup>73</sup>Sönmez, G., *Chem. Commun.*, 2005, **42**, 5251.
- <sup>74</sup>Sotzing, G. A., Reddinger, J. L., Katritzky, A. R., Soloducho, J., Musgrave, R., and Reynolds, J. R., *Chem. Mater.* 1997, **9**, 1578.
- <sup>75</sup>Fesser, K., Bishop, A. R., and Campbell, D. K., *Phys. Rev.*, 1983, **27**, 4804.
- <sup>76</sup>Sönmez, G., Schwendeman, I., Schottland, P., Zong, K., and Reynolds, J. R., *Macromolecules*, 2003, **36**, 639.

- <sup>77</sup>Skotheim, T. A., Elsenbaumer, R. A., and Reynolds, J. R., *Handbook of Conducting Polymers*, Marcel Dekker, New York, 1998.
- <sup>78</sup> Mudigonda, D.S.K.; Meeker, D.L.; Loveday, D.C.; Osborn, J.M.; Ferraris, J.P. *Polymer* **1999**, 40, 3407
- <sup>79</sup> Sapp, S.A.; Sotzing, G.A.; Reynolds, J.R. *Chem. Mater.* **1998**, 10, 2101
- <sup>80</sup> Meeker, D.L.; Mudigonda, D.S.K.; Osborn, J.M.; Loveday, D.C.; Ferraris, J.P. *Macromolecules* **1998**, 31, 2943
- <sup>81</sup> Oliver, R., Munoz, A., Ocampo, C., Aleman, C., and Estrany, F., *Chem. Phys.*, 2006, **328**, 299.
- <sup>82</sup>Ocampo, C., Aleman, C., Oliver, R., Arnedillo, M. L., Ruiz, O., and Estrany, F., *Polymer Int.*, 2007, **56**, 803.
- <sup>83</sup>Ocampo, C., Aleman, C., Oliver, R., Armelin, E., and Estrany, F., *J. Polymer Res.*, 2006, **13**, 193.
- <sup>84</sup>C. Bersellini, L. Garofano, M. Giannetto, F. Lusardi and G. Mori, *J. Forensic Sci.*, 2001, 46, 871.
- <sup>85</sup>Beresford, A. L. and Hillman, A. R., *Anal. Chem.*, 2010, **82**, 483–486.
- <sup>86</sup>Brown, R.M. and Hillman, A.R., *Phys. Chem. Chem. Phys.*, 2012, **14**, 8653.
- <sup>87</sup>Beresford, A. L., Brown, R. M., Hillman, A. R., and Bond, J. W., *J. Forensic Sci.*, 2011, **57(1)**, 93-102.
- <sup>88</sup>G. L. Thomas and T. E. Reynoldson, *J. Phys. D: Appl. Phys.*, 1975, 8, 724–729.

- <sup>89</sup>Abbott A.P. et al, *Phys. Chem. Chem. Phys.*, 2006, **8**, 4265-4279
- <sup>90</sup> Abbott, A. P., Boothby, D., Capper, G., Davies, D. L. and Rasheed, R. K., *Journal of the American Chemical Society*, 2004, **126**, 9142-9147.
- <sup>91</sup> Abbott, A. P., Capper, G., Davies, D. L. Rasheed, R. K., and Tambyrajah, V., *Chemical Communications*, 2003, 70-71.
- <sup>92</sup>Jones, R. A. L., and Richards, R. W., (1999), *"Polymers at Surfaces and Interfaces"*, Cambridge University Press, Cambridge, UK.
- <sup>93</sup>Lee, E. M., Thomas, R. K., Penfold, J., and Ward, R. C., *J. Phys. Chem*, 1989, **93**, 381.
- <sup>94</sup>Angus-Smyth, A., Campbell, R. A., & Bain, C. D., *Langmuir*, 2012, **28**, 12479-12492.
- <sup>95</sup>Halacheva, S. S., Penfold, J., Thomas, R. K., & Webster, J. R. P., *Langmuir*, 2012, **28**, 6336-6347.
- <sup>96</sup>Campbell, R. A., Yanez Arteta, M., Angus-Smyth, A., Nylander, T., & Varga, I., *J. Phys. Chem.*, 2011, **115**, 15202–15213.
- <sup>97</sup>Wadsater, M., Simonsen, J. B., Lauridsen, T., Grytli Tveten, E., Naur, P., Bjornholm, T., Wacklin, H., Mortensen, K., Arleth, L., Feidenhans, R., & Cardenas, M., *Langmuir*, 2011, **27**, 15065–15073.
- <sup>98</sup>Cardenas, M., Wacklin, H., Campbell, R. A., & Nylander, T., *Langmuir*, 2011, **27**, 12506-12514.
- <sup>99</sup>Zhang, X. L., Penfold, J., Thomas, R. K., Tucker, I. M., Petkov, J. T., Bent, J., Cox, A., & Campbell, R. A., *Langmuir*, 2011, **27**, 11316-11323.
- <sup>100</sup>Thomas, R. K., *Annu. Rev. Phys. Chem.*, 2004. **55**, 391–426.

- <sup>101</sup>Lee, L. T., Langevin, D., Mann, E. K., and Farnoux, B., *Physica B*, 1994, **198**, 83-88
- <sup>102</sup>Zarbaksh, A., Webster, J. R. P., Eames, E., *Langmuir*, 2009, **25 (7)**, 3953-3956.
- <sup>103</sup>Zarbaksh, A., Webster, J. R. P., and Wojciechowski, K., *Langmuir*, 2009, **25 (19)**, 11569-11575,
- <sup>104</sup> T. Cosgrove, J.S. Phipps and R.M. Richardson, *Colloids and Surfaces*, 1992, **62**, 159-206.
- <sup>105</sup>Strutwolf, J., Barker, A. L., Gonsalves, M., Caruana, D. J., Unwin, P. R., Williams, D. E., Webster, J. R. P., *J. Electroanal. Chem.*, 2000, **483 (1-2)**, 163-173.
- <sup>106</sup>Fleer, G. J., and Lyklema, J., (1983), "*Adsorption from Solution at the Solid/Liquid Interface*", Academic Press, New York.
- <sup>107</sup>Fragneto-Cusani, G., *J. Phys. Cond.Matter*, 2001, **13**, 4973-4989.
- <sup>108</sup>Penfold, J., Tucker, I. M., Thomas, R. K., *Langmuir*, 2005, **21**, 6330-6336.
- <sup>109</sup>Béziel, W., Fragneto, G., Cousin, F., and Sferrazza, M., *Phys. Rev. E.*, 2008, **78**, 22801.
- <sup>110</sup>Mitchell, W. J., Burn, P. L., Thomas, R. K., Fragneto, G., *J. Appl. Phys.*, 2004, **95 (5)**, 2391-2396.
- <sup>111</sup>Mitchell, W. J., Burn, P.L., Thomas, R.K., Fragneto, G., *Appl. Phys. Lett.*, 2003, **82**, 2724-2726.
- <sup>112</sup>Furrer, A., Mesot, J., Strässle, T., (2009) "*Neutron Scattering in Condensed Matter Physics*", World Scientific Publishing Co. Ltd, Singapore.

- <sup>113</sup>Squires, G. L., (1997), *“Introduction to the Theory of Thermal Neutron Scattering”*  
Dover Publications, New York, USA.
- <sup>114</sup>Willis, B. T. M., and Carlile, C. J., (2009), *“Experimental Neutron Scattering”*, Oxford  
University Press.
- <sup>115</sup>Brückel, T., Heger, G., Richter, D., Roth, G., and Zorn, R., (2010), *“Neutron Scattering”*,  
Forschungszentrum Jülich GmbH, Jülich, Germany.
- <sup>116</sup>Hippert, F., Geissler, E., Hodeau, J. L., Lelièvre-Berna, E., and Regnard, J. R., *“Neutron  
and X-ray Spectroscopy”*, Springer, Dordrecht, Netherlands.
- <sup>117</sup>Langridge, S., and Lovesey, S. W., *Radiation Physics and Chemistry*, 2001, **61**, 235-239.
- <sup>118</sup>Vettier, C., *Radiation Physics and Chemistry*, 2001, **61**, 235-239.
- <sup>119</sup>Ressouche, E., *Physica B: Condensed Matter*, 1999, **267**, 27-36
- <sup>120</sup>Weinberg, A. M., and Wigner, E. P., (1958), *“The Physical Theory of Neutron Chain  
Reactors”*, University of Chicago Press, USA.
- <sup>121</sup>Harvey, B. G., (1959), *“Progress in Nuclear Physics (Vol. 7)”*, Pergamon Press, Oxford,  
UK.

# 2. Methodology

---

## 2.1. Electrochemical Methods

Electrochemistry is the study of electron transfer reactions between electrodes and reactant molecules from a surrounding electrolyte i.e. the exchange between electrical and chemical energy. It has a wide range of applications including batteries<sup>1-7</sup>, corrosion protection<sup>8-13</sup>, electrowinning<sup>14-19</sup>, biosensors<sup>20-25</sup>, light emitting devices (LEDs)<sup>26-31</sup> and electrochromic devices<sup>32-37</sup>.

Electrochemical processes utilize oxidation and reduction reactions. Oxidation involves the loss of one or more electrons from a chemical species while a reduction is the gain of one or more electrons by a chemical species. During a redox reaction, electrons are transferred from the oxidized species, to the reduced species. This flow of electrons can either be spontaneously produced by the reaction and converted into electricity, as in a galvanic cell, or it can be imposed by an outside energy source to make a non-spontaneous reaction proceed, as in an electrolytic cell.

An electrochemical reaction is a chemical reaction that occurs when a voltage is applied (electrolysis), or a chemical reaction that produces a voltage (battery). The rates of these reactions can be controlled via electrode potential, the reactivity of the electrolyte, the nature of the electrode surface and the structure of the electron transfer interface<sup>38</sup>.

### 2.1.1. Cyclic Voltammetry

Voltammetric methods measure electrode currents as a function of potential in order to determine composition or reactivity of an analyte or to allow control over the rate and extent

of polymer deposition<sup>39,40</sup>. This technique was employed to electropolymerise homopolymer and copolymer modified electrodes in this thesis.

Cyclic voltammetry (CV) is one of many electrochemical techniques performed in a three electrode system consisting of a working electrode, a reference electrode and a counter electrode. The working electrode is the site of the reaction of interest, and a reference electrode has a known potential and is used to set the potential of the working electrode. A counter electrode connected to a potentiostat is used to ensure that no current flows through the reference electrode which could result in a change in its potential.

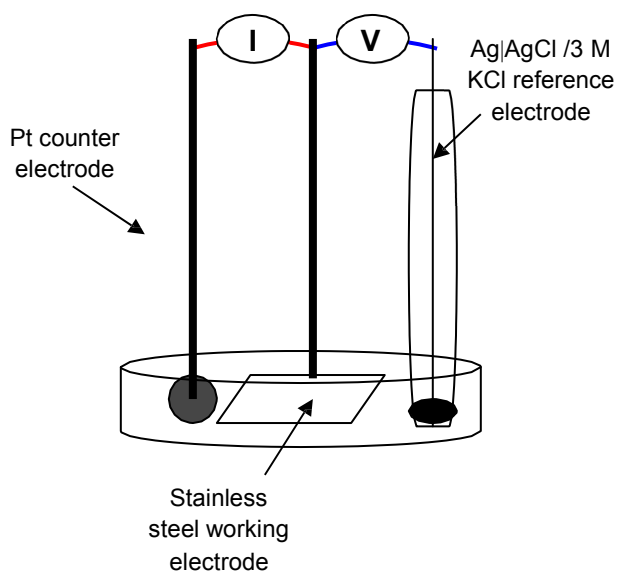


**Figure 2.1.** Schematic diagram of a three electrode cell.

Cyclic voltammetry involves linearly scanning the potential of the working electrode which is immersed in a solution containing an electrolyte (a solution containing free ions) and measuring the resulting current. The speed at which the potential is scanned is known as the scan rate ( $V s^{-1}$ ). The electrolyte solution contains an electroactive species R (in this case a monomeric species), which can undergo oxidation to form O (oxidised monomer) as seen in **Equation 2.1**.



Equation 2.1

If the rate of electron transfer is relatively fast, the forward (oxidation) and reverse (reduction) current peaks will be of the same magnitude and separated by a potential difference that is independent of scan rate. During the forward scan the potential is positively scanned from the initial potential to a value that is sufficiently oxidising for the electroactive species (R). At this point the current (I) starts to increase as the electroactive species (R) present on the working electrode becomes oxidised. Once all the R near the electrode has been oxidised to O, the current peaks ( $i_{pc}$ ) at potential  $E_{pc}$  and starts to decrease following a  $t^{1/2}$  decay as the process becomes diffusion dependant until the vertex potential ( $E_{vertex}$ ) is reached. In the reverse scan the potential is negatively scanned, causing the current to decrease until all of O near the electrode has been reduced, at which point the current peaks (negatively,  $i_{pa}$ ) at potential  $E_{pa}$  and starts to increase until the initial potential is reached and the scan is finished. This concept is illustrated in **Figure 2.2**:

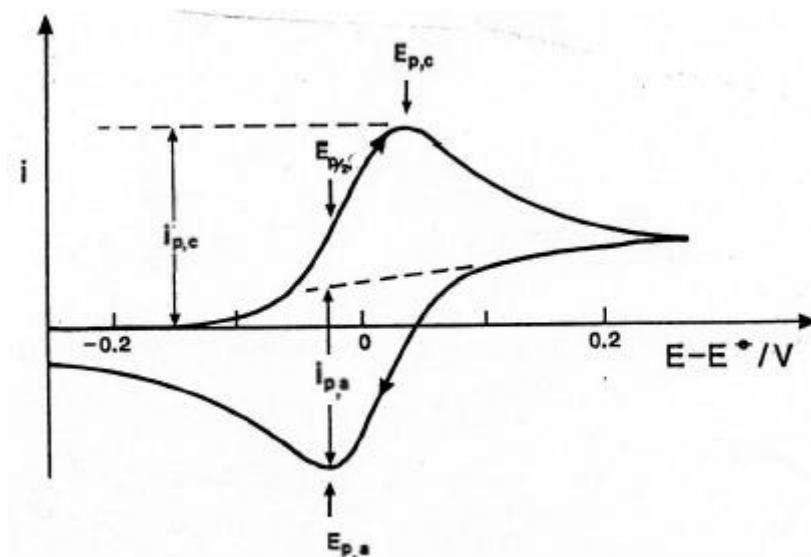


**Figure 2.2** Typical CV for a reversible 1 electron transfer reaction for which both oxidised and reduced species are in solution.



If all available sites are converted, this can then be used to calculate the molar coverage of the polymer, per unit area:

$$\Gamma = \frac{Q}{nFA} \quad \text{Equation 2.4}$$

where  $\Gamma$  is the molar coverage ( $\text{mol cm}^{-2}$ ),  $n$  = number of electrons lost from a single monomer unit during oxidation,  $F$  is Faraday's constant ( $\text{C mol}^{-1}$ ) and  $A$  is the area of the working electrode covered by the polymer ( $\text{cm}^2$ ).

Using this molar coverage along with the density and molar mass of the monomer, the thickness of the compact, solvent-free film can be calculated from **Equations 2.5** and **2.6**.

$$d = \frac{c}{\rho} \quad \text{Equation 2.5}$$

where  $c$  and  $\rho$  are the concentration and density of the monomer respectively and  $M_r$  is its molecular mass.

$$h_f = \frac{Q}{nF\rho} \quad \text{Equation 2.6}$$

where  $h_f$  = film thickness.

However, upon solvation these values might be expected to increase by 50-100 % as solvent volume fractions ( $\phi_{\text{solvent}}$ ) for electroactive polymer films are typically in the range of 0.3 - 0.5<sup>42-44</sup>. These thicknesses are only estimates based on the surface coverage of the polymer and assume complete film redox conversion on the experimental timescale. Neutron reflectivity can be used to accurately determine physical film thickness, both when dry and solvated, as well as determining precise solvation levels.

To calculate an estimate of the absorbance of the polymer films, the extinction coefficient ( $\text{L mg}^{-1} \text{cm}^{-1}$ ) is used along with the molar coverage.

**Equation 2.7**

where  $A$  = absorbance and  $\epsilon$  = extinction coefficient.

## **2.2. Microscopy**

### **2.2.1. Atomic Force Microscopy**

Atomic force microscopy (AFM) is a form of scanning probe microscopy that measures the topography of a surface. Using this instrument nanometre resolution can be achieved. The AFM works by rastering a cantilever (in this case silicon), with a sharp tipped probe, across the sample surface using a piezoelectric scanner. Variations in the height of the sample surface cause the cantilever to deflect up or down. The tip is mounted on a cantilever that reflects a laser, such that the tip and cantilever can move in response to the interatomic forces at the surface and the laser can detect this movement<sup>45</sup>. The forces experienced by the tip are a measure of the distance between the tip and the surface. In order to obtain a measurement, the position of the probe is monitored using the deflection of a laser beam onto an array of photodiodes<sup>46</sup> and the displacement of the tip is converted into a three dimensional image of the surface features.

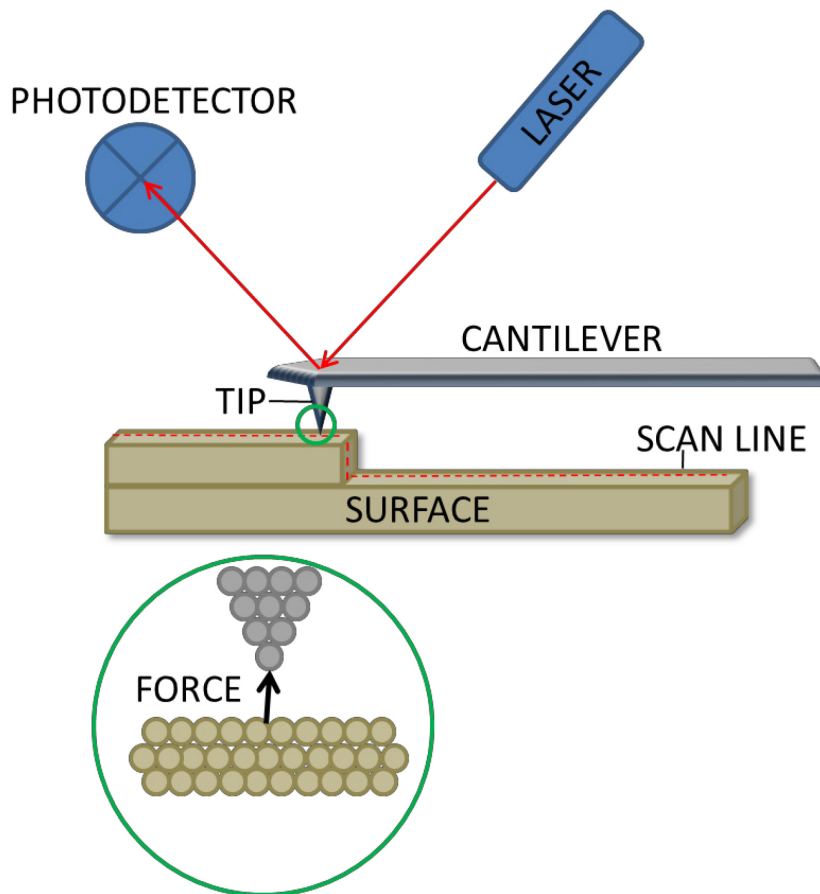


**Figure 2.3.** Schematic of an AFM.

There are three types of operating modes employed by the AFM, contact, non-contact and tapping mode. In contact mode, the repulsive forces between the surface and the probe are measured. This mode is destructive as it involves dragging the tip of the probe across the surface. Non-contact mode, on the other hand, is non-destructive as the probe is held a small distance above the sample surface. As a result of this distance, it is the attractive Van der Waals forces acting between the tip and the sample that are measured. As these forces are weak in comparison to those used in contact mode, the tip must be given a small oscillation to magnify the signal. Similarly, in tapping mode, the cantilever is oscillated using an external drive signal. This allows the intermittent probing of the attractive and repulsive interactions between the tip and the surface. In this mode, the frequency and phase of the cantilever oscillation are measured to obtain information on the sample surface. Scanning the tip at a

constant height would risk the tip of the probe colliding with the surface, causing damage. To avoid this, the tip-to-sample height is adjusted to maintain a constant force between the tip and the sample.

The main advantage of the AFM over other surface microscopy techniques is that it gives a three-dimensional surface profile but, unlike scanning tunnelling microscopy (STM), the surface does not have to be conducting. Additionally, samples viewed by AFM do not require any special treatments (metal/carbon coatings), that would irreversibly change the surface. It can also provide atomic scale resolution<sup>41</sup>. The limitations of the instrument mean that the sample must be small enough to mount. Also, the resolution and image quality obtained are dependent on the size and shape of the probe. Finally, highly sensitive instruments have a limited scan range.

The AFM used in this thesis consisted of a Veeco Dimension 3100 Scanning Probe Microscope that was operated by a computer using Nanoscope 6.12r1 software. The tips used were supplied by Veeco (model: RTESP, part: MPP-11100-10). The calibration of the instrument was checked by scanning over a silicon wafer reference. The image/scan size was 1 – 100  $\mu\text{m}^2$  with a scan rate of 0.6 Hz/120  $\mu\text{m s}^{-1}$ .

### **2.2.2. Optical Profilometry**

An optical profiler provides a 3D optical microscope image. Optical profiling, as opposed to stylus based profiling, is always non-contact. It measures height (the Z-axis) by combining the regions in focus from multiple optical microscopy images of X and Y lateral dimensions taken at a series of different step heights. Stylus based profilometers are, by nature, 2D as the stylus is rastered across the surface, sampling the height over a series of lines. Optical profiling allows the measurement of surface height and roughness in three dimensions using non-contact scanning. This provides a true colour 3D image with height information that is otherwise lost in a traditional 2D optical microscope image.

## 2.3. Spectroscopy

### 2.3.1. Fourier Transform Infrared Spectroscopy

Fourier transform infrared spectroscopy (FTIR) is a technique which is used to obtain an infrared spectrum of absorption from a sample. When exposed to infrared radiation, molecules absorb radiation of specific wavelengths which causes the change of dipole moment and the vibrational energy levels change from ground state to excited state. The frequency of the absorption peak is determined by the vibrational energy gap. The term Fourier transform refers to the mathematical process required to convert the raw frequency versus absorbance data to the corresponding IR spectrum<sup>47</sup>. IR spectroscopic methods are useful for the characterization of surface and thin film species in electrochemistry<sup>48-54</sup>. Reflectance FTIR spectra were acquired with p-polarised radiation incident at a reflectance angle of 55° using a Spectra-Tech reflectance accessory mounted on a Bomem MB120 infra-red instrument or with a Spotlight 400 SYS.

### 2.3.2. X-ray Photo Electron Spectroscopy

X-Ray Photoelectron Spectroscopy (XPS) or Electron Spectroscopy for Chemical Analysis (ESCA) is a surface sensitive technique (<10 nm) that can be used to determine elemental composition, chemical and electronic states. It has been widely used for studying electroactive polymer surfaces<sup>55-60</sup>. XPS is based upon the photoelectric effect; the phenomenon whereby a beam of x-rays of sufficient energy is used to excite the sample resulting in the ejection of so called photoelectrons (photoemission). The kinetic energy of the released photoelectrons is small, which limits the escape depth, so XPS is a surface sensitive probe, and unique to its environment (elemental, chemical and electronic). Therefore, the kinetic energy ( $E_k$ ) of the photoelectrons is measured and used to calculate the binding energy ( $E_b$ ) of the electron, prior to ejection, for a particular energy level using the Einstein relationship:

**Equation 2.8**

Plotting the number of photoelectrons detected against the binding energy generates a XPS spectrum. As this  $E_B$  is characteristic of a specific element, it can identify materials with unknown composition. The ratio of the peak areas can be used (incorporating instrument sensitivity factors and elemental cross sections) to determine the elemental composition of a surface. The shape of the peaks, along with the binding energy, is dependent on the environment of the component atom. An offset in the expected  $E_B$  is known as a chemical shift, which is defined as the difference in  $E_B$  values of one specific chemical state versus the BE of the pure element. The extent of this shift depends on the degree of electron bond polarization between the peak element and its neighbouring atoms. Peaks derived from peak-fitting a raw chemical state spectrum are due to the presence of different chemical states. As a result, XPS can also provide chemical bonding information.

## 2.4. Neutron Reflectivity

The principles behind neutron scattering were described in **Chapter 1.8**. Neutron reflectivity is used to probe the structure of flat, thin films such as conducting polymers<sup>61-67</sup>. Both static and time resolved measurements allow changes in composition, solvation and structure to be monitored during electrochemical and chemical reactions. This ability to probe internal structures in a spatially resolved manner, whilst maintaining sensitivity to chemical speciation, makes neutron reflectivity an invaluable characterisation tool. Neutron reflectivity is analogous to ellipsometry but instead of using light scattering to probe changes in refractive index, neutron scattering is used to probe changes in scattering length densities.

When a neutron beam encounters a lattice of point scatterers separated by a distance ( $d$ ) it is scattered simultaneously by the different points within the lattice<sup>68</sup>. **Figure 2.4** shows how scattering from different planes within the lattice structure provides constructive interference according to Bragg's law. Bragg diffraction occurs when two beams of equal wavelength and

phase are scattered from two atoms within neighbouring planes of a crystalline structure. The beam diffracted from the lower plane traverses an extra distance of  $2d \sin\theta$  (see **Figure 2.4/Equation 2.9**). If this distance is equal to an integer of the wavelength then the two beams remain in phase. This causes constructive interference, which produces a Bragg peak in the diffraction pattern. This allows probing of nanoscale structures, i.e. if  $d = 5 \text{ nm}$  and  $\theta = 3^\circ$  then  $\lambda = 5 \text{ \AA}$ . The distance between the two beams should be a multiple of the wavelength to obtain constructive interference.

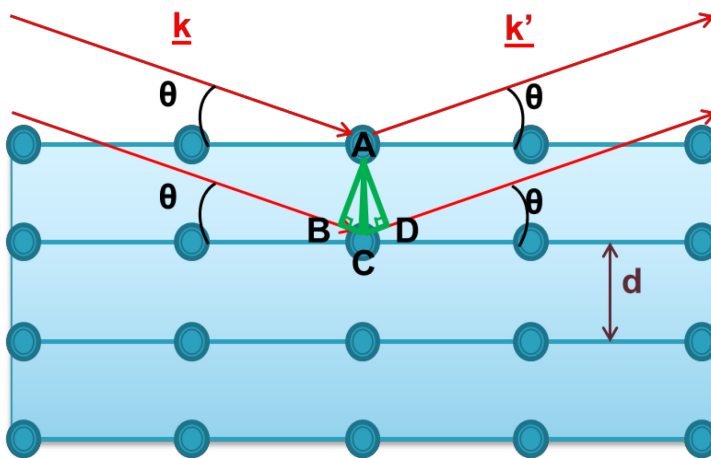


**Figure 2.4.** Elastic scattering of incident wave vector ( $k$ ) at a lattice point to give a reflected wave vector ( $k'$ ).

$$AC = d$$

$$BC = CD = d \sin \theta$$

$$BCD = 2d \sin \theta = n\lambda$$

**Equation 2.9**

Generally speaking there are two types of scattering that occur when a neutron interacts with a nucleus: elastic and inelastic. During elastic scattering, the kinetic energy of the reflected beam is the same as the incident beam, whereas in inelastic scattering the two energies are different. An example of elastic scattering is shown in **Figure 2.5**.

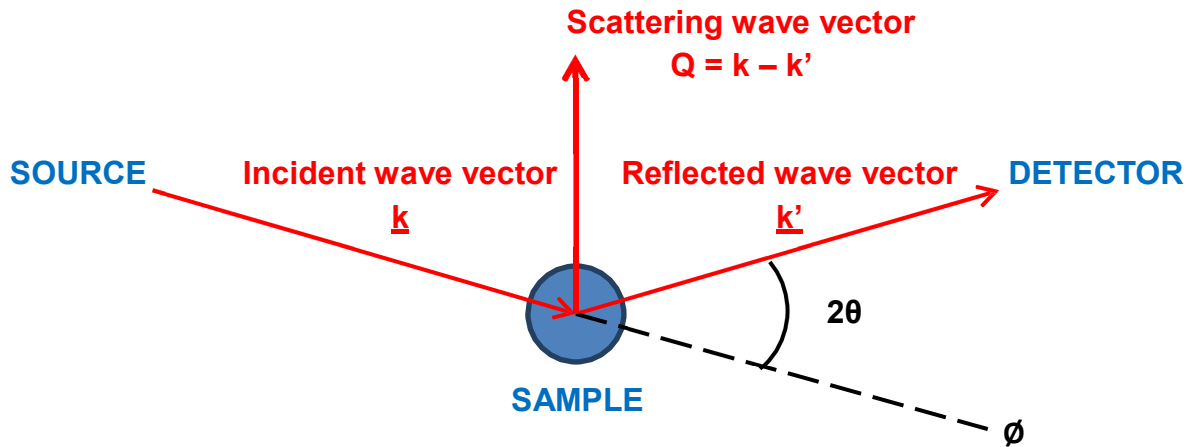


**Figure 2.5.** Cartoon representation of elastic scattering from a sample.

When a neutron from the incident wave vector  $k$  is elastically scattered it forms a reflected wave vector  $k'$  which has the same energy as  $k$ .

$$|k| = |k'| \tag{Equation 2.10}$$

$Q$  is the scattering wave vector/momentum transfer perpendicular to the interface and is given by the difference between the incident and reflected wave vectors.

$$Q = k - k' \tag{Equation 2.11}$$

$$Q = 2k \sin \theta \tag{Equation 2.12}$$

where  $\theta$  is the angle of incidence.

$$Q = 2k \sin \theta \tag{Equation 2.13}$$

When a neutron beam interacts with a nucleus it is scattered. Elastic scattering occurs mainly in solid, crystal structures where the scatterers are fixed in space. Therefore, none of the energy from the neutron beam is converted to kinetic energy. Elastic scattering occurs when the mass of the scatterers is high ( $m_{scatterer} \gg m_{neutron}$ ) and the temperature is low ( $k_B T \ll E_{neutron}$ ). However, if the scatterers are moving or are moved by the neutron, for example in a

liquid or a gas, then an energy transfer occurs resulting in inelastic scattering. This happens when the mass of the scatterers is low ( $m_{scatterer} \approx m_{neutron}$ ) and temperature is high ( $k_B T \approx E_{neutron}$ ).

Specular reflectivity, as shown in **Figure 2.6**, occurs if a surface is atomically flat.

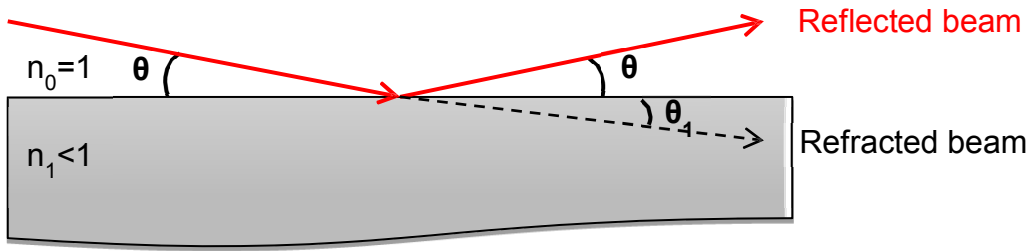


**Figure 2.6.** Total external reflection occurs when  $\theta_{incidence} < \theta_{critical}$ .

where  $n$  is the refractive index,  $\theta$  is the angle of incidence and  $\theta_1$  is the angle of refraction.

$$n_0 \sin \theta = n_1 \sin \theta_1 \tag{Equation 2.14}$$

where  $N_b$  is scattering length density and  $\delta$  is dispersion in the order of  $10^{-5} - 10^{-6}$ . This value is positive for most materials, as the scattering length is positive for most isotopes. Therefore,  $n$  is smaller than one and the transmitted beam refracts towards the interface.

$$n_1 = 1 - \delta \tag{Equation 2.15}$$

When  $n_1$  is less than 1, the neutron beam is refracted towards surface/interface. At a critical angle ( $\theta_c$ ) total external reflection occurs and  $\theta_1$  is zero.

$$\sin \theta_c = n_1 \tag{Equation 2.16}$$

If the angle is small, as it is in neutron reflectivity then **Equation 2.17** is obeyed.

(— )

Equation 2.17

If there is a single layer on the surface of the substrate then specular reflection occurs at both the surface and the interface allowing laterally averaged depth profiling.

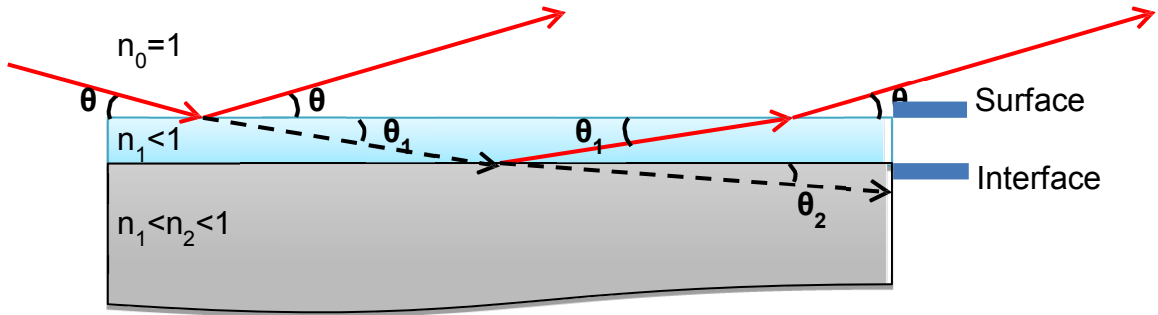


Figure 2.7. Specular reflection at both the surface and interface.

If the interface is rough then both specular and off-specular reflectivity occur providing information about the both the spatial and lateral planes.

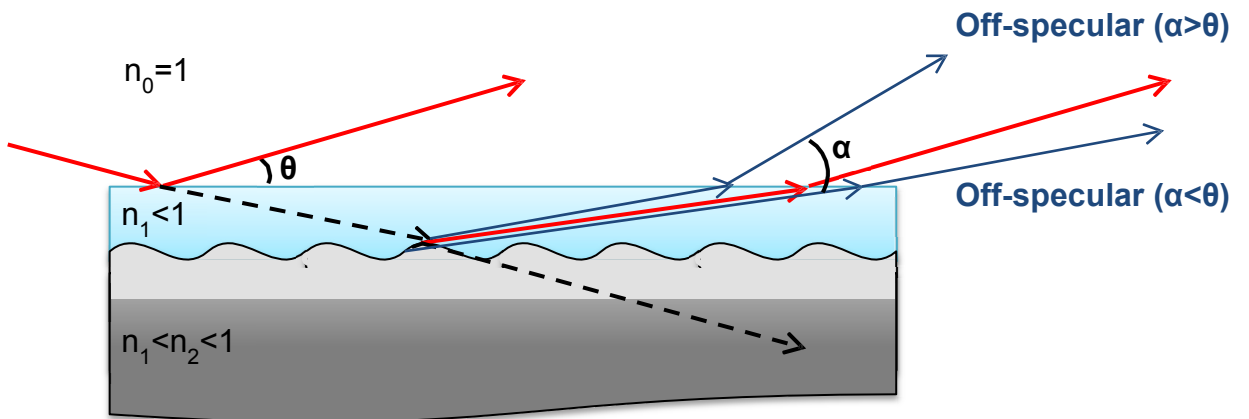


Figure 2.8. Off-specular reflection from a rough interface.

Neutron scattering experiments involve measuring the scattering wave vector ( $Q$ ) as a function of scattering intensity. This intensity is proportional to the cross section. The total neutron scattering cross section ( $\sigma_{tot}$ ) is for all neutrons scattered in any direction both elastically and inelastically.

$$\sigma_{\text{tot}} = x/\phi_0$$

Equation 2.18

where  $x$  is the total number of neutrons scattered per second and  $\phi_0$  is the incident neutron flux. The differential cross section selects only the neutrons scattered onto the detector over a solid angle ( $d\Omega$ ) as a result of elastic scattering in the direction  $2\theta$  and  $\phi$  (as shown in **Figure 2.9**).

---

Equation 2.19

where  $R$  is the rate of arrival of neutrons ( $s^{-1}$ ) onto the detector in the solid angle of  $\Delta\Omega$  (steradians) and  $N$  is the number of scatterers.

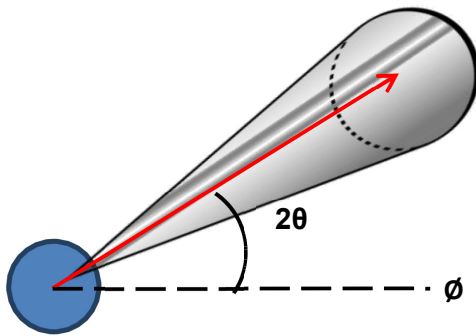


**Figure 2.9.** Solid angle  $d\Omega$  of neutrons on the detector.

This differential cross section contains contributions from both elastic and inelastic scattering. In order to separate these two components, a reflected wave energy must be selected. This provides the double differential cross section for inelastic scattering.

---

Equation 2.20

where  $R_{dE}$  is the rate of arrival of neutrons with a given energy range between the incident energy ( $E$ ) and the reflected energy ( $E + dE'$ )<sup>69</sup>.

Neutron reflectivity experiments involve measuring the intensity of reflected neutrons as a function of either wavelength ( $\lambda$ , time of flight mode) or angle of incidence ( $\theta$ , monochromatic mode) to yield a reflectivity profile of  $R$  versus  $Q$ .

Reflectivity is a function of the incident and transmitted wave vectors ( $k$  and  $k_i$ ).

Equation 2.21

where  $r$  is the probability amplitude of reflection.

$$[ \quad ]$$

Equation 2.22

where  $R_f$  is the Fresnel reflectivity  $Q_c$  is the point at which total internal reflection occurs.

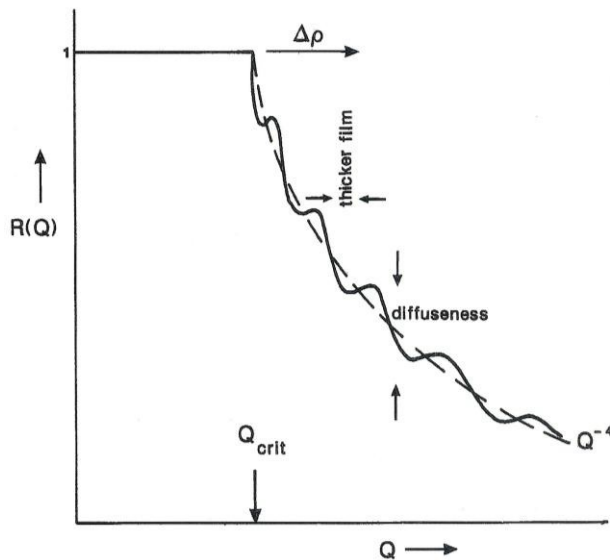


**Figure 2.10.** A typical reflectivity plot<sup>70</sup>.

The shape of the reflectivity profile yields information about the different layers causing the constructive interference. The height of the fringes is determined by the difference in scattering length densities of the different layers. The  $Q$  value corresponding to the critical edge,  $Q_c$ , is determined by the difference in the neutron scattering length densities of the two bulk materials,  $\Delta N_b$ .

/

**Equation 2.23**

Film thickness can be determined by the distance between the maxima of the fringes ( $\Delta Q$ ) which arise from the reflections at the interfaces of a layer as shown in **Figure 2.7**.

—

**Equation 2.24**

, therefore —

**Equation 2.25**

—, therefore —

**Equation 2.26**

The range of film thickness that can be measured is between 250-900 Å due to instrumental restrictions, which mean only a limited range of  $Q$  can be accessed due to restrictions to wavelength and  $\theta^{71}$ . This range is typically  $5 \times 10^{-3} - 0.12 \text{ \AA}^{-1}$  and resolution limits mean that there is essentially a data point every  $2.4 \times 10^{-3} \text{ \AA}^{-1}$ . Using **Equation 2.26** to estimate  $\Delta Q$  for layers 250 and 900 Å thick gives values of 25 and  $7 \times 10^{-3} \text{ \AA}^{-1}$ , respectively. In the first instance, this would only give up to four fringes over the accessible  $Q$  range, whilst in the latter there would be less than three data points per fringe. In both cases data fitting will be harder and more unreliable.

Roughness of the surface/interface ( $\sigma$ ) relates to the transition distance at an interface over which a change in  $N_b$  occurs (FWHM of the Gaussian in the  $N_b$  gradient at the interface). Experimentally, this can be observed as a drop in the reflectivity curve and by smoothing of the fringes.

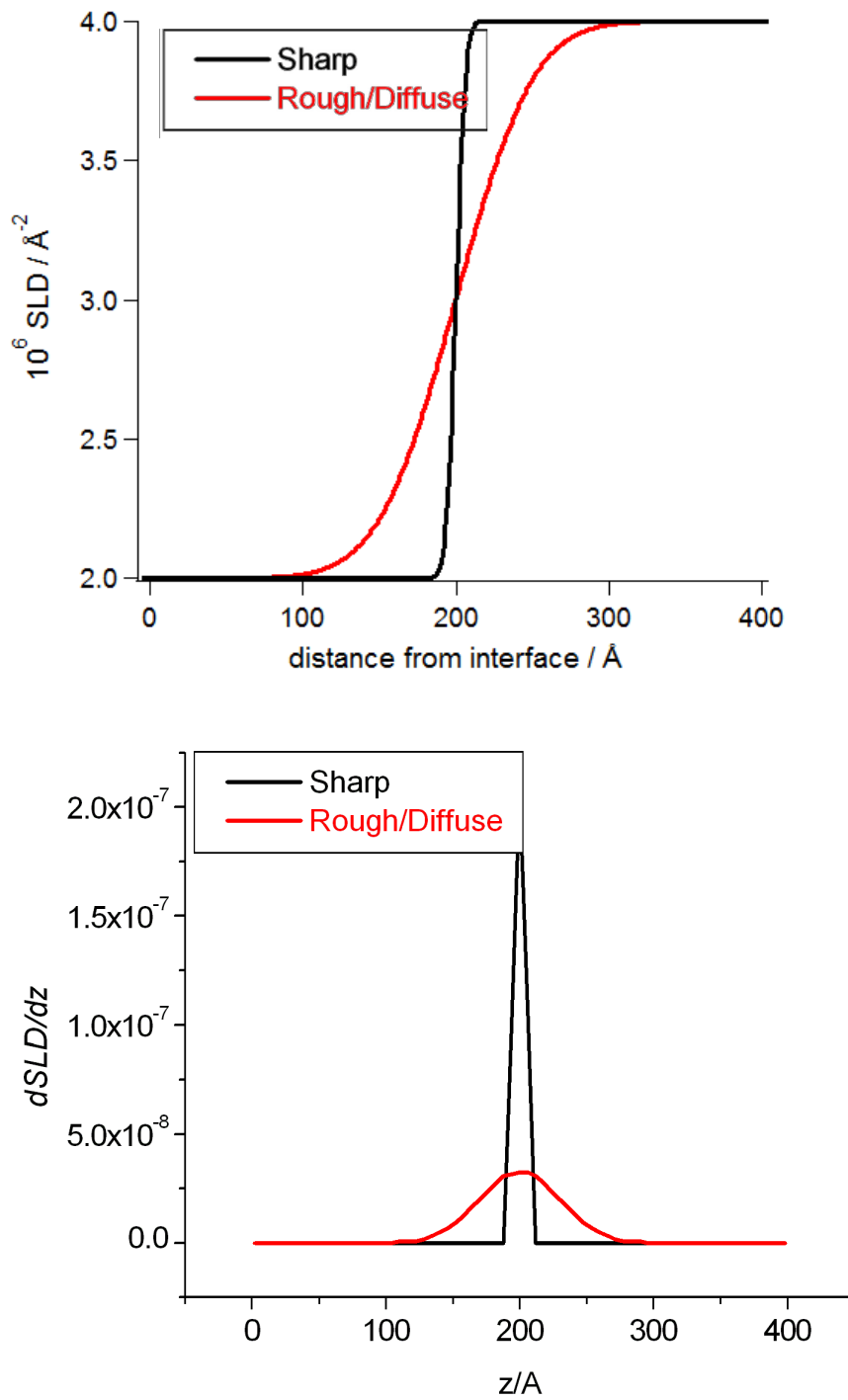


**Figure 2.11.** Scattering length density profile of a sharp and rough/diffuse interface (top) and the corresponding derivative of the step function (bottom).

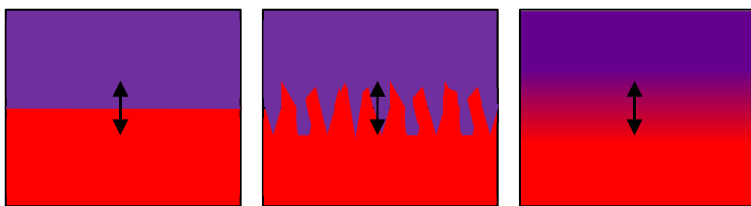


**Figure 2.12.** Schematic of sharp (left), rough (centre) and diffuse (right) interfaces.

Neutron reflectivity experiments were performed on D17<sup>72</sup> and FIGARO<sup>73</sup> at the Institute Laue Langevin, Grenoble, France and on INTER<sup>74</sup> and OFFSPEC<sup>75</sup> at ISIS, Oxford, UK. Measurements were performed in time-of-flight (TOF) mode. The scattering angle,  $\theta$ , is kept constant during any given measurement and all the available wavelengths in the beam are used. Multiple reflection angles are used to cover the desired range of  $Q$ . The equipment itself consists of: a radiation source, a wavelength selector or chopper(s), a system of collimation, sample chamber and a detector. The aim is to measure the reflectivity as a function of the wave vector ( $Q$ ), which is perpendicular to the reflecting surface (see **Figure 2.5**).

Measurements were taken for both dry films and films which were immersed in different electrolyte solutions using a specially designed electrochemical cell.

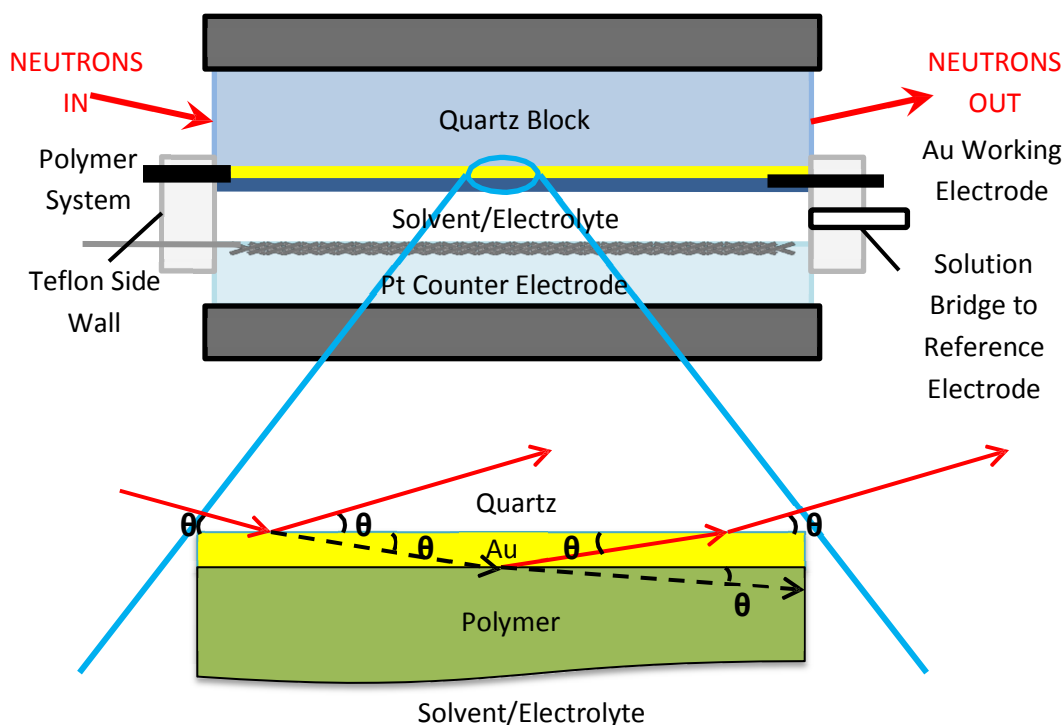


**Figure 2.13.** Schematic diagram of the electrochemical neutron reflectivity cell.

The cell consisted of Teflon walls with several valves to allow solvent uptake and the addition of counter and reference electrodes if the reflectometry was combined with electrochemical measurements. A glass block with Pt gauze formed the counter electrode and the quartz working electrode completed the cell (approximate working area = 18 cm<sup>2</sup>).

Once mounted in the sample chamber it was then roughly aligned using a laser. The detector was set at the correct specular scattering angle, and the height and angle of the sample to the beam were scanned for maximum intensity to the detector before being set to the optimum value.

### 2.4.1. Data Analysis

The variation with momentum transfer of reflectivity from an interface,  $R(Q)$ , is determined by the depth profile of the scattering length density  $N_b$ , where  $N$  represents the concentration of scattering atoms present and  $b$  is their scattering length. Scattering length is isotopically unique and medium independent. The scattering length density of a composite medium, for

example a solvated polymer film, is a weighted sum of the  $N_b$  values of its components with respect to the volume fractions of those components. Experimentally, this allows the tracking of any changes in film composition through changes in scattering length density and reflectivity.

#### 2.4.1.1. Reduction of Raw Data

To gain a reflectivity profile over a wide range of  $Q$  requires the use of multiple angles of incidence (**Equation 2.24**). The data from the different angles are then stitched together using a small region of  $Q$  where the two angles overlap. The data are then normalised so that the plateau before the critical edge is at 0.

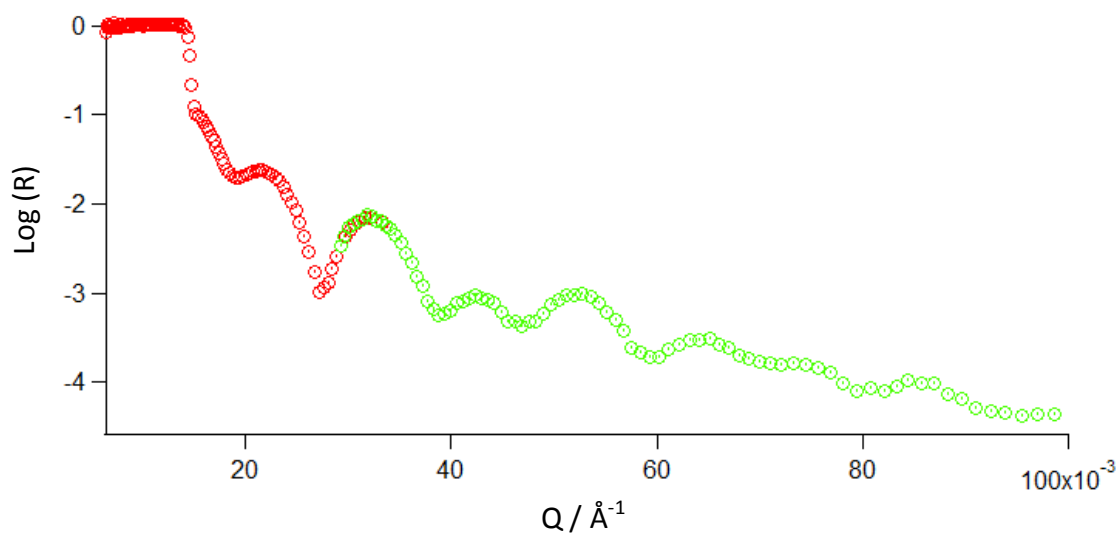


**Figure 2.14.** Example of combining  $Q$  ranges obtained from a small angle of incidence (red) and a large angle of incidence (green) to cover a wider range of  $Q$ .

All ILL data were reduced in LAMP<sup>76</sup> and ISIS data were reduced using either Open Genie or Mantid. These are all programs provided by the large scale facilities for raw data conversion for subsequent analysis.

### **2.4.1.2. Data Fitting**

Once the raw data have been spliced together it can then be imported into the fitting software Motofit<sup>77</sup>. This software uses genetic optimisation to allow the user to perform a rough fit, based on their knowledge of the system, and Levenberg-Marquardt fitting to finalise the fit to the lowest value of chi-squared ( $\chi^2$ ). Chi-squared is used as a means of evaluating the discrepancy between the data points and the reflectivity generated by the fitting function or model. Levenberg-Marquardt is a type of iterative fitting that attempts to minimize the chi-squared error. It is assumed that when the difference between the data and the model reflectivity profile approaches zero, the resultant scattering length density profile accurately represents the vertical composition and structure of the sample.

The Motofit software also allows for batch fitting of multiple datasets in different contrasts.

There are 4 parameters to fit for each layer within the system: thickness ( $d/\text{\AA}$ ), scattering length density ( $N_b/\text{\AA}^{-2} \times 10^{-6}$ ), roughness ( $\sigma/\text{\AA}$ ) and solvation (% v/v).

## 2.5. References

- <sup>1</sup>Suzuki, N., Cervera, R. B., Ohnishi, T., *J. Power Sources*, 2013, **231**, 186-189.
- <sup>2</sup>Vinodh, R., Sangeetha, D., *J. Appl. Polymer Sci.*, 2013, **128**, 1930-1938.
- <sup>3</sup>Shironita, S., Karasuda, K., Sato, M., *J. Power Sources*, 2013, **228**, 68-74.
- <sup>4</sup>Zhao, T., Chen, S., Li, L., *J. Power Sources*, 2013, **228**, 206-213.
- <sup>5</sup>Laoire, C. O., Mukerjee, S., Abraham, K. M., Plichta, E. J., Hendrickson, M. A., *J. Phys. Chem.*, 2010, **114 (19)**, 9178-9186.
- <sup>6</sup>Zaghib, K., Armand, M., and Gauthier, M., *J. Electrochem. Soc.*, 1998, **145 (9)**, 3135-3140.
- <sup>7</sup>MacDiarmid, A. G., YANG, L. S., HUANG, W. S., HUMPHREY, B. D., *Synthetic Metals*, 1987, **18 (1)**, 393-398.
- <sup>8</sup>Quiroga-Arganaraz, M. P., Ribotta, S. B., Folquer, M. E., *J. Solid State Electrochem.*, 2013, **17(2)**, 307-313
- <sup>9</sup>Park, S. A., Lee, S. H., Kim, J. G., *Metals & Materials Int.*, 2012, **18 (6)**, 975-987.
- <sup>10</sup>Mansfeld, F., *J. Appl. Electrochem.*, 1995, **25 (3)**, 187-202.
- <sup>11</sup>Sahu, S. C., Samantara, A. K., Seth, M., Parwaiz, S., Singh, B. P., Rath, P. C., Jena, B. K., *Electrochem. Commun.*, 2013, **32**, 22-26.
- <sup>12</sup>Huang, T. C., Yeh, T. C., Huang, H. Y., Ji, W. F., Chou, Y. C., Hung, W. I., Yeh, J. M., Tsai, M. H., *Electrochimica Acta*, 2011, **56 (27)**, 10151-10158.
- <sup>13</sup>Grundmeier, G., Schmidt, W., Stratmann, M., *Electrochimica Acta*, 2000, **45**, 2515–2533.
- <sup>14</sup>Clancy, M., Bettles, C. J., Stuart, A., *Hydrometallurgy*, 2013, **131**, 144-157.
- <sup>15</sup>Bertuol, D. A., Amado, F. D. R., Veit, H., *Chem. Eng. Tech.*, 2012, **12**, 2084-2092.
- <sup>16</sup>Nikoloski, A. N., Nicol, M. J., *Mineral Processing & Extracting Metallurgy Review*, 2008, **29 (2)**, 143-172.
- <sup>17</sup>Lantelme, F., and Groult, H., *Mineral Processing & Extractive Metallurgy*, 2010, **119 (2)**, 82-87.
- <sup>18</sup>Mohammadi, M., Mohammadi, F., and Alfantazi, A, *J. Electrochem. Soc.*, 2013, **160 (4)**, 35-43.
- <sup>19</sup>Liu, Z., Yu, X., Xie, G., Lu, Y., Hou, Y., *Hydrometallurgy*, 2012, **125-126**, 29-33.

- <sup>20</sup>Liang, B., Fang, L., Yang, G., *Biosensors & Bioelectronics*, 2013, **43**, 131-136.
- <sup>21</sup>Zhao, M., Huang, J., Zhou, Y., *Biosensors & Bioelectronics*, 2013, **43**, 226-230.
- <sup>22</sup>Pan, Y., Zhang, Y. Z., Li, Y., *J. App. Polymer Sci.*, 2013, **128 (1)**, 647-652.
- <sup>23</sup>Sadik, O. A., Mwilu, S. K., and Aluoch, A., *Electrochimica Acta*, 2010, **55 (14)**, 4287-4295.
- <sup>24</sup>Zhao, J., *Electrochem. Commun.*, 2011, **13 (1)**, 31-33.
- <sup>25</sup>Ronkainen, N. J., Halsall, H. B., and Heineman, W. R., *Chem. Soc. Rev.*, 2010, **39 (5)**, 1747-1763.
- <sup>26</sup>Evans, R.C., Douglas, P., Winscom, C. J., *Coord. Chem. Rev.*, 2006, **250**, 2093.
- <sup>27</sup>Marcilla, R., Mecerreyes, D., Winroth, G., Brovelli, S., Yebra, M. D. R., Cacialli, F., *Appl. Phys. Lett.*, 2010, **96**, 43308.
- <sup>28</sup>Matyba, P., Yamaguchi, H., Chhowalla, M., Robinson, N. D., Edman, L., *ACS Nano.*, 2011, **5 (1)**, 574-580.
- <sup>29</sup>Yu, Z., Niu, X. F., Liu, Z. T., Pei, Q. B., *Adv. Mater.*, 2011, **23 (34)**, 3989-3994.
- <sup>30</sup>Costa, R. D., Orti, E., Bolink, H. J., Graber, S., Housecroft, C. E., Constable, E. C., *J. Am. Chem. Soc.*, 2010, **132 (17)**, 5978-5980.
- <sup>31</sup>Matyba, P., Yamaguchi, H., Eda, G., Chhowalla, M., Edman, L., Robinson, N. D., *Acs Nano*, 2010, **4 (2)**, 637-642.
- <sup>32</sup>Mortimer, R. J., and Varley, T. S., *Solar Energy Materials and Solar Cells*, 2013, **109**, 275-279.
- <sup>33</sup>Thakur, V. K., Ding, G. Q., Ma, J., Lee, P. S., Lu, X. H., *Adv. Mater.*, 2012, **24 (30)**, 4070.
- <sup>34</sup>Nie, G., Zhou, L. J., Guo, Q. F., Zhang, S. S., *Electrochem. Commun.*, 2010, **12 (1)**, 160-163.
- <sup>35</sup>Mortimer, R. J., and Varley, T. S., *Chem. Mater.*, 2011, **23 (17)**, 4077-4082.
- <sup>36</sup>Mallouki, M., Aubert, P. H., Beouch, L., Vidal, F., Chevrot, C., *Synthetic Metals*, 2012, **162 (21)**, 1903-1911.
- <sup>37</sup>Zhao, L., Zhao, L., Xu, Y. X., Qiu, T. F., Zhi, L. J., Shi, G. Q., *Electrochimica Acta*, 2009, **55 (2)**, 491-497.
- <sup>38</sup>Fisher, A. C., (1996): *Electrode Dynamics*, United States, Oxford University Press.
- <sup>39</sup>Bard, A. J., Faulkner, L. R., (2000), "Electrochemical Methods: Fundamentals and Applications (2 ed.)", Wiley, New York, U.S.A.

- <sup>40</sup>Skotheim, T. A., Elsenbauner, P- L., Reynolds, J. R., (1998), "*Handbook of Conducting Polymers*", Merceel Dekker, New York.
- <sup>41</sup>Efimov, I. and Hillman, A. R., *Anal. Chem.*, 2006, **78**, 3616.
- <sup>42</sup>Glidle, A., Hillman, A. R., Ryder, K. S., Smith, E. L., Cooper, J. M., Gadegaard, N., Webster, J. R. P., Dalgliesh, R. M. and Cubitt, R., *Langmuir*, 2009, 25, 4093.
- <sup>43</sup>Glidle, A., Hillman, A. R., Ryder, K. S., Smith, E. L., Cooper, J. M., Dalgliesh, R. M, Cubitt, R. and Geue, T., *Electrochim. Acta*, 2009, **55**, 439.
- <sup>44</sup>Hillman, A. R., Mohamoud, M. A. and Efimov, I., *Anal. Chem.*, 2011, **83**, 5696.
- <sup>45</sup>G. Attard, and C. Barnes, (2008) "*Surfaces*", Oxford University Press.
- <sup>46</sup>D. Sarid, (1991), "*Scanning Force Microscopy*", United States, Oxford Series in Optical and Imaging Sciences, Oxford University Press.
- <sup>47</sup>Griffiths, P., de Hasseth, J.A., (2007) "*Fourier Transform Infrared Spectrometry (2nd ed.)*", Wiley-Blackwell.
- <sup>48</sup>Yavuz, A., Bezgin, B., Onal, A. M., *J. Appl. Polym. Sci.*, 2009, **114**, 2685.
- <sup>49</sup>Posudievsky, O. Y., Goncharuk, O. A., Barille, R., Pokhodenko, V. D., *Synth. Met.*, 2010, **160**, 462.
- <sup>50</sup>Nekrasov, A. A., Gribkova, O. L., Ivanov, V. F., Vannikov, A. V., *J. Solid State Electrochem.*, 2010, **14**, 1975.
- <sup>51</sup>Su, Z. H., Huang, J. H., Xie, Q. J., Fang, Z. F., Zhou, C., Zhou, Q. M., Yao, S. Z., *Phys. Chem. Chem. Phys.*, 2009, **11**, 9050.
- <sup>52</sup>Toth, P. S., Peintler-Krivan, E., Visy, C., *Electrochem. Commun.*, 2010, **12**, 598.
- <sup>53</sup>Parlak, E. A., Sarac, A. S., Serantoni, M., Bobacka, J., *J. Appl. Polym. Sci.*, 2009, **113**, 136.
- <sup>54</sup>Guler, F. G., Sarac, A. S., *Exp. Polym. Lett.*, 2011, **5**, 493.
- <sup>55</sup>Mahmood, N.; Busse, K.; Kressler, J. *J. Appl. Polym. Sci.* **2007**, 104, 1, 479
- <sup>56</sup>Bandeira, M.C.E.; Crayston, J.A.; Franco, C.V.; Glidle, A. *Phys. Chem. Chem. Phys.* **2007**, 9, 1003
- <sup>57</sup>Bach, C.M.G.; Reynolds, J.R. *J. Phys. Chem.* **1994**, 98, 13636
- <sup>58</sup>Schweiger, L.F.; Ryder, K.S.; Morris, D.G.; Glidle, A.; Cooper, J.M. *J. Mater. Chem.* **2000**, 10, 107
- <sup>59</sup>Ryder, K.S.; Schweiger, L.F.; Glidle, A.; Cooper, J.M. *J. Mater. Chem.* **2000**, 10, 1785

- <sup>60</sup>Glidle, A.; Swann, M.J.; Hadyoon, C.S.; Cui, L.; Davis, J.; Ryder, K.S.; Cooper, J.M. *J. Electron Spectrosc. Related Phenom.* **2001**, 121, 131
- <sup>61</sup>Glidle, A., Hillman, A. R., Ryder, K. S., Smith, E. L., Cooper, J., Gadegaard, N., Webster, J. R. P., Dalgliesh, R., Cubitt, R., *Langmuir*, 2009, **25**, 4093-4103.
- <sup>62</sup>Glidle, A., Hillman, A. R., Ryder, K. S., Smith, E. L., Cooper, J., Dalgliesh, R., Cubitt, R., Geue, T., *Electrochimica Acta*, 2009, **55**, 439-450.
- <sup>63</sup>Glidle, A., Hillman, A. R., Ryder, K. S., Smith, E. L., Cooper, J., Dalgliesh, R., Cubitt, R., Pearson, P. E., *J. Phys. Chem.*, 2007, **111**, 4043-4053.
- <sup>64</sup>Glidle, A., Hillman, A. R., Ryder, K. S., Smith, E. L., Cooper, J., Gadegaard, N., Webster, J. R. P., Dalgliesh, R., Cubitt, R., Wilson, R. W., Haydoon, C. S., *J. Phys. Chem.*, 2005, **109**, 14335-14343.
- <sup>65</sup>Glidle, A., Hillman, A. R., Ryder, K. S., Smith, E. L., Cooper, J., Gadegaard, N., Webster, J. R. P., Dalgliesh, R., Cubitt, R., Mortimer, R. J., *J. Am. Chem. Soc.*, 2004, **126**, 15362-15363.
- <sup>66</sup>Glidle, A., Hillman, A. R., Cooper, J., Bailey, L., Jackson, A., and Webster, J. R. P., *Langmuir*, 2003, **19**, 7746-7753.
- <sup>67</sup>Glidle, A., Hillman, A. R., Cooper, J., Bailey, L., Haydoon, C. S., Jackson, A., Webster, J. R. P., , Ryder, K. S., Saville, P. M., Swann, M. J., Wilson, R. W., *Anal. Chem.*, 2001, **73**, 5596-5606.
- <sup>68</sup>Pillai, S. O., (2009), *“Solid State Physics”*, New Age International Ltd, Delhi.
- <sup>69</sup>Silva, D. S., (2011), *“Elemental Scattering Theory”*, Oxford University Press, Oxford, UK.
- <sup>70</sup>[www.ill.fr](http://www.ill.fr)
- <sup>71</sup>Hillman, A.R.; Bailey, L.; Glidle, A.; Cooper, J.M.; Gadegaard, N.; Webster J.R.P. *J. Electroanal. Chem.*, 2002, **532**, 269.
- <sup>72</sup>R. Cubitt\*, G. Fragneto, *Appl. Phys.*, 2002, 74 [Suppl.], S329–S331.
- <sup>73</sup>Campbell, R. A., Wacklin, H. P., Sutton, I., Cubitt, R., Fragneto, G., *Eur. Phys. J. Plus.*, 2011, **126**, 107.
- <sup>74</sup>Webster, J. R. P., Langridge, S., Dalgliesh, R. M., and Charlton, T.R., *Eur. Phys. J. Plus*, 2011, **126**, 112.
- <sup>75</sup>Dalgliesh, R. M., Langridge, S., Plomp, J., DeHaan, V. O., VanWell, A. A., *Physica B*, 2011, **406**, 2346–2349.
- <sup>76</sup>LAMP, the Large Array Manipulation Program.  
[http://www.ill.fr/data\\_treat/lamp/front.html](http://www.ill.fr/data_treat/lamp/front.html)

<sup>77</sup>Nelson, A., *J. Appl. Crystallogr.*, 2006, **39**, 273.

# 3. Electrochromic Enhancement of Latent Fingerprints with Poly-(Pyrrole-co-EDOT)

---

## 3.1. Introduction

The evidential value of fingerprint evidence and the difficulty in capturing it from metallic surfaces is widely recognized. Currently, the most widely used enhancement techniques are powder dusting, cyanoacrylate (superglue) fuming and the use of wet powder. All these techniques rely on an interaction (either physical or chemical) between the applied reagent and the fingerprint deposit in order to visualise the ridge detail. Subsequent application of dyes and/or illumination with light of various wavelengths is also necessary after cyanoacrylate fuming to ensure optimal enhancement<sup>1</sup>. To address this challenge, a new method of latent fingerprint enhancement based on electrochromic conducting polymers has recently been developed using homopolymers of aniline (Ani)<sup>2</sup> and 3,4-ethylenedioxythiophene (EDOT)<sup>3</sup>. A recent comparison survey evaluating the ability of this method to enhance latent fingerprints subject to ageing in a range of environments suggests that there are practically relevant situations in which the methodology may be superior to methods traditionally employed<sup>4</sup>. Such niches include soap washed or heated samples.

Copolymers have been of growing interest in recent years as they show promise as a method of obtaining better electrochromic properties than the corresponding homopolymers<sup>5</sup>. Tao *et al* have shown how the copolymerization of EDOT and pyrrole (Py) may help to overcome the drawbacks of the individual homopolymers<sup>6</sup>. PEDOT is widely used in electrochromic applications as it shows good electrochemical stability as well as a fast switching speed<sup>7</sup>.

However, its low band gap means that PEDOT is restricted to only two colours: light blue in the doped state and dark blue in the neutral state which restricts its potential applications<sup>8</sup>. PPy on the other hand exhibits multi-chromic behaviours with a blue-violet doped state and is yellow/green when neutral<sup>9</sup>. It also has a wider band gap of 2.7 eV. In this instance stability is the restricting factor as PPy films degrade after repetitive redox cycling<sup>10</sup>. Fine-tuning the electrochromic properties of these two conducting polymers can be achieved through copolymerisation. In this chapter, the use of both the Py homopolymer and various ratios of P(Py-co-EDOT) for electrochromic latent fingerprint enhancement will be explored and compared to both PANi and PEDOT electrochromic enhancements as well as three traditional techniques (dusting, wet powder and superglue fuming) and a control<sup>a</sup>.

## **3.2. Experimental**

### **3.2.1. Instrumentation**

#### ***3.2.1.1. Electrochemistry***

An Ivium CompactStat potentiostat running IviumSoft 2.400 was used along with an Ag/AgCl reference electrode and a Pt counter electrode.

#### ***3.2.1.2. Superglue Fuming***

The Sandridge superglue fuming cabinet at the Northamptonshire Police chemical laboratory was used (MVC 5000; Foster and Freeman, Evesham, U.K.).

---

<sup>a</sup> Comparison survey of PEDOT, PANi, dusting, wet powder, superglue and control were all conducted during MChem research project with the aid of Dr Ann L. Beresford<sup>4</sup>.

### ***3.2.1.3. Fingerprint Visualisation***

The samples were photographed using a Canon A480 digital camera and were digitally enhanced using the GNU Image Manipulation Program 2.6.7. (G.I.M.P.). Videos were obtained using a Pentax Optio M40 digital camera. These were enhanced using iWisoft Free Video Converter video enhancement software. Fluorescent superglue samples were imaged with a Fuji Fine Pix S2 Pro digital camera with a 55 mm Nikkor micro lens. A blue, 4x4 Crime Lite (430 – 470 nm) was used along with a filter (476 nm) to obtain fluorescence and a Zeta 200 Optical Profiler was used to obtain 3D microscope images.

### ***3.2.1.4. X-ray Photoelectron Spectroscopy***

X-ray Photoelectron Spectroscopy (XPS) was performed by NEXUS (EPSRC XPS Users' Service) hosted by NanoLAB, University of Newcastle-upon-Tyne. The instrument used was a K-Alpha (Thermo Scientific) which uses a micro-focused monochromated Al K $\alpha$  x-ray source ( $h\nu = 1486.7$  eV).

### ***3.2.1.5. Fourier Transform Infrared Spectroscopy***

FTIR was performed on a Perkin Elmer Spotlight 400 FTIR imaging system. Images were taken in reflectance mode with a resolution of 8 cm<sup>-1</sup> and a pixel size of 6.26  $\mu\text{m}$ .

## **3.2.2. Procedures**

### ***3.2.2.1. Latent Fingerprint Deposition***

Stainless steel substrates were polished with Brasso (Reckitt Benckiser plc., Slough, UK) on one side for 2 minutes until a mirror like shine was achieved. After this they were washed with warm soapy water and acetone to remove any excess polish.

Fingerprint deposits were collected from five individuals, three men and two women, varying in age from 21 to 45 years. This range is designed to ensure a representational range of deposit composition and amount of deposit. To obtain sebaceous sweat the fingertips were

rubbed around the forehead and nose area. To ensure the sweat was distributed evenly across the fingertips, the fingers were rubbed together and across the palms. Donors deposited their prints by contact with the stainless steel surface for 1–2 sec with natural pressure. Prints were left overnight under ambient conditions before being subjected to their respective environments. In the case of the 1-day-old prints, pre-treatment commenced c. 4 h after deposition.

### ***3.2.2.2. Pre-Treatments***

The deposited fingerprints were subjected to a number of different pre-treatments/environments prior to their enhancement. The first was ambient conditions, where the samples were exposed to air at room temperature. High temperature samples were placed on a metal tray and stored in an oven at 150°C. Samples were also submerged under water at ambient temperature. Soap washed samples were rubbed in warm (40°C), soapy water for 30 sec; rinsed in soap-free water and left to dry naturally. Acetone washed samples were agitated in acetone for 30 sec and left to dry naturally. Both soap and acetone washed samples were subsequently stored under ambient conditions prior to enhancement. These treatments/environments were designed to represent a range of plausible evidential scenarios.

In order to compare the polymer enhancement technique to the methods currently employed by the police 1000 samples were prepared<sup>b</sup>. Samples were given names based on the type of development technique, the amount of time they were aged for, the code corresponding to the donor who gave the prints and the pre-treatment used:

---

<sup>b</sup> Comparison survey of PEDOT, PANi, dusting, wet powder, superglue and control were all conducted during MChem research project with the aid of Dr Ann L. Beresford<sup>4</sup>. PPy, 1:5, 1:10 and 1:20 P(Py-co-EDOT) were performed as part of this PhD research.

[Technique]:[age]:[donor]:[pre-treatment]

[C/D/S/W/A/E/P/5/10/20] : [1/7/14/28] : [a/b/c/d/e] : [A/B/O/S/W]

where C = control (prints photographed with no enhancement), D = powder dusting, S = superglue fuming, W = wet powder and A/E/P/5/10/12 = enhancement with conducting polymers (PAni/PEDOT/PPy/P(Py-co-EDOT) 1:5/1:10/1:20 feed ratios respectively). 1/7/14/28 refers to the age of the prints in days. a/b/c/d/e refers to the identity of the donor. For the pre-treatment references, A = washing in acetone, B = bench (ambient conditions), O = oven at 150 °C, S = soap wash and W = under water.

Photographs of all samples were taken both before and after enhancement.

### ***3.2.2.3. Comparison Techniques***

Dusting was performed with standard black powder (WA Products, Burnham on Crouch, Essex, UK), which was gently dusted back and forth using a mop head squirrel brush.

Wet Powder consists of a mixture of iron oxide and detergent (Kodak Professional Photo-Flo 200 [Kodak Eastman Company, Rochester, NY] and distilled water). It was made to a consistency viscous enough to coat a surface but sufficiently optically transmitting that the underlying surface could still be seen through the deposited film. Development was achieved by applying the wet powder in perpendicular directions to ensure that particles attached to the fingerprint ridges. Samples were then rinsed with water and placed in a drying cabinet (60°C) for 1 hour.

Superglue Fuming was performed in a superglue cabinet (MVC 5000; Foster and Freeman, Evesham, U.K.). A mixture of distilled water and cyanoacrylate was added to the incorporated hot plate. Samples were placed in the cabinet set to the auto glue function. After approximately 8 minutes, sufficient humidity (78.9%) was reached; after which 15 minutes of fuming at 119.4°C was performed. The samples were then removed from the cabinet and

dipped in a solution of Basic Yellow 40 dye (2 g /L in aqueous 60% ethanol, see **Figure 3.1**), and then rinsed with water. Samples were left in a drying cabinet (60°C) for 1 hour.

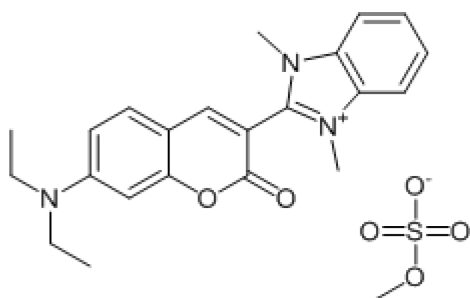


**Figure 3.1.** Structure of fluorescent dye BY40.

PAni deposition was performed potentiostatically ( $E = 900$  mV vs. Ag /AgCl/ saturated KCl) from a solution containing aniline (0.1 M) in aqueous  $H_2SO_4$  (1 M) solution. Deposition times ranged between 2 and 10 minutes.

PEDOT was deposited and the films handled under similar conditions to PAni deposition. The deposition potential was 900 mV vs a saturated Ag/AgCl reference electrode. The deposition solution contained EDOT (0.01 M)/ sodium dodecylsulfonate (SDS, 0.01 M) in aqueous  $H_2SO_4$  (0.1 M). The role of the SDS surfactant was to solubilize the EDOT monomer in the aqueous medium, thus eliminating the need for organic solvents. Deposition times ranged between 30 seconds – 5 minutes.

#### **3.2.2.4. Novel Electrochromic Enhancements:**

Ppy deposition was performed potentiostatically ( $E = 800$  mV vs. Ag /AgCl/ saturated KCl) from a solution containing pyrrole (0.01 M) and SDS (0.04 M) in  $LiClO_4$  (0.2 M). Deposition times were <5 seconds.

P(Py-co-EDOT) was electrochemically deposited from a solution containing the corresponding monomers; Py (0.002/0.004/0.008 M) and EDOT (0.04 M) in an aqueous solution of  $LiClO_4$  (0.2 M) and sodium dodecylsulfate (SDS) (0.04 M). Three different feed ratios (1:20, 1:10, and 1:5)

of the two corresponding monomers were used in order to vary the final ratio of PEDOT:PPy in the copolymer films. Films were grown potentiostatically ( $E = 800 \text{ mV vs. Ag/AgCl/ saturated KCl}$ ).

The electrode configuration was designed so the fingerprinted sample (working electrode) could be viewed allowing the enhancement to be visually monitored. When a suitable film was deposited, the working electrode (sample) was disconnected (with the film in the oxidized state), removed from the cell and rinsed with deionized water. This *ex-situ* observation downplayed the strength of the electrochromic method as previously demonstrated for PAni<sup>2</sup> and PEDOT<sup>3</sup> as subsequent control of optical contrast was sacrificed. This approach was adopted to provide a critical appraisal of this new technology.

### 3.2.3. Grading of Fingerprints

In order to assess the quality of the enhanced fingerprints, they were each graded according to the Bandey classification system<sup>11</sup>, which is currently employed by the Home Office. This employs a 5-point scale (0 = lowest to 4 = highest) based on the degree of ridge visualisation. A summary of this is given in **Table 3.1**. Many factors can affect the grade given to a fingerprint, from the amount of sweat present on the finger at the time of transfer, to the different components contained within the sweat itself, as well as the quality of surface on which the enhancement must take place.

Grade	Description
0	No development
1	No continuous ridges; all discontinuous or dotty
2	One third of the mark comprised of continuous ridges; remainder either show no development or dotty
3	Two thirds of the mark comprised of continuous ridges; remainder either show no development or dotty
4	Full development; whole mark comprised of continuous ridges

**Table 3.1.** Summary of the Bandey fingerprint classification system.

### 3.2.4. XPS Sample Preparation

Potentiostatic growth was performed from the above solutions at a series of potentials between 700-1000 mV (vs. Ag/AgCl/saturated KCl) at 50 mV intervals for 25 seconds on Au coated microscope slides. Potentiodynamic growth was achieved by cycling the potential between 0.13 – 1.2 V with an anodic current cap implemented at approximately 175  $\mu\text{A}$  at 20  $\text{mV s}^{-1}$ .

## 3.3. Results

### 3.3.1. Electropolymerisation

#### 3.3.1.1. Potentiostatic

The current time transients for samples of PEDOT, P(Py-co-EDOT) 1:20, 1:10, 1:5 feed ratios and PPy are shown in **Figures 3.2-6**. At high  $E_{\text{deposition}}$  the rate of electron transfer is fast and so the process is diffusion controlled and the current follows a  $t^{-1/2}$  decay. As  $E_{\text{deposition}}$  decreases, the process becomes more kinetically controlled and the different nucleation and growth mechanisms affect the shape of the current time transients.

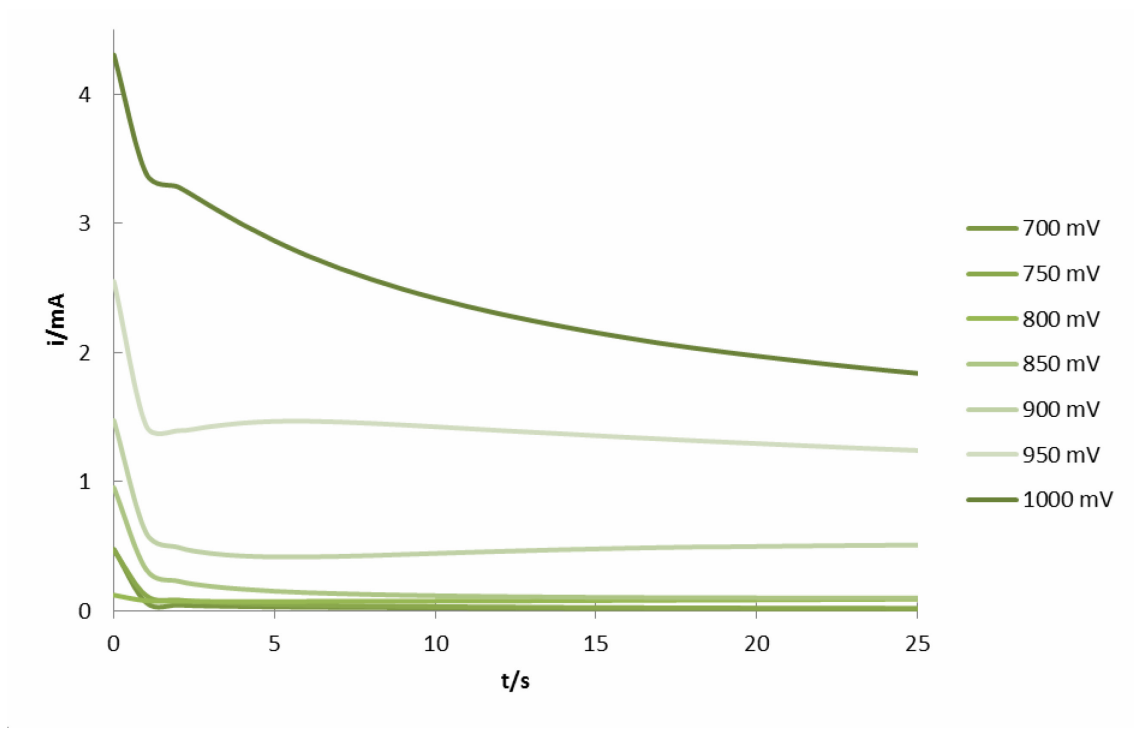


**Figure 3.2** Current-time transient of the potentiostatic growth of PEDOT homopolymer.

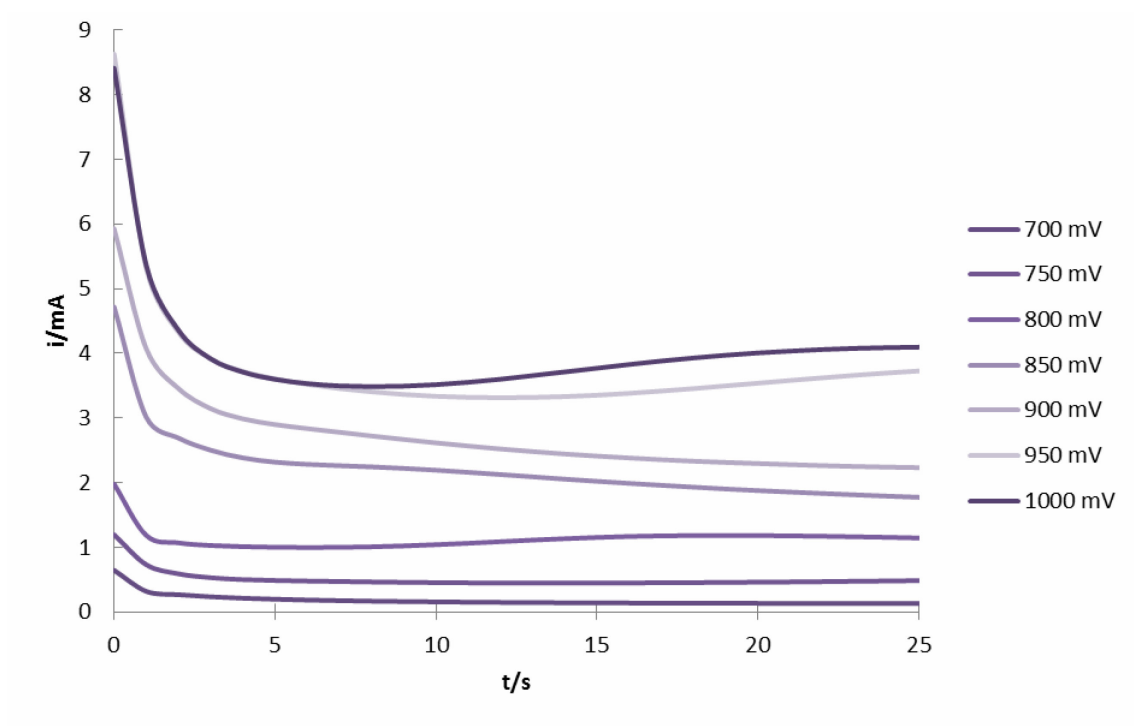


**Figure 3.3** Current-time transient of the potentiostatic growth of P(Py-co-EDOT) copolymer using a 1:20 Py:EDOT monomer concentration.

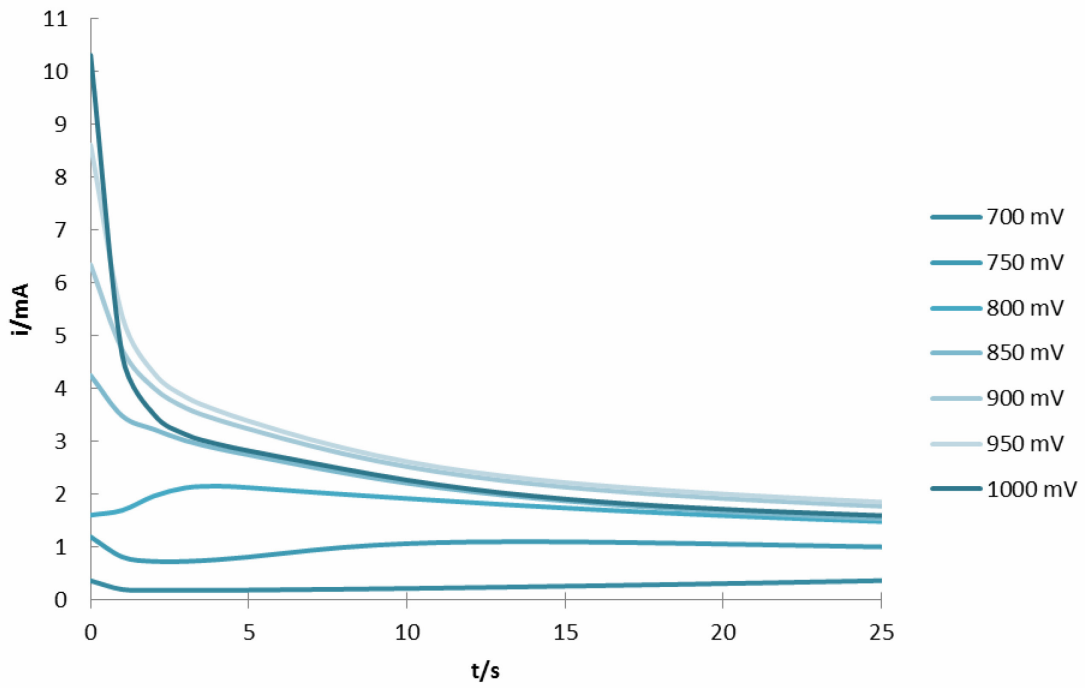


**Figure 3.4** Current-time transient of the potentiostatic growth of P(Py-co-EDOT) copolymer using a 1:10 Py:EDOT monomer concentration.

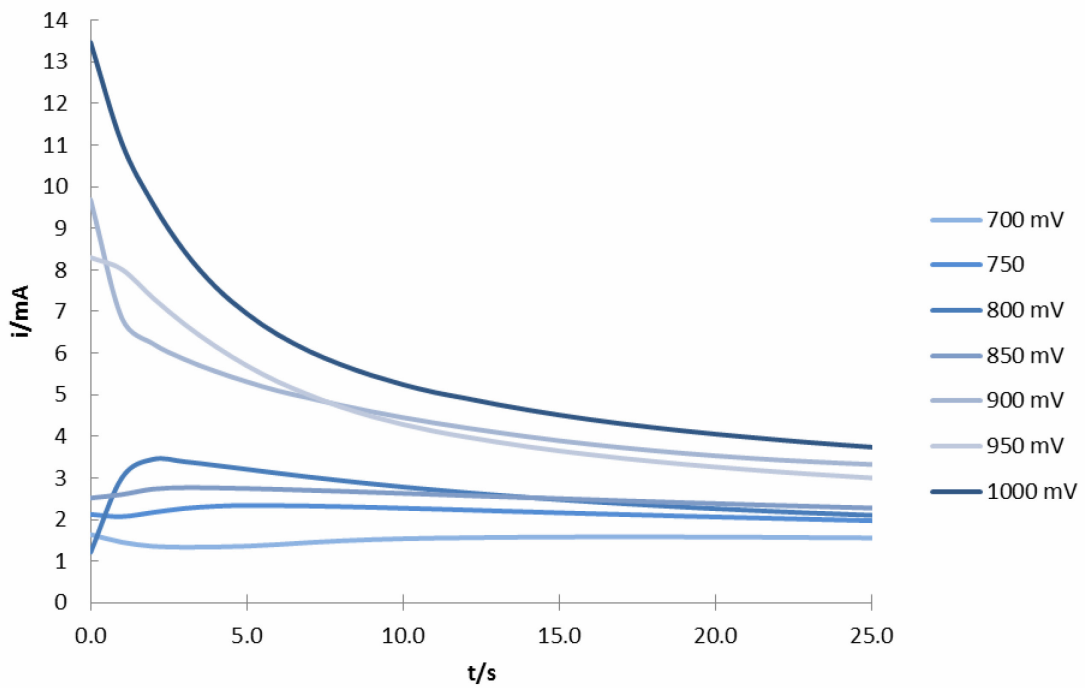


**Figure 3.5** Current-time transient of the potentiostatic growth of P(Py-co-EDOT) copolymer using a 1:5 Py:EDOT monomer concentration.

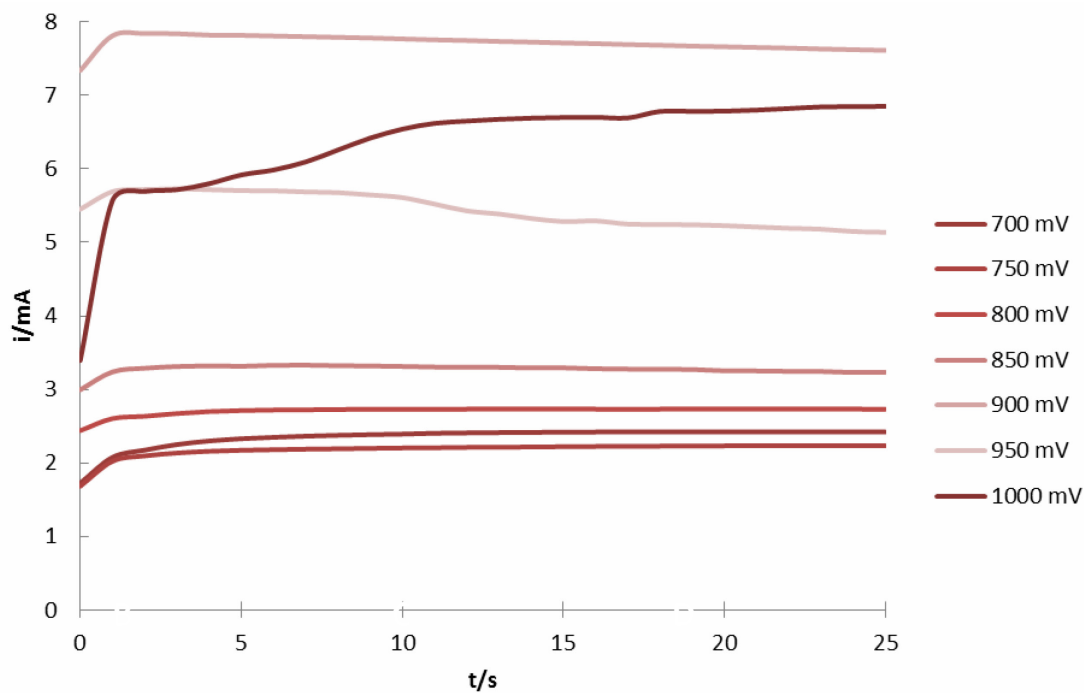


**Figure 3.6** Current-time transient of the potentiostatic growth of PPy homopolymer.

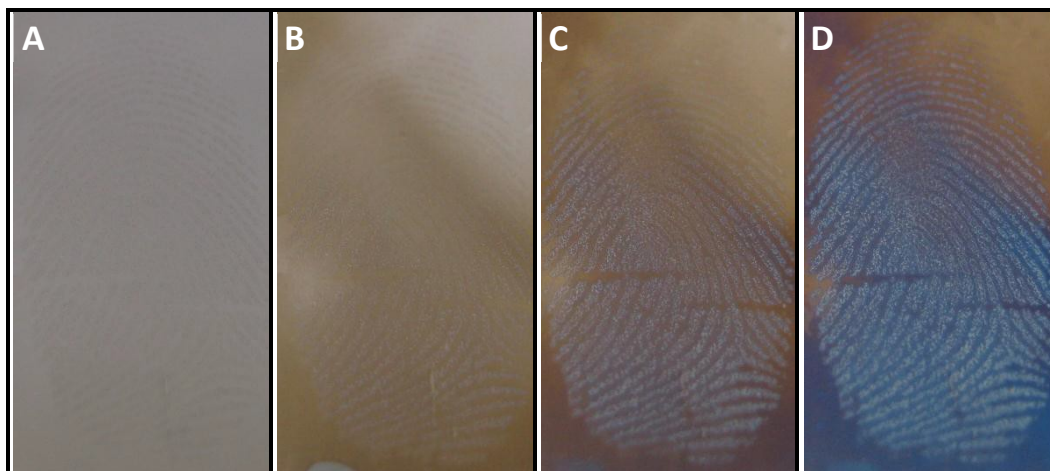


**Figure 3.7** The electrodeposition/enhancement progress of PPy onto stainless steel (sebaceous print deposit, 28 days old, kept under ambient conditions) at the following time intervals; (A) 0.5 s, (B) 1 s, (C) 1.5 s, (D) 2 s.

### 3.3.1.2. Potentiodynamic

Films were also grown potentiodynamically from the 5 monomer solutions.  $E_{ox}$  was shown to decrease with increasing Py concentration.

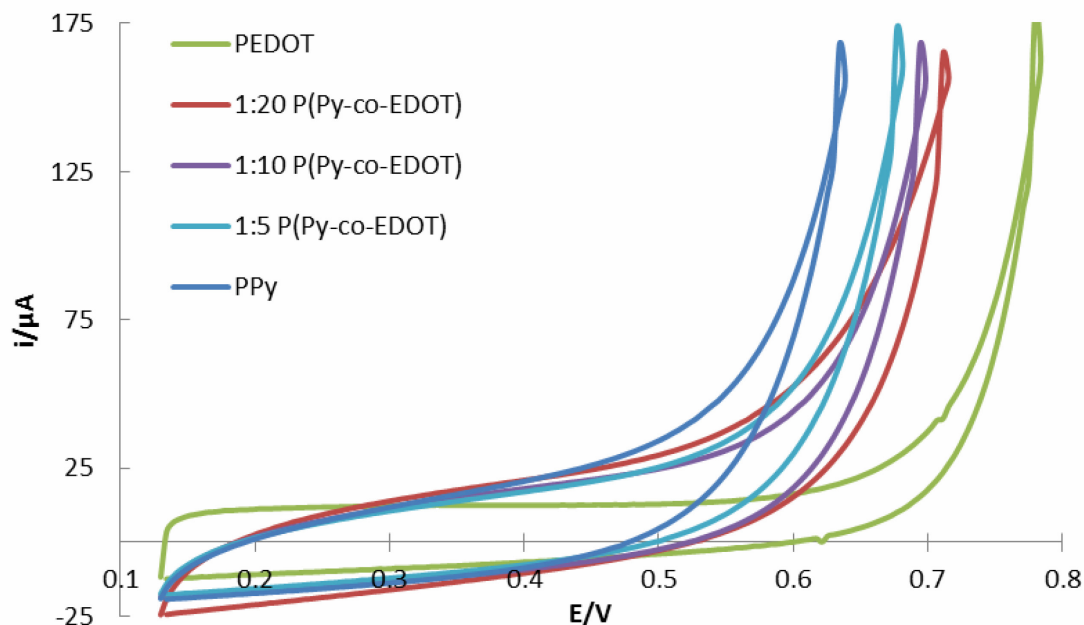


**Figure 3.8** Final growth cycle of potentiodynamic growth on Au electrodes with an anodic current limit to show decreasing  $E_{ox}$  ( $I_{max} = 175 \mu A$ ,  $v = 20 \text{ mV s}^{-1}$ ).

### 3.3.2. Electrochromism of P(Py-co-EDOT): a Comparison to the Corresponding Homopolymers PPy and PEDOT

The electrochromic properties of three copolymers of PPy and PEDOT were explored. Three different monomer feed ratios (1:5, 1:10 and 1:20 Py:EDOT) were used in order to vary the amounts of the corresponding polymers present in the resultant copolymer films. These films were then compared to PPy and PEDOT films grown under the same conditions from the same electrolyte solution.

Deposition potential was also varied to see if adding a kinetic component to the deposition would affect the final polymer ratio and/or the electrochromic behaviour of the polymer films. The electrochromic behaviour was analysed by viewing the resultant polymer films in monomer free electrolyte [aqueous  $\text{LiClO}_4$  (0.2 M)/SDS (0.04 M)] under static potential. The resultant colour changes are summarised in **Figures 3.9-13**.

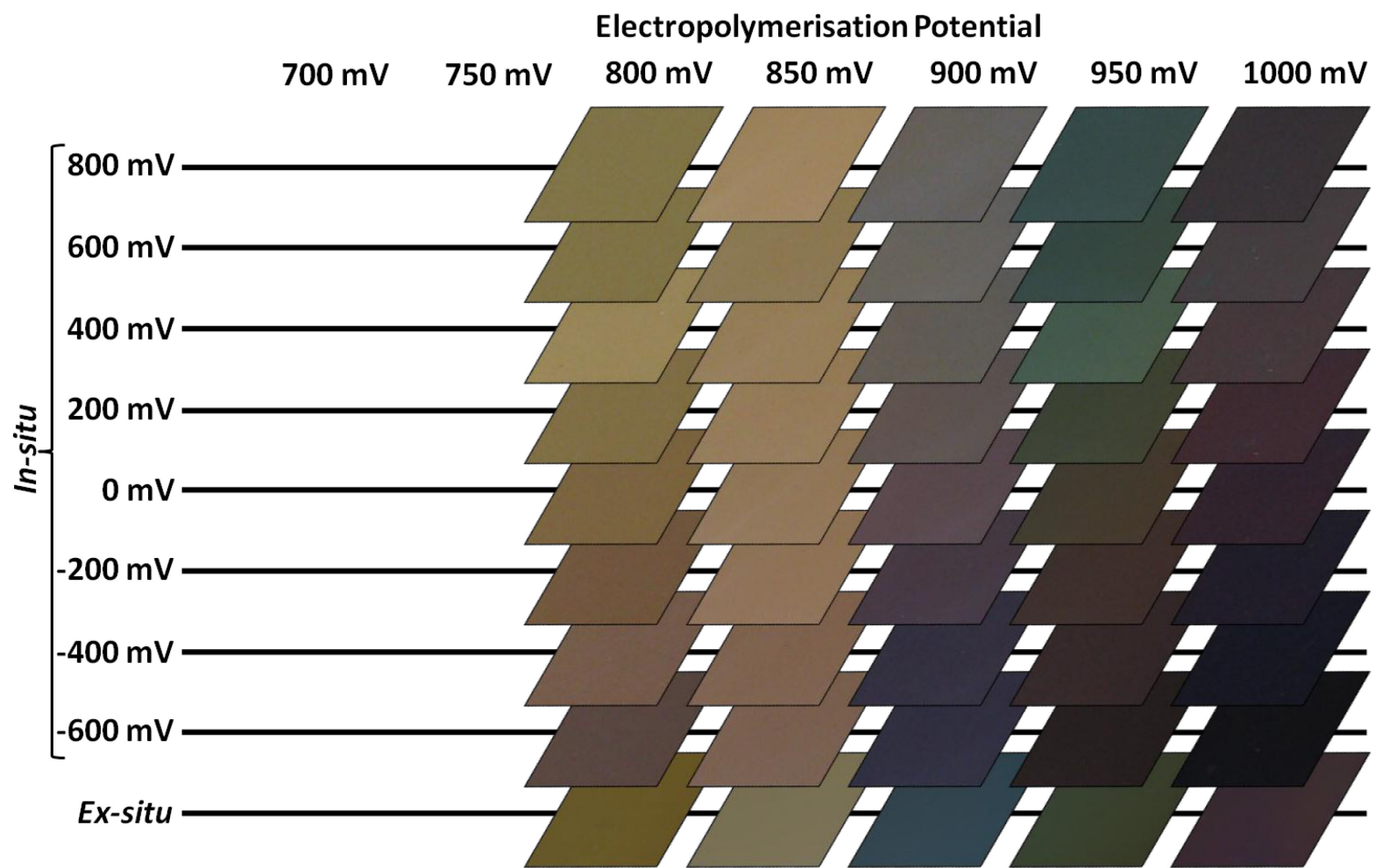


**Figure 3.9** PEDOT electrochromic behaviour (Au electrode).

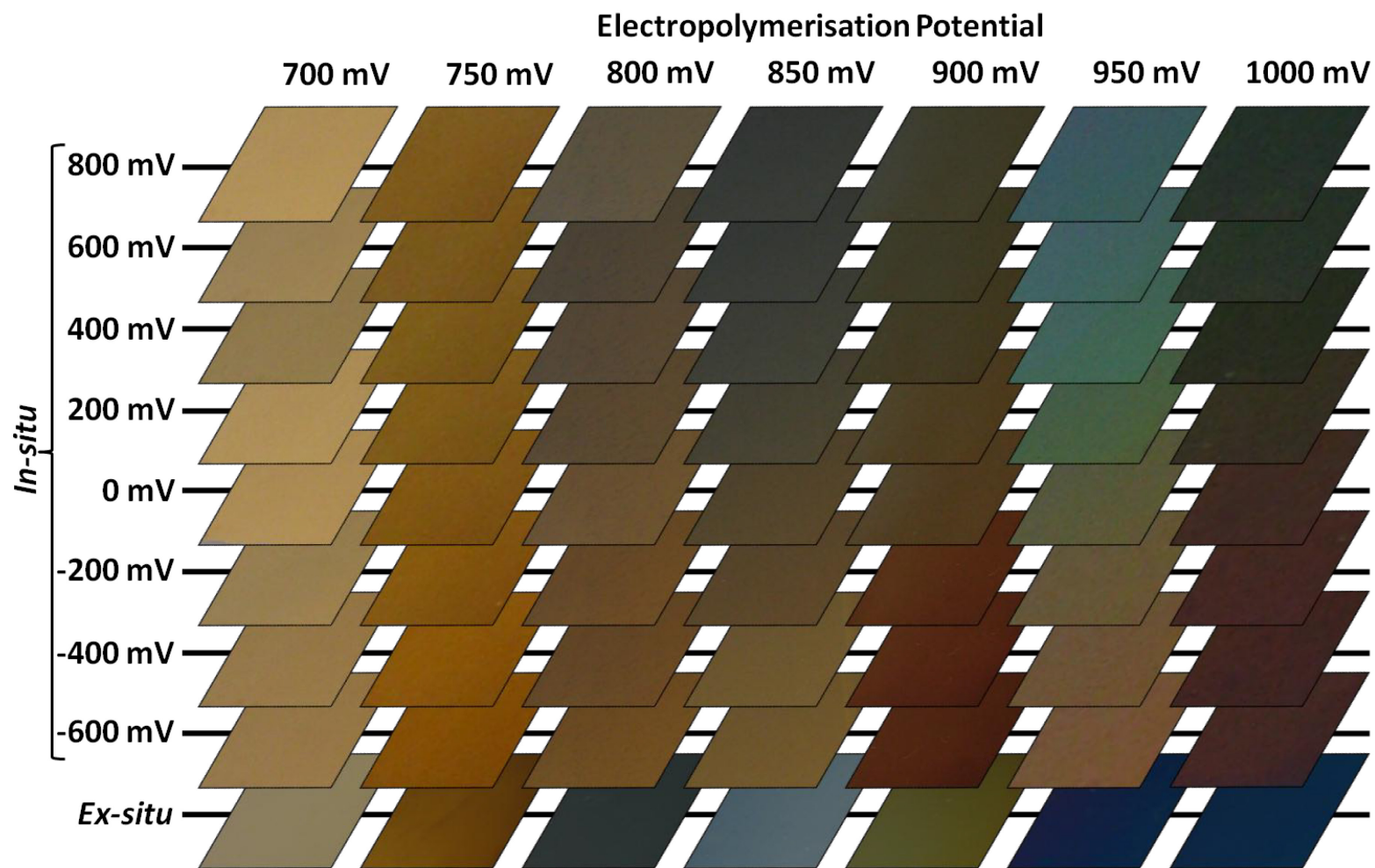


Figure 3.10 P(Py-co-EDOT) 1:20 electrochromic behaviour (Au electrode).

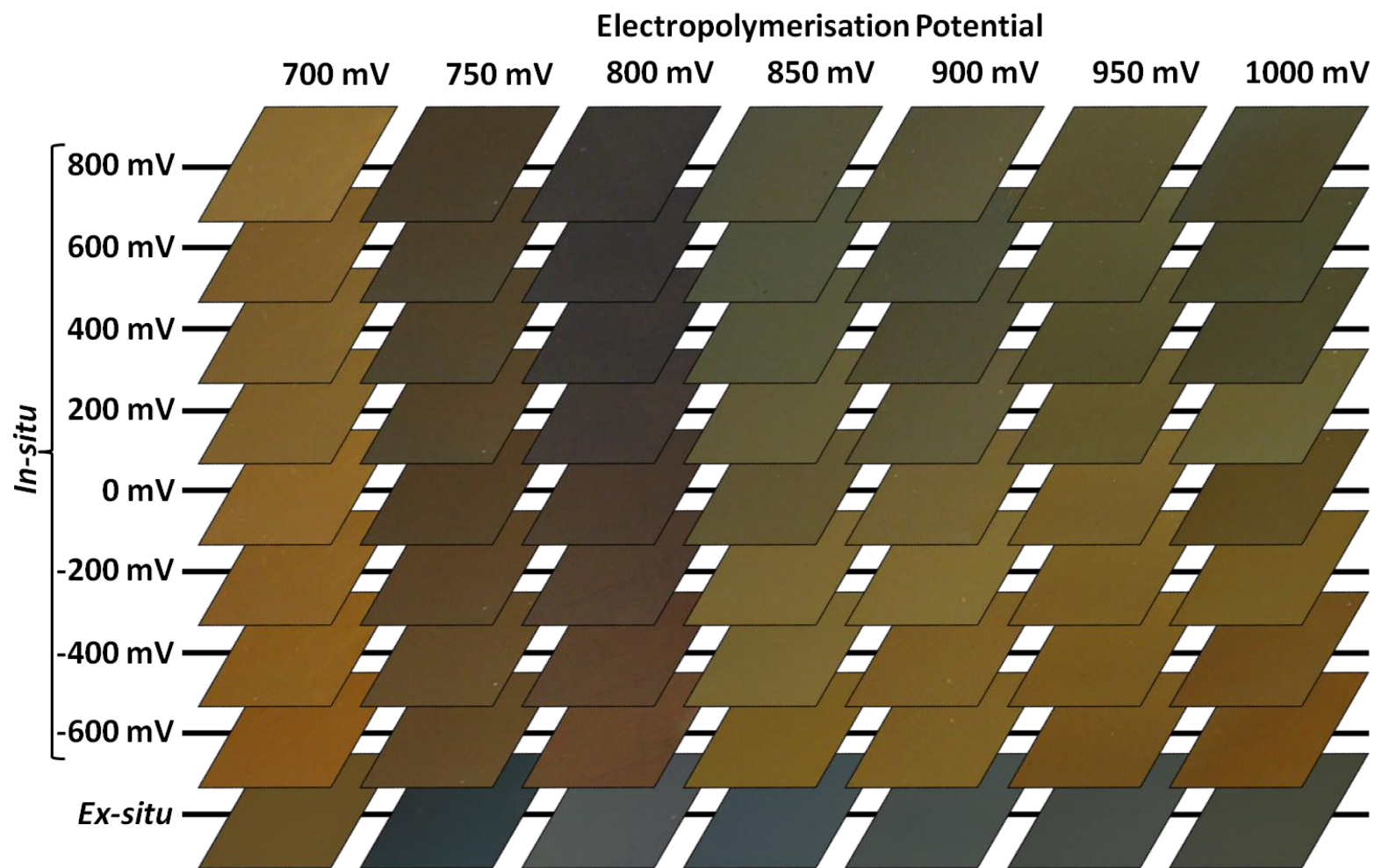


Figure 3.11 P(Py-co-EDOT) 1:10 electrochromic behaviour (Au electrode).

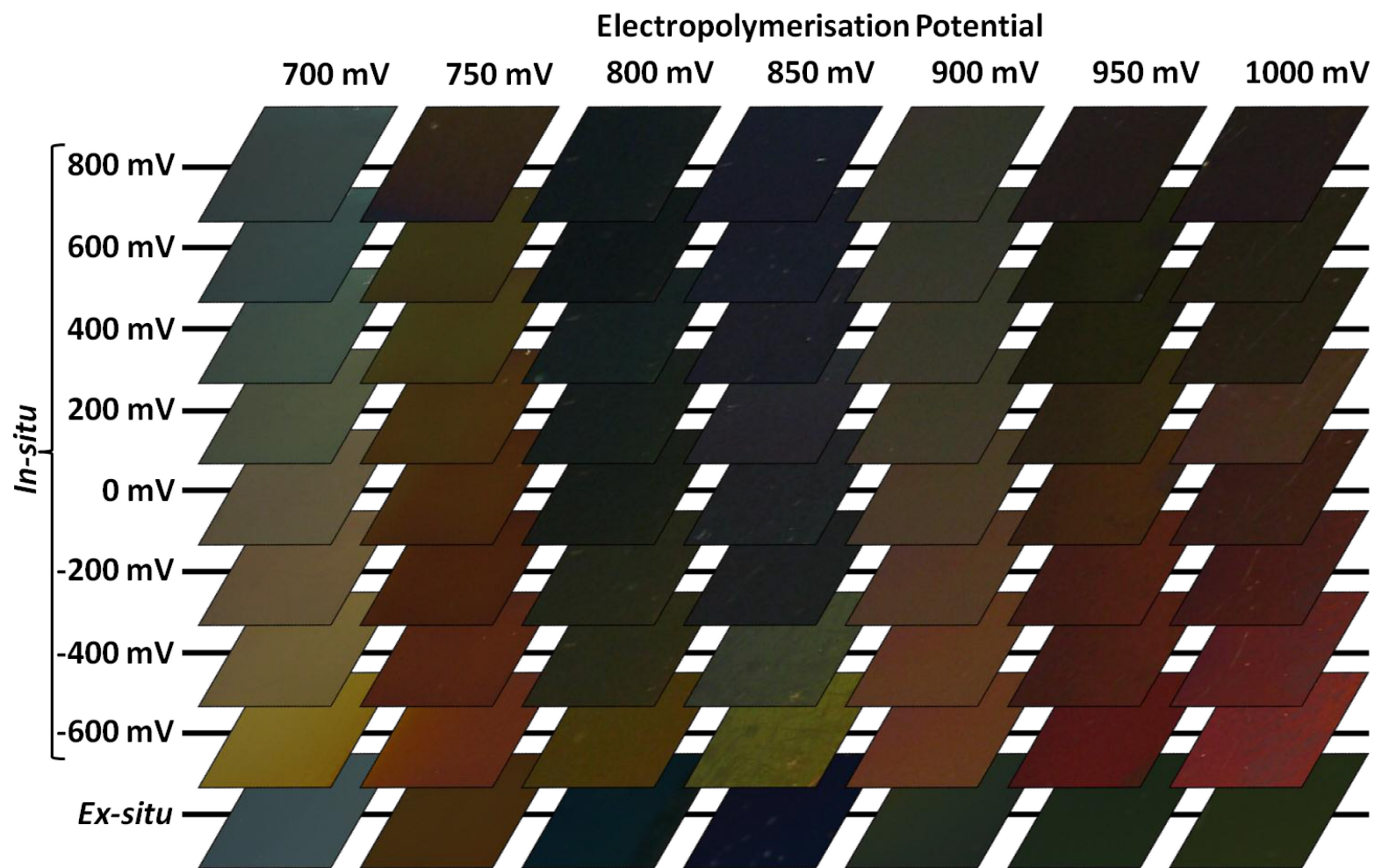


Figure 3.12 P(Py-co-EDOT) 1:5 electrochromic behaviour (Au electrode).

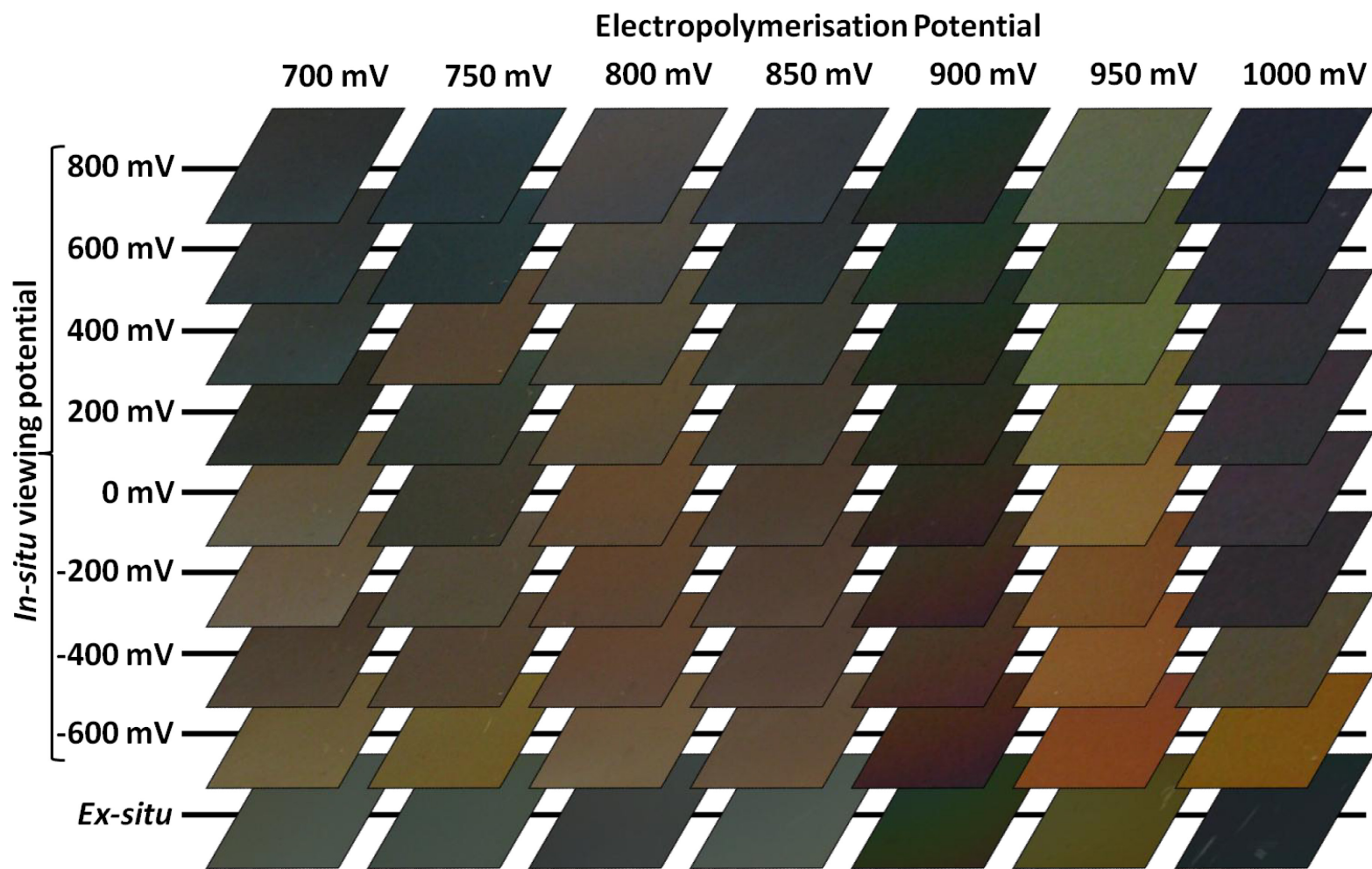
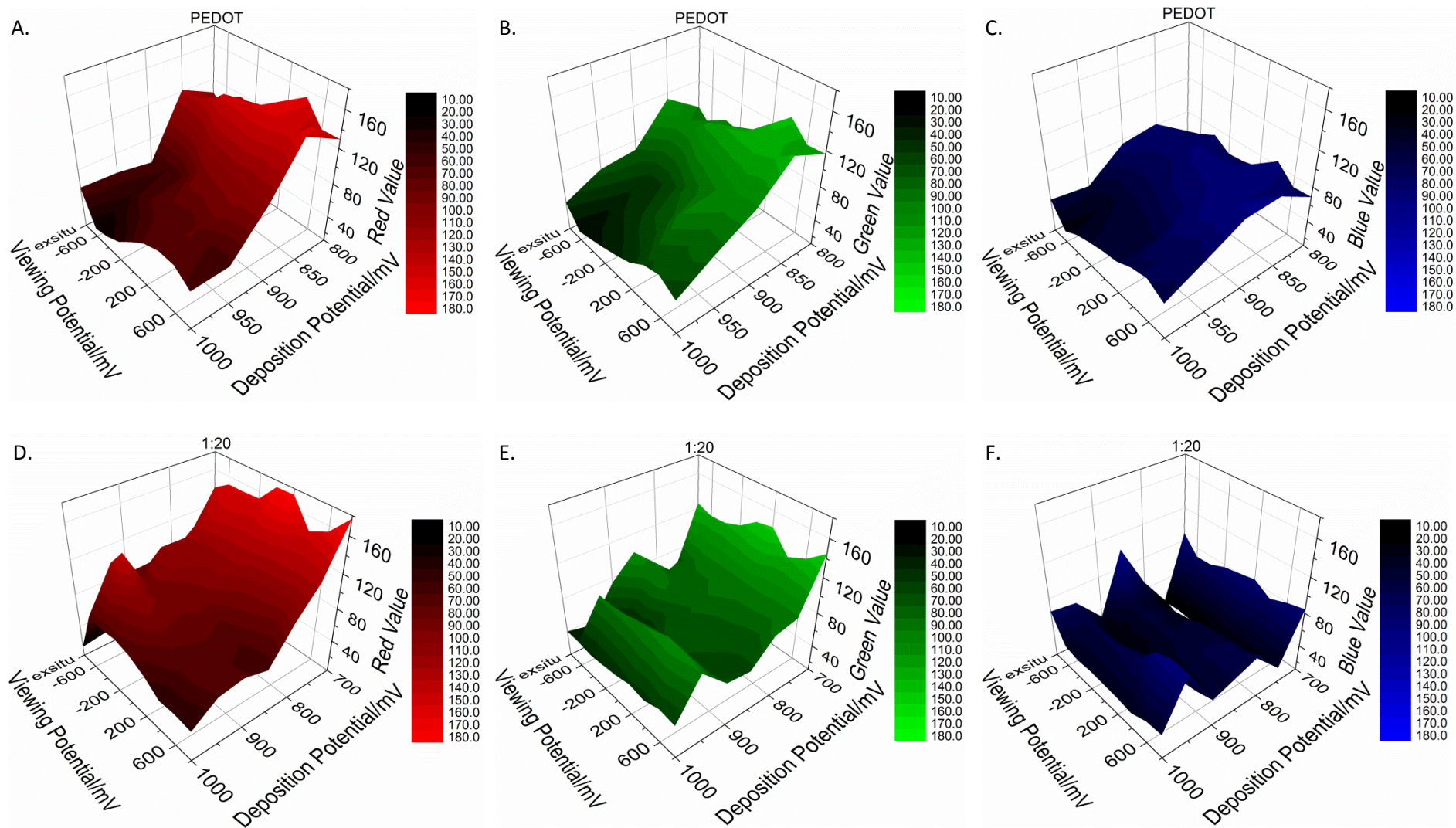
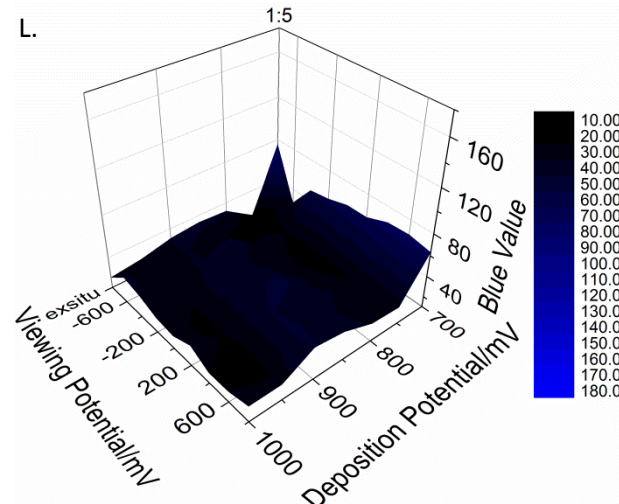
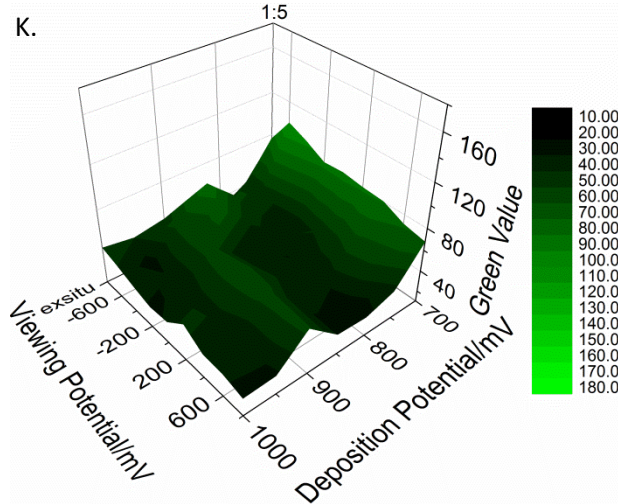
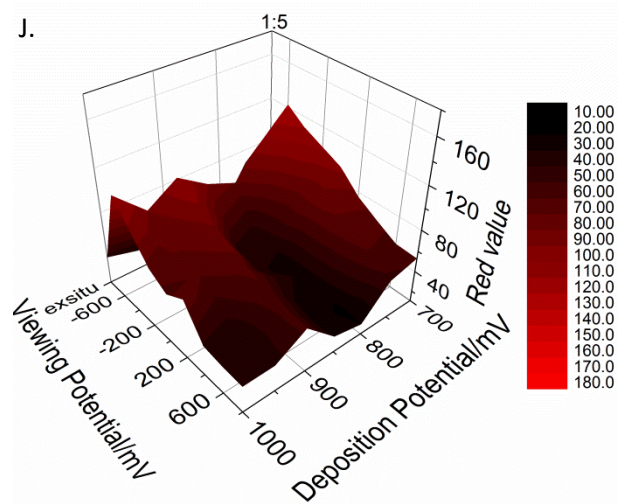
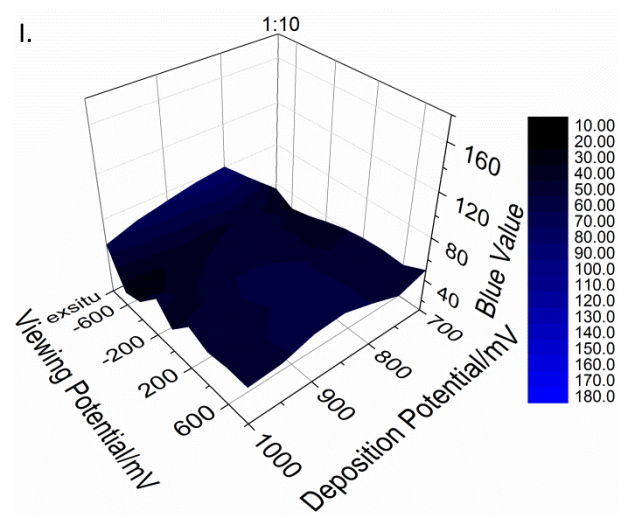
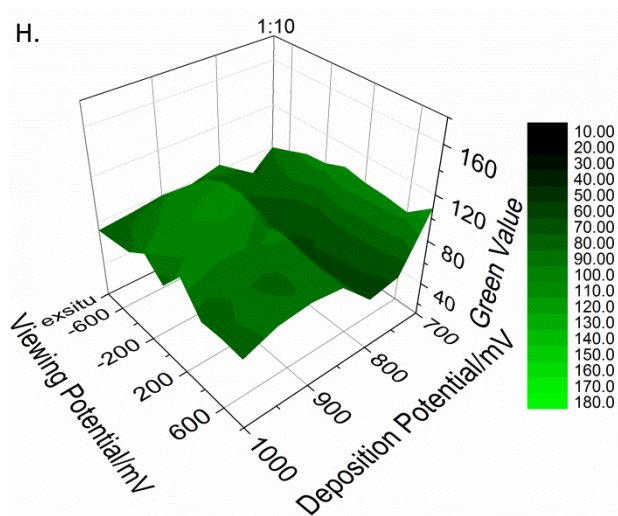
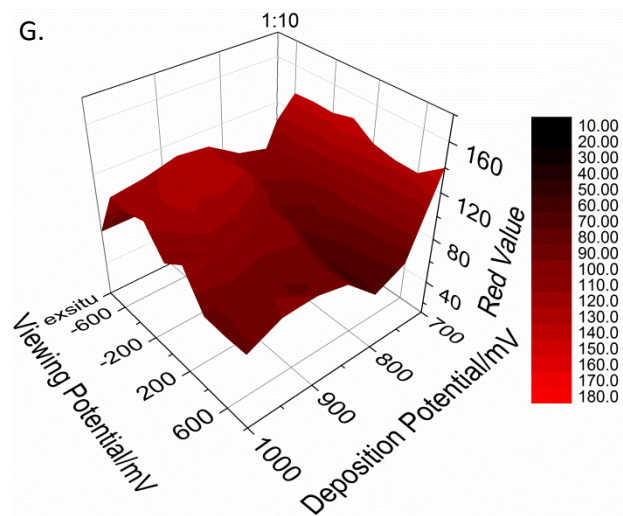
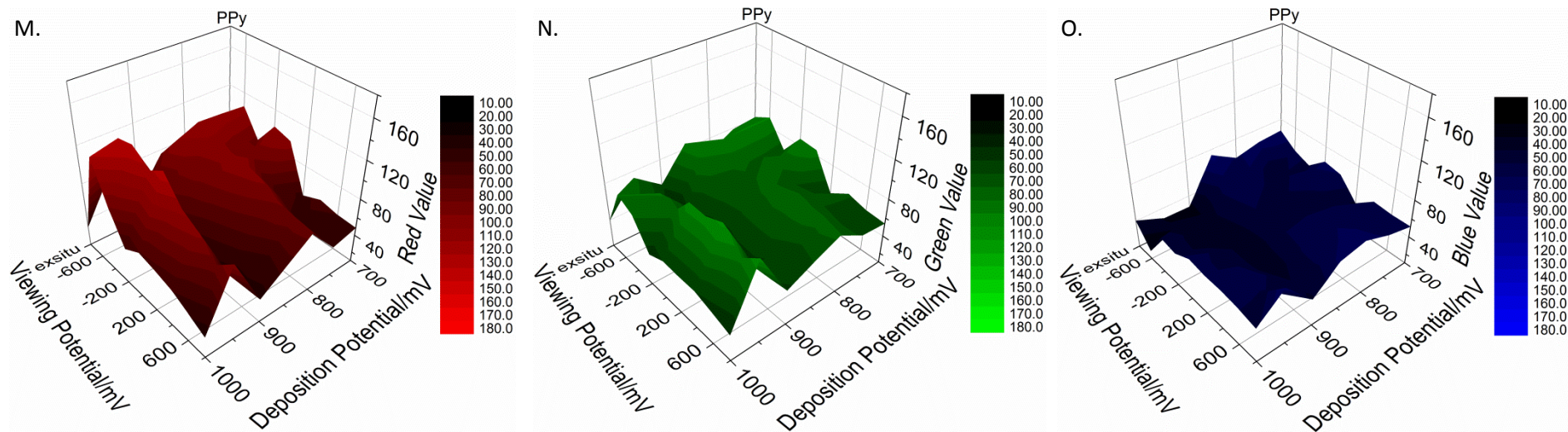


Figure 3.13 PPy electrochromic behaviour (Au electrode).

In order to quantify the colours seen in the electrochromism of the various polymers analysis of the RGB values in the above photographs was performed using Image J software (Wright Cell Imaging Facility, Toronto Western Research Institute, University Health Network). **Figure 3.14** shows the relationships between these so called RGB values and deposition/viewing potential.







**Figure 3.14** 3D plots showing RGB values versus deposition and viewing potentials for PEDOT (A-C), P(Py-co-EDOT) 1:20 (D-F), 1:10 (G-I), 1:5 (J-L) and PPy (M-O).

Panels A-C show that for pure PEDOT films the RGB values increase at lower deposition potentials and higher viewing potentials. Adding a small amount of PPy as in panels D-F for P(Py-co-EDOT) 1:20 feed ratio shows a minimising of the effect of viewing potential and appears to randomise the blue value. Continuing to increase the amount of PPy in the films (panels G-I and J-L) shows a minimisation of the effect of deposition potential as well and in the case of pure PPy the effect of viewing potential is reversed meaning that the values are larger for lower viewing potentials.

To see whether or not this could be a useful means of increasing the contrast between the fingerprint and the background in a forensic application an image of a fingerprint was split into the three colour channels. **Figures 3.15** and **3.16** show how different colour channels were more effective for different polymers. Panel (A) in **Figure 3.15** shows that the red channel is clearer for PEDOT whereas panel (C) in **Figure 3.16** shows that the blue channel is clearer for PPy.

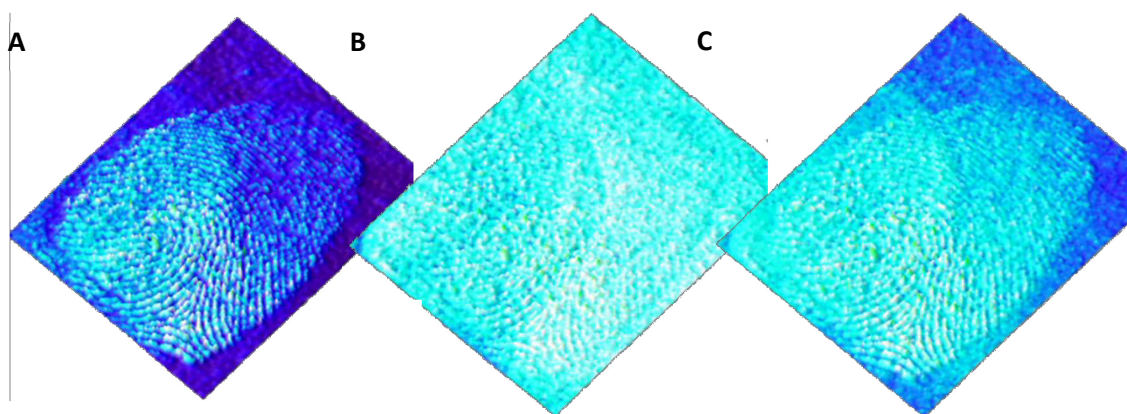


**Figure 3.15** PEDOT developed fingerprint photograph split into red (A), green (B) and blue (C) channels.

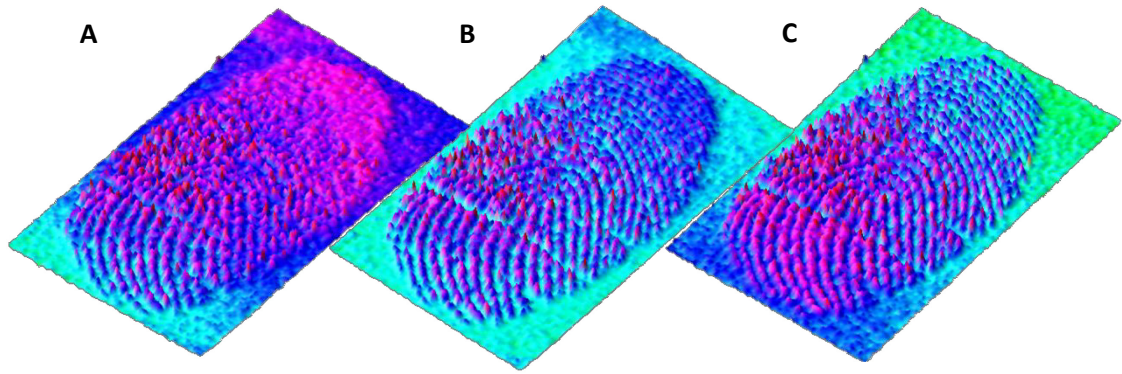


**Figure 3.16** PPy developed fingerprint photograph split into red (A), green (B) and blue (C) channels.

In reality these sorts of colour images would not be used by the police as the fingerprint experts currently work with only black and white images. However, **Figure 3.17** shows how this technology can be applied to the black and white images processed by fingerprint experts when confirming a match. Panel B showing the red channel only is clearer than the original “coloured” image merely made black and white (panel A). The lack of clarity, especially in the blue channel (panel D) supports the fact that doing a pseudo background subtraction of these lower contrast colour channels would help to increase the contrast in the image.

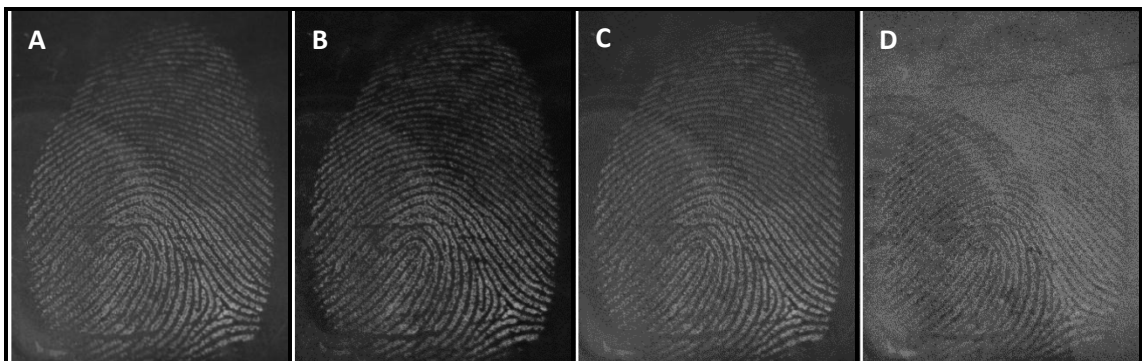


**Figure 3.17** PEDOT developed fingerprint (A) original colours grey scaled, (B) red channel, (C) green channel and (D) blue channel.

	Bare	<i>Ex situ</i>	+0.8 V	-0.6 V
PEDOT				
1:20				
1:10				
1:5				
PPy				

**Table 3.2** Series of latent fingerprints prior to enhancement, viewed *ex situ* and under potential control at 0.8 and -0.6 V in monomer free aqueous SDS (0.04 M) and LiClO<sub>4</sub> (0.2 M).

**Table 3.2** shows five representative examples of the electrochromic latent fingerprint enhancement on stainless steel substrates after their aging/pre-treatment regime: PEDOT six months old, ambient conditions; 1:20 and 1:10 one week old, kept at 150 °C (different donors); 1:5 two weeks old, kept at 150 °C and PPy one day old, kept under water. The first column shows the latent sebaceous fingerprints prior to enhancement, whilst in most instances there is obviously a fingerprint present, there is essentially no ridge detail visible (on the Bandey scale, a grade 1 print) or the ridges are visible but the contrast is insufficient. The second column shows the result of depositing a conducting polymer film and viewing the enhanced fingerprinted *ex situ*. As seen below in **Figure 3.18** viewing the fingerprint in this manner does not realise the full capability of the method, since the potential control that gives the added advantage of contrast manipulation through the film's electrochromic properties between the various colours of the un-doped and p-doped states. Whilst for a substrate like stainless steel substrate, this is not a significant limitation, for differently coloured substrates, potential control may prove more critical. The last two columns show the fingerprints under potential control in the p-doped (0.8 V) and un-doped (-0.6 V) states.

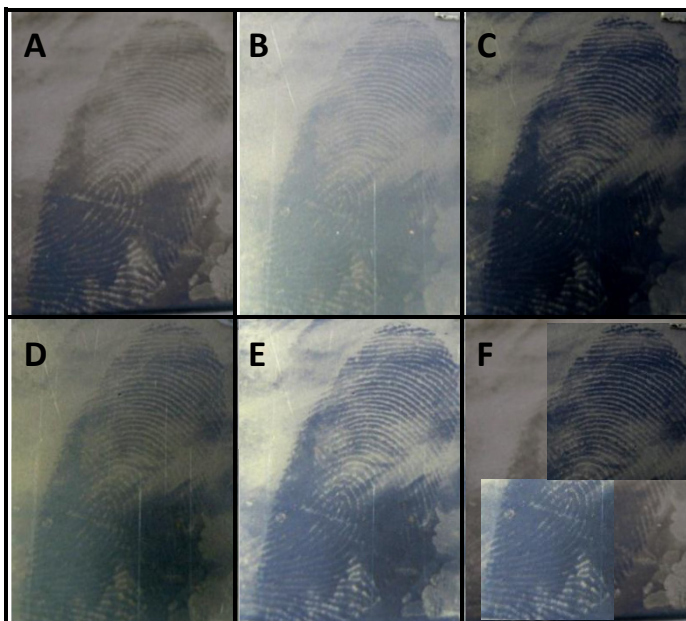


**Figure 3.18** Effects of ambient medium and applied potential on a fingerprint image subjected to enhancement by PEDOT deposition. All images are for the same sebaceous fingerprint, deposited on stainless steel, then stored for 3 days in ambient laboratory conditions prior to the observations shown. Final image quality on Bandey scale: grade 3. Sample environment: (A) *ex situ*; (B) and (C): *in situ* exposed to  $\text{H}_2\text{SO}_4$  (10 mM); (D) and (E): *in situ* exposed to  $\text{H}_2\text{SO}_4$  (0.01 M)/SDS (10 mM). Applied potential: (B) and (D) 0.80 V; (C) and (E) -0.80 V. (F) A combination of images (A), (C) and (E) to provide best overall contrast over areas where the film was under- and over-deposited.

### 3.3.3. FTIR

FTIR mapping of the P(Py-co-EDOT) enhanced fingerprint samples was performed in order to investigate the spatial selectivity of (A) the copolymer, (B) PPy within the copolymer and (C) PEDOT within the copolymer. The results of this are shown in **Figures 3.19-21**.

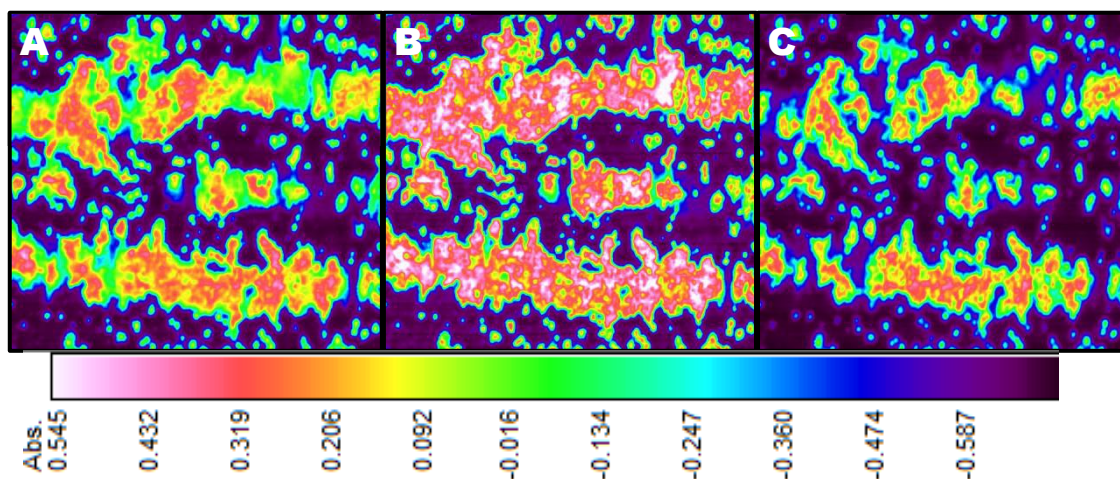


**Figure 3.19** P(Py-co-EDOT) 1:20 feed ratio (A) average absorbance, (B) picking out the absorbance of a single wavelength of 3402 cm<sup>-1</sup> representative of N-H stretching vibration in PPy<sup>12,13</sup> and (C) picking out the absorbance of a single wavelength of 1228 cm<sup>-1</sup> representative of stretching vibration between the aromatic C-O in PEDOT<sup>14</sup>.

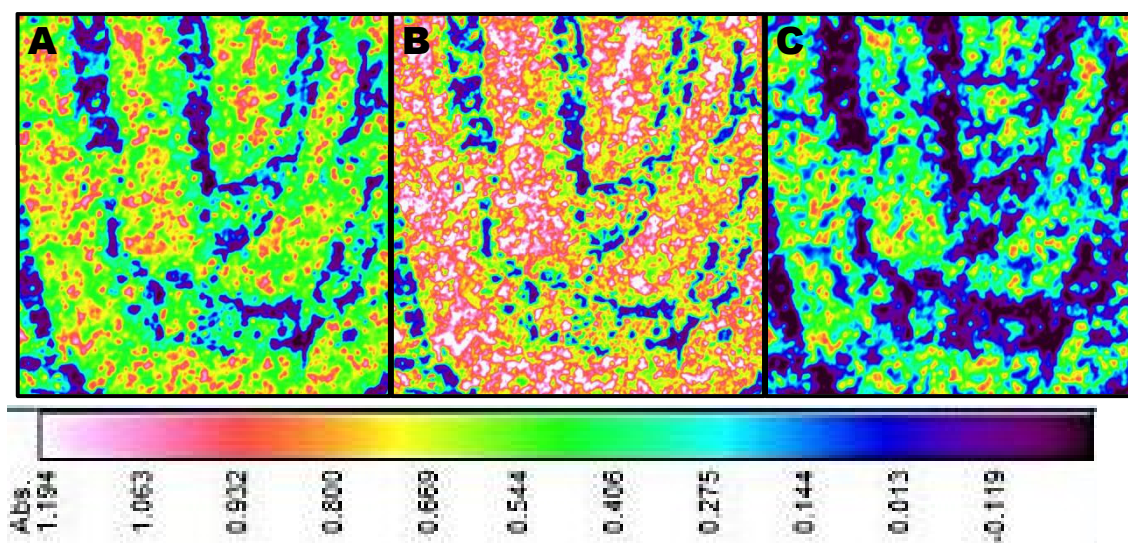


**Figure 3.20** P(Py-co-EDOT) 1:10 feed ratio (A) average absorbance, (B) picking out the absorbance of a single wavelength of 3402 cm<sup>-1</sup> representative of N-H stretching vibration in PPy and (C) picking out the absorbance of a single wavelength of 1228 cm<sup>-1</sup> representative of stretching vibration between the aromatic C-O in PEDOT.

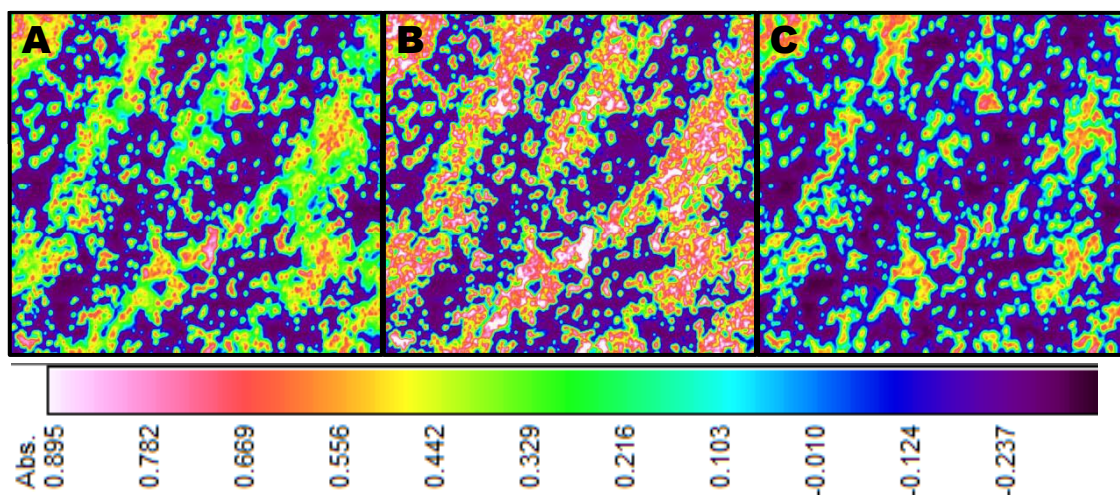


**Figure 3.21** P(Py-co-EDOT) 1:5 feed ratio (A) average absorbance, (B) picking out the absorbance of a single wavelength of  $3402\text{ cm}^{-1}$  representative of N-H stretching vibration in PPy and (C) picking out the absorbance of a single wavelength of  $1228\text{ cm}^{-1}$  representative of stretching vibration between the aromatic C-O in PEDOT.

These results qualitatively show that as the concentration of PPy is increased the relative absorbance of the PEDOT band in panel (C) decreases.

### 3.3.4. XPS

Monomer species with different structures or containing different functional groups, such as pyrrole and EDOT, are known to electropolymerise at varying rates. As a result of this the relative amounts of the two monomer units in the resulting copolymer films are often very different from that of the feed monomer solution<sup>15</sup>.

In order to quantify the amount of each homopolymer present in the copolymer films, XPS was performed on the same samples seen in **Figures 3.3-5** and **Figures 3.10-12**. Low resolution survey scans (**Figure 3.22**) were performed over a wide binding energy range (0-1350 eV) prior to performing higher resolution spectra around the N(1s) (393-410 eV) and S(2p) (157-175 eV) peaks. Quantification of the copolymer ratio was determined using the ratio of N:S atoms,

determined by integration of the N(1s) and S(2p) peaks. Note that the S(2p) peaks contain both a  $2p_{3/2}$  and  $2p_{1/2}$  resulting from spin-orbit splitting. The  $2p_{3/2}$  state is located at lower binding energies and the two have an energy separation of approximately 1.2 eV. The measurements were repeated over three different points within the same film (400  $\mu\text{m}$  spot size).

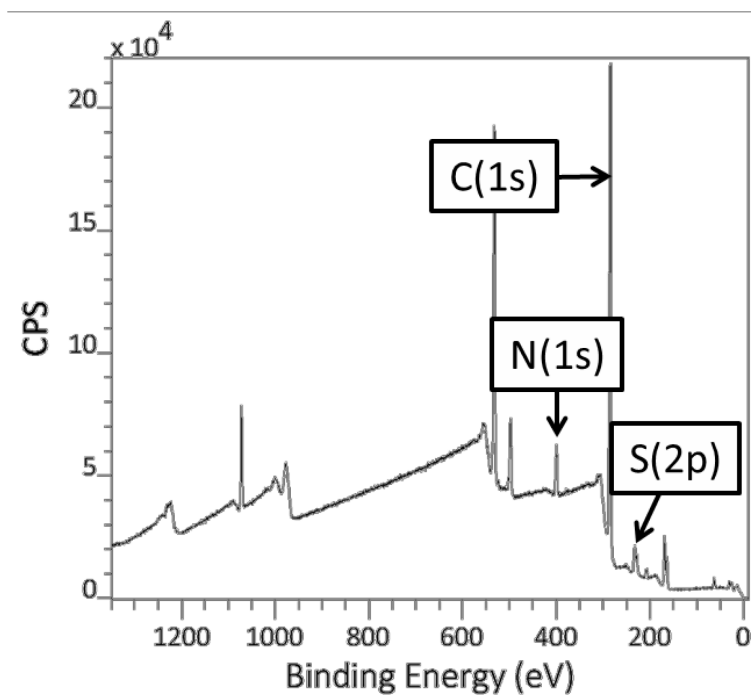


**Figure 3.22** Representative example of a low resolution survey spectrum of P(Py-co-EDOT) (deposited potentiostatically at 900 mV vs saturated Ag/AgCl for 25 seconds on Au).

**Figures 3.23** and **3.24** show the differences in the high resolution scans for each of the monomer feed ratios.

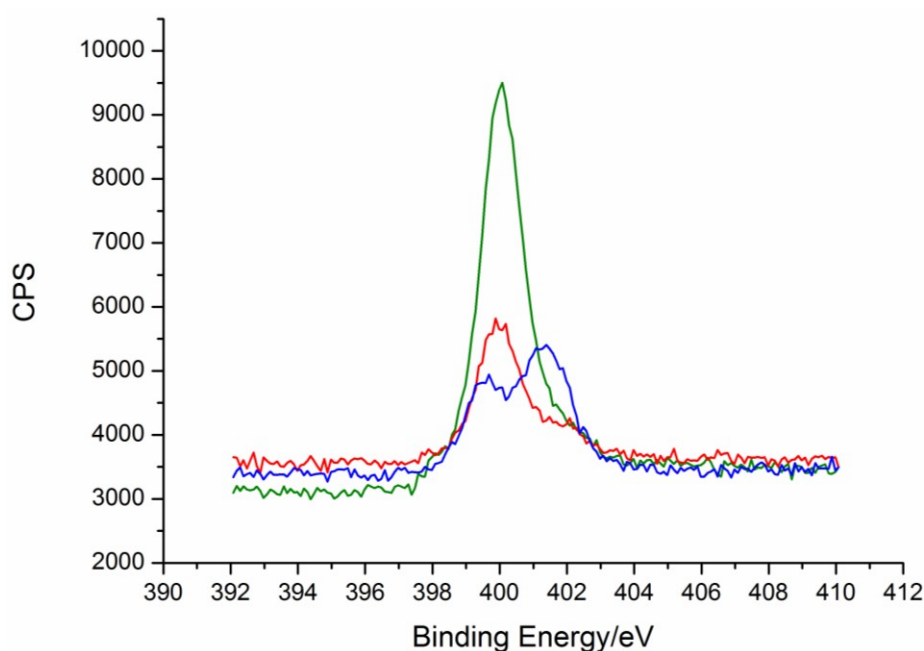


**Figure 3.23** Spectral differences in the N(1s) peak for three P(Py-co-EDOT) copolymers deposited at 1 V: 1:5 (green), 1:10 (red) and 1:20 (blue).

The N(1s) peak at a feed ratio of 1:5 consists of 1 main peak at 400 eV with a slight “shoulder” towards higher binding energy. At 1:10 this “shoulder” is more prominent and at 1:20 has become a distinct peak (401 eV) with more counts per second than the original peak at 400 eV. This can be attributed to the appearance of more PEDOT rings in the copolymer forming two environments for the PPy (next to other PPy units or next to PEDOT units).

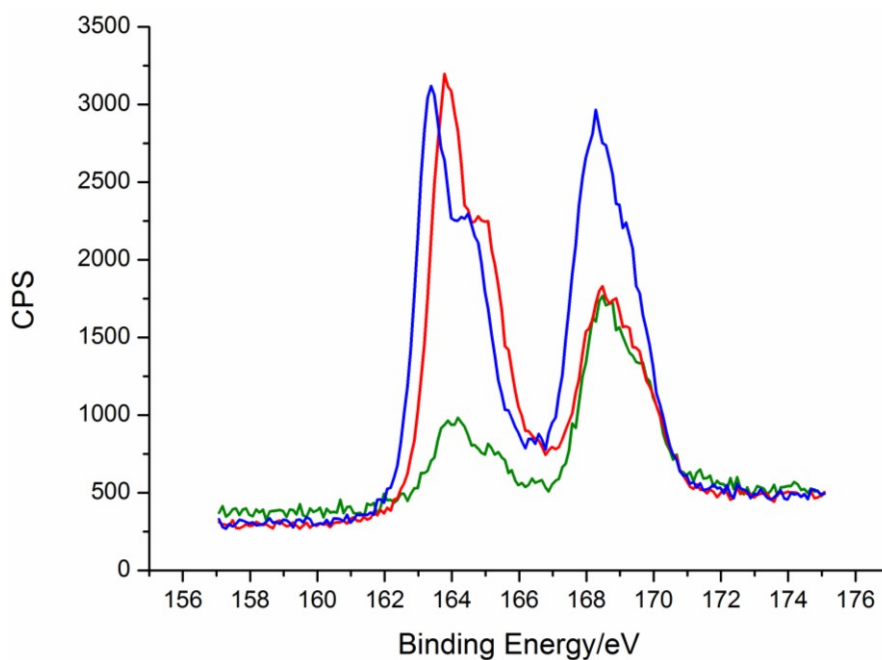


**Figure 3.24** Spectral differences in the S(2p) peak for the three P(Py-co-EDOT) copolymers deposited at 1 V: 1:5 (green), 1:10 (red) and 1:20 (blue).

The S(2p) peaks exhibit similar behaviour. The peak shown in **Figure 3.24** at 168 eV is present in the background scan. The peak at 163 eV corresponds to the S(2p<sub>3/2</sub>) state and the peak at 165 eV is the S(2p<sub>1/2</sub>) state. These peaks become more prominent as the ratio of EDOT in the monomer solution is increased.

The results of the N:S quantification are shown in **Figures 3.25-28**.

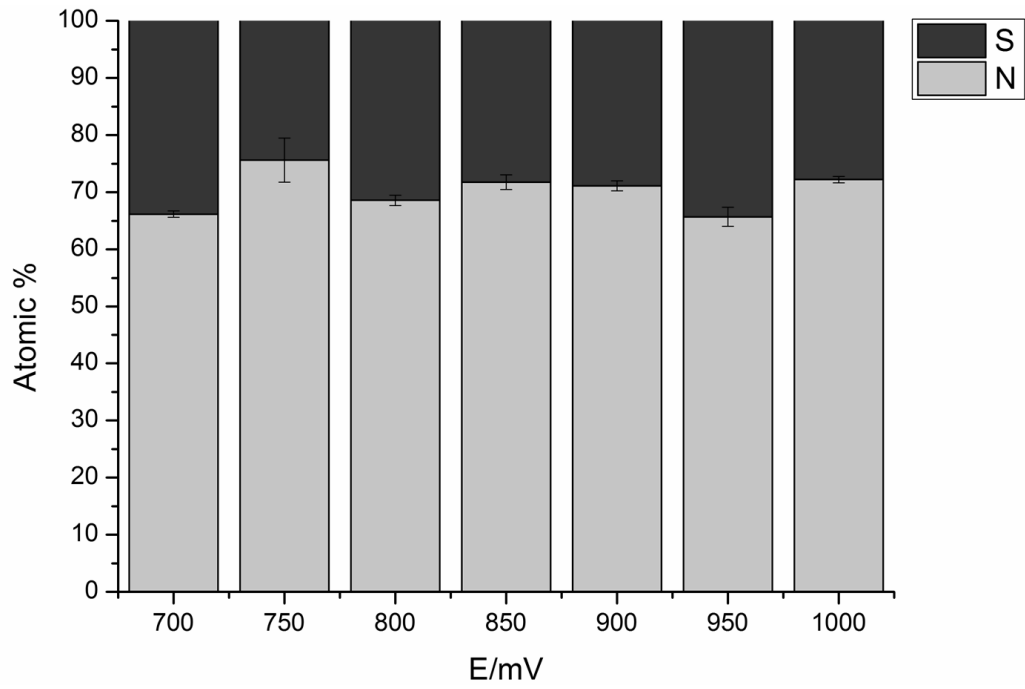


**Figure 3.25** Atomic percentages of N:S present in P(Py-co-EDOT) made with the 1:5 monomer solution as a function of deposition potential.

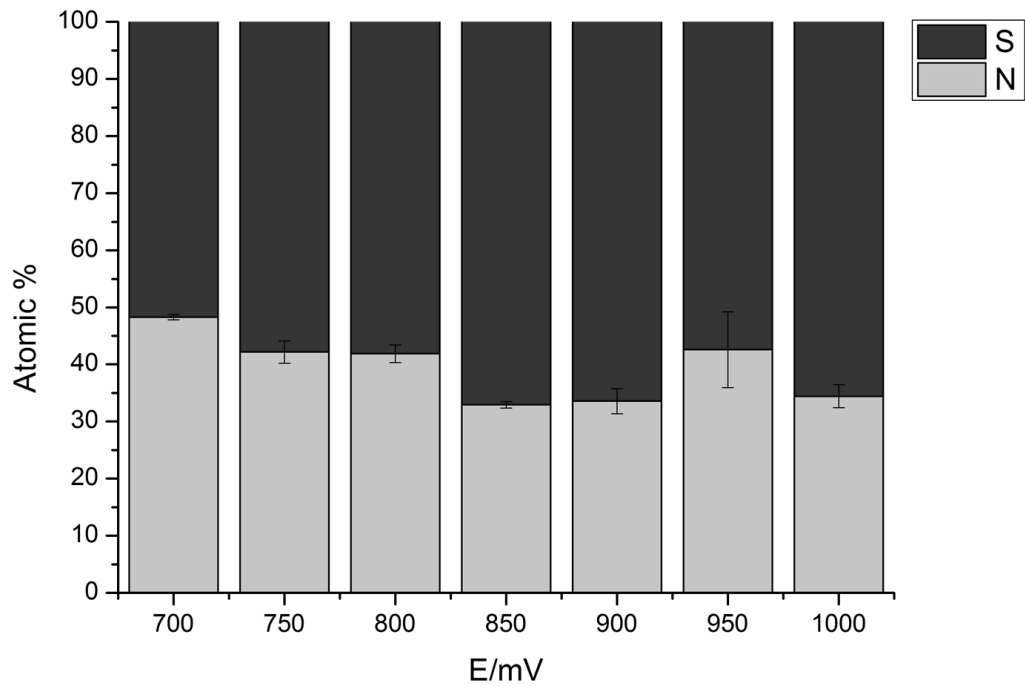


**Figure 3.26** Atomic percentages of N:S present in P(Py-co-EDOT) made with the 1:10 monomer solution as a function of deposition potential.

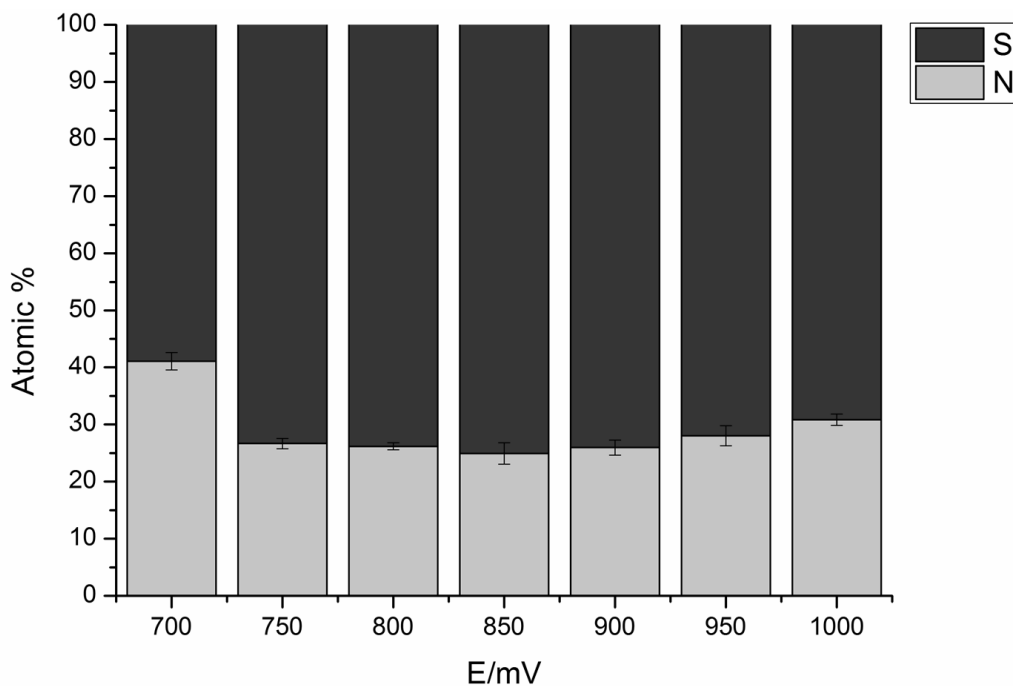


**Figure 3.27** Atomic percentages of N:S present in P(Py-co-EDOT) made with the 1:20 monomer solution as a function of deposition potential.

The results as a function of potential seem to show no systematic variation so if we take the average across the deposition potentials then a feed ratio of 1:5 Py:EDOT gives a copolymer film with 1:0.43 PPy:PEDOT; 1:10 gives 1:1.56 and 1:20 gives 1:2.45.

A similar trend in polymer composition was observed when XPS was performed on three samples grown potentiodynamically from each of the monomer solutions. As expected, the amount of sulphur in the polymer films increased with the amount of EDOT in the solution.

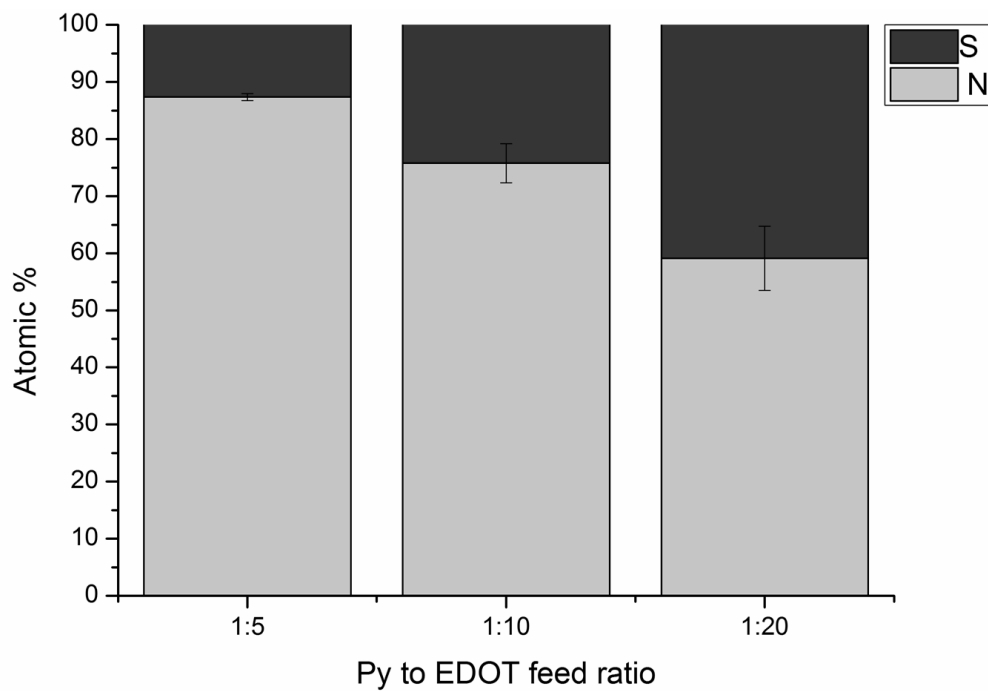


**Figure 3.28** Atomic percentages of N:S present in P(Py-co-EDOT) films grown potentiodynamically from the three monomer solutions.

Although in this chapter the effects of the different feedstock ratios are discussed these can be correlated to copolymer composition using **Figure 3.29**.

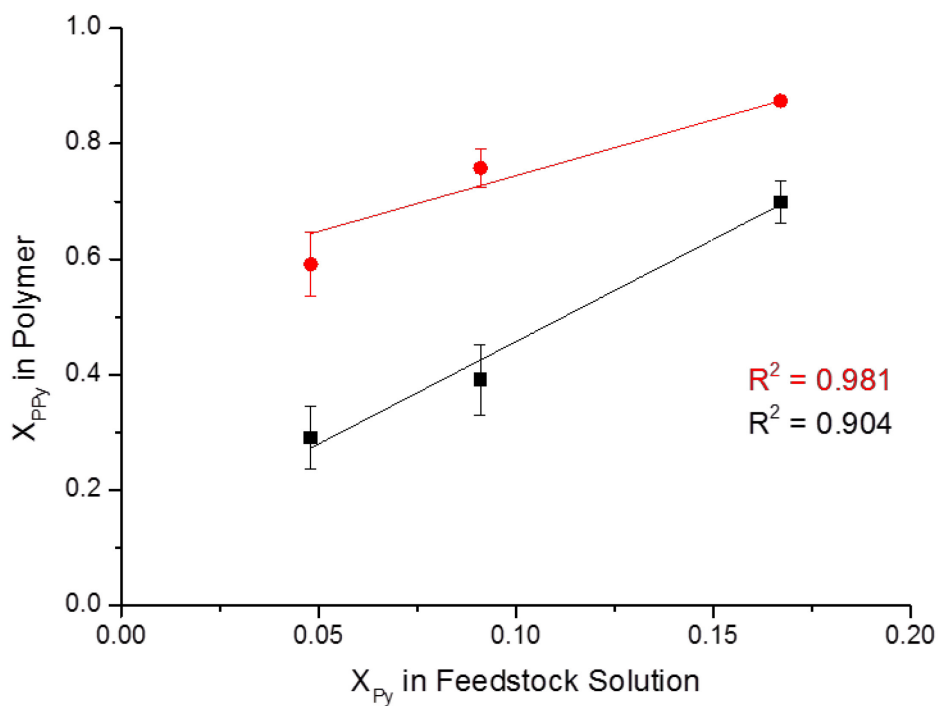


**Figure 3.29** Calibration curve correlating the mole fractions of PPy in the copolymers to the mole fractions of Py in the feedstock solution for both potentiostatic (black) and potentiodynamic (red) deposition.

### 3.3.5. 3D Profiling

In order to assess the quality of the lateral spatial selectivity of the five polymers three dimensional profiles were taken using a Zeta 200 optical profiler. The developed fingerprints and corresponding 3D profiles for the five polymers are shown below.

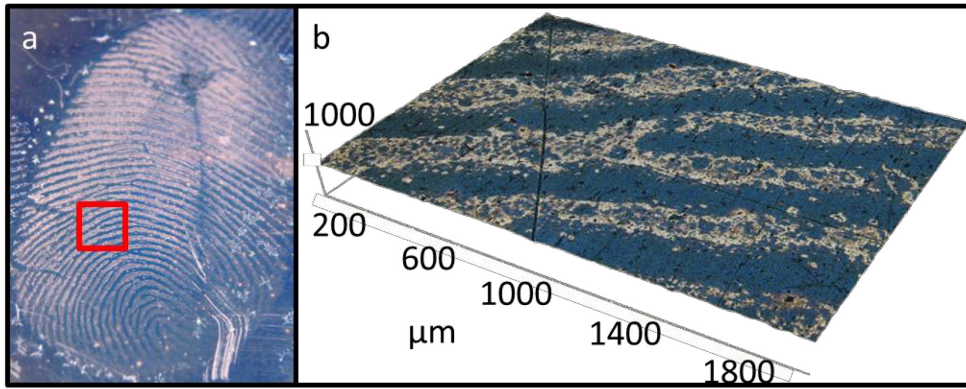


**Figure 3.30** PEDOT enhanced (as detailed in **Section 3.2.2.4**) sebaceous print on stainless steel: (a) photograph showing a highlighted area (bifurcation) subsequently imaged under the 3D profiler (b).

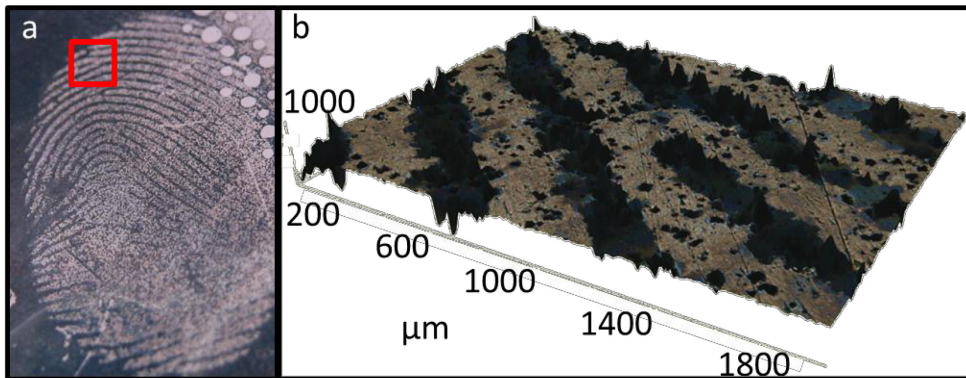


**Figure 3.31** P(Py-co-EDOT) [1:20 monomer ratio] enhanced (as detailed in **Section 3.2.2.4**) sebaceous print on stainless steel: (a) photograph showing a highlighted area (bifurcation) subsequently imaged under the 3D profiler (b).

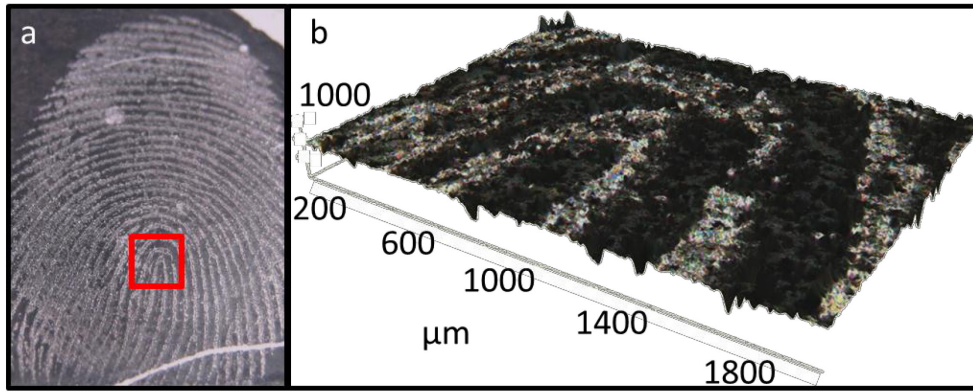


**Figure 3.32** P(Py-co-EDOT) [1:10 monomer ratio] enhanced (as detailed in **Section 3.2.2.4**) sebaceous print on stainless steel: (a) photograph showing a highlighted area (core loop of the fingerprint) subsequently imaged under the 3D profiler (b).

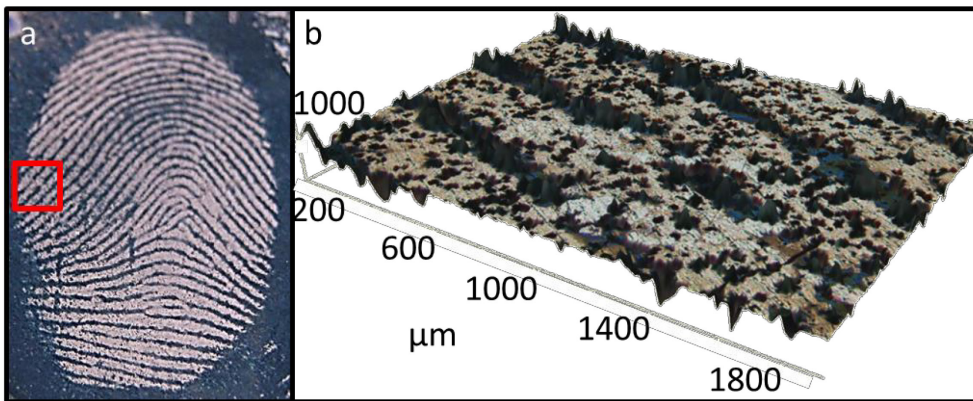


**Figure 3.33** P(Py-co-EDOT) [1:5 monomer ratio] enhanced (as detailed in **Section 3.2.2.4**) sebaceous print on stainless steel: (a) photograph showing a highlighted area (cross over) subsequently imaged under the 3D profiler (b).

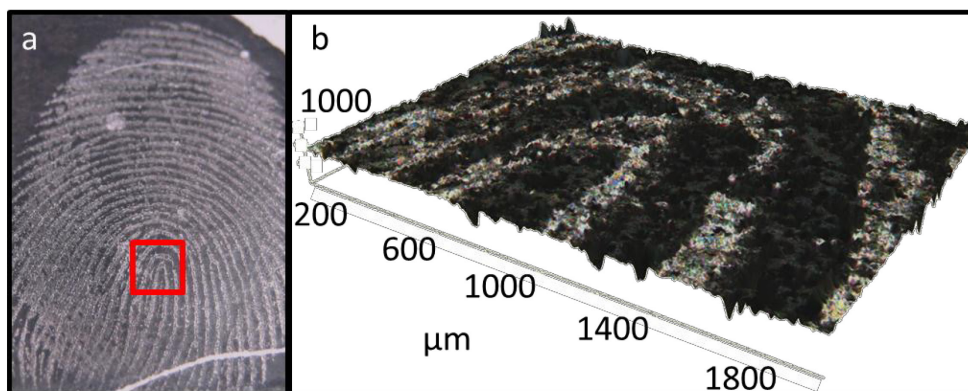


**Figure 3.34** PPy enhanced (as detailed in **Section 3.2.2.4**) sebaceous print on stainless steel: (a) photograph showing a highlighted area (ridge end) subsequently imaged under the 3D profiler (b).

These images show that PEDOT give a smoother more even deposit whereas PPy is rougher. However, each of the polymers is spatially selective enough to not only highlight the secondary features within the fingerprints (bifurcations, cross overs, ridge ends) but tertiary detail with the polymer also depositing in the “holes” in the sweat deposit formed by the sweat pores. These pores are typically only 10-40  $\mu\text{m}$  in diameter which highlights the ability of the conducting polymers to enhance latent fingerprint detail.

### 3.3.6. Comparison with Traditional Fingerprint Enhancement Techniques

Fingerprints on metallic surfaces are most commonly enhanced by dusting, cyanoacrylate (superglue) fuming, and the application of wet powder. Each one of these techniques is well established within the forensic community and all rely on the reagent interacting (physically or chemically) with the sweat deposit in order to visualize the ridge detail of the fingerprint.

In order to assess the ability of the electrochromic enhancement of latent fingerprints using conducting polymers, a comparison was made with these three techniques: dusting with black

powder, black Wet Wop powder and superglue fuming followed by dying with fluorescent BY40<sup>c</sup>.

**Figure 3.35** shows examples of 7 day old, grade 3/4 fingerprints that were kept under ambient conditions before enhancement from each of the different enhancement techniques.

---

<sup>c</sup> This was done with the help of Ann Beresford who developed samples using PANi and Northampton Police Headquarters Chemical Laboratory. The work on PEDOT homopolymer and the traditional techniques was performed as part of my MChem research project.

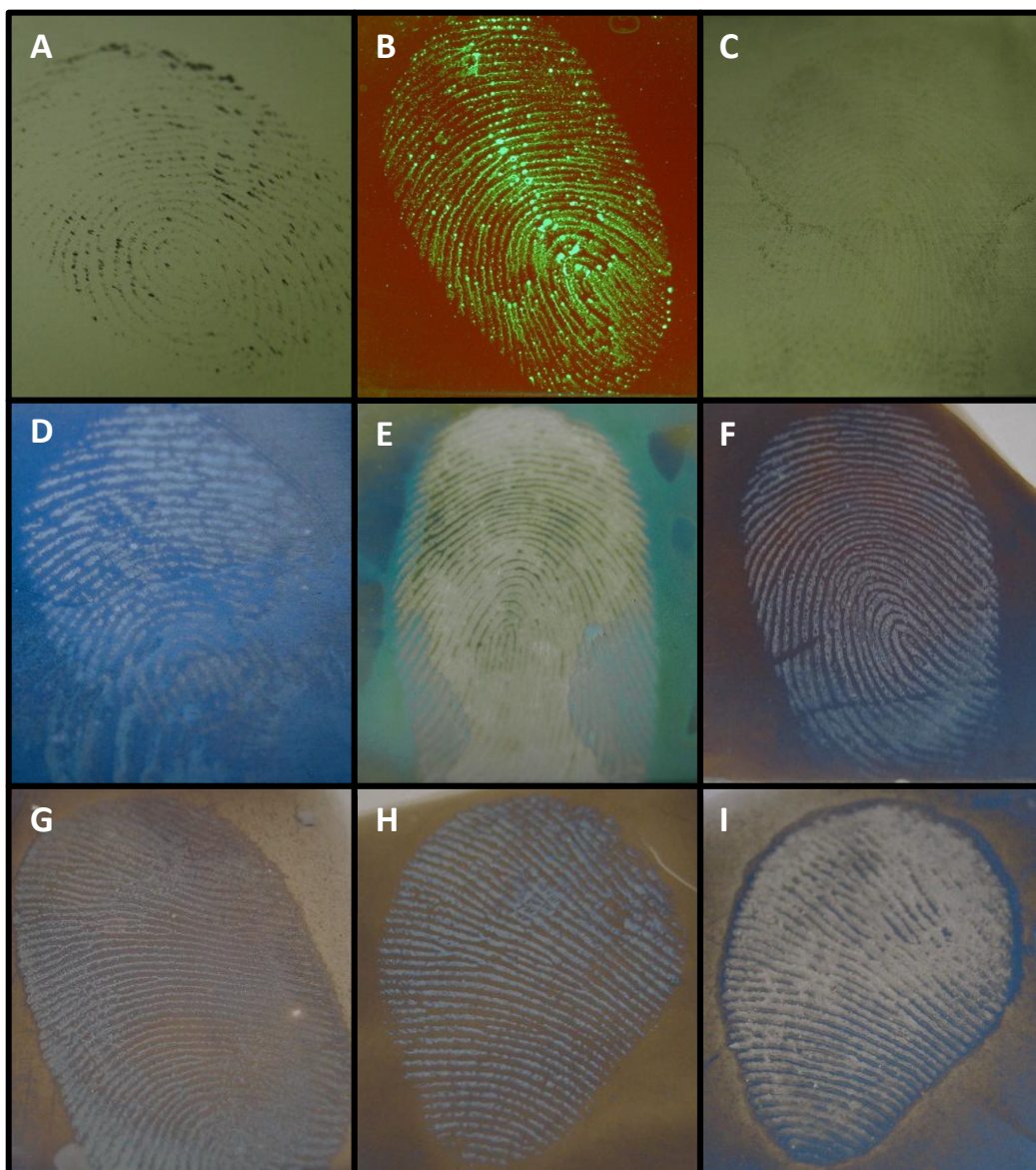


**Figure 3.35** Photographs of 7 day old enhanced fingerprints all grade 3 or 4 on the Bandey scale. Panels (A-C) are the traditional techniques: dusting, superglue fuming/BY40 and Wet Wop. Panels (D-F) are the three homopolymers: PEDOT, PAni and PPy and panels (G-I) are P(Py-co-EDOT) with monomer feed ratios of 1:5, 1:10 and 1:20 respectively (all photographed *ex situ*).

The photographs in **Figure 3.35** are examples of enhanced fingerprints that were left to age naturally in air for one week prior to development: this is the optimum condition for the traditional enhancement techniques as all of the moisture components in the sweat that they

adhere to/react with were still present. Despite this, the conducting polymers show greater contrast between the fingerprint and the background, providing a much clearer image. The fingerprint enhanced with superglue followed by dyeing and viewing under fluorescence also shows good contrast. However a special camera setup, including a fluorescent light and filter, has to be used in order to achieve this.

In order to test the two polymers ability against the traditional methods, the fingerprint deposits were also subjected to a series of harsh pre-treatments designed to remove or degrade the print deposits. These pre-treatments included heating in an oven to 150 °C, submerging in water for extended periods of time, washing with acetone and rubbing the print in warm soapy (40 °C) water. Work done by Patterson et al<sup>16</sup> indicated that these methods would be effective in the removal of latent fingerprint deposits. Similarly, Thomas et al<sup>17</sup> has demonstrated that a natural ageing of the fingerprints also leads to degradation/changes in composition. Therefore, after prints were subjected to the pre-treatments they were left to age either in ambient conditions (after washing with soap/acetone) or in the pre-treatment environment (oven/under water) for periods of 1, 7, 14 and 28 days before being enhanced.

A fingerprint achieving a grade 3 or 4 on the Bandey scale in a research scenario would be deemed useable in a court of law<sup>11</sup>. As such the fraction (expressed as a percentage) of samples for which the fingerprint was enhanced to any and to a useable level by each technique will both be assessed. **Figure 3.36** shows examples of P(Py-co-EDOT) enhanced fingerprint allocated different grades on the Bandey scale.

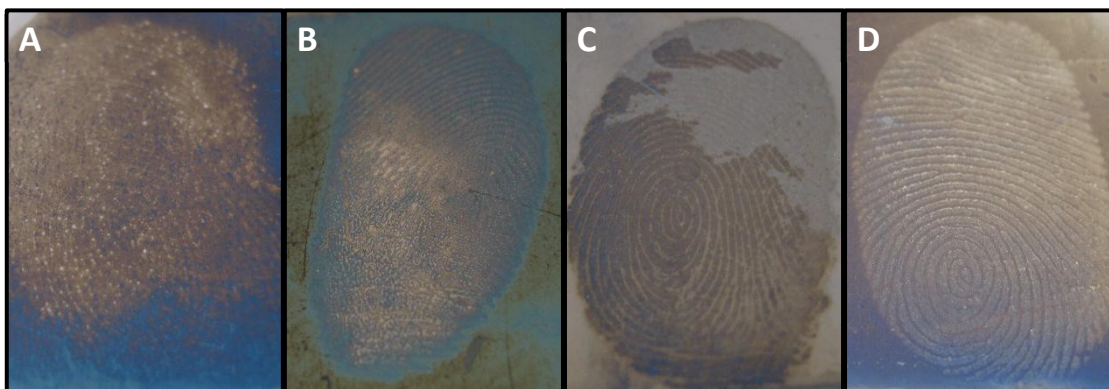


**Figure 3.36** Examples of P(Py-co-EDOT) (as detailed in **Section 3.2.2.4**) enhanced fingerprints of different grades: (A) grade 1 [1:5 feed ratio, 14 days old, acetone treated], (B) grade 2 [1:10, 7 days old, oven treated], (C) grade 3 [1:10, 28 days old, kept under water] and (D) grade 4 [1:20, 14 days old, acetone treated].

The following results summarise a survey conducted on 900 fingerprint samples. The survey was designed to assess 9 different enhancement techniques on fingerprints from 5 donors of varying sex and age. The fingerprints were subjected to 5 different environments with 4 varying lengths of time between the fingerprints being left on the surface and being enhanced.

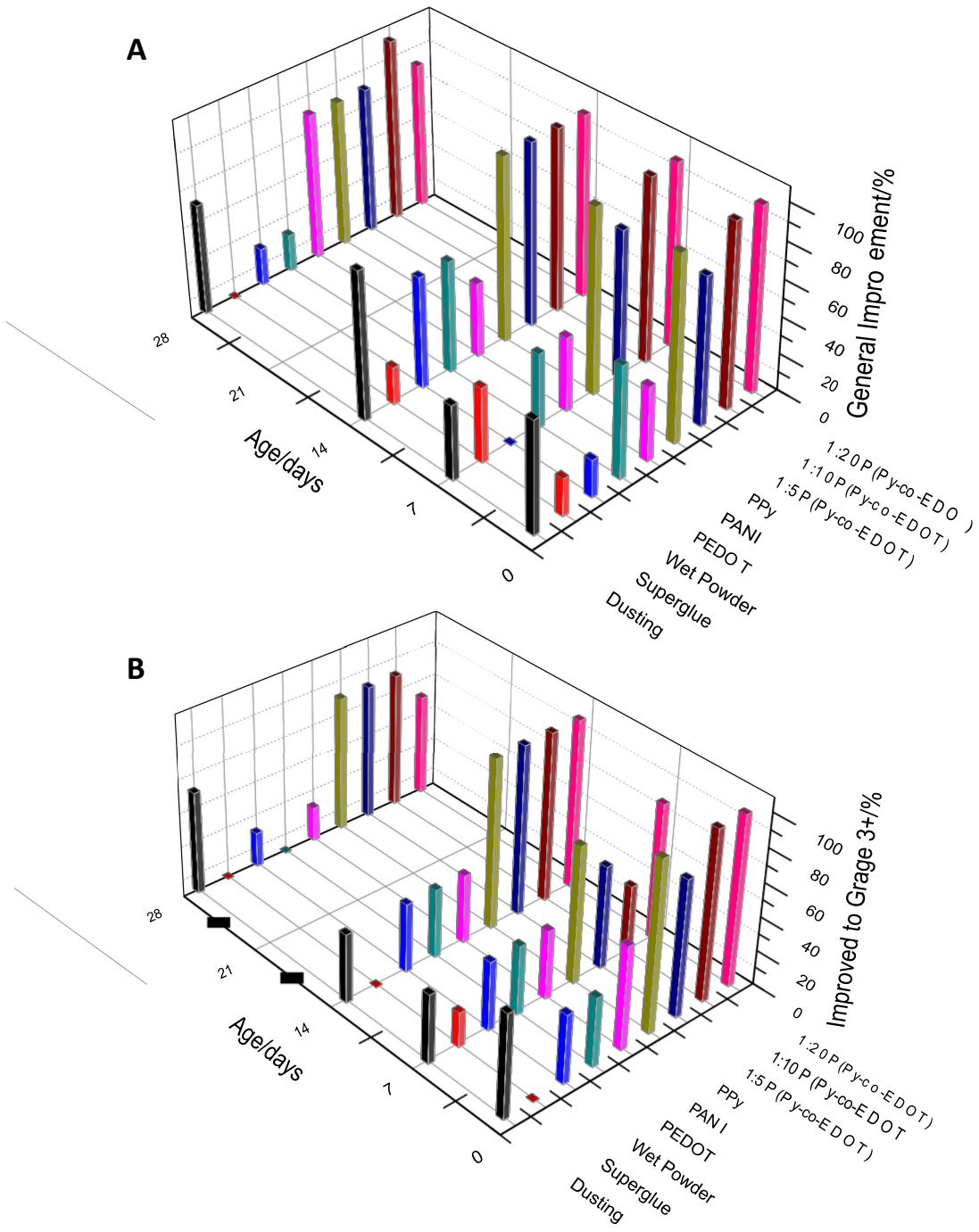


**Figure 3.37** 3D bar charts showing the percentage improvements achieved by each of the development techniques for samples subject to storage under ambient conditions. Each column represents the combined outcome from the five donors; the figure captures data from 180 prints. (A) Percentage of prints enhanced by the designated protocol; (B) percentage of prints enhanced to a useable level (grade 3 or 4) by the designated protocol.

Panel (A) in **Figure 3.37** shows that each of the traditional enhancement techniques offered reasonable enhancement; this is hardly surprising given that no intentional degradation to the sweat deposits (other than aging) has occurred. Interestingly, superglue fuming was shown to be the least effective treatment in this set of “control” measurements. The most effective procedure out of those currently employed by police was simple dusting with black powder. Of the electrochromic polymer treatments here assessed the two polymers explored previously, PANi and PEDOT appear to be weaker than PPy and the three copolymers.

However, panel (A) does not reveal whether the enhanced prints were of a useable quality. Panel (B) shows that under ambient conditions the enhancement quality between the traditional methods and the new set of electroactive polymers was over 40 % greater. However, this relatively unchallenging “control” environment was designed to be the most tolerant to the choice of enhancement procedure.

**Figures 3.38-41** show the analogous charts for the fingerprint sample subjected to harsher pre-treatments/environments.

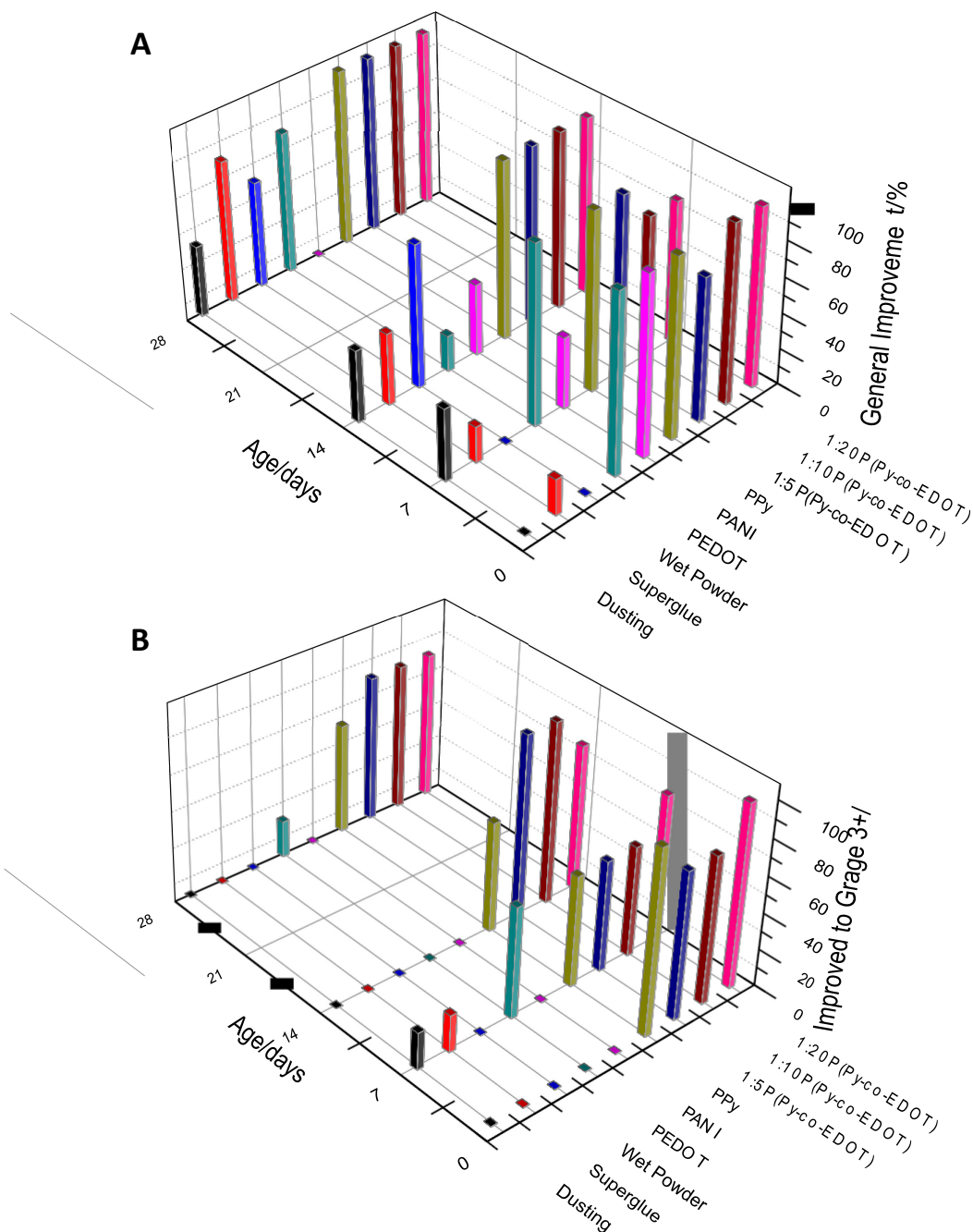


**Figure 3.38** 3D bar charts showing the percentage improvements achieved by each of the development techniques for samples subject to storage in an oven at 150 °C. Each column represents the combined outcome from the five donors; the figure captures data from 180 prints. (A) Percentage of prints enhanced by the designated protocol; (B) percentage of prints enhanced to a useable level (grade 3 or 4) by the designated protocol.

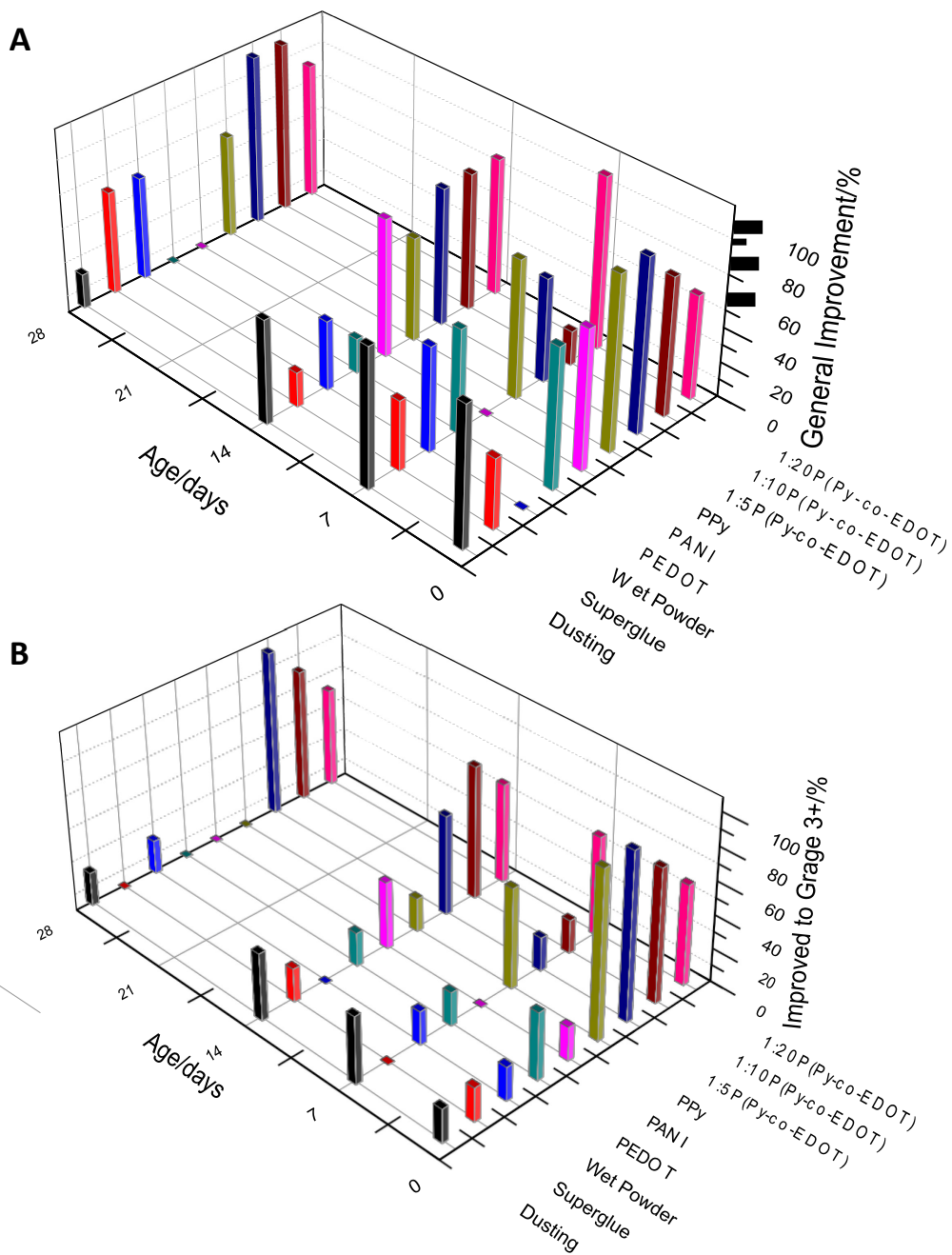


**Figure 3.39** 3D bar charts showing the percentage improvements achieved by each of the development techniques for samples subject to submergence under water. Each column represents the combined outcome from the five donors; the figure captures data from 180 prints. (A) Percentage of prints enhanced by the designated protocol; (B) percentage of prints enhanced to a useable level (grade 3 or 4) by the designated protocol.

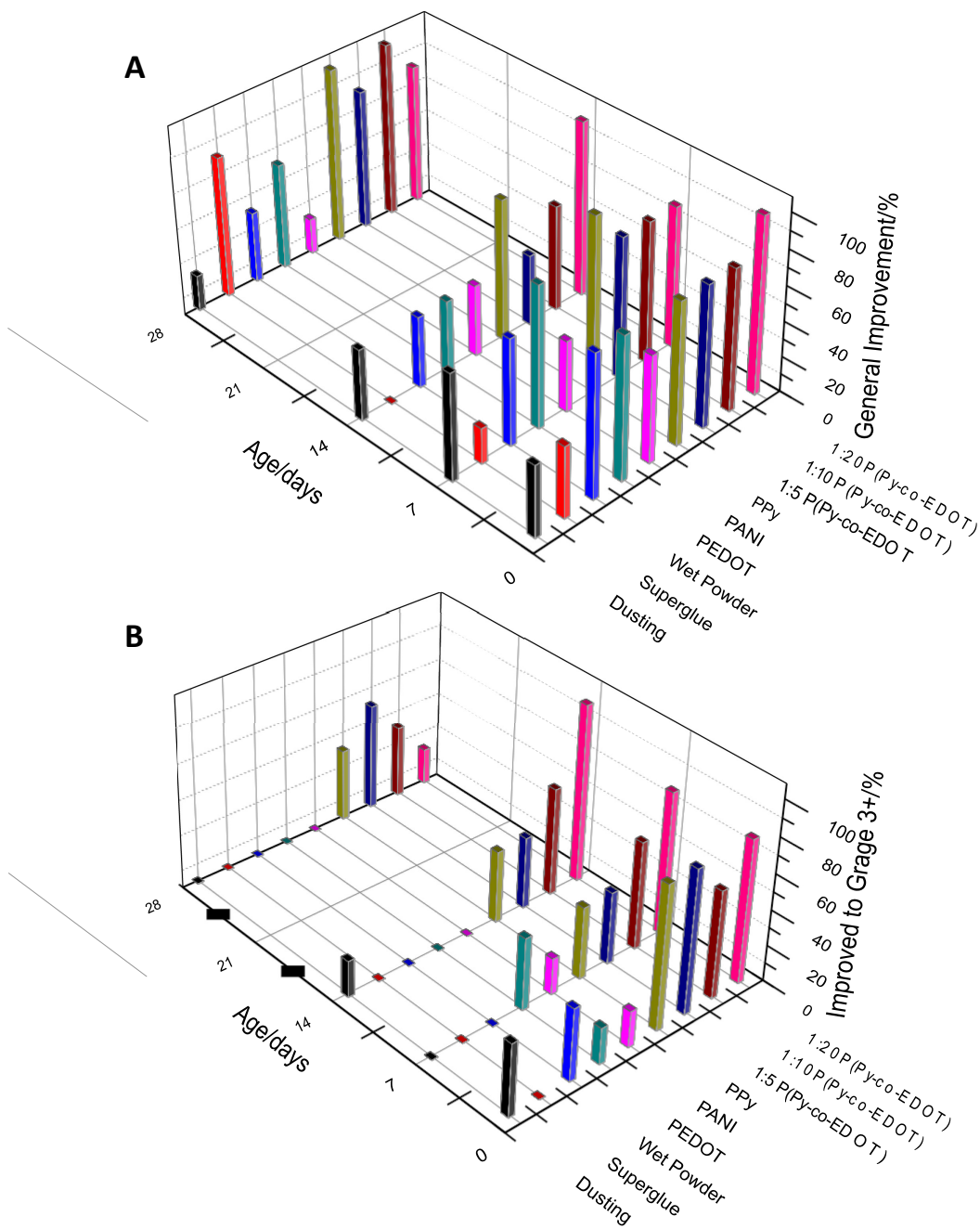


**Figure 3.40** 3D bar charts showing the percentage improvements achieved by each of the development techniques for samples subject to washing with acetone. Each column represents the combined outcome from the five donors; the figure captures data from 180 prints. (A) Percentage of prints enhanced by the designated protocol; (B) percentage of prints enhanced to a useable level (grade 3 or 4) by the designated protocol.

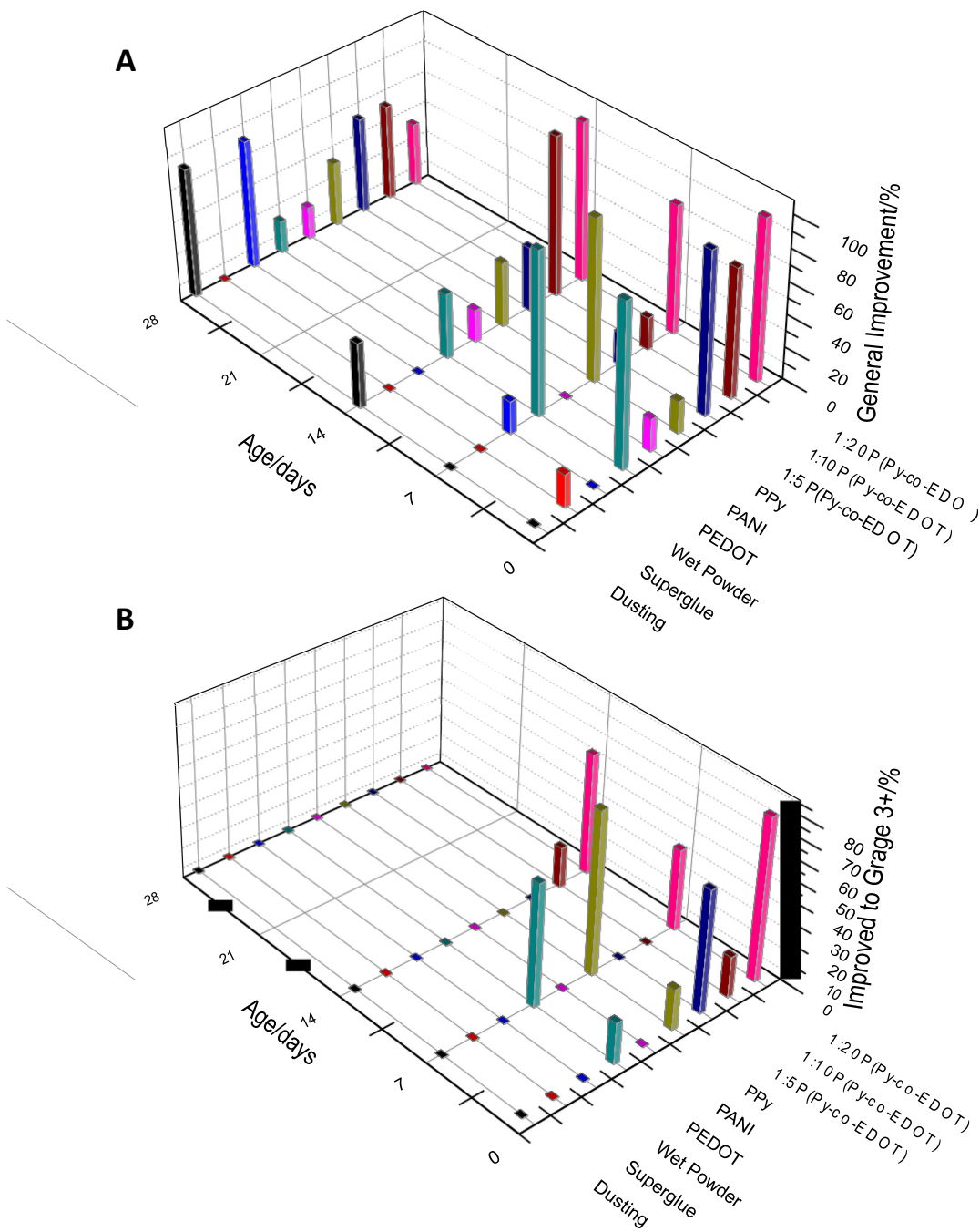


**Figure 3.41** 3D bar charts showing the percentage improvements achieved by each of the development techniques for samples subject to rubbing in warm (40 °C) soapy water. Each column represents the combined outcome from the five donors; the figure captures data from 180 prints. (A) Percentage of prints enhanced by the designated protocol; (B) percentage of prints enhanced to a useable level (grade 3 or 4) by the designated protocol.

This more environmentally challenging part of the survey highlighted the limitations of the traditional technique with very low recovery rates of useable fingerprints [panel (B) **Figures 3.38-41**]. For the samples kept at 150 °C during the aging process PEDOT previously offered the best prospect of recovery<sup>4</sup>. However all three of the P(Py-co-EDOT) ratios increased the rate of recovery significantly, particularly on older samples. More useable prints from samples kept under water and after washing with acetone were recovered with the copolymers than with the other techniques.

Formerly, PEDOT was the only enhancement procedure that offered any success on samples that had been hand washed in warm, soapy water. PPy showed a similar level of enhancement as both homopolymers showed some success on samples up to one week old. Importantly, using a copolymer of the two extended the time scale on which useable prints could be recovered by a factor of two with the 1:20 monomer feed ratio showing the most promise.

The observed drop in recovery rate as fingerprints age means that in a practical forensic scenario the immediate processing of evidence is necessary.

### **3.3.7. Over Oxidation**

When determining the anodic cycling limit using a soap washed fingerprint enhanced with a copolymer film that showed no evidence of a fingerprint an interesting phenomenon occurred: after irreversibly over oxidising the film the underlying fingerprint detail was revealed.

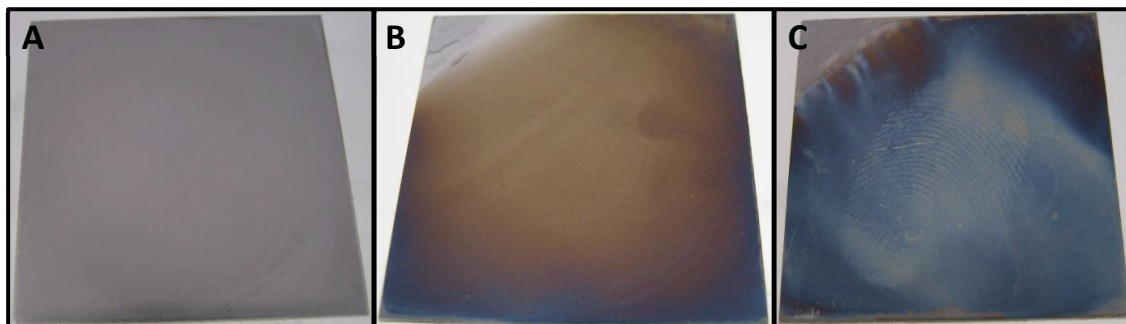


**Figure 3.42** Photographs of a 1 day old soap washed sample (A) sebaceous print before enhancement, (B) after initial enhancement with PPy and (C) after over oxidation of the PPy at 1.9 V for 1 minute.

This technique was applied to several films that were given a grade zero on the Bandey scale some of which showed a similar level of exposure seen in **Figure 3.42**. This behaviour is attributed to the fact that the layer of sweat deposit left after soap washing could be only a few nanometres. This could easily be covered with the first “nucleation layer” of polymer. However, it may affect the adhesion of the polymer onto the steel underneath it so over oxidising the polymer to a level where oxygen evolution starts to occur might be enough to rupture the adhesion of the polymer only where the fingerprint is present.

### 3.3.8. Application to Other Metal Surfaces and *Pseudo* Items of Evidence

Whilst stainless steel is a common metal for everyday items that might be of evidential value in a crime scene situation (tools, handles, knives) there are other metals that more evidentially important items (bullet casings) are made from. It is also important to test this technology on larger, more structurally challenging surfaces and not simply on flat squares of polished stainless steel.

**Figures 3.43-46** show the application of the four new polymers; PPy, P(Py-co-EDOT) 1:5, 1:10 and 1:20 to the processing of fresh prints (developed within a few hours) on pseudo items of evidence made from stainless steel, brass and nickel.

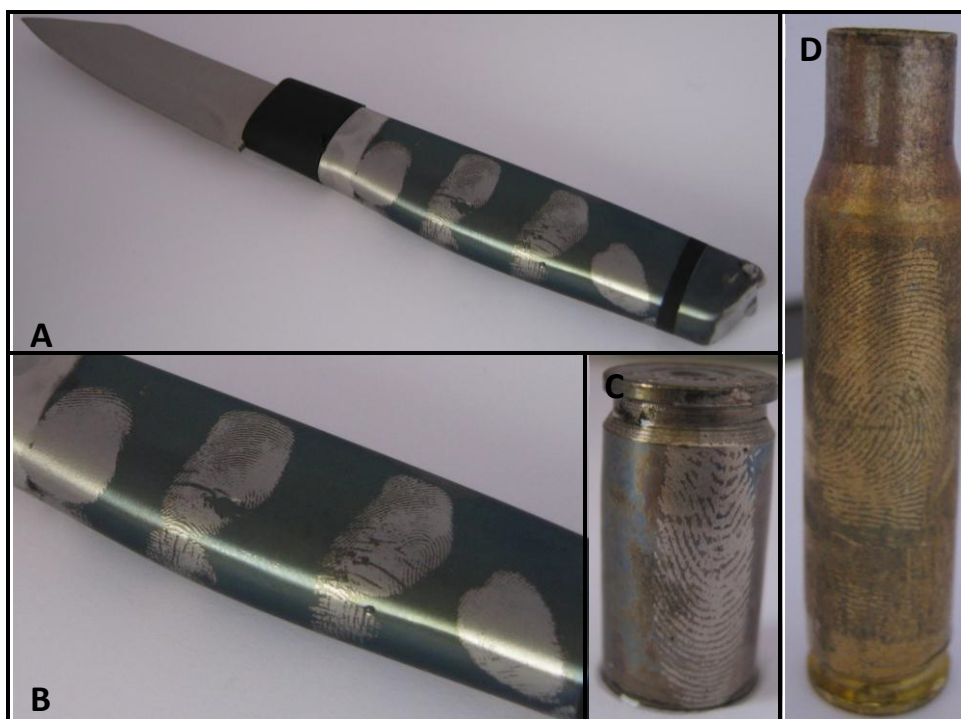


**Figure 3.43** PPy enhanced fresh sebaceous fingerprints on (A + B) a stainless steel knife, (C) a Ni coated brass bullet casing and (D) a brass bullet casing.

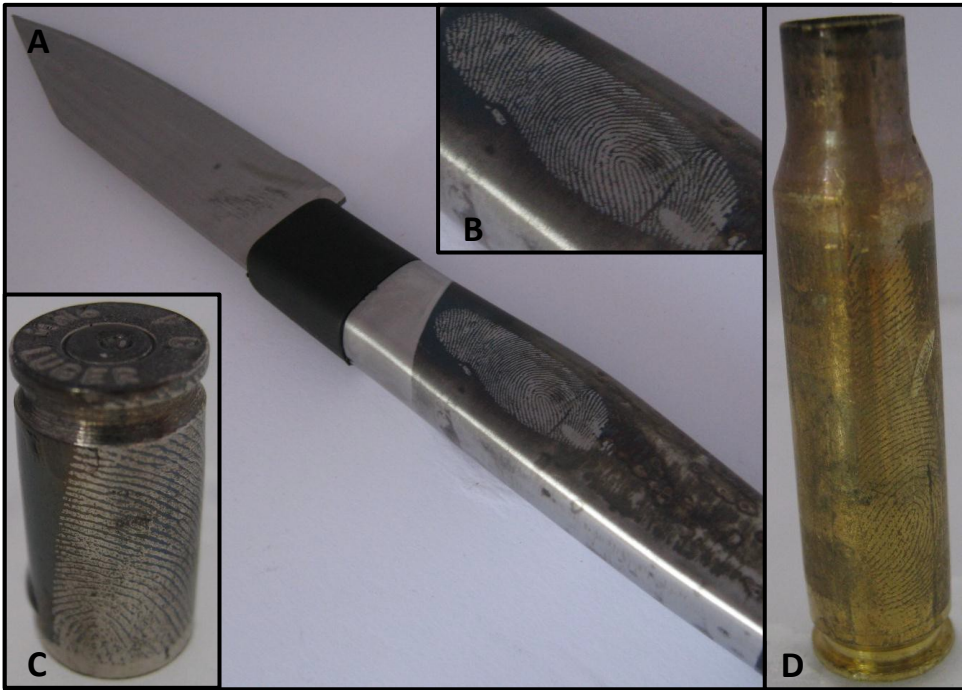


**Figure 3.44** P(Py-co-EDOT) 1:5 ratio enhanced fresh sebaceous fingerprints on (A + B) a stainless steel knife, (C) a Ni coated bullet casing and (D) a brass bullet casing.



**Figure 3.45** P(Py-co-EDOT) 1:10 ratio enhanced fresh sebaceous fingerprints on (A + B) a stainless steel knife, (C) a Ni coated bullet casing and (D) a brass bullet casing.



**Figure 3.46** P(Py-co-EDOT) 1:20 ratio enhanced fresh sebaceous fingerprints on (A + B) a stainless steel knife, (C) a Ni coated bullet casing and (D) a brass bullet casing.

The lack of acid in the solution along with the relatively high monomer concentrations in solution, low deposition potential and short deposition times mean that the same solution and electrochemical procedure can be applied to a range of metallic surfaces with different chemistries and colours. This opens the technique up to accessing a wider range of evidentially valuable items.

### 3.4. Conclusions

Out of over 200,000 items of fingerprint evidence that are processed each year in the UK, approximately 20,000 are metallic items. Surprisingly, despite the range of methods available, less than 10% of these produce useable fingerprints. Given the prevalence of metallic objects - weapons, tools, handles – in criminal investigations this is an important challenge.

Visualisation of latent fingerprints present on metallic surfaces has been demonstrated here by means of spatially selective deposition of the homopolymer PPy and the copolymer P(Py-co-EDOT) with three different feedstock ratios. This method is complementary to traditional enhancements, which require chemical or physical interaction with the fingerprint deposit, as it interacts with metallic surface around the fingerprint. It utilises the sweat deposit as an insulating mask resulting in the inhibition of electrochemical processes on regions “protected” by the fingerprint. This results in polymer deposition between the ridges, thus generating a negative image of the fingerprint. Subsequent variation of the applied potential and exploiting the polymer’s electrochromic properties means that the colour of the background (polymer) can be continuously and reversibly adjusted in order to optimise the contrast with the metal surface under the latent/invisible fingerprint deposit. The fact that this manipulation is reversible means that the contrast can be optimised separately in different regions of the image, for example in **Figure 3.18** where the fingerprint deposit is of variable thickness or definition.

For the practically challenging situations explored here, using stainless steel as a representative surface, the potentiostatic deposition of the comonomers in an aqueous SDS/LiClO<sub>4</sub> electrolyte solution showed not only a great advantage over traditional methods but in some instances a greater recovery rate than the three homopolymers explored: PANi<sup>2</sup>, PEDOT<sup>3</sup> and PPy. Suitable control of deposition rate, via monomer concentration, deposition potential and development time, permits progressive filling of trenches between fingerprint deposits until optimum contrast is achieved.

The major advantage of this new set of copolymers is that the development time has been cut compared to the homopolymers previously explored where a typical time to develop a print using PANi was 30 minutes and for PEDOT was approximately 10 minutes. Here the maximum deposition time used was only 10 seconds. This allowed deposition on more

challenging metal surfaces such as brass bullet casings. Microscopic observation of the polymer enhanced fingerprints on the metallic surfaces, using 3D profiling and FTIR mapping, showed good definition between the regions protected by the fingerprint sweat and the polymer covered furrows in between.

This novel technique involves the interaction of a visualizing reagent with the bare metal surface around the fingerprint deposit. It is complementary to traditional fingerprint enhancement methods, which are based on either a physical or a chemical interaction of a reagent with the fingerprint deposit itself. Future work should explore using both approaches sequentially, when one technique fails to give a print of evidential quality.

The survey assessment of the electrochromic technique, comparing the homopolymers and copolymers with more traditional techniques, revealed a greater ability to enhance latent fingerprints of evidentially useful quality from challenging and forensically relevant scenarios. These included attempts to remove the fingerprint with soap or acetone and extended exposure to water or heat. The results showed the electrochromic development was competitive with presently used methods across a broad range of scenarios and may exceed them in certain scenarios. Given that these results only took into account the initial polymer development and not any subsequent contrast manipulation of the polymers' electrochromic properties means that there is potential for the technique to distinguish itself further. The traditional approach for fingerprint comparison involves the use of monochrome black-and-white images but, by definition, electrochromic materials allow the manipulation of colour by application of a voltage. This has been shown to reveal more underlying detail, for example in areas where over filling of trenches may have occurred.

### 3.5. References

- <sup>1</sup> Bowman V., (2004) “*Manual of fingerprint development techniques, 2<sup>nd</sup> rev. edn.*” Sandridge, UK: Police Scientific Development Branch, Home Office.
- <sup>2</sup> Beresford, A. L., and Hillman, A. R., *Anal. Chem.*, 2010, **82**, 483–486.
- <sup>3</sup> Brown, R. M., and Hillman, A. R., *Phys. Chem. Chem. Phys.*, 2012, **14**, 8653.
- <sup>4</sup> Beresford, A. L., Brown, R. M., Hillman, A. R., and Bond, J. W., *J. Forensic Sci.*, 2011, **57(1)**, 93-102.
- <sup>5</sup> Zhang, C., Xu, Y., Wang, N., Xiang, W, Mi, O., Ma, C., *Electrochim. Acta*, 2009, **55**, 15.
- <sup>6</sup> Tao, Y., et al., *Synthetic Metals*, 2012, **162**, 728– 734.
- <sup>7</sup> Tarkuc, S., Sahmetlioglu, E., Tanyeli, C., Akhmedov, I. M., Toppare, L., *Opt. Mater*, 2008, **30**, 1489–1494.
- <sup>8</sup> Van, F. T., Beouch, L., Vidal, F., Yammineb, P., Teyssie, D., Chevrot, C., *Electrochim. Acta*, 2008, **53**, 4336–4343.
- <sup>9</sup> Ferreira, J., Santos, M. J. L., Matos, R., Ferreira, O. P., Rubira, A. F., Giroto, E. M., *J. Electroanal. Chem.* 2006, **591**, 27.
- <sup>10</sup> Somani, P. R., Radhakrishnan, S., *Mater. Chem. Phys.*, 2002, **77**, 118.
- <sup>11</sup> Bandey HL. “*Fingerprint development and imaging newsletter: the powders process, study 1.*” Sandridge, UK: Police Scientific Development Branch, Home Office, 2004; Report No.:54 / 04.
- <sup>12</sup> Tarkuc, S., Sahin, E., Toppare, L., Colak, D., Cianga, I., Yagci, I., *Polymer*, 2006, **47**, 2007.

<sup>13</sup> Cui, L., Li, J., Zhang, X., *Mater. Lett.* 2009, **63**, 685.

<sup>14</sup> Selvaganesh, S. Vinod and Mathiyarasu, J. and Phani, K. L. N. and Yegnaraman, V., *Nanoscale research Letters*, 2007, **2 (11)**, 546-549.

<sup>15</sup> Fred W. Billmeyer, *Textbook of Polymer Science*, John Wiley and Sons, New York, 1984 pp101-125

<sup>16</sup> Paterson, E., Bond, J. W., and Hillman, A. R., *J. Forensic Sci.*, 2010, **55(1)**, 221.

<sup>17</sup> Thomas, G. L., Reynoldson, T. E., *J. Phys. D: Appl. Phys.*, 1975, **8**, 724.

# 4. A Neutron Reflectivity Study of the Fluorescent-Electrochromic Enhancement of Latent Fingerprints

---

## 4.1. Introduction

As seen in **Chapter 3**, the electrochromic enhancement of latent fingerprints using conducting polymers is an effective means of visualizing latent fingerprints<sup>1,2</sup>. It utilises the fingerprint deposit as an insulating mask resulting in spatially selective deposition of the polymer on the bare metal surface in between the ridges of the fingerprint.

Here we describe an extension of the electrochromic concept, in which capability for emission (fluorescence) is added to that of absorption to combine fluorescent and electrochromic enhancements of latent fingerprints<sup>3</sup>. The objective was to expand the electrochromic enhancement, which relies on absorption of light, to include emission as a second means of visual contrast. This can be achieved through incorporation of a fluorophore into the polymer film. The challenge is that fluorophore-functionalised monomers are not polymerizable, almost certainly for steric reasons. The chemical/electrochemical route explored in this chapter involves the polymerization of a monomer (here, 3-(pyrrol-1-yl)propylamine, Py-NH<sub>2</sub>) functionalised with a relatively large leaving group (here, 9-fluorenylmethoxycarbonyl, Fmoc) that is sterically small enough for electropolymerisation. After film deposition, the amide-bound Fmoc is hydrolysed out, to leave nanoscale voids into which the fluorophores can be diffused, to bind with the polymer spine. The ease in which the bulky fluorophore moiety can

penetrate into the film will determine the intensity of emission that can be achieved, and hence the improvement in visual contrast. As a result of this, the enhancement of any latent fingerprint requires *lateral* resolution between the ridges of sweat deposit ( $\mu\text{m} \rightarrow \text{mm}$  length scales). To achieve this requires chemical control (FMOC hydrolysis and fluorophore penetration) in the *vertical* direction and on much smaller length scales ( $\text{nm} \rightarrow \mu\text{m}$ ).

In order to assess the amount of vertical chemical control of fluorophore penetration, neutron reflectivity was used to probe the structure of the polymer films during the different stages of the reaction shown in **Figure 4.3**. Neutron reflectivity measures the intensity of reflected neutrons as a function of either wavelength (time of flight mode) or angle of incidence (monochromatic mode) to yield a reflectivity profile. The shape of this profile yields information about the films' vertical spatial structure<sup>4-7</sup>. Kinetic measurements performed on INTER neutron reflectometer (ISIS) show how the depth profile of the polymer film alters during the hydrolysis in real time and static measurements performed on FIGARO/D17 (ILL) and OFFSPEC (ISIS) show the changes in reflectivity after subsequent reaction with a fluorophore. This allows the total penetration depth of the fluorophore into PPyNH<sub>2</sub> films with and without free volume generated by FMOC hydrolysis to be measured.

## 4.2. Experimental

### 4.2.1. Monomer Synthesis

#### 4.2.1.1. Reduction of *N*-cyanoethylpyrrole (PyCN) to yield 3-(pyrrol-1-yl)propylamine (PyNH<sub>2</sub>)

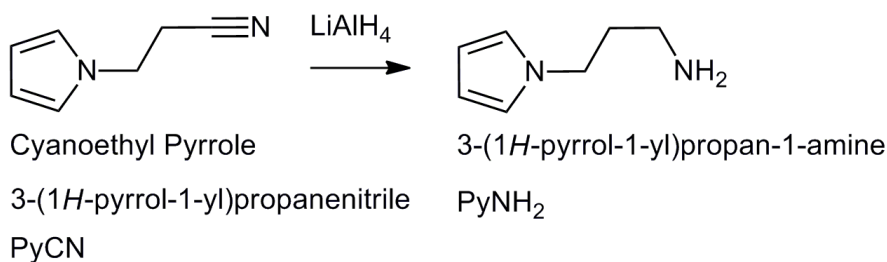


**Figure 4.1** Reduction of PyCN to PyNH<sub>2</sub>.

*N*-cyanoethylpyrrole (PyCN) was purified by Kugelrohr distillation at 133 °C before use. In a 250 ml, two neck round bottom flask fitted with a condenser equipped with a drying tube and a dropping funnel, LiAlH<sub>4</sub> (9.9, 0.26 mol) was dissolved in dry diethyl ether (150 ml). The flask was externally cooled in an ice bath. PyCN (7 g, 0.056 mol) dissolved in dry diethyl ether (50 ml) was then added to the solution drop wise over 30 minutes. The reaction was then left to stir for two hours. Excess LiAlH<sub>4</sub> was then neutralised using cold water. The solution was filtered, dried over MgSO<sub>4</sub>, and filtered. The solvent was then removed by rotary evaporation yielding 3-(Pyrrol-1-yl)propylamine (PyNH<sub>2</sub>) (yellow oil). This was purified by Kugelrohr distillation (6.1g, 84 % yield). FTIR of the PyNH<sub>2</sub> product showed that all of the PyCN had been reduced as the sharp peak at 2250 cm<sup>-1</sup> for the nitrile stretch had disappeared and two peaks forming a broad stretch had appeared around 3120 and 3295 cm<sup>-1</sup> for the 2 NH stretches (appendix 1).

**4.2.1.2. Amine Protection of PyNH<sub>2</sub> with 9-Fluorenylmethoxy carbonyl (FMOC) to yield (9H-fluoren-9-yl)methyl 3-(1H-pyrrol-1-yl)propylcarbamate (PyFMOC)**

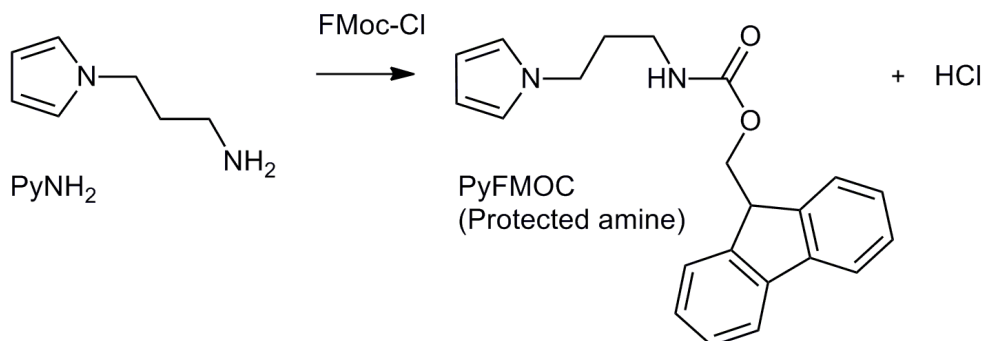


**Figure 4.2** Protection of PyNH<sub>2</sub> using FMOC.

PyNH<sub>2</sub> (2.5 g, 0.021 mol) in a solution of Na<sub>2</sub>CO<sub>3</sub> (3 g, 0.028 mol) in water/dioxane (60 ml, 1:1) was stirred in an ice bath. FMOC-Cl (5.5 g, 0.021 mol) in water/dioxane (60 ml, 1:1) was added and the mixture left to stir for two hours at room temperature. Water (50 ml) was added. The PyFMOC was extracted three times with ethyl acetate and one back extraction was performed to remove any NaCl. The solution was then dried over MgSO<sub>4</sub> and filtered. The solvent was removed via rotary evaporation yielding crude PyFMOC (5.5 g, 79 % yield, white solid). This was purified by column chromatography in DCM/diethyl ether (10:1) to yield pure PyFMOC (4.2 g, 60 %). The FTIR of the PyNH<sub>2</sub> monomer after reaction with the FMOC protecting group shows only one NH stretch at 3325 cm<sup>-1</sup>. A C=O stretch had also appeared for the ester in the FMOC group at 1705 cm<sup>-1</sup>.

## 4.2.2. Electrode Preparation

Gold coated microscope slides/quartz blocks were used as working electrodes, and were prepared as follows. The substrates were washed and sonicated in Decon, rinsed and sonicated in isopropanol twice before drying with compressed air. The substrates were held at reflux in isopropanol (400 ml) containing fresh MPTS (12 ml) and distilled water (12 ml) for

15 min. They were then rinsed and sonicated in clean isopropanol and blown dry with compressed air. This process was repeated twice. A Balzer's Turbo vacuum system was used to deposit gold onto the silanised surfaces.

### 4.2.3. Electropolymerisation

#### 4.2.3.1. PPyNH<sub>2</sub>

PPyNH<sub>2</sub> was grown potentiodynamically ( $0.13 < E/V$  vs. Ag/AgCl (saturated KCl)  $<$  anodic limit  $I_{\max} = 3.8$  mA,  $v = 20$  mVs<sup>-1</sup>, 30 cycles) from tetraethylammonium perchlorate (TEAP) (10 mM) and HBF<sub>4</sub> (10 mM, pH 4-5) in MeCN containing the monomer PyNH<sub>2</sub> (10 mM).

#### 4.2.3.2. PPyFMOC

PPyFMOC was grown potentiodynamically ( $0.13 < E/V$  vs. Ag/AgCl (saturated KCl)  $<$  anodic limit  $I_{\max} = 3.8$  mA,  $v = 20$  mVs<sup>-1</sup>, 30 cycles) from tetraethylammonium perchlorate (TEAP) (10 mM) and HBF<sub>4</sub> (10 mM, pH 4-5) in MeCN containing the monomer PyFMOC (10 mM).

### 4.2.4. Post Polymerisation Chemical Modifications

#### 4.2.4.1. Amine Deprotection

The base de-protection of PPyFMOC to yield PPyNH<sub>2</sub>-deprotected was carried out by soaking the films in a solution of piperidine (30 % v/v in ACN) for 30 minutes. The films were then washed with ACN to remove excess piperidine.

As the unprotected PPyNH<sub>2</sub> films are grown under acidic conditions they were deprotonated from PPyNH<sub>3</sub><sup>+</sup> prior to any further chemical modification. This was done by soaking the films in a 10 mM sodium carbonate buffer solution for 30 minutes and washing with water.

#### 4.2.4.2. Reaction with Fluorophore

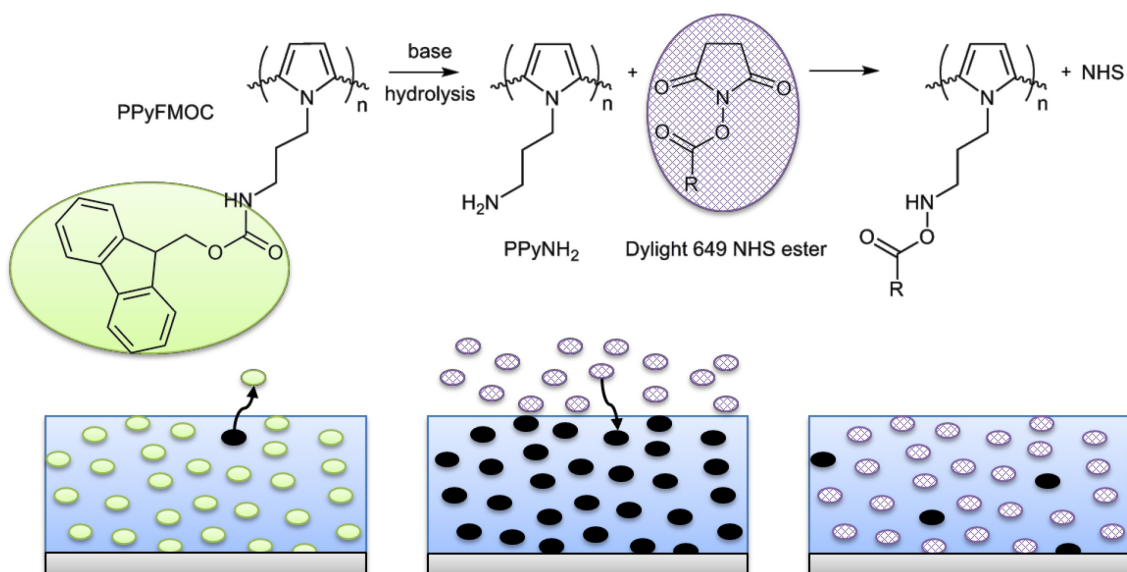


**Figure 4.3** Schematic representation of (i) PPyFmoc deposition, (ii) Fmoc (green) hydrolysis to create solvent “voids” (black); (iii) diffusion of fluorophore (purple) into voids and attachment to polymer.

In order to chemically bind the fluorophores to the PPyNH<sub>2</sub> films, fluorophores functionalised with NHS esters were used. The films were soaked in a solution of the NHS ester fluorophore [10 mM in DMSO/pH 7 potassium phosphate buffer (1:9 ml)]. The films were left to react for 30 minutes before rinsing with water.

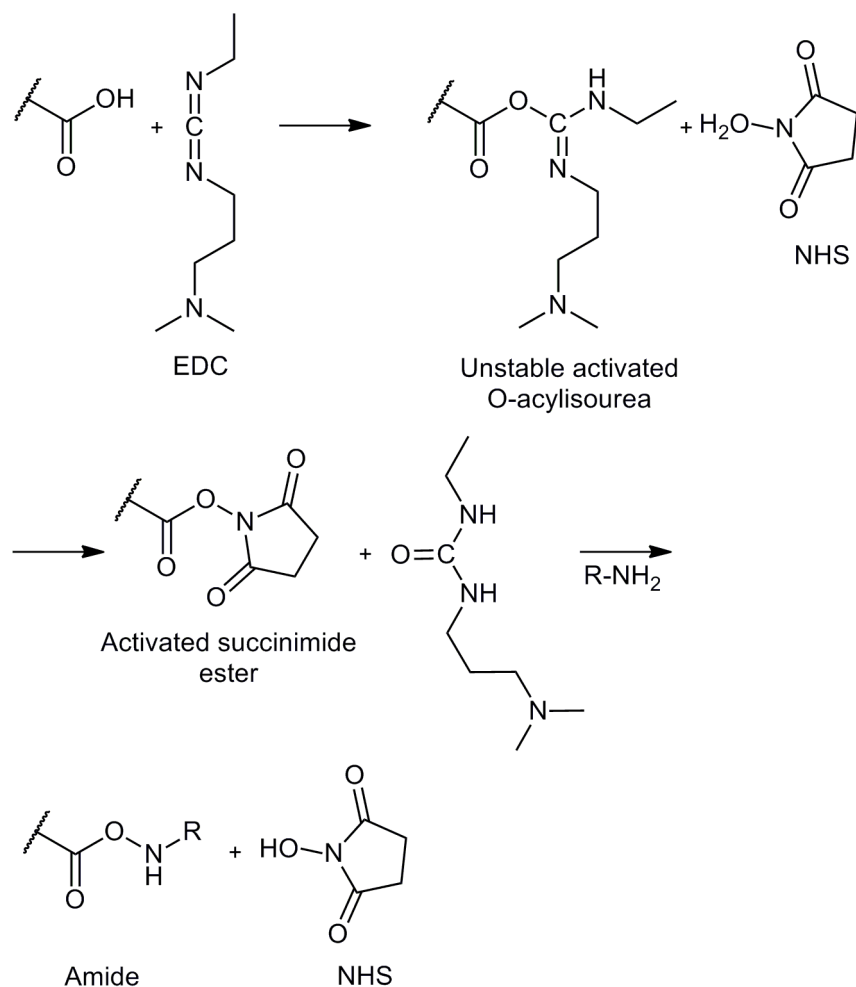


**Figure 4.4** General reaction scheme for activating a carbonyl group on an NHS ester in order to promote the formation of an amide bond in the presence of an amine.

In total three fluorophores were investigated: Dylight 649 NHS ester (structure unpublished), Cy3 and Cy7.5 (see **Figure 4.8**). As the structure of Dylight 649 is commercially protected physically reasonable approximations were used along with information provided by Thermo Fisher Scientific<sup>a</sup> in the scattering length density (SLD) calculations. The molar mass is 1008

---

<sup>a</sup> Thank you to Ines Carro-Muino (of Thermo Fisher Scientific) for helpful conversations relating to fluorophore NR calculations.

Daltons and there are four sulfonate groups to aid solubility on an essentially aromatic hydrocarbon skeleton.

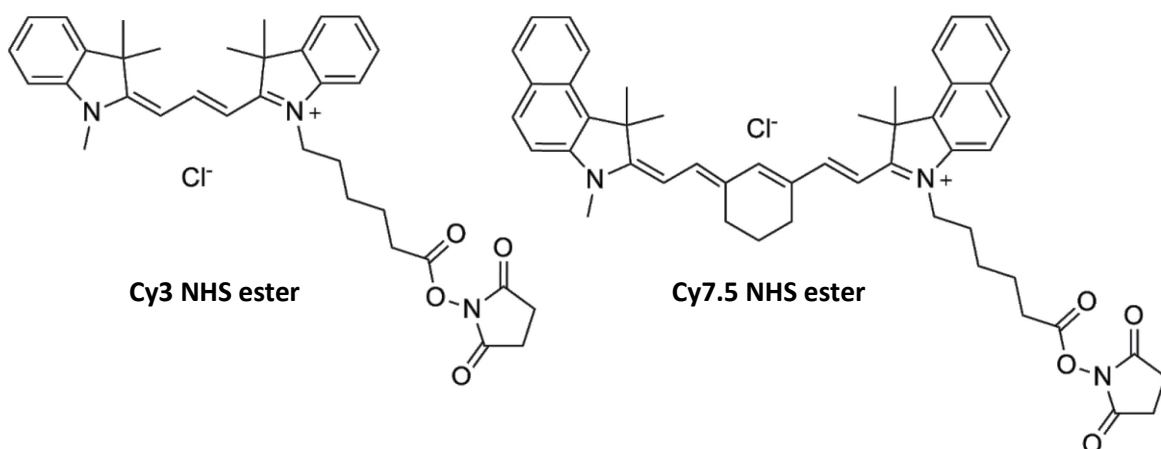


**Figure 4.5** Chemical structures of fluorophores Cy3 and Cy7.5 both of which have been functionalised with a NHS ester.

Films reacted with Dylight 649 NHS ester fluorophore were imaged under a Zeiss Axio Observer fluorescence microscope fitted with a Cy5 filter.

#### 4.2.1. Neutron Reflectivity

Neutron Reflectivity (NR) measurements were performed on FIGARO<sup>8</sup> and D17 at the Institut Laue-Langevin (Grenoble, France) and INTER<sup>9</sup> and OFFSPEC at ISIS, Appleton Rutherford Laboratory (Harwell, Oxford, UK). Static NR measurements were performed *ex situ*, on dry films (in air) as well as *in situ* in the relevant hydrogenous and deuterated solvents. The use of deuterated solvents maximises the contrast between the polymer and the electrolyte so that the solvation properties of the polymer could be probed. Comparing reflectivity profiles in both deuterated and hydrogenous solvents allows film solvation within the polymer to be more accurately probed. Kinetic measurements were taken in real time during the hydrolysis of the Fmoc protecting group. All NR measurements were performed on time-of-flight instrumentation with  $\lambda$  ranges of 2–30 Å (ILL) and 1.5–16 Å (ISIS). Different incident angles were used in order to maximise the accessible momentum transfer ( $Q_z$ ) range. Typically a  $Q_z$

range of  $0.004 < Q_z/\text{\AA}^{-1} < 0.12$  is suitable for samples of this type with the upper limit being defined by the point at which the reflectivity hits the background level ( $Q^4$  decay).  $Q$  corresponds to distance (see **Equation 4.4**) so a polymer film thicknesses of 300-700  $\text{\AA}$  were chosen for the experiments to give good periodicity in the fringes observed in the  $R(Q)$  profiles. Data acquisition times were ca. 1.5 h per static run and 10 min for kinetic runs.

Collimation slits were set to give a beam footprint of 30 x 60 mm on the sample; they also define the  $\Delta\theta/\theta$  resolution of the measurement. The  $\Delta\lambda/\lambda$  resolution is dependent on the neutron source (spallation at ISIS, reactor at ILL) and any associated instrumentation (for example chopper settings at ILL). In both cases, the resultant resolution in momentum transfer ( $\Delta Q/Q$ ) was 2–3%.

## 4.3. Results

### 4.3.1. Electropolymerisation

Polymer films were deposited potentiodynamically with an anodic current cap applied ( $i_{\text{max}} = 3.8 \text{ mA}$ ) to inhibit film roughness. By capping the oxidation current, a limited amount of polymer is deposited during each cycle. The slow scan rate used for deposition aids roughness control as the film is allowed to “settle” before another layer is deposited. **Figures 4.6** and **4.7** show growth curves and subsequent characterisation in monomer-free electrolyte for PPyFMOC and PPyNH<sub>2</sub> respectively.

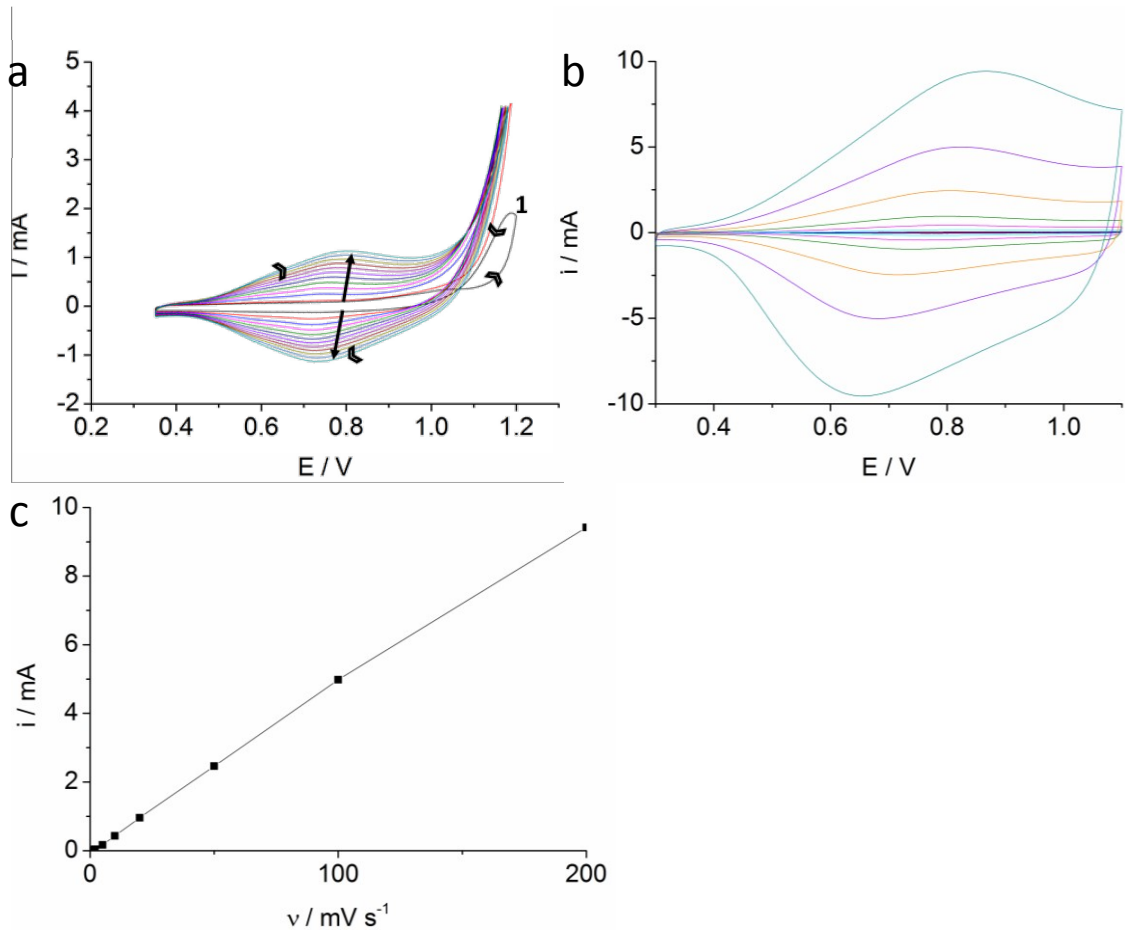


**Figure 4.6** Cyclic voltammogram of (a) PPyFmoc growth ( $v = 20 \text{ mV s}^{-1}$ ) and (b) post polymerisation characterisation in monomer free electrolyte  $v = 1, 2, 5, 10, 20, 50, 100$  and  $200 \text{ mV s}^{-1}$  (increasing “outwards”). Chevron arrows indicate scan direction. In panel (a) large arrows indicate the time sequence and “1” indicates the first deposition cycle (note the nucleation loop). Panel (c) shows the variation of cathodic peak current (from curves in panel (b)) with scan rate.

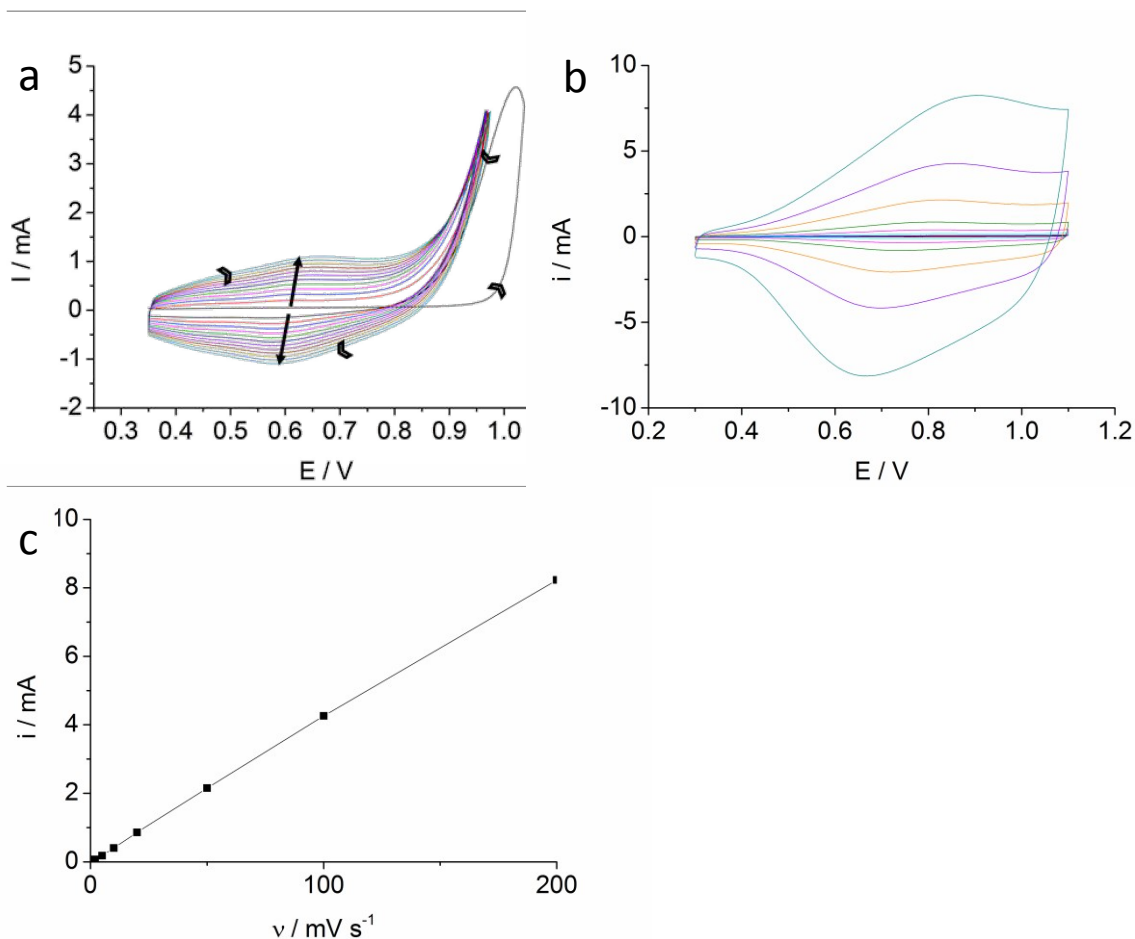


**Figure 4.7** Cyclic voltammogram of (a) PPyNH<sub>2</sub> growth ( $v = 20 \text{ mV s}^{-1}$ ) and (b) post polymerisation characterisation in monomer free electrolyte  $v = 1, 2, 5, 10, 20, 50, 100$  and  $200 \text{ mV s}^{-1}$  (increasing “outwards”). Chevron arrows indicate scan direction. In panel (a) large arrows indicate the time sequence and “1” indicates the first deposition cycle (note the nucleation loop). Panel (c) shows the variation of cathodic peak current (from curves in panel (b)) with scan rate.

Panel (c) in **Figures 4.6 and 4.7** shows that the cathodic peak currents are linearly proportional to the potential scan rate. This indicates complete redox conversion of the film on the experimental timescale, validating a coulometric assay of the surface population of polymer as discussed in **Chapter 2**.

Equation 4.1

where  $\Gamma$  is the surface coverage ( $\text{mol cm}^{-2}$ ),  $q$  is the charge (C),  $n$  is the number of electrons transferred (“doping level”,  $n = 0.33^{10}$ ),  $A$  is the electrode area ( $\text{cm}^2$ ) and  $F$  is the Faraday constant ( $\text{C mol}^{-1}$ ). In this case, the final polymer coverages were  $\Gamma_{\text{PPyFMOC}} = 20 \text{ nmol cm}^{-2}$  and  $\Gamma_{\text{PPyNH}_2} = 19 \text{ nmol cm}^{-2}$ , where in both cases the surface population is expressed in terms of monomer units. These surface coverages were then used to estimate film thickness.

Equation 4.2

where  $h_f$  = film thickness and  $c$  is the concentration of the monomer units which is equal to the density ( $\text{g cm}^{-3}$ ) divided by the molecular mass of the monomer. The RMM values of PyFMOC and PyNH<sub>2</sub> are 344 and 122  $\text{g mol}^{-1}$  respectively. Their respective densities are ca. 1.2 and 1.0  $\text{g cm}^{-3}$ . For compact, solvent-free (“dry”) films, these would correspond to film thicknesses of ca. 600 Å and 240 Å respectively. After solvation these values might be expected to increase by 50-100 % as solvent volume fractions ( $\phi_s$ ) for electroactive polymer films are typically in the range of 0.3 - 0.5<sup>3,12-14</sup>. These thicknesses are only estimates based on the surface coverage of the polymer and assume complete film redox conversion on the experimental timescale as indicated in panel (c) of **Figures 4.6 and 4.7**. Neutron reflectivity can be used to accurately determine physical film thickness, both dry and solvated, as well as determining precise solvation levels.

This observed difference in film thickness between PPyFMOC and PPyNH<sub>2</sub> films containing essentially the same number of monomer units (20 and 19  $\text{nmol cm}^{-2}$ ) shows the enormous capability for generating free volume during FMOc elution from the PPyFMOC film, which is over twice as thick. The fact that the thickness of the PPyNH<sub>2</sub> film is only 40 % of the thickness of the PPyFMOC suggests that up to 60 % of the film thickness of the latter film is due to the presence of the bulky FMOc protecting group.

### 4.3.2. Post Polymerisation Chemical Modifications

Conceptually, the simplest approach of generating fluorescence in a conducting polymer film is to functionalise the nitrogen of the pyrrole ring with a fluorophore and then to polymerise the film. However, the size of most fluorophores (required to give the fluorescence) creates significant steric hindrance. As a result of this, the substituted pyrrole monomer units cannot be polymerized.

The three step strategy schematically represented in **Figure 4.3** has been adopted to incorporate the fluorophore after the polymer film has been generated. In order to generate the maximum lateral contrast between the fingerprint and the “background” (spatially selective conducting polymer film) it is necessary to try and encompass as much fluorophore as possible to generate sufficient contrast via fluorescence. In order to accomplish this, sufficient free volume must be present within the polymer film to accommodate the fluorophore units. The tactic employed is to polymerize not PPyNH<sub>2</sub> itself, but a pyrrole amine film where the amine has been protected with a sterically bulky protecting group (Fmoc) prior to polymerization that can readily be removed post-deposition. Fmoc was chosen to strike a balance between using a substituent that is not so large as to inhibit polymerization but which is large enough to create significant free volume. The semi-fluid nature of the polymer film means that the randomly distributed free volume should be able to merge together to generate “voids” of sufficient size to accommodate larger fluorophore moieties. Choice of a fluorophore with NHS ester functionality provided the means of covalently bonding the fluorophore to the polymer via amide formation.

#### 4.3.2.1. Fluorescence Measurements

In order to demonstrate that the above strategy does indeed result in fluorophore immobilization within the PPyNH<sub>2</sub> film a series of measurements was performed. The first of these was the fluorescence measurement shown in **Figure 4.8**. This crude test shows two

PPyNH<sub>2</sub> films which have both been reacted with a droplet of fluorophore. Panel (A) shows four times greater fluorescence than panel (B). This preliminary observation proves the viability of fluorophore emission when in the film environment as the area (top left corner) that was reacted with the fluorophore shows up when illuminated ( $\lambda = 640$  nm) as a sharply defined region of enhanced brightness consistent with strong fluorophore emission. This is an encouraging result as the polymer film in panel (A) was synthesised through the PPyFMOC hydrolysis pathway whereas the film in panel (B) was electrodeposited from the PPyNH<sub>2</sub> monomer and so had no solvent “voids” to aid the penetration of the fluorophore as the PPyNH<sub>2</sub> film in panel (A) did. The fact that a film with these voids gives greater fluorescence is significant as the polymer film (when eventually applied to a fingerprint enhancement scenario) will give greater contrast to the fingerprint deposit itself.

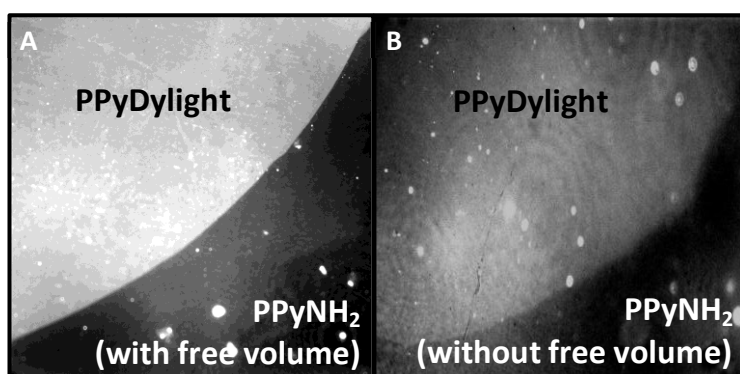


**Figure 4.8** Fluorescence image of two PPyNH<sub>2</sub> films after partial exposure to Dylight 649 NHS ester by contact with a droplet of fluorophore solution (top left corner in both cases), and subsequent removal of excess fluorophore by rinsing with water: (A) was prepared with solvent “voids” via the PPyFMOC hydrolysis pathway and (B) was electrochemically deposited from the PyNH<sub>2</sub> monomer. Both films were viewed *ex situ* and illuminated by light of wavelength 640 nm. In panel (A), the intensity was attenuated by a factor of four.

Although this method provides a functional appraisal, demonstrating the presence of the fluorophore in the film, it does not prove that the fluorophore is immobilised in the film. As such, elution of the fluorophore could still occur upon further exposure to electrolyte, thereby jeopardizing the potential combination of the fluorescence and electrochromic pathways. Consequently, a spectroscopic probe was used to provide direct evidence of fluorophore–polymer covalent bonding.

#### 4.3.2.1. FTIR

FTIR was used to show the presence (or absence) of carbonyl bands associated with the amide functionality thus demonstrating whether or not the NHS ester functionalised fluorophore had successfully bound to the PPyNH<sub>2</sub>. The amide band (1640-1690 cm<sup>-1</sup>) will be present in both the PPyFMOC and successfully immobilized PPy-Dylight film spectra, but should not be present in the PPyNH<sub>2</sub> spectrum. The results of the FTIR analysis are shown in **Figure 4.9**:

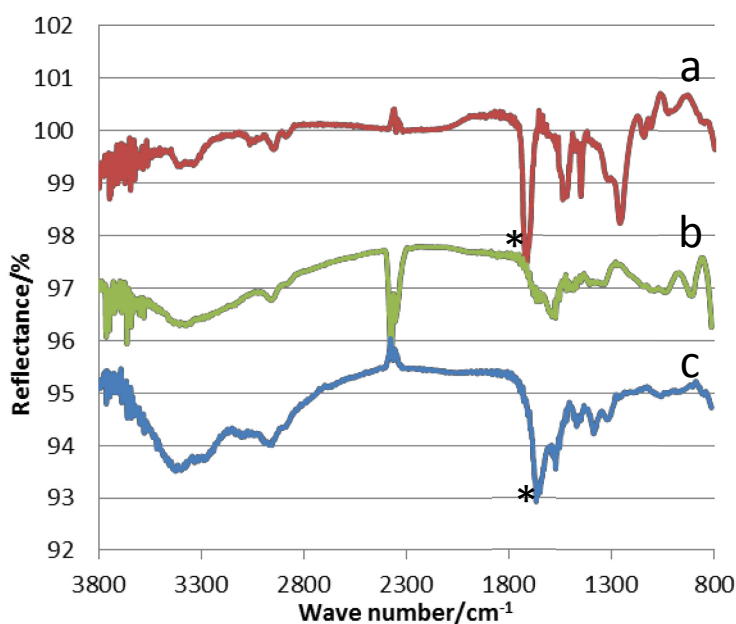


**Figure 4.9** FTIR spectra showing the different stages of the reaction depicted in **Figure 4.3**. (a) PPyFMOC as deposited, (b) PPyNH<sub>2</sub> film after FMOc hydrolysis and (c) PPy-Dylight. \*denotes the presence of amide peaks. Traces have been arbitrarily offset vertically for visual clarity.

Whilst the FTIR results demonstrate not only the permeation of fluorophore into the film but also its chemical immobilization they yield no information on the spatial distribution of the fluorophore or the factor(s) limiting its final population (for example, partial or complete collapse of the solvent “voids”). In order to examine these factors and further understand these reaction processes, a technique with vertical spatial resolution is required.

### 4.3.3. Neutron Reflectivity

There are two clear stages to the reaction described in **Figure 4.3**: Fmoc hydrolysis followed by a reaction of the resultant PPyNH<sub>2</sub> film with an NHS ester functionalized fluorophore. The functionality and therefore application of these polymer films is dependent on each of these reactions being uniform in the z direction (full hydrolysis and elution of “freed” Fmoc and complete penetration/maximum incorporation of the fluorophore moiety).

#### 4.3.3.1. Fmoc Hydrolysis

There are two key questions associated with the hydrolysis reaction: firstly, does the reaction go to completion in the allotted time and secondly how much of the free volume generated is retained? The second question is dependent on the rigidity of the polymer film. If the film is rigid then nearly all of the “voids” created will be filled by solvent but if the film is not rigid then the “voids” may collapse upon elution of the Fmoc before the solvent can fill the space. Some degree of film fluidity is necessary as it will allow the polymer to rearrange so that the smaller voids created by Fmoc elution can coalesce to accommodate the larger fluorophore entities but too much fluidity would cause the film to collapse resulting in a loss of free volume. Therefore, the main objective of this work was to assess the retention of free volume in the PPyFmoc/PPyNH<sub>2</sub> system and to optimise the level of film fluidity.

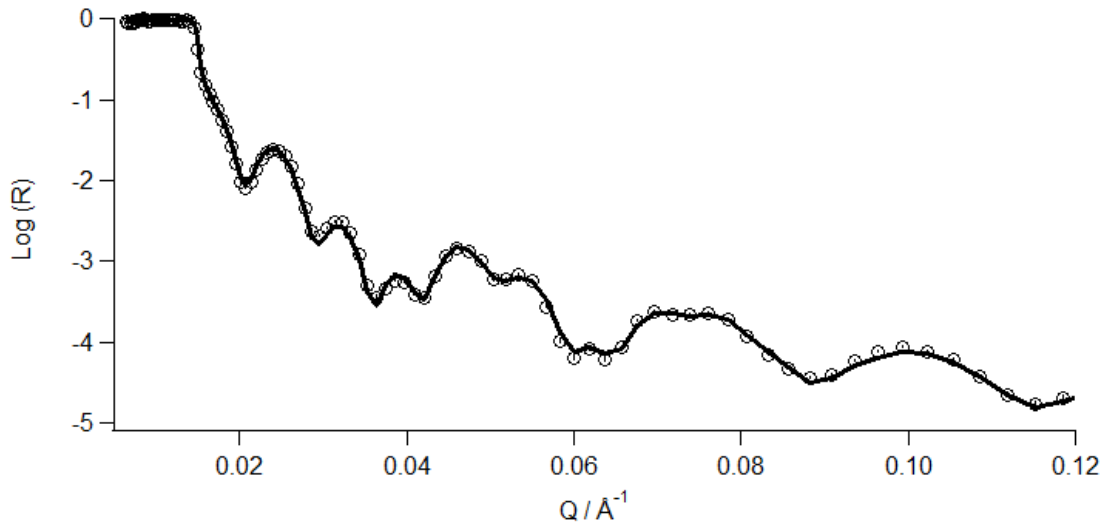


**Figure 4.10** Neutron reflectivity profile (INTER, ISIS) of a dry PPyFMOC film measured after polymerisation and prior to the hydrolysis of the FMOC protecting group. The circles represent the raw data and the line is the fit of that data ( $\chi^2 = 2.1$ , see **Table 4.1**).

**Figure 4.10** shows a typical NR measurement of a dry PPyFMOC film as deposited from the corresponding PyFMOC monomer. At low  $Q$  (here,  $Q < 0.0144 \text{ \AA}^{-1}$ ) total external reflection is observed ( $R = 1$ ) in the form of a critical edge. This is due to the positive difference in scattering length density (SLD) of the two bulk materials. In this case, the incident neutrons are transmitted through, air which has a SLD of zero, and are reflecting from quartz, which has a SLD of  $4.182 \times 10^{-6} \text{ \AA}^{-2}$ . The exact  $Q$  value corresponding to the critical edge,  $Q_c$ , is determined by this difference in SLD of the two bulk materials,  $\Delta N_b$ :

$$Q_c = \left( \frac{\Delta N_b}{2} \right)^{1/2} \tag{Equation 4.3}$$

If we take the value of the critical edge ( $Q_c = 0.0144$ ) and use **Equation 4.3** then the difference in SLD is  $4.182 \times 10^{-6} \text{ \AA}^{-2}$ . This is the SLD of quartz as the SLD of air is zero.

At higher  $Q$  there is a series of fringes whose spacing is determined by the thickness of the films present (binding layer of MPTS, Au electrode and polymer).

— **Equation 4.4**

If we take the value of  $\Delta Q$  for the final fringe in **Figure 4.10** ( $0.027 \text{ \AA}^{-1}$ ) and use **Equation 4.4** then the approximate thickness of the Au is  $233 \text{ \AA}$ ; this is entirely consistent with the nominal thickness of  $200 \text{ \AA}$  from the sputtering process and was confirmed through AFM.

The reflectivity value of these fringes is governed by the SLD contrast and sharpness of the interfaces between layers. At high  $Q$  (here,  $Q > 0.08 \text{ \AA}^{-1}$ ), the fringes can be attributed to the Au electrode. Although these are not of primary interest to the investigation, analysis of them does assist fitting of the full  $R(Q)$  profile from which the desired information on the polymer system can be obtained. At intermediate  $Q$ , these Au fringes are present but are seen in combination with the polymer derived fringes. These polymer fringes are not present at high  $Q$  due to the diffuseness of the polymer/air (or solution) interface.

In order to extract the information from the data it is necessary to fit the parameters of each layer. There are four parameters to fit for each layer within the system: thickness ( $d / \text{ \AA}$ ), SLD ( $10^6 N_b / \text{ \AA}^{-2}$ ), roughness ( $\sigma / \text{ \AA}$ ) and solvation (% v / v). This generates a SLD profile which is a plot of  $N_b$  versus distance in the vertical plane. The fit associated with the data in **Figure 4.10** is given below.

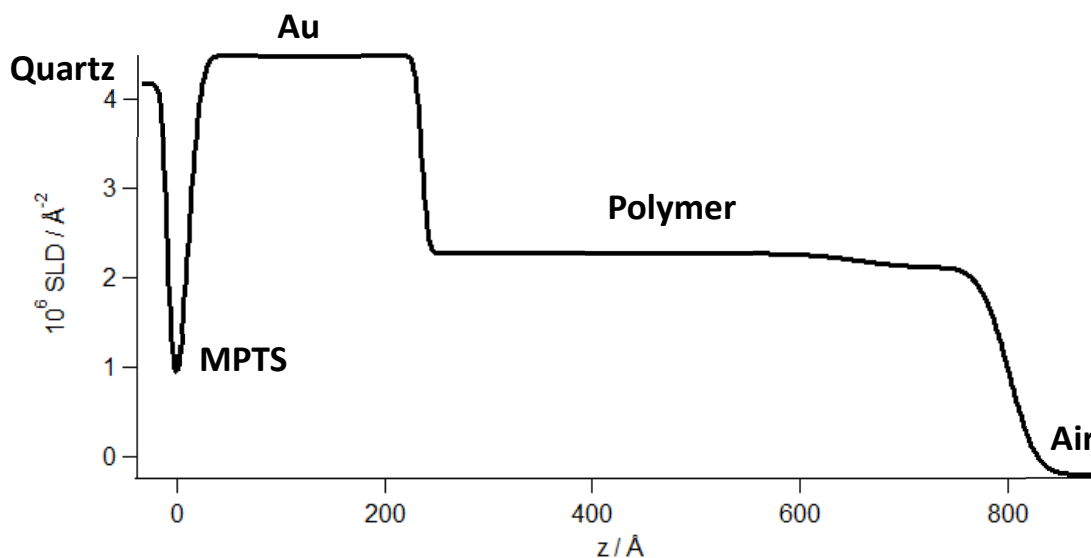


**Figure 4.11** SLD profile of the dry PPyFMOC film shown in **Figure 4.10**.

A summary of the fit parameters used is given in **table 4.1**.

Layer	$d / \text{Å}$	$10^6 N_b / \text{Å}^{-2}$	$\sigma / \text{Å}$
Air	Bulk	0	N/A
PPyFMOC <sub>outer</sub>	144.6	2.119	21.3
PPyFMOC <sub>inner</sub>	420.8	2.278	39.9
Au	225.1	4.490	5.0
MPTS	19.8	0.266	9.8
Quartz	Bulk	4.182	5.0

**Table 4.1** Fit parameters used in **Figure 4.10**.

The estimated thickness of the Au (233 Å) was slightly thicker than the value obtained from the fit (225 Å). This could be because of the relatively sharp polymer/air interface ( $\sigma = 21 \text{ Å}$ ) meaning that some of the polymer was still contributing to the fringes in this Q range. The PPyFMOC was split into two layers. The majority of the PPyFMOC formed an inner layer that was 421 Å thick. The second outer layer was 145 Å in thickness. This gives a total film thickness of 566 Å. The SLDs of the inner and outer layer are 2.28 and  $2.12 \times 10^{-6} \text{ Å}^{-2}$ , respectively; these values correspond to densities of 1.28 and  $1.19 \text{ g cm}^{-3}$ . This suggests that

as the polymer gets thicker it becomes more resistive and so deposition slows, resulting in a less compact outer layer.

Next the solvation of the PPyFMOC films was investigated. This was done by taking static neutron reflectivity measurements of the film in solution. In order to narrow down the solvent volume fraction in the PPyFMOC film it was measured in both  $\text{CH}_3\text{CN}$  and  $\text{CD}_3\text{CN}$ . The reflectivity and corresponding SLD profiles of these measurements are shown in **Figures 4.12** and **4.13**.

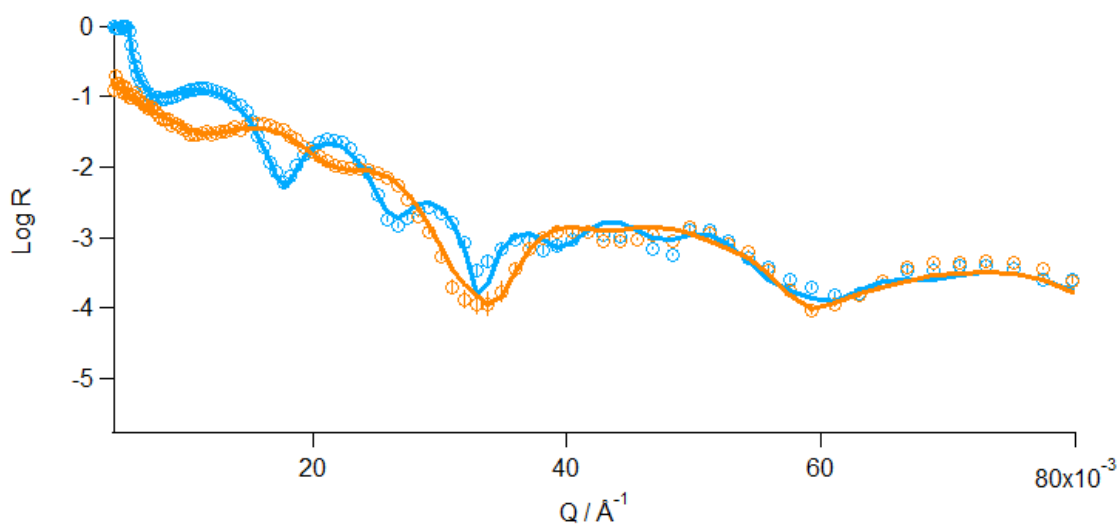


**Figure 4.12** Neutron reflectivity profile of the solvated PPyFMOC film in  $\text{CH}_3\text{CN}$  (orange) and  $\text{CD}_3\text{CN}$  (blue). The circles represent the raw data and the lines are the fits of that data ( $\chi^2 = 2.1$  and 2.5).

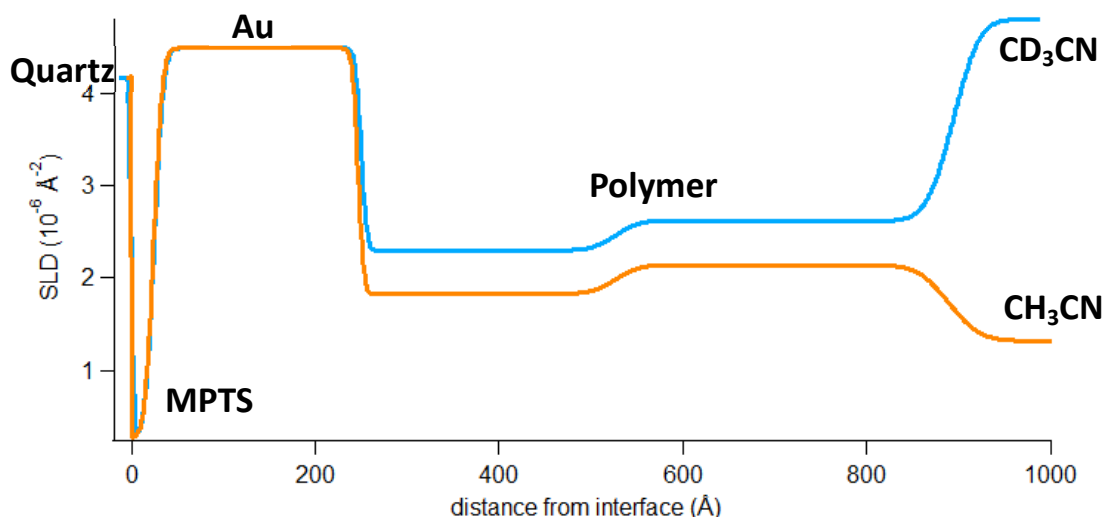


**Figure 4.13** SLD profile of the solvated PPyFMOC film in CH<sub>3</sub>CN (orange) and CD<sub>3</sub>CN (blue).

A summary of the fit parameters used is given in **table 4.2**.

Layer	d (Å)	N <sub>b</sub> (Å <sup>-2</sup> x10 <sup>-6</sup> )	σ (Å)
CH <sub>3</sub> CN/CD <sub>3</sub> CN	Bulk	1.320/4.802	N/A
PPyFMOC <sub>outer</sub>	365.0/367.1	2.139/2.620	22.5
PPyFMOC <sub>inner</sub>	278.6/276.9	1.831/2.300	20.0
Au	224.5	4.490	5.0
MPTS	24.2	0.266	8.0
Quartz	Bulk	4.182	5.0

**Table 4.2** Fit parameters used in **Figure 4.12**.

**Figure 4.13** demonstrates nicely the difference in contrast between the polymer layer and the two solvents with the CD<sub>3</sub>CN clearly having a larger difference in the SLDs. In this instance, the relevant bulk phases are the quartz block and the CD<sub>3</sub>CN to which the film is exposed; the scattering length densities are known for these materials (4.182 and approximately 4.8 respectively), giving  $\Delta N_b = 0.618 \text{ \AA}^{-2} \times 10^{-6}$ . Inserting this into **Equation 4.3**, we estimate  $Q_c = 0.0056 \text{ \AA}^{-1}$ . This is consistent with the experimental data. The total film thickness is 644 Å as

opposed to 566 Å in the dry film. This equates to 78 Å, or 14 % film swelling upon solvation. The inner and outer layers have also changed their thickness ratio with respect to one another. The inner layer is now less dense than the outer layer also suggesting high fluidity and rearrangement of polymer “packing” within the film. Before solvation the densities of the inner and outer layer were 1.28 and 1.19 g cm<sup>-3</sup> respectively. Upon solvation those values have changed to 1.03 and 1.22 g cm<sup>-3</sup>.

Now the initial film properties have been determined as a “control” experiment, the next stage was to monitor the hydrolysis and elution of the Fmoc from the film to yield PPyNH<sub>2</sub>. A preliminary investigation was performed on FIGARO at the ILL since there was no way of predicting the timescale of the reaction. The film was initially exposed to a relatively high concentration of piperidine (30 % v/v in ACN), with the aim of assessing the rate of the reaction.

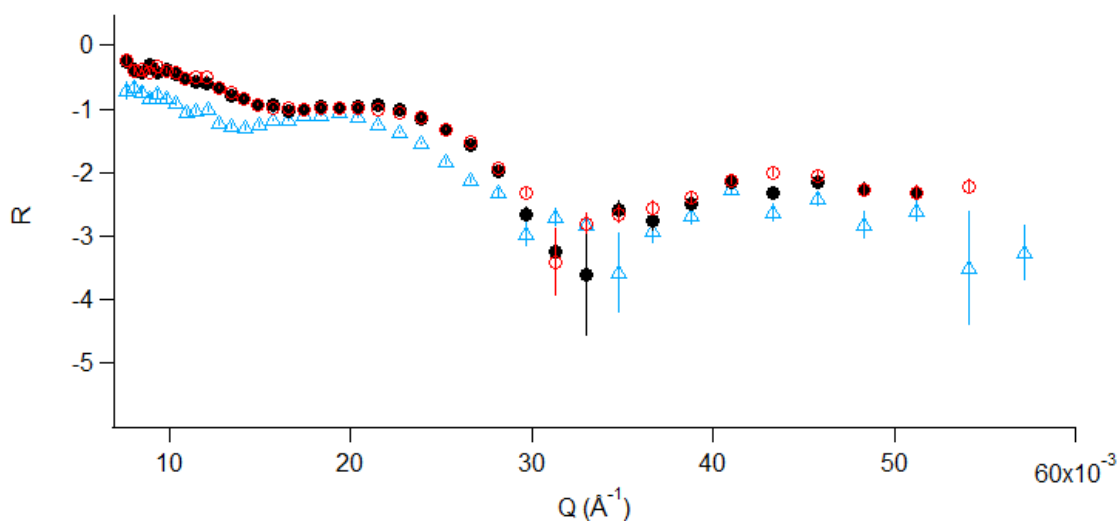


**Figure 4.14** Raw kinetic data for the base hydrolysis removal of the Fmoc protecting group in CH<sub>3</sub>CN.  $\Delta$  is the first measurement taken approximately 3 minutes after the solution was loaded into the neutron cell;  $\bullet$  was after 5 min and  $\circ$  after 31 min.

**Figure 4.14** depicts the raw NR data for an angle of  $0.624^\circ$  taken to assess the time scale of the hydrolysis reaction. It shows that the hydrolysis reaction is very fast in these conditions as the only significant changes in reflectivity are observed in the first 5 minutes as the location of the first fringe has shifted in both its value of reflectivity and Q. Whilst this time scale is ideal for its final application as a method of enhancing fingerprints it is too fast to perform any real time analysis using kinetic NR measurements. Therefore, in order to slow the reaction to a measurable rate, the concentration of piperidine was decreased.

The next set of measurements was performed on INTER (ISIS) show the hydrolysis of the same film seen in **Figures 4.10-13**. Initially, the concentration was decreased to 0.1 mM piperidine in ACN. As discussed previously, the hydrolysis reaction was conducted in  $\text{CD}_3\text{CN}$  medium to optimise the NR contrast.

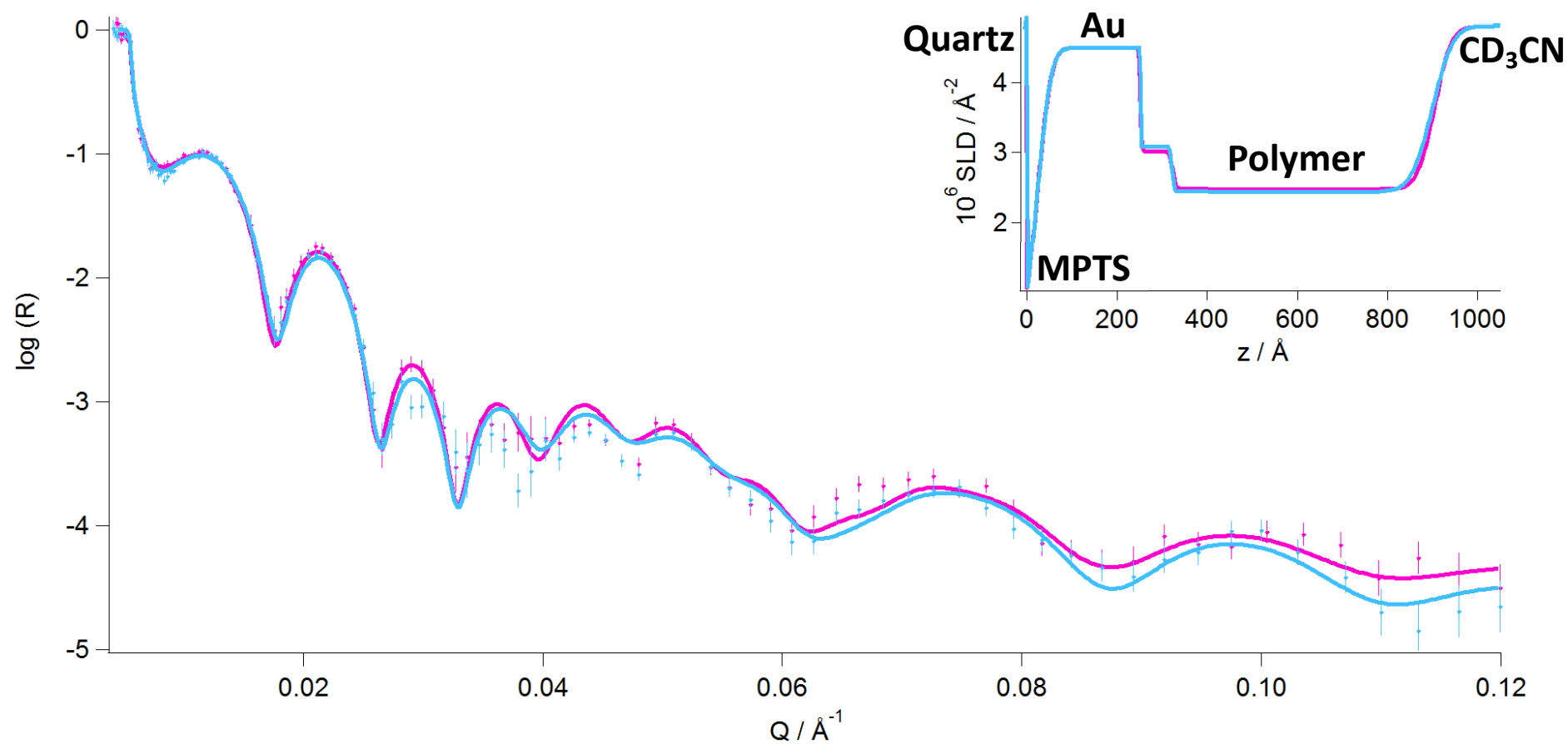


**Figure 4.15** Kinetic NR data ( $\bullet$ ), fits (line) and resultant SLD profiles (inset) showing the FMOc hydrolysis reaction progress in 0.1 mM piperidine/  $\text{CD}_3\text{CN}$  taken at the start of the reaction (pink) and after 4 hours (cyan). Film thicknesses = 653 and 648  $\text{\AA}$  ( $\chi^2 = 1.9$  and 1.8), respectively.

Layer	$d / \text{\AA}$	$10^6 N_b / \text{\AA}^{-2}$	$\sigma / \text{\AA}$
CD <sub>3</sub> CN	Bulk	4.788	N/A
PPyFMOc <sub>outer</sub>	581.3/577.9	2.483/2.449	30.5/36.8
PPyFMOc <sub>inner</sub>	71.9/70.5	3.012/3.083	5.7/3.9
Au	229.0	4.490	3.0(±1.4)
MPTS	22.3	0.266	24.5
Quartz	Bulk	4.182	5.0

**Table 4.3** Fit parameters used at the start (pink) and end (cyan) of the 0.01 mM hydrolysis reaction shown in **Figure 4.15**.

What **Figure 4.15** and **table 4.3** show is that even after 4 hours the reaction has hardly progressed with minimal changed in both thickness and SLDs of the two polymer layers. Measurements were taken every 10 minutes but the reaction progress every hour is summarised in **Figure 4.16**.

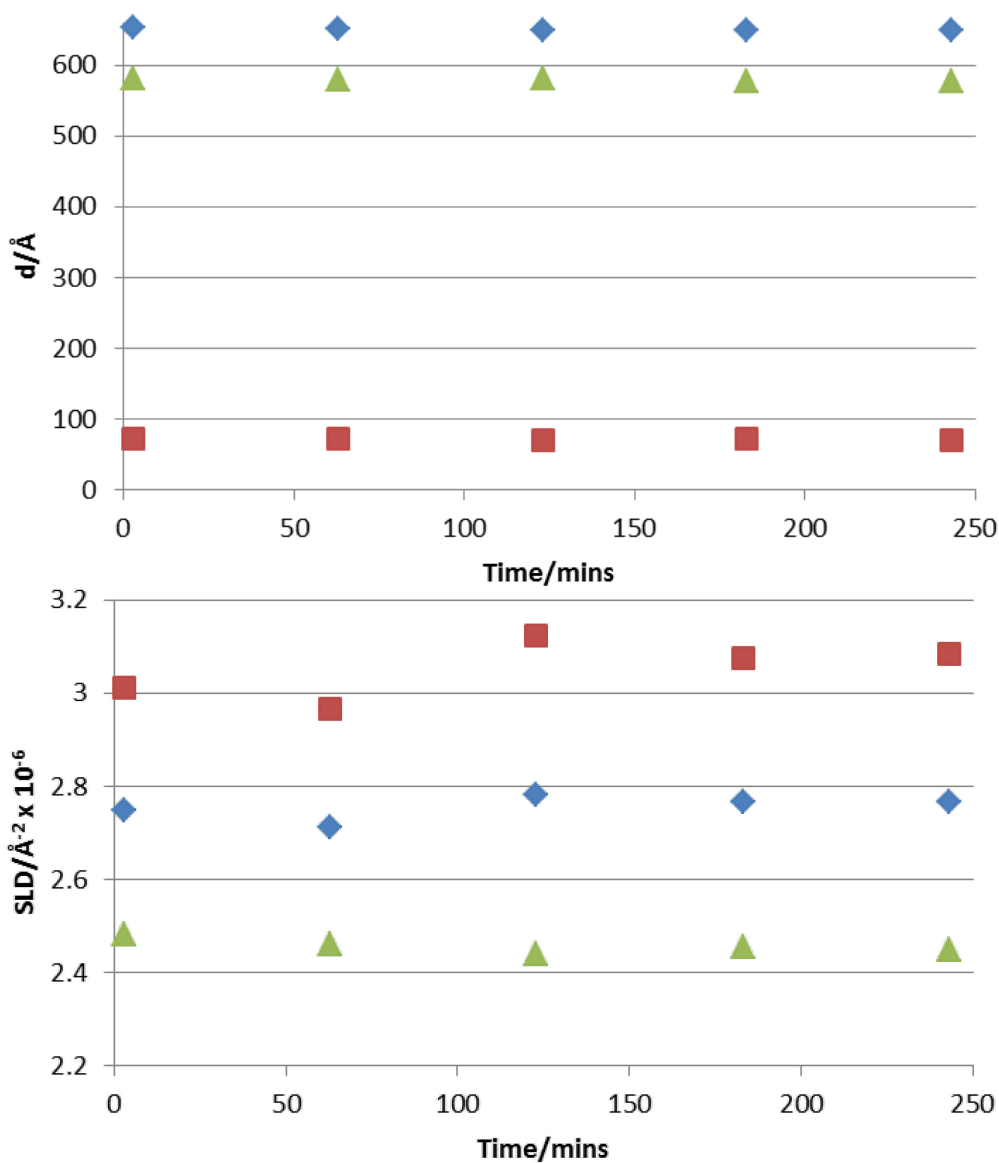


**Figure 4.16** Reaction progress of the inner (▲), outer (■) and total (◆) polymer later during the Fmoc hydrolysis reaction in 0.1 mM piperidine. Top graph is the change in thickness and bottom is the change in SLD.

As there was little visible reaction progress after 4 hours the measurement was stopped and the concentration of piperidine increased 100 fold from 0.1 mM to 10 mM. The analogous results in 10 mM piperidine are shown below.

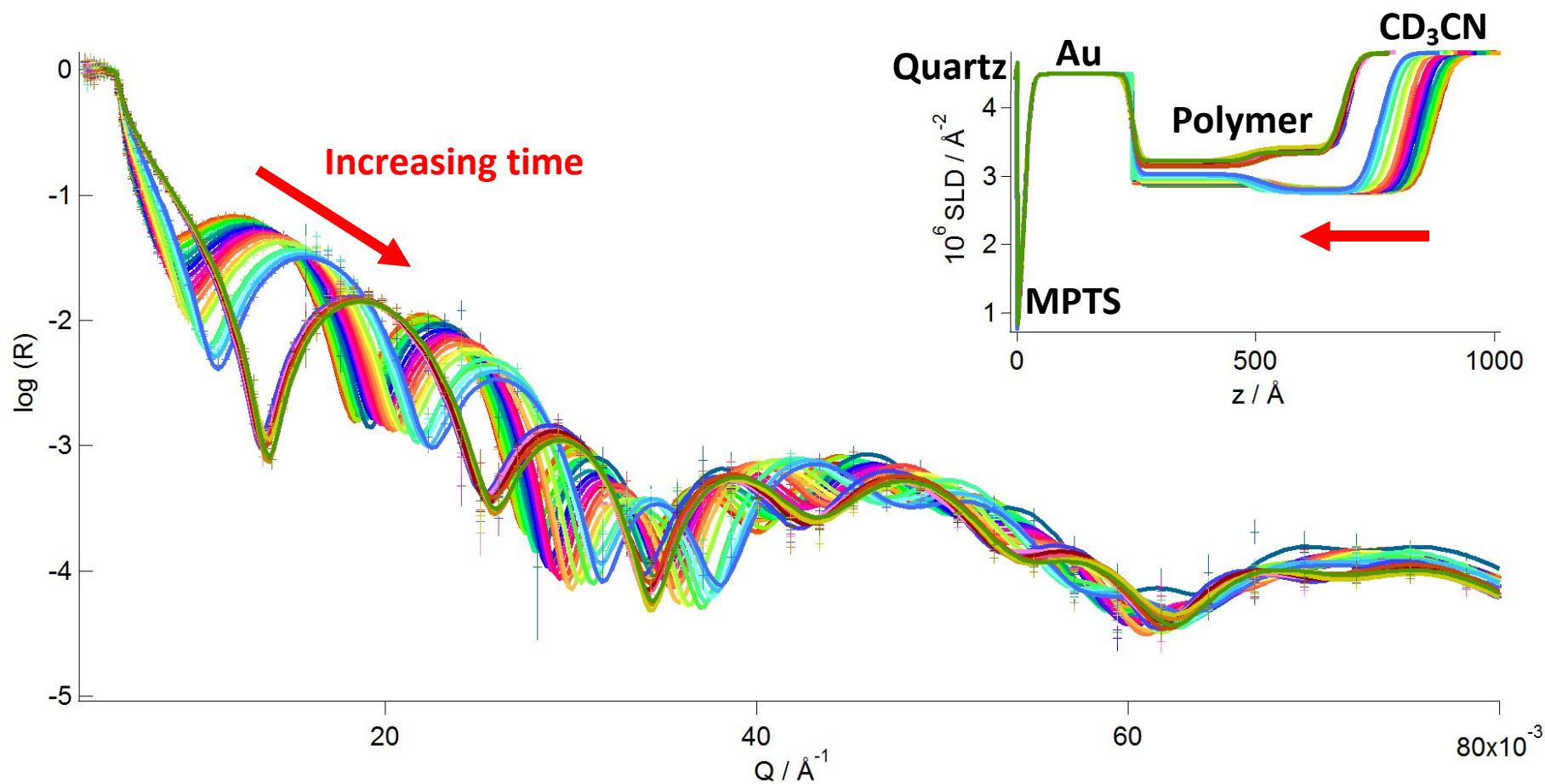


**Figure 4.17** Kinetic NR data ( $\bullet$ ), fits (line) and resultant SLD profiles (inset) showing the Fmoc hydrolysis reaction progress in 10 mM piperidine in  $\text{CD}_3\text{CN}$  taken every 10 minutes ( $X^2 = 1.3 - 2.4$ ) respectively.

Layer	$d / \text{Å}$	$10^6 N_b / \text{Å}^{-2}$	$\sigma / \text{Å}$
CD <sub>3</sub> CN	Bulk	4.802	N/A
PPyFMOc <sub>outer</sub>		See <b>table 4.5</b>	
PPyFMOc <sub>inner</sub>		See <b>table 4.5</b>	
Au	266.8	4.490	7.7(±3.9)
MPTS	14.3	0.266	11.9
Quartz	Bulk	4.182	5.0

**Table 4.4** Summary of the fit parameters for the solvent, Au, MPTS and quartz layers of the system used in **Figure 4.17**.

t / mins	PPyFMOC <sub>inner</sub>			PPyFMOC <sub>outer</sub>		
	d / Å	10 <sup>6</sup> N <sub>b</sub> / Å <sup>-2</sup>	σ / Å	d / Å	10 <sup>6</sup> N <sub>b</sub> / Å <sup>-2</sup>	σ / Å
3	314.1	2.869	19.6	320.0	2.815	31.1
13	313.1	2.902	44.3	319.5	2.795	27.5
23	319.2	2.910	20.9	309.9	2.759	34.6
33	313.0	2.934	32.2	315.1	2.832	27.2
43	324.6	2.876	12.5	294.3	2.779	31.6
53	307.6	2.921	16.4	305.9	2.774	28.7
63	302.3	2.887	39.1	307.5	2.778	32.0
73	291.7	2.948	30.0	314.4	2.797	23.3
83	297.6	2.913	11.7	301.1	2.775	29.6
93	306.7	2.950	31.6	286.8	2.772	29.3
103	295.2	2.936	28.8	293.6	2.811	29.0
113	293.7	2.930	11.0	288.7	2.803	28.8
123	282.0	2.914	19.7	291.7	2.773	25.2
133	305.8	2.948	24.5	265.5	2.818	26.6
143	315.9	2.969	20.0	250.3	2.858	29.2
153	264.4	2.926	8.4	291.8	2.784	28.1
163	289.9	2.944	10.1	262.8	2.806	27.5
173	275.8	2.981	28.2	260.4	2.806	29.7
183	241.7	2.972	20.4	291.7	2.786	25.3
193	255.0	3.001	24.7	272.7	2.770	29.6
203	259.1	3.016	36.9	263.0	2.760	28.1
213	271.5	3.033	38.0	246.2	2.801	30.3
363	261.1	3.147	38.6	195.0	3.419	17.2
373	251.1	3.146	29.3	200.2	3.347	23.7
383	257.7	3.182	21.4	195.0	3.387	23.6
393	247.9	3.158	32.0	200.4	3.380	22.0
403	251.2	3.208	30.9	199.6	3.404	19.9
413	267.4	3.146	29.9	178.1	3.331	21.8
423	231.0	3.228	13.4	212.9	3.346	22.4
433	232.8	3.214	46.1	211.5	3.427	21.9
443	245.2	3.224	19.5	197.5	3.348	23.1

**Table 4.5** Summary of the fit parameters for inner and outer layers of the PPyFMOC/PPyNH<sub>2</sub> system used in **Figure 4.17**.

**Figure 4.17** and **table 4.5** show the fringes in the intermediate Q region just above the critical edge are progressively widening as time increases. Since the momentum transfer, Q, is in reciprocal space, this stretching corresponds to a decrease in film thickness during Fmoc elution. This contraction suggests that not all of the free volume generated during the Fmoc

hydrolysis is retained by the resultant PPyNH<sub>2</sub> film. The quantitative question that follows is whether this loss in volume generated by the Fmoc is permanent or whether the fluidity of the film will allow the film to re-swell in order to incorporate the bulky fluorophore moieties.

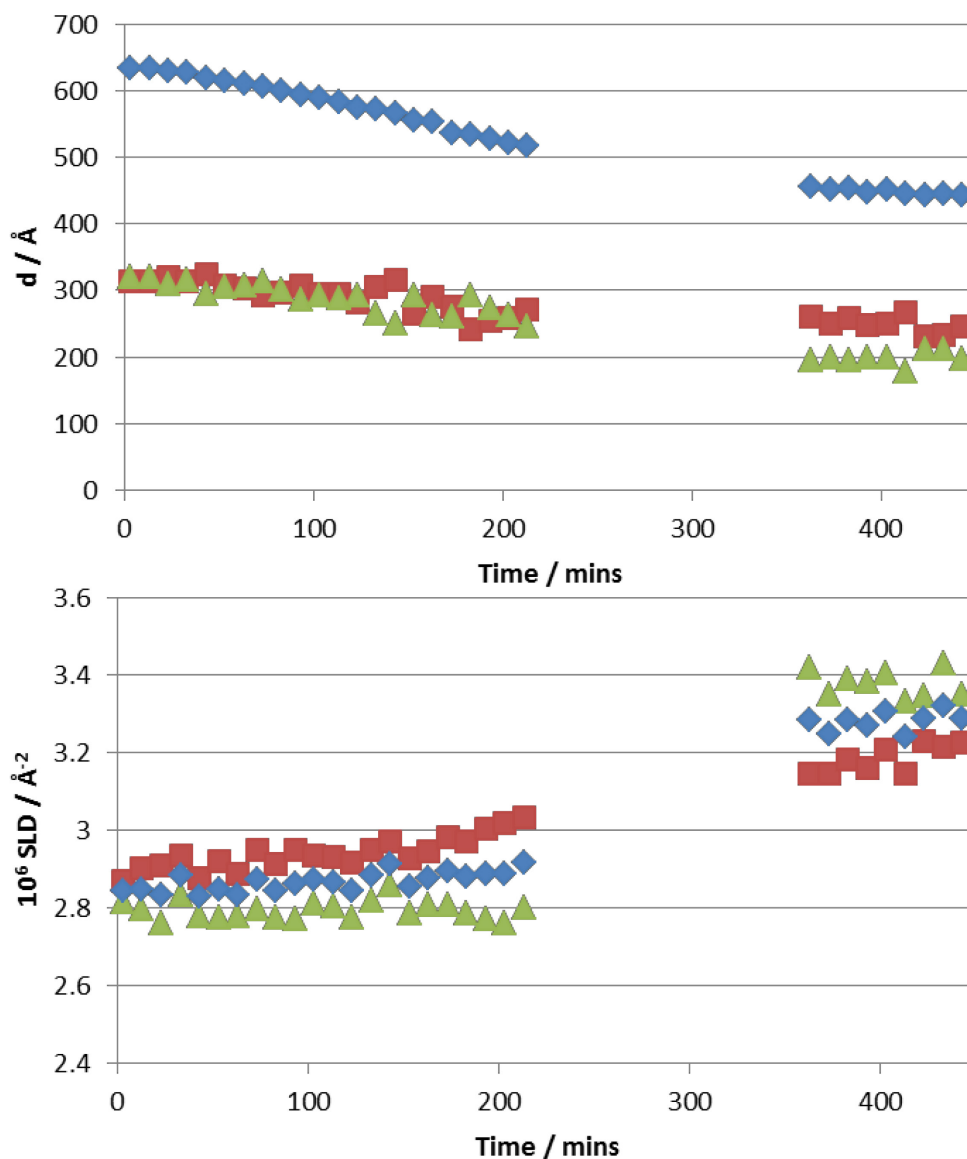


**Figure 4.18** Reaction progress of the inner ( $\blacktriangle$ ), outer ( $\blacksquare$ ) and total ( $\blacklozenge$ ) polymer layer during the Fmoc hydrolysis reaction in 10 mM piperidine. Top graph is the change in thickness and bottom is the change in SLD.

The gap in the data between 220 – 360 minutes was due to an instrumental malfunction in the spallation source at ISIS which resulted in the loss of the neutron beam for this period. The

SLDs of quartz, Au, PPyFMOC, the departing Fmoc, the remaining PPyNH<sub>2</sub> and CD<sub>3</sub>CN solvent are all known. The Au thickness is known (from a combination of fabrication protocol and the high Q data). **Figure 4.18** shows a total thickness change from 634 to 443 Å during the hydrolysis reaction. This corresponds to a collapse of 191 Å. The roughness of the polymer/solution interface is shown in **Figure 4.19**.

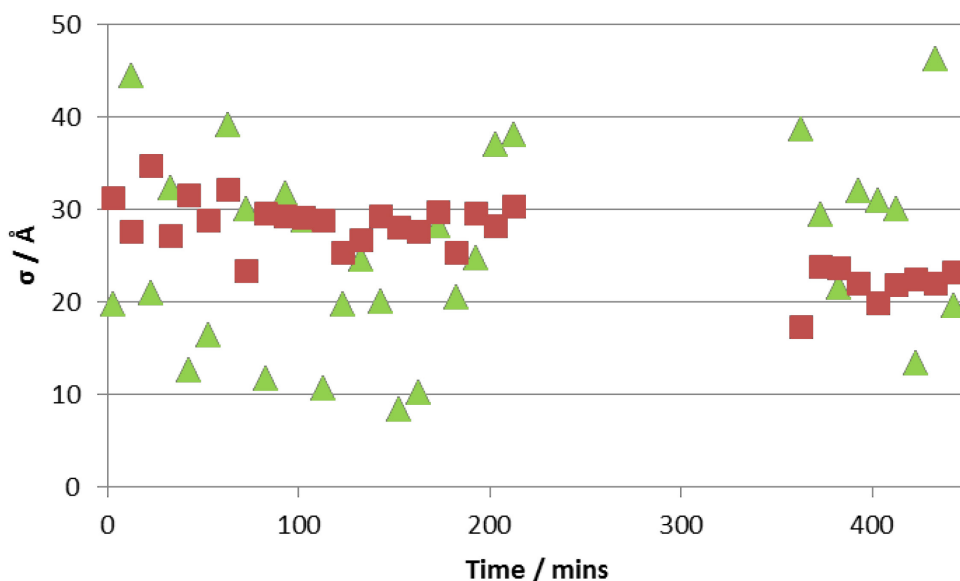


**Figure 4.19** Roughness of the polymer/polymer [inner (▲)] and polymer/solution interface [outer (■)] during the Fmoc hydrolysis reaction in 10 mM piperidine.

**Figure 4.19** shows that the polymer/polymer interfacial roughness fluctuates during hydrolysis (8 - 46 Å) whereas the polymer/solvent interfacial roughness decreases with time (35 - 22 Å). However, the internal composition of the film (ratio of PPyFMOC to hydrolysed PPyNH<sub>2</sub> and solvation level) are still unknown. These values can be extracted from the SLD values of the film during the different stages of the reaction as:

**Equation 4.5**

The results of these calculations are shown in **Figure 4.20** and **Figure 4.21**.

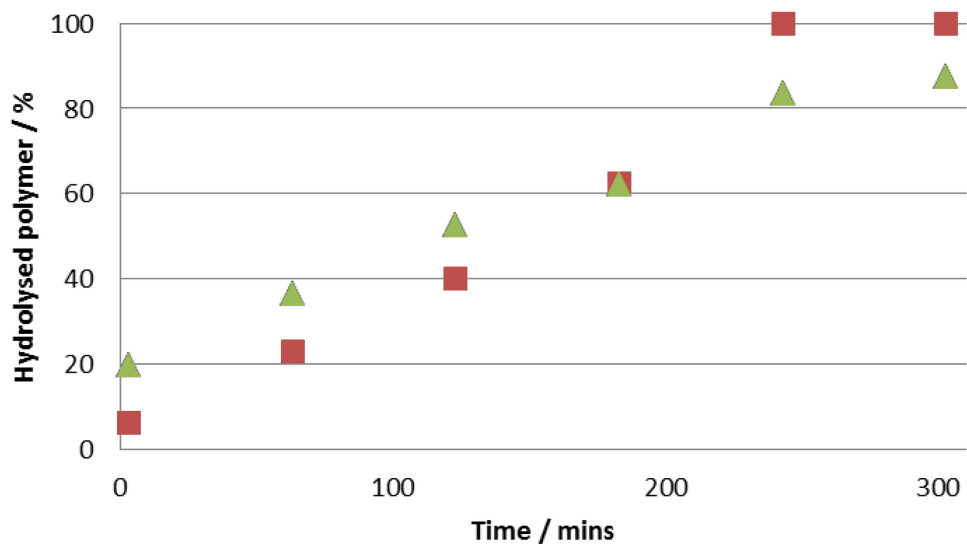


**Figure 4.20** Hydrolysis reaction progress represented by the percentage of hydrolysed polymer in the inner ( $\blacktriangle$ ) and outer ( $\blacksquare$ ) polymer layers.

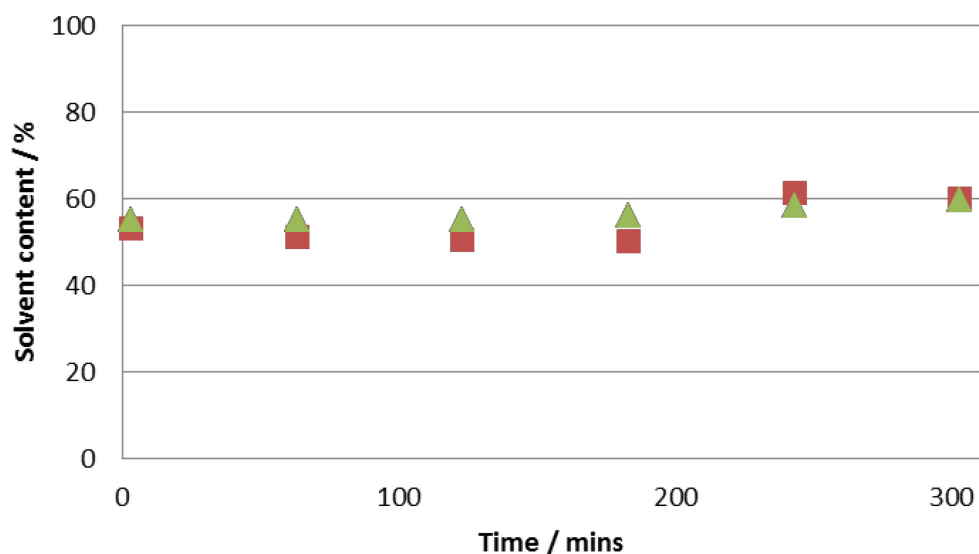


**Figure 4.21** Changes in solvent volume fraction ( $\phi_{\text{CD}_3\text{CN}}$ ) observed in the inner ( $\blacktriangle$ ) and outer ( $\blacksquare$ ) polymer layers during the 10 mM hydrolysis reaction.

**Figure 4.21** shows that the difference in  $\phi_{\text{CD}_3\text{CN}}$  between the inner and outer regions of the film is relatively small. Therefore, the average picture shows that  $\phi_{\text{polymer}}$  at the start of the reaction was 0.41. By the end of the reaction, this had increased to 0.60.

Once the reaction had gone to completion (no visible change in reflectivity over 30 min) the reaction was halted by the removal of the piperidine solution from the cell. The reflectivity of the film was then measured once again in both contrasts to more accurately determine the properties of the resulting PPyNH<sub>2</sub> film.

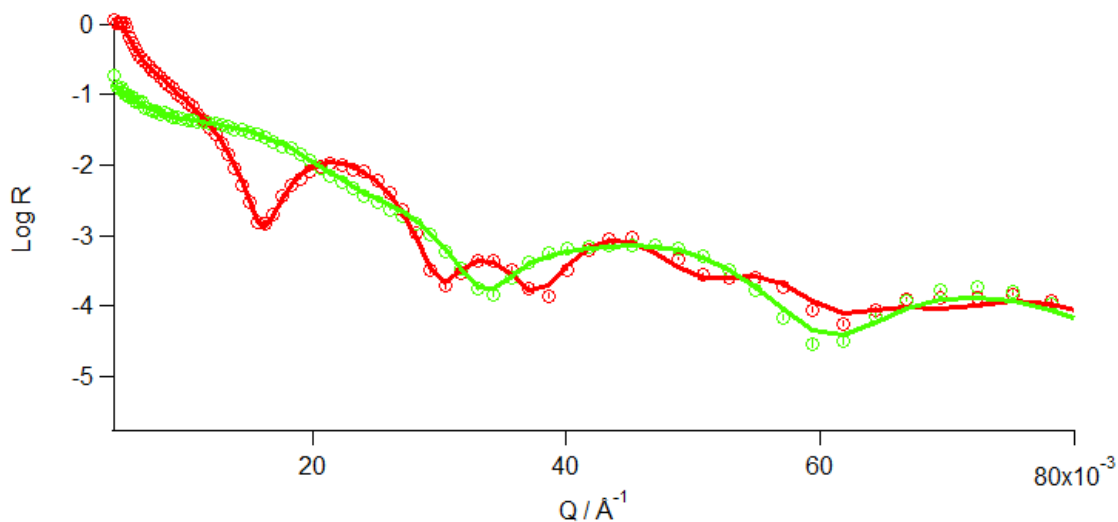


**Figure 4.22** NR profile of the solvated PPyNH<sub>2</sub> film after hydrolysis in CH<sub>3</sub>CN (green) and CD<sub>3</sub>CN (red). The circles represent the raw data and the line is the fit of that data ( $\chi^2 = 1.9$  and 2.2).

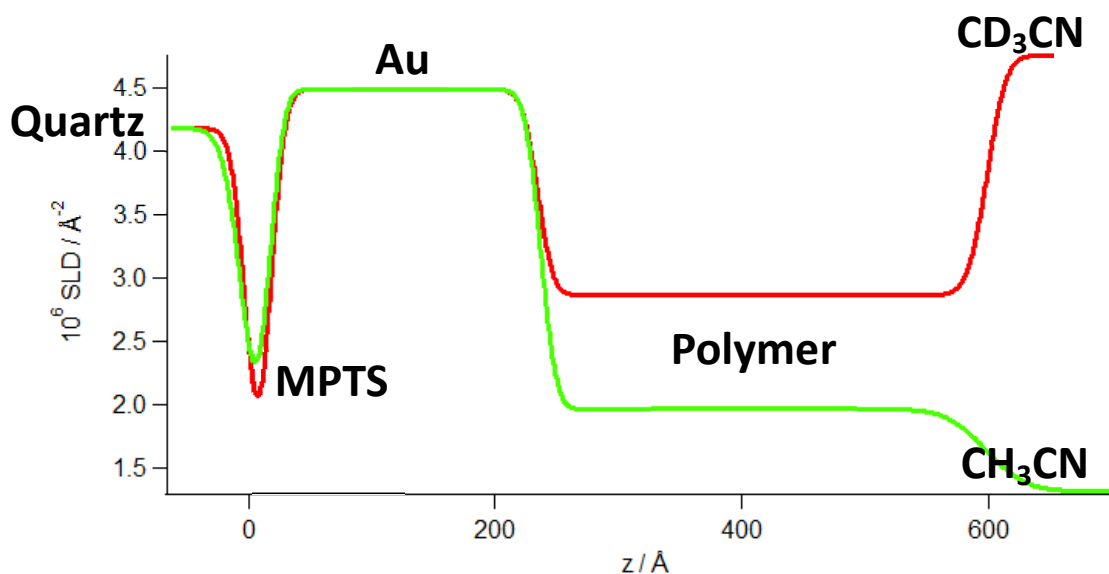


**Figure 4.23** SLD profile of the solvated PPyNH<sub>2</sub> film after hydrolysis in CH<sub>3</sub>CN (green) and CD<sub>3</sub>CN (red).

A summary of the fit parameters used is given in **Table 4.6**.

Layer	d / Å	10 <sup>6</sup> N <sub>b</sub> / Å <sup>-2</sup>	σ / Å
CH <sub>3</sub> CN/ CD <sub>3</sub> CN	Bulk	1.320/4.758	N/A
PPyNH <sub>2</sub>	361.7/363.7	1.967/2.869	29.2/12.6
Au	224.5	4.490	10.0
MPTS	24.2	0.266	10.0
Quartz	Bulk	4.182	10.0

**Table 4.6** Fit parameters used for the hydrolysed film in CH<sub>3</sub>CN (green) and CD<sub>3</sub>CN (red) shown in **Figure 4.22**.

The total film thickness is 363 Å as opposed to 443 Å at the end of the hydrolysis reaction. This is a secondary collapse of 80 Å. This can be attributed to polymer relaxation, which occurs on a longer timescale than the FMOC hydrolysis and elution.

Before hydrolysis, the densities of the inner and outer layers were  $1.03$  and  $1.22 \text{ g cm}^{-3}$ , respectively, and  $\phi_s$  was  $0.41$ . After the hydrolysis, the PPyNH<sub>2</sub> layer has a density of  $1.35 \text{ g cm}^{-3}$ . The solvent volume fraction has also decreased further from  $0.60$  to  $0.36$ . **Figures 4.24** and **4.25** summarise the changes in reflectivity and SLD profiles before and after the hydrolysis reaction. Note how the widening of the fringes in **Figure 4.24** corresponds to a decrease in polymer film thickness in **Figure 4.25**.

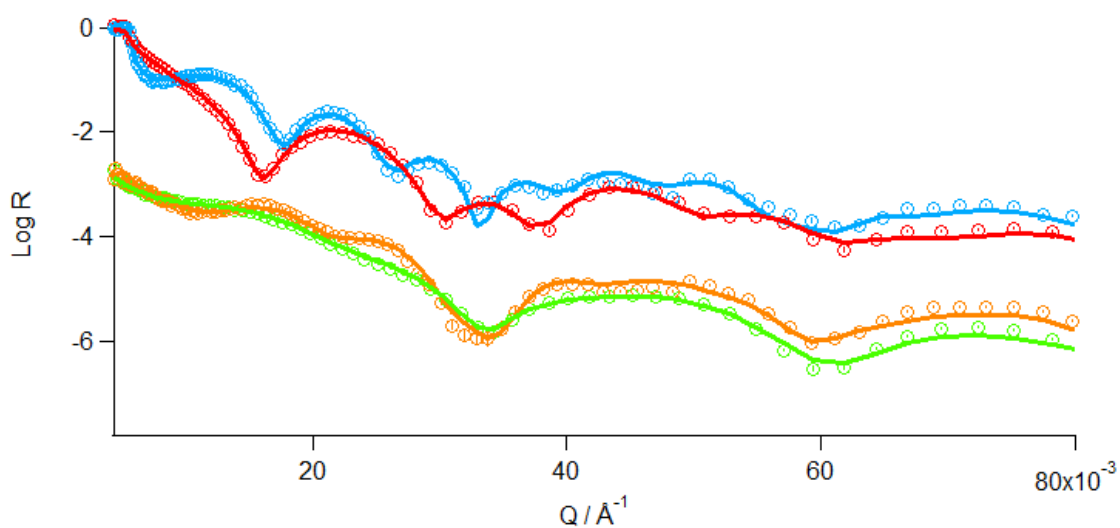


**Figure 4.24** Changes in reflectivity data before and after hydrolysis in CH<sub>3</sub>CN (orange and green, respectively) and CD<sub>3</sub>CN (blue and red, respectively). The circles represent the raw data and the line is the fit of that data. Note that datasets for the films in hydrogenous solvent have been manually offset in reflectivity for visual clarity.

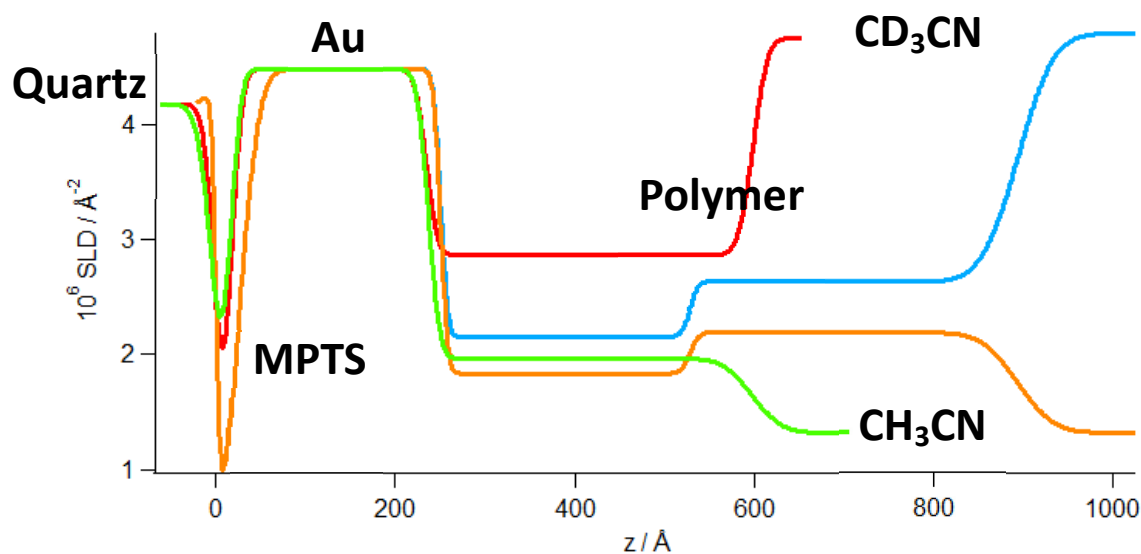


**Figure 4.25** Changes in SLD before and after hydrolysis in CH<sub>3</sub>CN (orange and green, respectively) and CD<sub>3</sub>CN (blue and red, respectively).

In order to check the validity of these findings the process was repeated with an analogous film (characterised in **Figures 4.26-4.29**) this time with the hydrolysis reaction taking place in CH<sub>3</sub>CN.

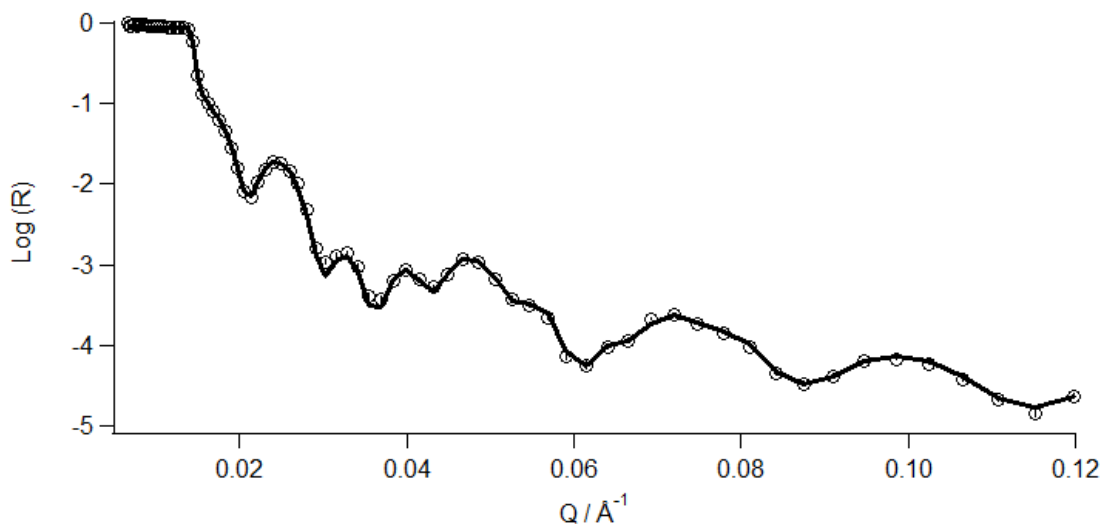


**Figure 4.26** Neutron reflectivity profile (INTER, ISIS) of a dry PPyFMOc film measured after polymerisation and prior to the hydrolysis of the FMOc protecting group. The circles represent the raw data and the line is the fit of that data ( $\chi^2 = 1.9$ ).

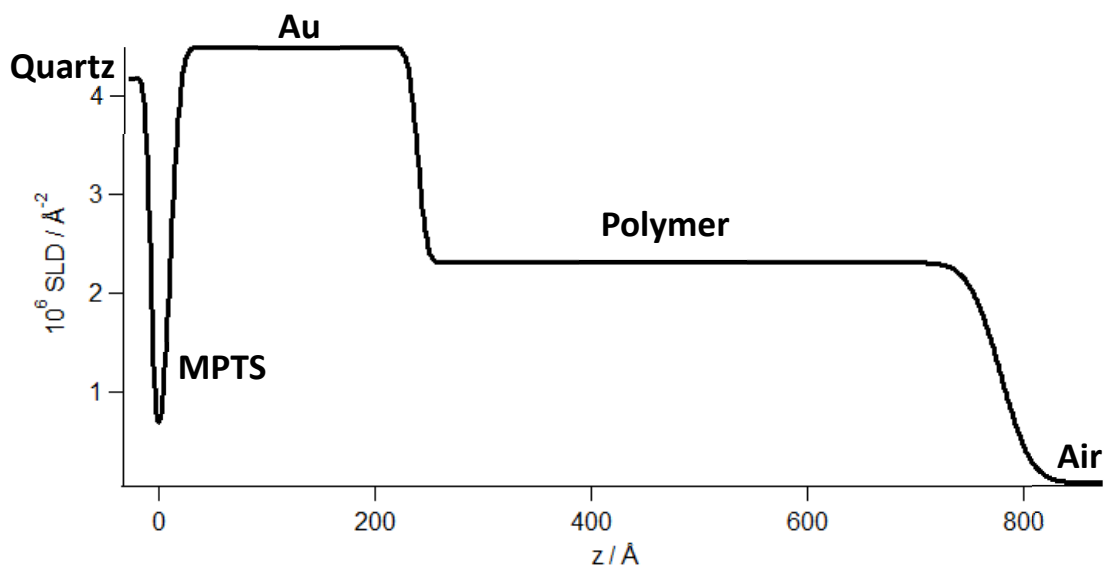


**Figure 4.27** SLD profile of the dry PPyFMOC film shown in **Figure 4.26**.

A summary of the fit parameters used is given in **Table 4.7**. In this instance the fitting parameters only required one layer of PPyFMOC to fit the dry film data:

Layer	$d / \text{Å}$	$10^6 N_b / \text{Å}^{-2}$	$\sigma / \text{Å}$
Air	Bulk	0	N/A
PPyFMOC	538.5	2.307	22.7
Au	228.3	4.490	6.8
MPTS	18.4	0.266	7.4
Quartz	Bulk	4.182	4.0

**Table 4.7** Fit parameters used in **Figure 4.26**.

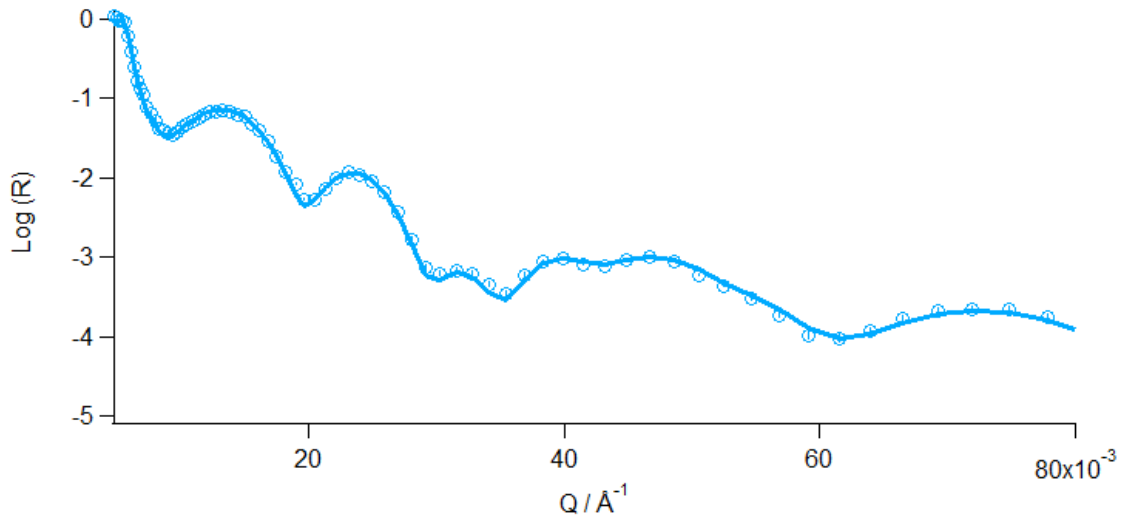


**Figure 4.28** Neutron reflectivity profile of the solvated PPyFMOC film in CD<sub>3</sub>CN ( $\chi^2 = 2.1$ ). The circles represent the raw data and the line is the fit of that data.

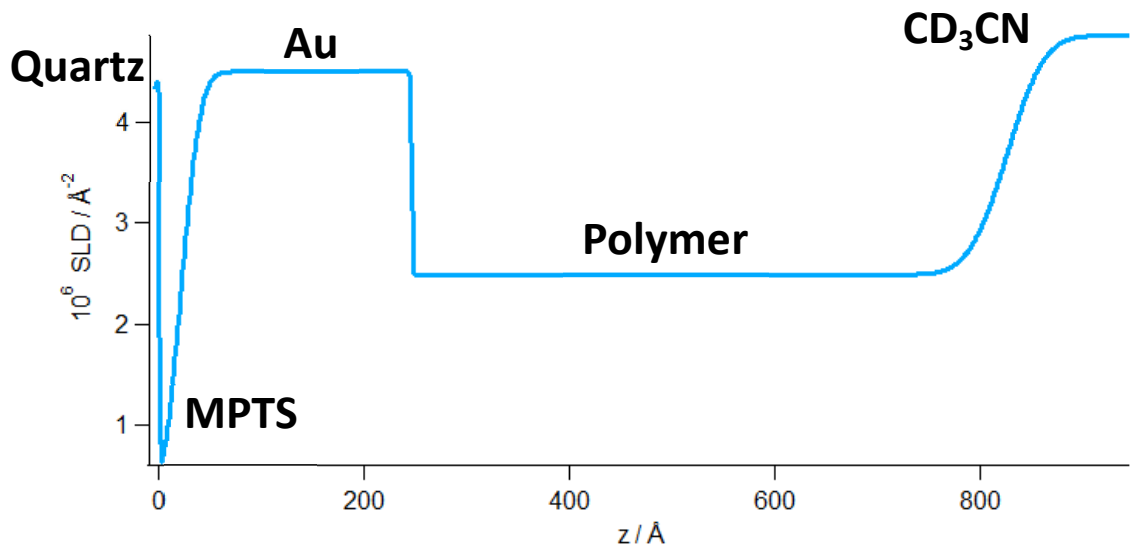


**Figure 4.29** SLD profile of the solvated PPyFMOC film in CD<sub>3</sub>CN.

A summary of the fit parameters used is given in **Table 4.8**.

Layer	d / Å	$10^6 N_b / \text{Å}^{-2}$	$\sigma / \text{Å}$
CH <sub>3</sub> CN/ CD <sub>3</sub> CN	Bulk	4.846	N/A
PPyFMOc	579.0	2.488	28.8
Au	222.54.5	4.490	5.0
MPTS	21.6	0.266	11.6
Quartz	Bulk	4.182	5.0

**Table 4.8** Fit parameters used in **Figure 4.28**.

Here the total film thickness is 579.0 Å, compared to 538.5 Å for the dry film. This is a swelling of 41 Å or 8 % upon solvation. This increase in thickness during solvation was accompanied by a decrease in the density of the polymer film. Before solvation the density of the PPyFMOc layer was 1.30 g cm<sup>-3</sup> and upon solvation this changed to 1.22 g cm<sup>-3</sup>.

Next the film was monitored during hydrolysis in 10 mM piperidine in CH<sub>3</sub>CN.

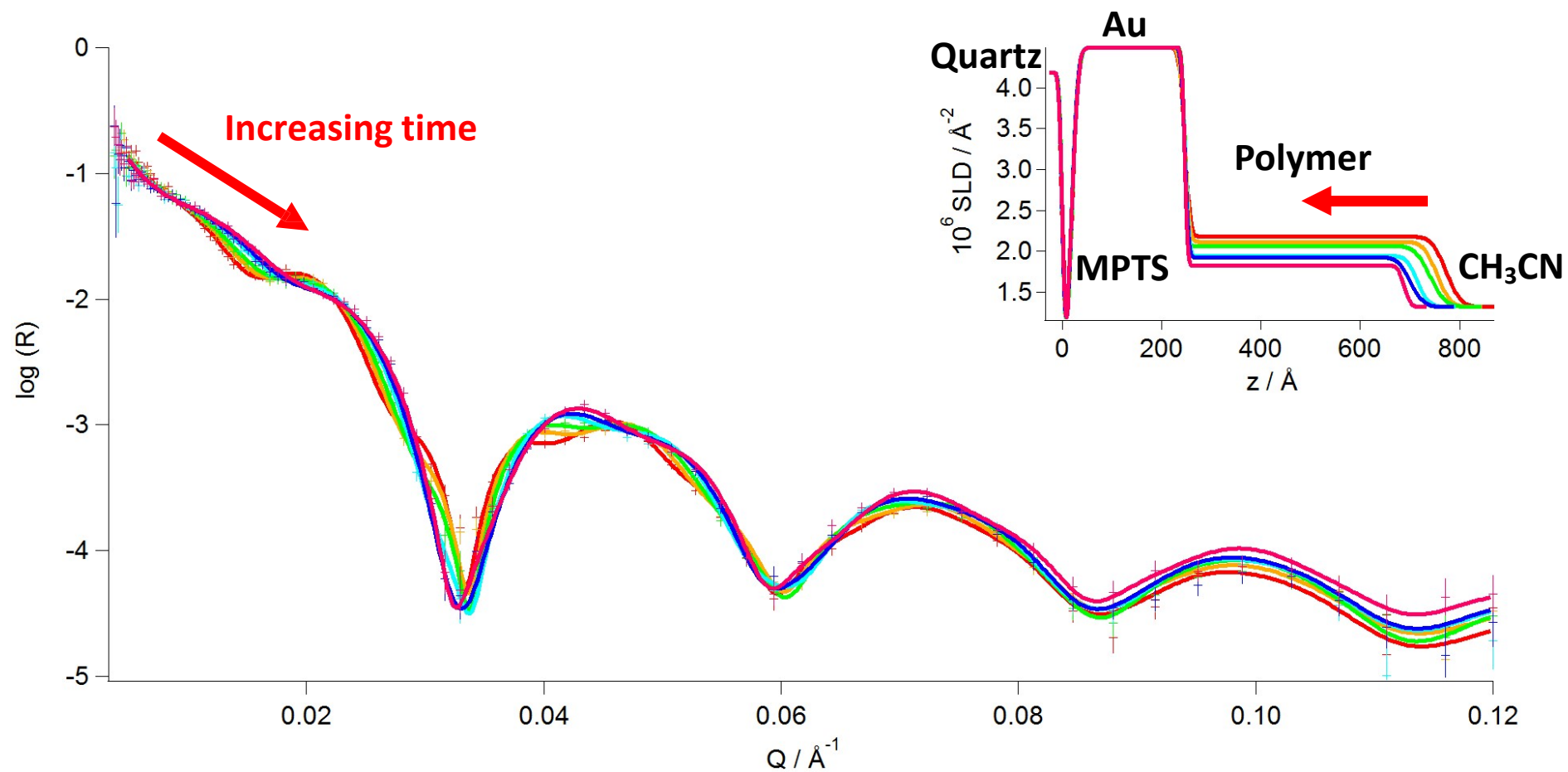


**Figure 4.30** Kinetic NR data ( $\bullet$ ), fits (line) and resultant SLD profiles (inset) showing the Fmoc hydrolysis reaction progress in 10 mM piperidine in CH<sub>3</sub>CN taken every 10 minutes ( $X^2$  1.2 - 2.2) respectively.

<b>CH<sub>3</sub>CN</b>	Bulk	1.320	N/A
<b>PPyFMOc</b>	See <b>Table 4.10</b>		
<b>Au</b>	228.1	4.490	5.7(±2.0)
<b>MPTS</b>	18.3	0.266	10.4
<b>Quartz</b>	Bulk	4.182	5.2

**Table 4.9** Summary of the fit parameters for the solvent, Au, MPTS and quartz layers of the system used in **Figure 4.30**.

<b>PPyFMOc</b>			
<b>t / min</b>	<b>d / Å</b>	<b>10<sup>6</sup> N<sub>b</sub> / Å<sup>-2</sup></b>	<b>σ / Å</b>
3	526.7	2.179	23.1
13	517.3	2.065	13.5
23	514.8	2.139	21.9
33	508.2	2.116	21.5
43	503.3	2.085	26.7
53	494.6	1.999	16.1
63	494.4	2.067	24.6
73	482.0	2.038	21.6
83	480.8	1.981	24.1
93	469.5	1.943	17.8
103	466.3	1.957	20.0
113	464.1	1.923	20.7
123	455.5	1.926	20.5
133	449.1	1.923	22.1
143	445.3	1.843	18.7
153	442.1	1.826	10.2
283	408.6	1.695	5.9
293	406.7	1.680	6.4

**Table 4.10** Summary of the fit parameters for inner and outer layers of the PPyFMOc/PPyNH<sub>2</sub> system used in **Figure 4.30**.

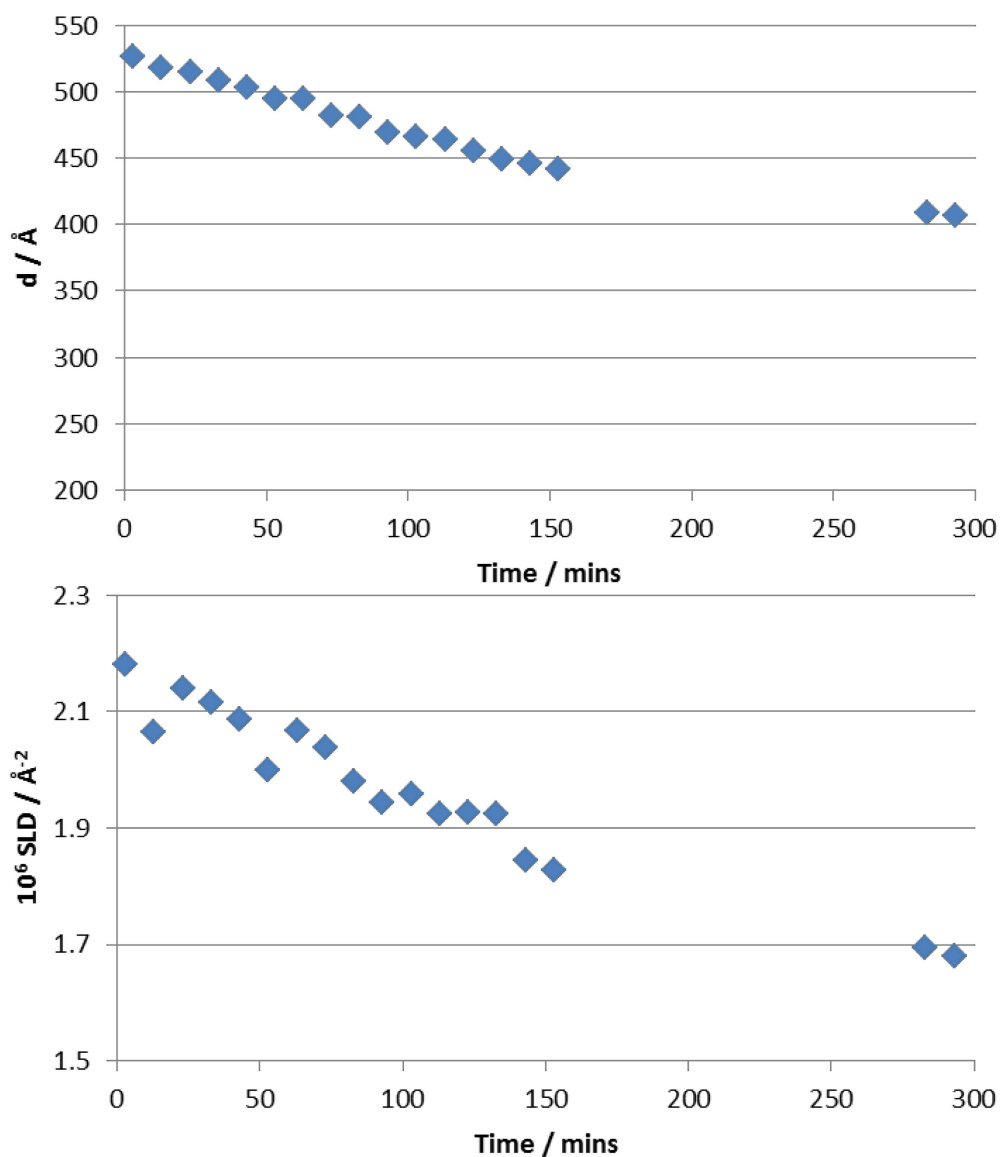


**Figure 4.31** Reaction progress of the total (◆) polymer layer during the Fmoc hydrolysis reaction in 10 mM piperidine. Top graph is the change in thickness and bottom is the change in SLD.

**Figure 4.31** shows a thickness change from 526.7 to 406.7 Å during the hydrolysis reaction. This corresponds to a collapse of 120 Å. The reaction progress and film solvation are depicted in **Figures 4.32** and **4.33**.

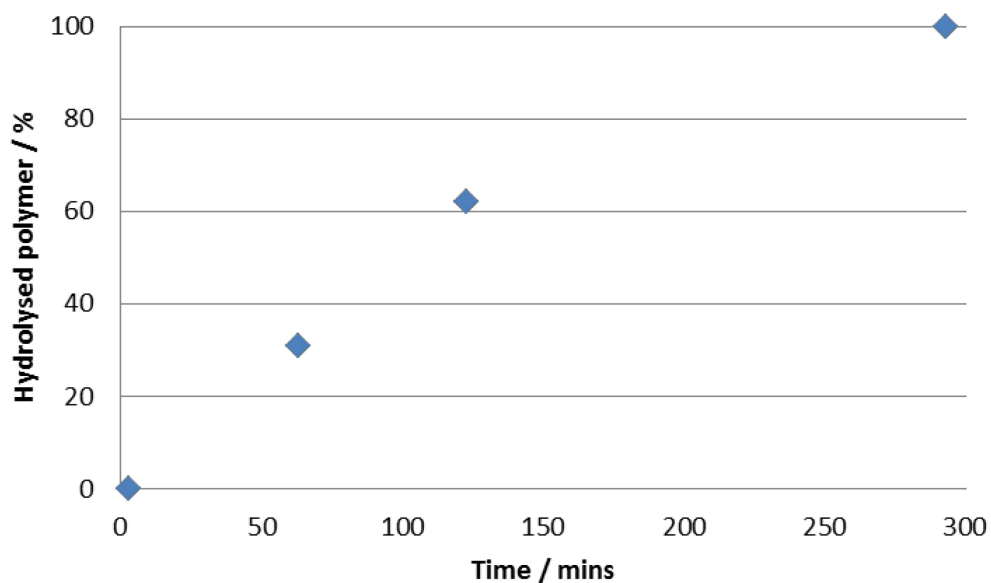


**Figure 4.32** Hydrolysis reaction progress represented by the percentage of hydrolysed polymer.

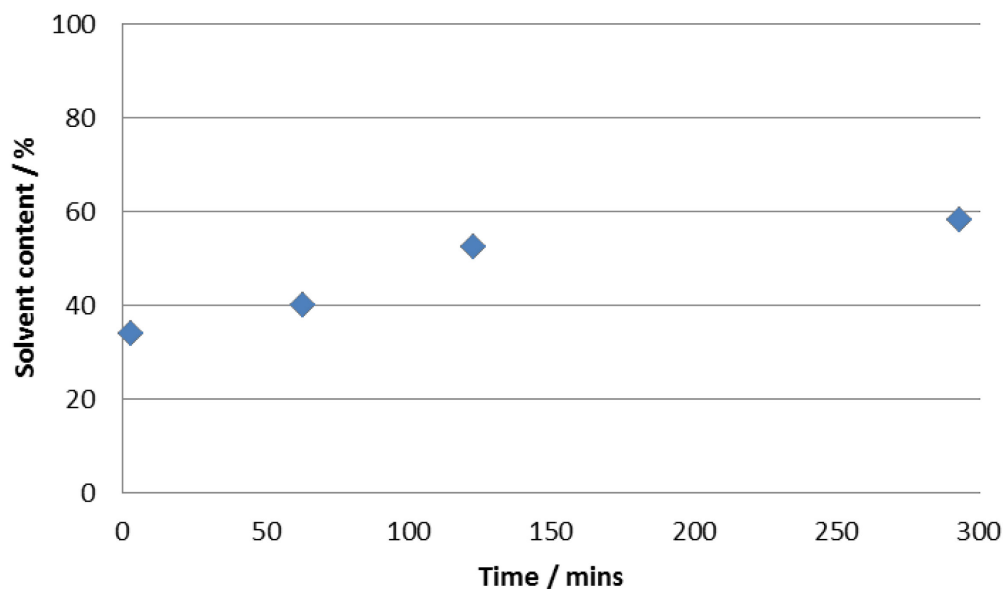


**Figure 4.33** Changes in solvent volume fraction ( $\phi_{\text{CH}_3\text{CN}}$ ) observed in the polymer during the 10 mM hydrolysis reaction.

Again, once the reaction had gone to completion the reaction was stopped and the reflectivity of the film was measured in both contrasts.

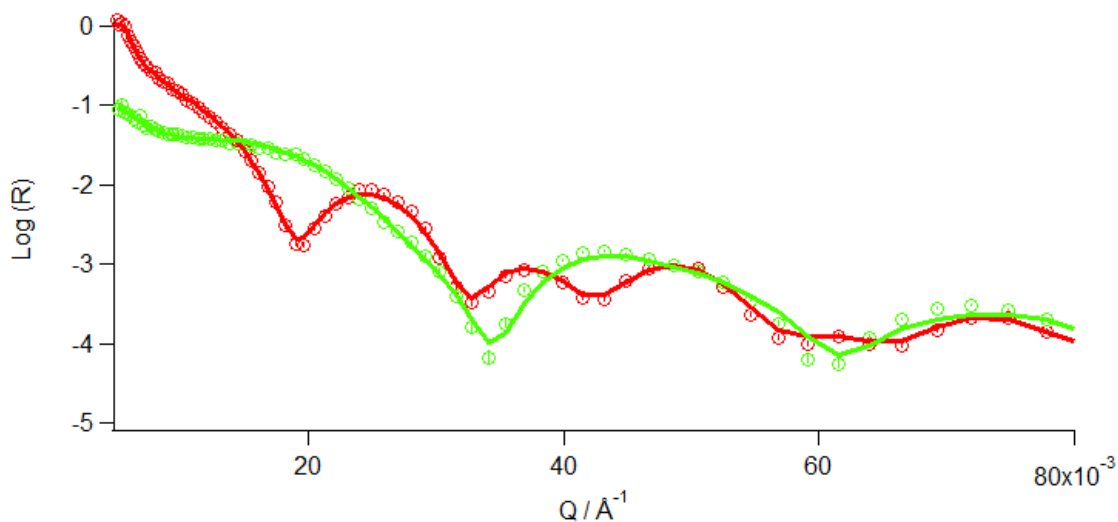


**Figure 4.34** NR profile of the solvated PPyNH<sub>2</sub> film after hydrolysis in CH<sub>3</sub>CN (green) and CD<sub>3</sub>CN (red). The circles represent the raw data and the line is the fit of that data ( $\chi^2 = 2.1$  and  $2.0$ ).

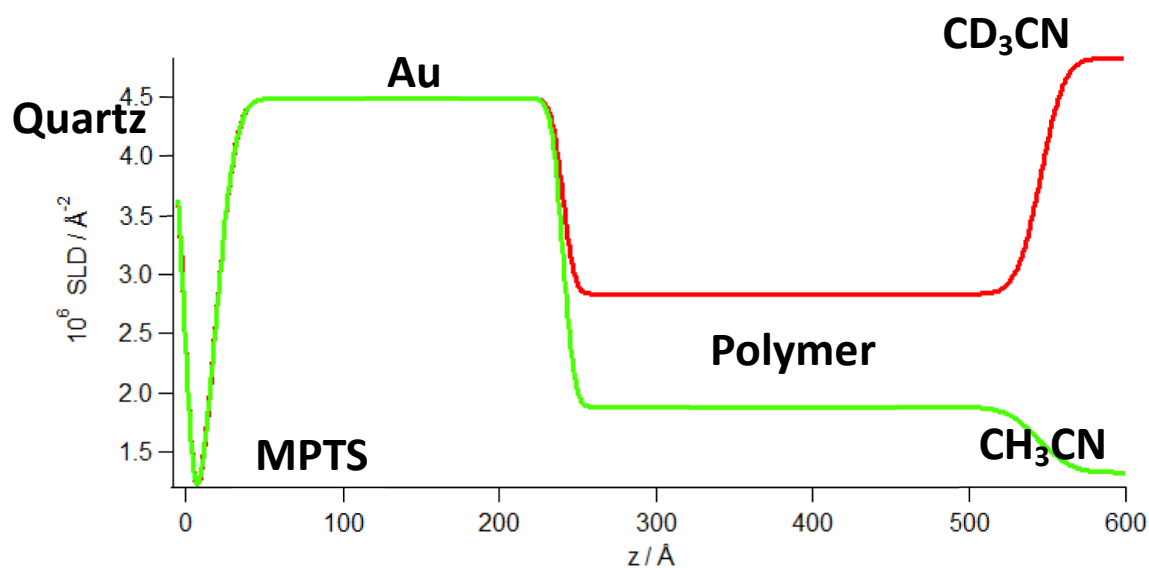


**Figure 4.35** SLD profile of the solvated PPyNH<sub>2</sub> film after hydrolysis in CH<sub>3</sub>CN (green) and CD<sub>3</sub>CN (red).

A summary of the fit parameters used is given in **Table 4.11**.

Layer	d / Å	$10^6 N_b / \text{Å}^{-2}$	$\sigma / \text{Å}$
CH <sub>3</sub> CN/ CD <sub>3</sub> CN	Bulk	1.320/4.828	N/A
PPyNH <sub>2</sub>	304.0/305.1	1.877/2.834	16.4/12.2
Au	222.8	4.490	5.9
MPTS	17.9	0.266	10.7
Quartz	Bulk	4.182	5.0

**Table 4.11** Fit parameters of the solvated PPyNH<sub>2</sub> film after hydrolysis in CH<sub>3</sub>CN (green) and CD<sub>3</sub>CN (red) used in **Figure 4.34**.

The total film thickness is 304.5 Å, compared with 406.7 Å at the end of the hydrolysis reaction. This is a further collapse of 101.5 Å. The fact that this secondary collapse occurred in both films supports the theory that this must be because of polymer relaxation occurring on a longer timescale than the FMOC hydrolysis and elution.

Before hydrolysis the density of the PPyFMOC layer was 1.22 g cm<sup>-3</sup>. After the hydrolysis the solely PPyNH<sub>2</sub> layer has a density of 1.32 g cm<sup>-3</sup>. The initial  $\phi_s$  of the PPyFMOC was 0.35. This rose to 0.58 immediately after hydrolysis and subsequently relaxed back to 0.37. **Figures 4.36** and **4.37** highlight the changes in both reflectivity and SLD profiles before and after hydrolysis.

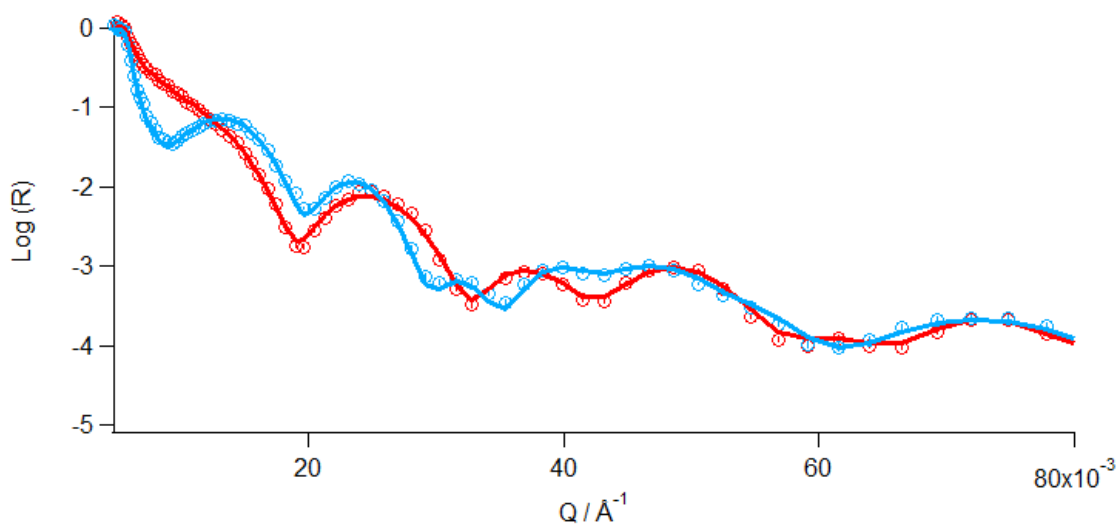


**Figure 4.36** Changes in reflectivity data before and after hydrolysis  $\text{CD}_3\text{CN}$  (blue and red, respectively). The circles represent the raw data and the line is the fit of that data.

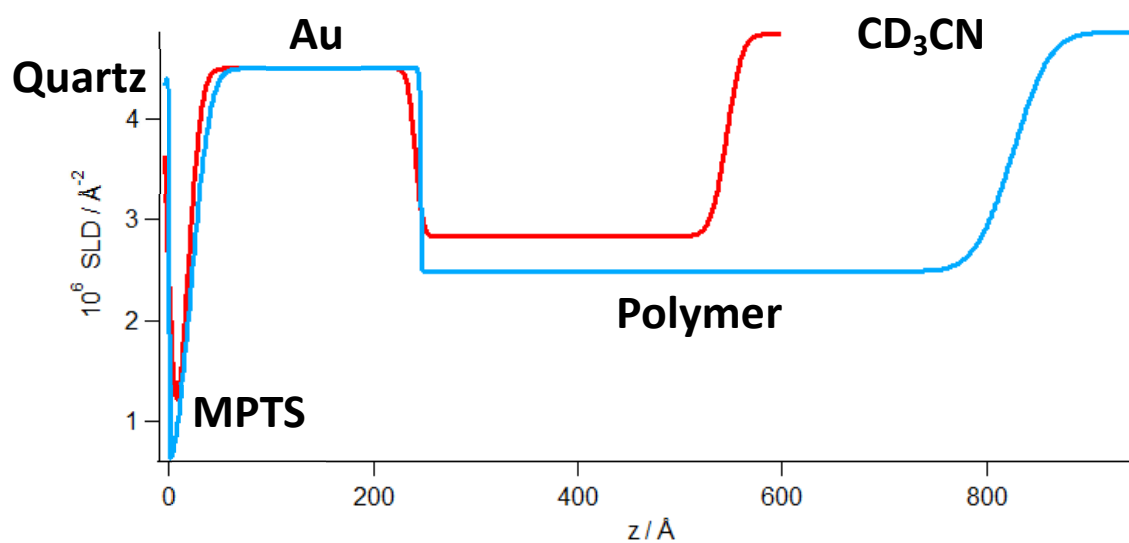


**Figure 4.37** Changes in SLD before and after hydrolysis in  $\text{CD}_3\text{CN}$  (blue and red, respectively).

**Figure 4.38** shows a cartoon representation of the changes in film properties observed by NR during Fmoc hydrolysis and elution.

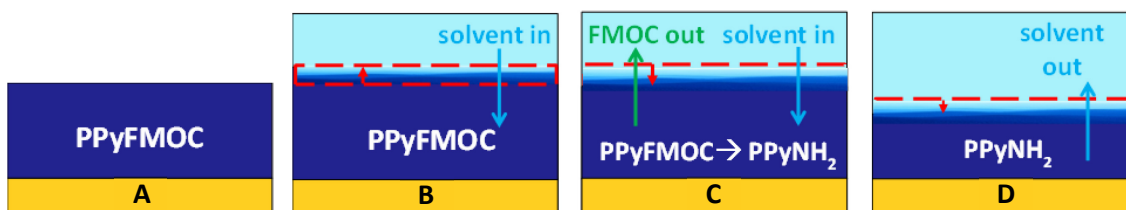


**Figure 4.38** Cartoon representation of film changes occurring during the different neutron reflectivity measurements taken to assess the hydrolysis reaction. (A) dry PPyFmoc film, (B) PPyFmoc film swelling due to solvation in acetonitrile, (C) PPyFmoc film undergoing hydrolysis with Fmoc elution and solvent incorporation and (D) secondary collapse of deprotected PPyNH<sub>2</sub> film due to polymer relaxation.

#### 4.3.3.2. Reaction with Fluorophores

Once the first stage of the reaction depicted in **Figure 4.3** had been evaluated, the final stage of the reaction was considered. This involved reacting the PPyNH<sub>2</sub> films with a sterically bulky, NHS ester functionalized fluorophore. NR was used to assess a series of films (analogous to those used to assess the hydrolysis reaction) before and after the fluorophore reaction. In total three fluorophores were assessed; Dylight 649, Cy3 and Cy7.5 all of which were functionalised with a NHS ester in order to chemically bind to the amine.

Dylight 649 NHS Ester

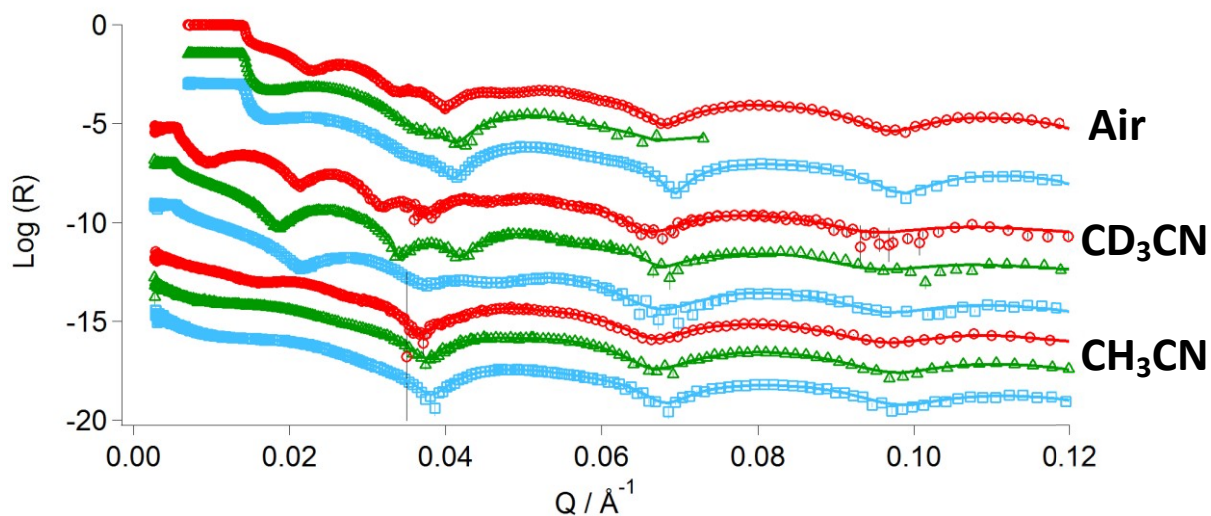


**Figure 4.39** NR data for a PPyFmoc film prior to hydrolysis (○), the PPyNH<sub>2</sub> film resulting from hydrolysis (△) and the PPyDylight film following exposure to the fluorophore (□). For visual comparison purposes, R(Q) profiles are grouped according to medium (see annotations) and are progressively offset in reflectivity ( $\chi^2 = 1.4-2.7$ ).

As expected because of the positive difference in SLD between quartz and air and CD<sub>3</sub>CN and quartz, the dry and CD<sub>3</sub>CN exposed films show a critical edge at low Q. However, there is no critical edge in CH<sub>3</sub>CN as  $\Delta N_b$  is negative ( $1.32-4.182 \times 10^{-6} \text{ \AA}^{-2}$ ).

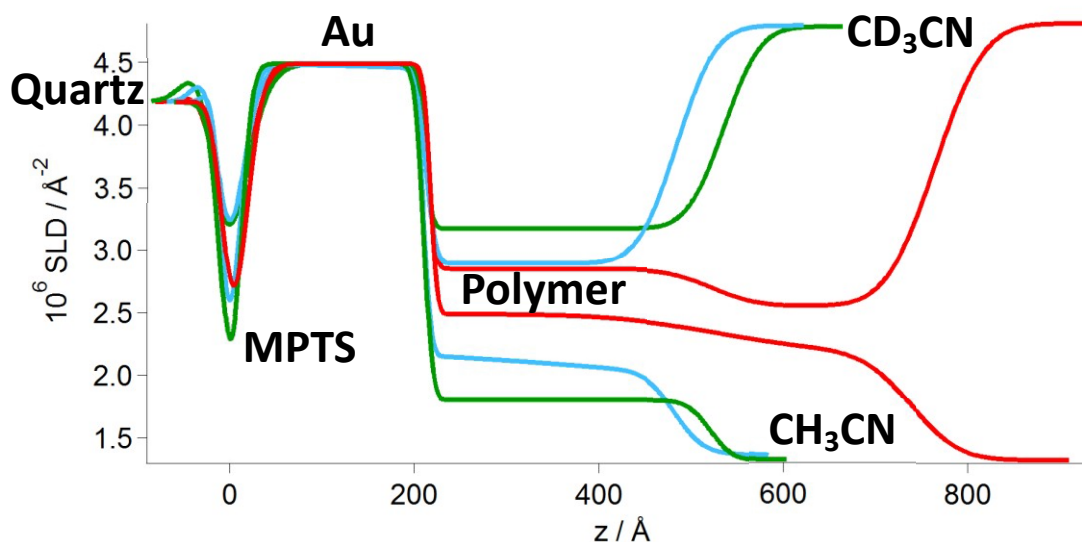


**Figure 4.40** SLD profiles for the film exposed to  $\text{CH}_3\text{CN}$  (bottom three traces in polymer section) and  $\text{CD}_3\text{CN}$  (top three traces in polymer section) at each of the three stages of the process: nominally PPyFMOC (red), PPyNH<sub>2</sub> (green) and PPyDylight (cyan).

	$d / \text{\AA}$	$10^6 N_b / \text{\AA}^{-2}$	$\sigma / \text{\AA}$	$d / \text{\AA}$	$10^6 N_b / \text{\AA}^{-2}$	$\sigma / \text{\AA}$	$d / \text{\AA}$	$10^6 N_b / \text{\AA}^{-2}$	$\sigma / \text{\AA}$
Air	Bulk	0	N/A	Bulk	0	N/A	Bulk	0	N/A
PPyX <sub>outer</sub>	303.4	2.298	35.9	256.9	1.915	28.5	267.4	1.978	29.6
PPyX <sub>inner</sub>	172.7	2.383	11.2						
Au	208.9	4.490	6.8	208.0	4.490	7.0	208.7	4.490	7.5
MPTS	15.7	0.266	16.5	17.1	0.266	18.5	13.1	0.266	16.1
Quartz	Bulk	4.182	9.7	Bulk	4.182	10.2	Bulk	4.182	7.1

**Table 4.12** Fit parameters used for the dry films: PPyFMOC (red), PPyNH<sub>2</sub> (green) and PPyDylight (cyan).

In order to fit the thicker PPyFMOC film it was necessary to model the polymer as two layers. As with the film in **Figures 4.10** and **4.11** the higher  $N_b$  of the inner layer relates to a higher density of the polymer closer to the electrode surface ( $\rho_{\text{inner}} = 1.34 \text{ g cm}^{-3}$ ,  $\rho_{\text{outer}} = 1.29 \text{ g cm}^{-3}$ ). The densities of the PPyNH<sub>2</sub> and PPyDylight layers were 1.40 and 1.42 g cm<sup>-3</sup>. The total film thicknesses of the PPyFMOC, PPyNH<sub>2</sub> and PPyDylight films were 476, 257 and 267 Å, respectively. The significant change observed in the SLD profiles in **Figure 4.40** clearly demonstrates a change in film composition. This change took place within the first 15 min of the exposure to the Dylight fluorophore solution. When measured again after an hour there was no further change. This is attributed to the more fluid-like environment of the film following hydrolysis and the creation of the solvent “voids”. Instrumental issues (such as sample alignment prior to measurement) and time restraints on experiments meant it was not possible to do a kinetic measurement in real time during the fluorophore reaction, but from a practical perspective in future applications such a quick reaction time with the fluorophore is obviously beneficial.

**Tables 4.13** and **4.14** show the properties of the three films upon solvation in acetonitrile.

	$d / \text{\AA}$	$10^6 N_b / \text{\AA}^{-2}$	$\sigma / \text{\AA}$	$d / \text{\AA}$	$10^6 N_b / \text{\AA}^{-2}$	$\sigma / \text{\AA}$	$d / \text{\AA}$	$10^6 N_b / \text{\AA}^{-2}$	$\sigma / \text{\AA}$
<b>CD<sub>3</sub>CN</b>	Bulk	4.812	N/A	Bulk	4.787	N/A	Bulk	4.796	N/A
<b>PPyX<sub>outer</sub></b>	241.2	2.554	41.7	324.5	3.172	31.1	272.2	2.887	12.8
<b>PPyX<sub>inner</sub></b>	308.4	2.844	38.1						
<b>Au</b>	214.5	4.490	6.5	214.5	4.490	6.5	214.0	4.490	21.3
<b>MPTS</b>	12.5	0.266	23.4	12.7	0.266	28.3	9.7	0.266	9.0
<b>Quartz</b>	Bulk	4.182	16.2	Bulk	4.182	16.2	Bulk	4.182	33.3

**Table 4.13** Fit parameters used for the solvated films in CD<sub>3</sub>CN: PPyFMOC (red), PPyNH<sub>2</sub> (green) and PPyDylight (cyan).

	$d / \text{\AA}$	$10^6 N_b / \text{\AA}^{-2}$	$\sigma / \text{\AA}$	$d / \text{\AA}$	$10^6 N_b / \text{\AA}^{-2}$	$\sigma / \text{\AA}$	$d / \text{\AA}$	$10^6 N_b / \text{\AA}^{-2}$	$\sigma / \text{\AA}$
<b>CH<sub>3</sub>CN</b>	Bulk	1.320	N/A	Bulk	1.320	N/A	Bulk	1.320	N/A
<b>PPyX<sub>outer</sub></b>	205.6	2.179	41.4	311.0	1.800	12.2	87.9	1.935	24.4
<b>PPyX<sub>inner</sub></b>	316.3	2.482	95.5				184.0	2.190	174.9
<b>Au</b>	208.3	4.490	6.0	200.6	4.490	10.7	206.5	4.490	7.0
<b>MPTS</b>	14.8	0.266	17.7	15.4	0.266	7.8	12.3	0.266	15.7
<b>Quartz</b>	Bulk	4.182	12.0	Bulk	4.182	12.2	Bulk	4.182	8.6

**Table 4.14** Fit parameters used for the solvated films in CH<sub>3</sub>CN: PPyFMOC (red), PPyNH<sub>2</sub> (green) and PPyDylight (cyan).

The higher roughness at the polymer/polymer interface for the PPyFMOC film in hydrogenous acetonitrile is attributed to a contrast effect. As there is less contrast between CH<sub>3</sub>CN and

PPyFMOc than CD<sub>3</sub>CN the layers appear to be more diffuse as the neutrons are not able to highlight the difference between the layers as effectively. The outer interfaces are also diffuse. In the NR profiles, this is seen as damping of the film-based fringes. In terms of reactivity, this would undoubtedly aid faster permeation of the fluorophore moieties.

Based on the solvation properties it is estimated that there was one fluorophore entity for every ca. four-five PyNH<sub>2</sub> monomer units. This approximation is based on the N<sub>b</sub> of the PPyNH<sub>2</sub> polymer that was determined through the NR measurements above and the limited information available on the structure of Dylight 649 NHS ester (structure is commercially protected). The molecular mass is on the order of 1000 Daltons and there are four sulfonate groups (to provide adequate solubility) on an essentially aromatic hydrocarbon skeleton.

**Figure 4.40** shows that the N<sub>b</sub>, and thus composition of the PPyDylight film shows only modest dependence on depth (none in deuterated media and a high polymer/polymer interfacial roughness in hydrogenous). This indicates that diffusion of reactant into the film is not a limiting factor in the fluorophore reaction; if it were, then there would be a clear step in N<sub>b</sub>/composition representing fluorophore penetration. Despite the entry of fluorophore into the polymer, the films shrink slightly during the reaction. This indicates that the volume of solvent expelled exceeds the volume of fluorophore entering, suggesting that transport processes are not so slow that mobile species (here, solvent) are trapped within the film. However, the dry film thickness of PPyDylight is ca. 10 Å greater than the PPyNH<sub>2</sub> film. This supports the previous statement that the solvated thicknesses are dependent on solvent volume fraction. Finally, the overall thicknesses of the dry films are not much less than for the solvated films yet there is still appreciable solvent in the immersed films. This suggests that the film does not collapse upon emersion (any free volume is retained).

	$\phi_{\text{Acetonitrile}}$	
	Inner	Outer
PPyFmoc	0.34	0.38
PPyNH <sub>2</sub>	0.47	
PPyDylight	0.40	0.62

**Table 4.15** Summary of film solvent volume fractions at different stages of the reaction process.

**Figure 4.41** shows *ex situ* AFM images of the polymer films shown in **Figures 4.39-40**.

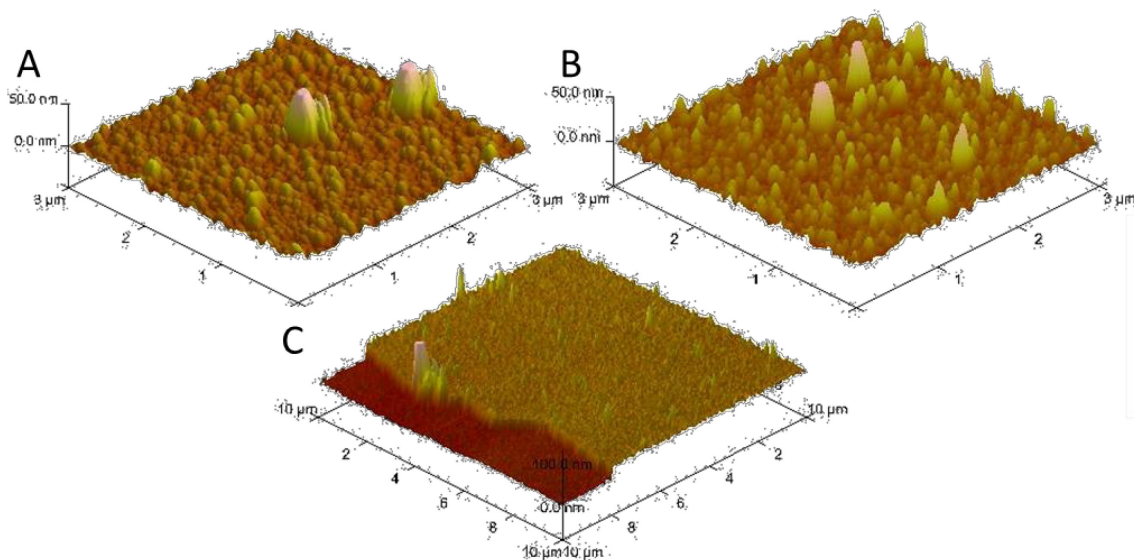


**Figure 4.41** *Ex situ* AFM images of (A) PPyFmoc before NR experiment, (B) PPyDylight after NR experiment and (C) step height of PPyDylight after NR experiment.

In order to qualitatively assess the value of the extra hydrolysis step in the incorporation of the bulky fluorophore molecules the same set of neutron experiments were performed on a PPyNH<sub>2</sub> film that was deposited from the corresponding PyNH<sub>2</sub> monomer (no solvent “voids”). The results are shown in **Figures 4.42** and **4.43**.

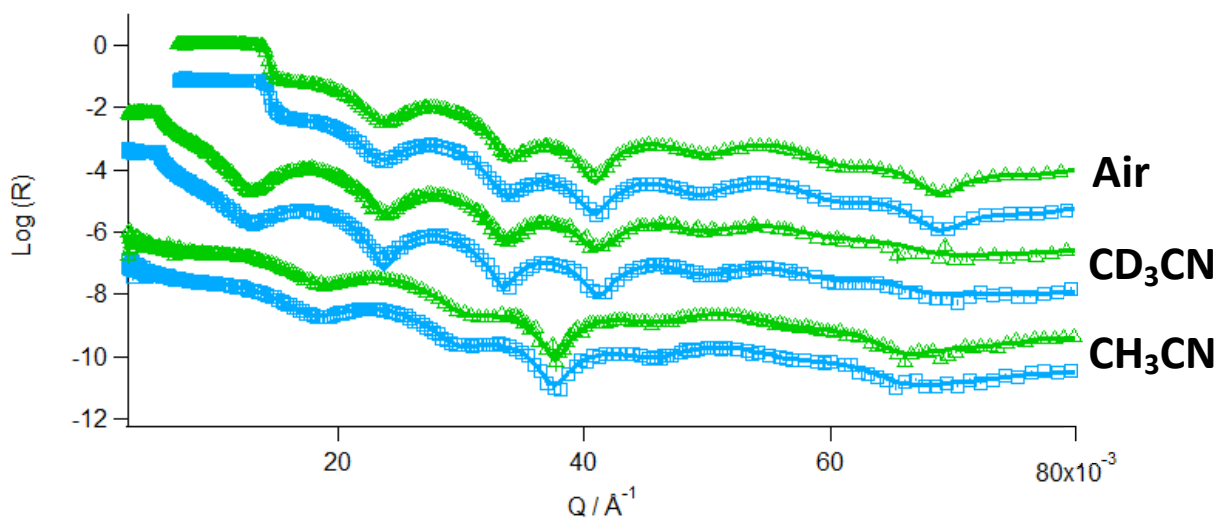


**Figure 4.42** NR data for a PPyNH<sub>2</sub> film as electrodeposited ( $\Delta$ ) and the PPyDylight film following exposure to the fluorophore ( $\square$ ). For visual comparison purposes, R(Q) profiles are grouped according to medium (see annotations) and are progressively offset in reflectivity ( $\chi^2 = 1.2-2.9$ ).

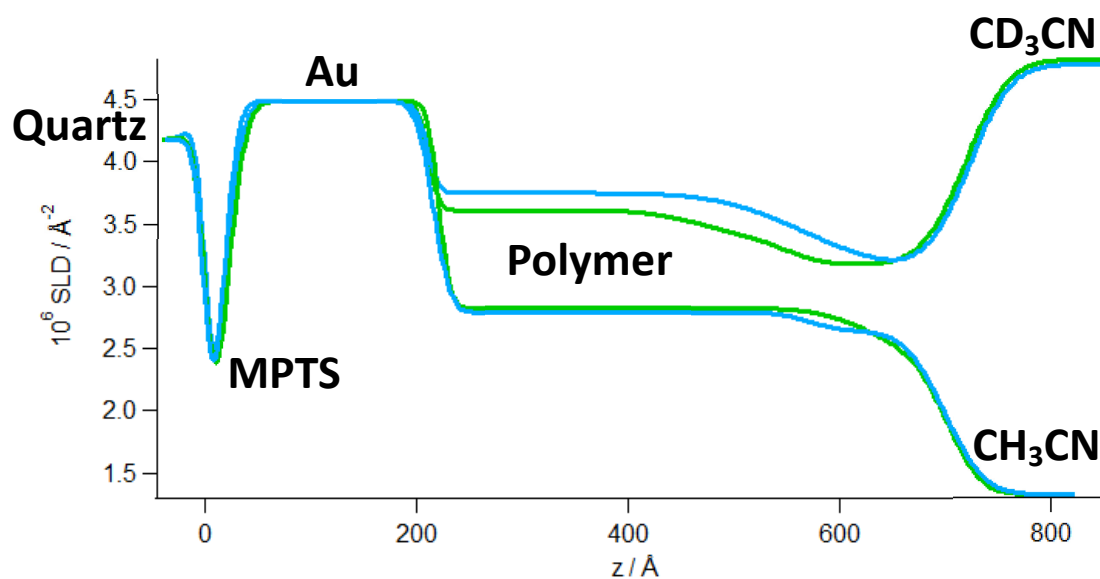


**Figure 4.43** SLD profiles for the film exposed to CH<sub>3</sub>CN and CD<sub>3</sub>CN at each of the three stages of the process: PPyNH<sub>2</sub> (green) as electrodeposited and PPyDylight (cyan).

	$d$ (Å)	$N_b$ (Å <sup>2</sup> x10 <sup>-6</sup> )	$\sigma$ (Å)	$d$ (Å)	$N_b$ (Å <sup>2</sup> x10 <sup>-6</sup> )	$\sigma$ (Å)
<b>Air</b>	Bulk	0	N/A	Bulk	0	N/A
<b>PPyX<sub>outer</sub></b>	117.8	2.465	25.5	132.3	2.354	25.2
<b>PPyX<sub>inner</sub></b>	342.8	2.610	37.8	334.0	2.664	47.1
<b>Au</b>	205.7	4.490	8.0	204.3	4.490	9.5
<b>MPTS</b>	17.1	0.266	15.9	15.0	0.266	13.8
<b>Quartz</b>	Bulk	4.182	7.6	Bulk	4.182	5.7

**Table 4.16** Fit parameters used for the dry films: PPyNH<sub>2</sub> (green) and PPyDylight (cyan).

In this instance the only noticeable change between the two systems is a slight lowering of the SLD of the outer polymer layer. Once again in the PPyNH<sub>2</sub> film (as electropolymerised) there is a denser inner layer (1.90 g cm<sup>-3</sup>) and a less dense outer layer (1.80 g cm<sup>-3</sup>) and it is this less dense layer only that seems able to react with the sterically bulky fluorophore molecules. To assess the extent of the reaction the corresponding solvated measurements were performed in CH<sub>3</sub>CN and CD<sub>3</sub>CN.

	$d$ (Å)	$N_b$ (Å <sup>-2</sup> x10 <sup>-6</sup> )	$\sigma$ (Å)	$d$ (Å)	$N_b$ (Å <sup>-2</sup> x10 <sup>-6</sup> )	$\sigma$ (Å)
<b>CD<sub>3</sub>CN</b>	Bulk	4.825	N/A	Bulk	4.786	N/A
<b>PPyX<sub>outer</sub></b>	167.5	3.176	32.8	155.9	3.133	32.1
<b>PPyX<sub>middle</sub></b>	80.7	3.378	27.8	-	-	-
<b>PPyX<sub>inner</sub></b>	260.3	3.612	42.7	356.7	3.751	64.8
<b>Au</b>	196.3	4.490	8.0	196.9	4.490	9.0
<b>MPTS</b>	14.3	0.266	15.0	12.5	0.266	15.0
<b>Quartz</b>	Bulk	4.182	9.0	Bulk	4.182	8.0

**Table 4.17** Fit parameters used for the solvated films in CD<sub>3</sub>CN: PPyNH<sub>2</sub> (green) and PPyDylight (cyan).

	$d$ (Å)	$N_b$ (Å <sup>-2</sup> x10 <sup>-6</sup> )	$\sigma$ (Å)	$d$ (Å)	$N_b$ (Å <sup>-2</sup> x10 <sup>-6</sup> )	$\sigma$ (Å)
<b>CH<sub>3</sub>CN</b>	Bulk	1.320	N/A	Bulk	1.320	N/A
<b>PPyX<sub>outer</sub></b>	66.1	2.381	24.7	127.1	2.640	29.7
<b>PPyX<sub>inner</sub></b>	415.8	2.826	44.7	356.8	2.790	24.4
<b>Au</b>	205.5	4.490	8.7	202.4	4.490	12.7
<b>MPTS</b>	15.1	0.266	15.8	12.8	0.266	12.0
<b>Quartz</b>	Bulk	4.182	9.1	Bulk	4.182	8.5

**Table 4.18** Fit parameters used for the solvated films in CH<sub>3</sub>CN: PPyNH<sub>2</sub> (green) and PPyDylight (cyan).

The total film thicknesses of the solvated PPyNH<sub>2</sub> and PPyDylight films were 509 and 513 Å respectively in CD<sub>3</sub>CN and 482 and 484 Å in CH<sub>3</sub>CN. As there is no physical reason for the thickness to be different in the two contrasts (essentially the same medium) this must be a contrast effect. Perhaps the lower roughness also observed in the hydrogenous medium is actually higher and simply cannot be seen due to a lack of contrast in reflectivity. In order to check that this contrast effect was not simply a case of the film relaxing over time the PPyNH<sub>2</sub> was measured in CD<sub>3</sub>CN followed by CH<sub>3</sub>CN and PPyDylight was measured in CH<sub>3</sub>CN first and then in CD<sub>3</sub>CN. The effect was seen in both instances and therefore must be related to neutron reflectivity contrast and not film aging.

The solvation properties of each polymer were determined utilising the two solvent contrasts.

The results are summarised in **Table 4.19**:

	$\Phi_{\text{Acetonitrile}}$		
	Inner	Middle	Outer
PPyNH <sub>2</sub>	0.22	0.24	0.26
PPyDylight	0.26	-	0.26

**Table 4.19** Summary of film solvent volume fractions at different stages of the reaction process. Note that the middle layer in the PPyNH<sub>2</sub> film was only seen in the deuterated contrast.

The PPyNH<sub>2</sub> film in this instance is significantly less solvated than the corresponding film created through the PPyFMOC hydrolysis pathway. This suggests that there is less free volume. The inner layer of the PPyDylight film (357 Å) comprises unreacted PPyNH<sub>2</sub>. This layer is more solvated than the inner layer present in the unreacted PPyNH<sub>2</sub> film. This can be attributed to the bulky fluorophore molecules pushing solvent into the film as it enters. The outer layer (127-156 Å) contains one fluorophore molecule to every 6.7 monomer units. For the film as a whole this equates to only 3-4 % of the amines in the film being bound to the

fluorophore. Therefore, the 18 % seen in the deprotected PPyFmoc film, with the free volume created by Fmoc hydrolysis, is significantly higher and therefore a worthwhile step.

The Dylight 649 NHS ester has a molecular mass of  $1008 \text{ g mol}^{-1}$ . In order to see how much the steric bulk of the fluorophore determines its incorporation into the polymer film two further fluorophores were explored; Cy7.5 NHS ester ( $616.2 \text{ g mol}^{-1}$ ) and Cy3 NHS ester ( $474.2 \text{ g mol}^{-1}$ ).

**Figure 4.44** shows *ex situ* AFM images of the polymer films shown in **Figures 4.42-43**.

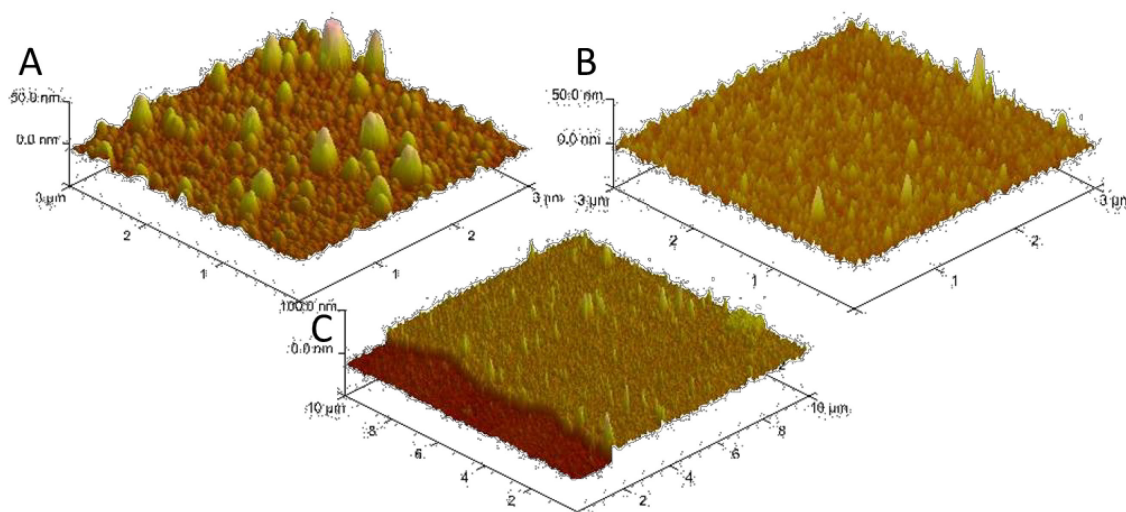


**Figure 4.44** *Ex situ* AFM images of (A) PPyNH<sub>2</sub> before NR experiment, (B) PPyDylight after NR experiment and (C) step height of PPyDylight after NR experiment.

#### Cy7.5 NHS Ester

Unfortunately issues with the fluorophore precipitating in solution during the time scale of the neutron experiment meant that the data interpretation would not be reliable. As such these results will not be discussed. More work could be done to improve the solubility of the fluorophores in solution, for example by the addition of more DMSO to get the data for this intermediate sized fluorophore.

### Cy3 NHS Ester

The smaller NHS ester had greater solubility and so was characterised, this time in air and D<sub>2</sub>O.

In this instance the CD<sub>3</sub>CN and CH<sub>3</sub>CN measurements showed little to no contrast in the R(Q) profiles as shown in **Figure 4.45**.

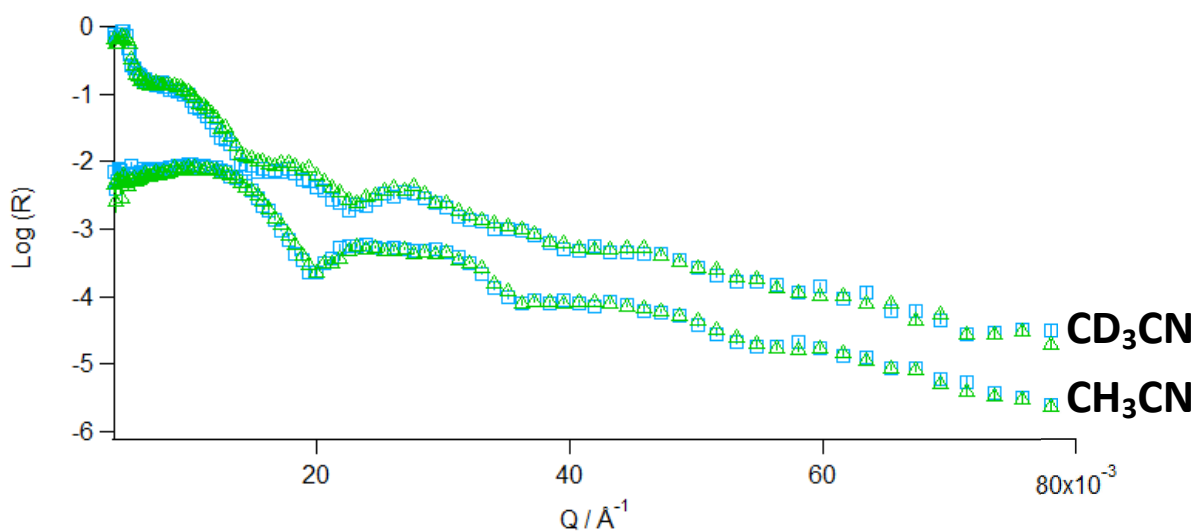


**Figure 4.45** NR data for PPyNH<sub>2</sub> as electrodeposited ( $\Delta$ ) and the PPyCy3 film following exposure to the fluorophore ( $\square$ ). For visual comparison purposes, R(Q) profiles are group according to medium (see annotations) and are offset in reflectivity.

Once again, PPyNH<sub>2</sub> film with solvent “voids” created through the Fmoc hydrolysis pathway was compared to a film with no extra free volume electropolymerised directly from the PyNH<sub>2</sub> monomer. **Figures 4.46** and **4.47** show the reflectivity and SLD profiles for the PPyFmoc film at the different stages of the reaction.

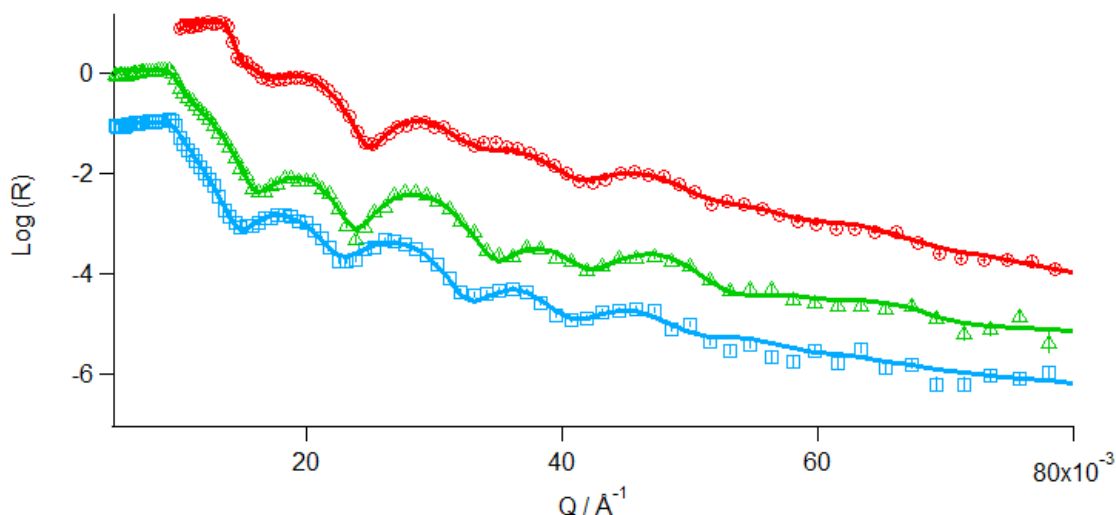


**Figure 4.46** NR data for a dry PPyFMOC film prior to hydrolysis (○), the PPyNH<sub>2</sub> film resulting from hydrolysis in D<sub>2</sub>O (△) and the PPyCy<sub>3</sub> film following exposure to the fluorophore in D<sub>2</sub>O (□). For visual comparison purposes, R(Q) profiles are progressively offset in reflectivity ( $\chi^2 = 1.1-2.1$ ).

The sloping of the critical edges in **Figure 4.46** was seen in the samples run with the samples/cells in a horizontal alignment (FIGARO/OFFSPEC) but not in a vertical alignment (D17). This was proved with a series of measurements, on the same film in both configurations, to be because of a gravitational drop of the long wavelength neutrons. These neutrons are colder and travel slower than shorter wavelength neutrons. They follow a parabolic incident pathway which causes them to arrive before the sample's centre of rotation. Short  $\lambda$  neutrons follow a "linear" pathway as they travel faster and so reach the samples centre of rotation before they experience a gravitational drop. This drop in the long  $\lambda$  neutrons not only changes the illuminated area but in the case of our short gap cells where the beam has already been highly collimated to put the beam footprint within the cell boundaries it was shown that at angles as low as 0.1° on OFFSPEC the difference in the illumination path length was 30 mm. As the footprint of the beam was set to 60 mm in length this equates to the loss of half the longest wavelength neutrons (12-15 Å) as they drop off

before entering the cell and are blocked by the Teflon sides. It also changes the resolution in  $Q$  where the low range neutrons occur as the angle of incidence is steeper than it is meant to be due to the curved pathway.  $\Delta\theta/\theta$  is therefore different for short and long wavelength neutrons meaning that the resolution at low  $Q$  is different to that at high  $Q$ , making the fitting of data more problematic<sup>b</sup>.

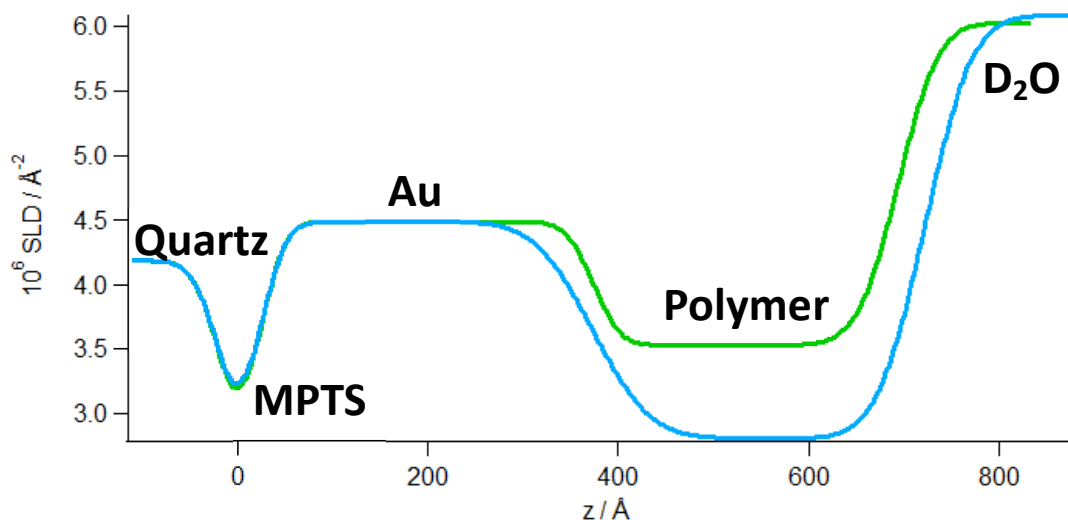


**Figure 4.47** SLD profiles for the solvated films in  $D_2O$ : the PPyNH<sub>2</sub> film resulting from hydrolysis (green) and the PPyCy3 film following exposure to the fluorophore in  $D_2O$  (cyan).

The less well defined dip for the MPTS layer in **Figure 4.47** was attributed to a build-up of MPTS over several experiments causing a roughening of the quartz/thickening of the MPTS layer itself. The SLD profiles show a uniform reaction of the film with the Cy3 NHS ester. The gold/polymer interface also appears rougher after the reaction with the fluorophore. As the structure of the gold electrode is unlikely to roughen itself this effect is more likely to be a

---

<sup>b</sup> Acknowledgement and thanks to Dr Robert M. Dalgliesh for his help and expertise in understanding the problem of sloping critical edges.

result of the polymer rearranging itself to incorporate the bulky fluorophore. This could also have happened with the PPyDylight film but perhaps it can only be seen in the greater contrast of D<sub>2</sub>O and not in acetonitrile.

	$d / \text{\AA}$	$10^6 N_b / \text{\AA}^{-2}$	$\sigma / \text{\AA}$	$d / \text{\AA}$	$10^6 N_b / \text{\AA}^{-2}$	$\sigma / \text{\AA}$	$d / \text{\AA}$	$10^6 N_b / \text{\AA}^{-2}$	$\sigma / \text{\AA}$
<b>Media</b>	Bulk	0	N/A	Bulk	6.029	N/A	Bulk	6.086	N/A
<b>PPyX</b>	291.2	2.603	32.4	319.9	3.532	33.7	348.6	2.813	39.7
<b>Au</b>	360.8	4.490	33.9	360.8	4.490	22.8	361.0	4.490	47.7
<b>MPTS</b>	50.7	0.266	33.2	17.1	0.266	23.4	16.8	0.266	24.0
<b>Quartz</b>	Bulk	4.182	18.3	Bulk	4.182	25.2	Bulk	4.182	25.0

**Table 4.20** Fit parameters used for the dry PPyFMOC (red) film and the solvated films in D<sub>2</sub>O: PPyNH<sub>2</sub> (green) and PPyDylight (cyan).

The dry PPyFMOC film has a scattering length density of  $2.603 \times 10^{-6} \text{\AA}^{-2}$  corresponding to a polymer density of  $1.46 \text{ g cm}^{-3}$ . The PPyNH<sub>2</sub> film formed after elution of the FMOC protecting group had a solvated thickness of 320 Å in D<sub>2</sub>O ( $\phi_s = 0.48$ ). After the reaction with the fluorophore, this had swollen to 349 Å (an increase of 29 Å). This increase in thickness was accompanied by a uniform decrease of the  $N_b$  of the polymer layer. Calculation showed that this was due to the inclusion of one Cy3 fluorophore to every 2.33 monomer units ( $\phi_{\text{PPyCy3}} = 0.3$ ) and the expulsion of solvent ( $\phi_s = 0.36$ ). This is significantly more fluorophore incorporation than for the larger Dylight 649, as predicted.

**Figure 4.48** shows *ex situ* AFM images of the polymer films shown in **Figures 4.45-47**.

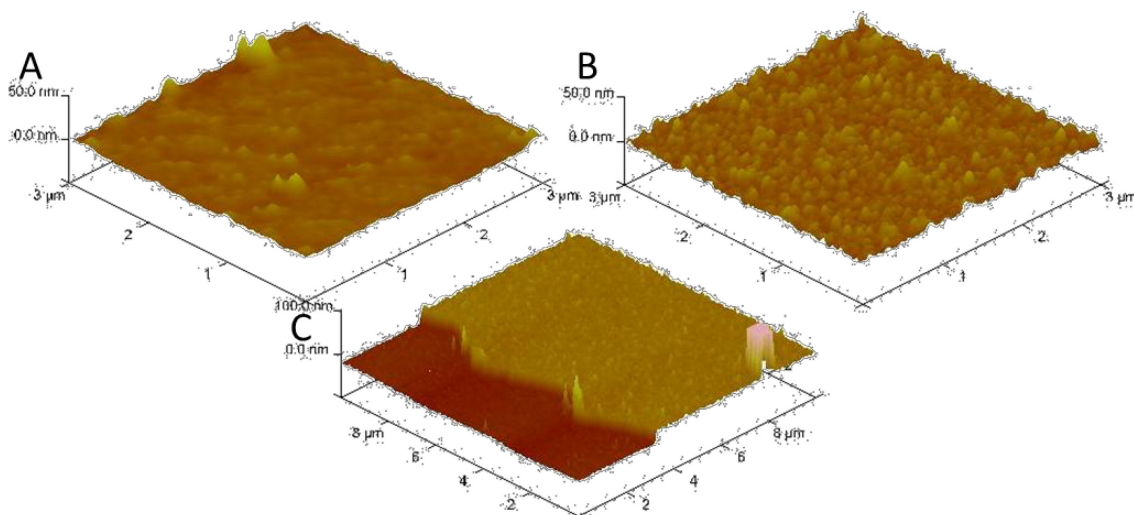


**Figure 4.48** *Ex situ* AFM images of (A) PPyFMOC before NR experiment, (B) PPyCy3 after NR experiment and (C) step height of PPyCy3 after NR experiment.

The question now is whether the corresponding electropolymerised PPyNH<sub>2</sub> film will fare any better with a smaller molecule to incorporate. **Figures 4.49** and **4.50** show the reflectivity and SLD profiles of the PPyNH<sub>2</sub> film.

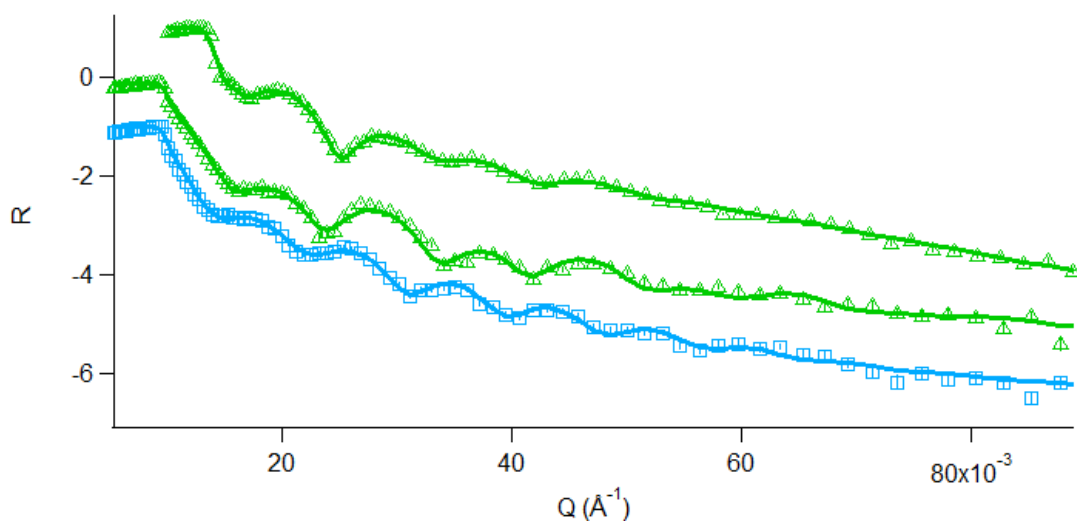


**Figure 4.49** NR data for the PPyNH<sub>2</sub> film resulting from hydrolysis in air and D<sub>2</sub>O ( $\Delta$ ) and the PPyCy3 film following exposure to the fluorophore in D<sub>2</sub>O ( $\square$ ). For visual comparison purposes,  $R(Q)$  profiles are progressively offset in reflectivity ( $\chi^2 = 1.3-2.1$ ).

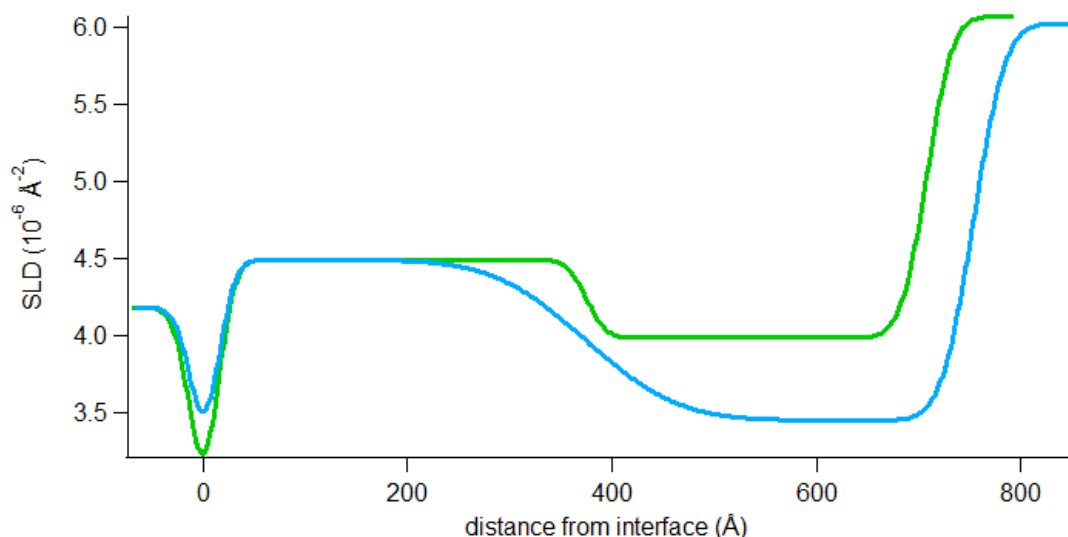


**Figure 4.50** SLD profiles for the solvated films in  $D_2O$ : the PPYNH<sub>2</sub> film electropolymerised directly (green) and the PPYCy3 film following exposure to the fluorophore in  $D_2O$  (cyan).

The fit parameters used in **Figure 4.49** are summarised in **Table 4.21**.

	$d$ (Å)	$N_b$ ( $\text{Å}^{-2} \times 10^{-6}$ )	$\sigma$ (Å)	$d$ / Å	$10^6 N_b / \text{Å}^{-2}$	$\sigma$ / Å	$d$ / Å	$10^6 N_b / \text{Å}^{-2}$	$\sigma$ / Å
<b>Media</b>	Bulk	0	N/A	Bulk	6.073	N/A	Bulk	6.027	N/A
<b>PPyX</b>	294.1	2.792	35.8	332.5	3.984	20.0	378.5	3.447	24.6
<b>Au</b>	354.3	4.490	43.1	368.9	4.490	15.0	368.6	4.490	71.3
<b>MPTS</b>	37.3	0.266	23.1	10.4	0.266	15.0	7.7	0.266	15.0
<b>Quartz</b>	Bulk	4.182	15.3	Bulk	4.182	15.0	Bulk	4.182	15.0

**Table 4.21** Fit parameters used for the dry PPYNH<sub>2</sub> (olive green) film and the solvated films in  $D_2O$ : PPYNH<sub>2</sub> (green) and PPYDylight (cyan).

The dry PPYNH<sub>2</sub> (as deposited) has a polymer density of  $2.03 \text{ g cm}^{-3}$ . Its dry thickness was 294 Å, this increases by 39 Å to 333 Å when solvated in  $D_2O$  ( $\phi_{\text{solvent}} = 0.30$ ). A further swelling of

46 Å was seen upon reaction with the Cy3 fluorophore. This increase in thickness is more than that seen in the corresponding FMOc PPyNH<sub>2</sub> film shown in **Figure 4.47**. Again, the change in N<sub>b</sub> observed in the polymer layer was uniform suggesting that, unlike with the bulkier Dylight 649, the Cy3 fluorophore molecules had managed to penetrate the full depth of the film. However, calculations showed that there was only one fluorophore molecule to every five monomer units ( $\phi_{\text{solvent}} = 0.18$ ); significantly less than the 1:2.33 observed with the solvent “voids”.

**Figure 4.51** shows *ex situ* AFM images of the polymer films shown in **Figures 4.49-50**.

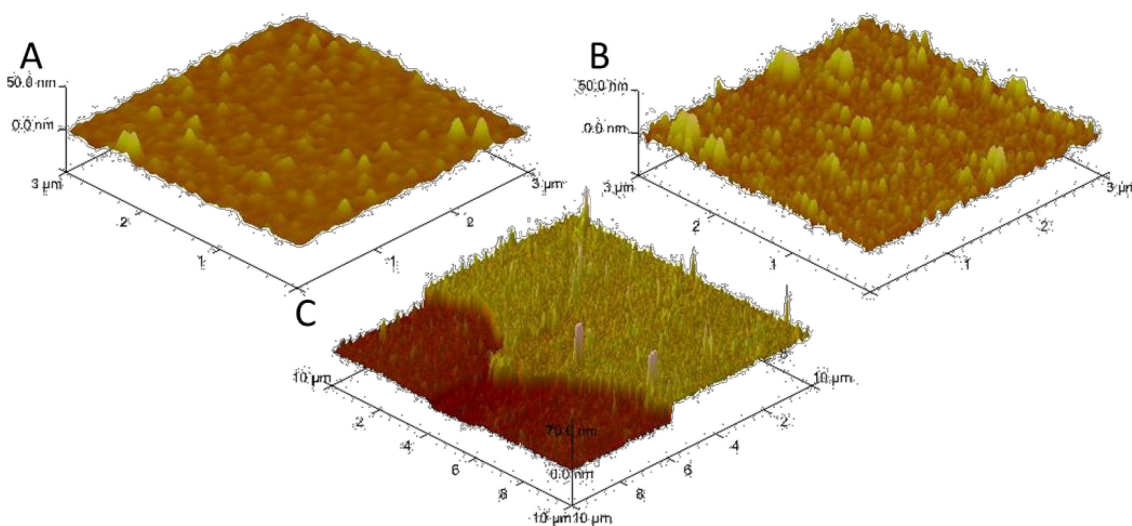


**Figure 4.51** *Ex situ* AFM images of (A) PPyNH<sub>2</sub> before NR experiment, (B) PPyCy3 after NR experiment and (C) step height of PPyCy3 after NR experiment.

#### 4.4. Conclusions and Future Work

The aim of this work has been to understand the spatial parameters involved in immobilizing a fluorophore within a conducting polymer matrix. A combination of electrochemical, spectroscopic and neutron-based techniques have been used to provide insight into the deposition and subsequent chemical functionalization of conducting polymer films for use in the joint fluorescent-electrochromic enhancement of latent fingerprints.

Electrochemistry allows manipulation and coulometric analysis of the surface population of the polymer matrix where the chemical modifications occur. Fluorescence measurements and FTIR spectroscopy was used to qualitatively demonstrate the post-deposition chemical modification of the polymer films throughout the functionalization process by both the presence of fluorescence in the final stage and through the disappearance and reappearance of the amide band.

Neutron reflectivity was used to accurately determine film composition, thickness and solvent content at each stage. The solvent volume fractions were 0.37 ( $\pm 0.03$ ) for the PPyFmoc films, 0.59 ( $\pm 0.01$ ) immediately after hydrolysis and 0.47 ( $\pm 0.04$ ) after relaxation (where these data originate from both kinetic and non-kinetic experiments). After fluorophore entry, the film contracts slightly. It has been shown that the additional step to create free volume within the polymer matrix through the elution of the bulky amine protecting group (Fmoc) is beneficial as it results in the incorporation of more fluorophore. Eventually this will lead to greater contrast between the masked regions of the fingerprint and the fluorescent polymer. Significantly, the diffusion of fluorophore into the polymer film was shown to vary with the size of the molecule to be incorporated. The volume fractions of the smaller Cy3 NHS ester in PPyNH<sub>2</sub> films as deposited and made through the Fmoc hydrolysis pathway were 0.17 and 0.30, respectively. These were significantly lower for the larger Dylight 649 NHS ester (0.04 and 0.18, respectively). In the latter case, the PPyNH<sub>2</sub> film with no voids only had an outer layer containing the Dylight 649 fluorophore as it proved too sterically bulky to penetrate any further.

Future work should focus on determination of the polymers electrochromic properties at the different stages of the reaction and the properties of the immobilized fluorophore. One of the major technical issues that still needs addressing is whether the proximity of the immobilized

fluorophore molecules to the working electrode will result in any fluorescence significant quenching.

This preliminary study does not attempt to address the lateral issue of imaging a full fingerprint, but focuses solely on the viability of the joint polymer-fluorophore system by understanding the reactivity and composition in the vertical direction at distance scales from 10–100 nm. The potential for a combined absorption/fluorescence strategy in latent fingerprint enhancement is clear with the next step being the application of this strategy to a fingerprinted surface.

## 4.5. References

- <sup>1</sup>Hillman, A. R. and Beresford, A. L., *Anal. Chem.*, 2010, **82**, 483.
- <sup>2</sup>Brown, R.M. and Hillman, A.R., *Phys. Chem. Chem. Phys.*, 2012, **14**, 8653.
- <sup>3</sup>Sapstead (nee Brown), R. M., Ryder, K. S., Fullarton, C., Skoda, M., Dalglish, R. M., Watkins, E. B., Beebee, C., Barker, R., Glidle, A., and Hillman, A. R., *Faraday Discussions*, 2013, **164**, 319.
- <sup>4</sup>Penfold, J., and Thomas, R. K., *J. Phys.: Condens. Matter*, 1990, **2**, 1369-1412.
- <sup>5</sup>Russell, T. P., *Physica B*, 1996, **221**, 267-283.
- <sup>6</sup>Penfold, J., *Current Opinion in Colloid & Interface Science*, 2002, **7**, 139-147.
- <sup>7</sup>Torikai, N., Yamada, N. L., Noro, A., Harada, M., Kawaguchi, D., Takano, A., and Matsushita, Y., *Polymer Journal*, 2007, **39 (12)**, 1238–1246.
- <sup>8</sup>Campbell, R. A., Wacklin, H. P., Sutton, I., Cubitt, R. and Fragneto, G., *Eur. Phys. J. Plus*, 2011, **126**, 107.
- <sup>9</sup>Webster, J. R. P., Langridge, S., Dalglish, R. M. and Charlton, T. R., *Eur. Phys. J. Plus*, 2011, **126**, 112.
- <sup>10</sup>Cho, S. H., Song, K. T. and Lee, J. Y., in Skotheim, T. A. and Reynolds, J. R. (eds.) (2007), *“Handbook of Conducting Polymers (3<sup>rd</sup> edn.)”*, CRC Press, Boca Raton, Ch. 8, p. 8-3.
- <sup>11</sup>Efimov, I. and Hillman, A. R., *Anal. Chem.*, 2006, **78**, 3616.
- <sup>12</sup>Glidle, A., Hillman, A. R., Ryder, K. S., Smith, E. L., Cooper, J. M., Gadegaard, N., Webster, J. R. P., Dalglish, R. M. and Cubitt, R., *Langmuir*, 2009, **25**, 4093.

<sup>13</sup>Glidle, A., Hillman, A. R., Ryder, K. S., Smith, E. L., Cooper, J. M., Dalgliesh, R. M,

Cubitt, R. and Geue, T., *Electrochim. Acta*, 2009, **55**, 439.

<sup>14</sup>Hillman, A. R., Mohamoud, M. A. and Efimov, I., *Anal. Chem.*, 2011, **83**, 5696.

# 5. Probing the Segregation and Solvation of Multi-Component Conducting Polymer Films

---

## 5.1. Introduction

The tuning of electrochromic properties of a polymer material has been explored through random<sup>1</sup>, or block co-polymerisation of two discrete monomer units (**Chapter 3**). The two other ways in which this can be achieved are through homopolymerisation of a hybrid co-monomer (see **Chapter 6**) and secondly, by deposition of the individual homopolymers in multi-layered structures<sup>2-5</sup>. These three approaches offer varying levels of control over the final composition of the resultant polymer film and all result in the optical properties being either intermediate to those of the homopolymers, or displaying separate new properties<sup>6-9</sup>.

The advantage of layering the individual homopolymers to create a composite is that each stage of deposition involves only control of a pure phase, which is often already well established. The nature of the polymer/polymer interface is central to the rectifying (segregated) or capacitive (interdiffused) characteristics of the multi-layered films<sup>10,11</sup>, such that the spatial distribution of the different polymer components determines the optical and electronic properties of the films. These properties are important for the potential applications of these multi-component systems in energy storage. The operational goal is a polymeric material with rapid charge/discharge capability and the facility to take up charge across a wide voltage range.

*En route* to this final application, determination of film composition and structure must be achieved. In this chapter, the specific objectives are the determination of polymer component segregation vs. interpenetration and the determination of equal vs. differentiated solvation levels of the different polymer components. In addition it is important to understand dynamics of mobile species such as solvent or counterions across these interfacial boundaries and to quantify these properties as a function of the different oxidation states of the electrochromic material. Another key objective is to try and tune the physical properties of the polymer/polymer interfaces.

## 5.2. Experimental

### 5.2.1. Monomer Synthesis

#### 5.2.1.1. *Base Hydrolysis of PyCN to Form 3-(pyrrol-1-yl)propanoic Acid (PyCOOH)*

3-(pyrrol-1-yl)propionitrile (7.5 g, 62.5 mmol) was added to an aqueous solution of NaOH (10 g, 0.25 mol, 50 cm<sup>3</sup>) in a 250 cm<sup>3</sup> round bottom flask fitted with a condenser. The mixture was refluxed until no ammonia evolution was seen (*ca.* 7 hrs.). This was tested with moist indicator paper at the top of the condenser. Cold water (25 cm<sup>3</sup>) was run down the condenser and the mixture allowed to cool in an ice bath. H<sub>2</sub>SO<sub>4</sub> (50 %, 15 cm<sup>3</sup>, 0.28 mol) was added causing the mixture to separate. The product (upper oily phase) was extracted with diethyl ether (4 x 30 ml) and dried with anhydrous Na<sub>2</sub>SO<sub>4</sub> overnight. Ether was removed by rotary evaporation to yield a cream, waxy solid (8.392 g, 59.4 mmol, 96 %).

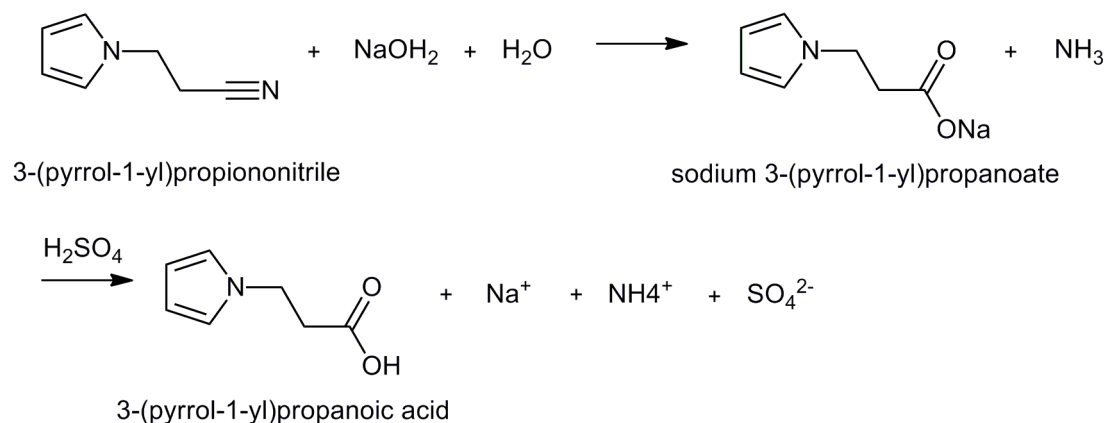


**Figure 5.1** Base hydrolysis of PyCN to form PyCOOH.

### 5.2.1.2. Coupling of Pentafluorophenol with PyCOOH to Yield Pentafluorophenyl 3-(pyrrol-1-yl)propanoate

A solution of dicyclohexylcarbodiimide (DCC) (9 g, 44 mmol) and pentafluorophenol (8 g, 44 mmol) in dry MeCN (80 cm<sup>3</sup>) was added to a stirred solution of 3-(pyrrol-1-yl)propanoic acid (6 g, 44 mmol) in dry MeCN (15 cm<sup>3</sup>). The mixture was stirred overnight. The white precipitate (dicyclohexylurea, 8.9 g, 39.7 mmol) was filtered off and the MeCN removed under vacuum to yield golden oil. This was taken up in hexane (250 cm<sup>3</sup>) and placed in a freezer (*ca.* 2hrs). Golden needles precipitated out which were filtered off and dried under vacuum (12.06 g, 39.5 mmol, 89 %).

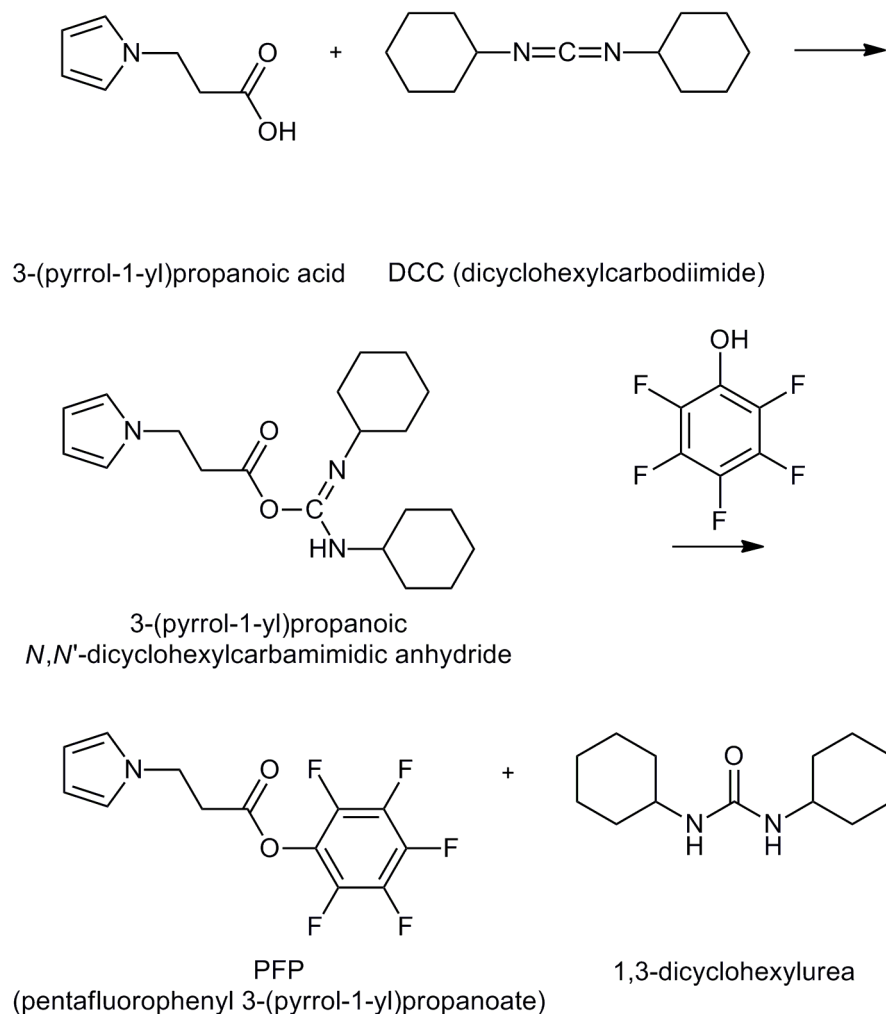


**Figure 5.2** Coupling of PyCOOH with pentafluorophenol to yield PFP.

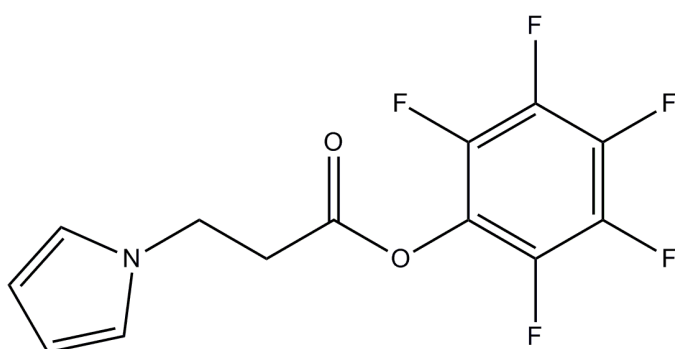
## 5.2.2. Electropolymerisation

### 5.2.2.1. PEDOT/PPFP Multilayers

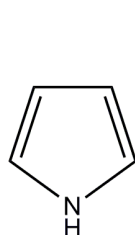
Multi-layered films were deposited potentiodynamically onto gold working electrodes ( $0.13 < E/V$  vs. Ag/AgCl (saturated KCl)  $<$  anodic limit  $I_{\max} = 1.8$  mA,  $v = 20$  mV s<sup>-1</sup>, 12 cycles) from tetrabutylammonium perchlorate/TBAP (0.1 M) in CH<sub>3</sub>CN containing the desired monomer (10 mM). After each layer was deposited the films were rinsed in CH<sub>3</sub>CN and allowed to dry before depositing the next layer. Two systems were deposited: Au/PEDOT/PPFP bilayer and Au/PEDOT/PPFP/PEDOT trilayer.

### 5.2.2.2. PEDOT/PPy Multilayers

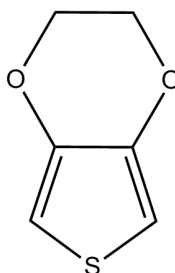
Bilayers of PPy and PEDOT were deposited potentiodynamically onto gold working electrodes ( $0.13 < E/V \text{ vs. Ag} < \text{anodic limit}$ ,  $I_{\text{max}} = 1.8 \text{ mA}$ ,  $v = 20 \text{ mV s}^{-1}$ , 12 cycles) from lithium perchlorate (0.1 M) in  $\text{CH}_3\text{CN}$  containing the desired monomer (10 mM). After each layer was deposited the films were rinsed in  $\text{CH}_3\text{CN}$  and allowed to dry before depositing the next layer. Two systems were investigated:  $\text{Au}/h_4\text{-PEDOT}/d_3\text{-PPy}$  and  $\text{Au}/d_2\text{-PPy}/h_4\text{-PEDOT}$ .



Pentafluorophenyl 3-(pyrrol-1-yl)propanoate



Pyrrole



3,4-Ethylenedioxythiophene

**Figure 5.3** Structures of the hydrogenous monomers used in the multilayer systems.

### 5.2.3. Neutron Reflectivity Measurements

Neutron reflectivity measurements were performed on FIGARO (Institut Laue-Langevin, Grenoble, France) and INTER (ISIS, Appleton Rutherford Laboratories, Harwell, UK). Measurements of the films were performed dry in air as well as  $\text{CH}_3\text{CN}/\text{CD}_3\text{CN}$ . Deuterated solvents were used to maximise contrast between the polymer and the electrolyte so that the solvation properties of the polymer could be more accurately determined. All of the multilayered systems described above were held in both their fully oxidised and fully reduced

states. Reflectivity was measured at incident angles of 0.624 and 3.78° (dry) and 0.624, 1.98 and 3.78° (in acetonitrile) giving a usable momentum transfer range of  $0.004 < Q/\text{\AA}^{-1} < 0.15$  before the reflectivity of the sample drops below the background level. The collimation slits were set to give a beam footprint on the sample of 60 mm x 30 mm and a momentum transfer ( $Q$ ) resolution of 3 %. Data acquisition times were 2-3 hrs. per run. Model fitting of the reflectivity profiles was performed using Motofit software<sup>12</sup>.

### 5.3. Results: PEDOT/PPFP Systems

#### 5.3.1. Electrodeposition

**Figure 5.4** shows representative final growth curves for each polymer layer in the PEDOT/PPFP bilayer system.

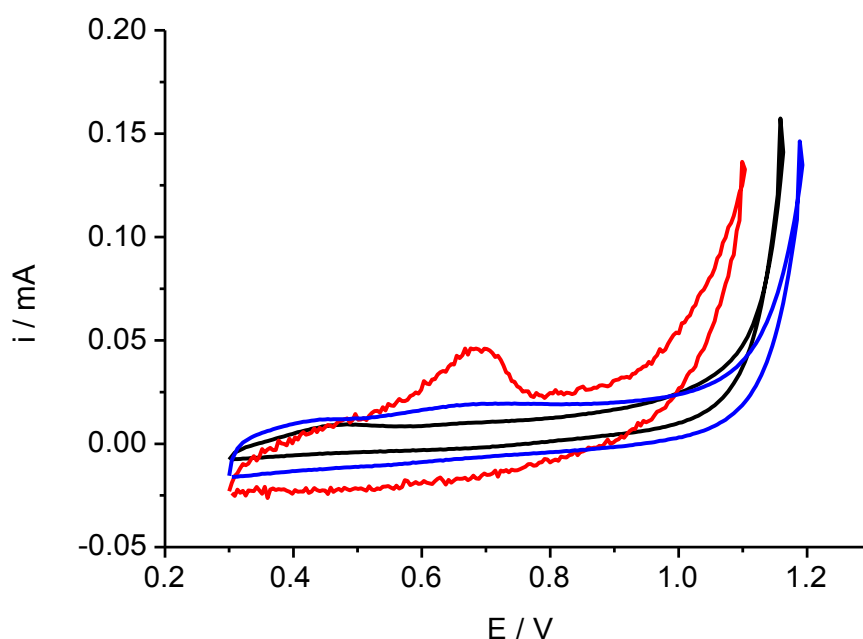


**Figure 5.4** Final growth curves for PEDOT on Au (black), PPFP on PEDOT/Au (blue) and PEDOT on PPFP/PEDOT/AU (red) [ $0.13 < E/V$  vs. Ag/AgCl (saturated KCl)  $<$  anodic limit  $I_{\text{max}} = 0.16$  mA,  $v = 20$  mV s<sup>-1</sup>, 12 cycles]. Note this deposition was done on a smaller gold working electrode than the neutron blocks (25 x 16 mm).

### 5.3.2. Au/PEDOT/PPFP Bilayer

#### 5.3.2.1. NR Measurements of the Dry Film

The dry  $R(Q)$  and SLD profiles of the bilayer system after deposition are shown in **Figure 5.5** and **Figure 5.6**.

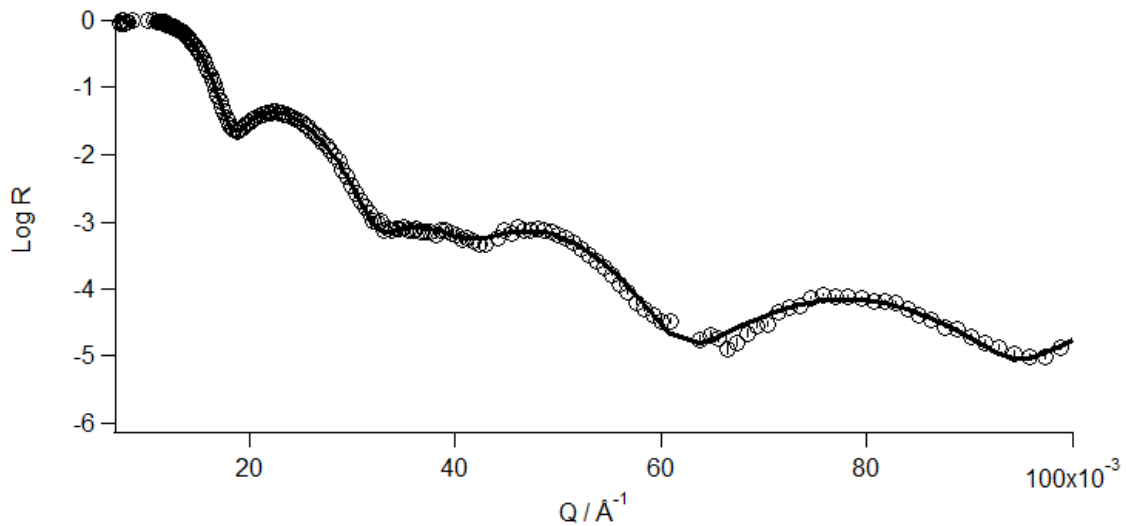


**Figure 5.5**  $R(Q)$  profile of the dry Au/PEDOT/PPFP bilayer system. O is the raw data and the black line is the fit of the data ( $\chi^2 = 1.7$ ).

As described in **Chapter 3**, at low  $Q$  total external reflection is observed ( $R = 1$ ), in the form of a critical edge, as a result of air having a lower scattering length density (SLD) than silicon. In this instance the critical edge is not well defined and appears to merge into the first fringe indicative of a rough polymer/air interface. The  $Q$  value corresponding to the critical edge,  $Q_c$ , is determined by the difference in the neutron SLDs of the two bulk materials,  $\Delta N_b$ .

$$\left( \frac{Q_c}{k} \right)^2 = \frac{\Delta N_b}{N_b}$$

**Equation 5.1**

If we take the value of the critical edge from **Figure 5.5** ( $Q_c = 0.0102$ ) and use **Equation 5.1**

then the difference in SLD is  $2.073 \text{ \AA}^{-2} \times 10^{-6}$  which is the  $N_b$  of the silicon block as the SLD of air is zero. Si blocks were used for this experiment as all quartz blocks were being used.

## Equation 5.2

As described in previous chapters, taking the value of  $\Delta Q$  for the final fringe in **Figure 5.5** ( $0.0319 \text{ \AA}^{-1}$ ) and using **Equation 5.2** allows the thickness of the Au to be calculated. This gives a value of  $197 \text{ \AA}$ , which is consistent with the objective thickness of  $200 \text{ \AA}$  in the sputtering process.

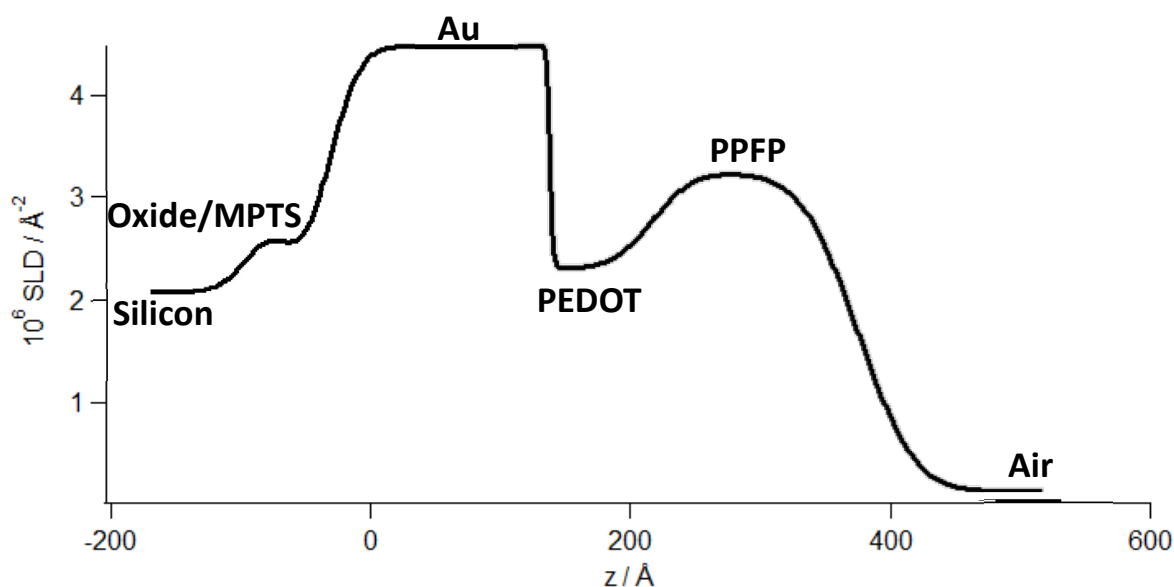


**Figure 5.6** SLD profile of the dry Au/PEDOT/PPFP bilayer film shown in **Figure 5.5**.

Layer	$d / \text{\AA}$	$10^6 N_b / \text{\AA}^{-2}$	$\sigma / \text{\AA}$
Air	Bulk	0	N/A
PPFP	160.1	3.187	34.7
PEDOT	80.0	2.215	24.3
Au	197.9	4.490	2.0
MPTS	19.5	0.266	21.1
Oxide Layer	18.4	4.182	20.3
Silicon	Bulk	2.073	21.5

**Table 5.1** Summary of the fit parameters used in **Figure 5.5**.

**Table 5.1** shows that there were two distinct layers: a thin inner layer of PEDOT and a thicker outer layer of PPF. The SLDs of these two layers were fitted at 2.215 and  $3.187 \times 10^{-6} \text{ \AA}^{-2}$ , respectively. These correspond to densities of 1.31 and  $1.53 \text{ g cm}^{-3}$ , which were used in the fitting process later on to determine solvation and doping values. The two layers were segregated but there was a roughness of 24.3 Å. As shown in **Figure 2.11**, this roughness value does not represent topographical roughness but the distance over which one scattering length density changes to another. In this instance, there is a distance of 24.3 Å over which pure PEDOT becomes pure PPF. This is a good indication of the amount of segregation/interpenetration of the two layers.

### ***5.3.2.2. Solvated Film NR Measurements Under Potential Control***

In order to assess how the amount of segregation/interpenetration changes, depending on oxidation/cycling of the multi-layered system, the bilayer system was measured at a series of potentials in both deuterated and hydrogenous acetonitrile/0.1 M TEAP electrolyte. The potentials chosen were -700, 0, and 700 mV. These represented fully reduced, resting and fully oxidised film states that were observed during redox cycling. The R(Q) profiles of the PEDOT/PPFP bilayer in these three oxidation states are given in **Figures 5.7-9**.

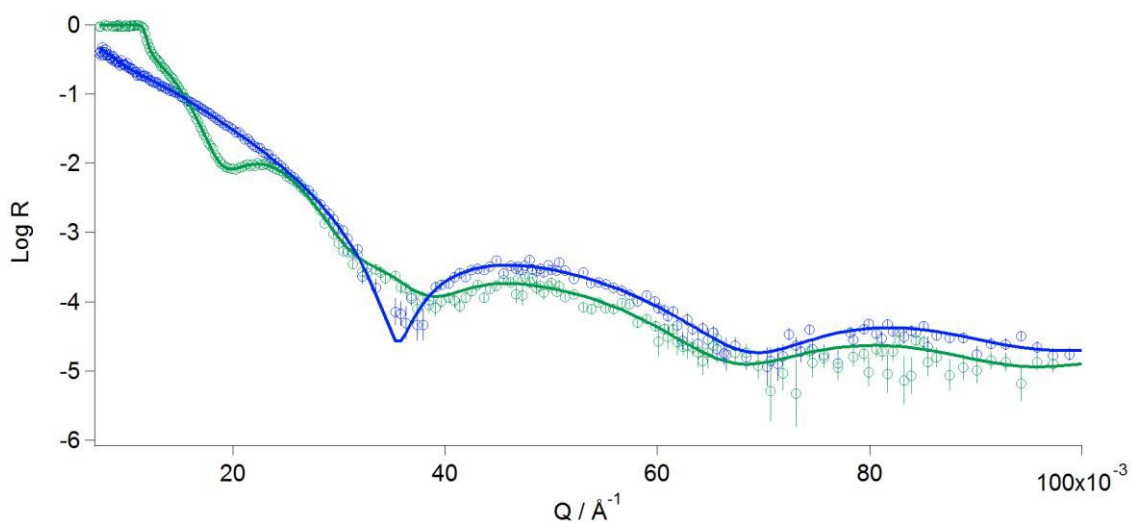


**Figure 5.7**  $R(Q)$  profile of the PEDOT/PPFP bilayer fully reduced at  $-700$  mV in  $\text{CH}_3\text{CN}$  (blue) and  $\text{CD}_3\text{CN}$  (green). Circles represent the raw data and the solid lines are the fits of the data ( $\chi^2 = 1.29$  and  $1.42$ ).

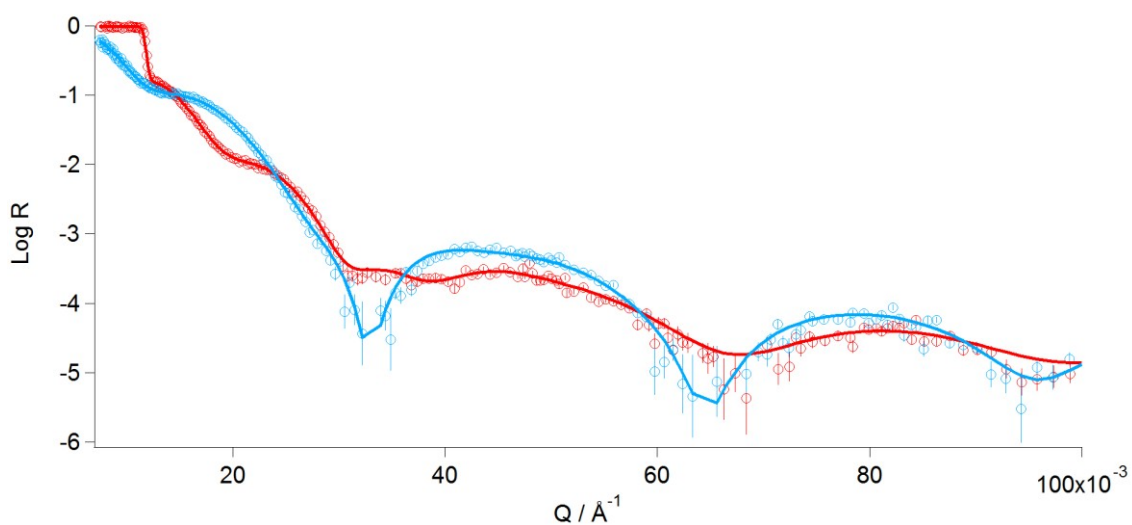


**Figure 5.8**  $R(Q)$  profile of the PEDOT/PPFP bilayer at  $0$  mV in  $\text{CH}_3\text{CN}$  (cyan) and  $\text{CD}_3\text{CN}$  (red). Circles represent the raw data and the solid lines are the fits of the data ( $\chi^2 = 1.55$  and  $1.61$ ).

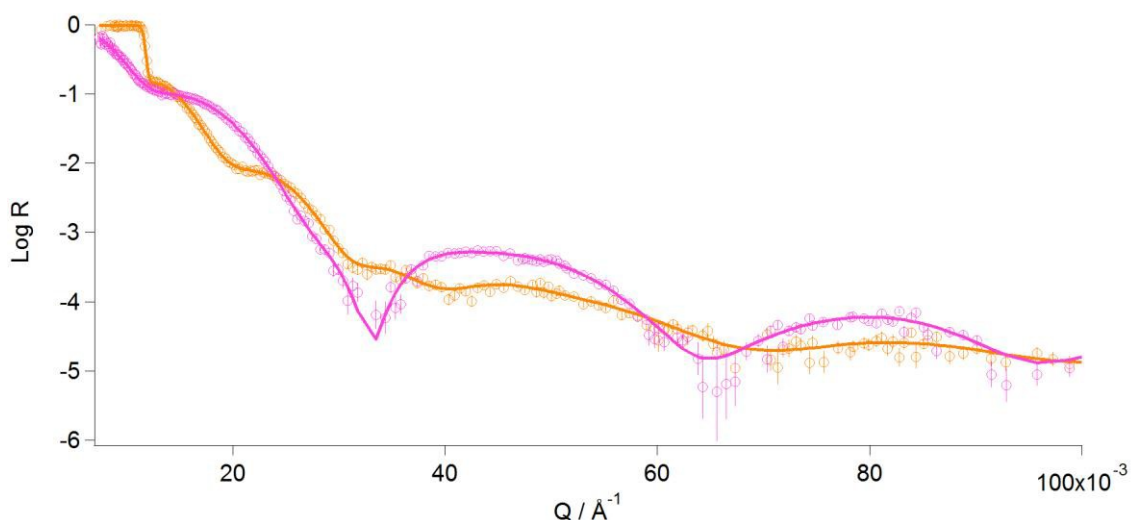


**Figure 5.9**  $R(Q)$  profile of the PEDOT/PPFP bilayer fully oxidised at 700 mV in  $\text{CH}_3\text{CN}$  (pink) and  $\text{CD}_3\text{CN}$  (orange). Circles represent the raw data and the solid lines are the fits of the data ( $\chi^2 = 1.34$  and  $1.17$ ).

SLD calculations for the PEDOT layer were performed in order to calculate the differences in solvation for each oxidation state and the doping level of  $\text{ClO}_4^-$  for the oxidised film. However, for the PPFP layer these calculations, for the pairs of measurements given above in **Figures 5.7-9**, were unsuccessful and the numbers were significantly different to one another for the  $\text{CH}_3\text{CN}$  and  $\text{CD}_3\text{CN}$  datasets. This suggested an additional change in the films during/between the different NR measurements. This was proved through SLD calculations and IR spectroscopy to be the hydrolysis of the poly-pentafluorophenyl 3-(pyrrol-1-yl)propanoate (PPFP) to yield poly-3-(pyrrol-1-yl)propanoic Acid (PPyCOOH). As a result of this, the data are now presented in chronological order in **Figure 5.10** rather in the analogous redox state pairs shown above.

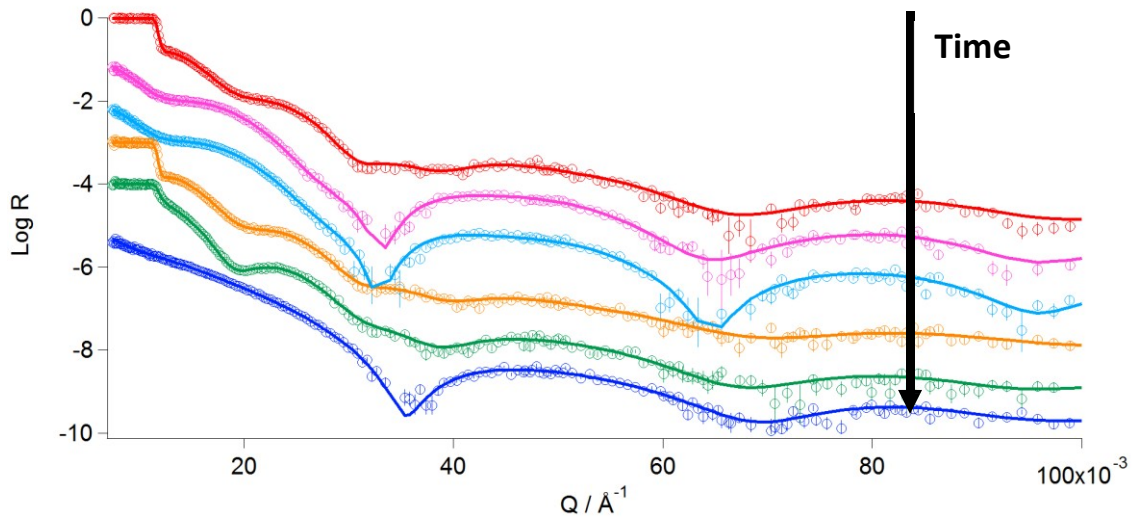


**Figure 5.10** R(Q) profiles of the PEDOT/PPFP bilayer offset in reflectivity in chronological order so that:

- Log R = 0: 0 mV in CD<sub>3</sub>CN/TEAP (red)
- Log R = -1: 700 mV in CH<sub>3</sub>CN/TEAP (pink)
- Log R = -2: 0 mV in CH<sub>3</sub>CN/TEAP (cyan)
- Log R = -3: 700 mV in CD<sub>3</sub>CN/TEAP (orange)
- Log R = -4: -700 mV in CD<sub>3</sub>CN/TEAP (green)
- Log R = -5: -700 mV in CH<sub>3</sub>CN/TEAP (blue)

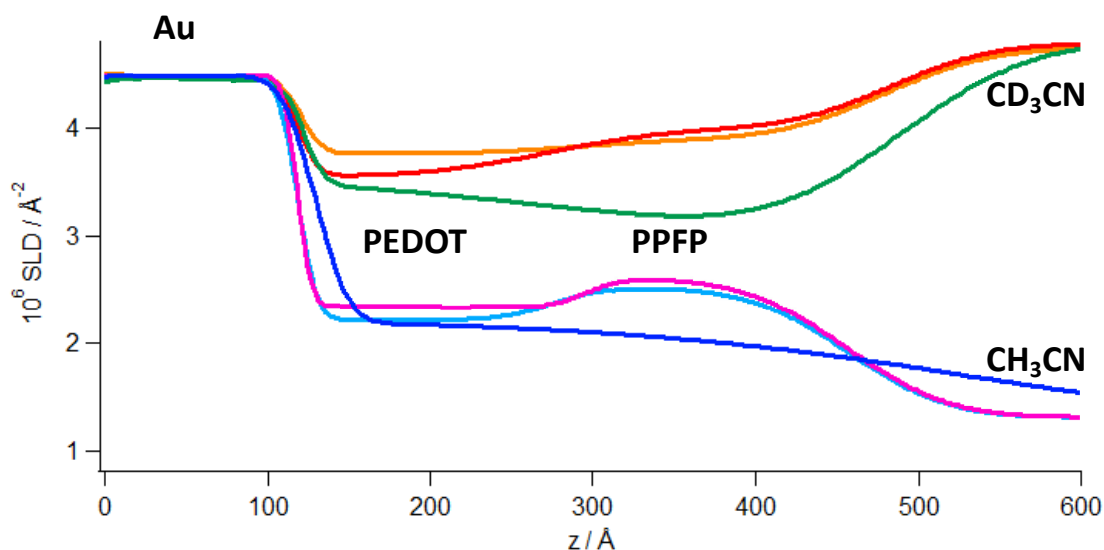


**Figure 5.11** Corresponding SLD profiles of the PEDOT/PPFP bilayer film shown in **Figure 5.10**: -700 mV in  $\text{CD}_3\text{CN}/\text{TEAP}$  (green) and  $\text{CH}_3\text{CN}/\text{TEAP}$  (blue); 0 mV in  $\text{CD}_3\text{CN}/\text{TEAP}$  (red) and  $\text{CH}_3\text{CN}/\text{TEAP}$  (cyan); 700 mV in  $\text{CD}_3\text{CN}/\text{TEAP}$  (orange) and 700 mV in  $\text{CH}_3\text{CN}/\text{TEAP}$  (pink).

Summaries of the fit parameters used are given in **Tables 5.2-5**.

Layer	$d / \text{Å}$	$10^6 N_b / \text{Å}^{-2}$	$\sigma / \text{Å}$
$\text{CH}_3\text{CN}/\text{CD}_3\text{CN}$	Bulk	1.320/4.773	N/A
PPFP	See <b>Table 5.3</b>		
PEDOT	See <b>Tables 5.4 and 5.5</b>		
Au	200.5( $\pm 7.6$ )	4.490	9.8( $\pm 4.1$ )
MPTS	26.4( $\pm 8.2$ )	0.266	16.5( $\pm 7.4$ )
Oxide	17.3( $\pm 7.0$ )	4.182	20.8( $\pm 8.8$ )
Silicon	Bulk	2.073	9.2( $\pm 7.6$ )

**Table 5.2** Average fit parameters used in **Figure 5.10** for the Au, MPTS, oxide and silicon layers.

Conditions	$d / \text{\AA}$	$10^6 N_b / \text{\AA}^{-2}$	$\sigma / \text{\AA}$	Solvent	Anion
				volume fraction / $\phi_s$	doping level
0 mV, CD <sub>3</sub> CN	157.2	3.549	59.3	0.49	0
700 mV, CH <sub>3</sub> CN	179.4	2.342	17.6	0.51	0.33
0 mV, CH <sub>3</sub> CN	156.7	2.224	26.4	0.49	0
700 mV, CD <sub>3</sub> CN	173.3	3.763	50.3	0.51	0.33
-700 mV, CD <sub>3</sub> CN	157.5	3.550	145.2	0.49	0
-700 mV, CH <sub>3</sub> CN	156.5	2.201	100.9	0.49	0

**Table 5.3** Fit parameters used in **Figure 5.10** for the inner PEDOT layer listed in chronological order.

**Table 5.3** shows that the thickness of the PEDOT layer increases when the film is oxidised (700 mV). This increase in thickness is accompanied by an increase in solvent volume fraction of 0.02 as well as the ingress of perchlorate anions to counteract the positive charge shared over every three monomer units of PEDOT. The roughness of the polymer/polymer interface increases ( $\sigma$  in **Table 5.3**) significantly with time meaning that the two polymer layers become more interdiffused over time which would allow more capacitive behaviour.

Conditions	$d / \text{\AA}$	$10^6 N_b / \text{\AA}^{-2}$	$\sigma / \text{\AA}$	Solvent	Anion
				volume fraction / $\phi_s$	doping level
0 mV, CD <sub>3</sub> CN	210.2	4.000	49.0	0.56	0
700 mV, CH <sub>3</sub> CN	158.9	2.610	49.1	0.47	0.33
0 mV, CH <sub>3</sub> CN	178.3	2.531	48.3	0.56	0
700 mV, CD <sub>3</sub> CN	186.5	3.904	50.8	0.47	0.33
-700 mV, CD <sub>3</sub> CN	209.4	2.984	64.4	0.30	0
-700 mV, CH <sub>3</sub> CN	209.0	2.082	132.3	0.30	0

**Table 5.4** Fit parameters used in **Figure 5.10** for the outer PPFPP/PPyCOOH layer listed in chronological order.

**Table 5.4** shows the changes in the PPFPP layer of the film over the course of the neutron experiment. However, the interpretation of any trends in thickness/roughness is hindered as it is unclear whether these effects are due to film aging/relaxing over time, redox state or the added factor of the PPFPP hydrolysing to give PPyCOOH during the course of the experiment (see **Table 5.5**).

Conditions	Volume fraction of PPyCOOH / $\phi_{\text{PPyCOOH}}$
0 mV, CD <sub>3</sub> CN	0.00
700 mV, CH <sub>3</sub> CN	0.62
0 mV, CH <sub>3</sub> CN	0.75
700 mV, CD <sub>3</sub> CN	1.00
-700 mV, CD <sub>3</sub> CN	1.00
-700 mV, CH <sub>3</sub> CN	1.00

**Table 5.5** Fit parameters used in **Figure 5.10** for the outer PPF/PPyCOOH layer showing the amount of hydrolysis of PPF to PPyCOOH.

The hydrolysis was confirmed by measuring the bilayer dry after the solvated NR experiments and comparing the  $R(Q)$  (**Figure 5.12**) and SLD (**Figure 5.13**) profiles to those seen in **Figures 5.5** and **5.6**.

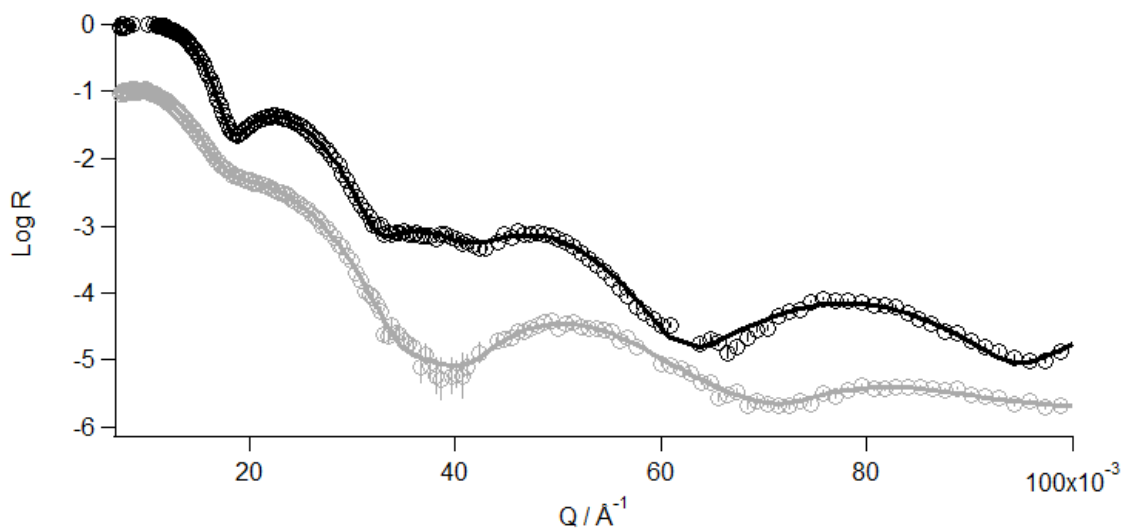


**Figure 5.12**  $R(Q)$  profile of the dry Au/PEDOT/PPFP bilayer system before the solvated NR experiments (black, **Figure 5.6**) and of the dry Au/PEDOT/PPyCOOH bilayer system after the solvated NR experiments (grey). O is the raw data and the line is the fit of the data ( $\chi^2 = 1.7$  and 1.2, respectively).

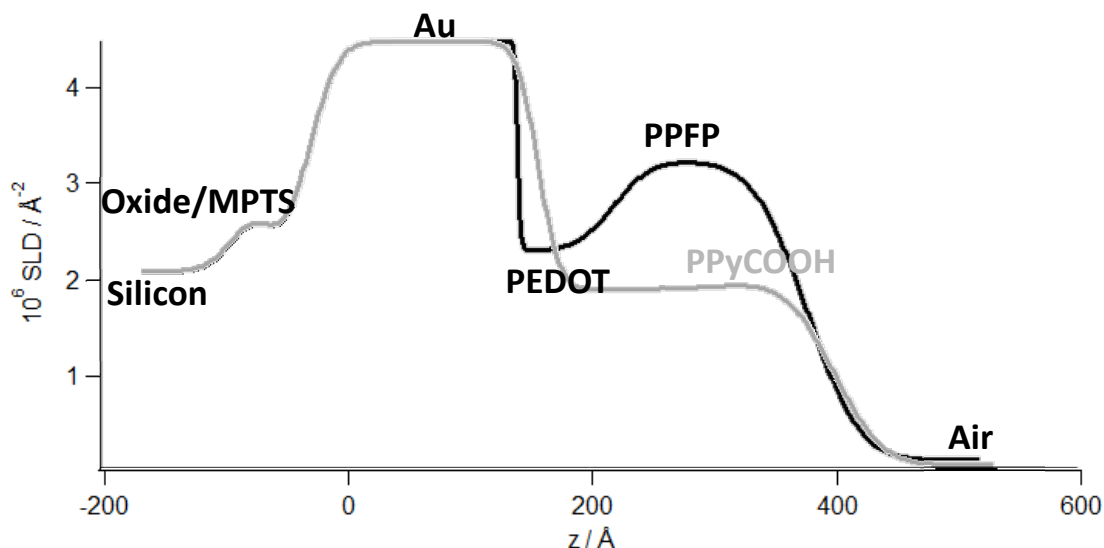


**Figure 5.13** SLD profiles of the dry Au/PEDOT/PPFP bilayer system before the solvated NR experiments (black) and of the dry Au/PEDOT/PPyCOOH bilayer system after the solvated NR experiments (grey) shown in **Figure 5.12**.

Layer	$d / \text{Å}$	$10^6 N_b / \text{Å}^{-2}$	$\sigma / \text{Å}$
Air	Bulk	0	N/A
PPyCOOH	143.2	1.924	46.4
PEDOT	112.3	2.068	20.3
Au	197.9	4.490	2.0
MPTS	19.5	0.266	21.1
Oxide Layer	18.4	4.182	20.3
Silicon	Bulk	2.073	21.5

**Table 5.6** Summary of the fit parameters used for the dry Au/PEDOT/PPyCOOH in **Figure 5.12**.

The PEDOT/PPFP bilayer showed interesting properties in terms of bilayer segregation, with two distinct polymer layers showing a relatively large degree of interpenetration at the polymer/polymer interface (**Table 5.3**). This was shown as a high roughness factor at the interface. This inter-diffusion of the two polymer layers would aid the movement of counterions throughout the film during REDOX. The PPFP was also hydrolysing so a trilayer

was also analysed with a layer of PPFPP “sandwiched” between two layers of PEDOT to see how this would affect the rate of hydrolysis.

After the neutron experiment the step heights of the polymer layer and the gold were determined using an AFM (**Figure 5.14**). This showed the gold thickness to be 206 Å and the combined polymer layers to be 240 Å. This is consistent with the final NR measurement of the dry film (see **Table 5.6**).

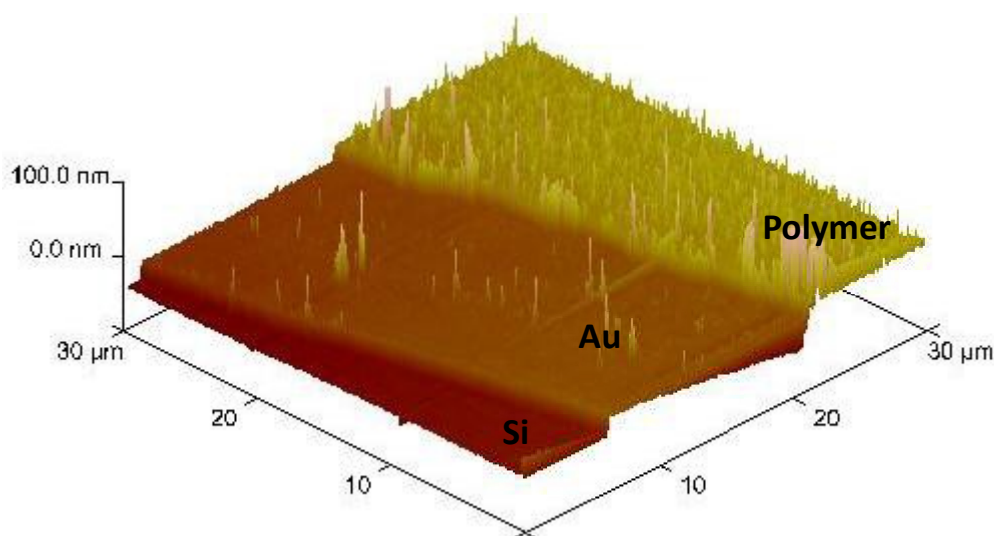


**Figure 5.14** AFM image of Au and the PEDOT/PPyCOOH bilayer on Silicon shown in **Figures 5.5-5.13**.

### 5.3.3. Au/PEDOT/PPFP/PEDOT Trilayer

#### 5.3.3.1. NR Measurements of the Dry Film

A try layer system was also analysed to assess how a third layer would affect the rate of hydrolysis as well as assessing interfacial properties in systems with multiple polymer/polymer interfaces. The dry  $R(Q)$  and SLD profiles of the trilayer system after deposition are shown in **Figures 5.15** and **5.16**.

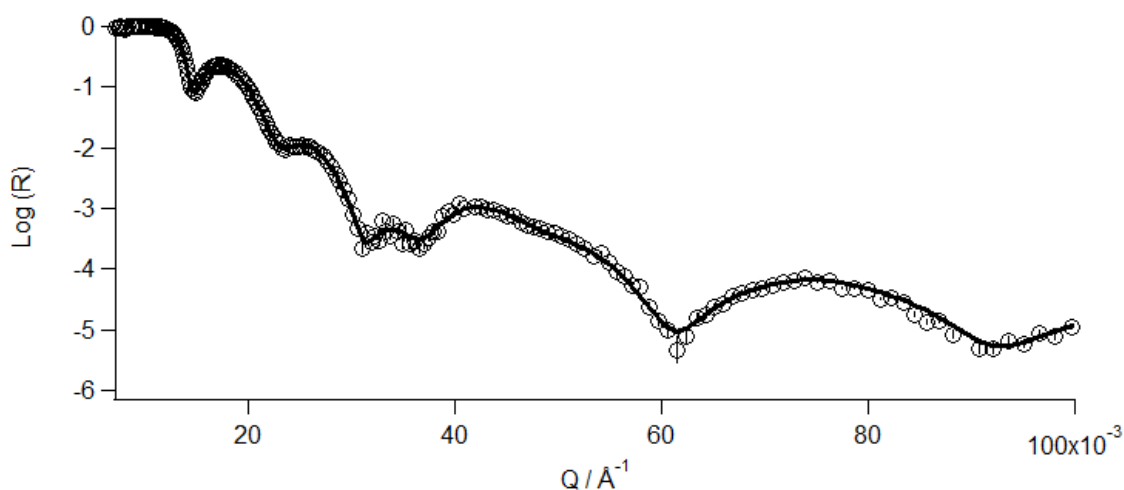


**Figure 5.15** R(Q) profile of the dry Au/PEDOT/PPFP/PEDOT trilayer system. Circles are the raw data and the line is the fit of the data ( $\chi^2 = 1.8$ ).

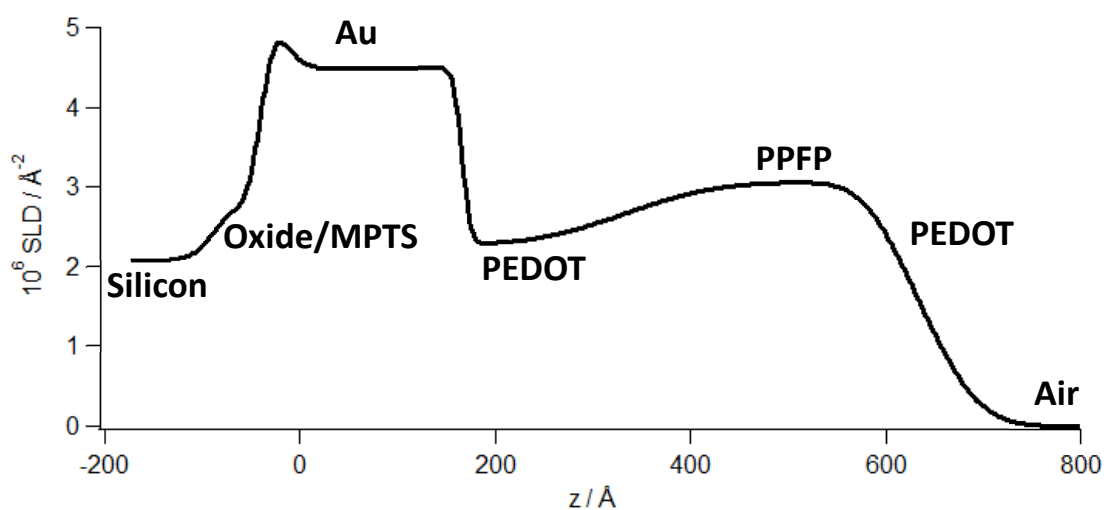


**Figure 5.16** SLD profile of the dry Au/PEDOT/PPFP/PEDOT trilayer shown in **Figure 5.15**.

The hump at the MPTS/Au interface is an effect of the combined roughness of the oxide and MPTS layers. Using the  $\Delta Q$  ( $0.0307 \text{ \AA}^{-1}$ ) of the final fringe in **Equation 5.2** to approximate the thickness of the Au gives a value of  $205 \text{ \AA}$ .

Layer	$d / \text{\AA}$	$10^6 N_b / \text{\AA}^{-2}$	$\sigma / \text{\AA}$
Air	Bulk	0	N/A
PEDOT	206.5	2.711	44.4
PPFP	261.3	3.064	22.7
PEDOT	45.6	2.303	68.9
Au	206.4	4.490	5.5
MPTS	3.3	0.266	12.9
Oxide Layer	25.3	4.182	22.2
Silicon	Bulk	2.073	2.0

**Table 5.7** Fit parameters used for the dry Au/PEDOT/PPFP/PEDOT trilayer shown in **Figure 5.15**.

**Table 5.7** shows that once again each polymer has a distinct layer. The outer layer of PEDOT was significantly thinner than the inner two polymer layers of PEDOT and PPFP. This was attributed to more of the oxidation current applied being used to oxidise the inner layers already present on the electrode and the resistivity created by their presence. The SLDs of the two PEDOT layers were 2.711 and 2.303  $\times 10^{-6} \text{\AA}^{-2}$ . These correspond to densities of 1.60 and 1.36  $\text{g cm}^{-3}$ , respectively. The SLD of the PPFP layer was 3.064  $\times 10^{-6} \text{\AA}^{-2}$ , which gives a density of 1.47  $\text{g cm}^{-3}$ .

### 5.3.3.1. Solvated Film NR Measurements Under Potential Control

As with the bilayer in **Section 5.3**, the trilayer was measured at a series of potentials in both deuterated and hydrogenous acetonitrile/0.1 M TEAP electrolyte to assess any changes in the amount of segregation/interpenetration. An additional NR measurement, at an intermediate potential, was performed for the more complex trilayer system: -700, 0, 400 and 700 mV representing fully reduced, resting and partially and fully oxidised film states. Once again the R(Q) profiles were analysed in chronological order to assess the amount of hydrolysis in the PPFP (**Figure 5.17**).

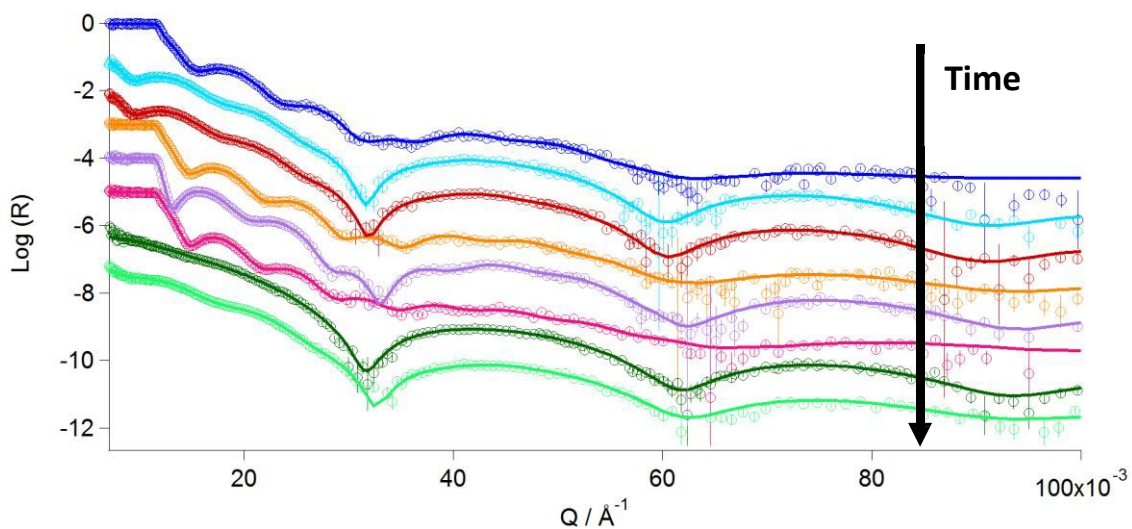


**Figure 5.17** R(Q) profiles of the PEDOT/PPFP/PEDOT trilayer offset in reflectivity in chronological order so that:

- Log R = 0: 0 mV in CD<sub>3</sub>CN/TEAP ( $\chi^2 = 1.9$ , blue)
- Log R = -1: 0 mV in CH<sub>3</sub>CN/TEAP ( $\chi^2 = 1.2$ , cyan)
- Log R = -2: 400 mV in CH<sub>3</sub>CN/TEAP ( $\chi^2 = 1.3$ , red)
- Log R = -3: 400 mV in CD<sub>3</sub>CN/TEAP ( $\chi^2 = 1.6$ , orange)
- Log R = -4: -700 mV in CD<sub>3</sub>CN/TEAP ( $\chi^2 = 1.5$ , purple)
- Log R = -5: 700 mV in CD<sub>3</sub>CN/TEAP ( $\chi^2 = 1.7$ , pink)
- Log R = -6: -700 mV in CH<sub>3</sub>CN/TEAP ( $\chi^2 = 2.6$ , dark green)
- Log R = -7: 700 mV in CH<sub>3</sub>CN/TEAP ( $\chi^2 = 1.8$ , green)

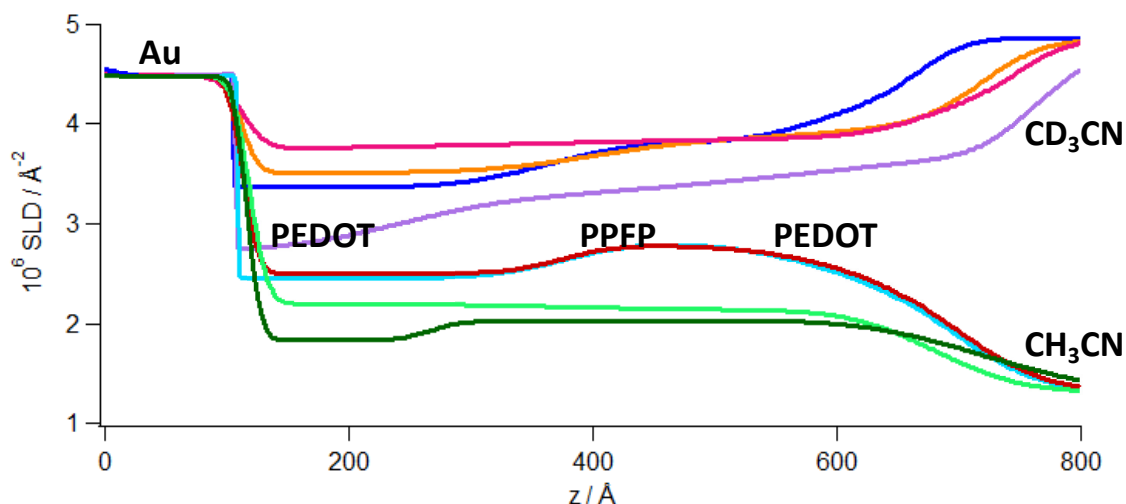


**Figure 5.18** Corresponding SLD profiles of the Au/PEDOT/PPFP/PEDOT trilayer film shown in **Figure 5.17**: -700 mV in CD<sub>3</sub>CN/TEAP (dark green) and CH<sub>3</sub>CN/TEAP (purple); 0 mV in CD<sub>3</sub>CN/TEAP (blue) and CH<sub>3</sub>CN/TEAP (cyan); 400 mV in CD<sub>3</sub>CN/TEAP (orange) and 700 mV in CH<sub>3</sub>CN/TEAP (red); and 700 mV in CD<sub>3</sub>CN/TEAP (pink) and 700 mV in CH<sub>3</sub>CN/TEAP (green).

Layer	d / Å	10 <sup>6</sup> N <sub>b</sub> / Å <sup>-2</sup>	σ / Å
CH <sub>3</sub> CN/CD <sub>3</sub> CN	Bulk	1.320/4.773	N/A
PEDOT		See <b>Table 5.12</b>	
PPFP		See <b>Tables 5.10-11</b>	
PEDOT		See <b>Table 5.9</b>	
Au	207.5(±8.0)	4.490	8.9(±4.9)
MPTS	10.5(±5.2)	0.266	9.1(±6.2)
Oxide	13.1(±9.0)	4.182	15.5(±11.6)
Silicon	Bulk	2.073	11.6(±9.5)

**Table 5.8** Average fit parameters used in **Figure 5.17** for the Au, MPTS, oxide and silicon layers.

Conditions	$d / \text{\AA}$	$10^6 N_b / \text{\AA}^{-2}$	$\sigma / \text{\AA}$	Solvent volume fraction / $\phi_s$	Anion level	Cation level
0 mV, CD <sub>3</sub> CN	262.2	3.300	60.2	0.34	0	0
0 mV, CH <sub>3</sub> CN	268.6	2.460	47.6	0.34	0	0
400 mV, CH <sub>3</sub> CN	261.6	2.511	35.4	0.34	0.25	0
400 mV, CD <sub>3</sub> CN	292.2	3.513	73.1	0.34	0.25	0
-700 mV, CD <sub>3</sub> CN	166.1	2.689	70.9	0.43	0.16	0.16
700 mV, CD <sub>3</sub> CN	353.3	3.744	92.2	0.37	0.25	0
-700 mV, CH <sub>3</sub> CN	150.4	1.833	32.1	0.43	0.09	0.09
700 mV, CH <sub>3</sub> CN	265.5	2.198	74.4	0.37	0.25	0

**Table 5.9** Fit parameters used in **Figure 5.17** for the inner PEDOT layer in chronological order.

**Table 5.9** shows that the thickness of the PEDOT layer increases when the film is oxidised (400 and 700 mV). This increase can best be seen in the deuterated contrast. As with the bilayer system this swelling is accompanied by a slight increase in solvent volume fraction of 0.03 as well as the ingress of perchlorate anions to counteract the positive charge shared over every four monomer units of PEDOT, in this case suggesting less redox activity than in the bilayer. This could be attributed to the thicker multilayer system as a whole or the other two outer layers hindering the mobility of the counter ion(s). This conclusion is supported further by the fact that after the initial oxidation the anion seems to be trapped and cation is incorporated into the film to balance the negative charge of the anions. The roughness of the polymer/polymer interface is high suggesting a degree of interpenetration of the PFP layer with the PEDOT.

Conditions	$d / \text{\AA}$	$10^6 N_b / \text{\AA}^{-2}$	$\sigma / \text{\AA}$	Solvent volume fraction / $\phi_s$	Anion level
0 mV, CD <sub>3</sub> CN	215.4	3.811	42.2	0.42	0
0 mV, CH <sub>3</sub> CN	242.4	2.820	80.1	0.42	0
400 mV, CH <sub>3</sub> CN	262.5	2.792	78.1	0.42	0.25
400 mV, CD <sub>3</sub> CN	236.3	3.873	71.3	0.42	0.25
-700 mV, CD <sub>3</sub> CN	285.2	2.954	215.4	0.29	0
700 mV, CD <sub>3</sub> CN	223.2	3.878	46.5	0.46	0.25
-700 mV, CH <sub>3</sub> CN	252.1	2.021	107.8	0.29	0
700 mV, CH <sub>3</sub> CN	215.3	2.000	200.1	0.46	0.25

**Table 5.10** Fit parameters used in **Figure 5.17** for the middle PFP/PPyCOOH layer in chronological order.

**Table 5.10** shows the changes in the PFP layer of the film over the course of the neutron experiment. As with the bilayer system the PFP is hydrolysing to give PPyCOOH over the course of the experiment. The amount of hydrolysed PFP in each measurement is shown in **Table 5.11**.

Conditions	Volume Fraction of PPyCOOH / $\phi_{\text{PPyCOOH}}$
0 mV, CD <sub>3</sub> CN	0
0 mV, CH <sub>3</sub> CN	0.48
400 mV, CH <sub>3</sub> CN	0.48
400 mV, CD <sub>3</sub> CN	0.48
-700 mV, CD <sub>3</sub> CN	1.00
700 mV, CD <sub>3</sub> CN	1.00
-700 mV, CH <sub>3</sub> CN	1.00
700 mV, CH <sub>3</sub> CN	1.00

**Table 5.11** Fit parameters used in **Figure 5.17** for the middle PFP/PPyCOOH layer showing the amount of hydrolysis of PFP to PPyCOOH in chronological order.

The properties of the outer PEDOT layer are given in **Table 5.12**. Interestingly, in both the measurements at 400 mV the outer PEDOT layer contained 0.24 volume fraction of hydrolysed pentafluorophenol that was “seeping out” from the PFP/PPyCOOH layer underneath.

Conditions	$d / \text{\AA}$	$10^6 N_b / \text{\AA}^{-2}$	$\sigma / \text{\AA}$	Solvent volume fraction / $\phi_s$	Anion level
0 mV, CD <sub>3</sub> CN	91.1	4.240	32.6	68.9	0
0 mV, CH <sub>3</sub> CN	90.0	2.111	49.1	68.9	0
400 mV, CH <sub>3</sub> CN	90.7	2.241	51.5	66.7	0.25
400 mV, CD <sub>3</sub> CN	81.4	4.073	39.4	66.7	0.25
-700 mV, CD <sub>3</sub> CN	196.4	3.922	37.7	62.7	0
700 mV, CD <sub>3</sub> CN	71.5	4.384	30.6	69.4	0.25
-700 mV, CH <sub>3</sub> CN	200.2	2.112	167.6	69.5	0
700 mV, CH <sub>3</sub> CN	95.0	2.092	56.1	69.3	0.25

**Table 5.12** Fit parameters used in **Figure 5.17** for the outer PEDOT layer in chronological order.

As with the bilayer system, the trilayer was measured in air after the solvated NR experiments to confirm the hydrolysis. **Figures 5.19** and **5.20** show the dry film R(Q) and SLD profiles at the start and end of the NR experiment.

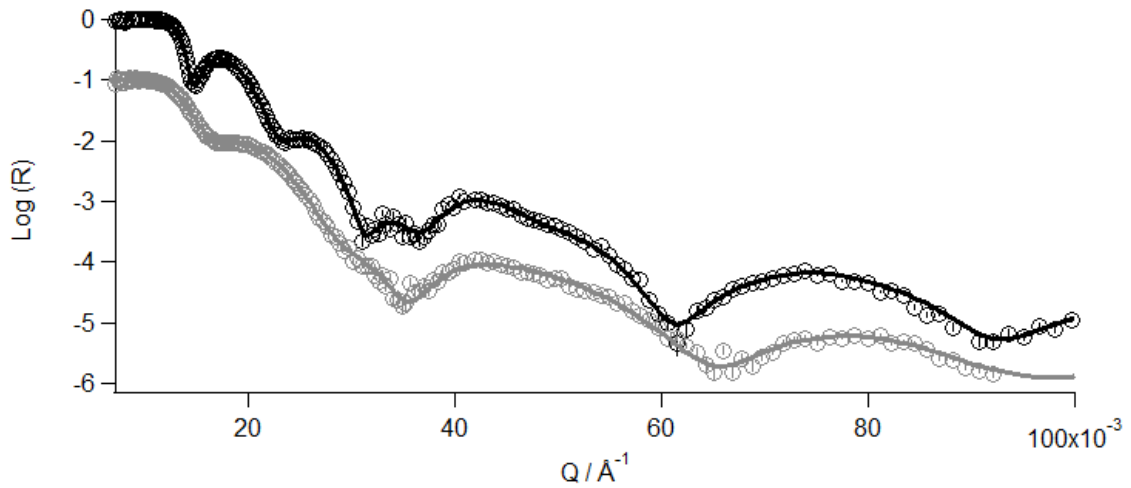


**Figure 5.19**  $R(Q)$  profile of the dry Au/PEDOT/PPFP/PEDOT trilayer system before the solvated NR experiments (black) and of the dry Au/PEDOT/PPyCOOH/PEDOT trilayer system after the solvated NR experiments (grey).  $\circ$  is the raw data and the line is the fit of the data ( $\chi^2 = 1.8$  and  $2.0$ , respectively).

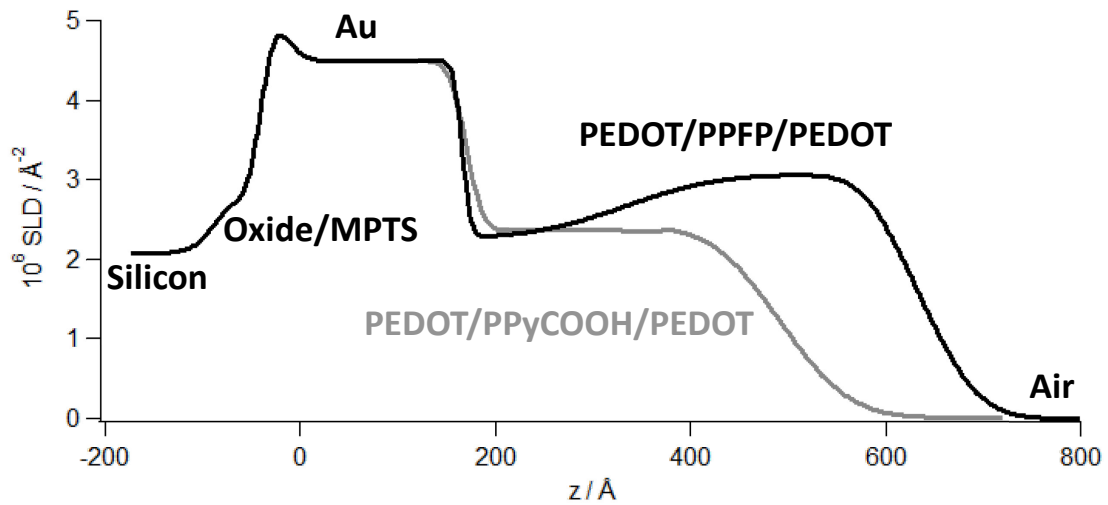


**Figure 5.20** SLD ( $z$ ) profiles of the dry Au/PEDOT/PPFP/PEDOT trilayer system before the solvated NR experiments (black) and of the dry Au/PEDOT/PPyCOOH/PEDOT trilayer system after the solvated NR experiments (grey) shown in **Figure 5.19**.

Layer	$d / \text{\AA}$	$10^6 N_b / \text{\AA}^{-2}$	$\sigma / \text{\AA}$
Air	Bulk	0	N/A
PEDOT	45.6	2.300	55.5
PPyCOOH	80.3	2.414	32.4
PEDOT	200.2	2.360	4.7
Au	206.4	4.490	5.5
MPTS	3.3	0.266	12.9
Oxide Layer	25.3	4.182	22.2
Silicon	Bulk	2.073	2.0

**Table 5.13** Summary of the fit parameters used for the dry Au/PEDOT/PPyCOOH/PEDOT in **Figure 5.19**.

After the neutron experiment the step height of the combined trilayer was measured by AFM. This thickness of 315.7 nm is consistent with the final dry NR measurement (see **Table 5.6**).

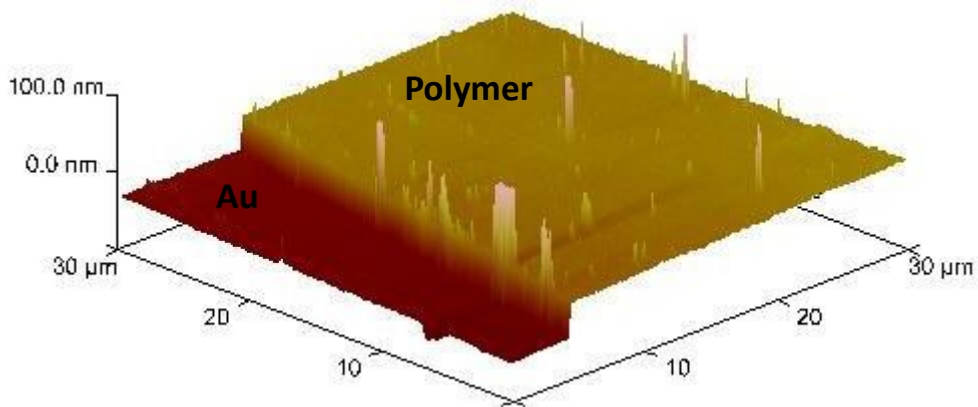


**Figure 5.21** AFM image of Au and the PEDOT/PPyCOOH trilayer on silicon shown in **Figures 5.15-20**.

## 5.4. Results: PEDOT/PPy Systems

In order to better understand the effects of redox states on the segregation and solvation of multi-layered films a simpler set of bilayers, based on PEDOT and PPy, were analysed with neutron reflectivity. This removes the added variable of hydrolysis seen in the case of PFPF and focuses solely on the properties of the conducting polypyrrole backbone.

### 5.4.1. Au/h<sub>4</sub>-PEDOT/d<sub>2</sub>-PPy Bilayer

#### 5.4.1.1. Electropolymerisation

The first layer of h<sub>4</sub>-PEDOT was grown before the neutron experiment and its R(Q) profile was measured prior to the formation of the bilayer. After these measurements, a second layer of d<sub>2</sub>-PPy was grown on top of the h<sub>4</sub>-PEDOT and the bilayer was studied with NR. This was grown from d<sub>4</sub>-Py monomer and two D atoms were lost during polymerisation. The use of both hydrogenous and deuterated polymers for different layers was chosen to highlight the polymer/polymer interfacial characteristics. The growth and monomer-free electrochemical i-E characterisation curves are shown in **Figure 5.22**.

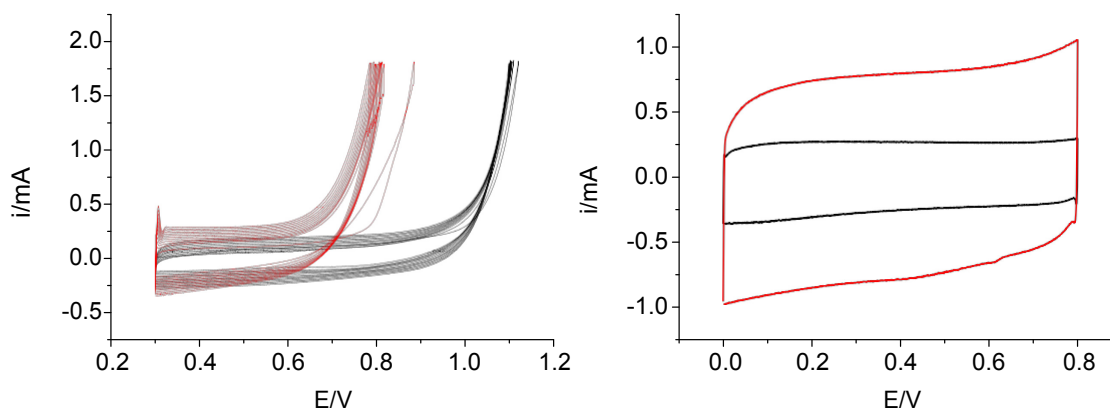


**Figure 5.22** Left: growth curves for  $h_4$ -PEDOT on Au (black) and  $d_2$ -PPy on Au/ $h_4$ -PEDOT (red) [ $0.3 < E/V$  vs. Ag  $<$  anodic limit  $I_{\max} = 0.18$  mA,  $\nu = 20$   $\text{mV s}^{-1}$ , 12 cycles]. Right: Au/ $h_4$ -PEDOT (black) and Au/ $h_4$ -PEDOT/ $d_2$ -PPy bilayer post deposition cycling in  $\text{LiClO}_4/\text{acetonitrile}$  [ $0.3 < E/V$  vs. Ag/AgCl (saturated KCl)  $<$  0.8,  $\nu = 50$   $\text{mV s}^{-1}$ ].

A coulometric assay can be achieved by integrating the current of the half cycle in panel b performed in monomer free electrolyte, which is not complicated by contributions from the (irreversible) anodic polymerization current contribution. The accuracy of the coulometric assay relies upon complete film redox conversion on the experimental timescale.

On this basis, the surface coverage,  $\Gamma$  ( $\text{mol cm}^{-2}$ ), is equal to  $q/nFA$ , where  $q$  (C) is the charge,  $n$  is the number of electrons transferred (“doping level”,  $n = 0.33$ ),  $A$  is the electrode area ( $\text{cm}^{-2}$ ) and  $F$  is Faraday’s constant ( $\text{C mol}^{-1}$ ). In this instance, the polymer coverages are  $5.9$   $\text{nmol cm}^{-2}$  for the  $h_4$ -PEDOT single layer and  $14$   $\text{nmol cm}^{-2}$  for the  $h_4$ -PEDOT/ $d_2$ PPy bilayer. For compact, solvent-free (“dry”) films, these would correspond to film thicknesses of ca.  $85$   $\text{\AA}$  and  $300$   $\text{\AA}$ .

#### 5.4.1.1. NR measurements of the Dry Film

The dry  $R(Q)$  and SLD profiles of the  $h_4$ -PEDOT single layer after deposition are shown in **Figures 5.23** and **5.24**.

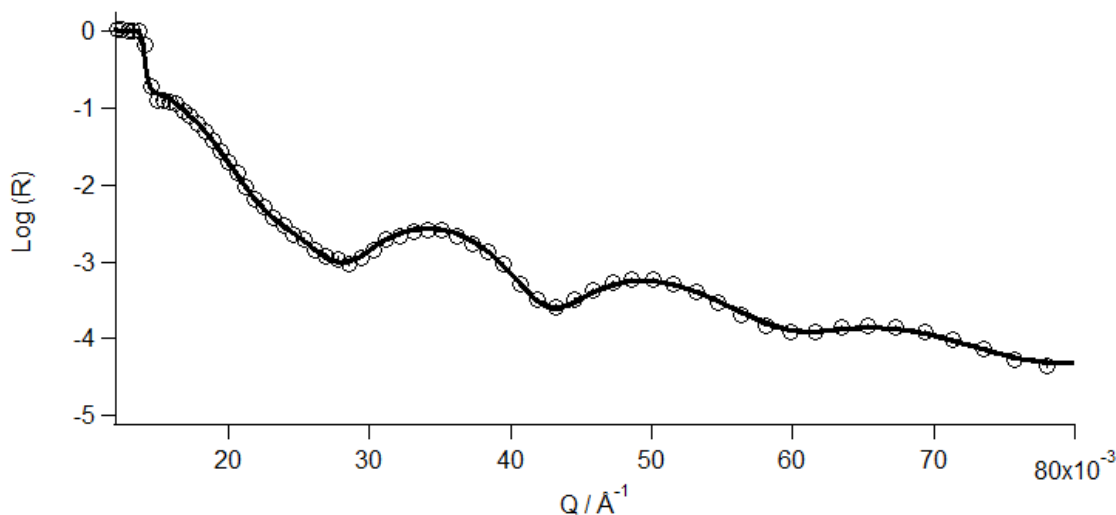


**Figure 5.23** R(Q) profile of the dry  $h_4$ -PEDOT single layer. Circles are the raw data and the line is the fit of the data ( $\chi^2 = 0.9$ ). Refer to **Figure 5.24** for SLD profile and **Table 5.14** for fit parameters.

Using **Equation 5.2** to calculate the thickness of the Au using the  $\Delta Q$  ( $0.0182 \text{ \AA}^{-1}$ ) of the final fringe in **Figure 5.23** gives a value of  $345 \text{ \AA}$ .

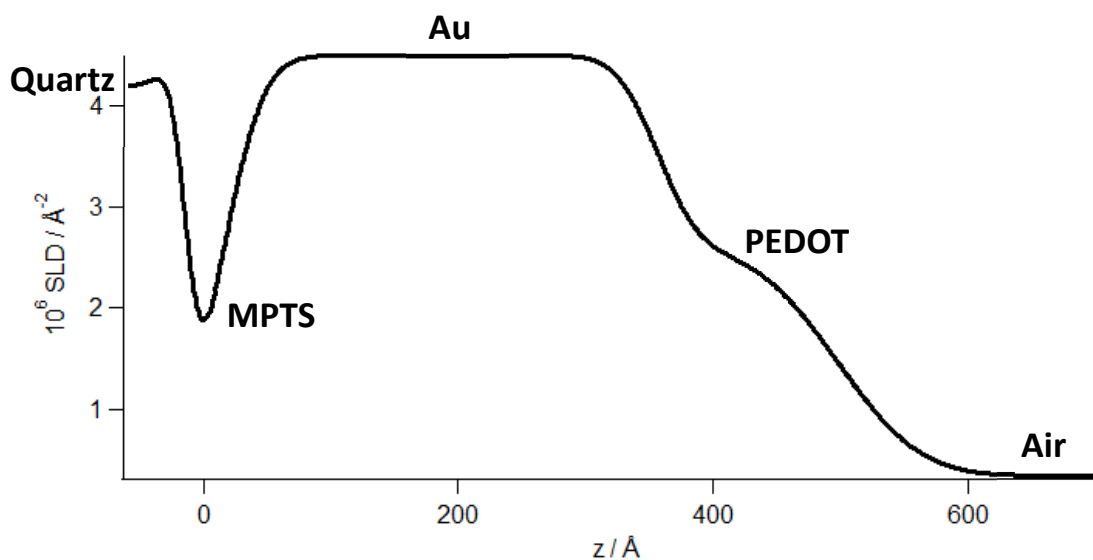


**Figure 5.24** SLD profile of the dry  $h_4$ -PEDOT single layer shown in **Figure 5.23**. Refer to **Table 5.14** for fit parameters used.

Layer	d / Å	$10^6 N_b / \text{Å}^{-2}$	$\sigma / \text{Å}$
Air	Bulk	0	N/A
$h_4$ -PEDOT	141.7	2.600	51.3
Au	343.1	4.490	25.4
MPTS	27.1	0.266	26.3
Quartz	Bulk	4.182	10.0

**Table 5.14** Fit parameters used for the dry  $h_4$ -PEDOT single layer shown in **Figure 5.23**.

The PEDOT single layer has a SLD of  $2.600 \times 10^{-6} \text{Å}^{-2}$ , which corresponds to a density of  $1.54 \text{ g cm}^{-3}$ . Measuring the thickness and roughness of the  $h_4$ -PEDOT single layer, before the addition of the  $d_2$ -PPy to form the bilayer, allows for a more detailed analysis of the polymer/polymer interface.

#### ***5.4.1.2. Solvated $h_4$ -PEDOT Single layer NR Measurements Under Potential Control***

To understand any changes seen in the bilayer system, the properties of the  $h_4$ -PEDOT single layer system needed to be analysed under potential control in both its fully oxidised and fully reduced states. The R(Q) and SLD profiles are given in **Figures 5.25** and **5.26**.

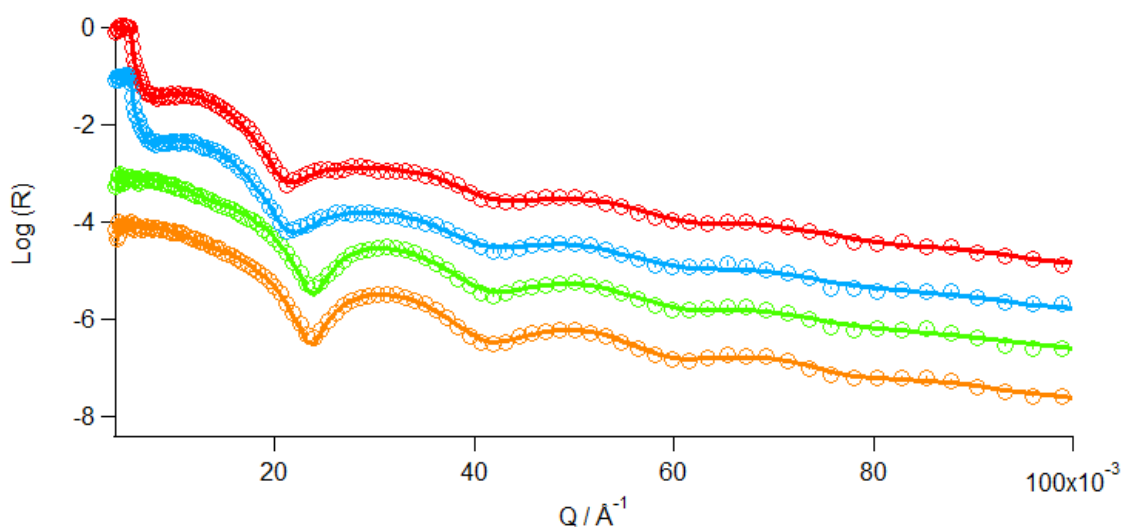


**Figure 5.25** R(Q) profile of the  $h_4$ -PEDOT single layer: fully oxidised at 800 mV in  $CD_3CN$  (red) and  $CH_3CN$  (green); and fully reduced at 0 mV in  $CD_3CN$  (cyan) and  $CH_3CN$  (orange). Circles represent the raw data and the solid lines are the fits of the data ( $\chi^2 = 0.61, 0.88, 0.78$  and  $1.02$ ). Refer to **Figure 5.26** for SLD profile and **Tables 5.15** and **5.16** for fit parameters.

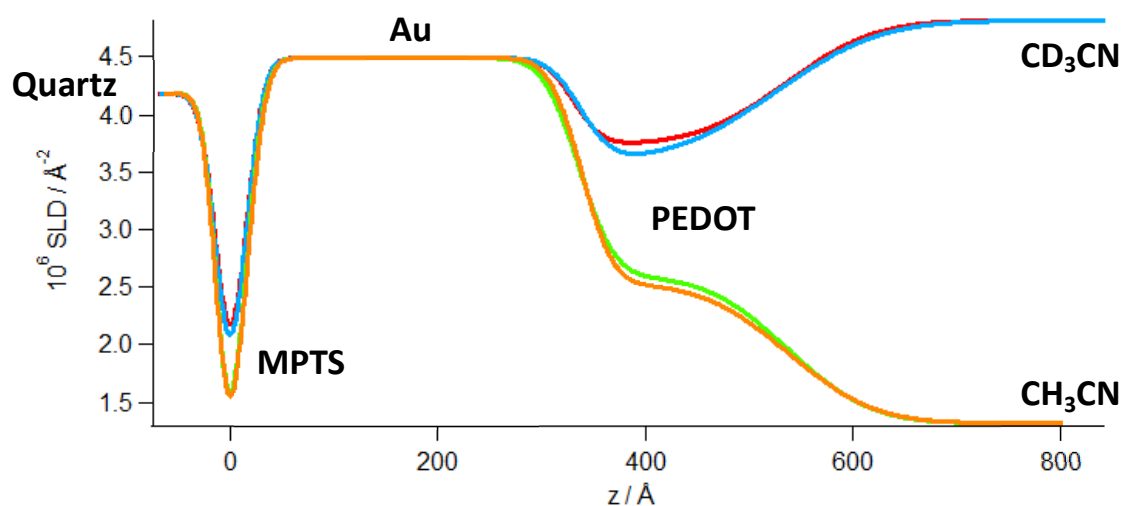


**Figure 5.26** SLD profiles of the  $h_4$ -PEDOT single layer: fully oxidised at 800 mV in  $CD_3CN$  (red) and  $CH_3CN$  (green); and fully reduced at 0 mV in  $CD_3CN$  (cyan) and  $CH_3CN$  (orange) shown in **Figure 5.25**. Refer to **Tables 5.15** and **5.16** for fit parameters used.

The fit properties used in **Figure 5.25** to produce the SLD profiles shown in **Figure 5.26** are given in **Tables 5.15** and **5.16**.

Layer	d / Å	$10^6 N_b / \text{Å}^{-2}$	$\sigma / \text{Å}$
CH <sub>3</sub> CN/CD <sub>3</sub> CN	Bulk	1.320/4.815	N/A
h <sub>4</sub> -PEDOT	201.7/205.0	2.604/3.739	62.6/67.4
Au	322.7/320.5	4.490	27.0/21.7
MPTS	25.7/20.8	0.266	15.0/15.0
Quartz	Bulk	4.182	11.2/13.7

**Table 5.15** Fit parameters for the oxidised h<sub>4</sub>-PEDOT film in CH<sub>3</sub>CN (green) and CD<sub>3</sub>CN (red) shown in **Figure 5.25**.

Layer	d / Å	$10^6 N_b / \text{Å}^{-2}$	$\sigma / \text{Å}$
CH <sub>3</sub> CN/CD <sub>3</sub> CN	Bulk	1.32/4.814	N/A
h <sub>4</sub> -PEDOT	199.8/190.0	2.534/3.599	65.2/77.8
Au	324.2/326.6	4.490	24.1/24.1
MPTS	26.5/21.5	0.266	15.0/15.0
Quartz	Bulk	4.182	11.6/13.3

**Table 5.16** Fit parameters for the reduced h<sub>4</sub>-PEDOT film in CH<sub>3</sub>CN (orange) and CD<sub>3</sub>CN (cyan) shown in **Figure 5.25**.

**Tables 5.15** and **5.16** show that the thickness of the PEDOT layer increases slightly when the film is oxidised as seen already in **Sections 5.3.2** and **5.3.3**. This increase can best be seen in CD<sub>3</sub>CN as this has the greatest contrast in terms of scattering length densities between the hydrogenous polymer and the deuterated solvent. This swelling is attributed to the ingress of perchlorate anions to counteract the positive charge shared over every four monomer units of PEDOT despite the fact that the level of solvation remains the same ( $\phi_s$  0.40). These

conclusions are corroborated by the change in SLD between the oxidised and reduced states in both  $\text{CH}_3\text{CN}$  and  $\text{CD}_3\text{CN}$ .

#### 5.4.1.3. Solvated $h_4$ -PEDOT/ $d_2$ -PPy Bilayer NR Measurements Under Potential Control

Once the single layer had been fully characterised, a layer of  $d_2$ -PPy was grown on top (see **Figure 5.22**). After growth the film was re-characterised in its oxidised and reduced states. The  $R(Q)$  and SLD profiles are shown in **Figures 5.27** and **5.28**.

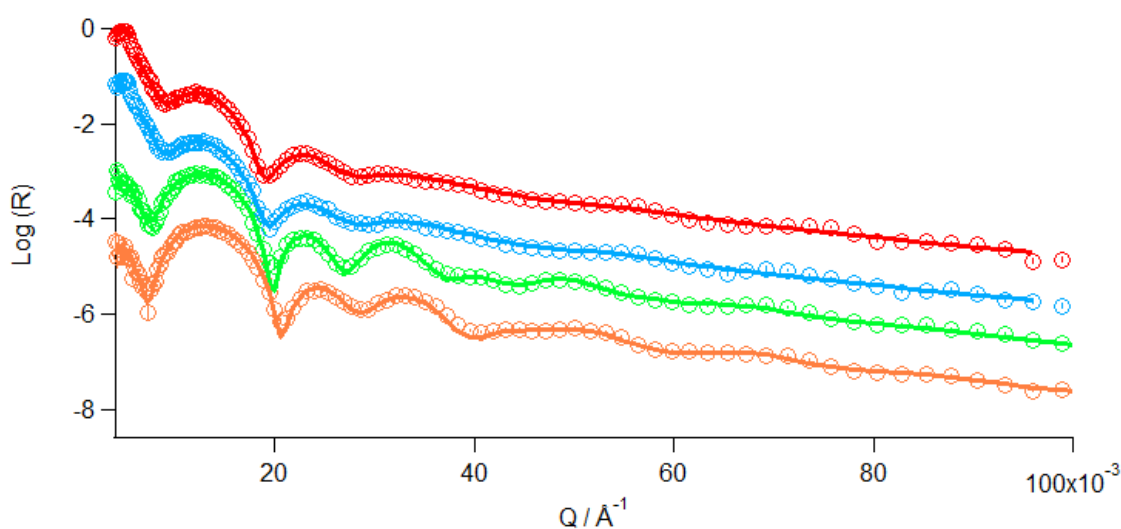


**Figure 5.27**  $R(Q)$  profile of the  $h_4$ -PEDOT/ $d_2$ -PPy bilayer: fully oxidised at 800 mV in  $\text{CD}_3\text{CN}$  (red) and  $\text{CH}_3\text{CN}$  (green); and fully reduced at 0 mV in  $\text{CD}_3\text{CN}$  (cyan) and  $\text{CH}_3\text{CN}$  (orange). Circles represent the raw data and the solid lines are the fits of the data ( $\chi^2 = 0.97, 1.34, 0.89$  and  $1.42$ ).

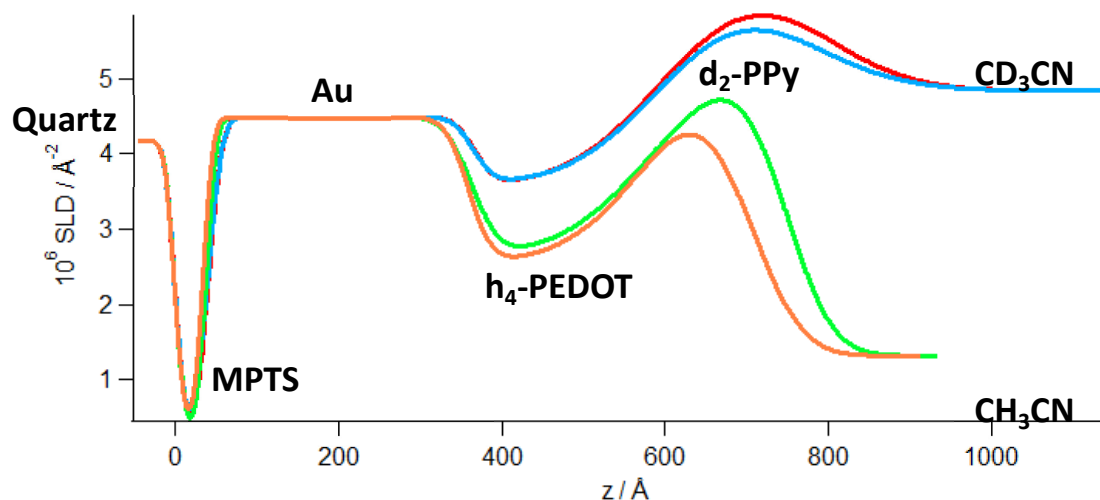


**Figure 5.28** SLD profiles of the  $h_4$ -PEDOT/ $d_2$ -PPy bilayer: fully oxidised at 800 mV in  $CD_3CN$  (red) and  $CH_3CN$  (green); and fully reduced at 0 mV in  $CD_3CN$  (cyan) and  $CH_3CN$  (orange) shown in **Figure 5.27**.

The fit parameters used for the solvated  $d_2$ -PPy/ $h_4$ -PEDOT bilayer are given in **Tables 5.17** and **5.18**.

Layer	$d / \text{Å}$	$10^6 N_b / \text{Å}^{-2}$	$\sigma / \text{Å}$
$CH_3CN/CD_3CN$	Bulk	1.320/4.889	N/A
$d_2$ -PPy	160.8/162.7	5.377/6.776	45.4/67.8
$h_4$ -PEDOT	222.6/236.0	2.660/3.581	89.4/83.2
Au	325.0/325.0	4.490	26.6/20.0
MPTS	38.4/45.3	0.266	10.0/10.5
Quartz	Bulk	4.182	10.0/10.0

**Table 5.17** Fit parameters for the oxidised  $h_4$ -PEDOT/ $d_2$ -PPy film in  $CH_3CN$  (green) and  $CD_3CN$  (red) shown in **Figure 5.27**.

Layer	$d / \text{\AA}$	$10^6 N_b / \text{\AA}^{-2}$	$\sigma / \text{\AA}$
CH <sub>3</sub> CN/CD <sub>3</sub> CN	Bulk	1.32/4.898	N/A
d <sub>2</sub> -PPy	104.2/100.5	5.777/7.441	51.9/77.8
h <sub>4</sub> -PEDOT	237.1/240.9	2.560/3.609	88.2/85.1
Au	325.0/325.0	4.490	22.6/20.0
MPTS	34.4/43.1	0.266	10.0/11.9
Quartz	Bulk	4.182	10.0/10.0

**Table 5.18** Fit parameters for the reduced h<sub>4</sub>-PEDOT/d<sub>2</sub>-PPy film in CH<sub>3</sub>CN (orange) and CD<sub>3</sub>CN (cyan) shown in Figure 5.27.

The inner h<sub>4</sub>-PEDOT layer in **Tables 5.17** and **5.18** shows very similar properties to the single layer in **Tables 5.15** and **5.16** in terms of solvation ( $\phi_s$  0.40), density ( $\rho = 1.53 \text{ g cm}^{-3}$ ) and anion doping level when oxidised ( $n = 0.33$ ). However, the changes in thickness during redox switching are reversed with the film shrinking, rather than swelling, during oxidation. The h<sub>4</sub>-PEDOT/d<sub>2</sub>-PPy interface shows a higher roughness than the corresponding h<sub>4</sub>-PEDOT/solvent interface in the single layer. As discussed previously, this roughness is not topographical but rather the distance over which a layer with one scattering length density changes into a second layer with a different scattering length density. This is therefore a good indication of interpenetration of the two polymers suggesting that PPy fills any voids present in the PEDOT single layer producing a graded interface between two distinct layers of homopolymers. This was attributed to PPy tendency to form chemical crosslinks<sup>13</sup>. Both polymers in the bilayer also have the same solvation and doping levels.

This initial characterisation provided an insight into the properties of the multi-layer film “as deposited”. However, for all of the potential applications of thin polymer films the properties of the film during/after repetitive redox cycling are of paramount importance. To explore this question the bilayer was reanalysed after 100 cycles.

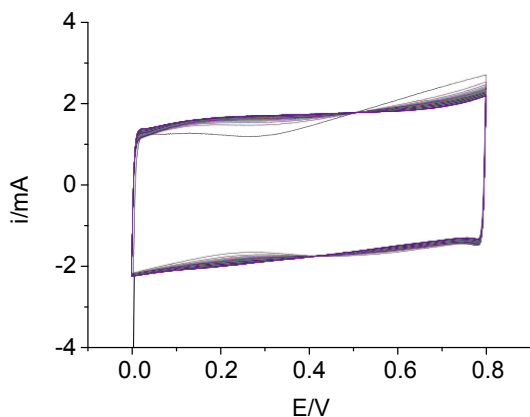


**Figure 5.29** 100 cycles of the  $h_4$ -PEDOT/ $d_2$ -PPy bilayer in  $LiClO_4$ /acetonitrile [ $0 < E/mV$  vs.  $Ag < 800, v = 100 \text{ mV s}^{-1}$ ].

The post cycling  $R(Q)$  and SLD profiles are shown in **Figures 5.30** and **5.31**.

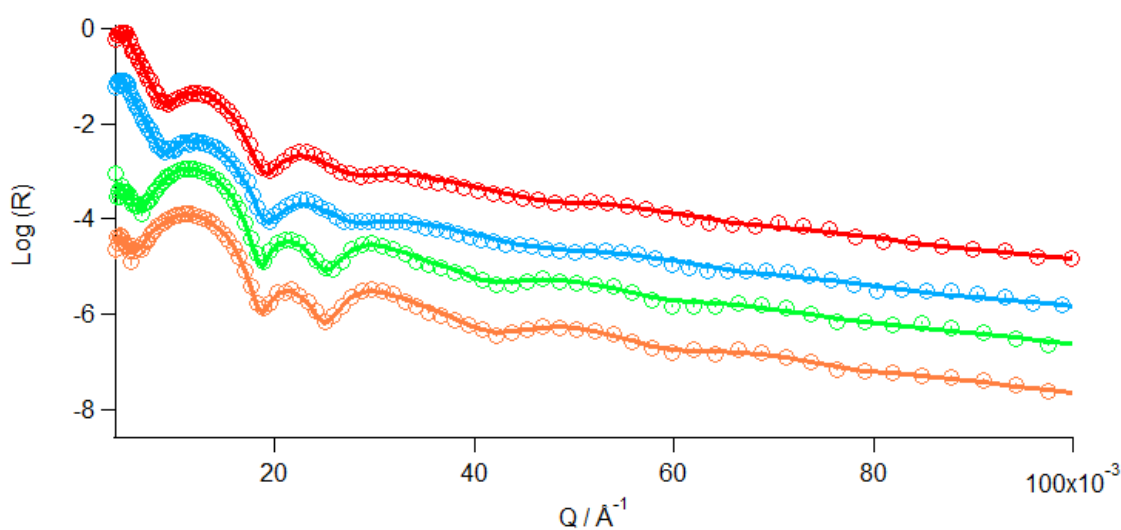


**Figure 5.30**  $R(Q)$  profile of the  $h_4$ -PEDOT/ $d_2$ -PPy bilayer after repetitive cycling: fully oxidised at 800 mV in  $CD_3CN$  (red) and  $CH_3CN$  (green); and fully reduced at 0 mV in  $CD_3CN$  (cyan) and  $CH_3CN$  (orange). Circles represent the raw data and the solid lines are the fits of the data ( $\chi^2 = 0.97, 1.34, 0.89$  and  $1.42$ ).

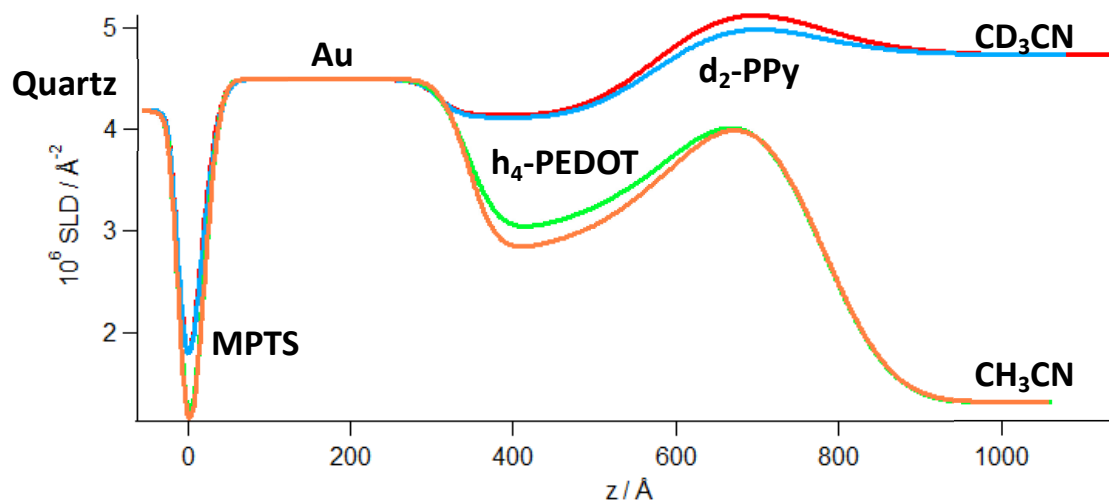


**Figure 5.31** SLD profiles of the  $h_4$ -PEDOT/ $d_2$ -PPy bilayer after repetitive cycling: fully oxidised at 800 mV in  $CD_3CN$  (red) and  $CH_3CN$  (green); and fully reduced at 0 mV in  $CD_3CN$  (cyan) and  $CH_3CN$  (orange) shown in **Figure 5.30**.

The post-cycling  $R(Q)$  and SLD profiles shown in **Figures 5.30** and **5.31** provide a direct comparison with the pre cycling profiles shown in **Figures 5.27** and **5.28**. The fringes in **Figure 5.30** have visibly dampened after cycling which is indicative of interfacial roughening. The fit parameters used for the solvated  $h_4$ -PEDOT/ $d_2$ -PPy bilayer are given in **Tables 5.19** and **5.20**.

Layer	$d / \text{Å}$	$10^6 N_b / \text{Å}^{-2}$	$\sigma / \text{Å}$
$CH_3CN/CD_3CN$	Bulk	1.320/4.878	N/A
$d_2$ -PPy	124.9/37.6	5.322/7.491	71.1/127.0
$h_4$ -PEDOT	304.2/284.4	2.964/4.167	124.7/94.1
Au	325.0/325.0	4.490	26.6/20.0
MPTS	30.0/23.8	0.266	10.0/10.5
Quartz	Bulk	4.182	10.0/10.0

**Table 5.19** Fit parameters for the oxidised  $h_4$ -PEDOT/ $d_2$ -PPy film in  $CH_3CN$  (green) and  $CD_3CN$  (red) shown in **Figure 5.30**.

Layer	$d / \text{\AA}$	$10^6 N_b / \text{\AA}^{-2}$	$\sigma / \text{\AA}$
CH <sub>3</sub> CN/CD <sub>3</sub> CN	Bulk	1.32/4.735	N/A
d <sub>2</sub> -PPy	129.9/16.7	5.301/8.882	70.7/116.5
h <sub>4</sub> -PEDOT	297.5/282.6	2.773/4.142	116.8/98.9
Au	325.0/325.0	4.490	22.6/20.0
MPTS	30.5/24.5	0.266	10.0/11.9
Quartz	Bulk	4.182	10.0/10.0

**Table 5.20** Fit parameters for the reduced h<sub>4</sub>-PEDOT/d<sub>2</sub>-PPy film in CH<sub>3</sub>CN (orange) and CD<sub>3</sub>CN (cyan) shown in **Figure 5.30**.

The cycling of the bilayer film has had an effect on the structure of the two layers as shown in **Tables 5.19** and **5.20**. The inner layer of h<sub>4</sub>-PEDOT layer appears thicker after repetitive cycling. There is also an increase in the SLD of the layer suggesting that some of the d<sub>2</sub>-PPy, which has a higher SLD, has penetrated into the lower SLD h<sub>4</sub>-PEDOT layer. The increase in roughness at the polymer/polymer interface also supports the conclusion that the two polymer layers have become more interdiffused during repetitive redox switching. This could be advantageous in terms of observing capacitive behaviour in the multilayers<sup>10,11</sup>.

A summary of the overall thicknesses of the bilayer before and after cycling is given in **Table 5.21**.

Redox State/Solvent Contrast	Thickness before cycling / Å	Thickness after cycling / Å
Oxidised/CH <sub>3</sub> CN	383.4	429.1
Reduced/CH <sub>3</sub> CN	341.3	427.4
Oxidised/CD <sub>3</sub> CN	398.7	322.0
Reduced/CD <sub>3</sub> CN	341.4	299.3

**Table 5.21** Changes in the h<sub>4</sub>-PEDOT/d<sub>2</sub>-PPy bilayer film thicknesses before and after repetitive cycling.

The bilayer film has got thicker after redox cycling and the changes between oxidised and reduced states are significantly less. This can be seen best in the hydrogenous contrast as the outer layer of deuterated polymer has greater contrast with the CH<sub>3</sub>CN than the CD<sub>3</sub>CN (see **Figure 5.31**). The deceptively low thicknesses after cycling in **Table 5.21** are because the lack of contrast means that the outer film thickness is instead modelled as a greater polymer/solvent interfacial roughness, which is not seen in the hydrogenous contrast. Therefore, the values in **Table 5.21** are only the locally homogeneous layer thickness. Even so, the hydrogenous contrast does show that the polymer/solvent interfacial roughness is greater after cycling than before which would aid the penetration of counter anions during oxidation and subsequent expulsion during reduction. Interestingly, the layer of MPTS binding the gold to the quartz is thinner after the repetitive cycling.

After the neutron experiment the bilayer film was analysed by AFM. The results are shown in **Figure 5.32**. This *ex situ* measurement showed the h<sub>4</sub>-PEDOT single layer to be 137 Å thick, which is entirely consistent with the NR measurements of the dry film (**Table 5.14**). The dry *ex situ* thickness of the h<sub>4</sub>-PEDOT/d<sub>2</sub>-PPy film was 333 Å.

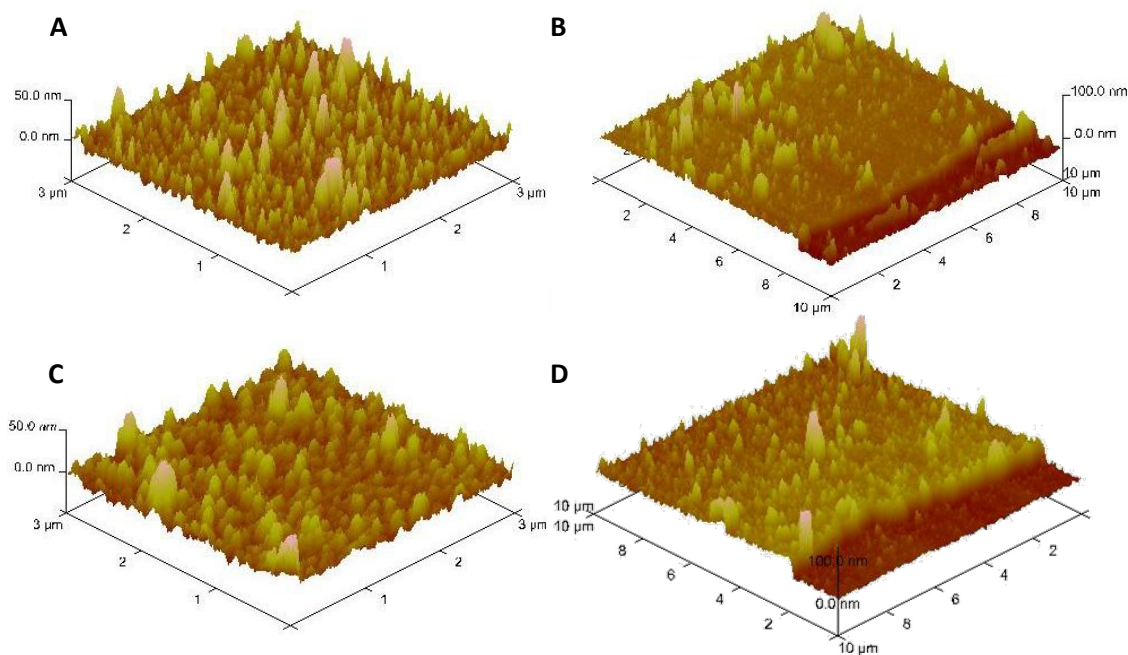


**Figure 5.32** AFM images of the  $h_4$ -PEDOT/ $d_2$ -PPy bilayer after the neutron experiment:  $h_4$ -PEDOT surface (A) and step height (B);  $h_4$ -PEDOT/ $d_2$ -PPy surface (C) and step height (D).

## 5.4.2. Au/ $d_2$ -PPy/ $h_4$ -PEDOT Bilayer

### 5.4.2.1. Electropolymerisation

As with **Section 5.4.1**, the first layer of  $d_2$ -PPy was grown prior to the neutron experiment and was characterised before a layer of  $h_4$ -PEDOT was grown on top. Again the reflectivity of the film(s) was measured in both hydrogenous and deuterated solvents. The growth and monomer-free electrochemical characterisation curves are shown in **Figure 5.33**.

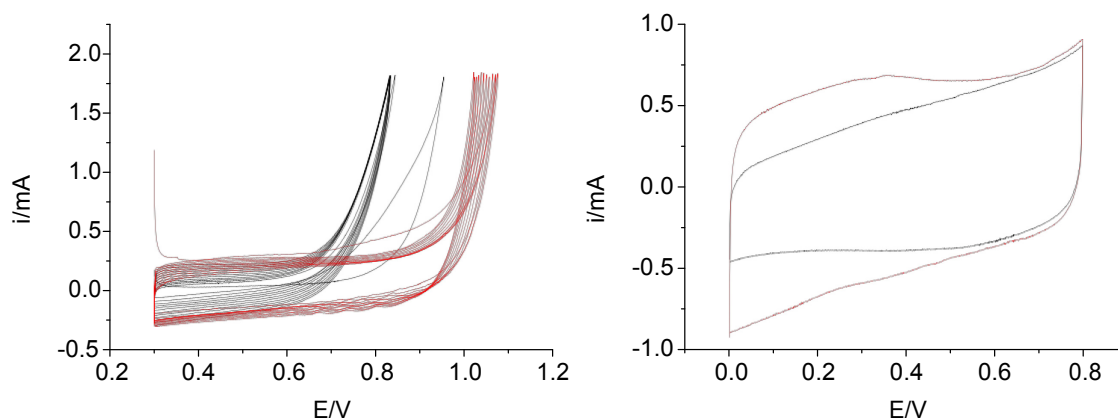


**Figure 5.33** Left: growth curves for  $d_2$ -PPy on Au (black) and  $h_4$ -PEDOT on Au/ $d_2$ -PPy (red) [ $0.3 < E/V$  vs. Ag < anodic limit  $I_{\max} = 0.18$  mA,  $\nu = 20$   $\text{mV s}^{-1}$ , 12 cycles]. Right: Au/ $d_2$ -PPy (black) and Au/ $d_2$ -PPy/ $h_4$ -PEDOT bilayer post deposition cycling in  $\text{LiClO}_4/\text{acetonitrile}$  [ $0.3 < E/V$  vs. Ag/AgCl (saturated KCl) < 0.8,  $\nu = 50$   $\text{mV s}^{-1}$ ].

Coulometric assay showed the polymer coverages were  $8.6$   $\text{nmol cm}^{-2}$  for the  $d_2$ -PPy single layer and  $14$   $\text{nmol cm}^{-2}$  for the  $d_2$ -PPy/ $h_4$ -PEDOT bilayer, which correspond to film thicknesses of ca.  $60$  Å and  $300$  Å, respectively.

#### 5.4.2.2. NR measurements of the Dry Film

The  $R(Q)$  and SLD profiles of the dry  $d_2$ -PPy single layer after deposition are shown in **Figures 5.34** and **5.35**.

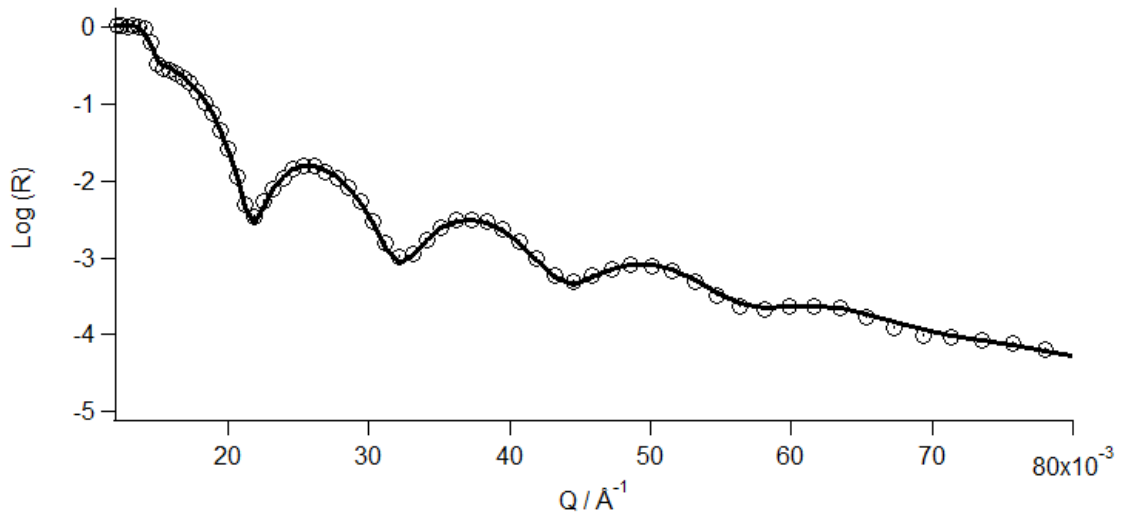


**Figure 5.34** R(Q) profile of the dry d<sub>2</sub>-PPy single layer from **Figure 5.33**. Circles are the raw data and the line is the fit of the data ( $\chi^2 = 1.9$ ).

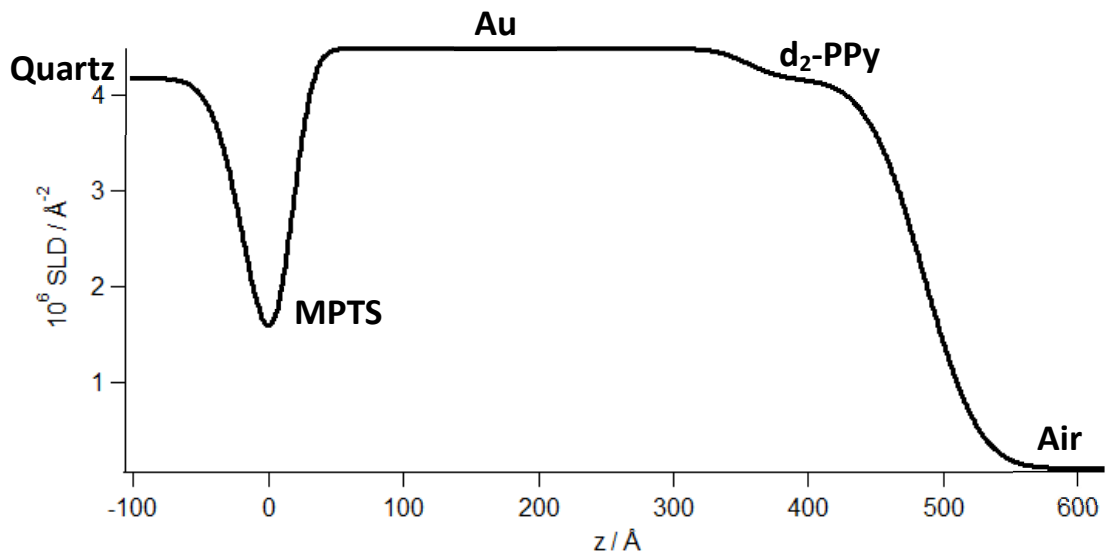


**Figure 5.35** SLD profile of the dry d<sub>2</sub>-PPy single layer shown in **Figure 5.34**.

The fitting parameters used in **Figure 5.34** are given in **Table 5.22**.

Layer	$d / \text{\AA}$	$10^6 N_b / \text{\AA}^{-2}$	$\sigma / \text{\AA}$
Air	Bulk	0	N/A
$d_2$ -PPy	126.1	4.171	32.3
Au	342.0	4.490	20.0
MPTS	31.2	0.266	12.7
Quartz	Bulk	4.182	20.8

**Table 5.22** Fit parameters used for the dry  $d_2$ -PPy single layer shown in **Figure 5.34**.

The PPy single layer has a SLD of  $4.171 \times 10^{-6} \text{\AA}^{-2}$ , which corresponds to a density of  $1.05 \text{ g cm}^{-3}$ , which is suggestive of a very diffuse layer compared to those seen previously in this thesis.

#### *5.4.2.1. Solvated $d_2$ -PPy Single layer NR Measurements Under Potential Control*

As in **Section 5.4.1** the properties of the  $d_2$ -PPy single layer system were measured when both fully oxidised and fully reduced.

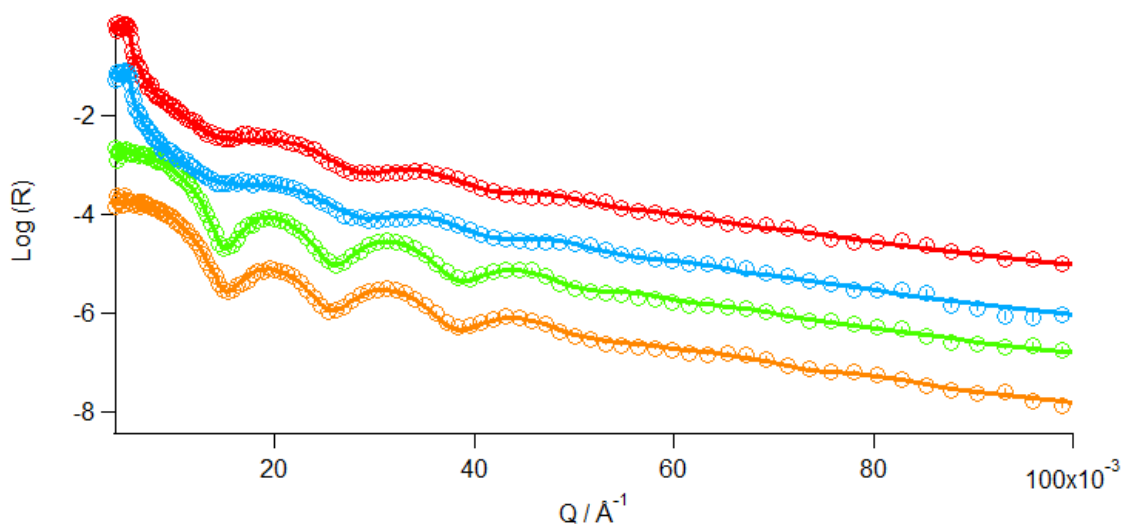


**Figure 5.36** R(Q) profile of the d<sub>2</sub>-PPy single layer: fully oxidised at 800 mV in CD<sub>3</sub>CN (red) and CH<sub>3</sub>CN (green); and fully reduced at 0 mV in CD<sub>3</sub>CN (cyan) and CH<sub>3</sub>CN (orange). Circles represent the raw data and the solid lines are the fits of the data ( $\chi^2 = 1.68, 1.68, 0.61$  and  $0.74$ ).

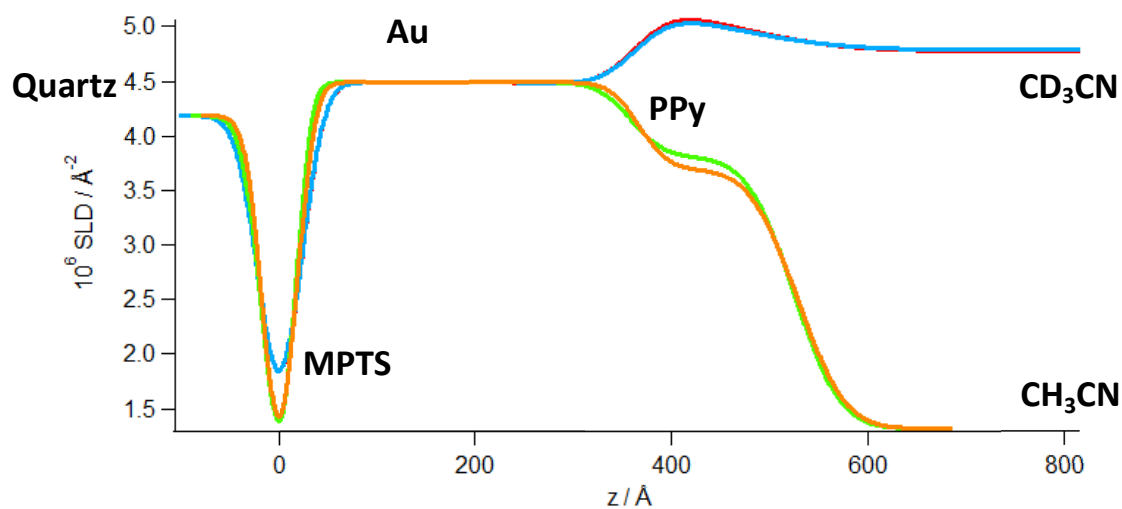


**Figure 5.37** SLD profiles of the d<sub>2</sub>-PPy single layer: fully oxidised at 800 mV in CD<sub>3</sub>CN (red) and CH<sub>3</sub>CN (green); and fully reduced at 0 mV in CD<sub>3</sub>CN (cyan) and CH<sub>3</sub>CN (orange) shown in **Figure 5.36**.

The fit parameters used in **Figure 5.36** to produce the SLD profiles are given in **Tables 5.23** and **5.24**.

Layer	$d / \text{\AA}$	$10^6 N_b / \text{\AA}^{-2}$	$\sigma / \text{\AA}$
CH <sub>3</sub> CN/CD <sub>3</sub> CN	Bulk	1.320/4.815	N/A
d <sub>2</sub> -PPy	165.4/103.4	3.808/5.217	37.5/87.4
Au	342.6/340.5	4.490	27.7/21.5
MPTS	32.2/30.7	0.266	12.8/15.0
Quartz	Bulk	4.182	17.1/16.7

**Table 5.23** Fit parameters for the oxidised d<sub>2</sub>-PPy film in CH<sub>3</sub>CN (green) and CD<sub>3</sub>CN (red) shown in **Figure 5.36**.

Layer	$d / \text{\AA}$	$10^6 N_b / \text{\AA}^{-2}$	$\sigma / \text{\AA}$
CH <sub>3</sub> CN/CD <sub>3</sub> CN	Bulk	1.32/4.814	N/A
d <sub>2</sub> -PPy	160.6/100.0	3.697/3.599	38.5/88.8
Au	351.0/346.6	4.490	24.1/24.1
MPTS	32.0/27.5	0.266	15.5/15.0
Quartz	Bulk	4.182	14.4/13.3

**Table 5.24** Fit parameters for the reduced d<sub>2</sub>-PPy film in CH<sub>3</sub>CN (orange) and CD<sub>3</sub>CN (cyan) shown in **Figure 5.36**.

The conclusion in **Section 5.4.2.2** that the low density of the single layer was due to the film being more diffuse than those in **Section 5.4.1.1** is supported by the higher solvation level calculated from the solvated scattering length densities. The solvent volume fraction of the d<sub>2</sub>-PPy single layer is 0.50 which is 0.10 greater than the h<sub>4</sub>-PEDOT single layer in **Section 5.4.1.1**. The oxidised film was doped with one ClO<sub>4</sub><sup>-</sup> to every three monomer units, as expected based on the behaviour seen in **Section 5.4.1.1**. However, sole anion egress during

oxidation would have resulted in a SLD higher than that of the oxidised film<sup>a</sup>. Total anion egress would give a SLD of  $4.037 \times 10^{-6} \text{ \AA}^{-2}$ , but the value obtained from the fits in **Figure 5.36** is  $3.697 \times 10^{-6} \text{ \AA}^{-2}$ . This is suggestive of cation ingress to balance the charge. However, sole cation egress to balance the charge gives a SLD of  $3.292 \times 10^{-6} \text{ \AA}^{-2}$ , which is too low. Therefore, to get a SLD of  $3.697 \times 10^{-6} \text{ \AA}^{-2}$ , there must be a combination of the two processes: partial anion egress and some cation ingress to balance any retained anion. This change in doping behaviour could be due to the more diffuse nature of the film meaning that counter ions can flow more freely. Calculations showed that approximately one anion to every eight monomer units is retained in the film during reduction and are balanced by  $\text{Li}^+$  (SLD =  $3.701 \times 10^{-6} \text{ \AA}^{-2}$ ). The SLDs obtained from the deuterated fits supported these conclusions.

#### ***5.4.2.2. Solvated $d_2$ -PPy/ $h_4$ -PEDOT Bilayer NR Measurements Under Potential Control***

Once the single layer had been fully characterised, a bilayer was made with the addition of a layer of  $h_4$ -PEDOT. After growth the film was re-characterised in its oxidised and reduced states. The R(Q) and SLD profiles are shown in **Figures 5.38** and **5.39**.

---

<sup>a</sup> Note here that values discussed are in  $\text{CH}_3\text{CN}$  as this provides the best contrast with the deuterated polymer.

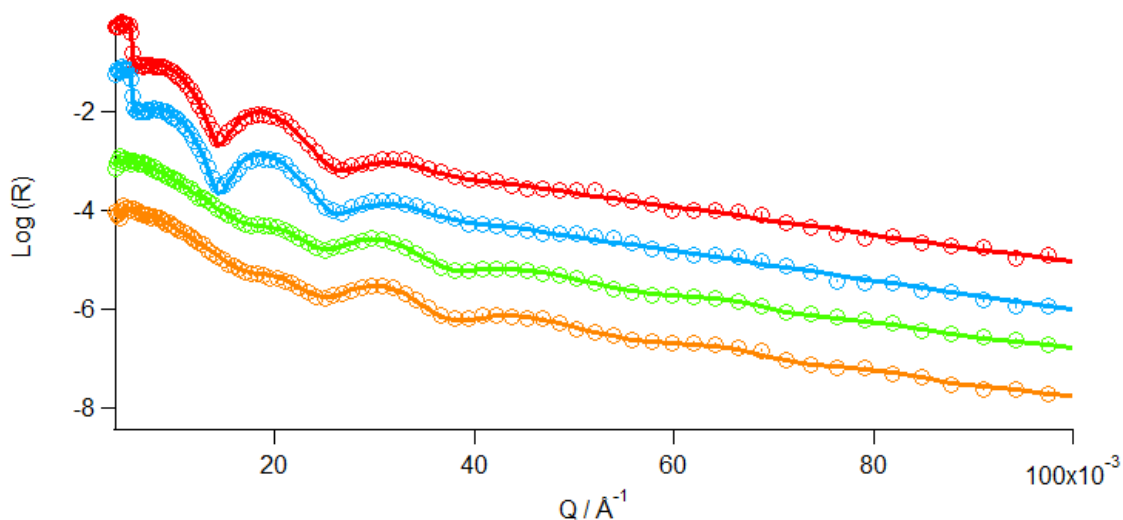


**Figure 5.38**  $R(Q)$  profile of the  $d_2$ -PPy/ $h_4$ -PEDOT bilayer: fully oxidised at 800 mV in  $CD_3CN$  (red) and  $CH_3CN$  (green); and fully reduced at 0 mV in  $CD_3CN$  (cyan) and  $CH_3CN$  (orange). Circles represent the raw data and the solid lines are the fits of the data ( $\chi^2 = 0.45, 0.48, 0.95$  and  $1.20$ ).

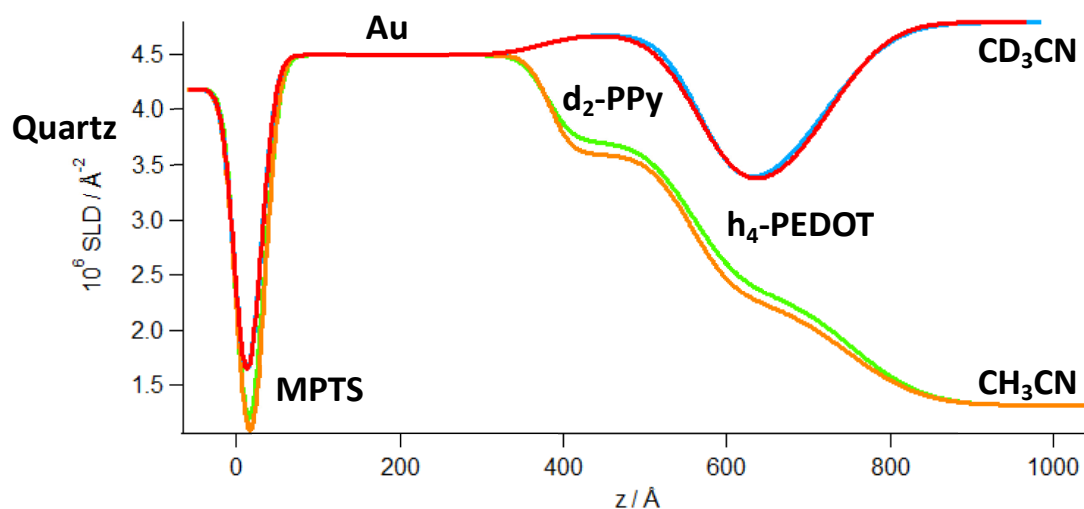


**Figure 5.39** SLD profiles of the  $d_2$ -PPy/ $h_4$ -PEDOT bilayer: fully oxidised at 800 mV in  $CD_3CN$  (red) and  $CH_3CN$  (green); and fully reduced at 0 mV in  $CD_3CN$  (cyan) and  $CH_3CN$  (orange) shown in **Figure 5.38**.

The fit parameters used for the solvated  $d_2$ -PPy/ $h_4$ -PEDOT bilayer are given in **Tables 5.25** and **5.26**.

Layer	$d / \text{\AA}$	$10^6 N_b / \text{\AA}^{-2}$	$\sigma / \text{\AA}$
CH <sub>3</sub> CN/CD <sub>3</sub> CN	Bulk	1.320/4.769	N/A
h <sub>4</sub> -PEDOT		195.7/196.7	2.368/3.188
d <sub>2</sub> -PPy		177.2/175.1	3.708/4.673
Au		4.490	24.4/23.3
MPTS		0.266	15.6/15.5
Quartz	Bulk	4.182	12.2/12.3

**Table 5.25** Fit parameters for the oxidised d<sub>2</sub>-PPy/h<sub>4</sub>-PEDOT film in CH<sub>3</sub>CN (green) and CD<sub>3</sub>CN (red) shown in **Figure 5.38**.

Layer	$d / \text{\AA}$	$10^6 N_b / \text{\AA}^{-2}$	$\sigma / \text{\AA}$
CH <sub>3</sub> CN/CD <sub>3</sub> CN	Bulk	1.32/4.748	N/A
h <sub>4</sub> -PEDOT		190.4/200.5	2.296/3.213
d <sub>2</sub> -PPy		173.5/240.9	3.595/4.613
Au		4.490	21.6/20.0
MPTS		0.266	13.7/11.9
Quartz	Bulk	4.182	13.6/10.0

**Table 5.26** Fit parameters for the reduced d<sub>2</sub>-PPy/h<sub>4</sub>-PEDOT film in CH<sub>3</sub>CN (orange) and CD<sub>3</sub>CN (cyan) shown in **Figure 5.38**.

The inner layer of d<sub>2</sub>-PPy is less solvated in the bilayer than it was in the single layer:  $\phi_{\text{acetonitrile}}$  was 0.40 and 0.50, respectively. This suggests that some of the solvent has been displaced by the interpenetrating h<sub>4</sub>-EDOT during the formation of the bilayer. The polymer/polymer interfacial roughness is lower in this PPy/PEDOT bilayer than it was in the PEDOT/PPy bilayer in **Section 5.4.1**. The order in which layers are polymerised could therefore be used to tune the properties of the film.

The doping level of the inner  $d_2$ -PPy film was again 0.33 when oxidised, with charge balance being achieved through anion ingress. A level of approximately 0.125 was again retained during reduction and was charge balanced through the ingress of  $\text{Li}^+$ . The doping level of the outer  $h_4$ -PEDOT layer was also 0.33 with one anion entering the film during oxidation for every three monomer units. Total anion egress was observed upon reduction and the solvation level was 0.40 regardless of oxidation state.

This initial characterisation provided an insight into the properties of the multi-layer film “as deposited”. The bilayer was measured again after 100 cycles during which the electrochemistry showed the film to be remarkably stable.

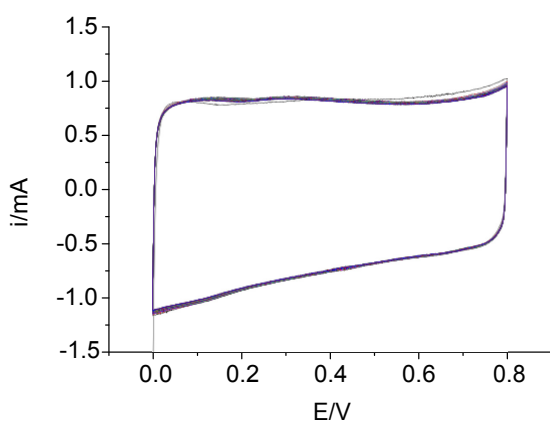


**Figure 5.40** 100 cycles of the  $d_2$ -PPy/  $h_4$ -PEDOT bilayer in  $\text{LiClO}_4/\text{acetonitrile}$  [ $0 < E/\text{mV}$  vs.  $\text{Ag} < 800$ ,  $\nu = 100 \text{ mV s}^{-1}$ ].

The  $R(Q)$  and SLD profiles are shown in **Figures 5.41** and **5.42**.

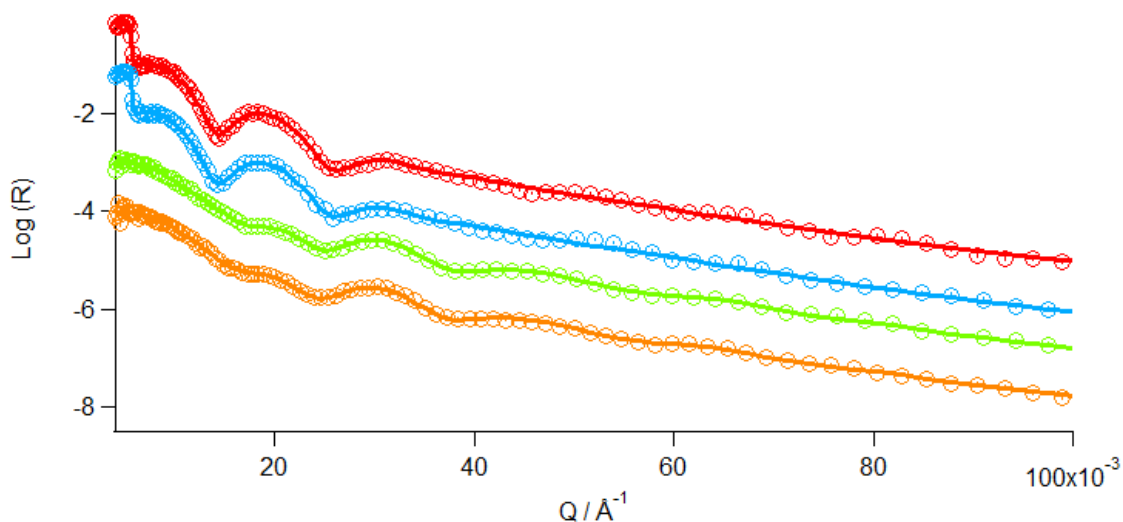


**Figure 5.41** R(Q) profile of the d<sub>2</sub>-PPy/h<sub>4</sub>-PEDOT bilayer after repetitive cycling: fully oxidised at 800 mV in CD<sub>3</sub>CN (red) and CH<sub>3</sub>CN (green); and fully reduced at 0 mV in CD<sub>3</sub>CN (cyan) and CH<sub>3</sub>CN (orange). Circles represent the raw data and the solid lines are the fits of the data ( $\chi^2 = 0.35, 0.77, 0.71$  and  $0.68$ ).

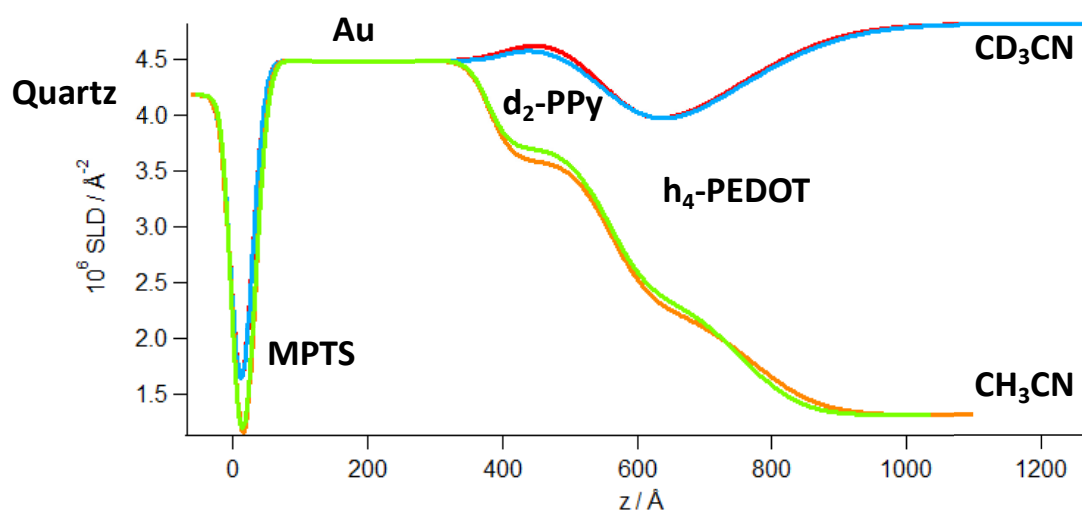


**Figure 5.42** SLD profiles of the d<sub>2</sub>-PPy/h<sub>4</sub>-PEDOT bilayer after repetitive cycling: fully oxidised at 800 mV in CD<sub>3</sub>CN (red) and CH<sub>3</sub>CN (green); and fully reduced at 0 mV in CD<sub>3</sub>CN (cyan) and CH<sub>3</sub>CN (orange) shown in **Figures 5.41**.

The fit parameters used for the solvated d<sub>2</sub>-PPy/h<sub>4</sub>-PEDOT bilayer are given in **Tables 5.27** and **5.28**.

Layer	$d / \text{\AA}$	$10^6 N_b / \text{\AA}^{-2}$	$\sigma / \text{\AA}$
CH <sub>3</sub> CN/CD <sub>3</sub> CN	Bulk	1.320/4.756	N/A
h <sub>4</sub> -PEDOT		2.368/3.188	69.6/91.0
d <sub>2</sub> -PPy		3.708/4.672	47.4/47.4
Au		4.490	24.3/23.5
MPTS		0.266	15.5/15.3
Quartz	Bulk	4.182	12.2/12.0

**Table 5.27** Fit parameters for the oxidised d<sub>2</sub>-PPy/h<sub>4</sub>-PEDOT film in CH<sub>3</sub>CN (green) and CD<sub>3</sub>CN (red) shown in **Figures 5.41**.

Layer	$d / \text{\AA}$	$10^6 N_b / \text{\AA}^{-2}$	$\sigma / \text{\AA}$
CH <sub>3</sub> CN/CD <sub>3</sub> CN	Bulk	1.32/4.735	N/A
h <sub>4</sub> -PEDOT		2.296/3.213	81.5/80.7
d <sub>2</sub> -PPy		3.595/4.613	46.4/48.9
Au		4.490	26.3/26.0
MPTS		0.266	14.3/14.9
Quartz	Bulk	4.182	13.8/13.8

**Table 5.28** Fit parameters for the reduced d<sub>2</sub>-PPy/h<sub>4</sub>-PEDOT film in CH<sub>3</sub>CN (orange) and CD<sub>3</sub>CN (cyan) shown in **Figures 5.41**.

The d<sub>2</sub>-PPy/h<sub>4</sub>-PEDOT bilayer showed remarkable stability during cycling when compared to the h<sub>4</sub>-PEDOT/d<sub>2</sub>-PPy bilayer in **Section 5.4.1**. Aside from a slight increase in roughness of the polymer/solvent interface the film properties before and after cycling are almost the same.

After the neutron experiment the bilayer film was analysed by AFM. The results are shown in

**Figure 5.43.**

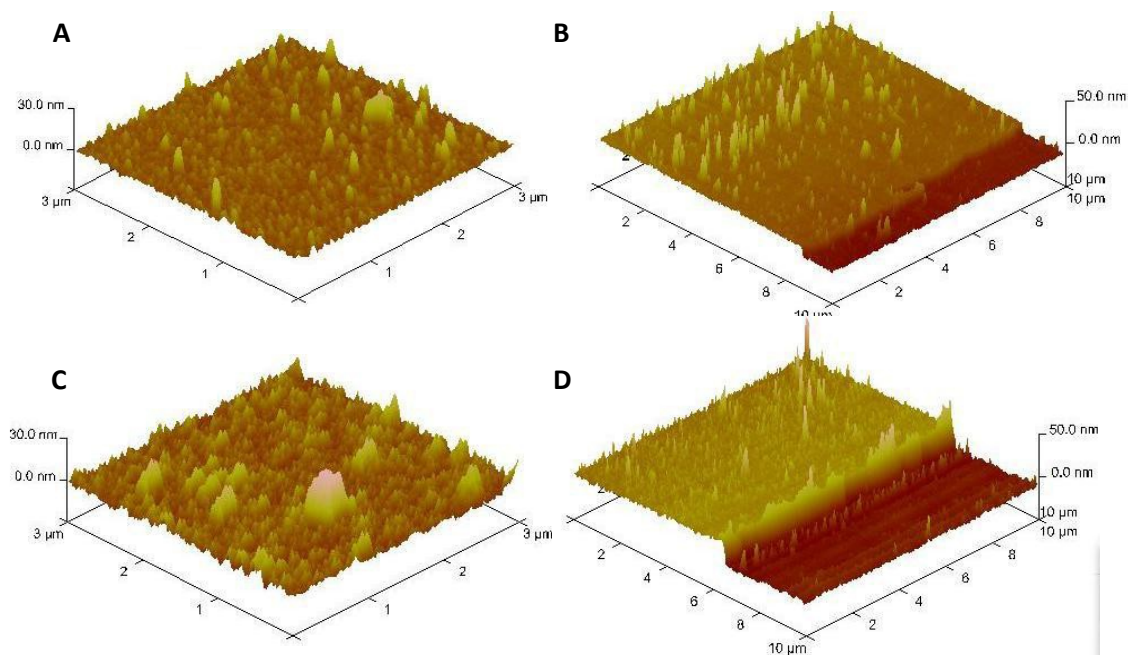


**Figure 5.43** AFM images of the  $d_2$ -PPy/ $h_4$ -PEDOT bilayer after the neutron experiment:  $d_2$ -PPy surface (A) and step height (B);  $d_2$ -PPy/ $h_4$ -PEDOT surface (A) and step height (B).

This *ex situ* measurement showed the  $d_2$ -PPy single layer to be 130 Å thick, which is entirely consistent with the NR measurements of the dry film (**Table 5.14**). The dry *ex situ* thickness of the  $d_2$ -PPy/ $h_4$ -PEDOT film was 302 Å.

## 5.5. Conclusions

The properties of two multicomponent layer by layer deposition systems were explored using neutron reflectivity. The first comprised PEDOT and PFPF, which showed interesting properties in terms of segregation. The fitting of the NR data revealed two distinct polymer layers, which showed a large degree of interpenetration at the polymer/polymer interface parameterised as a high roughness factor at the polymer/polymer interface. This roughness factor increased with time meaning that the two polymer layers become more interdiffused over time which would allow more capacitive behaviour.

The thickness of the inner PEDOT layer increased during oxidation due to an increase in solvation from  $\phi_s = 0.49$  to  $\phi_s = 0.51$  as well as the ingress of perchlorate anions to counteract the positive charge shared over every three monomer units of PEDOT. However, over time the PFPF layer also hydrolysed to PPyCOOH, complicating the interpretation by the introduction of a time dependent effect. This meant that it was unclear whether the observed changes were a result of polymer backbone interactions or due to the chemical change occurring on the functionalised nitrogen of the PPy backbone in the PFPF.

In order to better understand the effects of redox states and time on the segregation and solvation of multi-layered films a chemically stable set of bilayers, based on PEDOT and PPy were also analysed. This removed the added variable of hydrolysis seen in the PFPF layers and focused solely on the properties of the conducting pyrrole backbone.

It was found that the order of the respective polymers in the multi-layered system greatly affected the properties and stability of the bilayers. As the nature of the polymer/polymer interface is central to the rectifying (segregated) or capacitive (interdiffused) characteristics of the multi-layered films understanding this means that bi- or multi-layer film properties can be tuned based on the order in which the layers are deposited.

Depositing PEDOT first leads to a greater degree of polymer/polymer interfacial roughness which increases with repetitive cycling, whereas depositing PPy first leads to a higher degree of segregation which remains remarkably stable during repetitive cycling. This is significant as the properties of multi-layered systems can be tuned by the individual components deposition sequence, to actively select interpenetration/segregation, depending on whether capacitive or rectifying effects are desired.

## 5.6. References

- <sup>1</sup> Billmeyer, F. W., Textbook of Polymer Science, John Wiley & Sons, 1984, 3<sup>rd</sup> edition, Chapter 5
- <sup>2</sup> Kranz, C., Wohlschlager, H., Schmidt, H.L., Schuhmann, W., *Electroanalysis*, **10**, 1998, 546–552.
- <sup>3</sup> Hao, Q., Wang, X., Lu, L., Yang, X., Mirsky, V. M., *Macromol. Rapid Commun.*, 2005, **26**, 1099–1103.
- <sup>4</sup> Kranz, C., Wohlschlaeger, H., Schmidt, H. L., Schuhmann, W., *Electroanal.*, 1998, **10**, 546.
- <sup>5</sup> Lukkari, J., Salomaeki, M., Aeaeritalo, T., Loikas, K., Laiho, T., Kankare, J., *Langmuir* 2002, **18**, 8496.
- <sup>6</sup> Skotheim, T. A., Elsenbaumer, R. A., and Reynolds, J. R., (1998) “*Handbook of Conducting Polymers*”, Marcel Dekker, New York.
- <sup>7</sup> Oliver, R., Munoz, A., Ocampo, C., Aleman, C., and Estrany, F., *Chem. Phys.*, 2006, **328**, 299.
- <sup>8</sup> Ocampo, C., Aleman, C., Oliver, R., Arnedillo, M. L., Ruiz, O., and Estrany, F., *Polymer Int.*, 2007, **56**, 803.
- <sup>9</sup> Ocampo, C., Aleman, C., Oliver, R., Armelin, E., and Estrany, F., *J. Polymer Res.*, 2006, **13**, 193.
- <sup>10</sup> Aradilla, D., Estrany, F., and Aleman, C., *J. Phys. Chem.*, 2011, **115**, 8430–8438.
- <sup>11</sup> Sellam and Hashmi, S. A., *ACS Appl. Mater. Interfaces*, 2013, **5**, 3875–3883.

<sup>12</sup> A. Nelson, *J. Appl. Crystallogr.*, 2006, **39**, 273.

<sup>13</sup> Alemán, C., Casanovas, J., Torras, J., Bertrán, O., Armelin, E., Oliver R, *Polymer*, 2008, **49**, 1066.

# 6. Thiophene-Pyrrole Comonomer: a Promising Material for Rechargeable Batteries

---

## 6.1. Introduction

Electronically conducting polymers based on functionalised pyrrole and thiophene monomer units have continued to generate academic interest due to their wide range of potential applications. These include portable power supplies (supercapacitors<sup>1,2</sup> and batteries<sup>3</sup> of various types) for numerous mobile or remotely operated electronic entities, from implantable clinical devices<sup>4</sup>, through mobile phones<sup>5</sup> and computers<sup>6-10</sup>.

One of these energy storage applications is the creation of a new class of fast rechargeable zinc/polymer batteries for hybrid/small electric vehicle applications<sup>11</sup>. This has been the primary focus of the Polyzion project<sup>12</sup> (E.U. FP7 funded framework programme).

In the current market electric vehicles use either lead acid (e.g. Ford Ranger EV), NiMH (e.g. Toyota Prius) or lithium ion batteries (post 2004 Toyota Prius)<sup>13</sup>. However, lead acid and NiMH batteries have limited power and energy density resulting in the need for a large number of cells to sustain the high output current required in an electric vehicle. Lithium ion batteries have a high output but suffer from other drawbacks, such as decreased lifetime compared to lead acid/NiMH batteries, as well as temperature dependent performance and safety concerns over the structure of the batteries themselves, which are sealed in a polymer bag that may rupture upon impact. In some instances, they may not be sufficiently lightweight or well suited to fabrication as an integrated part of the device.

The Polyzion initiative is working towards a novel Zn cathode/polymer anode battery, which aims to overcome these issues. The electrochemical redox properties of pyrrole and thiophene have been widely investigated<sup>14-19</sup>. However, their prospective application as part of a charge storage device is hindered by the rate of (dis)charge/available current density, the available voltage and (electro)chemical stability to repetitive charge/discharge cycling.

Polyzion are aiming to combine conducting polymers with the novel properties of choline chloride based Deep Eutectic Solvents (DES) which have wide electrochemical windows, high stability and low toxicity as well as being relatively cost effective.

In energy storage devices, the movement of ions and solvent into/out of the polymer film during redox cycling is key to the DC capacitance behaviour (extent of charge storage), as well as adhesion/stability of the film. This chapter will discuss the behaviour of polymer films derived from the novel comonomer 2-thiophen-2-yl-1H pyrrole (ThPy) in both a conventional organic electrolyte ( $\text{LiClO}_4$  in acetonitrile) and the DES Ethaline. Specifically, NR will be used to probe the vertical structure of P(ThPy) in terms of thickness, roughness and any differences in solvation and doping levels in the depth profile.

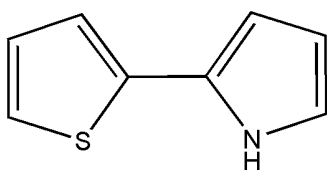


**Figure 6.1** Novel ThPy comonomer.

## 6.2. Experimental

The neutron-electrochemical cell as described previously<sup>20</sup> consists of a Teflon spacer (forming the walls) between a ~30 nm thin-film Au working electrode mounted on a quartz block and a Pt coated Ti gauze counter electrode mounted on a glass block. Also incorporated into the cell was a Ag/AgCl wire pseudo reference electrode.

### 6.2.1. Electrode Fabrication

The working electrode was prepared by sputter coating gold onto a polished single-crystal quartz block (80 x 50 mm, Mark Optics) coated with a monolayer of 3-mercaptopropyltrimethoxysilane (Sigma Aldrich) to promote adherence. Poly-(thiophene-pyrrole) was grown potentiodynamically ( $-0.3 < E/V$  vs. Ag/AgCl (saturated KCl)  $<$  anodic limit  $I_{\max} = 4$  mA,  $v = 20$  mVs<sup>-1</sup>, 30 cycles) from thiophene-pyrrole (25 mM) in LiClO<sub>4</sub> (0.1 M) in acetonitrile.

### 6.2.2. Neutron Reflectivity Measurements

Neutron reflectivity measurements were performed on FIGARO<sup>21</sup> at the Institut Laue-Langevin, Grenoble, France. The reflectivity of the films was measured dry in air as well as in h<sub>4</sub>/d<sub>4</sub>-ethaline and h<sub>3</sub>/d<sub>3</sub>-acetonitrile. Deuterated solvents were used to maximise contrast between the polymer and the electrolyte so that the solvation properties of the polymer could be probed. In total three films were studied. Two of the films were held at static potentials, one in acetonitrile/LiClO<sub>4</sub> (0.1 M) [P(ThPy)-1] and one in Ethaline [P(ThPy)-2]. Both films were held in both their fully oxidised (0.5 and 0.55 V respectively) and fully reduced (-0.2 and -0.22 V) states. The third film [P(ThPy)-3] was cycled in acetonitrile/LiClO<sub>4</sub> ( $-0.2 < E < 0.5$  V,  $v = 1$  mV s<sup>-1</sup>) whilst kinetic measurements were taken every 50 mV, i.e. every 50 seconds. The reflectivity of the films was measured at incident angles of 0.624 and 2.5° when dry and solvated in ethaline and at 0.312, 0.624, and 2.5° when solvated in acetonitrile. This provided momentum transfer ranges of  $0.004 < Q/\text{\AA}^{-1} < 0.15$  and of  $0.007 < Q/\text{\AA}^{-1} < 0.15$ , respectively. The collimation slits were set to give a beam footprint on the sample of 60 mm x 30 mm and a momentum transfer (Q) resolution of 2.1 %. Data acquisition times were ca. 2hrs per run. Model fitting of the reflectivity profiles was performed using Motofit software<sup>22</sup>.

## 6.3. Results

### 6.3.1. Electropolymerisation of P(Th-Py)

P(ThPy) films were deposited potentiodynamically with an anodic current cap applied ( $i_{\max} = 0.1 \text{ mA cm}^{-2}$ ) to inhibit film roughness by limiting the amount of oxidation/polymerisation within each cycle. Two of the films were grown from the same batch of monomer [P(ThPy)-1 and P(ThPy)-2]. Both their growth cycles and post growth characterisation in monomer free electrolyte (0.1 M  $\text{LiClO}_4/\text{acetonitrile}$ ) were very similar as shown in **Figures 6.2-4**.

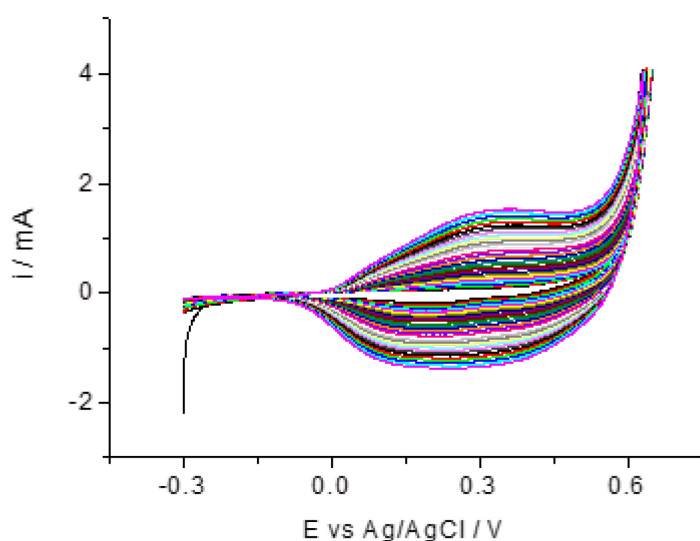


**Figure 6.2** Cyclic voltammogram showing the growth of P(ThPy)-1 (26.7 mM) in acetonitrile (0.1 M) [ $-0.3 < E/\text{V vs. Ag/AgCl (wire)} < \text{anodic limit } I_{\max} = 0.1 \text{ mA cm}^{-2}, v = 20 \text{ mV s}^{-1}, 30 \text{ cycles}$ ].

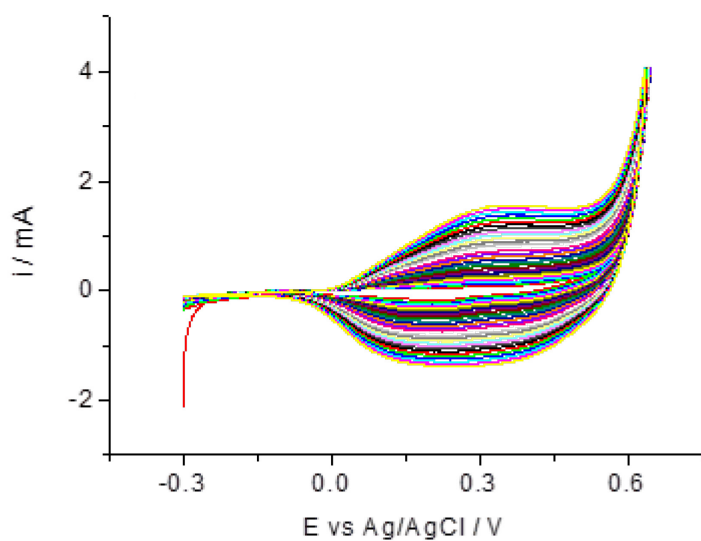


**Figure 6.3** Cyclic voltammogram showing the growth of P(ThPy)-2 (26.7 mM) in acetonitrile (0.1 M) [ $-0.3 < E/V$  vs. Ag/AgCl (wire)  $<$  anodic limit  $I_{\max} = 0.1$  mA  $\text{cm}^{-2}$ ,  $v = 20$   $\text{mV s}^{-1}$ , 30 cycles].

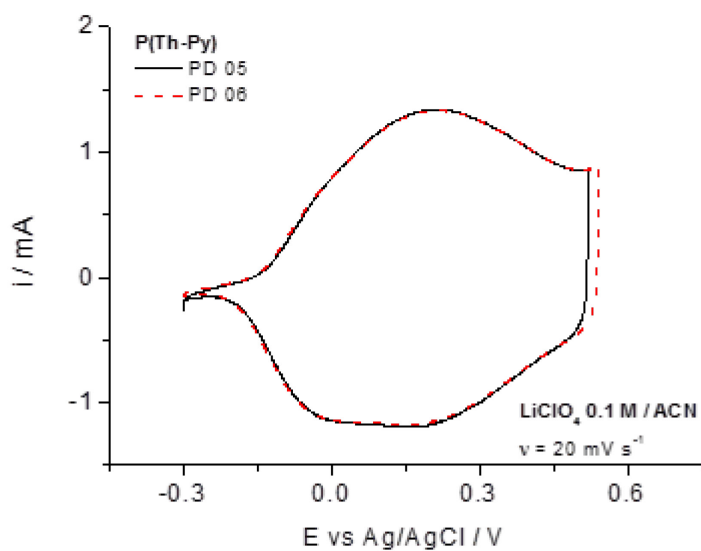


**Figure 6.4** Post polymerisation characterisation of P(ThPy)-1 and P(ThPy)-2 in monomer-free electrolyte.

However, P(ThPy)-3 was grown from a different batch of ThPy monomer under the same conditions and exhibited a similar growth curve but showed an increase in  $I_a$  and  $I_c$  compared with the first 2 films.

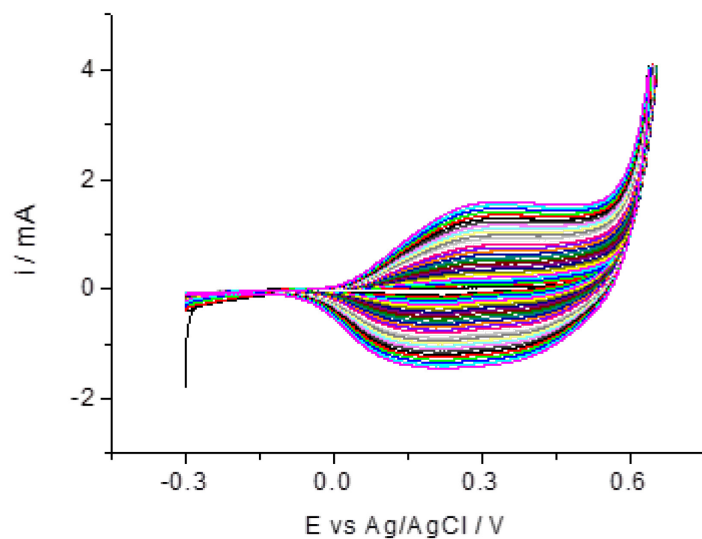


**Figure 6.5** Cyclic voltammogram showing the growth of P(ThPy)-3 (19.6 mM) in acetonitrile (0.1 M) [ $-0.3 < E/V$  vs. Ag/AgCl (wire)  $<$  anodic limit  $I_{\max} = 0.1 \text{ mA cm}^{-2}$ ,  $v = 20 \text{ mV s}^{-1}$ , 30 cycles].

**Figure 6.6** shows a comparison of the final growth cycle for all three P(ThPy) films, which shows excellent reproducibility.

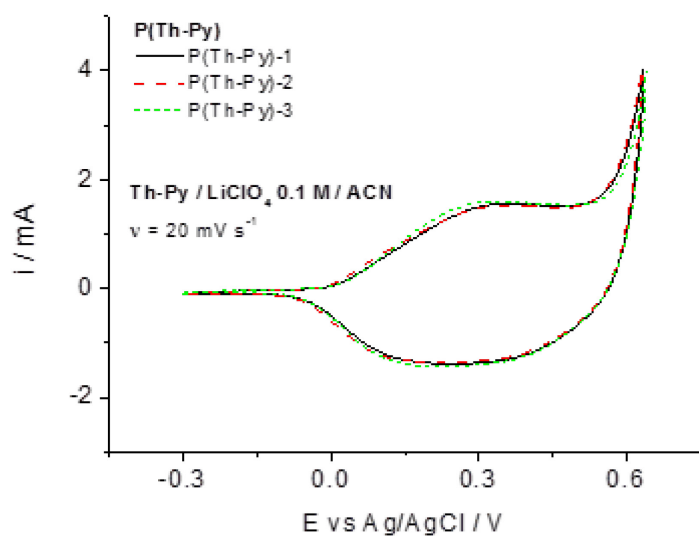


**Figure 6.6** Comparison of the final growth cycle of all three P(ThPy) films.

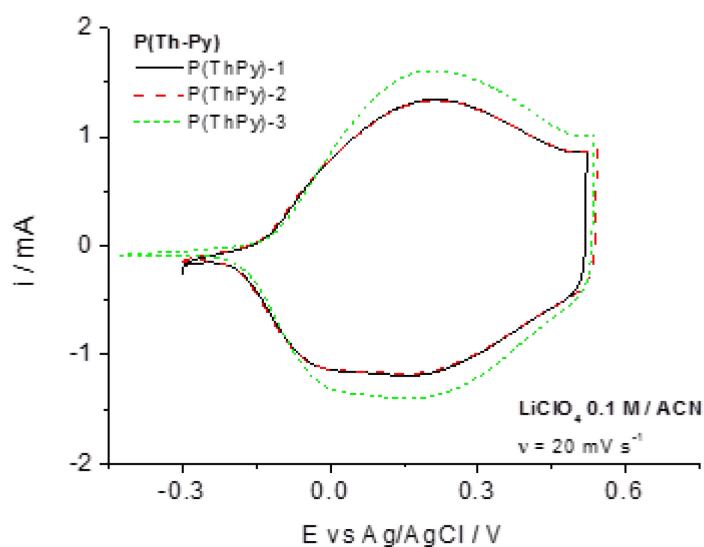


**Figure 6.7** Comparison of post growth characterisation in monomer electrolyte between batch one [P(ThPy)-1 and P(ThPy)-2] and batch two [P(ThPy)-3] of the ThPy monomer.

Despite having similar polymerisation currents, the two batches showed significant variations in film thickness both when estimated using coulometry from CVs taken before the

experiment (**Figure 6.7**) and when measured with the AFM after the neutron experiment (**Figure 6.8**). Coulometric calculations of the surface coverage, ( $\text{mol cm}^{-2}$ ,  $\Gamma = q/nFA$ ) were 26, 25 and  $30 \text{ nmol cm}^{-2}$ , respectively for the three films. For compact, solvent-free (“dry”) films, these would correspond to film thicknesses of ca. 282, 284 and  $340 \text{ \AA}$ , respectively. AFM measurements showed that films 1 and 2 were 220 and  $248 \text{ \AA}$  thick, respectively whereas film 3 was  $344 \text{ \AA}$  thick. This accounts for the increase in  $I_a$  and  $I_c$  of film 3 in **Figure 6.7**.

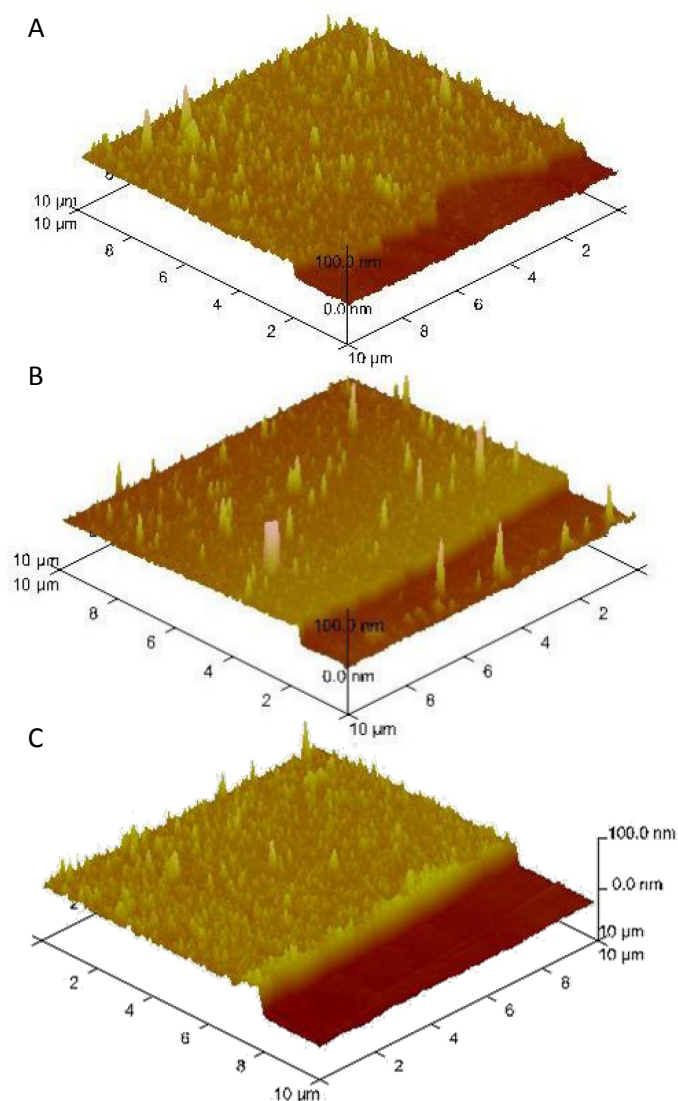


**Figure 6.8** AFM images showing the step heights of films 1-3 (A-C respectively).

Despite this difference in thickness the topographical roughness measured by the AFM was similar for all 3 films (ca. 5 nm).

## 6.3.2. Neutron Reflectivity

### 6.3.2.1. Measurements of Dry Films

Prior to any electrochemical measurements, all three P(ThPy) films were characterised in the dry state by neutron reflectivity. In the case of dry film NR measurements, both the incident and reflected neutron beams travel through air (**Figure 6.9**) i.e. reflection occurs at the polymer/air interface.

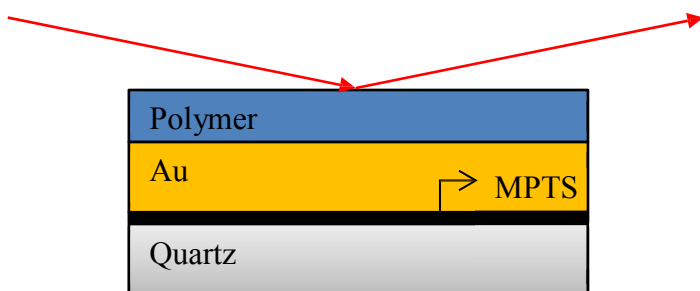


**Figure 6.9** Schematic representation of a dry film neutron reflection.

In the case of P(ThPy) the scattering length density of the polymer films ( $N_b$ ) can be expressed in terms of the volume fractions ( $\phi$ ) of the polymer film and any additional media such as air or solvent/electrolyte.

**Equation 6.1**

As the scattering length density ( $N_b$ ) of air =  $0 \text{ \AA}^{-2}$  then the latter half of **Equation 6.1** can be ignored so that:

**Equation 6.2**

This allows us to calculate the dry film density of the polymer film.

$\Sigma$

**Equation 6.3**

This provides a good estimation when calculating the volume fractions of polymer and solvent in any future solvated film measurements.

**Figure 6.10** shows the dry film NR measurements of the three P(ThPy) films after deposition from the two bespoke monomer solutions. As seen in previous chapters, at  $Q < 0.0144 \text{ \AA}^{-1}$  total external reflection is observed ( $R = 1$ ) in the form of a critical edge as a result of air having a lower scattering length density (SLD) than quartz ( $\Delta N_b = 4.182 \text{ \AA}^{-2} \times 10^{-6}$ ).

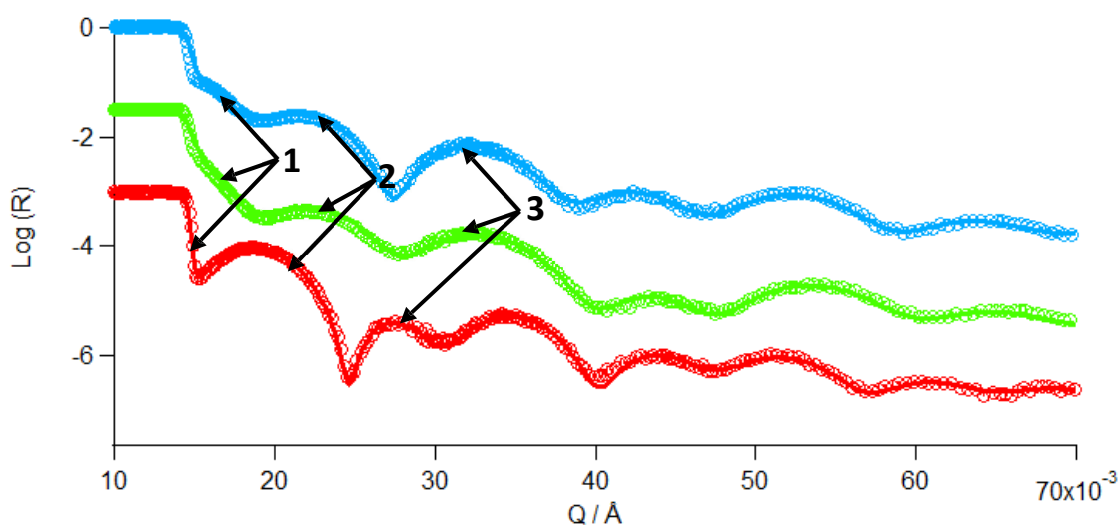


**Figure 6.10** Dry film neutron reflectivity profiles (FIGARO, ILL) of the three films: P(ThPy)-1 (cyan), P(ThPy)-2 (green) and P(ThPy)-3 (red). The circles represent the raw data and the line is the fit of that data ( $\chi^2 = 2.1-2.5$ ).  $R(Q)$  profiles are manually offset in reflectivity for visual clarity.

P(ThPy)-1 and P(ThPy)-2 were from the same batch of monomer and AFM measurements showed they were similar in thickness (229.7 and 220.7  $\text{\AA}$ , respectively) as expected due to **Figure 6.8**. This is supported by the fact that the  $d$  spacing of the fringes in **Figure 6.10** is almost the same for both films. P(ThPy)-3 on the other hand shows a decrease in the fringe spacing. This is hard to see as the reflectivity profiles look so different. Simplistically, if one looks at the first three fringes labelled in **Figure 6.2**, the first fringe seen in P(ThPy)-1 and P(ThPy)-2 disappears into the critical edge in the reflectivity profile of P(ThPy)-3. The second

fringe is more defined in the P(ThPy)-3 R(Q) profile and the third fringe clearly shows a decrease in the fringe spacing which is indicative of the film being thicker (354.3 Å) as Q is in reciprocal space.

However, the fringes are less well defined in the P(ThPy)-2 trace than in the other two which indicates a roughening of one or more of the layers in the system. **Figure 6.11** shows the corresponding scattering length density (SLD) profiles of the three dry films. Here we can see that the binding layer of MPTS is much thinner than in the other two films and has a higher thickness:interfacial ratio. This was attributed to using non-degraded MPTS in the silanisation process for P(ThPy)-1 and 3.

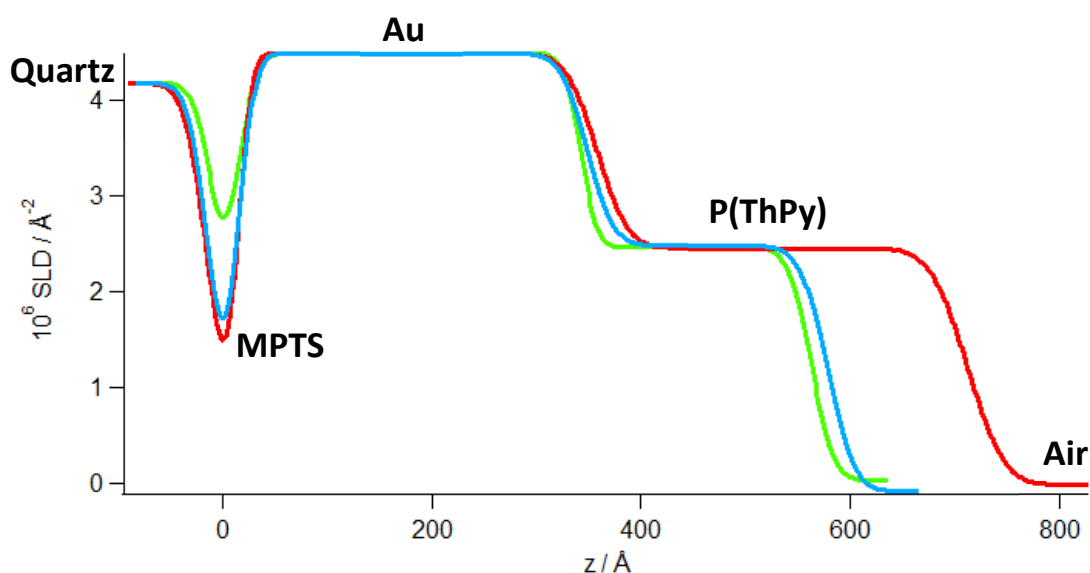


**Figure 6.11** SLD profiles of the three films shown in **Figure 6.10**: P(ThPy)-1 (cyan), P(ThPy)-2 (green) and P(ThPy)-3 (red).

The fit parameters used in **Figure 6.10** are summarised in **Tables 6.1-3**.

Layer	$d / \text{\AA}$	$10^6 N_b / \text{\AA}^{-2}$	$\sigma / \text{\AA}$
Air	Bulk	0	N/A
P(ThPy)-1	229.7	2.486	20.7
Au	334.5	4.490	20.3
MPTS	26.2	0.266	12.6
Quartz	Bulk	4.182	16.3

**Table 6.1** Summary of the fit parameters used in **Figure 6.10** for P(ThPy)-1.

Layer	$d / \text{\AA}$	$10^6 N_b / \text{\AA}^{-2}$	$\sigma / \text{\AA}$
Air	Bulk	0	N/A
P(ThPy)-2	220.7	2.468	17.2
Au	332.9	4.490	12.8
MPTS	15.0	0.266	15.0
Quartz	Bulk	4.182	15.0

**Table 6.2** Summary of the fit parameters used in **Figure 6.10** for P(ThPy)-2.

Layer	$d / \text{\AA}$	$10^6 N_b / \text{\AA}^{-2}$	$\sigma / \text{\AA}$
Air	Bulk	0	N/A
P(ThPy)-3	354.3	2.460	27.9
Au	343.5	4.490	23.4
MPTS	27.9	0.266	10.3
Quartz	Bulk	4.182	17.9

**Table 6.3** Summary of the fit parameters used in **Figure 6.10** for P(ThPy)-3.

The SLDs of all three P(ThPy) films were between  $2.460\text{-}2.486 \times 10^{-6} \text{\AA}^{-2}$  which corresponds to a density range of  $1.29\text{-}1.30 \text{ g cm}^{-3}$ . This shows the growth to be remarkably consistent at producing films of similar structures. All three films showed one uniform layer of polymer, indicating that there was no dense inner layer/diffuse outer. This is promising for its potential application in the charge storage industry as it should “react” uniformly during redox switching maximising its charge storage capacity.

### 6.3.2.2. *P(ThPy)-1: Static NR Measurements of P(ThPy) in LiClO<sub>4</sub>/acetonitrile*

Before analysing this novel copolymer's behaviour in a novel DES its behaviour was first characterised in a traditional electrolyte medium, LiClO<sub>4</sub> in acetonitrile. To achieve this, P(ThPY)-1 was held in oxidised (p-doped, 0.50 V) and reduced (undoped, -0.2 V) states in both hydrogenous and deuterated acetonitrile. Both contrasts were used to more accurately measure the solvent volume fraction ( $\phi_{ACN}$ ) and track the movement of any counterions into and out of the film during the static holds at the extreme redox states (fully oxidised and reduced). The R(Q) profiles from these measurements are shown in **Figure 6.12**.

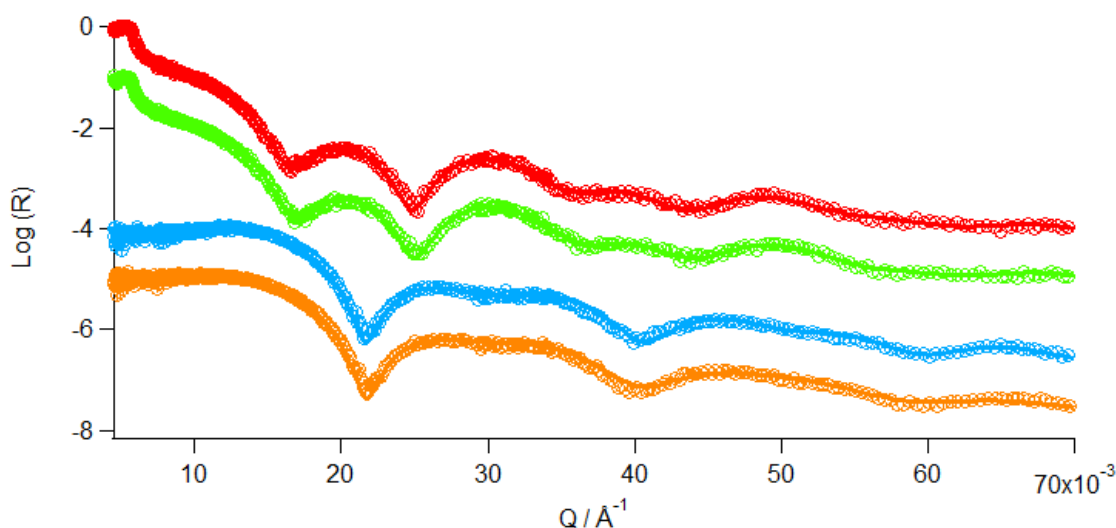


**Figure 6.12** NR profiles of P(ThPy)-1 in LiClO<sub>4</sub>/acetonitrile: oxidised (red) and reduced (green) in CD<sub>3</sub>CN; oxidised (cyan) and reduced (orange) in CH<sub>3</sub>CN ( $\chi^2 = 1.3-1.6$ ). R(Q) profiles are manually offset in reflectivity for visual clarity.

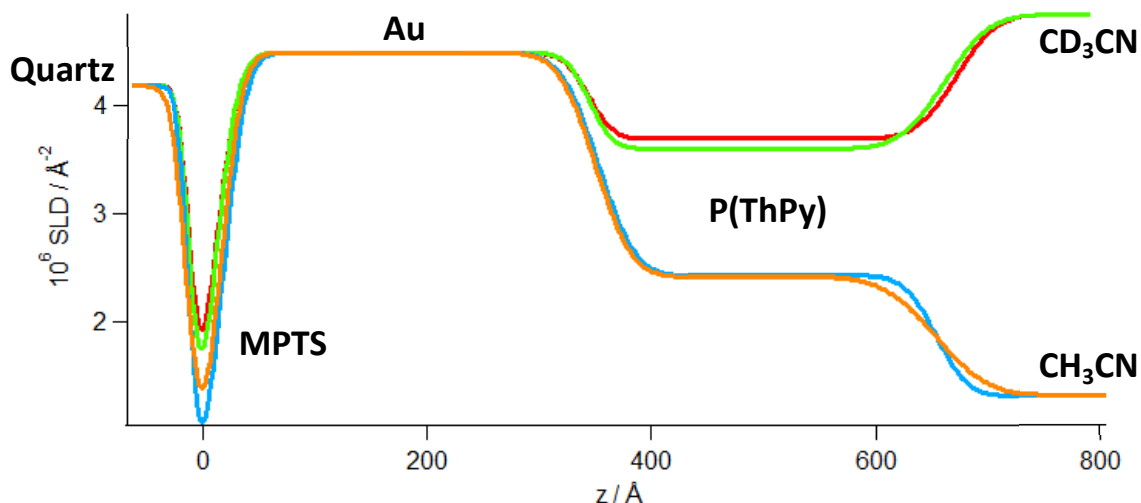


**Figure 6.13** SLD profiles of P(ThPy)-1 in  $\text{LiClO}_4/\text{acetonitrile}$ : oxidised (red) and reduced (green) in  $\text{CD}_3\text{CN}$ ; oxidised (cyan) and reduced (orange) in  $\text{CH}_3\text{CN}$ .

The film parameters used in the fit parameters for the oxidised and reduced films are given in **Tables 6.4 and 6.5**.

Layer	$d / \text{Å}$	$10^6 N_b / \text{Å}^2$	$\sigma / \text{Å}$
$\text{CH}_3\text{CN} / \text{CD}_3\text{CN}$	Bulk	1.320/4.843	N/A
P(ThPy)	301.1/328.0	2.430/3.695	22.4/27.9
Au	335.0	4.490	25.9/17.4
MPTS	30.5/20.5	0.266	16.5/17.4
Quartz	Bulk	4.182	9.0

**Table 6.4** Fit parameters for the oxidised film in  $\text{CH}_3\text{CN}$  (cyan) and  $\text{CD}_3\text{CN}$  (red) **Figure 6.12**.

Layer	$d / \text{\AA}$	$10^6 N_b / \text{\AA}^{-2}$	$\sigma / \text{\AA}$
CH <sub>3</sub> CN / CD <sub>3</sub> CN	Bulk	1.320/4.842	N/A
P(ThPy)	303.6/316.9	2.415/3.604	37.0/31.3
Au	335.0	4.490	25.5/16.2
MPTS	28.7/21.6	0.266	15.7/16.6
Quartz	Bulk	4.182	9.0

**Table 6.5** Fit parameters for the reduced film in CH<sub>3</sub>CN (orange) and CD<sub>3</sub>CN (green) in **Figure 6.12**.

The slight discrepancies between the fit parameters for the Au and MPTS layers between measurements are due to a problem experienced on the experiment with sample misalignment. This produced an offset in the sample angle  $\theta$  which in turn caused a change in the reflected pixel position on the instruments detector. This caused both the reflectivity data to shift in its value of  $Q$  and the fringes to stretch/compress. This meant that the position of the critical edge was offset and that the different angles measured did not overlap, so that the data at different incident angles could not be spliced.

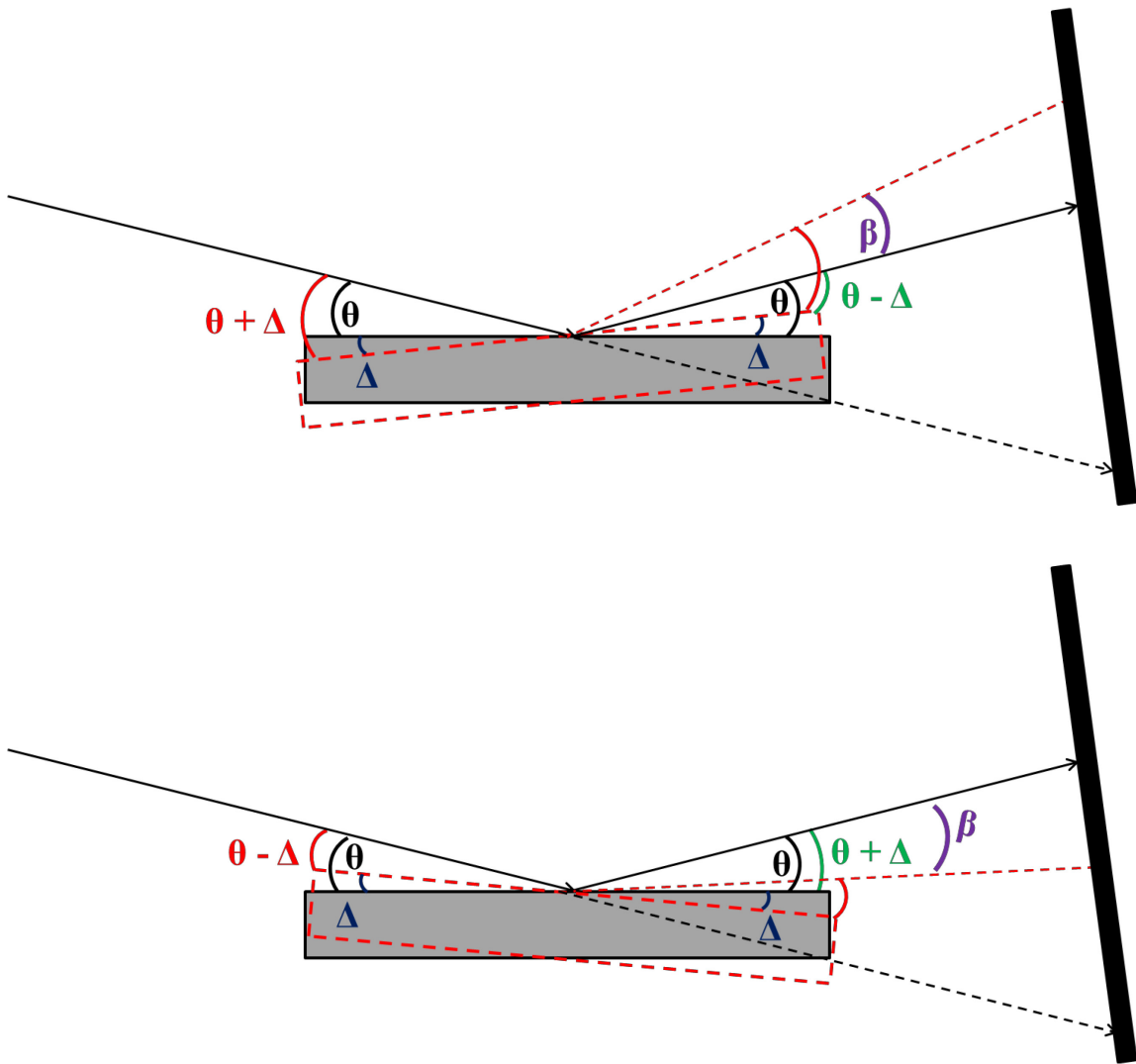


**Figure 6.14** Schematic of the 2 variations in sample angle misalignment seen in this data set.  $\theta$  is the intended sample angle and  $\Delta$  is the offset due to misalignment.  $\beta$  is the difference in pixel position on the detector [ $\beta = (\theta + \Delta) - (\theta - \Delta) = 2\Delta$ ].

This difference in pixel position was corrected for by manually calculating the correct pixel position on the detector, using the known position of the critical edge in the air measurement, and manually adjusting the value until  $Q_c$  and the overlap issues were corrected for all data sets.

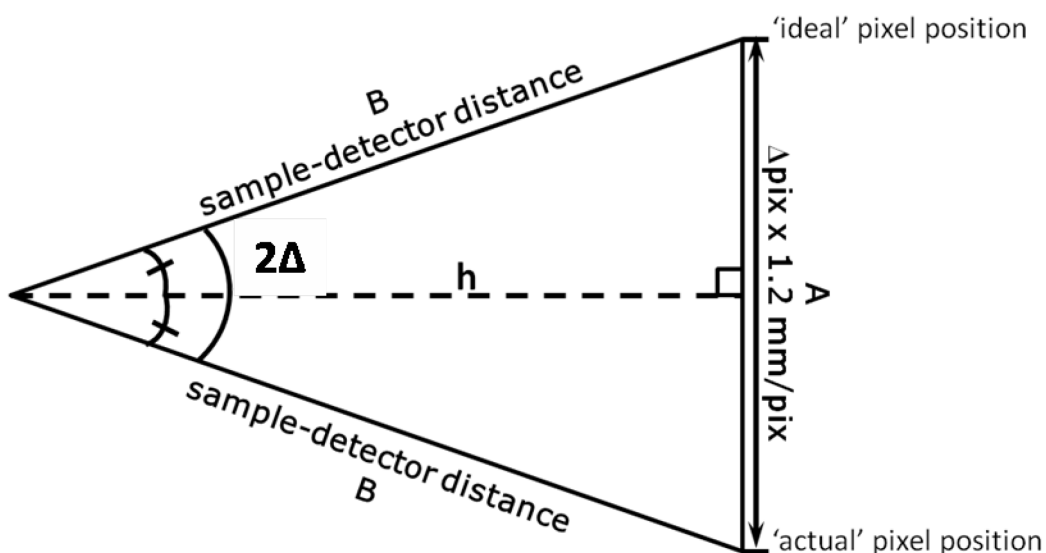


**Figure 6.15** Schematic showing the geometry applied in the  $\theta$  correction process.

The offset ( $\Delta$ ) in sample angle ( $\theta$ ) was calculated as follows:

$$\frac{\Delta \text{pix} \times 1.2 \text{ mm/pix}}{D}$$

**Equation 6.4**

**Equation 6.5**

where  $\Delta \text{pix}$  is the offset from the "ideal" pixel position, 1.2 is the pixel size (mm/pix) and  $D$  is the distance between the sample and the detector (2808.6 mm).  $\Delta \text{pix}$  was calculated to be 63.56.

Whilst the application of this correction set corrected the data, the samples were all slightly misaligned and each alignment was different causing the area of the polymer film beneath the footprint of the neutron beam to be different after each alignment. This meant that the lateral averaging over the areas was slightly different in each measurement accounting for the discrepancies in the chemically/physically unchanging layers in the system.

The total film thickness is 317 Å when reduced (un-doped). This equates to 87 Å or 38 % film swelling upon solvation. As seen in previous chapters there are apparent differences in

thickness and roughness of the polymer film between hydrogenous and deuterated measurements due to the differences in reflectivity contrast. The solvent volume fraction ( $\phi_{\text{ACN}}$ ) was calculated as 0.49 using **Equation 6.1**.

Upon oxidation, a further film swelling of 11 Å was observed corresponding to the incorporation of two anions to every three ThPy monomer units to compensate for the positive charge that delocalises over every three rings in the polymer backbone. There was no change in the overall solvation of the P(ThPy) film.

Once the movement of counterions, film solvation and physical characteristics had been quantified in this traditional electrolyte a second film was subjected to the same protocol in the deep eutectic solvent Ethaline (shown in **Section 6.3.2.3**).

#### ***6.3.2.3. P(ThPy)-2: Static NR Measurements of P(ThPy) in Ethaline***

P(ThPY)-2 was held in its oxidised (p-doped, 0.55 V) and reduced (undoped, -0.22 V) states in both hydrogenous and deuterated Ethaline. The fact that Ethaline is a mixture of two components, ethylene glycol and choline chloride, gave an added advantage of deuterating one component allowing an additional contrast between the resultant cations and anions highlighting and distinguishing between their movements within the film. D<sub>4</sub>-ethylene glycol was chosen. The measured reflectivity and SLD profiles are given in **Figures 6.16** and **6.17**.

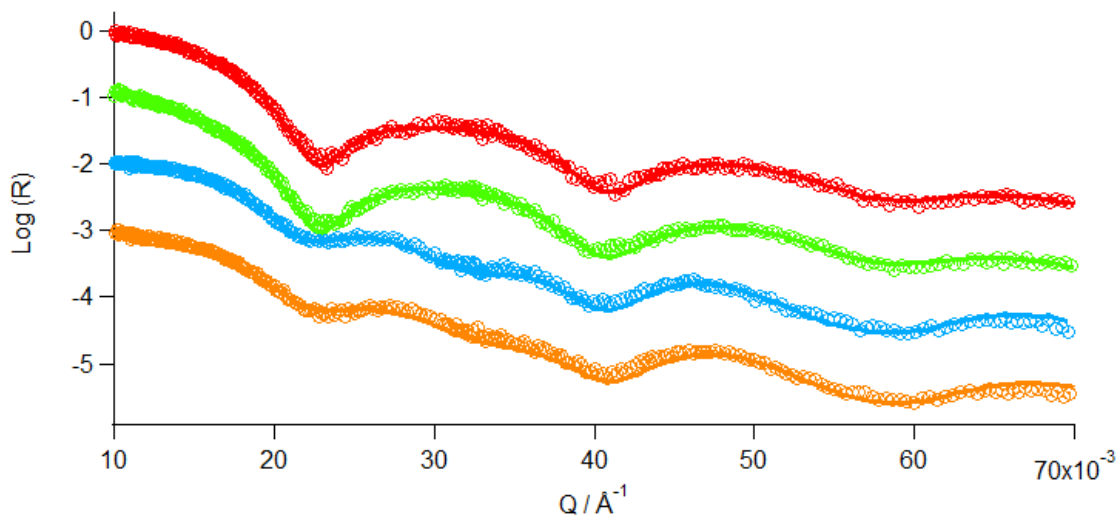


**Figure 6.16** NR profiles of P(ThPy)-2 in Ethaline: oxidised (red) and reduced (green) in  $d_8$ -Ethaline; oxidised (cyan) and reduced (orange) in h-Ethaline ( $\chi^2 = 1.9$ -2.5). R(Q) profiles are manually offset in reflectivity for visual clarity.

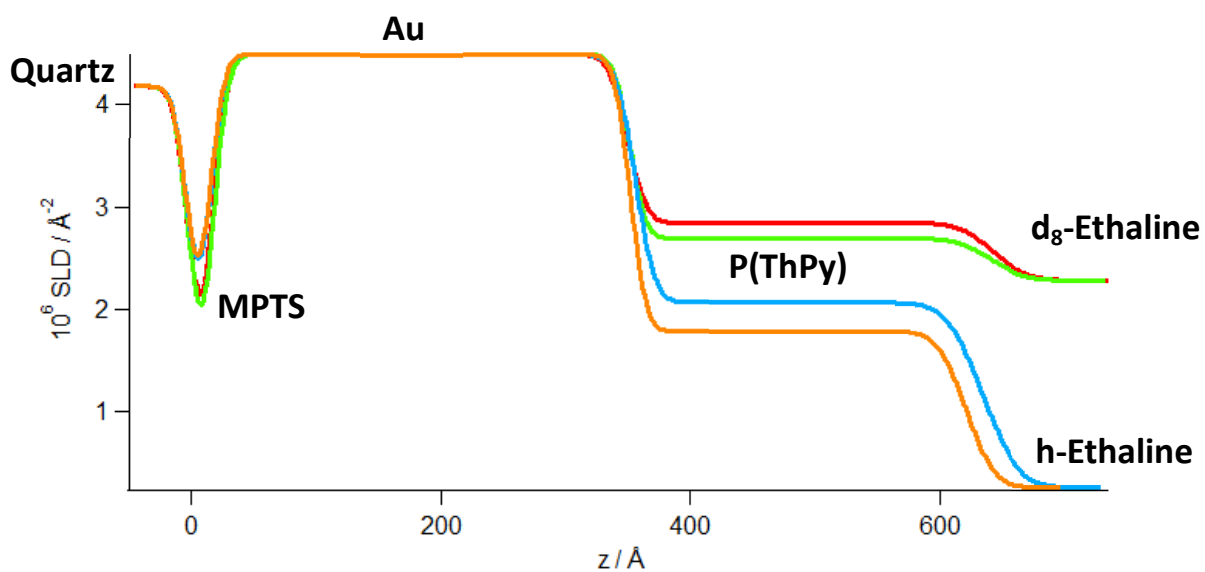


**Figure 6.17** SLD profiles of P(ThPy)-2 in Ethaline: oxidised (red) and reduced (green) in  $d_8$ -Ethaline; oxidised (cyan) and reduced (orange) in h-Ethaline ( $\chi^2 = 1.8$ -2.5).

The lack of a critical edge in the R(Q) for the film immersed in deuterated Ethaline is because there are still 18 hydrogen atoms present and only 8 atoms of deuterium. This means that the SLD of  $d_8$ -Ethaline is  $2.290 \times 10^{-6} \text{ \AA}^{-2}$  meaning that  $\Delta N_b$  is negative (see **Equation 2.22**). This

complicated the fitting process as there is no way to calculate the scale factor for the data so one has to be calculated by batch fitting all four data sets to find a scale factor that works in all cases. In fact, the roles of the hydrogenous and deuterated solvent are now reversed, compared to what has previously been seen in acetonitrile, as there is now more contrast between the hydrogenous Ethaline and P(ThPy) than there is with the deuterated Ethaline.

The film parameters used in the fit parameters for the oxidised and reduced films are given in **Tables 6.6** and **6.7**.

Layer	d / Å	$10^6 N_b / \text{Å}^2$	$\sigma / \text{Å}$
h/d <sub>8</sub> -Ethaline	Bulk	0.265/2.290	N/A
P(ThPy)	279.1/293.9	2.070/2.846	22.7/22.0
Au	336.0	4.490	10.0
MPTS	15.0	0.266	10.0
Quartz	Bulk	4.182	10.0

**Table 6.6** Fit parameters for the oxidised film in hydrogenous (cyan) and deuterated (red) Ethaline in **Figure 6.16**.

Layer	d / Å	$10^6 N_b / \text{Å}^2$	$\sigma / \text{Å}$
h/d <sub>8</sub> -Ethaline	Bulk	0.265/2.290	N/A
P(ThPy)	269.4/289.9	1.790/2.696	18.1/22.0
Au	336.0	4.490	10.0
MPTS	15.0	0.266	10.0
Quartz	Bulk	4.182	10.0

**Table 6.7** Fit parameters for the reduced film in hydrogenous (orange) and deuterated (green) Ethaline in **Figure 6.16**.

The total film thickness is 269 Å when reduced (un-doped). This equates to 48 Å or 22 % film swelling upon solvation. As discussed in previous chapters, there are differences in thickness and roughness of the polymer film between hydrogenous and deuterated measurements with

the hydrogenous Ethaline giving the best contrast. Interestingly, a lower volume fraction solvent volume fraction ( $\phi_{\text{Ethaline}}$ ), which was calculated as 0.20 using **Equation 6.1**, was observed in the deep eutectic medium than in acetonitrile. This is attributed to the sterically bulky nature and high viscosity of the Ethaline which results in less solvent ingress and less film swelling.

During polymer oxidation, a further 10 Å of film swelling was observed. However, the deuterated ethylene glycol, forming the anion complex with the chloride  $[(\text{EG})_2\text{Cl}^-]$  through hydrogen bonding, was not acting as a counterion like the  $\text{ClO}_4^-$  anion in the traditional organic medium. Instead the choline cation  $[\text{Ch}^+]$  was expelled upon polymer oxidation to neutralise the positive charge, i.e. oxidising  $[\text{P}^0\text{A}^-\text{C}^+]$  to  $[\text{P}^+\text{A}^-]$ . Again, calculations showed that there was one counterion transferred for every three rings in the polymer backbone. This was accompanied by an increase in the overall solvation of the P(ThPy) film from 0.20 to 0.26.

#### ***6.3.2.4. P(ThPy)-3: Dynamic NR Measurements of P(ThPy) in $\text{LiClO}_4/\text{acetonitrile}$***

Now that the static behaviour of this novel copolymer has been established, in both a traditional organic electrolyte, and the novel DES Ethaline, the next stage was to track the movements of the counterions in real time during a neutron experiment. To achieve this, P(ThPy)-3 was cycled in  $\text{LiClO}_4/\text{acetonitrile}$  at  $1 \text{ mV s}^{-1}$  for 9 cycles. A neutron measurement was acquired in 50 second intervals, dividing the resultant CV into 32 slices.

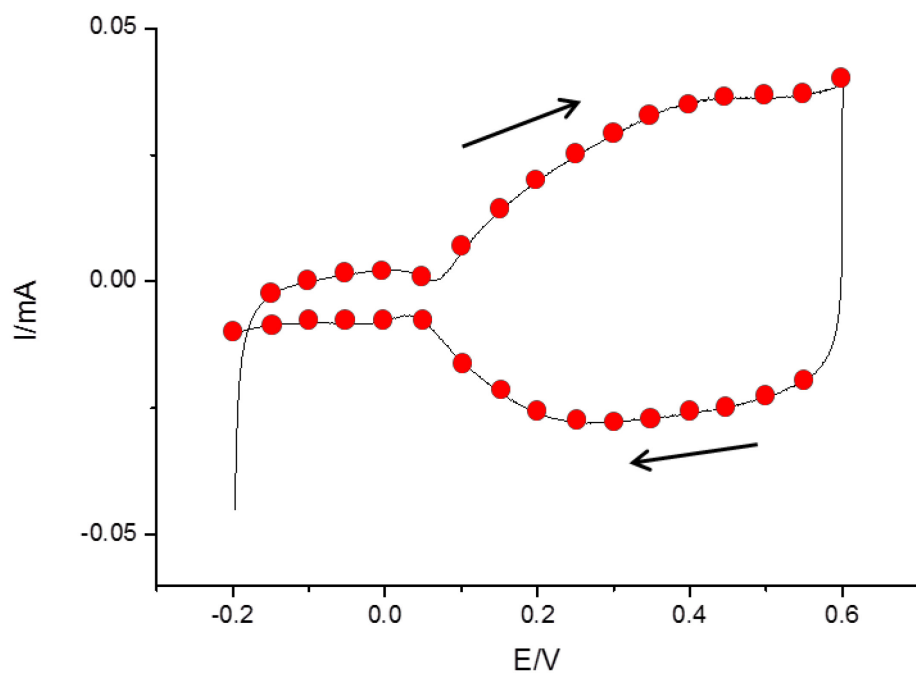


**Figure 6.18** CV of P(ThPy)-3 in ACN/0.1 M LiClO<sub>4</sub> ( $\nu = 1 \text{ mV s}^{-1}$ ). Red dots indicate the starting position in the CV of each of the 32 neutron measurements taken throughout the course of the CV. After each of the 9 cycles of the experiment the data was binned and the statistics from each slice were added from each cycle.

The resultant R(Q) profiles as a function of potential in CH<sub>3</sub>CN and CD<sub>3</sub>CN are shown in **Figures 6.19** and **6.20**.

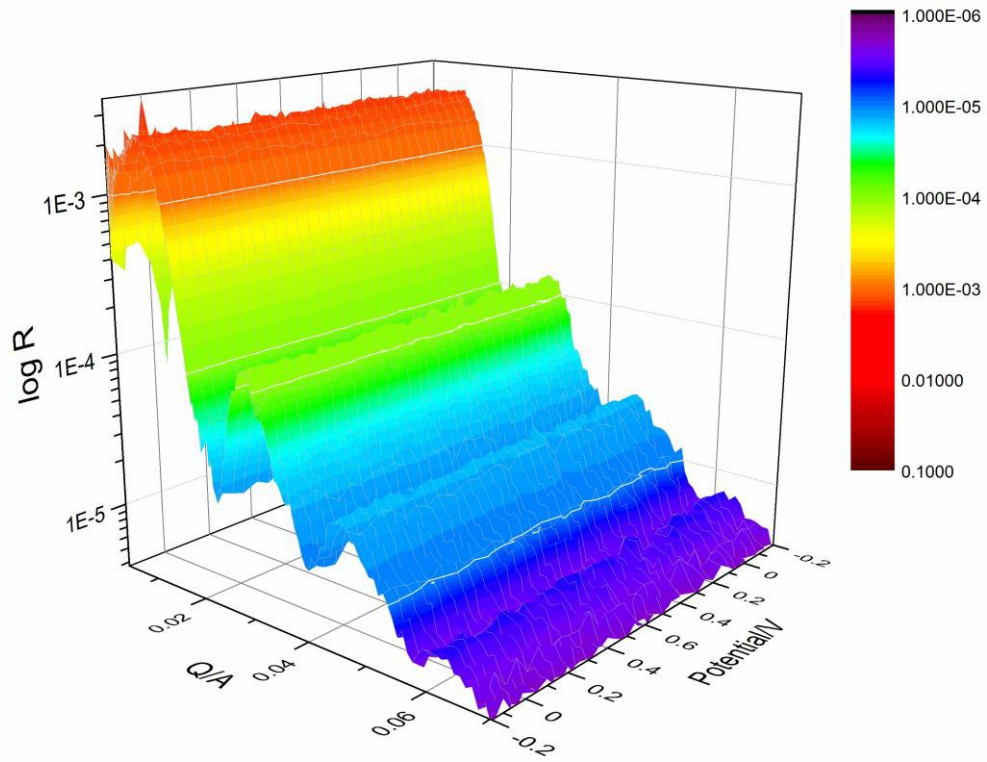


**Figure 6.19** 3D plot of  $R(Q)$  as a function of potential in  $\text{CH}_3\text{CN}/\text{LiClO}_4$ .

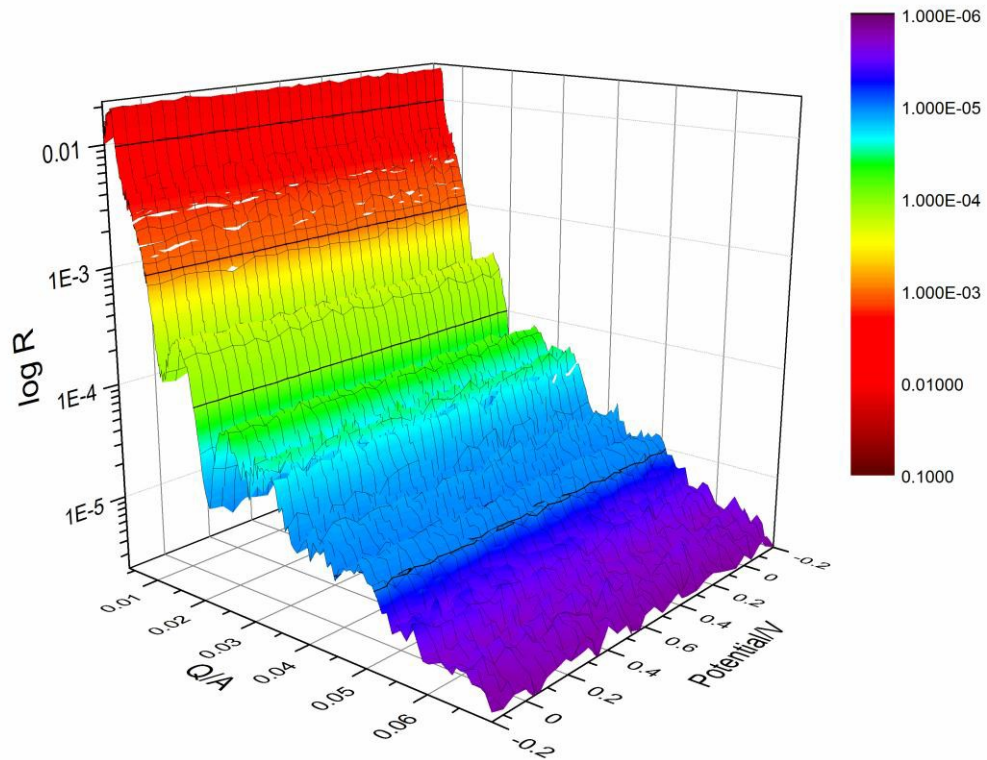


**Figure 6.20** 3D plot of  $R(Q)$  as a function of potential in  $\text{CD}_3\text{CN}/\text{LiClO}_4$ .

The behaviour at the extreme redox states (at  $E = 0.6$  and  $-0.2$  V) was the same as seen in the static measurements performed on P(ThPy)-1. The SLD profiles resulting from the fits at these two extremes are shown in **Figure 6.21** and the fit parameters are given in **Tables 6.8** and **6.9**.

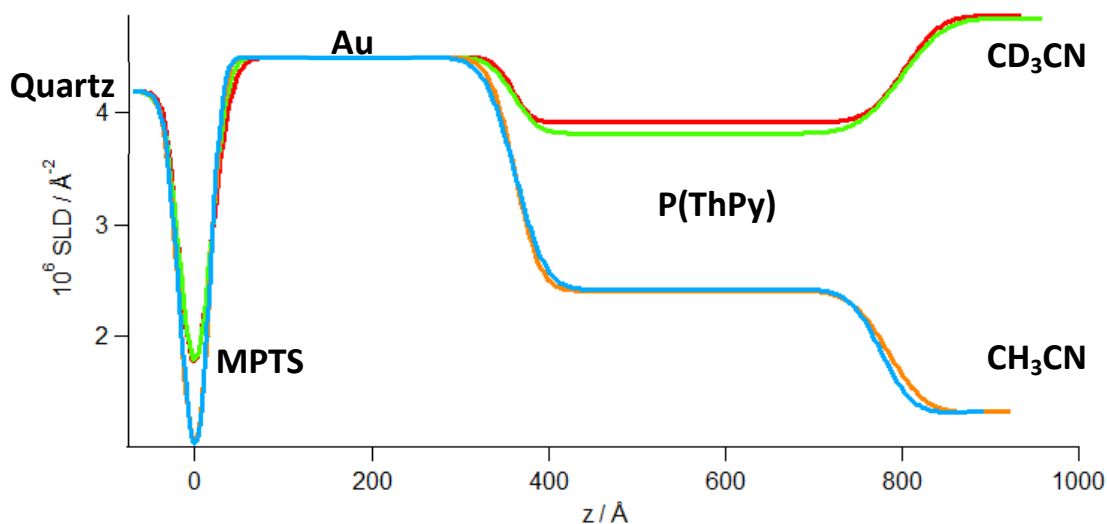


**Figure 6.21** SLD profiles of the fully oxidised and reduced state from the dynamic measurements shown in **Figures 6.19** and **6.20** ( $\chi^2 = 1.1-1.2$ ).

Layer	$d / \text{Å}$	$10^6 N_b / \text{Å}^{-2}$	$\sigma / \text{Å}$
CH <sub>3</sub> CN / CD <sub>3</sub> CN	Bulk	1.320/4.863	N/A
P(ThPy)	413.0/443.3	2.420/3.91	27.3/32.0
Au	346.0	4.490	25.9/16.8
MPTS	33.0/29.4	0.266	11.4/19.7
Quartz	Bulk	4.182	13.6

**Table 6.8** Fit parameters for the oxidised film in CH<sub>3</sub>CN (cyan) and CD<sub>3</sub>CN (red) in **Figures 6.19** and **6.20**.

Layer	$d / \text{Å}$	$10^6 N_b / \text{Å}^{-2}$	$\sigma / \text{Å}$
CH <sub>3</sub> CN / CD <sub>3</sub> CN	Bulk	1.320/4.843	N/A
P(ThPy)	422.0/439.7	2.410/3.813	33.4/38.4
Au	346.0	4.490	22.3/21.8
MPTS	33.6/28.2	0.266	12.2/15.7
Quartz	Bulk	4.182	15.0

**Table 6.9** Fit parameters for the reduced film in CH<sub>3</sub>CN (orange) and CD<sub>3</sub>CN (green) in **Figures 6.19** and **6.20**.

In this slightly thicker film, with a lower density, the solvent volume fraction ( $\phi_{\text{ACN}}$ ) was slightly higher at 0.54 than in **Section 6.3.2.2**. The same level of film swelling was seen upon oxidation, again as a result of the ingress of two anions to compensate for the positive charge that delocalises over every three ThPy monomer units.

### 6.3.3. Atomic Force Microscopy

The topography of each of the films in **Sections 6.3.1** and **6.3.2** was analysed by an AFM.

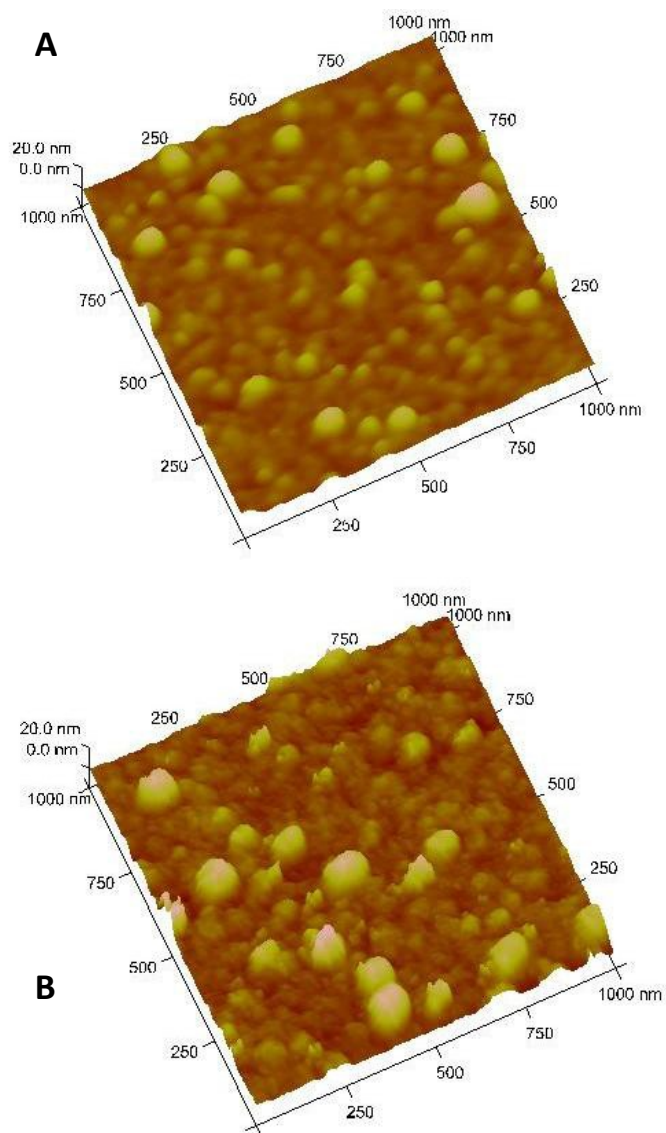


**Figure 6.22** Changes in topography of P(ThPy)-1 (A) before and (B) after the neutron experiments in **Figure 6.12**.

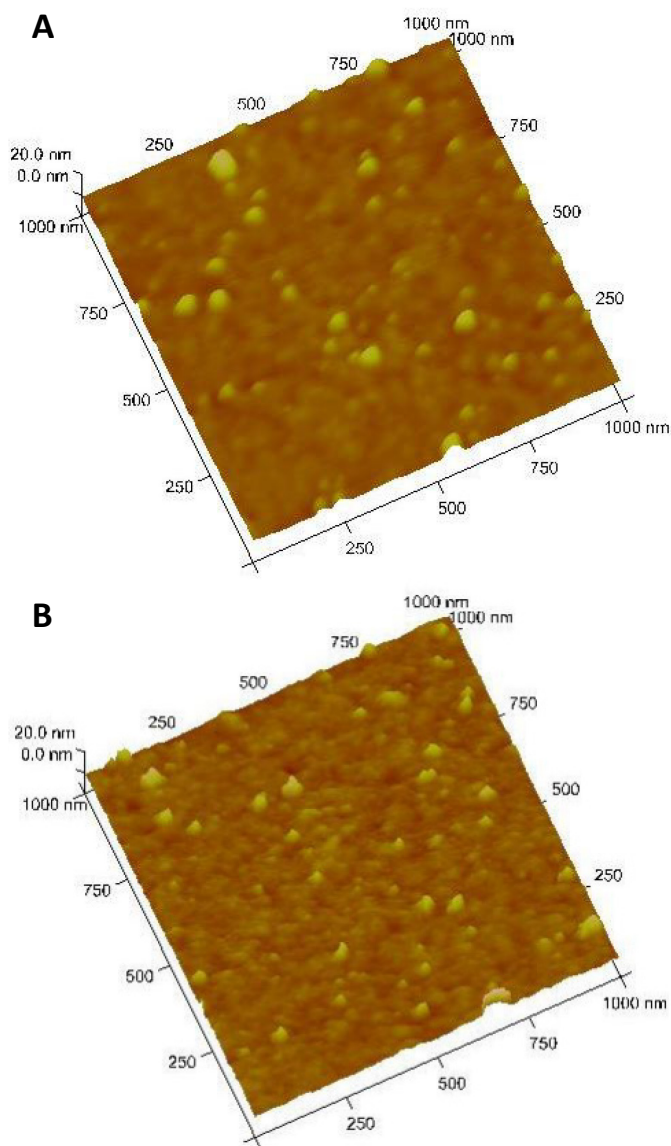


**Figure 6.23** Changes in topography of P(ThPy)-2 (A) before and (B) after the neutron experiments in **Figure 6.16**.

Both the films that were held under static potentials showed very little change in surface topography and roughness. However, P(ThPy)-3 that was cycled showed an increase in the size of the globules of the polymer on the surface as well as an increase in surface roughness. This has an important implication for future applications, as roughening will increase film mobility and ion transport but may, over time, decrease stability.

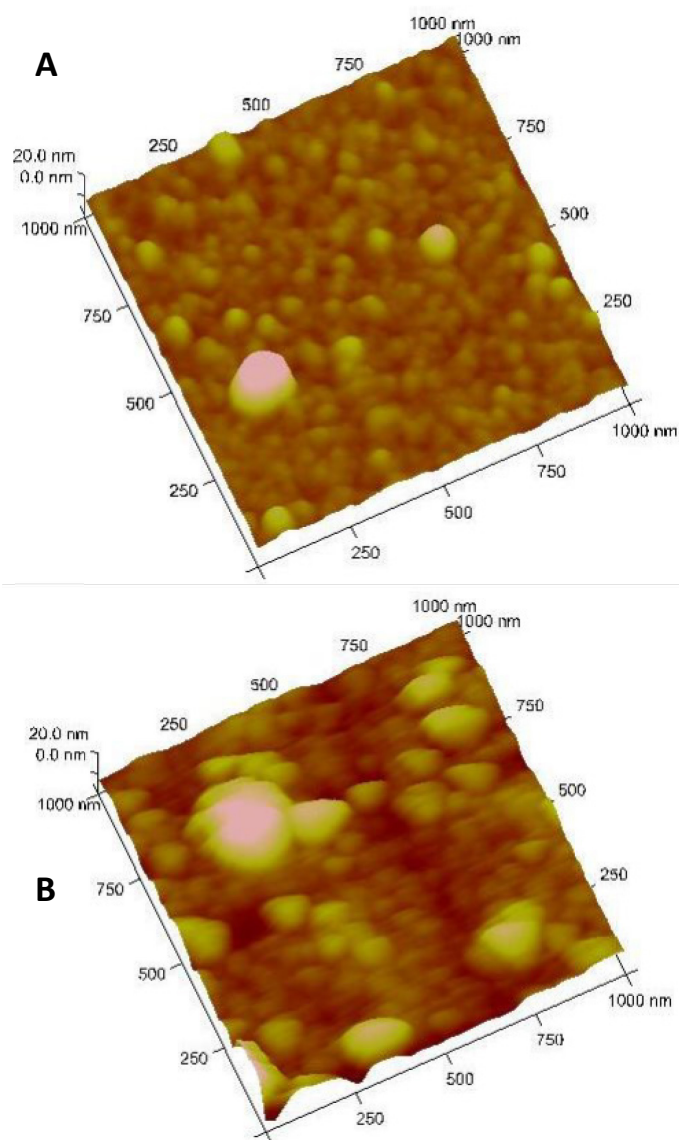


**Figure 6.24** Changes in topography of P(ThPy)-3 (A) before and (B) after the neutron experiments in **Figures 6.19** and **6.20**.

### 6.3.4. Electrochemical Characterisation

The following figures show the electrochemistry of the films performed during the above neutron experiments.

#### 6.3.4.1. *P(ThPy)-1*

Figures 6.25 and 6.26 show the electrochemical data to accompany the NR data in Figures 6.12 and 6.13.

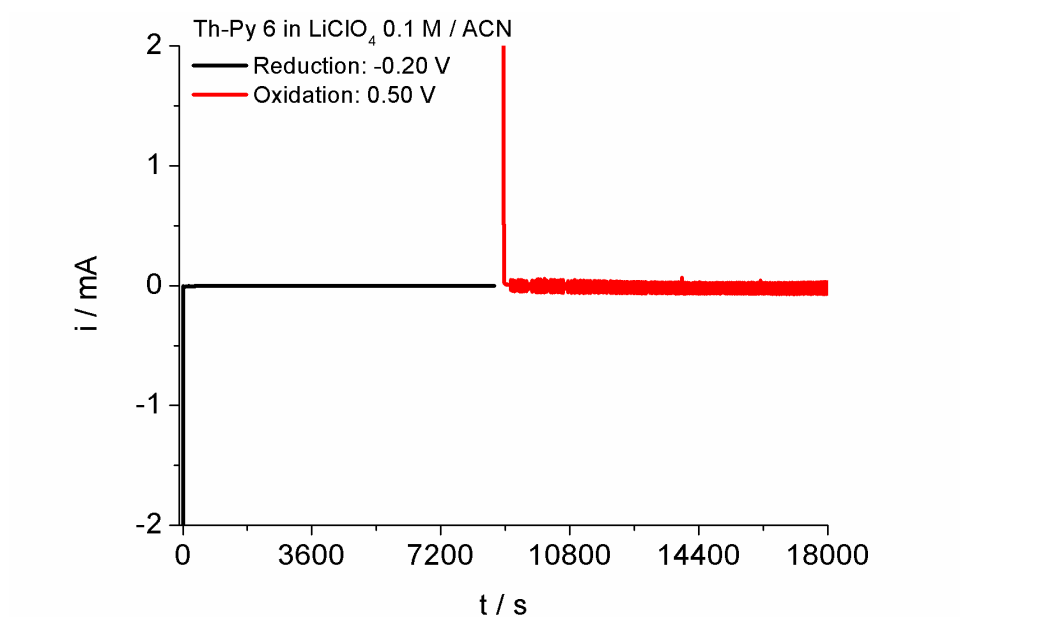


**Figure 6.25** Current-time transients for the neutron measurements for *P(ThPy)-1* in Section 6.3.2.2.

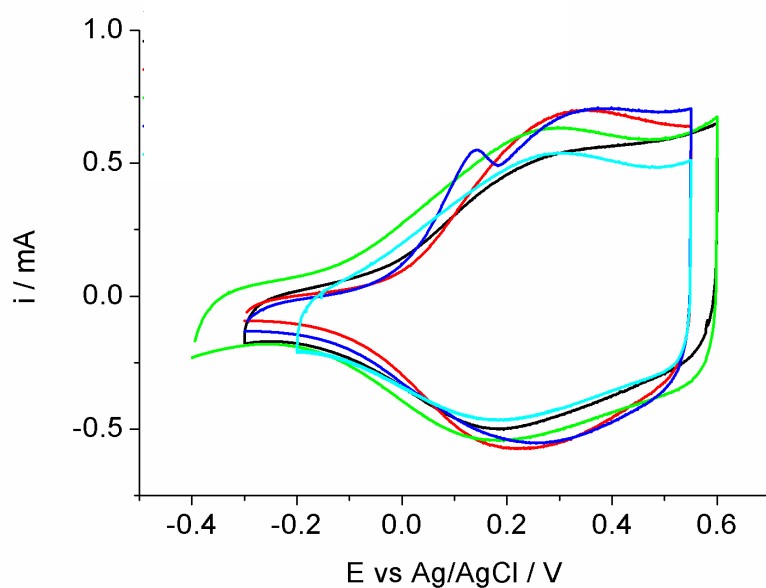


**Figure 6.26** Film characterisation between the neutron measurements for P(ThPy)-1 in **Section 6.3.2.2** performed in 0.1 M LiClO<sub>4</sub>/acetonitrile ( $\nu = 20 \text{ mV s}^{-1}$ ): before (black) and after (red) reduction in CD<sub>3</sub>CN, after oxidation in CD<sub>3</sub>CN (green), after reduction (blue) and after oxidation in CH<sub>3</sub>CN.

#### 6.3.4.2. *P(ThPy)-2*

**Figures 6.27** and **6.28** show the electrochemical data to accompany the NR data in **Figures 6.16** and **6.17**.

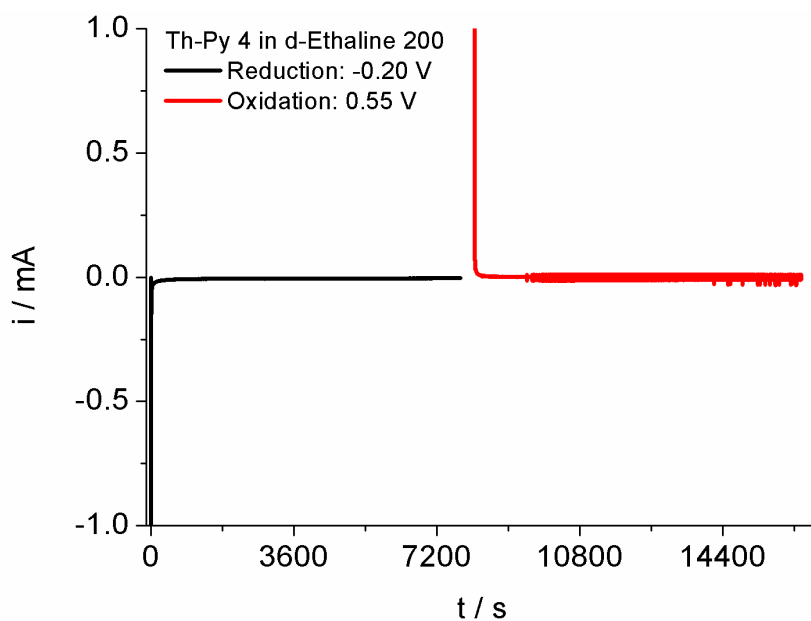


**Figure 6.27** Current-time transients for the static potential holds during the neutron measurements for P(ThPy)-2 in **Section 6.3.2.3**.

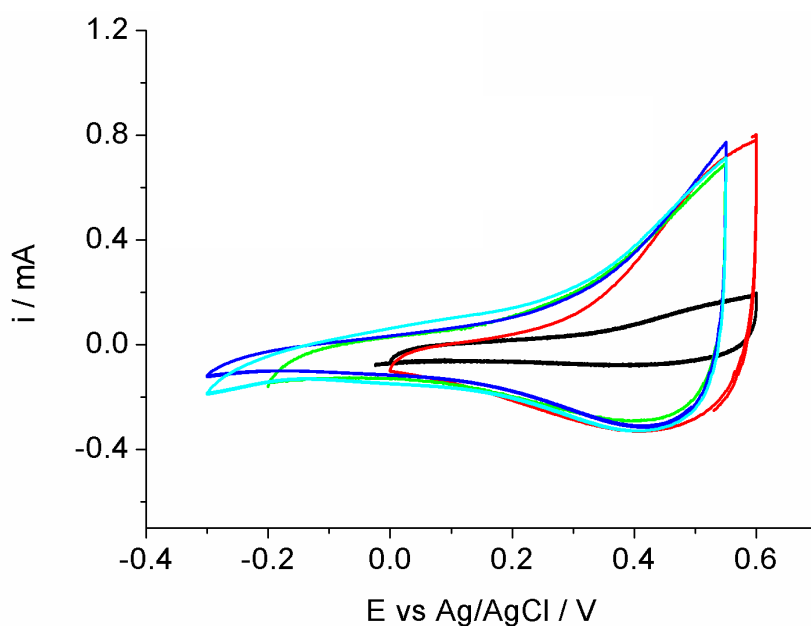


**Figure 6.28** Film characterisation between the neutron measurements for P(ThPy)-2 in **Section 6.3.2.3** performed in Ethaline ( $\nu = 20 \text{ mV s}^{-1}$ ): before (black) and after (red) reduction in  $\text{CD}_3\text{CN}$ , after oxidation in  $\text{CD}_3\text{CN}$  (green), after reduction (blue) and after oxidation in  $\text{CH}_3\text{CN}$ .

The small current observed in the black trace once the film was initially exposed to Ethaline suggests that it takes more time than in seen in acetonitrile for the film to solvate in the more viscous DES.

### 6.3.4.3. *P(ThPy)*-3

Figure 6.29 shows the final cycle of each kinetic measurement in Section 6.3.2.4.

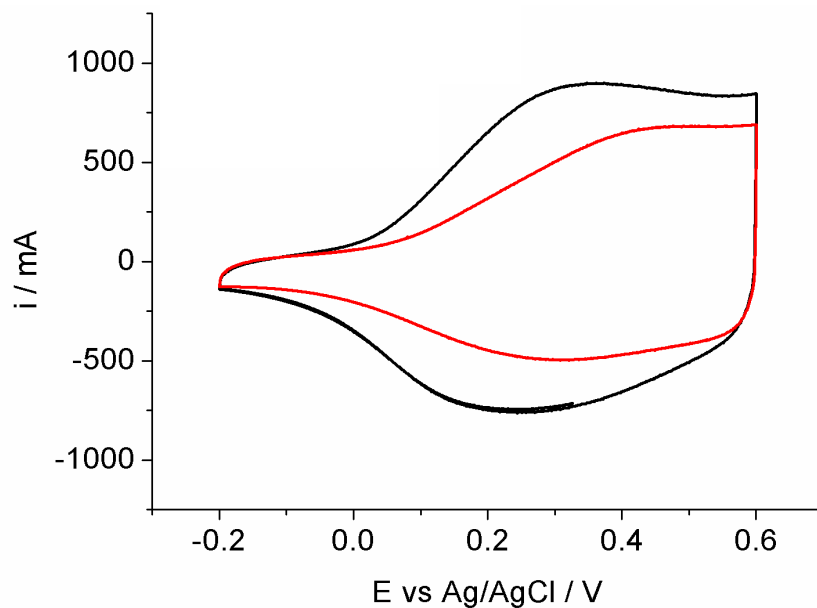


**Figure 6.29** Cyclic voltammograms showing the drop in current after NR measurements in  $\text{CH}_3\text{CN}$  (red) and  $\text{CD}_3\text{CN}$  (black) for *P(ThPy)*-3 in Section 6.3.2.4.

The NR measurement in  $\text{CD}_3\text{CN}$  was performed first, suggesting a 33 % loss of electroactivity after extensive cycling at this low scan rate ( $\nu = 1 \text{ mV s}^{-1}$ ).

## 6.4. Conclusions and Future Work

NR measurements were made on thin films of a new copolymer material, based on a hybrid bespoke monomer derived from thiophene and pyrrole. The resultant P(ThPy) material is a promising candidate for one electrode of a battery or supercapacitor. The electropolymerisation curves in **Figure 6.6** show a high degree of reproducibility in the growth of the polymer, which would be key for the production of polymer anodes in the Polyzion project. NR showed that this produced compositionally homogeneous films that were uniformly solvated.

The novelty of the system is enhanced by the use of a room temperature ionic liquid, Ethaline, comprising a 2:1 mixture of ethylene glycol (EG) and choline chloride (ChCl). From an NR perspective, this choice of solvent medium allowed the practical advantage of using deuterated materials for one component of the mixture allowing cation and anion movement within the system to be separated. Industrially, the advantage of DESs over traditional electrolytes is the increased film ionic conductivity, which is often a limiting factor in (dis)charge rate.

NR measurements were used to answer questions regarding the concentration and spatial distribution of both DES “electrolyte” and to compare this to the distribution of a more standard electrolyte (LiClO<sub>4</sub>/ACN) within the P(ThPy) film. This provides insight into the films charge storage dynamics and permitting design of next generation materials. Films containing the more viscous Ethaline were less solvated ( $\phi_s = 0.20 - 0.26$ ) than the films solvated with acetonitrile ( $\phi_s = 0.49 - 0.54$ ).

Ethaline, is composed of solely of choline chloride (Ch+Cl<sup>-</sup>) and ethylene glycol (EG) in the formulation in a 1:2 ratio, so that the electrolyte solution is a mixture of Ch<sup>+</sup> cations and [(EG)<sub>2</sub>Cl]<sup>-</sup> anions containing no neutral “solvent”. LiClO<sub>4</sub>/ACN on the other hand is a salt in molecular solvent. The use of NR to compare film composition and structure in these two

contrasting media revealed different routes to achieving electroneutrality during redox switching (p-doping/un-doping). It was shown that in LiClO<sub>4</sub>/ACN charge compensation upon oxidation is achieved through the ingress of two ClO<sub>4</sub><sup>-</sup> anions to every three ThPy monomer units [P<sup>0</sup> → P<sup>+</sup>A<sup>-</sup>]. Film solvation during this change in redox state remained the same and the film swelled to incorporate the anions. In the DES Ethaline however the polymer film however, charge compensation was achieved through the egress of two Ch<sup>+</sup> cations to every three ThPy monomer units [P<sup>0</sup>A<sup>-</sup>C<sup>+</sup> → P<sup>+</sup>A<sup>-</sup>]. Film solvation and resultant swelling were significantly less in the more viscous Ethaline than it was in acetonitrile.

Future work should complete this set of measurements by performing dynamic NR experiments in hydrogenous and deuterated Ethaline. This set of measurements could not be performed during the course of this project due to the closure of the ILL for maintenance.

## 6.5. References

- <sup>1</sup> Yue, B., Wang, C., Wagner, P., Yang, Y., Ding, X., Officer, D. L., Wallace, G. G., *Synthetic Metals*, 2012, **162 (24)**, 2216-2221.
- <sup>2</sup> Mini P. A., Balakrishnan, A., Nair, S. V., and Subramanian, K. R. V., *Chem. Commun.*, 2011, **47**, 5753-5755.
- <sup>3</sup> Nyholm, L., Nyström, G., Mhramyan, A., Strømme, M., *Adv. Mater.*, 2011, **23**, 3751-3769.
- <sup>4</sup> Weiss, Z., Mandler, D., Shustak, G., Domb, A. J., *J. Polym. Sci.*, 2004, **42 (7)**, 1658-1667.
- <sup>5</sup> Möller, S., Forrest, S. R., Perlov, C., Jackson, W., and Taussig, C., *J. Appl. Phys.*, 2003, **94**, 7811.
- <sup>6</sup> Skotheim, T.A., and Reynolds, J. R., (2007) *Handbook of Conducting Polymers, 3rd Ed.*, CRC Press, U.S.A.
- <sup>7</sup> Li, X.C., Siringhaus, H., Garnier, F., Holmes, A.B., Moratti, S.C., Feeder, N., Clegg, W., Teat, S.J., Friend, R.H. *J. Am. Chem. Soc.* 1998, **120**, 2206.
- <sup>8</sup> Siringhaus, H., Tessler, N., Friend, R.H. *Science* 1998, **280**, 1741.
- <sup>9</sup> Brown, A.R., Pomp, A., Hart, C.M., de Leeuw, D.M. *Science*, 1995, **270**, 972.
- <sup>10</sup> Garnier, F., Hajlaoui, R., Yassar, A., Srivastava, P. *Science* 1994, **265**, 1684
- <sup>11</sup> Guerfia, A., Trottiera, J., Boyanob, I., De Meatzab, I., Blazquezb, J. A., Brewerc, S., Ryderd, K. S., Vijha, A., Zaghiba, K., *J. Power Sources*, 2013, **248**, 1099-1104.
- <sup>12</sup> [www.polyzion.eu](http://www.polyzion.eu)

- <sup>13</sup> Spotnitz, R., IEEE Vehicle Power and Propulsion Conference, 2005, 334-337.
- <sup>14</sup> MacDiarmid, A. G., *Angew. Chem., Int. Ed.*, 2001, **40**, 2581-2590.
- <sup>15</sup> McNeill, R., Siudak, R., Wardlaw, J. H., Weiss, D. E., *Aust. J. Chem.*, 1963, **16**, 1056-75.
- <sup>16</sup> Bartuš, J., *J. Macromol. Sci.: Part A – Chemistry*, 1991, **28 (9)**, 917–924.
- <sup>17</sup> Roncali, J., *Chem. Rev.*, 1992, **92 (4)**, 711.
- <sup>18</sup> Schopf, G.; Koßmehl, G., *Adv. Polym. Sci.*, 1997, **129**, 1–166.
- <sup>19</sup> Vernitskaya, T. V., and Efimov, O. N., *Russ. Chem. Rev.* 1997, **66**, 443.
- <sup>20</sup> Wilson, R. W., Cubitt, R., Glidle, A., Hillman, A. R., Saville, P. M., Vos, J. G., *J. Electrochem. Soc.*, 1998, **145**, 1454-1461.
- <sup>21</sup> Campbell, R. A., Wacklin, H. P., Sutton, I., Cubitt, R., and Fragneto, G., *Eur. Phys. J. Plus*, 2011, **126**, 107.
- <sup>22</sup> Nelson, A., *J. Appl. Crystallogr.*, 2006, **39**, 273.

## 7. Conclusions

---

Most fingerprints at crime scenes are "latent", i.e. non-visible, so they must be treated chemically to make them visible. However, despite all the methods available the success rate for metallic items (weapons, handles, and tools) is very low. Out of over 200,000 items of fingerprint evidence that are processed each year in the UK, approximately 20,000 are metallic items. Surprisingly, despite the range of methods available, less than 10% of these produce useable fingerprints. Given the prevalence of metallic objects - weapons, tools, handles – in criminal investigations this is an important challenge.

Traditionally employed techniques for enhancing fingerprints on non-porous metallic substrates rely on some form of physical or chemical interaction between a reagent and the sweat deposit transferred when handling an item or surface. Such enhancement results in a positive image of the fingerprint.

Visualisation of latent fingerprints present on metallic surfaces has been previously demonstrated by means of spatially selective deposition of the polymers; PANi<sup>2</sup> and PEDOT<sup>3</sup>. This method is complementary to traditional enhancements, which require chemical or physical interaction with the fingerprint deposit, as it interacts with metallic surface around the fingerprint. It utilises the sweat deposit as an insulating mask resulting in the inhibition of electrochemical processes on regions "protected" by the fingerprint. This results in polymer deposition between the ridges, thus generating a negative image of the fingerprint. Subsequent variation of the applied potential and exploiting the polymer's electrochromic properties means that the colour of the background (polymer) can be continuously and reversibly adjusted in order to optimise the contrast with the metal surface under the

latent/invisible fingerprint deposit. The fact that this manipulation is reversible means that the contrast can be optimised separately in different regions of the image, for example in **Figure 3.18** where the fingerprint deposit is of variable thickness or definition.

Most electroactive polymers are restricted to two colours or two shades of the same colour<sup>1</sup>. Changing the electronic character of the polymer backbone moves the position of the  $\pi - \pi^*$  transition across the electromagnetic spectrum so that when different conducting polymers are doped different optical properties are observed<sup>2,3</sup>. This thesis explored the effect of the copolymerisation of two distinct monomer units (EDOT and Py) on the optical properties of the resultant polymer. Suitable control of deposition rate, via monomer concentration, deposition potential and development time, was accomplished. This allowed the progressive filling of trenches between fingerprint deposits until optimum contrast was achieved.

A comparison of this enhancement methodology with commonly used fingerprint enhancement methods (dusting with powder, application of wet powder suspensions and cyanoacrylate fuming) showed promising performance in a variety of scenarios of practical forensic interest. For the practically challenging situations explored here, using stainless steel as a representative surface, the potentiostatic deposition of the comonomers in an aqueous SDS/LiClO<sub>4</sub> electrolyte solution showed not only a great advantage over the traditional methods but in some instances a greater recovery rate than the three homopolymers explored: PANi, PEDOT and PPy. The ability of the method to reveal fingerprints of various ages and subjected to plausible environmental histories was clearly demonstrated during this wide spectrum survey. The electrochromic enhancement outperformed traditional techniques when the sample environment had significantly decreased the amount of fingerprint residue left on the surface, for example when subjected to high temperatures and when washed with soap<sup>4</sup>. This was attributed to the fact that an insulating layer of fingerprint residue is enough to prevent electropolymerisation so only a fraction of the original fingerprint deposit, which

can be several microns thick<sup>5</sup>, is required for a successful enhancement. This is significantly less than the amount required by traditional development techniques.

The major advantage of this new set of copolymers is that the development time has been cut compared to the homopolymers previously explored where a typical time to develop a print using PANi was 30 minutes and for PEDOT was approximately 10 minutes. Here the maximum deposition time used was only 10 seconds.

An extension of the electrochromic concept, to combine fluorescent and electrochromic enhancements of latent fingerprints, was also explored<sup>6</sup>. The objective was to expand the electrochromic enhancement; which relies on absorption of light, to include emission as a second means of visual contrast. This was achieved through the incorporation of a fluorophore into the polymer film. The challenge was that fluorophore-functionalised monomers were not polymerizable, almost certainly for steric reasons. The chemical/electrochemical route explored in this thesis involved the polymerization of a monomer (here, Py-NH<sub>2</sub>) functionalised with a large leaving group (here, Fmoc). After film deposition, the amide-bound Fmoc was hydrolysed out, to leave nanoscale voids into which the fluorophores could be diffused, to bind with the polymer spine.

As the ease in which the bulky fluorophore moiety could penetrate into the film would determine the intensity of emission achieved, and hence the improvement in visual contrast analysis of the chemical control (Fmoc hydrolysis and fluorophore penetration) in the *vertical* direction (nm/ $\mu$ m scale) was performed using neutron reflectivity. This technique was chosen as cold neutron wavelengths are comparable with interatomic spacings. They are highly penetrating allowing bulk properties to be measured and their isotopic sensitivity allows contrast variation, which can be used to highlight structural and chemical changes in the vertical plane.

Neutron reflectivity was used to accurately determine film composition, thickness and solvent content at each stage. Kinetic NR measurements performed on INTER (ISIS) show how the depth profile of the polymer film alters during the hydrolysis in real time. The solvent volume fractions were 0.37 ( $\pm 0.03$ ) for the PPyFmoc films, 0.59 ( $\pm 0.01$ ) immediately after hydrolysis and 0.47 ( $\pm 0.04$ ) after relaxation (where these data originate from both kinetic and non-kinetic experiments).

Static NR measurements performed on FIGARO/D17 (ILL) and OFFSPEC (ISIS) show the changes in reflectivity after subsequent reaction with a fluorophore. This allows the total penetration depth of the fluorophore into PPyNH<sub>2</sub> films with and without free volume generated by Fmoc hydrolysis to be measured. After fluorophore entry, the film contracts slightly. It has been shown that the additional step to create free volume within the polymer matrix through the elution of the bulky amine protecting group (Fmoc) is beneficial as it results in the incorporation of more fluorophore. Eventually this will lead to greater contrast between the masked regions of the fingerprint and the fluorescent polymer. Significantly, the diffusion of fluorophore into the polymer film was shown to vary with the size of the molecule to be incorporated. The volume fractions of the smaller Cy3 NHS ester in PPyNH<sub>2</sub> films as deposited and made through the Fmoc hydrolysis pathway were 0.17 and 0.30, respectively. These were significantly lower for the same polymer films containing the larger Dylight 649 NHS ester (0.04 and 0.18, respectively). In the latter case, the PPyNH<sub>2</sub> film with no voids only had an outer layer containing the Dylight 649 fluorophore as it proved too sterically bulky to penetrate any further.

Electrochemical methods allowed the coulometric analysis of the surface population of the polymer matrix with which the chemical modifications occur. Fluorescence measurements and FTIR spectroscopy was used to qualitatively demonstrate the post-deposition chemical modification of the polymer films throughout the functionalization process by both the

presence of fluorescence in the final stage and through the disappearance and reappearance of the amide band.

Future work should focus on determination of the polymers' electrochromic properties at the different stages of the reaction and the properties of the immobilized fluorophore. One of the major technical issues that still needs addressing is whether the proximity of the immobilized fluorophore molecules to the working electrode will result in any significant fluorescence quenching.

This preliminary study did not attempt to address the lateral issue of imaging a full fingerprint, but focused solely on the viability of the joint polymer-fluorophore system by understanding the reactivity and composition in the vertical direction at distance scales from 10–100 nm. The potential for a combined absorption/fluorescence strategy in latent fingerprint enhancement is clear with the next step being the application of this strategy to a fingerprinted surface.

Interest in conducting polymers has been growing since the 1970's<sup>7-9</sup> due to their wide spectrum of applications ranging from photo-voltaic devices<sup>10,11</sup> and organic-based light emitting devices<sup>12</sup> to integrated circuits<sup>13-16</sup> to use in the automotive industry<sup>17</sup>. The desire to extend this scope to further technological applications means that there is always a need to refine electrodeposition conditions in order to increase the stability of the resulting polymer and to extend to different substrates<sup>18</sup>.

The properties of two multicomponent layer by layer deposition systems were explored using neutron reflectivity. The first comprised PEDOT and PFP, which showed interesting properties in terms of segregation. The fitting of the NR data revealed two distinct polymer layers, which showed a large degree of interpenetration at the polymer/polymer interface parameterised as a high roughness factor at the polymer/polymer interface. This roughness

factor increased with time meaning that the two polymer layers become more interdiffused over time which would allow more capacitive behaviour.

The thickness of the inner PEDOT layer increased during oxidation due to an increase in solvation from  $\phi_s = 0.49$  to  $\phi_s = 0.51$  as well as the ingress of perchlorate anions to counteract the positive charge shared over every three monomer units of PEDOT. However, over time the PPFp layer also hydrolysed to PPyCOOH, complicating the interpretation by the introduction of a time dependent effect. As a result, it was unclear whether this was due to the polymer backbone interactions or because of the chemical change occurring on the functionalised nitrogen of the PPy backbone in the PPFp.

In order to better understand the effects of redox states and time on the segregation and solvation of multi-layered films a chemically stable set of bilayers, based on PEDOT and PPy were also analysed. This removed the added variable of hydrolysis seen in the PPFp layers and focused solely on the properties of the conducting pyrrole backbone.

It was found that the order of the respective polymers in the multi-layered system greatly affected the properties and stability of the bilayers. As the nature of the polymer/polymer interface is central to the rectifying (segregated) or capacitive (interdiffused) characteristics of the multi-layered films understanding this means that bi- or multi-layer film properties can be tuned based on the order in which the layers are deposited.

Depositing PEDOT first leads to a greater degree of polymer/polymer interfacial roughness which increases with repetitive cycling, whereas depositing PPy first leads to a higher degree of segregation which remains remarkably stable during repetitive cycling. This is significant as the properties of multi-layered systems can be tuned by the individual components deposition sequence, to actively select interpenetration/segregation, depending on whether capacitive or rectifying effects are desired.

The advantage of layering the individual homopolymers to create a composite is that each stage of deposition involves only control of a pure phase, which is often already well established. The nature of the polymer/polymer interface is central to the rectifying (segregated) or capacitive (interdiffused) characteristics of the multi-layered films<sup>19,20</sup>, such that the spatial distribution of the different polymer components determines the optical and electronic properties of the films. These properties are important for the potential applications of these multi-component systems in energy storage. The operational goal is a polymeric material with rapid charge/discharge capability and the facility to take up charge across a wide voltage range.

*En route* to this final application, determination of film composition and structure must be achieved. It has been shown in this thesis that polymer component segregation vs. interpenetration and equal vs. differentiated solvation levels of the different polymer components can be accurately determined via neutron reflectivity. In addition, NR can also be used to probe the dynamics of mobile species such as solvent or counterions across these interfacial boundaries and to quantify these properties as a function of the different oxidation states of the electrochromic material.

In another application area, creating a new class of fast rechargeable zinc/polymer batteries for hybrid/small electric vehicle applications has been the primary focus of Polyzion<sup>21</sup> (E.U. FP7 funded framework programme). It aims to overcome the issues of batteries currently used, such as lead acid (e.g. Ford Ranger EV), NiMH (e.g. Toyota Prius) or lithium ion batteries (post 2004 Toyota Prius). Lead acid and NiMH batteries have limited power and energy density resulting in the need for a large number of cells to sustain the high output current required in an electric vehicle, whereas, lithium ion batteries have decreased lifetime compared to lead acid/NiMH batteries as well as temperature dependent performance and safety concerns.

The electrochemical redox properties of pyrrole and thiophene have been widely investigated<sup>22-27</sup>. However, their prospective application as part of a charge storage device are hindered by the rate of (dis)charge/available current density, the available voltage and (electro)chemical stability to repetitive charge/discharge cycling. Polyzion are combining conducting polymers with the novel properties of choline chloride based Deep Eutectic Solvents (DES) which have wide electrochemical windows, high stability and low toxicity as well as being relatively cost effective.

In energy storage devices, the movement of ions and solvent into/out of the polymer film during redox cycling is key to the DC capacitance behaviour (extent of charge storage) as well as adhesion/stability of the film.

NR measurements were made on thin films of a new copolymer material, based on a hybrid bespoke monomer derived from thiophene and pyrrole. The resultant P(ThPy) material is a promising candidate for one electrode of a battery or supercapacitor. Electropolymerisation curves revealed a high degree of reproducibility in the growth of the polymer, which is key for the production of polymer anodes in the Polyzion project. NR showed that this produced compositionally homogeneous films that were uniformly solvated.

The novelty of the system was enhanced by the use of a room temperature ionic liquid, Ethaline, comprising a 2:1 mixture of ethylene glycol (EG) and choline chloride (ChCl). From an NR perspective, this choice of solvent medium allowed the practical advantage of using deuterated materials for one component of the mixture allowing cation and anion movement within the system to be separated. Industrially, the advantage of DESs over traditional electrolytes is the increased film ionic conductivity, which is often a limiting factor in (dis)charge rate.

NR measurements were used to answer questions regarding the concentration and spatial distribution of both DES “electrolyte” and to compare this to the distribution of a more standard electrolyte ( $\text{LiClO}_4/\text{ACN}$ ) within the P(ThPy) film. This provides insight into the films charge storage dynamics and permitting design of next generation materials.

Ethaline, is composed of solely of choline chloride ( $\text{Ch}+\text{Cl}^-$ ) and ethylene glycol (EG) in the formulation in a 1:2 ratio, so that the electrolyte solution is a mixture of  $\text{Ch}^+$  cations and  $[(\text{EG})_2\text{Cl}]^-$  anions containing no neutral “solvent”.  $\text{LiClO}_4/\text{ACN}$  on the other hand is a salt dissolved in a molecular solvent. The use of NR to compare film composition and structure in these two contrasting media revealed different routes to achieving electroneutrality during redox switching (p-doping/un-doping). It was shown that in  $\text{LiClO}_4/\text{ACN}$  charge compensation upon oxidation is achieved through the ingress of two  $\text{ClO}_4^-$  anions to every three ThPy monomer units [ $\text{P}^0 \rightarrow \text{P}^+\text{A}^-$ ]. Film solvation during this change in redox state remained the same and the film swelled to incorporate the anions. In the DES Ethaline however the polymer film however, charge compensation was achieved through the egress of two  $\text{Ch}^+$  cations to every three ThPy monomer units [ $\text{P}^0\text{A}^+\text{C}^- \rightarrow \text{P}^+\text{A}^-$ ]. Film solvation and resultant swelling were significantly less in the more viscous Ethaline than it was in acetonitrile. Future work should complete this set of measurements by performing dynamic NR experiments in hydrogenous and deuterated Ethaline.

## 7.1. References

- <sup>1</sup> Sotzing, G. A., Reddinger, J. L., Katritzky, A. R., Soloduchko, J., Musgrave, R., and Reynolds, J. R., *Chem. Mater.* 1997, **9**, 1578.
- <sup>2</sup> Fesser, K., Bishop, A. R., and Campbell, D. K., *Phys. Rev.*, 1983, **27**, 4804.
- <sup>3</sup> Sönmez, G., Schwendeman, I., Schottland, P., Zong, K., and Reynolds, J. R., *Macromolecules*, 2003, **36**, 639.
- <sup>4</sup> Beresford, A. L., Brown, R. M., Hillman, A. R., and Bond, J. W., *J. Forensic Sci.*, 2011, **57(1)**, 93-102.
- <sup>5</sup> Thomas, G. L., and Reynoldson, T. E., *J. Phys. D: Appl. Phys.*, 1975, **8**, 724–729.
- <sup>6</sup> Sapstead (nee Brown), R. M., Ryder, K. S., Fullarton, C., Skoda, M., Dalglish, R. M., Watkins, E. B., Beebee, C., Barker, R., Glidle, A., and Hillman, A. R., *Faraday Discussions*, 2013, **164**, 319.
- <sup>7</sup> Shirakawa, H., Louis, E., McDiarmid, A., Chiang, C., and Heeger, A. J., *J. Chem. Soc. Chem. Commun.*, 1977, 758.
- <sup>8</sup> Skotheim, T. A., Elsenbaumer, R. L., and Reynolds, J. R., *Handbook of conducting polymers 2<sup>nd</sup> edition*, Marcel Dekker, New York, 1988.
- <sup>9</sup> Nalwa, H. S., *Handbook of organic conductive molecules and polymers*, John Wiley and Sons, Chichester, 1997.
- <sup>10</sup> Halls, J. J. M., Walsh, C.A., Greenham, N.C., Marseglia, E.A., Friend, R.H., Moratti, S.C., Holmes, A.B. *Nature* **1995**, 376, 498.
- <sup>11</sup> Sariciftci, N.S., Smilowitz, L., Heeger, A.J, Wudl, F. *Science* **1992**, 258, 1474.

- <sup>12</sup>Friend, R.H., Gymer, R.W., Holmes, A.B., Burroughes, J.H., Marks, R.N., Taliani, C., Bradley, D.D.C.; Dos Santos, D.A., Brédas, J.L., Lögdlund, M., Salaneck, W.R. *Nature* **1999**, 397, 121.
- <sup>13</sup>Li, X.C., Sirringhaus, H., Garnier, F., Holmes, A.B., Moratti, S.C., Feeder, N., Clegg, W., Teat, S.J., Friend, R.H. *J. Am. Chem. Soc.* **1998**, 120, 2206.
- <sup>14</sup>Sirringhaus, H., Tessler, N., Friend, R.H. *Science* **1998**, 280, 1741.
- <sup>15</sup>Brown, A.R., Pomp, A., Hart, C.M., de Leeuw, D.M. *Science* **1995**, 270, 972.
- <sup>16</sup>Garnier, F., Hajlaoui, R., Yassar, A., Srivastava, P. *Science* **1994**, 265, 1684
- <sup>17</sup>De Paoli, M. A., and Gazotti, W. A., *J. Braz. Chem. Soc.*, 2002, **13**, 410.
- <sup>18</sup>Saraç, A. S., Sönmez, G., and Cebeci, F. Ç., *J. App. Electrochem.*, 2003, **33**, 295-301.
- <sup>19</sup>Aradilla, D., Estrany, F., and Aleman, C., *J. Phys. Chem.*, 2011, **115**, 8430–8438.
- <sup>20</sup>Sellam and Hashmi, S. A., *ACS Appl. Mater. Interfaces*, 2013, **5**, 3875–3883.
- <sup>21</sup>[www.polyzion.eu](http://www.polyzion.eu)
- <sup>22</sup>MacDiarmid, A. G., *Angew. Chem., Int. Ed.*, 2001, **40**, 2581-2590.
- <sup>23</sup>McNeill, R., Siudak, R., Wardlaw, J. H., Weiss, D. E., *Aust. J. Chem.*, 1963, **16**, 1056-75.
- <sup>24</sup>Bartuš, J., *J. Macromol. Sci.: Part A – Chemistry*, 1991, **28 (9)**, 917–924.
- <sup>25</sup>Roncali, J., *Chem. Rev.*, 1992, **92 (4)**, 711.
- <sup>26</sup>Schopf, G.; Koßmehl, G., *Adv. Polym. Sci.*, 1997, **129**, 1–166.
- <sup>27</sup>Vernitskaya, T. V., and Efimov, O. N., *Russ. Chem. Rev.* 1997, **66**, 443.

# Publications

---

1. Brown, R. M. and Hillman, A. R., *Electrochromic enhancement of latent fingerprints by poly(3,4-ethylenedioxythiophene)*, Physical Chemistry Chemical Physics, 2012,14, 8653-8661 <http://hdl.handle.net/2381/28821>
2. Beresford, A. L., Brown, R. M., Hillman, A. R., and Bond, J. W., *Comparative Study of Electrochromic Enhancement of Latent Fingerprints with Existing Development Techniques\**, Journal of Forensic Sciences, 2011, 57 (1) pp. 93-102 DOI: 10.1111/j.1556-4029.2011.01908.x (Article removed from electronic thesis due to copyright restrictions)
3. Sapstead (nee Brown), R. M., Ryder, K. S., Fullarton, C., Skoda, M., Dalgliesh, R. M., Watkins, E. B., Beebee, C., Barker, R., Glidle, A., and Hillman, A. R., *Nanoscale control of interfacial processes for latent fingerprint enhancement*, Faraday Discussions, 2013, 164, pp 391 – 410 <http://hdl.handle.net/2381/28822>

Cite this: DOI: 10.1039/c2cp40733g

www.rsc.org/pccp

PAPER

## Electrochromic enhancement of latent fingerprints by poly(3,4-ethylenedioxythiophene)†

Rachel M. Brown and A. Robert Hillman\*

Received 7th March 2012, Accepted 2nd May 2012

DOI: 10.1039/c2cp40733g

Spatially selective electrodeposition of poly-3,4-ethylenedioxythiophene (PEDOT) thin films on metallic surfaces is shown to be an effective means of visualizing latent fingerprints. The technique exploits the fingerprint deposit as an insulating mask, such that electrochemical processes (here, polymer deposition) may only take place on deposit-free areas of the surface between the ridges of the fingerprint deposit; the end result is a negative image of the fingermark. Use of a surfactant (sodium dodecylsulphate, SDS) to solubilise the EDOT monomer allows the use of an aqueous electrolyte. Electrochemical (coulometric) data provide a total assay of deposited material, yielding spatially averaged film thicknesses, which are commensurate with substantive filling of the trenches between fingerprint deposit ridges, but not overflowing to the extent that the ridge detail is covered. This is confirmed by optical microscopy and AFM images, which show continuous polymer deposition within the trenches and good definition at the ridge edges. Stainless steel substrates treated in this manner and transferred to background electrolyte (aqueous sulphuric acid) showed enhanced fingerprints when the contrast between the polymer background and fingerprint deposit was optimised using the electrochromic properties of the PEDOT films. The facility of the method to reveal fingerprints of various ages and subjected to plausible environmental histories was demonstrated. Comparison of this enhancement methodology with commonly used fingerprint enhancement methods (dusting with powder, application of wet powder suspensions and cyanoacrylate fuming) showed promising performance in selected scenarios of practical interest.

### Introduction

Fingerprints have been used as a means of biometric identification since the mid 1800s and, despite the rise of other methods such as those based on DNA, remain a cornerstone of the identification of individuals for forensic and other purposes. Accordingly, the last century has seen great innovation of physical and chemical methods for visualizing fingerprints on diverse surfaces.<sup>1</sup>

Nevertheless, the reality is that the success rate in extracting fingerprints of adequate quality for unequivocal identification remains low – in the case of metallic surfaces, only a few percent.<sup>2–4</sup> While incremental improvements to existing methods undoubtedly have value, it is clear that substantive progress requires the advent of radically different approaches. Here we describe one such approach, the basis of which requires an order of magnitude less fingerprint residue than typical methods and the nature of which introduces the additional dimension of externally variable optical properties to optimise visual contrast.

The attractions of using fingerprints for identification are that they are unique to an individual,<sup>1</sup> are unchanged throughout life, can survive superficial damage to the skin<sup>1</sup> and persist for a significant time after death.<sup>5</sup> Their intricate spatial form also means that it is extremely difficult to "contaminate" an object with a perfectly formed fingerprint. Formation of a fingermark on a surface is an example of the classic Locard's principle,<sup>6,7</sup> commonly expressed as "every contact leaves a trace". There are three types of fingermark: *patent* (in which the transfer of a coloured substance leaves a visible image), *plastic* (when pressure from the finger on a soft material leaves

a 3D imprint) and *latent* (when the material exchanged with the surface is not visible). The last of these is the most common source of forensic evidence but, by definition, such fingerprints require treatment to reveal the image.

Most latent fingerprints are attributable to secretions from two types of sweat gland: eccrine glands found on the hands and sebaceous glands found on the facial areas. Eccrine sweat has a very high water content,<sup>1</sup> in which the predominant solutes are inorganic salts (some at a sufficiently high concentration to corrode metal surfaces<sup>8</sup>) as well as lipids and amino acids, whose presence is exploited in fingerprint development with ninhydrin. Sebaceous sweat comprises a complex mixture of fatty acids,

Department of Chemistry, University of Leicester, Leicester, LE1 7RH, UK. E-mail: arh7@le.ac.uk

† Electronic supplementary information (ESI) available. See DOI: 10.1039/c2cp40733g

phospholipids, wax esters, sterols and squalene, collectively referred to as *sebum*.<sup>1</sup>

Broadly speaking, current fingerprint development methods involve interaction of the chosen reagent with one of the water soluble or lipid components of the sweat deposit; lack of knowledge of the fingerprint history introduces uncertainty into the enhancement process. Traditional reagents and delivery methods include dusting with powders (of a fluorescent,<sup>9</sup> magnetic,<sup>2,13</sup> or thermoplastic nature), dipping in (or spraying with) ninhydrin solution,<sup>14</sup> vacuum metal deposition,<sup>15</sup> small particle reagent,<sup>15</sup> physical developer<sup>5</sup> and fuming with cyanoacrylate<sup>16,17</sup> ("super glue"). In the latter instance, the white polymeric product is commonly visualized by soaking in solutions of basic dyes such as Basic Yellow 40, Rhodamine 6G (Basic Red 1), Safranin O (Basic Red 2) and Basic Red 14 and the objects viewed under fluorescent conditions. A variant of the fluorescence approach is the use of cadmium sulphide nanocomposites, which bond with the fatty acid and amino acid components in fingerprint deposits.<sup>18</sup> Recent physically-based approaches include using a Scanning Kelvin Probe<sup>19,20</sup> to map surface work function variations and high voltage-driven spatially selective local adhesion of carbon particulates to semi-conducting oxides formed on brass surfaces (e.g. bullet casings).<sup>21</sup>

While analysis of the complex spatial patterns of fingerprints<sup>22</sup> is not the focus of the present work, an appreciation of their form is required to define the challenge of their visual enhancement. Fingerprint detail is considered at three levels. First level detail describes the general type of fingerprint pattern: a loop, a whorl or an arch. Second level detail corresponds to characteristic *minutiae* within the fingerprint: a *ridge ending*, a *bifurcation*, a *lake* (where two split ridges rejoin after a bifurcation), a *dot*, an *island* (a short independent ridge), a *spur* or a *crossover* (running between two parallel ridges). Third level detail corresponds to smaller features, such as pores, on the ridges. First level detail clearly cannot provide identification, but can be useful for elimination purposes. Currently, the spatial relationship between – though not the identity of – second level features is the basis of fingerprint identification; their unambiguous imaging is thus critical. Third level detail, which is commonly not resolved, is not presently used in isolation for identification purposes. However, it may be used in combination with second (or even first) level detail in a holistic approach, exploiting all the available information to reach a decision on identification. Thus, techniques capable of resolving third level detail hold considerable future promise, notably for partial fingerprints or other situations where unambiguous second level detail is sparse.

We now report the successful implementation of a new concept, based on the use of the fingerprint deposit as a template, or "mask", through which the visualizing reagent may be deposited, to give a negative image of the fingerprint. The approach is complementary to most visualization methods, in that it involves interaction *not* with the fingerprint but with the *WICKED* regions of the substrate. This first stage of the concept (illustrated in Scheme 1) was described by Bersellini *et al.*,<sup>23</sup> who deposited polypyrrole electrochemically on fingerprinted metal surfaces such as Pt, Au, Ag and Ergal (Al alloy).<sup>23</sup> The fundamental extension pursued here is subsequent potential control of the deposited polymer to vary its optical properties,



**Scheme 1** Schematic representation of strategy for visualizing latent fingerprints by deposition of electrochromic polymer. Panel a: surface with deposited fingerprint, prior to treatment; panel b: fingerprinted surface immersed in monomer solution, prior to initiation of film deposition; panel c: regions of bare (inter-ridge) surface covered with thin layer of polymer in early stages of deposition; panel d: surface optimally covered with polymer; panel e: excess polymer deposited, resulting in overfilling of trenches and partial obscuring of fingerprint detail; panel f: sample after transfer to monomer-free electrolyte and held at a different potential, generating a contrasting image (violet colour change) to that in panel d.

*i.e.* colour. The practical significance of this is that one can then optimise fingerprint visual contrast, yielding excellent second level detail and significant third level detail.

Irrespective of the detailed fingerprint composition (*vide supra*), the premise is that it contains sufficient non-conductive material to form an insulating mask on the surface. Electron transfer- and thus polymer deposition – is prevented by an insulating layer only a few nanometres thick. Since the initial fingerprint deposit may be several microns thick,<sup>24</sup> one only requires retention of a small fraction of the initially deposited material – far less than would be commonly required to give a visible mark by interaction with traditional chemical enhancement agents. The practical significance of this is the potential to image old fingerprints or ones that have been subjected to environmental deterioration.

A preliminary communication demonstrated the electrochromic enhancement concept using polyaniline as the active material.<sup>25</sup> We now implement this strategy using poly(3,4-ethylenedioxythiophene), PEDOT, a widely studied conducting polymer<sup>6,32</sup> with excellent (electro)chemical stability and electrochromic properties. In principle, with a wide operating potential range, one could access three states of distinct optical properties: 11-doped, undoped and p-doped. However, for practical reasons, we elect to operate in aqueous media – facilitated by using a surfactant to effect micellar monomer solubilisation – and thus focus on the interchange of the latter two redox states, which are readily accessible within the aqueous potential window under the conditions employed.

Summarizing the preceding arguments, the generic goal is visualization of latent fingerprints on metallic objects, for the overwhelming majority of which conventional methods do not yield useable images. Specific objectives related to the present study include (i) identification of conditions (media and electrochemical protocols) for PEDOT deposition that do not simultaneously degrade the fingerprint; (ii) demonstration of PEDOT electrochromic enhancement of latent fingerprints; (iii) morphological characterization distinguishing trench filling (desired) from ridge coverage (undesired), showing directly that the PEDOT deposit yields a faithful image of the fingerprint deposit; and (iv) demonstration that enhancement with PEDOT as the active agent is competitive with existing methods. This report

focuses on fundamental aspects of these objectives, extending the polyaniline-based proof-of-concept,<sup>25</sup> complementary performance aspects and the subject of a parallel report." As we shall show, PEDOT deposition from aqueous media provides a powerful means of latent fingerprint enhancement on metals, with access to second and third level detail via the added visual dimension of electrochromism.

## Experimental

### Materials

PEDOT films were deposited from aqueous 0.01 mol dm<sup>-3</sup> EDOT (Sigma Aldrich)/0.1 mol dm<sup>-3</sup> H<sub>2</sub>SO<sub>4</sub> (Sigma Aldrich), in selected cases (see figure legends) also containing either 0.01 mol dm<sup>-3</sup> sodium dodecylsulphate (SDS) (Sigma Aldrich) or 0.02 mol dm<sup>-3</sup> sodium N-lauroylsarcosinate (SLS) (Sigma Aldrich) to facilitate solubilisation of EDOT monomer. All reagents were used as supplied. Subsequent cyclic voltammetric measurements for film characterization and coulometric assay involved exposure of the films to nitrogen-purged aqueous 0.1 mol dm<sup>-3</sup> H<sub>2</sub>SO<sub>4</sub>, in selected instances (see figure legends) with SDS or SLS present.

For exploratory purposes, four deposition solution formulations were used: (i) 0.1 mol dm<sup>-3</sup> LiClO<sub>4</sub>/0.07 mol dm<sup>-3</sup> SDS/0.05 mol dm<sup>-3</sup> EDOT; (ii) 0.1 mol dm<sup>-3</sup> KCl/0.1 mol dm<sup>-3</sup> SDS/0.01 mol dm<sup>-3</sup> EDOT; (iii) 0.1 mol dm<sup>-3</sup> H<sub>2</sub>SO<sub>4</sub>/0.01 mol dm<sup>-3</sup> SDS/0.01 mol dm<sup>-3</sup> EDOT; (iv) 0.1 mol dm<sup>-3</sup> H<sub>2</sub>SO<sub>4</sub>/0.02 mol dm<sup>-3</sup> SLS/0.01 mol dm<sup>-3</sup> EDOT. For reasons described below, formulation (iii) was used most extensively.

The substrates were stainless steel 304 plates (2.5 cm × 2.5 cm × 0.08 cm; one face insulated to give an exposed (electrochemically active) geometric area, A = 6.25 cm<sup>2</sup>). These were incorporated as the working electrode in a single compartment three-electrode cell, with a Pt Hag counter electrode and a Ag/AgCl/KCl (saturated) reference electrode, against which all potentials were controlled and are quoted.

Reagents and associated procedures for standard fingerprint visualization methods (for comparison purposes) are described in the Supporting Information.

### Instrumentation

Electrochemical measurements were made under potential control using a JIAUTOLAB type 11 potentiostat. Optical microscopy images were taken with a Meiji Techno MT7100 trinocular microscope operated by uEye (IDS GmbH). The atomic force microscope (AFM) was a Veeco Dimension 3100 Scanning Probe Microscope operated by a computer using Nanoscope 6.1.2r1 software. The silicon nitride tips were supplied by Veeco (model: RTESP; part: MPP-1 1100-10). Calibration was effected by scanning over a silicon wafer reference. Images (100 μm × 100 μm) were acquired in tapping mode (resonant frequency 200 kHz) at a scan rate of 0.6 Hz, i.e. 120 lines s<sup>-1</sup>.

### Procedures

The metal substrates were washed to remove any protective grease and one side polished with Brasso to a mirror finish. They were then washed again with warm soapy water and acetone to

remove the excess polish and left to dry at room temperature. In separate experiments, eccrine and sebaceous fingerprints were analysed. In both cases, donors first washed their hands with soapy water to remove contaminants. Eccrine fingerprints were produced by the donor wearing powder-free nitrile gloves for 2 h, then depositing the print. Sebaceous fingerprints were generated by rubbing the fingertips around the forehead and nose area prior to deposition. In both cases, minimal force was used: this minimizes distortion and provides a more realistic test of any enhancement method. The data presented are representative of fingerprints from a range of donors; the operational implications of their attributes (characteristics such as age and gender) are outside the scope of the present fundamental study.

Potentiodynamic and potentiostatic control functions were explored for EDOT polymerization. Deposition via potentiodynamic mode typically involved 20 cycles (guided by visual appraisal of film development) with a cathodic potential limit in the range -0.6 to -0.5 V and an anodic potential limit of 0.9 to 1.2 V at scan rates in the range 20 < v/mV s<sup>-1</sup> < 100. Potentiostatic deposition was in the range 0.9 to 1.2 V for times in the range 140-3600 s. Conditions specific to a given experiment are listed in the relevant figure legend but, in general for the fingerprint application considered here, films produced in the absence of H<sub>2</sub>SO<sub>4</sub> were either uneven (beyond the variations imposed by fingerprint deposit) or failed to show electrochromic behaviour. As described below, films deposited under potentiostatic control gave the best outcomes in terms of image contrast; irrespective of the deposition control function, films were transferred to monomer-free electrolyte and characterized potentiodynamically. All measurements were made at room temperature (20 ± 2 °C).

### Image interpretation

Coulometric assays of PEDOT surface coverage were made on films immersed in nitrogen-purged, monomer-free 0.1 mol dm<sup>-3</sup> H<sub>2</sub>SO<sub>4</sub>. For voltammetric measurements the potential limits were -0.8 V to 0.8 V. Scan rates in the range 1 < v/mV s<sup>-1</sup> < 250 were used to establish complete film electroactivity (or otherwise); for coulometric assay the optimum scan rate for films of sufficient optical density to be practically useful was v = 30 mV s<sup>-1</sup>. The total charge (Q/C) was used to estimate the laterally spatially averaged population density (Γ/mol cm<sup>-2</sup>) using

$$\Gamma = \frac{Q}{nFA} \quad (1)$$

where n = 0.33 is the maximum doping level during oxidation,<sup>35</sup> F is the Faraday constant and A (cm<sup>2</sup>) is the total exposed electrode area. We note that removal of oxygen, and thereby minimization of the partial current associated with oxygen reduction, is critical to accurate coulometric assay of deposited polymer in a fundamental study but that this would not be required in practical application. In the latter instance, one simply wishes to use applied potential to establish a particular oxidation state (colour); the charge required to do so is not a measured parameter. Since oxygen is not electroactive in the potential range used for EDOT polymerization, its removal at that stage is also not critical.

As discussed in more detail in the supporting information, while eqn (1) provides an unequivocal coulometric assay of the

total amount (moles) of polymer present on the surface. the spatial distribution- both laterally and vertically- requires more careful consideration. If the polymer were deposited as a uniform, dense (unsolvated) slab on the surface, its thickness would be:

$$\frac{0}{n_{r,av}} = \frac{r}{c} \quad (2)$$

where the zero superscript signifies the absence of solvent, the "av" subscript signifies a laterally averaged value and  $c$  is the concentration of monomer units in the film (approximated at the reciprocal of monomer molar volume). The fact that the lateral distribution of polymer is *not* uniform is, of course, the entire basis of the methodology presented here. Although there are variations from sample to sample, in a typical situation, the deposited film marks obscures *ca.* 50% of the surface so, in those unobscured ("bare") regions of the surface where electrochemistry does occur, the local film thickness,  $h = 2h_{av}$ . Further, *in situ* solvation of electroactive polymers is known to occur and in this configuration will swell the film *vertically*. Anecdotal, it is accepted that electroactive polymer film solvent volume fractions vary with polymer charge state, solvent and electrolyte composition, but they are commonly in the range 0.2-0.5, *i.e.* may swell the polymer by a further factor of up to two (1.25 *hr* 2 *hr*). To summarize, the total population of polymer is unambiguously known, but local estimates of film thickness require some (reasonable) assumptions.

Images of full PEDOT enhanced fingerprints were captured using a Canon A480 digital camera and digitally enhanced using the GNU Image Manipulation Program 2.6.7 (GIMP). Details of nuorescence, lighting, filters and still image capture for fingerprints enhanced by standard methods are given in the Supporting Information. In different instances, films were viewed either *ex situ* or under potential control *in situ*: details are given in the figure legends.

Fingerprint images prior to and subsequent to enhancement were graded according to the Bandey scale<sup>36</sup> (see Supporting Information for details), a five point scale running from 0 (no development) to 4 (full development). Although this scale is designed for research rather than legal application, it is broadly accepted that images of grades 3 and 4 would provide unequivocal (legally undisputed) identification.

## Results

### Electrochemistry and review of PEDOT films

PEDOT film quality was judged *visually* by evenness of colour on non-fingerprinted sample regions and by uniformity of ridge definition across the fingerprinted area, *electrochemically* by charge injection/recovery as functions of potential scan rate and repetitive cycling, and *morphologically* by microscopic imaging. Details of these individual assessments are given below, but the summary is that the highest quality films were generated from EDOT deposition solutions containing  $H_2SO_4$  and SDS, and vigorously stirred immediately prior to use to ensure good monomer dispersion. Accordingly, we focus here on PEDOT films deposited potentiostatically (at  $E = 0.9$  V) from such solutions; comments on the outcomes for less effective protocols are provided in the Supporting Information.

These films had electrochemical signatures (voltammetric  $i$ - $E$  curves in oxygen-free background electrolyte) typical of relatively thick PEDOT films<sup>32, 37</sup> (see Supporting Information). We do not explore the details of coupled electron/ion (dopant) transfer, which have been discussed previously for diverse electrolytes.<sup>38</sup> save to note the practically critical feature that voltammetric currents were linear with potential scan rate and (necessarily) that injected/recovered charge was independent of scan rate in the range  $1 < \nu/mV s^{-1} < 250$ . These films were stable to extended potential cycling in the range  $-0.4 < E/V < 0.8$ ; within this range the electrochemical response was attributable solely to PEDOT (no solvent decomposition) and full (un)doping could be accomplished. Although not required for practical purposes, reasonable stability to application of more extreme potentials (from a cathodic limit of  $E = -1.4$  V to an anodic limit of  $E = 1.5$  V) was found; beyond this range the severe gas evolution associated with solvent decomposition resulted in film rupture. (At least in the case of the cathodic limit, at which the film will be reduced and very resistive, we recognize that ohmic drop may be significant, so the applied potential may not reflect the potential at the film/solution interface.) Films subject only to the potential regime  $-0.8 < E/V < 0.8$  showed electrochromism that could be regenerated by re-immersion in background electrolyte after extended dry storage, were not detached from the surface by washing with water or acetone, but could be damaged by abrasion (*e.g.* scratching the surface).

Based on coulometric assay (see eqn (1) and (2)), the range of film thickness explored was  $83 < h/nm < 530$ . As discussed above (see Experimental procedures and supporting information), the implication is that local solvated film thickness values were in the range  $0.33 < h/nm < 2.1$ . Quite generally, the height of a fingerprint deposit can range from 10 nm to 2  $\mu m$ , according to the amount of sweat present on the finger and the pressure applied during deposition,<sup>39</sup> so the selected *hr* range spans low level filling (Scheme 1, panel *c*) to overfilling (Scheme 1, panel *e*) of the trenches; this distinction is explored below using AFM imaging. Based on literature data for PEDOT optical properties,<sup>40</sup> the peak absorbances of PEDOT films in this coverage ( $r$ ) range should lie in the ranges 0.4-2.4 and 0.2-1.1 when the films are maintained in the undoped and p-doped states, respectively. Although transmission measurements cannot be made on the metal substrates (and in any case would not be meaningful for films that are, necessarily in this situation, laterally varying in thickness), this estimated absorbance range is consistent with both the needs of visual fingerprint appraisal (*i.e.* giving images whose film/fingerprint deposit contrast gave feature definition at the grade 3 or 4 level on the Bandey scale; see Supporting information) and the observation that films were readily visible but not totally opaque.

### PEDOT electrochromic enhancement – the effect of applied potential

A representative example of latent fingerprint enhancement on a stainless steel substrate is shown in Fig. 1 for the case of a three day old fingerprint stored under ambient conditions. Panel *a* shows the latent sebaceous fingerprint as deposited; while one can deduce qualitatively that there is a fingerprint

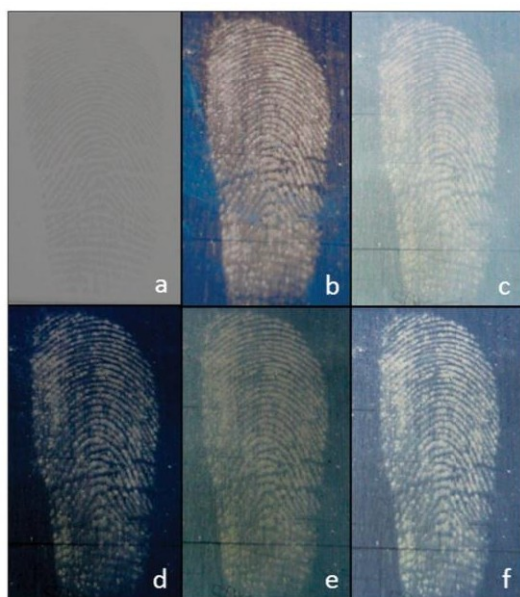


Fig. 1 Effects of ambient medium and applied potential on a fingerprint image subjected to enhancement by PEDOT deposition. All images are for the same sebaceous fingerprint, deposited on stainless steel, then stored for 3 days in ambient laboratory conditions prior to the observations shown. Panel *a*: fingerprint prior to enhancement; panels *b-f* following PEDOT deposition (see main text; deposition time 150 s); final image quality on Bandy scale: grade 3. Sample environment: panel *b*: *ex situ*; panels *c* and *d*: *in situ* exposed to  $1 \text{ mol dm}^{-3} \text{ H}_2\text{SO}_4$ ; panels *e* and *f*: *in situ* exposed to  $1 \text{ mol dm}^{-3} \text{ H}_2\text{SO}_4/0.01 \text{ mol dm}^{-3} \text{ SDS}$ . Applied potential: panels *c* and *e*:  $0.80 \text{ V}$ ; panels *d* and *f*:  $-0.80 \text{ V}$ .

present, there is essentially no ridge detail visible (on the Bandy scale, a grade 0 print). Panels *b-f* show the result of depositing a PEDOT film (from an acidic SDS monomer solution, procedure (iii); see above) and then viewing the enhanced fingerprinted surface under variously controlled conditions. In all cases, it is clear that the image has been significantly enhanced, although differently according to the imposed conditions. For the present, we focus on the effect of applied potential. Comparing panels *c* and *d* and panels *e* and *f* – where each pair corresponds to exposure to the same electrolyte – the result is that active maintenance of the film in a reduced (undoped) state gives a more strongly contrasted image for the case of the stainless steel substrate. In the case of panel *b*, for which the sample was simply removed from the deposition solution, rinsed and viewed *ex situ*, the result is similar to the undoped state. However, while the colour of the PEDOT film is obvious, in this image the full potential (literally) of the method is not realised, since the sample is necessarily not subject to the potential control that allows manipulation of film electrochromic properties between the dark and light blue colours, respectively, of the undoped and p-doped states. For the stainless steel substrate, this is not a significant limitation, but for differently coloured substrates one might imagine that potential control would be more critical.

Replicate PEDOT deposition experiments on fingerprints of varying ages and subject to different environmental histories (see below) required polymer deposition times on the order of hundreds of seconds (as judged visually to give good contrast). Performance variation with fingerprint age and environmental history has been the subject of a separate operationally-oriented study<sup>34</sup> but transformation of grade 0 images (on the Bandy scale) for an as deposited latent fingerprint to grade 3 or 4 images (as shown in Fig. 1) was commonly achievable for fingerprints left under ambient conditions for extended periods of time. Typically, deposition times in excess of 20 min lead to decreased contrast. The hypothesis, explored below, is that this is a consequence of overfilling the trenches between fingerprint ridges, the scenario represented by panel *e* of Scheme 1.

The *in situ* images of Fig. 1 were acquired with potentiostatic control. More obvious variation of contrast was observed under potentiodynamic conditions, with video recording of the (variably) enhanced image.

#### Effect of electrolyte composition

Given the widely recognized variation in PEDOT electrochemical (*i-E*) responses in the presence of different electrolytes (a typical feature of conducting polyheterocycle films), the effects of the presence and identity of anionic surfactant were determined. The first of these can be seen by comparison of panels *c* and *e* and panels *d* and *f*. In the latter instance of each pair, the background electrolyte contained SDS; in the former instance of each pair, it did not. Since the two optical responses are different, we deduce that (at least some of) the dodecylsulfonate anion transfers into the film as an anionic dopant upon PEDOT oxidation. If the only dopant were bisulfate (the dominant sulfate species at this pH), then the presence of SDS would make no difference; the fact that it does make a difference unequivocally signals its participation as a transferrable dopant. This differs from the conclusion of Li *et al.*,<sup>41</sup> who deduced that OS<sup>-</sup> anions were immobile in Au-supported PEDOT films cycled in SDS and LiBF<sub>4</sub>. In noting the effect of the presence of SDS in the background electrolyte used for redox cycling the film, it should be recalled that all the images in Fig. 1 relate to the same fingerprint and that those in panels *b-f* all relate to the sample following its PEDOT enhancement from an EDOT/SDS deposition solution. The conclusion here is that the response is predominantly determined not by the deposition solution (presence or otherwise of SDS), but rather by the solution to which the film is exposed when the electrochromic effect is exploited.

The fact that anionic surfactant influences film electrochromism prompted the use of a different surfactant, the amino acid-based sodium N-lauroylsarcosinate (SLS), in place of SDS as the solubilising vehicle for EDOT. The outcome, shown in Fig. 2, was a black PEDOT film. Unfortunately, despite the use of apparently similar conditions to a previous report of electrochromism,<sup>42</sup> the fingerprint-templated PEDOT films here did not show an electrochromic response. Practically, the dark film does provide excellent contrast and enhancement for the stainless steel substrate used in Fig. 2, but the loss of electrochromism is in general detrimental.

It was also found that PEDOT films at open circuit showed a response to solution pH. In acidic solution the films were



Fig. 2 Sebaceous fingerprint on stainless steel enhanced by PEDOT deposition from EDOT monomer solution containing  $1 \text{ mol dm}^{-3} \text{H}_2\text{SO}_4/0.01 \text{ mol dm}^{-3} \text{SLS}$ . Deposition (3500 s) on freshly fingerprinted stainless steel. Viewed *ex situ*; BAMLEY (C&D); GNUJIT: 3.



Fig. 3 Effect of pH on PEDOT enhancement for a sebaceous fingerprint on stainless steel (age 24 h under ambient conditions). Panel a: *ex situ*; panel b: *in situ* immersed in  $1 \text{ mol dm}^{-3} \text{H}_2\text{SO}_4$ ; panel c: *in situ* immersed in  $1 \text{ mol dm}^{-3} \text{KOH}$  (Bamley scale: grade 4).

light blue and in basic solution film were dark blue, as shown in Fig. 3. These are analogous to oxidized and reduced films, respectively, although the basis of this effect is less obvious, given the absence of readily (de-)protonatable sites in PEDOT.

#### Imaging at different spatial resolution

The visual assessment of fingerprint enhancement was extended by observations at progressively increasing magnification using optical and then atomic force microscopy. Fig. 4 shows a series of optical microscope images of a sebaceous fingerprint kept under water for one day, then enhanced by PEDOT deposition. For illustrative purposes to indicate the spatial resolution of the technique, we show images centred on a representative second level feature (here, a bifurcation) that would be used for identification purposes. The contrast between the fingerprint ridge detail and PEDOT deposited between the ridges is excellent. The highest magnification optical image (nominally  $\times 20$  magnification; see panel c) that contains the entire feature shows its unambiguous and clear outlines. It is clear that, despite the inevitable dissolution of a substantive fraction of the fingerprint deposit, the enhancement procedure is successful.

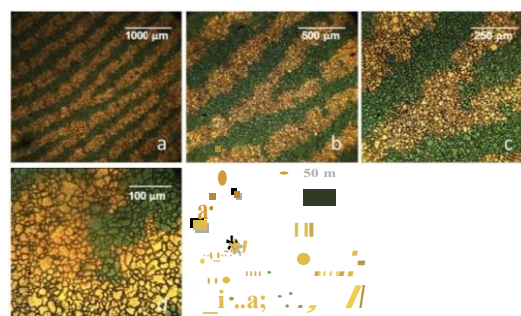
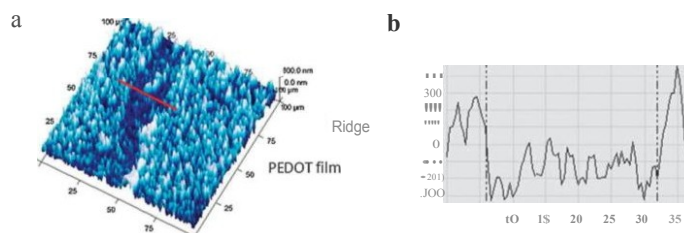


Fig. 4 Optical microscope images (viewed *ex situ*) of progressively increasing magnification (nominally: a:  $\times 5$ ; b:  $\times 10$ ; c:  $\times 20$ ; d:  $\times 50$ ; e:  $\times 100$ ; see scale bars for absolute dimensions). Fingerprint deposited on stainless steel, kept under water for 1 day, then PEDOT enhanced (see main text; deposition time: 230 s). The images focus in on a second level detail feature, a bifurcation. In panel e, red circle highlights onset of overfilling (see main text).

The higher magnification images of Fig. 4 (panels d and e) do not contain the full second level feature, but do allow one to inspect the PEDOT/ridge interface. This is relatively sharp, but higher magnification is required to assess this fully. Accordingly, Fig. 5 shows an AFM image of a (necessarily) small section of ridge detail subject to PEDOT enhancement. The fingerprint deposit and PEDOT are morphologically distinct: the PEDOT is rougher and more globular in nature, as seen for many conducting polymer films. The primary issue at stake is the extent of trench (over)filling, as represented in the cartoons of Scheme 1. Specifically, we wish to determine whether the polymer surface population is sufficiently high to be visualized, but sufficiently low that there is still substantial uncovered ridge detail against which the deposited polymer contrasts. In the event that the polymer surface population were too great, the rising level of PEDOT might be expected to spread across the ridge detail (see Scheme 1, panel e). While there is some evidence (see red circled area in panel e of Fig. 4) of limited spread of PEDOT across the fingerprint ridges, visual appraisal suggests that this does not seem to be widespread. The fundamental reason for this is revealed by images of the type shown in panel a of Fig. 5, which shows a slightly surprising – but undoubtedly advantageous – outcome. Although the trench is overfilled, *i.e.* the level of PEDOT is higher than the upper surface of the fingerprint deposit, the PEDOT does not flow fully across the ridge. The effect is more obvious in the 1D section across the ridge, shown in panel b of Fig. 5, in which the initial fingerprint "ridge" appears as a valley. Practically this is extremely helpful, since one cannot *a priori* know the dimensions of a given fingerprint and thus cannot anticipate the optimum polymer coverage,  $\Gamma$ .

Exploring this in more quantitative fashion, the exposed width of the ridge is  $26 \text{ μm}$  and the PEDOT film rises  $300 \text{ nm}$  above the top of the fingerprint ridge. Coulometrically, we calculate  $\Gamma_{\text{av}} = 353 \text{ nm}$ . In this *ex situ* measurement, it is likely that most of the solvent will have evaporated so, if the film collapses to reflect this fact, then —  $700 \text{ nm}$ . (If solvent evaporation is not accompanied by film collapse, then the film thickness may be a little larger, but most probably not as large



**Fig. 5** *Ex situ* AFM image of a section of fingerprint ridge and surrounding PEDOT. Fingerprint was deposited on stainless steel, stored for 11 days under ambient laboratory conditions, then enhanced by PEDOT deposition (250 s). Panel a: 3D image; panel b: 1D line section perpendicular to ridge (see red line in panel a).

as a factor of two for a fully solvated film.) By difference, we deduce that the height of the fingerprint deposit above the metal substrate was 490 nm. According to Thomas *et al.*,<sup>39,43,44</sup> the width of a ridge in a latent fingerprint deposit can be anywhere between 1–50  $\mu\text{m}$  and the height between 10 nm to 2  $\mu\text{m}$  (depending on load when deposited and time elapsed since deposition). The experimental observations fall within these bounds and are consistent with a mid-range deposit that is substantially, but incompletely, covered.

The example of Fig. 5 was a fingerprint aged for 11 days under ambient conditions, during which time evaporation of the more volatile components will have decreased the ridge width and height.<sup>39</sup> From the perspective of a topographic image, this may in part explain the relatively narrow fingerprint ridge and its less regular shape. Loss of volatile components will increase the viscosity of the deposit, making rheological distinction between the viscoelastic<sup>37</sup> PEDOT and fingerprint deposit components less marked. The obvious control experiment of imaging the fingerprint as deposited was not possible due to its fluid-like nature prior to loss of volatile components: the AFM tip was simply dragged through the soft deposit. Nonetheless, the evidence of Fig. 5 is that their different morphological characteristics permit differentiation of the PEDOT and fingerprint deposit components.

#### Assessment of performance and comparison with existing enhancement techniques

To assess the efficacy of the PEDOT electrochromic enhancement technique, its capability to visualize fingerprints subjected to plausible environmental degradation scenarios was tested. These scenarios were ambient exposure (the least challenging scenario), continuous immersion in water, washing with soap solution followed by ambient exposure, washing with acetone followed by ambient exposure, and continuous exposure to high temperature (ISO C: the most challenging scenario). In each case, samples were imaged after periods of 1, 7, 14 and 28 days. Replicate sets of samples (from different donors) were also treated with three commonly used enhancement methods, namely dusting with black powder, cyanoacrylate ("superglue") fuming followed by dyeing with the fluorescent yellow dye BY40, and a suspension of iron oxide in detergent (Codeco and distilled water, "wet Wop."). The empirical outcomes of such a survey executed for

five donors are presented elsewhere<sup>34</sup> without explanation of the underlying electrochemistry. Here we focus on these more

fundamental issues, through illustrative examples of scenarios where the PEDOT enhancement shows particular promise.

Figs. 6 and 7 show images of PEDOT-enhanced fingerprints previously subjected, respectively, to heat and washing with soap solution. The practical significance of these environments is that both diminish the amount of sweat deposit present on the surface, thereby compromising techniques that involve interaction with the fingerprint itself. For example, traditional techniques (using powder, wet powder and cyanoacrylate ("superglue") treatments) showed poor success rates. Moreover, interest in samples subjected to these environments is motivated by the efficacy of the PEDOT treatment in visualizing these latent fingerprints.<sup>3</sup> For example, across a number of enhancement

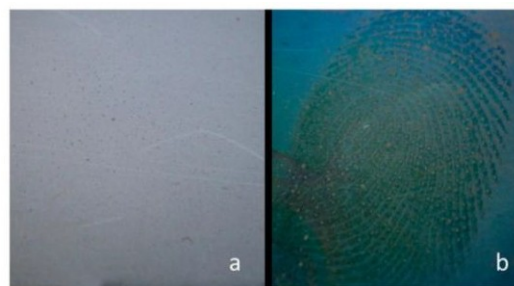


**Fig. 6** Images of sebaceous fingerprint kept in an oven at 150 °C for 28 days prior to enhancement with PEDOT. Panel a: fingerprint prior to enhancement (Bandy scale: grade 1); panel b: *ex situ* after PEDOT deposition (Bandy scale: grade 4).

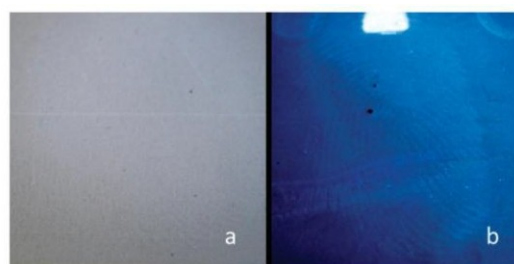


**Fig. 7** Images of sebaceous fingerprint hand washed in warm (40 °C) soapy water then kept in ambient conditions for 7 days prior to enhancement with PEDOT. Panel a: fingerprint prior to enhancement (Bandy scale: grade 1); panel b: *ex situ* after PEDOT deposition (Bandy scale: grade 4).

techniques used to enhance samples subject to heat treatment. PEDOT deposition was responsible over 50% of the successful visualizations, and on 7 day old samples PEDOT showed improved images of 60% of fingerprints washed (with gentle abrasion) with soap solution. For the two examples shown, these high quality PEDOT-enhanced images, showing excellent second level detail and (at least in the case of Fig. 6) significant third level detail, demonstrate clear niche applications for the PEDOT approach.

Although enhancement was possible with both eccrine and sebaceous print residues, sebaceous fingerprints produced higher quality images. We attribute this to the fatty deposits derived from sebaceous fingerprints acting as better insulators and being more resistant to dissolution in the aqueous electrolyte than is the case for the analogous deposits for eccrine fingerprints. Practically, this is beneficial since fingerprints in a forensic context commonly contain a mixture of eccrine and sebaceous sweat. In particular, one rarely finds pure eccrine fingerprint deposits, since they are frequently contaminated with sebaceous residues as a result of contact of the fingertips with the face or hair.

The overall picture, set in the context of complementary and competing methods, is summarised in Fig. 8. This figure aggregates the outcomes of a survey involving over 500 samples, involving fingerprints from different donors, subjected to different environments/histories, sampled after different time intervals and enhanced using different methods. The detailed effects of these parameters from an operational perspective are described elsewhere<sup>34</sup> for the majority of this dataset. The purpose of showing the integrated data set is to assert the potential efficacy

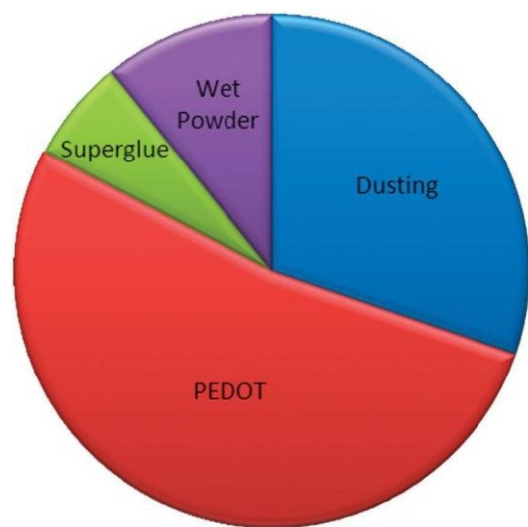


Fig. 8 Summary of success rates (image enhanced to Bandey scale grade 3 or 4) using various latent fingerprint enhancement methods: black powder, wet powder, cyanoacrylate fuming and PEDOT electrochromic polymer (as annotated). For the three traditional methods, survey size was 100 samples each and for PEDOT the survey size was 130 samples. In all cases, samples spanned a range of ages (1–28 days) and environmental exposures (see ref. 34 for details). For each enhancement methodology, the success rate was normalized to the number of samples.

of the electrochromic treatment. The simplistic view is that the PEDOT enhancement method and powder dusting are the two most effective methods, although this superficial assessment conceals the fact that the strengths of the two best methods are somewhat complementary. The poor performance of "superglue" is perhaps surprising, but it should be emphasised that it is an excellent method for imaging latent fingerprints on plastics and other insulating surfaces, for which the electrochromic approach cannot be used.

We end the discussion with some comments on issues related to practitioner uptake of this novel approach. The choice of instrumentation will depend upon the object to be processed, but capital costs need not be more than for the cyanoacrylate (superglue fuming) cabinet that is a feature of every well-founded fingerprint laboratory. There is a wide selection of such instruments commercially available and choice would be based on the current requirement: objects of larger area will require passage of larger current, *i.e.* a potentiostat of greater compliance. Reagent costs are modest. Operation is simple and processing time will be comparable to that of existing chemical treatment techniques. We do not envisage substantial barriers to exploitation associated with typical laboratory infrastructure, safety issues or economic factors.

## Conclusions

The principle of using the locally insulating characteristics of a fingerprint deposit on a metal surface as a mask, or template, for the spatially selective electrodeposition of PEDOT films has been demonstrated. The facility to alter the optical properties – simplistically, colour – of the deposited film *via* the application of an external voltage provides a means to optimise contrast within the image. This introduces a new dimension to fingerprint imaging. Further, the reversibility of this latter process means that one can independently optimise contrast in different regions of the image, for example where the fingerprint deposit is of variable thickness or definition.

For the situations explored – on stainless steel as a representative surface – potentiostatic polymerization of EDOT monomer in an aqueous SDS surfactant dispersion was found to be optimum. Suitable control of deposition rate, *via* monomer concentration and deposition potential and time, permits progressive filling of trenches between fingerprint deposits until optimum contrast is achieved. Both eccrine and sebaceous latent fingerprint deposits were developed on stainless steel, although sebaceous prints provided the highest quality images. This is attributed to the greater insulating nature of the predominantly hydrocarbon-based deposits resulting from these fingerprints.

Microscopic observation of the polymer/fingerprint deposit structures on the surface show good definition. For the particular material used, PEDOT, it turns out that some element of overfilling of the trenches can be tolerated, since the polymer grows preferentially vertically (outwards) rather than laterally (across the top of the fingerprint deposit). While one would naturally attempt to avoid overfilling of the trenches, this may in practice be difficult for marks of variable deposit thickness, so this tolerance has practical value. An additional attractive practical attribute of this system is the option of using

an aqueous electrolyte for both deposition and film redox state variation. In the deposition step, this requires use of a surfactant to solubilise the monomer: limited exploration of surfactant options suggests this may be an additional area for useful optimisation and/or colour manipulation.

From an operational perspective, this method reveals latent fingerprints of evidentially useful quality from challenging and practically relevant situations, including attempts to remove the fingerprint and extended exposure to water or heat. In the latter two instances, it is surmised that this is a result of removal of water-soluble (conducting) components, such that the insulating organic components are concentrated on the surface to provide a more effective template for polymer deposition. In the case of heat treatment, water will also be removed. Across a range of fingerprint histories and ages, PEDOT enhancement outperforms cyanoacrylate and wet powder enhancements. Overall, it has a similar success rate to dusting with black powder, but the strengths of these two reagents are complementary.

The approach of a visualizing reagent interacting with the bare surface is complementary to the majority of fingerprint enhancement methods, which are based on interaction of some reagent with the fingerprint deposit itself. This offers the promise, to be explored in future work, of using both approaches without mutual exclusion. Other areas of future enquiry will include application to other metals, variation of deposition solution formulation (for example using other surfactants with potential generation of different optical properties), and assessment of the extent of third level detail present.

### Acknowledgements

We thank Dr John Bond, Dr Karl Ryder and Mark Rowe (Northamptonshire Police) for helpful conversations on practical issues. RMB thanks the University of Leicester for a scholarship.

### References

- 1 H. C. Lee and R. E. Gaensslen. *Advances in Fingerprint Technology*. CRC Press. Boca Raton. 2nd edn. 2001.
- 2 S. P. Wargacki, L. A. Lewis and M. D. Dadmun. *J. Forensic Sci.* 2008, **53**, 1138-1144.
- 3 P. Cuce, G. Polimeni, A. P. Lazzaro and G. De Fulvio. *Forensic Sci. Int.*, 2004, **146**, 7-8.
- 4 M. Zhang and H. H. Girauh. *Analyst*. 2009, **134**, 25-30.
- 5 R. Fields and D. K. Molina. *J. Forensic Sci.* 2008, **53**, 952-955.
- 6 J. R. W. Jackson and J. M. Jackson, *Forensic Science*. Pearson Prentice House. Harlow, UK. 2004.
- 7 C. Champod, C. J. Lennard, P. Margot and M. Stoilovic. *Fingerprints and Other Ridge Skin Impressions (International Forensic Science and Investigation)*. CRC Press. Boca Raton. 2004.
- 8 O. Jensen and E. Nielsen. *Acta Derm.* 1979, **59**, 139-143.
- 9 N. Akiba, N. Saitoh and K. Kuroki. *J. Forensic Sci.* 2007, **55**, 180.
- 10 M. J. Choi, T. Smoother, A. A. Martin, A. M. McDonagh, P. J. Maynard, C. Lennard and C. Roux. *Forensic Sci. Int.* 2007, **173**, 154.
- 11 J. Ahnog, G. Levinton-Shamuilov, Y. Cohen and M. Azoury. *J. Forensic Sci.* 2007, **52**, 1057.
- 12 J. D. James, C. A. Pounds and B. Wilshire. *J. Forensic Sci.* 1993, **38**, 391.
- 13 L. K. Seah, U. S. Dinis, W. F. Phang, Z. X. Chao and V. M. Murukeshan. *Forensic Sci. Int.* 2005, **152**, 249.
- 14 A. R. W. Jackson and J. M. Jackson. *Forensic Science*, Pearson Prentice House. Harlow, UK, 2004.
- 15 *Annual of fingerprint development techniques*, ed. V. Bowman. Sandridge, UK, 2nd rev. edn, 2004: Police Scientific Development Branch, Home Office.
- 16 P. Czekanski, Y. Fasola and J. Allison. *J. Forensic Sci.* 2006, **51**, 1323.
- 17 M. Colella, A. Parkinson, T. Evans, C. Lennard and C. Roux. *J. Forensic Sci.* 2009, **54**(3), 583-590.
- 18 K. K. Bouldin, E. R. Menzel, M. Takatsu and R. H. Murdock. *J. Forensic Sci.* 2000, **45**, 1239.
- 19 G. Williams, H. M. McMurray and D. A. Worsley. *J. Forensic Sci.* 2001, **46**, 1085.
- 20 G. Williams and N. McMurray. *Forensic Sci. Int.* 2007, **167**, 102.
- 21 J. W. Bond. *Rev. Sci. Instrum.* 2009, **80**, 075108.
- 22 E. Gutierrez-Redomero, C. Alonso-Rodriguez, L. E. Hernandez-Hurtado and J. L. Rodriguez-Villalba. *Forensic Sci. Int.* 2011, **208**, 79-90.
- 23 C. Bersellini, L. Garofano, M. Giannico, F. Lusardi and G. Mori. *J. Forensic Sci.* 2001, **46**, 871.
- 24 G. L. Thomas and T. E. Reynoldson. *J. Phys. D: Appl. Phys.* 1975, **8**, 724-729.
- 25 A. L. Beresford and A. R. Hillman. *Anal. Chem.* 2010, **82**, 483-486.
- 26 F. Blanchard, B. Carre, F. Bonhomme, P. Biensan, H. Pages and D. Lemordant. *J. Electroanal. Chem.* 2004, **569**, 203-210.
- 27 A. Bund and S. Neudeck. *J. Phys. Chem. B* 2004, **108**, 17845-17850.
- 28 L. Iu, C. Kvarnstrom and A. Ivaska. *J. Electroanal. Chem.* 2004, **569**, 151-160.
- 29 L. Pigani, A. Heras, A. Colina, R. Seeber and J. Lopez-Palacios. *Electroanal. Chem.* 2004, **6**, 1192-1198.
- 30 W. Plieth, A. Bund, U. Rammeh, S. Neudeck and L. M. Due. *Electrochim. Acta* 2006, **51**, 2366-2372.
- 31 F. Petraki, S. Kennou, S. Nespurek and M. Bilcer. *Org. Electron.* 2010, **11**, 1411-1431.
- 32 D. C. Martin, J. Wu, C. M. Shaw, Z. King, S. A. Spanninga, S. Richardson-Burns, J. Hendricks and J. Yang. *Polym. Rev.* 2010, **50**, 340-384.
- 33 H. K. Song, E. J. Lee and S. M. Oh. *Chem. Mater.* 2005, **17**, 2232.
- 34 A. L. Beresford, R. M. Brown, A. R. Hillman and J. W. Bond. *J. Forensic Sci.* 2012, **57**(1), 93-102.
- 35 L. B. Groenendall, F. Jonas, D. Freitag, H. Pielartzik and J. R. Reynolds. *Adv. Mater.* 2000, **12**, 481-494.
- 36 V. G. Sears, S. M. Bleay, H. L. Bandey and V. J. Bowman. *Sci. Justice* 2011. DOI: 10.1016/j.scjus.2011.10.006. in press.
- 37 A. R. Hillman, I. Efimov and K. S. Ryder. *J. Am. Chem. Soc.* 2005, **127**(47), 16611-16620.
- 38 A. R. Hillman, S. J. Daisley and S. Bruckenstein. *Phys. Chem. Chem. Phys.* 2007, **9**, 2379-2388.
- 39 G. L. Thomas and T. E. Reynoldson. *J. Phys. D: Appl. Phys.* 1975, **8**, 724.
- 40 E. G. Tolstopyatova, N. A. Pogulaichenko, S. Eliseeva and V. V. Kondratiev. *Russ. J. Electrochem.* 2009, **45**(3), 252-262.
- 41 C. Li and T. Imae. *Macromolecules* 2004, **37**, 2411.
- 42 Y. Wen, J. Xu, H. He, B. Lu, Y. Li and B. Dong. *J. Electroanal. Chem.* 2009, **634**, 49-58.
- 43 G. L. Thomas. *Thin Solid Films* 1974, **24**, 52.
- 44 G. L. Thomas. *J. Phys. E: Sci. Instrum.* 1978, **11**, 722.

## PAPER

## Nanoscale control of interfacial processes for latent fingerprint enhancement

Rachel M. Sapstead (nee Brown),<sup>a</sup> Karl S. Ryder,<sup>a</sup> Claire Fullarton,<sup>a</sup> Maximilian Skoda,<sup>b</sup> Robert M. Dalgliesh,<sup>b</sup> Erik B. Watkins,<sup>c</sup> Charlotte Beebee,<sup>c</sup> Robert Barker,<sup>c</sup> Andrew Glidled and A. Robert Hillman\*<sup>a</sup>

Received 15th April 2013, Accepted 17th May 2013

DOI: 10.1039/c3fd00053b

Latent fingerprints on metal surfaces may be visualized by exploiting the insulating characteristics of the fingerprint deposit as a "mask" to direct electrodeposition of an electroactive polymer to the bare metal between the fingerprint ridges. This approach is complementary to most latent fingerprint enhancement methods, which involve physical or chemical interaction with the fingerprint residue. It has the advantages of sensitivity (a nanoscale residue can block electron transfer) and, using a suitable polymer, optimization of visual contrast. This study extends the concept in two significant respects. First, it explores the feasibility of combining observation based on optical *absorption* with observation based on *fluorescence*. Second, it extends the methodology to materials (here, polypyrrole) that may undergo post-deposition substitution chemistry, here binding of a fluorophore whose size and geometry preclude direct polymerization of the functionalised monomer. The scenario involves a *lateral* spatial image (the whole fingerprint, *first level* detail) at the centimetre scale, with identification features (minutiae, *second level* detail) at the 100–200 nm scale and finer features (*third level* detail) at the 10–50 nm scale. However, the strategy used requires *vertical* spatial control of the (electro)chemistry at the 10–100 nm scale. We show that this can be accomplished by polymerization of pyrrole functionalised with a good leaving group, ester-bound Fmoc, which can be hydrolysed and eluted from the deposited polymer to generate solvent "voids". Overall the "void" volume and the resulting effect on polymer dynamics facilitate entry and amide bonding of Dylight 649 NHS ester, a large fluorophore. FTIR spectra demonstrate the spatially integrated compositional changes. Both the hydrolysis and fluorophore functionalization were followed using neutron reflectivity to determine *vertical* spatial composition variations, which control image development in the *lateral* direction.

<sup>a</sup>University of Leicester, Leicester LE1 7RH. E-mail: arh7@le.ac.uk

<sup>b</sup>Rutherford Appleton Laboratory, Didcot, Oxfordshire. OX11 0QX UK

<sup>c</sup>Institut Laue Langevin, Grenoble, Cedex 9, France

<sup>d</sup>Glasgow University, Glasgow, G12 8LT, UK

## Introduction

Fingerprints provide an example of pattern formation in nature, carrying information that uniquely identifies an individual. Notwithstanding the rise of sophisticated genetic methods, they remain the cornerstone of many criminal investigations and have a number of non-criminal applications based upon identification of an individual. The efficacy of this approach is in large measure associated with the complexity of a fingerprint and the consequent practical difficulty of forgery; powerful software tools for analysis and recognition facilitate exploitation of this potential. The power of fingerprint evidence for analytical purposes in general is anecdotally recognized by the use of the term in other contexts, such as the "fingerprint" region of IR spectra and DNA "fingerprinting". The challenge in realizing this analytical opportunity lies in visualization of the interfacial chemical transfer that constitutes a fingerprint, primarily in the case of *latent* fingerprints, for which the nature and extent of the deposit mean that they are not immediately visible to the eye. Here we explore how this can be accomplished by a novel electroanalytical approach based upon spatially selective deposition of electroactive polymers with variable optical properties. The intellectual novelty lies in the need to control the (electro)chemistry on different length scales and in both the lateral and vertical directions.

When a finger contacts a surface, exchange of material with the surface leaves behind a trace of this contact which resembles the pattern present on the finger. Dependent on the substrate and the nature of the contact, the fingerprint may be visible, latent or plastic. Since they are not immediately visible to the eye, and thus less readily "wiped", latent fingerprints are the greatest source of forensic evidence. To give an indication of scale, in the UK on the order of 700 000 objects are fingerprinted per annum. In response to this demand, numerous methods and reagents have been developed to effect latent fingerprint visualization but, perhaps surprisingly, the operational success rate is only *ca.* 10%. While there may be local variations in demand and/or success rate for specific types of object, the global need for improvement is clear.

The existence of fingerprint patterns was recognized in ancient times: they have been identified on hand-formed building materials in Jericho dating back to 7000 BC and on the reverse of Chinese clay seals from 300 BC. Much later they were used as accompaniments to signatures by citizens claiming damages following the siege of Londonderry in 1691<sup>5</sup> and by the engraver Bewick who used an engraved fingerprint as a signature on his work. The first documented study of fingerprints was in the 17th century by Grew,<sup>6</sup> followed by attempts at pattern classification in 1823 by Purkinje,<sup>7</sup> and later by Henry.<sup>8</sup>

Development of these historical observations for forensic application was reliant upon three crucial deductions made during the 19th century. First, Herschel<sup>9</sup> made the critical observation – on his own hands – that fingerprints do not change during the life of an individual. "Indeed, the friction ridge skin pattern that constitutes a fingerprint persists after death, thereby enabling *post mortem* identification." Second, by removing skin from the fingers and allowing it to re-grow, it was demonstrated that injury does not change fingerprint patterns.<sup>10</sup> Third, in 1892 Galton<sup>9</sup> estimated that the odds of two individuals having identical fingerprints were 64 billion to 1; thus, for all practical purposes, they are unique to an individual. Combination of these observations pointed to the value of

fingerprints in criminal investigations.<sup>10</sup> The outcome of this, in the first decade of the 20th century, was establishment of the UK's first fingerprint bureau<sup>5</sup> and the use of fingerprint evidence to secure a murder conviction.<sup>6</sup>

Fingerprint patterns fall into three basic categories (so-called *first level* detail): loops, whorls and arches.<sup>7</sup> While differences at this gross level can clearly eliminate certain individuals, positive identification relies on the *minutiae* (or *second level* detail) within the pattern: these include such features as ridge endings, crossovers (bridges), short independent ridges, islands, bifurcations, spurs, dots and lakes.<sup>8</sup> The standard for matching a crime scene fingermark to one from a database varies with jurisdiction: in some cases there is a set minimum number of points of similarity (although the number is not universal) and in others (including the UK) it is decreed a matter for a recognized expert to decide. As a rule of thumb, identification of around 16 points of similarity can be expected to be considered conclusive.<sup>9</sup> There are also finer features (*third level* detail) present in a fingerprint image: these include the detailed shapes of the ridges and individual sweat pores. While not currently used in fingerprint identification, there is considerable research interest in third level detail, since it may in future permit analysis of smaller fragments of marks left by a finger, *i.e.* partial fingerprints.

Here we focus on latent fingerprints, since these are the primary source of forensic evidence. In general terms, the traditional approach has been to apply a reagent that interacted with the residues left by contact of the finger. We do not rehearse the diverse methods available, since these have been reviewed elsewhere recently,<sup>13–15</sup> but rather show how the apparently diverse methods used in fact have some similarities that limit their efficacy and motivate the novel approach developed here. The classical approach is to apply a powder (either dry or as a suspension) that adheres physically to the sweat residues; the powder may be fluorescent,<sup>16</sup> magnetic<sup>19,20</sup> or thermoplastic. In each case, this method is reliant upon there being sufficient residue present for adhesion of a powder with adequate optical contrast to the substrate.<sup>21–26</sup> More recent developments involve (by dipping, spraying or gas phase delivery, according to the chemistry) ninhydrin solution,<sup>27</sup> vacuum metal deposition,<sup>28</sup> small particle reagent/<sup>29</sup> physical developer/<sup>30</sup> cyanoacrylate ("superglue") polymerization in conjunction with a suitable dye/<sup>30</sup> S<sub>2</sub>N<sub>2</sub> polymerization<sup>31</sup> and cadmium sulphide nanocomposites.<sup>32</sup> In some cases the interaction of the reagent may be relatively unspecific (physical adhesion of powders), in others it may involve moderately specific chemistry (CdS binding with fatty acids and amino acids generally found in fingerprint deposits) and in oilier cases it may be very specific (reaction with secreted drug metabolites of antibody-functionalised nanoparticles.<sup>33</sup> However, the common factor is that the reagent interacts with the deposited residue. This makes all these technologies vulnerable to loss or deterioration of fingerprint residue, *e.g.* as a consequence of ageing, environmental exposure or abuse (attempted washing).

The approach developed here is complementary to those described above, in that the "reagent" is applied to the bare substrate surface that lies between the deposited fingermark ridges. The means of accomplishing this is to use the fingerprint deposit as a "mask" or template, whose broadly insulating characteristics preclude electron transfer from a metal substrate to a solution precursor. Since electron tunnelling can only take place over very short distances, only a very thin layer (*ca.* 1–2 nm) of fingerprint residue is required – far less (by an order of magnitude) than required in the conventional strategies listed above. We have recently demonstrated

proof-of-concept for this strategy<sup>35</sup> in the context of electropolymerization of aromatic solution precursors<sup>36</sup> to generate conducting polymer films. Other applications of electrochemically-based methods of latent fingerprint visualization include imaging using the SECM<sup>38,41</sup> and deposition of Au nanoparticles.<sup>42</sup>

In the case of electroactive polymer enhancement, after transfer to a background electrolyte, the electrochromic properties of these materials were exploited to adjust the visual contrast between the polymer and the metal substrate. Evaluation of the ability of this approach to visualize fingerprints subject to ageing in a range of environments suggests that there are practically relevant situations in which the methodology may be superior to currently employed methods, for example involving powders and cyanoacrylate.<sup>37</sup>

The aim of the present study is to extend the concept of the electrochromic polymer enhancement strategy in two significant respects. First, we wish to explore the possibility of combining observation based on optical *absorption* (as above) with observation based on *emission*. Since the advantages, notably sensitivity, of fluorescence detection are appreciated in fingerprint visualization, translation to practical application would be facilitated by existing instrumentation. In the context of "superglue" enhancement, subsequent use of fluorescent dyes is a necessity, since the cyanoacrylate polymer is not coloured. This leads naturally to our second generic goal, use of electropolymerized films permitting excellent spatial control but with sub-optimal optical properties. In particular, we wish to move from thiophene<sup>5</sup> and aniline-based materials to pyrrole-based systems, for which there is much greater opportunity for manipulation of properties by substituent chemistry on the  $\alpha$ -N-H functionality. Here we focus on the underlying fundamental (electro)chemistry of this approach.

The future viability of enhancement and analysis of latent fingerprints using this strategy relies on "writing" (electropolymerization and post-deposition reaction) and "reading" (absorption and emission observations) of spatial information at different length scales. The precise figures will vary from one individual to another, but typically this is at *ca.* 1 cm for first level detail (the whole print), at 100–200  $\mu$ m for second level detail and at 10–50  $\mu$ m (third level detail). These feature sizes set the chemical challenge: control of enhancement chemistries with commensurate *lateral* spatial resolution to the feature size. However, the requirement for *vertical* resolution is somewhat different. Typical fingerprint deposits may be a few microns thick as-deposited, but evaporative and other environmental losses will typically decrease this to 100s of nm before enhancement is undertaken. This defines the *vertical* resolution required for the (electro)chemistry: there is an optimum to be found between the lower limit of detection of deposited material and over-filling<sup>15</sup> of the trenches between fingerprint ridge deposits. To summarize, this singular analytical challenge of uniquely identifying an individual based on electroanalytical visualization of their fingerprint requires simultaneous control of (electro)chemical processes on length scales from the nanometre to the centimetre regime and in both lateral and vertical directions.

## Experimental

Reagents, materials and electrodes

N-Cyanoethylpyrrole (PyCN), piperidine, tetrabutylammonium perchlorate (TBAP), perchloric acid, hydrogenous and deuterated acetonitrile were all used as supplied

## Paper

## Faraday Discussions

(Sigma Aldrich). N-Aminopropylpyrrole (PyNH<sub>2</sub>) was synthesised *via* reduction of PyCN (0.056 mol) with LiAlH<sub>4</sub> (0.26 mol) in anhydrous ether. The reaction was stirred for 2 h before excess LiAlH<sub>4</sub> was neutralised with water. The solution was dried over MgSO<sub>4</sub> before evaporating to dryness to yield a yellow oil (84% yield).

(9H-Fluoren-9-yl)methyl-3-(1H-pyrrol-1-yl)propylcarbamate (PyFMOC) was made using a Merrifield synthesis. Fmoc-Cl (0.021 mol) in water-dioxane (60 ml, 1 : 1) was added to a solution of PyNH<sub>2</sub> (0.021 mol) and Na<sub>2</sub>CO<sub>3</sub> (0.028 mol) in water-dioxane (60 ml, 1 : 1) in an ice bath. The solution was then stirred at room temperature for 2 h. PPyFMOC was extracted with ethyl acetate and dried over MgSO<sub>4</sub> before evaporating to dryness to yield a white solid (78% yield).

For the neutron reflectivity (NR) experiments, the working electrode was prepared by sputter coating gold onto a polished single-crystal quartz block (100 x 50 mm, Gooch and Hou sego) coated with a monolayer of 3-mercaptopropyltrimethoxysilane (MPTS) (Sigma Aldrich) to promote adhesion. The nominal Au film thickness was 20 nm. For other experiments, the electrodes were metal sheet, as indicated in the figure legends. The counter electrode was in each case a Pt gauze, of adequate size to ensure that the counter electrode reaction was not limiting. The reference electrode was a double junction Ag|AgCl|KCl (saturated) electrode. These were assembled into a standard three electrode cell configuration; for the NR measurements, the purpose built cell has been described elsewhere.<sup>43,44</sup>

### Instrumentation

NR measurements were performed on FIGARO\*s and D17 at the Institut Laue-Langevin (Grenoble, France) and on INTER<sup>46</sup> at the ISIS Facility of the Rutherford Appleton Laboratory (Harwell Oxford, UK). Static neutron reflectivity measurements were performed *ex situ* in air ("dry") and *in situ* immersed in H<sub>2</sub> and d<sub>3</sub>-acetonitrile before and after the film fabrication stage (see Fig. 3, below). Deuterated solvents were used to maximise contrast between the polymer and the electrolyte so that the solvation within the polymer could be probed. Kinetic measurements were recorded during the hydrolysis stage of the reaction (see Fig. 3), using time-of-flight instrumentation with ranges of 2-30 Å (ILL) and 1.5-16 Å (ISIS). Using different incident angles, this provides an accessible momentum transfer range of  $0.004 < Q/\text{Å}^{-1} < 0.12$ , where  $Q$  is defined as  $(4\pi/\lambda) \sin\theta$ ;  $\lambda$  is the wavelength of the neutron and  $\theta$  is the incident angle. (Strictly, this is  $Q_z$  but since we only consider specular reflection we use the simpler notation  $Q$ .) The collimation slits were set to give a beam footprint on the sample of 60 mm x 30 mm; they also define the  $\Delta\theta/\theta$  resolution. The  $\Delta\lambda/\lambda$  resolution is dependent on the source (spallation source at ISIS, reactor at ILL) and associated instrumentation (chopper settings at ILL). In both cases, the resultant resolution in momentum transfer was  $\Delta Q/Q \approx 2-3\%$ . Data acquisition times were *ca.* 1.5 h per static run and 10 min for kinetic runs.

Photographs were taken with a Canon A480 digital camera and were digitally enhanced using the GNU Image Manipulation Program 2.6.7. (G.I.M.P.). 3D profiles were recorded with a Zeta 200 Optical Profiler. Reflectance FTIR spectra were acquired with p-polarised radiation incident at a reflectance angle of 55° using a Spectra-Tech reflectance accessory mounted on a Bomem MB120 infra-red instrument.

## Procedures

Poly(3,4-ethylenedioxythiophene) (PEDOT) films were deposited potentiostatically ( $E = 0.90$  V) from an aqueous solution containing 0.01 M EDOT monomer in 0.01 M SDS-0.1 M  $H_2SO_4$ . Polypyrrole (PPy) films were deposited potentiostatically ( $E = 0.90$  V) from an aqueous solution containing 0.01 M pyrrole monomer in 0.1 M  $LiClO_4$ . In both cases, the film thickness was controlled by deposition time. PPyFMOC and PPyNH<sub>2</sub> films were deposited, respectively, from 10 mM PyFMOC in 0.1 M TBAP-CH<sub>3</sub>CN and 10 mM PPyNH<sub>2</sub> in 0.1 M TBAP-CH<sub>3</sub>CN/ $HClO_4$  (pH 4.5). The films were grown potentiodynamically ( $v = 20$  mV s<sup>-1</sup>) in the potential range  $0.3 < E < E_{max}$  where the anodic limit  $E_{max}$  (typically 1.15 V) was set to cap the anodic current to 4 mA. This procedure was designed to avoid uncontrollably rapid growth; the amount of deposited polymer was varied with adequately fine control by varying the number of deposition cycles. All measurements were made at room temperature,  $20 \pm 2$  °C. PPyFMOC films were deprotected using a 30% v/v piperidine solution in CH<sub>3</sub>CN to yield PPyNH<sub>2</sub>. PPyNH<sub>2</sub> films were reacted with 0.01 M Dylight 649 NHS ester (hereafter referred to as "Dylight", for brevity) (Thermo Scientific) in DMSO-pH7 phosphate buffer in water (1 : 9 ml).

## Data analysis

The principles of neutron reflectivity data analysis<sup>47</sup> and the issues arising for samples involving "wet" interfaces under electrochemical control<sup>8</sup> have been described elsewhere. The variation with momentum transfer of reflectivity from an interface,  $R(Q)$ , is determined by the depth profile of the scattering length density,  $Nb$ , where  $N$  represents the concentration of scattering atoms present and  $b$  is their scattering length; the value of  $b$  is isotopically unique and medium independent. The scattering length density of a composite medium, here a solvated polymer film, is a weighted sum of the  $Nb$  values of its components: film composition determines scattering length density and thence reflectivity. Experimentally, we invert the process and use reflectivity,  $R$ , to determine composition – in practice, the volume fractions of polymer and solvent – by model fitting the reflectivity profile,  $R(Q)$ . This was accomplished using the box-model approach, implemented in the Motofit software.<sup>9</sup>

## Results

## Electrochromic enhancement of latent fingerprints – basic observations in absorption mode

Before attempting to exploit the substitution chemistry opportunities presented by the N–H function in pyrrole, it is first necessary to demonstrate that PPy films can in fact be deposited with spatial selectivity directed by a fingermark on a metallic substrate. Fig. 1 and Fig. 2 show representative images of two fingermarks on 304 stainless steel substrates, following enhancement by electrodeposition of PEDOT and PPy, respectively. In panel (a) of each figure, the paler (nominally white) regions correspond to the fingermark itself, *i.e.* the complex mixture of materials secreted from pores along the ridges on the fingertip. The darker regions (blue for PEDOT in Fig. 1 and black for polypyrrole in Fig. 2) correspond to polymer deposited on the bare metal *between* the fingerprint deposits. The PEDOT enhanced image acts as a control; this material has

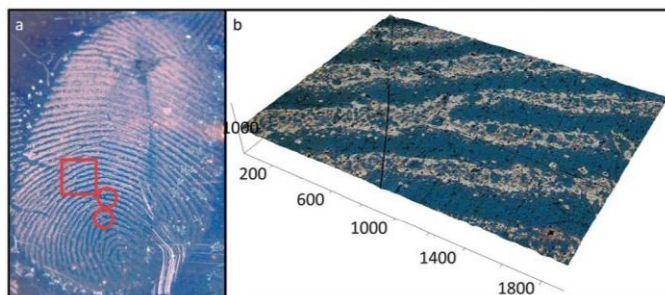


**Fig. 1** PEDOT enhanced sebaceous fingerprint on 304 stainless steel. Deposition conditions as in main text; deposition time,  $t_{\text{dep}} = 3000$  s. Panel (a): whole fingerprint image. Dark (blue) regions correspond to PEDOT and lighter regions to fingerprint deposit. Circles highlight examples of second level detail, a bifurcation and a ridge ending. Panel (b): optical microscope image of selected area from panel (a) (as defined by the rectangle). Larger dark circular regions within light areas represent individual sweat pores. Vertical and horizontal distance scales (expressed in  $\mu\text{m}$ ) are relative.

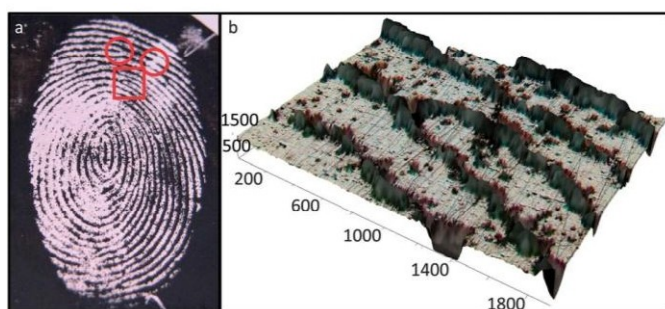


**Fig. 2** PPy enhanced sebaceous fingerprint on 304 stainless steel. Deposition conditions as in main text; deposition time,  $t_{\text{dep}} = 3000$  s. Panel (a): whole fingerprint image. Dark regions correspond to PPy and lighter regions to fingerprint deposit. Circles highlight examples of second level detail, a crossover and a ridge ending. Panel (b): optical microscope image of selected area from panel (a) (as defined by the rectangle). Larger dark circular regions within light areas represent individual sweat pores. Vertical and horizontal distance scales (expressed in  $\mu\text{m}$ ) are relative.

previously been demonstrated to provide good visualization of latent fingerprints, with high fidelity and controllable visual contrast.<sup>3,5</sup>

We have quite deliberately shown examples that might be typical of real evidence, rather than highly controlled ("groomed") model examples. Thus, one can see evidence of damage to the fingerprint and of adjacent fingerprints in Fig. 1 and of smearing (for example, caused by motion of the finger on the surface) and variable amounts of residue in Fig. 2. These and other imperfections represent practical challenges to be addressed.

At the coarsest level of interpretation, *first level* detail, the fingerprints in Fig. 1 and Fig. 2 are, respectively, a loop and a whorl. While this is clearly not sufficient for identification purposes, it is clear that there is much *second level* detail present within these images. Panel (b) in each of Fig. 1 and Fig. 2 shows higher magnification optical images of the samples in panels (a). By any reasonable standard (see above), it would be possible to achieve an evidentially acceptable identification from images such as these using various combinations of *second level* detail.

To illustrate the principle, we simply identify two such features on each image. It is also possible to identify a large number of pores, seen as dots along the ridges where the absence of contact with the substrate permits polymer deposition; these are examples of *third level* detail.

#### Overview of extension to emission mode visual enhancement

The qualitative conclusion of the preliminary experiments shown above is that polypyrrole can be added to the set of electrochromic materials (to date, polyaniline<sup>34</sup> and PEDOT<sup>35</sup>) that permit visualization of latent fingerprints on metallic substrates by means of their optical absorption properties; note that the work of Bersellini<sup>36</sup> in this respect demonstrated the facility to electrodeposit polypyrrole, but did not go on to exploit its electrochromic properties. We therefore proceed to the more challenging goal of developing a polymeric system with suitable absorption *and* fluorescence characteristics. Conceptually, the simplest approach is to functionalise the nitrogen of the pyrrole ring with a fluorophore. In practice, the (necessarily) large size of most fluorophores creates such steric hindrance that the substituted pyrrole monomers cannot polymerize. We therefore arrive at the three step strategy schematically represented in Fig. 3.

The essential idea is to functionalize pyrrole units with the fluorophore post-deposition. However, in order to accomplish this, there is still a requirement to create sufficient free volume within the polymer film to accommodate the fluorophore units. The tactic employed is to polymerize not pyrrole itself, but an N-functionalized derivative that can readily be removed post-deposition. The balance to be struck is use of a substituent that is not so large as to preclude polymerization but that is large enough to create appreciable free volume. The functionality chosen was the widely used Fmoc protecting group. Thus, we set out to polymerize the N-substituted Fmoc derivative of pyrrole (PPyFmoc), then hydrolyze and leach out the protecting group to leave an amine-functionalized polypyrrole film. The semi-fluid nature of the polymer film means that the

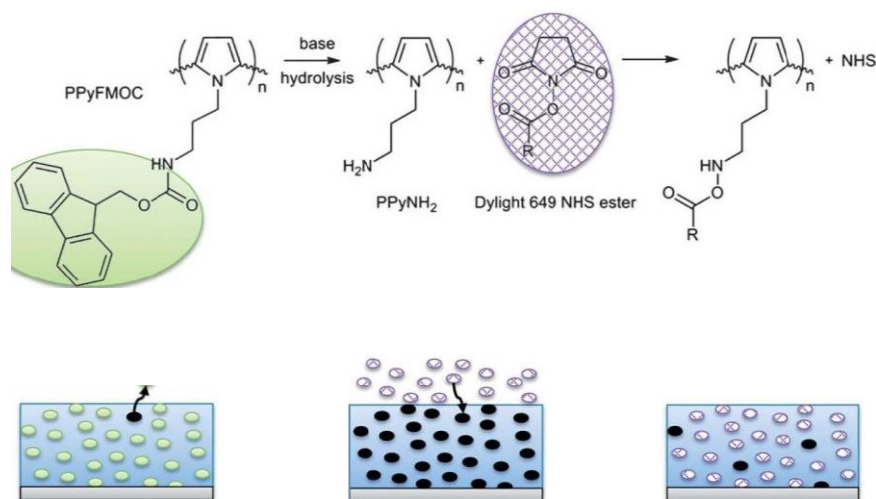


**Fig. 3** Cartoon representation of (i) PPy Fmoc deposition, (ii) Fmoc hydrolysis to create solvent "voids"; (iii) diffusion of fluorophore into voids and attachment to polymer. Stylised ellipsoids (simplicially, of similar size) represent Fmoc (pale green), solvent (black) and fluorophore (diamond chequered).

randomly distributed free volume can aggregate to generate "voids" of sufficient size to accommodate larger fluorophore moieties. Choice of a fluorophore with an ester functionality provides the means of covalent bonding by amide formation (see Fig. 3).

In the experimental realisation of the strategy indicated in Fig. 3, critical issues are the completion of hydrolysis, the extent to which departing FMOc is replaced by solvent *cf.* film contraction, the vertical (perpendicular to the interface) spatial distribution of replaceable solvent and the penetration of fluorophore into the film. The outcomes, which will ultimately determine performance, are addressed using a combination of spectroscopic and neutron reflectivity measurements.

### Optimization of film deposition

The limited aim of this study is establishment and assessment of the strategy of Fig. 3 on clean (*i.e.* non-fingermarked) metal surfaces. The deliberate absence of *lateral* spatial variation focuses attention on the required control of film composition in the *vertical* direction. Fig. 4 and Fig. 5, respectively, show the voltammetric responses of PPyFMOc and PPyNH<sub>2</sub> films on Au during electropolymerization (panels (a)) and after transfer to background electrolyte (panels (b)). Both sets of responses provide information relating to polymer deposition. In the former instance, the integrated current provides cycle-by-cycle monitoring to facilitate deposition of the chosen amount of polymer. In practice, use of the cathodic half cycle response is better, since this is not complicated by contributions from the (irreversible) anodic polymerization current contribution.

The coulometric assay described above is reliant upon complete film redox conversion on the experimental timescale; that this is accomplished is demonstrated by the data in Fig. 4b and Fig. 5b. In these measurements (following completion of film deposition) there is no monomer present in the solution, so the issue of distinguishing polymerization and film redox chemistry is irrelevant. For films of suitable coverage, *i.e.* appropriate both to the NR experiment (giving multiple well-defined interference fringes within the accessible Q range) and to future forensic exploitation (not so thick as to obscure all image detail when a fingerprint is present), we find that the peak currents are linearly proportional to the potential scan rate (see Fig. 4c and Fig. 5c). This indicates complete redox

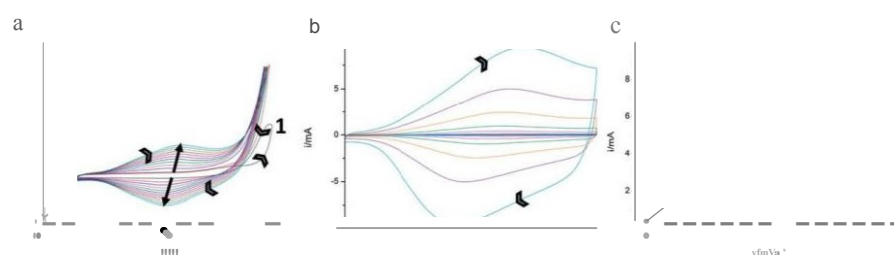


**Fig. 4** *i*-*E* responses for a PPyFMOc film. Panel (a): during potentiodynamic electropolymerization ( $v = 20 \text{ mV s}^{-1}$ ); panel (b): after transfer to a monomer-free background electrolyte (subsequent to the final cycle of panel (a)), during cycling at  $v = 1, 2, 5, 10, 20, 50, 100$  and  $200 \text{ mV s}^{-1}$  (increasing "outwards"); panel (c): variation of cathodic peak current (from curves in panel (b)) with scan rate. Solution compositions as described in the main text. In panels (a) and (b), chevron arrows indicate scan direction. In panel (a) large arrows indicate the time sequence and "1" indicates the first deposition cycle (note the nucleation loop).

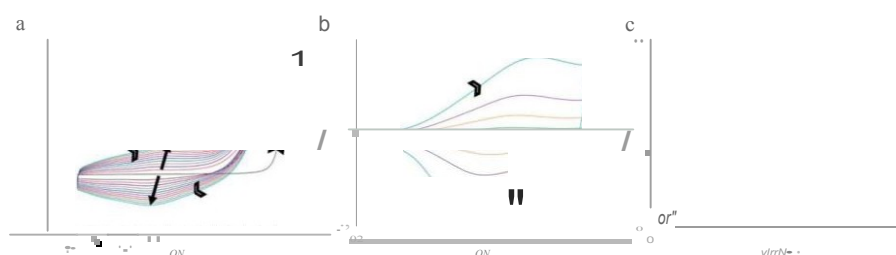


**Fig. 5**  $i$ - $E$  responses for a PPyNH<sub>2</sub> film. Panel (a): during potentiodynamic electropolymerization ( $\nu = 20 \text{ mV s}^{-1}$ ); panel (b): after transfer to a monomer-free background electrolyte (subsequent to the final cycle of panel (a)), during cycling at  $\nu = 1, 2, 5, 10, 20, 50, 100$  and  $200 \text{ mV s}^{-1}$  (increasing "outwards"); panel (c): variation of cathodic peak current (from curves in panel (b)) with scan rate. Solution compositions as described in main text. In panels (a) and (b), chevron arrows indicate scan direction. In panel (a) large arrows indicate the time sequence and "1" indicates the first deposition cycle (note the nucleation loop).

conversion of the film on the experimental timescale, validating a coulometric assay of the spatially integrated surface population of polymer. On this basis, the surface coverage,  $\Gamma/\text{mol cm}^{-2}$ , is determined as  $q/nFA$ , where  $q/C$  is the charge,  $n$  is the number of electrons transferred ("doping level",  $n = 0.33$ )<sup>50</sup>,  $A$  is the electrode area and  $F$  is the Faraday constant. For the data shown, the final polymer coverages are  $\Gamma^{\text{PPyFMoc}} = 20 \text{ nmol cm}^{-2}$  and  $\Gamma^{\text{PPyNH}_2} = 19 \text{ nmol cm}^{-2}$ , where in both cases the surface population is expressed in terms of monomer units.

These surface coverages can be used to estimate a physical film thickness, as follows. The molar volume of monomer units,  $v_{01}/\text{cm}^3 \text{ mol}^{-1}$  (*i.e.* the reciprocal of the volume concentration of monomer units), can be estimated as the quotient of monomer molar mass and density,  $RMM/p$ . The approximation here is that the monomer units in the polymer pack essentially the same as in pure monomer. For a compact, solvent-free ("dry") polymer, the film thickness  $h^* = v_{01}\Gamma$ . The RMM values of PPyFMOC and PPyNH<sub>2</sub> are 344 and 122  $\text{g mol}^{-1}$ , respectively. Their respective densities are *ca.* 1.2 and 1.0  $\text{g cm}^{-3}$ . Combining these with the values of  $\Gamma^{\text{PPyFMoc}}$  and  $\Gamma^{\text{PPyNH}_2}$  from the previous paragraph, we estimate "dry" (*i.e.* collapsed, solvent-free) film thicknesses of *ca.* 600 Å and 240 Å for the PPyFMOC and PPyNH<sub>2</sub> films, respectively. Looking ahead to the NR part of the study, solvation might be expected to increase these values by 50-100%, since typical solvent volume fractions for electroactive polymer films are in the range  $0.3 < \phi_s < 0.5$ . This overall scenario is appropriate both for a NR experiment (to explore structure) and filling of the inter-ridge "trenches" in a typical fingerprint deposit (to accomplish practical visualization). As a final observation, the different thicknesses of these two PPyFMOC and PPyNH<sub>2</sub> films containing essentially the same number of monomer units (irrespective of whether one compares two dry films or two solvated films) shows the potential for generation of free volume by Fmoc elution from a film.

#### Observation of changes in surface composition using spectroscopic measurements

Before addressing the more sophisticated issue of spatial distribution of active components within the film, it is necessary to demonstrate that the strategy of Fig. 3 does indeed result in fluorophore immobilization. In principle, one might consider accomplishing this using either a fluorescence measurement or some other

spectroscopic probe. Superficially, a fluorescence measurement has the attraction of also providing a more direct functional appraisal. However, while this could demonstrate the *presence* of the fluorophore, it might not do so if quenching were an issue; in either instance, it would not provide evidence of its *immobilization*. The concern here is that, unless covalent attachment to the polymer is achieved, facile entry of the fluorophore could just as easily be followed by its elution upon further exposure to electrolyte, thereby jeopardizing the entire surface synthetic strategy. Consequently, we sought a spectroscopic probe able to provide direct evidence of fluorophore-polymer binding. Qualitatively, this can be accomplished using vibrational spectroscopy, with particular focus on the presence (or absence) of carbonyl bands associated with the amide functionality, which will be present in an PPyFMOC film (at the start) and a successfully functionalized PPy-Dylight film (at the end), but should be absent in PPyNH<sub>2</sub> (following hydrolysis of the PPyFMOC film).

Representative data are shown in Fig. 6. Trace (a), representing a PPyFMOC film, has a strong absorption band at 1660 cm<sup>-1</sup>. Trace (b), for the hydrolysed film, has no significant amide band, demonstrating removal of the Fmoc functionality. Trace (c), for the hydrolysed film after exposure to Dylight solution, shows a strong band at 1630 cm<sup>-1</sup>, showing the formation of an amide. Significantly, the last of these observations demonstrates not only the permeation of fluorophore into the film but also its chemical immobilization. Overall, these data show elution of Fmoc and binding of fluorophore, but give no insight into the spatial distribution of the fluorophore or the factor(s) limiting its final population. We now address these issues using NR.

#### Determination of vertical spatial structure using neutron reflectivity

The second stage of the strategy in Fig. 3 is the creation of free volume in the PPyFMOC film by the hydrolysis and elution of the Fmoc moieties. Importantly,

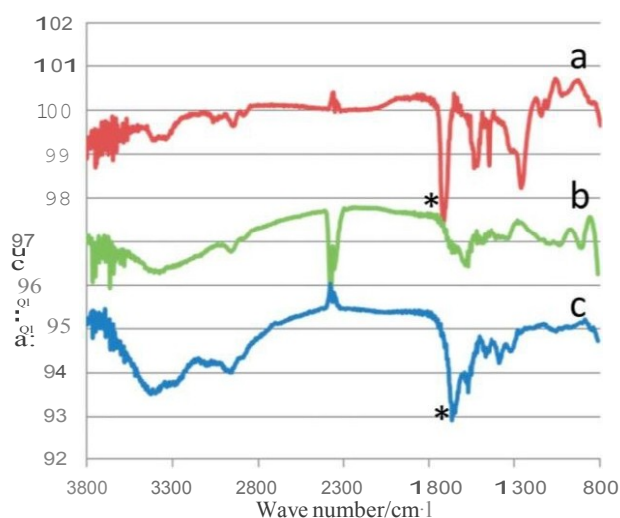


**Fig. 6** Reflectance infra-red spectra for a PPyFMOC film subject to the reaction sequence of Fig. 3. Trace (a): PPyFMOC film, as deposited; trace (b): PPyFMOC film after hydrolysis, notionally a PPyNH<sub>2</sub> film; trace (c): film of panel (b) after reaction with Dylight solution. Traces are arbitrarily offset vertically for visual clarity. Reaction conditions as in main text. The asterisks on traces (a) and (c) indicate the amide peaks referred to in the main text.

we require this free volume to be created throughout the film. Fig. 7 shows neutron reflectivity data acquired at different times during the hydrolysis process, conducted in a deuterated solvent medium to optimise the contrast. The data shown in Fig. 7 in fact represent the second –and, in reaction terms, productive – phase of the experiment. Since there was no means *a priori* to predict the time-scale of the hydrolysis-elution process, the film was initially exposed to a low (0.01 mM) concentration of piperidine, with the aim of slowing the reaction to a measurable rate. This approach turned out to be more than successful, in that the rate of hydrolysis was immeasurably slow. However, this had the advantage of providing a film solvation profile at a true “ $t = 0$ ”; the outcome of this is cited below in the discussion of Fig. 7c. The hydrolysis solution was then exchanged to higher piperidine concentration (10 mM) and the data shown in Fig. 7a acquired.

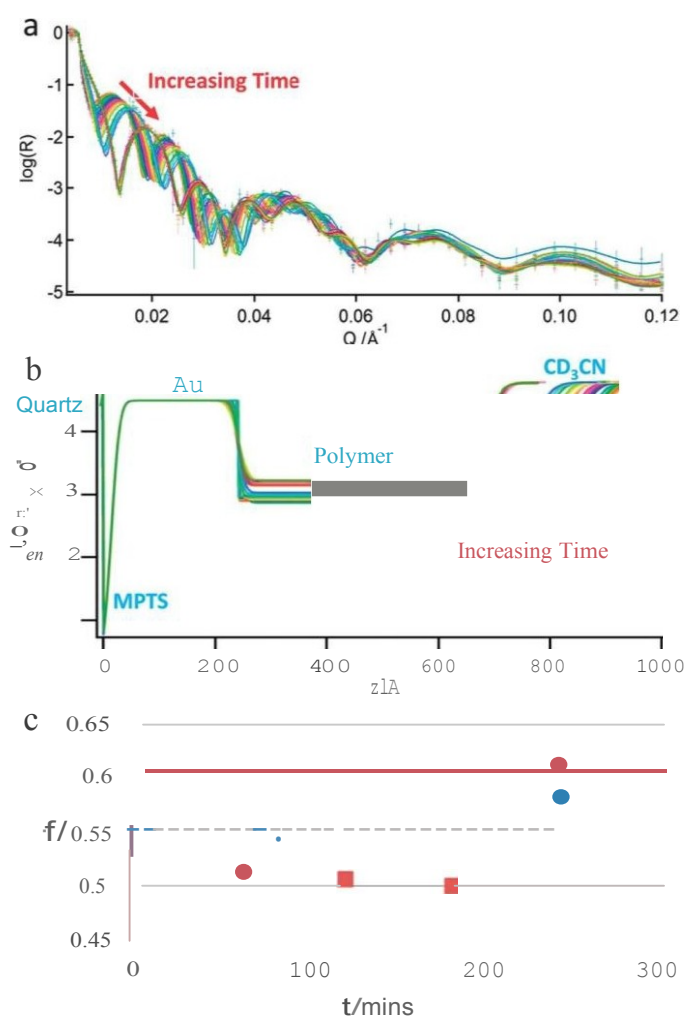


**Fig. 7** Time-resolved NR experiment for PPyFMOc hydrolysis to give PPy-voids. Panel (a):  $R(Q)$  profiles as a function of time (indicated by arrows); panel (b) model fitted scattering length density profiles as a function of time (from the data of panel (a)); panel (c): solvent volume fraction in the film at selected time intervals (see main text for comment on absolute values) during the hydrolysis. (—: inner polymer layer; +: outer polymer layer).

The time taken for cell mounting and alignment and for initiation of data acquisition was on the order of 30 min. Hence the time axis in Fig. 7c has an offset of this order; since there is no attempt to extract kinetic or diffusional parameters, this is not critical.

Broadly speaking, the  $R(Q)$  profiles of Fig. 7a comprise three regions. At low  $Q$  (here,  $Q < 0.0055 \text{ \AA}^{-1}$ ) there is total external reflection ( $R = 1$ ); this is a consequence of the substrate material the neutrons are transmitted through (quartz) having a lower scattering length density than the material they are reflecting from (the deuterated solvent). Beyond this, there is a series of fringes whose periodicity is dictated by the thickness of the films present (Au electrode and polymer) and whose amplitude is dictated by the scattering length density contrast and sharpness of the interfaces between layers. At high  $Q$  (here,  $Q > 0.06 \text{ \AA}^{-1}$ ), the fringes seen are attributable to the Au electrode. Although these are not central to the aims of the experiment *per se*, their quantitation does assist fitting of the full  $R(Q)$  profile from which we extract the polymer film data. At intermediate  $Q$ , the Au-derived fringes are seen, but superimposed on these are fringes that result from the polymer film. The latter do not persist to high  $Q$  as a consequence of the diffuse polymer/solution interface.

Independent of any model, we can make four deductions from the data. Trivially, the presence of a critical edge shows that the film scattering length density is below that of the solution. The position of the critical edge,  $Q^* = (167t \text{ bY})^{1/2}$ , where

corresponds to the difference in scattering length densities

two bulk phases in the sample. In this instance, the relevant bulk phases are the quartz block supporting the electrode and the bathing solution to which the film is exposed; the scattering length densities are known for these materials, giving  $\Delta\rho = 0.62 \times 10^{-6} \text{ \AA}^{-2}$ . Inserting this into the expression above, we estimate  $Q^* = 0.0056 \text{ \AA}^{-1}$ , consistent with the experimental data of Fig. 7. Secondly, the time invariance of the fringes at high  $Q$  allows these to be assigned to the Au electrode, the composition and thickness of which (necessarily) do not vary with time. Thirdly, an Au electrode thickness of 210 Å can be estimated from the periodicity of the fringes,  $6.Q = 0.03 \text{ \AA}^{-1}$ , via the equation  $6.Q = 27/t/d$  (where  $d$  = film thickness); this is entirely consistent with the nominal thickness of 200 Å from the sputtering process. Fourthly, the higher frequency fringes present only in the intermediate  $Q$  region can be seen progressively to stretch out with time. Since the momentum transfer,  $Q$ , is in reciprocal space, this stretching corresponds to some element of contraction of film thickness with hydrolysis of the FMOC groups. The quantitative question that follows is whether this contraction results in loss of some or all of the "void" volume generated by the FMOC departure.

To address this last question, detailed fitting of the data is required. Full details of this standard procedure are given in the Experimental section and elsewhere,<sup>47, 48</sup> but the essential points are as follows. The scattering lengths of all the components present (quartz, Au, PPyFMOC, the departing FMOC, the remaining PPy-amine and CD<sub>3</sub>CN solvent) are all known. The Au thickness is known (from a combination of fabrication protocol, bare electrode observations and the high  $Q$  data of Fig. 7). The unknowns are therefore the internal composition of the film (predominantly, solvation level), film thickness and the roughness of the polymer/solution interface.

The outcomes of the fitting process are shown in Fig. 7b and 7c. In the first of these, the scattering length density of the system, from the quartz block supporting the electrode through to the bulk solution, is shown as a function of

## Faraday Discussions

## Paper

distance,  $z$  (perpendicular to the interface). The values for quartz, Au and solvent represent bulk values for the pure components. The sharp dip between the quartz support and the Au electrode represents the MPTS bonding layer used to ensure good Au adhesion. For the purposes of this work, the region of interest is from the Au electrode outwards. The interface between the Au and the film is relatively sharp; a small amount of diffuseness (typically 10 Å) is required to account for the finite roughness of the Au surface. Interestingly, the polymer film is *not* compositionally homogeneous at any point in the process: there is a relatively diffuse outer region (a transition from "bulk" film to bulk solution over 40 Å) and the interior of the film comprises compositionally distinct inner and outer regions. A single polymer layer with high interfacial roughness was insufficient to model the film. The key outcome is a substantial shrinkage of the film as hydrolysis proceeds. For the example shown, the dry film thickness (measured in air) was 561 Å, and the solvated film thickness (measured upon exposure to solvent, prior to hydrolysis) was 639 Å, and the latter shrunk to 443 Å following completion of FMOc hydrolysis and elution.

The significance of this in solvation terms is shown in the solvent volume fraction data of Fig. 7c. While the fitting unquestionably demands that some film inhomogeneity be recognized (see Fig. 7b), the difference in scattering length density (and thence solvation) between the inner and outer regions of the film is relatively small. We therefore look at the average picture. The film solvent volume fraction at the outset, as solvated PPyFMOc exposed to a low piperidine concentration (as explained above) is 0.41. By the end of the hydrolysis process, this increases to 0.60, but it subsequently falls to 0.52. The latter decrease is the result of polymer relaxation, which occurs on a longer timescale than the FMOc hydrolysis and elution.

It is of course not possible to make the analogous measurements in hydrogensolvent ( $\text{CH}_3\text{CN}$ ) for the *same* film, since the hydrolysis reaction is a one-time process. However, such measurements were made on a nominally identical film and the outcome, in summary form for the analogue of Fig. 7c, was an initial solvent volume fraction of 0.35, rising to 0.58 immediately after hydrolysis and subsequently relaxing back to 0.44. The common conclusion from these experiments is that FMOc removal increases the film solvent volume fraction by  $\Delta\phi_s \approx 0.2$  in the short term, but this increase is subsequently diminished to  $\Delta\phi_s \approx 0.1$ . While this may seem modest, we note that relatively small *changes* in solvent content can have profound effects on polymer chain mobility, for example as manifested in viscoelastic properties,<sup>54,55</sup> which would facilitate permeation of fluorophore reactant. In an absolute sense, a replaceable solvent volume fraction  $\phi_s > 0.4$  is more than adequate to give a high (and thus visible) fluorophore population.

This leads to consideration of the final step in the scheme of Fig. 3, fluorophore functionalization of the PPy-NH<sub>2</sub> film. What reaction did occur – and the significant changes in  $R(Q)$  profiles do unequivocally demonstrate change, quantified below – took place within the first 15 min of exposure to fluorophore solution. We attribute this to the more fluid-like environment of the film following hydrolysis (see above). From a mechanistic perspective, this removed the opportunity to follow the kinetics of the process (largely due to instrumental issues such as sample alignment prior to measurement), but from a practical perspective in future application it is obviously beneficial.

Consequently, on a separate (but nominally similar) film to that of Fig. 7, a separate set of measurements were made, as follows. First,  $R(Q)$  data were acquired for a PPyFMOC film in the dry state (solvent-free) and exposed to  $h_3$ - and  $d_3$ -acetonitrile, prior to hydrolysis. Second, the film was hydrolysed (with no attempt to monitor the time-dependence of this process) and  $R(Q)$  data acquired for the resultant PPyNH<sub>2</sub> film in the three environments (air,  $h_3$  and  $d_3$ -acetonitrile). Finally, the film was Dylight functionalised and  $R(Q)$  data acquired in the same three environments. This last part of the experiment is complementary to the hydrolysis step, in that the aim is entry of a large reactant to consume free volume, rather than elution of a large leaving group to generate free volume. As compensation for sacrifice of any kinetic information, this suite of measurements provided data in different solvent contrasts for the same film, which (through co-refinement) gives greater certainty in fitting. The resulting  $R(Q)$  profiles are shown in Fig. 8a, grouped according to the film environment; the general form of the profiles is analogous to those of Fig. 7.

The key parameters of interest are film thickness and solvent content at each stage. To extract these, we need to consider the contributions of the polypyrrole spine, fluorophore and solvent components to the scattering length density. For the polypyrrole and solvent components, the scattering length and physical density are known. For the fluorophore, whose structure is commercially protected, this is not so straightforward, but acceptable approximations are possible,

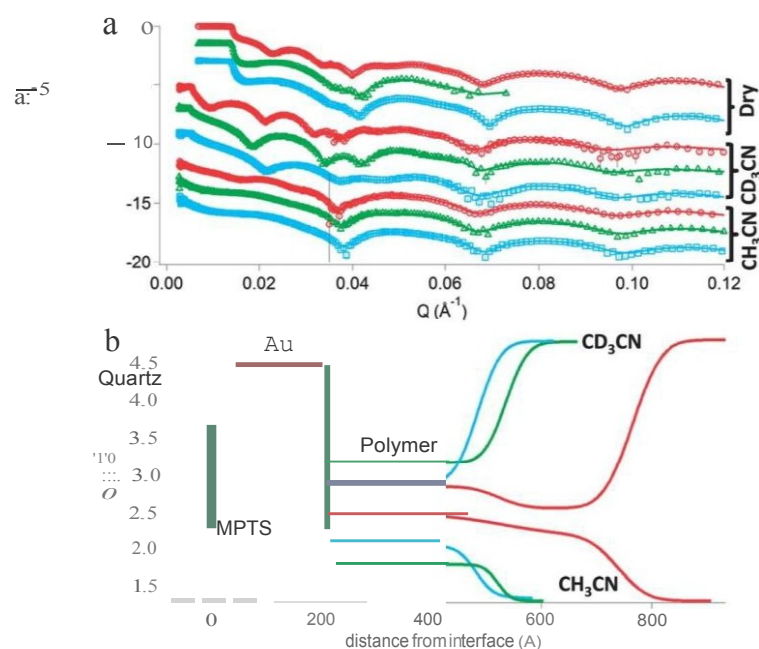


**Fig. 8** Panel (a):  $R(Q)$  data for a PPyFMOC film prior to hydrolysis (O), the PPyNH<sub>2</sub> film resulting from hydrolysis (L), and the PPy-Dylight film following exposure to the fluorophore (D). Points represent data; lines represent fits (see panel (b)). For visual comparison purposes,  $R(Q)$  profiles are grouped according to the ambient medium (see annotations). Data are progressively offset downwards for presentational purposes; for the dry and  $d_3$ -acetonitrile exposed films, a critical edge is seen, below which  $R = 1$ . Panel (b). model fitted scattering length density profiles for the film exposed to  $h_3$ -acetonitrile and  $d_3$ -acetonitrile at each of the three stages of the process: nominally PPyFMOC (red traces), PPyNH<sub>2</sub> (green traces) and PPy-Dylight (blue traces).

as follows. The molar mass is on the order of 1000 Daltons and there are four sulfonate groups (to provide adequate solubility) on an essentially aromatic hydrocarbon skeleton. We thus have an entity that comprises *ca.* 320 Daltons of "SO<sub>3</sub><sup>-</sup>" and *ca.* 680 Daltons of "CH"; we make the plausible approximation that the overall density is unity. With these physically reasonable approximations, combining the data sets for the h<sub>3</sub>-acetonitrile and d<sub>3</sub>-acetonitrile environments, we estimate that there is one fluorophore entity for every *ca.* five pyrrole monomer units. Physically, this is plausible, given the geometrical constraints of the cartoon representation of Fig. 3 and practically this is expected to be useful.

The model scattering length density profiles best fitting the data are shown in Fig. 8b and the  $R(Q)$  fits (lines) are shown alongside the data (points) in Fig. 8a; the agreement is good across the accessible  $Q$  range. We particularly highlight four characteristics. First, the outer interfaces are diffuse. In the  $R(Q)$  profiles, this accounts for the damping of the film-based fringes. In terms of reactivity, it undoubtedly contributes to the faster permeation of the fluorophore molecules. Second, once one progresses to the interior of the film, its scattering length density, and thus composition, shows at most only modest dependence on depth (actually, none for PPyNH<sub>2</sub>). This indicates that diffusion of reactant into the film is not a limiting factor; if it were, then there would be a clear gradient of composition representing fluorophore penetration. Third, despite the *entry* of fluorophore into the polymer, the films *shrink* slightly during the process (compare the traces for PPyNH<sub>2</sub> and PPy-Dylight). This indicates that the volume of solvent expelled exceeds the volume of fluorophore entering, suggesting that transport processes are not so slow that mobile species (here, solvent) are trapped within the film. Finally, while the outer interface is slightly sharper for the dry film (profile not shown), the overall thickness is not much less than for the solvent-exposed film. Since (see Table 1) there is still appreciable solvent in the immersed films, this suggests that the film does not collapse upon emersion.

The characteristics of the model profiles are summarized in Table 1. Considering first the thickness data, the dramatic collapse of the PPyFMOc film upon hydrolysis (by *ca.* 40%) is accompanied by an *increase* in solvent content of the resulting PPyNH<sub>2</sub> film. This apparently counter-intuitive result is a consequence of the size of the FMOc group; recall the earlier estimations of film thickness accompanying the coulometry, when it was noted that the FMOc group constitutes *ca.* 60% of the film volume. Turning to the solvent volume fraction, the values for PPyFMOc ( $l/l_s = 0.36$ ) and PPyNH<sub>2</sub> ( $l/l_s = 0.47$ ) are satisfyingly consistent

**Table 1** Summary of film thickness and solvent content values at each stage of assembly of the surface architecture represented schematically in Fig. 3. PPyNH<sub>2</sub> films could be modelled as a single layer (*i.e.* were internally homogeneous), so "inner" and "outer" regions are merged

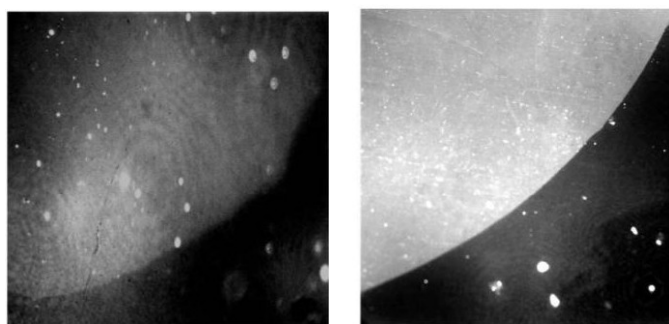
Environment	Air ("dry")		Exposed to acetonitrile			
	Thickness/Å		Thickness/Å		Solvent volume fraction/cps	
Parameter	Inner	Outer	Inner	Outer	Inner	Outer
PPyFMOc	173	303	312 (±18)	223 (±4)	0.34	0.38
PPyNH <sub>2</sub>		257	318 (±8)		0.47	
PPy-Dylight	104	164	188 (±3)	84 (±3)	0.40	0.62

with those of  $\phi^s = 0.38$  and  $\phi^s = 0.48$  at the same points in the surface chemistry of Fig. 3 determined by averaging the outcomes of the two kinetic experiments of Fig. 7 and its  $\text{h}_3$ -acetonitrile counterpart.

#### Functional viability of the fluorophore-modified film

This report focuses on construction of the interfacial architecture and, *via* the NR measurements, on establishing spatial control of fluorophore immobilization within the polymer matrix; essentially, this represents the *compositional* and *structural* aspects of the strategy. In a subsequent phase of the work, the focus will shift to determination of the polymer chromophore and immobilized fluorophore properties; these represent the *functional* aspects of the strategy. The latter will involve a substantive programme of measurements, notably as functions of excitation and observational wavelengths and of polymer charge state (*i.e.* doping level, manipulated *via* applied potential). Nonetheless, in advance of such a future report, there is merit in a forward look to establish at a qualitative level fluorophore activity in the polymer film context. The technical issue here is whether (or not) proximity of the fluorophore sites to the underlying electrode results in fluorescence quenching.

Fig. 9 shows two images of PPy-based films representing two stages – simplistically, in the absence and presence of fluorophore, respectively – of the assembly process shown in Fig. 3. This preliminary observation does not attempt to address the spatial issue of imaging a full fingerprint, but focuses solely on the viability of fluorophore emission when in the film environment. The left hand image shows a section of a PPyNH<sub>2</sub> film deposited on an Au substrate (using the procedure of Fig. 5, terminating at the cathodic end of a potential cycle to establish the undoped redox state), removed from solution and viewed *ex situ* (dry) under illumination by light of wavelength 640 nm. This control observation shows a few brighter areas, but nothing systematic or substantive. The right hand image shows



**Panel a**

**Panel b**

Fig. 9 Panel (a): PPy film on Au (deposition procedure as in main text); this represents the control experiment, in the absence of fluorophore. Panel (b): PPyNH<sub>2</sub> film prepared by hydrolysis of a PPyFmoc film (deposition and subsequent treatment as in main text) after partial exposure to Dylight 649 NHS ester by contact with a droplet of fluorophore solution, and subsequent removal of excess fluorophore by rinsing. The top left part of the viewed region includes part of the droplet-exposed area. In both cases, the films were in the reduced (undoped) state and were viewed *ex situ* under illumination by light of wavelength 640 nm. In panel (b), the intensity was attenuated by a factor of 4.

a partially Dylight 649 ester functionalised film, prepared as follows. A PPyFMOc film was deposited on Au and hydrolysed (as discussed earlier with reference to Fig. 7), then a droplet of Dylight 649 NHS ester solution placed on one part of the surface, followed by rinsing with pure water (to remove unbound and surface/exterior fluorophore) and air drying (at room temperature for *ca.* 15 min). The resultant film was viewed *ex situ* under illumination with light of wavelength 640 nm. The top left part of the viewed region in panel (b) of Fig. 9 includes part of the droplet-exposed area. The sharply defined region of enhanced brightness is consistent with strong fluorophore emission; note that the intensity was attenuated (see legend) so the distinction between the images in panels (a) and (b) is significant. Although this is not a quantitative measure of the fluorescence efficiency and does not totally exclude quenching – perhaps from fluorophore sites closer to the electrode (see Fig. 8 for evidence of deep penetration of fluorophore) – it is clear that at least some fluorophore sites are sufficiently distant from the electrode that they are not vulnerable to quenching. Pragmatically, the practical viability of the interfacial (electro)chemical strategy is established.

## Conclusions

A combination of spectroscopic, electrochemical and neutron-based techniques provides the capability to follow and quantify deposition and subsequent functionalization of electroactive polymer films relevant to latent fingerprint visualization. This approach has been used to explore the (electro)chemistry of pyrrole-FMOc electropolymerization and deposition, followed by hydrolysis of the FMOc leaving group, then permeation and bonding of the fluorophore Dylight 649 NHS ester. By revealing the presence, removal and reintroduction of amide functionalities, FTIR spectroscopy demonstrates qualitative success of this post-deposition functionalization strategy. Electrochemistry provides control over (and coulometric assay of) the surface population of polymer, the electrochromic matrix into which the fluorophore is introduced. Neutron reflectivity provides insight into the *vertical* spatial distribution of the permeating fluorophore and the changes in film population of the solvent that must leave to create space for it. Together, these techniques provide insights into film composition, structure and (in the cases of the electrochemical and neutron data) dynamics; simplistically, they address the tersely expressed questions "*what, how much and where?*"

We have demonstrated that the portfolio of materials suitable for electrochromic enhancement of latent fingerprints can be extended from the previously used aniline and thiophene (PEDOT) families to include pyrrole-based materials. Specifically, this was accomplished for the parent polypyrrole, N-propylamine functionalised pyrrole and FMOc functionalised pyrrole. In future, in addition to the substitution chemistry explored here, this will provide a wider colour palette with which to optimise latent fingerprint visual contrast against the substrate.

In the post-deposition functionalization of PPyFMOc, the hydrolysis process (leading to FMOc removal) is relatively slow (*ca.* 3 h under the conditions employed), which allowed the progress of the reaction to be monitored by neutron reflectivity. The subsequent entry of fluorophore (Dylight 649 NHS ester) is much more rapid – too rapid to follow readily using neutron reflectivity – which is attributed to the higher solvent volume fraction and thence greater fluidity of the film. During this sequence of events, the solvent volume fraction rises by *ca.*

0.2 immediately upon hydrolysis and Fmoc elution, but then falls by *ca.* 0.1, presumably as a consequence of polymer relaxation in the now highly plasticised film. In absolute terms, the solvent volume fractions are 0.37 ( $\pm 0.03$ ) for PPyFmoc prior to hydrolysis, 0.59 ( $\pm 0.01$ ) immediately after hydrolysis and 0.47 ( $\pm 0.04$ ) after relaxation (where these data originate from both kinetic and non-kinetic experiments). After fluorophore entry, the film contracts slightly.

Future prospects for a combined absorption/fluorescence strategy in latent fingerprint enhancement appear promising. The next step is implementation of the strategy described here to fingerprinted surfaces. Having established control of reactivity and composition in the *vertical* direction at distance scales from 10-100 nm, this fine control can now be applied to the *lateral* direction. Since the fingerprint feature sizes are at the scale of  $>10$  nm, the prospect of high resolution, high fidelity fingerprint images is excellent.

## Acknowledgements

We thank the Institut Laue Langevin and ISIS Facility of the Rutherford Appleton Laboratory for provision of neutron beam time. R. M. B. thanks the University of Leicester for financial support. We thank Ines Carro-Muino (of Thermo Fisher Scientific) for helpful conversations relating to fluorophores and Zeta Instruments for helpful discussions regarding sample analysis using 3D optical profiling.

## References

- 1 *Advances in Fingerprint Technology* (2nd edn), ed. H. C. Lee and R. E. Gaensslen, CRC Press, Boca Raton, 2001.
- 2 R. S. Ramotowski, in *Advances in Fingerprint Technology* (2nd edn), ed. H. C. Lee and R. E. Gaensslen, CRC Press, Boca Raton, 2001, p. 63.
- 3 R. D. Olsen and H. D. Lee, *Advances in Fingerprint Technology* (2nd edn), ed. H. C. Lee and R. E. Gaensslen, CRC Press, Boca Raton, 2001, p. 41.
- 4 P. Voss-De Haan, *Contemp. Phys.*, 2006, 47, 209.
- 5 J. Berry and D. A. Stoney, in *Advances in Fingerprint Technology* (2nd edn), ed. H. C. Lee and R. E. Gaensslen, CRC Press, Boca Raton, 2001, p. 1.
- 6 J. G. Barnes, in *The Fingerprint Source Book*, ed. A. McRoberts, National Institute of Justice, Washington, 2011, ch. 1. Available from <http://www.nij.gov/pubs-sum/225320.htm>.
- 7 W. J. Herschel, *Nature*, 1880, 23, 76.
- 8 K. Barnett, in *Crime Scene to Court: the Essentials of Forensic Science* (1st edn), ed. P. White, Royal Society of Chemistry, Cambridge, UK, 1998, p. 98.
- 9 F. Galton, *Finger Prints*, Macmillan, London, 1892.
- 10 H. Faulds, *Nature*, 1880, 22, 605.
- 11 M. Kucken, *Forensic Sci. Int.*, 2007, 171, 85.
- 12 I. W. Evett and R. L. Williams, *J. Forensic Ident.*, 1996, 46, 49.
- 13 *Advances in Fingerprint Technology* (3rd edn), ed. R. S. Ramotowski, CRC Press, Boca Raton, 2013.
- 14 S. Bell, *Annu. Rev. Anal. Chem.*, 2009, 2, 297.
- 15 T. A. Brettell, J. M. Butler and J. R. Almirall, *Anal. Chem.*, 2011, 83, 4539.
- 16 N. Akiba, N. Saitoh and K. Kuroki, *J. Forensic Sci.*, 2007, 55, 180.
- 17 M. J. Choi, T. Smoother, A. A. Martin, A. M. McDonagh, P. J. Maynard, C. Lennard and C. Roux, *Forensic Sci. Int.*, 2007, 173, 154.
- 18 J. Almog, G. Levinton-Shamuilov, Y. Cohen and M. Azoury, *J. Forensic Sci.*, 2007, 52, 1057.
- 19 J. D. James, C. A. Pounds and B. Wilshire, *J. Forensic Sci.*, 1993, 38, 391.
- 20 L. K. Seah, U. S. Dinis, W. F. Phang, Z. X. Chao and V. M. Murukeshan, *Forensic Sci. Int.*, 2005, 152, 249.
- 21 V. Bowman, *Manual of Fingerprint Development Techniques* (2nd edn), Police Scientific Development Branch, Home Office, Sandridge, UK, 2004.
- 22 H. L. Bandy and T. Kent, *Superglue Treatment of Crime Scenes 30/03*, Police Scientific Development Branch, Home Office, Sandridge, UK, 2003.

- 23 A. A. Cantu, D. A. Leben, R. Ramotowski, J. Kopera and J. R. Simms, *J. Forensic Sci.*, 1998, 43, 294.
- 24 C. Kauffman and K. Smith, *J. Forensic Dent.*, 2001, 51, 9.
- 25 Y. Migron and D. Mandler, *J. Forensic Sci.*, 1997, 42, 986.
- 26 G. S. Sodhi and J. Kaur, *Forensic Sci. Int.*, 2001, 120, 172.
- 27 A. R. W. Jackson and J. M. Jackson, *Forensic Science*, Pearson Prentice House, Harlow, UK, 2004.
- 28 A. A. Cantu, in *Optics and Photonics for Counterterrorism and Crime Fighting* iii, *SPIE-Int. Soc. Opt. Eng.*, ed. C. Lewis, 2007, vol. 6741, p. D7410.
- 29 P. Czekanski, M. Fasola and J. Allison, *J. Forensic Sci.*, 2006, 51, 1323.
- 30 M. Colella, A. Parkinson, T. Evans, C. Lennard and C. Rom<, *J. Forensic Sci.*, 2009, 54, 583.
- 31 P. F. Kelly, R. S. P. King and R. J. Mortimer, *Chern. Commun.*, 2008, 6111.
- 32 K. K. Bouldin, E. R. Menzel, M. Takatsu and R. H. Murdock, *J. Forensic Sci.*, 2000, 45, 1239.
- 33 R. Leggett, E. E. Lee-Smith, S. M. Jickells and D. A. Russell, *Angew. Chem, Int. Ed.*, 2007, 46, 4100.
- 34 A. L. Beresford and A. R. Hillman, *Anal. Chern.*, 2010, 82, 483.
- 35 R. M. Brown and A. R. Hillman, *Phys. Chern. Chem Phys.*, 2012, 14, 8653.
- 36 C. Bersellini, L. Garofano, M. Giannetto, F. Lusardi and G. Mori, *J. Forensic Sci.*, 2001, 46, 871.
- 37 A. L. Beresford, R. M. Brown, A. R. Hillman and J. W. Bond, *J. Forensic Sci.*, 2012, 57, 93.
- 38 F. Cortes-Salazar, J. M. Busnel, F. Li and H. H. Girault, *J. Electroanal. Chern.*, 2009, 635, 69.
- 39 M. Zhang and H. H. Girault, *Analyst*, 2009, 134, 25.
- 40 F. Cortes-Salazar, M. Q. Zhang, A. Becue, J. M. Busnel, M. Prudent, C. Champed and H. H. Girault, *Chin. Chem. Lett.*, 2009, 40, 580.
- 41 M. Q. Zhang and H. H. Girault, *Electrochem. Commun.*, 2007, 9, 1778.
- 42 G. Qin, M. Zhang, Y. Zhang, Y. Shu, S. Liu, W. Wu and X. Zhang, *J. Electroanal. Chern.*, 2013, 693, 12.
- 43 A. Glidle, A. R. Hillman, K. S. Ryder, E. L. Smith, J. M. Cooper, N. Gadegaard, J. R. P. Webster, R. M. Dalgliesh and R. Cubitt, *Langmuir*, 2009, 25, 4093.
- 44 A. Glidle, A. R. Hillman, K. S. Ryder, E. L. Smith, J. M. Cooper, R. M. Dalgliesh, R. Cubitt and T. Geue, *Electrochim. Acta*, 2009, 55, 439.
- 45 R. A. Campbell, H. P. Warkentin, I. Suttun, R. Cubitt and G. Fragnaud, *Eur. Phys. J. Plus*, 2011, 126, 107, DOI:10.1140/epjp/i2011-11107-8.
- 46 J. R. P. Webster, S. Langridge, R. M. Dalgliesh and T. R. Charlton, *Eur. Phys. J. Plus*, 2011, 126, 112, DOI:10.1140/epjp/i2011-11112-y.
- 47 J. Penfold, R. M. Richardson, A. Zorbakhsh, J. R. P. Webster, D. G. Bucknall, A. R. Rennie, R. A. L. Jones, T. Cosgrove, R. K. Thomas, J. S. Higgins, P. D. I. Fletcher, E. Dickinson, S. J. Roser, I. A. McLure, A. R. Hillman, R. W. Richards, E. J. Staples, A. N. Burgess, E. A. Simister and J. W. White, *J. Chem. Soc., Faraday Trans.*, 1997, 93, 3899.
- 48 A. Glidle, J. Cooper, A. R. Hillman, L. Bailey, A. Jackson and J. R. P. Webster, *Langmuir*, 2003, 19, 7746.
- 49 A. Nelson, *J. Appl. Crystallogr.*, 2006, 39, 273.
- 50 S. H. Cho, K. T. Song and J. Y. Lee, in *Handbook of Conducting Polymers* (3rd edn), ed. T. A. Skotheim and J. R. Reynolds, CRC Press, Boca Raton, 2007, ch. 8, pp. 8-3.
- 51 I. Efimov and A. R. Hillman, *Anal. Chern.*, 2006, 78, 3616.
- 52 A. Glidle, A. R. Hillman, K. S. Ryder, E. L. Smith, J. M. Cooper, N. Gadegaard, J. R. P. Webster, R. M. Dalgliesh and R. Cubitt, *Langmuir*, 2009, 25, 4093.
- 53 A. Glidle, A. R. Hillman, K. S. Ryder, E. L. Smith, J. M. Cooper, R. M. Dalgliesh, R. Cubitt and T. Geue, *Electrochim. Acta*, 2009, 55, 439.
- 54 A. R. Hillman, M. A. Mohamoud and I. Efimov, *Anal. Chern.*, 2011, 83, 5696.
- 55 A. R. Hillman, I. Efimov and K. S. Ryder, *J. Am. Chem. Soc.*, 2005, 127, 16611.